2020

# Full-wave modeling of ultrasonic scattering for non-destructive evaluation

Praveen Gurrala
*Iowa State University*

**Full-wave modeling of ultrasonic scattering for non-destructive evaluation**

by

**Praveen Gurrala**

A dissertation submitted to the graduate faculty

in partial fulfillment of the requirements for the degree of

DOCTOR OF PHILOSOPHY

Major: Electrical Engineering (Electromagnetics, Microwave, and Nondestructive Evaluation)

Program of Study Committee:
Jiming Song, Co-major Professor
Liang Dong, Co-major Professor
Leonard J. Bond
Ronald A. Roberts
Mani Mina

The student author, whose presentation of the scholarship herein was approved by the program of study committee, is solely responsible for the content of this dissertation. The Graduate College will ensure this dissertation is globally accessible and will not permit alterations after a degree is conferred.

Iowa State University

Ames, Iowa

2020

# TABLE OF CONTENTS

**Page**

LIST OF TABLES . . . . . v

LIST OF FIGURES . . . . . vii

LIST OF ABBREVIATIONS . . . . . xiv

ACKNOWLEDGMENTS . . . . . xvii

ABSTRACT . . . . . xviii

CHAPTER 1. INTRODUCTION . . . . . 1
1.1 Evolution of NDE . . . . . 1
1.2 Significance of NDE Modeling . . . . . 4
1.3 Goals and Scope of the Thesis . . . . . 7
1.4 Review of UNDE Models . . . . . 12
1.4.1 CIVA . . . . . 12
1.4.2 UTSIM . . . . . 14
1.4.3 UTDefect . . . . . 16
1.4.4 IZFP Models . . . . . 17
1.4.5 Distributed Point Source Model . . . . . 18
1.4.6 Finite Element Method . . . . . 19
1.4.7 Boundary Element Method . . . . . 21
1.5 Summary and Organization of the Thesis . . . . . 23

CHAPTER 2. APPLICATION OF FULL-WAVE SCATTERING MODELS TO BENCHMARK PROBLEMS . . . . . 24
2.1 Introduction . . . . . 24
2.2 Measurement Model for Immersion Testing . . . . . 27
2.2.1 Composite Measurement Model . . . . . 27
2.2.2 Beam Model . . . . . 33
2.2.3 Extraction of System Efficiency Factor . . . . . 34
2.2.4 Scattering Model . . . . . 37
2.3 Simulations of Benchmark Problems . . . . . 38
2.3.1 Benchmark Problems of 2004 . . . . . 38
2.3.2 Benchmark Problems of 2005 . . . . . 53
2.3.3 Polystyrene Sphere in TransOptic Specimen . . . . . 66
2.4 Conclusions . . . . . 70

CHAPTER 3. NUMERICAL STUDY OF HIGH-ORDER NYSTRÖM METHOD FOR ELASTIC WAVE SCATTERING . . . 72
3.1 Introduction . . . 72
3.2 High-order Nyström Method . . . 73
3.3 Numerical Study of Error and Convergence Rates . . . 77
3.4 Comparison of Simulation Times and Memory Usage . . . 80
3.4.1 Rigid Cube . . . 82
3.4.2 Rigid Sphere . . . 82
3.4.3 Elastic Sphere . . . 85
3.5 Conclusions . . . 88

CHAPTER 4. A HIGH-ORDER BOUNDARY ELEMENT METHOD FOR ELASTIC WAVE SCATTERING . . . 92
4.1 Introduction . . . 92
4.2 Derivation of the CFIE . . . 93
4.2.1 Equation of Motion . . . 94
4.2.2 Reciprocity Relation . . . 95
4.2.3 Fundamental Solutions . . . 98
4.2.4 Integral Representation . . . 100
4.2.5 Elastic Wave Scattering Problem . . . 104
4.2.6 Conventional Boundary Integral Equation . . . 108
4.2.7 Hypersingular Boundary Integral Equation . . . 112
4.2.8 Combined Field Integral Equation . . . 116
4.2.9 Limit-to-the-Boundary Approach . . . 118
4.2.10 Boundary Integral Equations for Scattering from Thin Bodies . . . 118
4.3 Discretization . . . 121
4.3.1 Mesh Interpolation . . . 122
4.3.2 Field Expansion . . . 124
4.3.3 Field Interpolation Points . . . 126
4.3.4 Matrix Equations . . . 128
4.3.5 Far-field Matrix Elements . . . 130
4.3.6 Near-field Matrix Elements . . . 131
4.4 Incident Field Calculation . . . 141
4.5 Semi-Analytical Solution for Scattering from a Circular Crack . . . 142
4.6 Numerical Results . . . 146
4.6.1 Convergence Rates . . . 146
4.6.2 Scattering Cross Section for a Circular Crack . . . 148
4.7 Summary . . . 150

CHAPTER 5. MULTILEVEL FAST MULTIPOLE METHOD FOR COMBINED FIELD FORMULATION . . . 153
5.1 Introduction . . . 153
5.2 Principle of the Fast Multipole Method . . . 155
5.3 Multipole Expansions of CFIE Kernels . . . 159
5.4 Factorization of Far-field Matrix Elements . . . 166
5.5 Application of FMM to Matrix-Vector Products of Influence Matrix . . . 168

5.5.1 Single Level Implementation . . . 169
5.5.2 Multilevel Implementation . . . 171
5.6 Numerical Results . . . 174
5.6.1 Helical Strip . . . 174
5.6.2 Traction-free Sphere . . . 174
5.6.3 CPU Time and Memory Scaling . . . 177
5.7 Concluding Remarks . . . 177

CHAPTER 6. IRREGULAR FREQUENCIES IN ELASTODYNAMIC BOUNDARY INTEGRAL EQUATIONS . . . 180
6.1 Introduction . . . 180
6.2 Mathematical Description . . . 182
6.3 Eigenfrequencies of Sphere . . . 185
6.3.1 Rigid Boundary . . . 188
6.3.2 Traction-free Boundary . . . 191
6.4 Numerical Examples . . . 196
6.4.1 Condition Number of BEM Matrix . . . 196
6.4.2 Scattering Amplitude . . . 199
6.4.3 Convergence Rate of Iterative Solution . . . 207
6.4.4 Pulse-echo from FBH . . . 209
6.5 Conclusions . . . 210

CHAPTER 7. CONCLUSIONS AND DIRECTIONS FOR FUTURE WORK . . . 213

BIBLIOGRAPHY . . . 216

APPENDIX A. KIRCHHOFF APPROXIMATION FORMULAS FOR SPHERICAL SCATTERER . . . 233

APPENDIX B. EVALUATION OF LIMITS IN THE DERIVATIONS OF INTEGRAL REPRESENTATION AND CBIE . . . 236
B.1 Limits in the Derivation of Integral Representation . . . 236
B.2 Convergence of CPV Integrals . . . 238
B.3 Continuity Requirements of Displacement Field in HBIE . . . 239
B.4 Jump Relation . . . 239

APPENDIX C. EVALUATION OF SINGULAR AND NEAR-SINGULAR INTEGRALS . . . 246
C.1 Singular Integrals . . . 246
C.1.1 Laurent Series Expansions . . . 246
C.1.2 Coefficients of Taylor Series Expansions . . . 249
C.2 Nearly-Singular Integrals . . . 258
C.2.1 H-kernel . . . 258
C.2.2 K-Kernel . . . 262
C.2.3 U-Kernel . . . 265
C.2.4 T-Kernel . . . 266
C.2.5 Analytical Integration of Nearly-Singular Terms . . . 268

# LIST OF TABLES

**Page**


Table 2.1 Pulse-echo amplitudes (in mV) for the spherical cavity inspection with planar transducer. . . . 41

Table 2.2 Pulse-echo amplitudes (in mV) for spherical cavity inspection with focused transducer. . . . 44

Table 2.3 Pulse-echo amplitudes (in mV) for the FBH inspection with planar transducer. 48

Table 2.4 Pulse-echo amplitudes (in mV) for the FBH inspection with focused transducer. . . . 52

Table 2.5 Pulse-echo amplitudes (in mV) from Crack C for normal incidence. . . . 55

Table 2.6 Pulse-echo amplitudes (in mV) for Crack C for 30° incidence at point A. . . 57

Table 2.7 Pulse-echo amplitudes (in mV) for Crack C for 45° incidence at point A. . . 61

Table 2.8 Pulse-echo amplitudes (in mV) for Crack C for 30° incidence at point B. . . 64

Table 2.9 Pulse-echo amplitudes (in mV) for Crack C for 45° incidence at point B. . . 64

Table 2.10 Parameters for the inspection in Section 2.3.3. . . . 68

Table 2.11 Pulse-echo amplitudes (in mV) for the TransOptic inspection. . . . 70

Table 3.1 CPU time and memory usage for scattering from rigid cube. . . . 82

Table 3.2 CPU time and memory usage for scattering from rigid sphere. . . . 85

Table 3.3 CPU time and memory usage for scattering from spherical inclusion. . . . 87

Table 3.4 Comparison of performance metrics of Rule-22 and Rule-11 for the spherical inclusion problem. . . . 88

Table 4.1 Quadrature rules . . . 126

Table 4.2 Convergence of semi-analytical solution for $\Sigma_p/\pi$ with increasing $N_q$ ($k_2 = 6$, $\nu = 0.25$). . . . 145

Table 4.3 Symmetric quadrature rule used in Rule-24. . . . . 150

Table 6.1 Eigenfrequencies for rigid boundary condition. . . . . 192

Table 6.2 Eigenfrequencies for traction-free boundary condition. . . . . 197

Table 6.3 Comparison of number of iterations and relative errors of different BIE formulations for scattering from a spherical cavity. . . . . 209

# LIST OF FIGURES

**Page**


Figure 1.1 Schematic of immersion testing setup for detecting a defect inside a test block. 7

Figure 2.1 Schematics of the two states considered for modeling the flaw response. State 1 is the conventional immersion testing experiment, reproduced from Figure 1.1. In state 2, the defect is absent, and the receiving transducer is excited. . . . . 29

Figure 2.2 Schematics of calibration measurements for spherically focused transducers and planar transducers. . . . . 35

Figure 2.3 Schematic of pulse-echo measurement of a fused-quartz specimen with a spherical cavity. . . . . 39

Figure 2.4 Measured and simulated pulse-echo signals for spherical cavity with planar transducer. . . . . 39

Figure 2.5 Measured and simulated scattering amplitudes of a spherical void. Measurement curve is extracted from planar transducer measurement. . . . . 43

Figure 2.6 Normalized magnitudes of $B(\omega)$, $\tilde{B}(\omega)$ and $\beta(\omega)$ for spherical void with planar transducer. Each curve is normalized by its maximum value in the given frequency range. The plots of $\beta(\omega)$ and $|\tilde{B}(\omega)|$ correspond to $\epsilon_1$=0.03. 43

Figure 2.7 Measured and simulated pulse-echo signals for the spherical void with focused transducer. . . . . 45

Figure 2.8 Measured and simulated scattering amplitudes of the spherical void. Measurement curve is extracted from focused transducer measurement. . . . . 45

Figure 2.9 Schematic of pulse-echo measurement of a steel specimen containing an FBH. 47

Figure 2.10 Magnitude of the diffraction coefficient corresponding to the planar transducer at the surface of the FBH. . . . . 47

Figure 2.11 Measured and simulated pulse-echo signals for the FBH with planar transducer. . . . . 49

Figure 2.12 Measured and simulated scattering amplitudes of the FBH. Measurement curve is extracted from planar transducer measurement. . . . . 49

Figure 2.13 Measured and simulated pulse-echo signals for the FBH with focused transducer. . . . . 51

Figure 2.14 Measured and simulated scattering amplitudes of the FBH. Measurement curve is extracted from focused transducer measurement. . . . . 51

Figure 2.15 Schematic of pulse-echo measurement of a Titanium alloy containing a crack-like void. . . . . 54

Figure 2.16 Measured and simulated pulse-echo signals for the pillbox void at normal incidence. . . . . 54

Figure 2.17 Magnitude of the integral $I(\omega)$ for the pillbox benchmark problem at normal incidence. . . . . 56

Figure 2.18 Schematic of pulse-echo measurement of a Titanium alloy containing a crack-like void. Oblique incidence on the left tip (point A). . . . . 56

Figure 2.19 Pulse-echo signals for the pill-box flaw corresponding to 30° incidence at point A. . . . . 58

Figure 2.20 Magnitude of the integral $I(\omega)$ for the pill-box flaw for 30° incidence at point A. . . . . 58

Figure 2.21 Pulse-echo signals for the pill-box flaw corresponding to 45° incidence at point A. . . . . 60

Figure 2.22 Magnitude of the integral $I(\omega)$ for the pill-box flaw for 45° incidence at point A. . . . . 60

Figure 2.23 Schematic of pulse-echo measurement of a Titanium alloy containing a crack-like void. Oblique incidence on point B. . . . . 62

Figure 2.24 Pulse-echo signals for the pill-box flaw corresponding to 30° incidence on the right tip (point B). . . . . 62

Figure 2.25 Magnitude of the integral $I(\omega)$ for the pill-box flaw for 30° incidence at point B. . . . . 63

Figure 2.26 Pulse-echo signals for the pill-box flaw corresponding to 45° incidence at point B. . . . . 63

Figure 2.27 Magnitude of the integral $I(\omega)$ for the pill-box flaw for 45° incidence at point B. . . . . 65

Figure 2.28 Schematic of pulse-echo measurement of a TransOptic$^{TM}$ specimen containing a polystyrene sphere. . . . . 65

Figure 2.29 Front-wall reflection from the TransOptic$^{TM}$ sample in the calibration measurement. . . . . 67

Figure 2.30 Pulse-echo signals obtained from the polystyrene sphere embedded in the TransOptic$^{TM}$ sample. . . . . 67

Figure 2.31 Pulse-echo signals for the TransOptic$^{TM}$ inspection with longitudinal wave speed of the inclusion modified to $c_p = 2350$ m/s. . . . . 69

Figure 2.32 Measured and simulated scattering amplitudes for the spherical polystyrene inclusion in the TransOptic$^{TM}$ specimen. . . . . 69

Figure 3.1 Relative error for $k_p a = \pi$ as a function of the average number of interpolation nodes per shear wavelength. . . . . 79

Figure 3.2 Relative error for $k_p a = \pi$ for all combinations of field and geometry discretizations. . . . . 79

Figure 3.3 Relative error for $k_p a = 2.648\pi$ as a function of the average number of interpolation nodes per shear wavelength. . . . . 81

Figure 3.4 Relative error for $k_p a = 3.216\pi$ as a function of the average number of interpolation nodes per shear wavelength. . . . . 81

Figure 3.5 Magnitude of scattered displacement field at $r = 5a$ due to a longitudinal plane-wave incident on a rigid cube in an elastic solid ($k_p a = 20$). Radial component is $u_r$. Polar component is $u_t$. Fields are normalized by the variable $a$. . . . . 83

Figure 3.6 Magnitude of scattered displacement field at $r = 5a$ due to scattering from a rigid sphere in an elastic solid ($k_p a = 20$). Radial component is $u_r$. Polar component is $u_t$. Fields are normalized by the variable $a$. . . . . 84

Figure 3.7 Relative errors in the radial and polar components of the displacement field for scattering from rigid sphere ($k_p a = 20$). . . . . 84

Figure 3.8 Magnitude of surface displacement field on a cut-plane for scattering from a spherical elastic inclusion in an elastic solid ($k_p a = 8$). Radial component is $u_r$. Polar component is $u_t$. Fields are normalized by the variable $a$. . . . . 86

Figure 3.9 Relative errors in the radial and polar components of the surface displacement field for scattering from a spherical elastic inclusion in an elastic solid ($k_p a = 8$). . . . . 86

Figure 3.10 Magnitude of surface displacement field in the spherical inclusion problem ($k_p a = 8$). NM result is generated from Rule-11 with 1280 mesh elements. Radial component is $u_r$. Polar component is $u_t$. Fields are normalized by the variable $a$. . . . . 89

Figure 3.11 Relative errors in the radial and polar components of the surface displacement field on the spherical inclusion for Rule-11 with 1280 mesh elements. . 89

Figure 3.12 Magnitude of surface displacement field in the spherical inclusion problem ($k_p a = 8$). NM result is generated from Rule-11 with 5120 mesh elements. Radial component is $u_r$. Polar component is $u_t$. Fields are normalized by the variable $a$. . . . . 90

Figure 3.13 Relative errors in the radial and polar components of the surface displacement field on the spherical inclusion for Rule-11 with 5120 mesh elements. 90

Figure 4.1 Schematic of an elastic solid occupying a volume $V$ and bounded by a surface $S$. An imaginary sphere centered at $\mathbf{x}'$ and of radius $\epsilon$ is excluded from $V$ for applying the divergence theorem. Orientations of the unit surface normal vectors on the surfaces $S$ and $S_\epsilon$ are indicated by the vectors $\hat{\mathbf{n}}(\mathbf{x})$ and $\hat{\mathbf{n}}(\mathbf{y})$, respectively. The surface $S_\epsilon$ is fictitious and does not represent material inhomogeneity. . . . . 100

Figure 4.2 An unbounded and otherwise homogeneous elastic solid containing an inclusion. . . . . 103

Figure 4.3 An unbounded and homogeneous elastic solid with a background displacement field $\mathbf{u}^I(\mathbf{x})$. Dashed line represents the surface $S$. . . . . 103

Figure 4.4 A model for elastic wave scattering in UNDE applications. The incident field is assumed to be generated by body forces present inside $V_f$. . . . . 106

Figure 4.5 An imaginary surface $S_\epsilon$ is used to exclude the point $\mathbf{x}$ from the volume in which the divergence theorem is applied. . . . . 110

Figure 4.6 The imaginary surface $S_\epsilon$ projects into the scatterer. Divergence theorem can be applied inside the scatterer minus the volume excluded by $S_\epsilon$. . . . . 111

Figure 4.7 Real part of $F(\xi_m, \eta)$ as a function of $\eta$ ($\xi_m = 0.4$). Derivative is discontinuous at $\eta = \xi_m$. . . . . 144

Figure 4.8 Relative error in scattering amplitude of longitudinal wave for a spherical cavity ($k_p a = \pi$) as a function of the average number of interpolation nodes per shear wavelength. Simulation results are based on the CFIE formulation with coupling parameter $\beta = -(1+i)$. . . . . 147

Figure 4.9 Relative error in scattering amplitude of shear wave for a spherical cavity ($k_p a = \pi$) as a function of the average number of interpolation nodes per shear wavelength. Simulation results are based on the CFIE formulation with coupling parameter $\beta = -(1+i)$. . . . . 147

Figure 4.10 Relative error in scattering amplitude of longitudinal wave for a circular crack ($\nu = 0.25$, $k_s a = 4\pi$) as a function of the average number of interpolation nodes per shear wavelength. Simulation results are are based on the HBIE formulation. . . . . 149

Figure 4.11 Relative error in scattering amplitude of shear wave for a circular crack ($\nu = 0.25$, $k_s a = 4\pi$) as a function of the average number of interpolation nodes per shear wavelength. Simulation results are are based on the HBIE formulation. . . . . 149

Figure 4.12 Normalized scattering cross section of a circular crack as a function of the shear wavelength. . . . . 151

Figure 4.13 Relative error in the scattering cross section computed using BEM. . . . . 151

Figure 5.1 A representation of $M$ groups of source and observation points. . . . . 157

Figure 5.2 An illustration of source and observation points in Equation (5.10). The source point is $\mathbf{x}'$, observation point is $\mathbf{x}$, and multipole and local expansion centers are $\mathbf{x}'_0$ and $\mathbf{x}_0$, respectively. . . . . 158

Figure 5.3 A representation of a closed surface $S$ with a single-layer source $h(\mathbf{x})$. The point $\mathbf{x}$ represents the location where the radiated field is evaluated. . . . . 162

Figure 5.4 The two-dimensional scatterer, represented by the boundary $S$, is embedded in a fictitious grid. Collocation point $\mathbf{x}$ lies in the group with index $l$. Groups that are adjacent to group $l$ are marked in red. . . . . 169

Figure 5.5 An illustration of a multilevel grouping scheme in two dimensions. Collocation point is $\mathbf{x}$ . . . . . 171

Figure 5.6 A traction-free helical strip. . . . . 175

Figure 5.7 Relative error for elements in the first column of influence matrix. For any index $j$, $Z_{1j}$ represents the matrix element in column 1 and row $j$. . . . . 175

Figure 5.8 Magnitude of scattered displacement field at $r = 5a$. Radial and polar components are represented as $u_r$ and $u_t$, respectively. All fields are normalized by the radius of the sphere. . . . . 176

Figure 5.9 Relative error in the scattered displacement at $r = 5a$. . . . . 176

Figure 5.10 Relative errors for the longitudinal and shear wave components of the scattered displacement field at $r = 5a$. . . . . 178

Figure 5.11 CPU time per iteration and memory requirement as a function of the number of DOFs for solving a scattering from a traction-free sphere using HBIE formulation. An $\mathcal{O}(N \log N)$ curve is shown for reference. . . . . 178

Figure 6.1 Condition number of BEM matrix for the CBIE formulation and rigid spherical scatterer. Vertical lines mark the positions of Class 1 and Class 2 eigenfrequencies of a rigid sphere. . . . . 198

Figure 6.2 Condition number of BEM matrix for the CBIE formulation and soft spherical scatterer. Vertical lines mark the positions of Class 1 and Class 2 eigenfrequencies of a rigid sphere. . . . . 198

Figure 6.3 Condition number of BEM matrix for the HBIE formulation and rigid spherical scatterer. Vertical lines mark the positions of Class 1 and Class 2 eigenfrequencies of a traction-free sphere. . . . . 200

Figure 6.4 Condition number of BEM matrix for the HBIE formulation and soft spherical scatterer. Vertical lines mark the positions of Class 1 and Class 2 eigenfrequencies of a traction-free sphere. . . . . 200

Figure 6.5 Condition number of BEM matrix for the CFIE formulation ($\beta = i$) in case of both soft and rigid spherical scatterers. . . . . 201

Figure 6.6 Magnitude of longitudinal wave scattering amplitude for the rigid spherical scatterer computed using the CBIE formulation. . . . . 203

Figure 6.7 Magnitude of longitudinal wave scattering amplitude for the soft spherical scatterer computed using the CBIE formulation. . . . . 203

Figure 6.8 Magnitude of longitudinal wave scattering amplitude for the rigid spherical scatterer computed using the HBIE formulation. . . . . 204

Figure 6.9 Magnitude of longitudinal wave scattering amplitude for the soft spherical scatterer computed using the HBIE formulation. . . . . 204

Figure 6.10 Magnitude of longitudinal wave scattering amplitude for the rigid spherical scatterer computed using the CFIE formulation ($\beta = i$). . . . . 205

Figure 6.11 Magnitude of longitudinal wave scattering amplitude for the soft spherical scatterer computed using the CFIE formulation ($\beta = i$). . . . . 205

Figure 6.12 Magnitude of scattered radial displacement at $r = 5a$ for a soft spherical scatterer ($k_s a = 2\pi$). Coupling coefficient in CFIE formulation is $\beta = i$. . . . 206

Figure 6.13 Relative error in scattered radial displacement at $r = 5a$ for a soft spherical scatterer ($k_s a = 2\pi$). Coupling coefficient in CFIE formulation is $\beta = i$. . . . 206

Figure 6.14 Longitudinal wave scattering amplitude for a spherical cavity at the first four Class 2 eigenfrequencies. . . . . 207

Figure 6.15 Longitudinal wave scattering amplitude for spherical cavity at the first four Class 2 eigenfrequencies. Coupling coefficient in CFIE formulation is $\beta = i$. 208

Figure 6.16 Measured and simulated pulse-echo signals for the FBH benchmark problem with planar transducer. Coupling coefficient in CFIE formulation is $\beta = -(1 + i)$. . . . . 211

Figure 6.17 Magnitude of the integral $I(\omega)$ for the FBH benchmark problem. Coupling coefficient in CFIE formulation is $\beta = -(i + 1)$. . . . . 211

Figure A.1 KA for scattering from a sphere. . . . . 234

Figure C.1 Analytical integration of nearly-singular integrals. Projection point $\boldsymbol{\eta}_0$ is assumed to lie outside the triangular integration domain. . . . . 268

# LIST OF ABBREVIATIONS

**ACA** . . . . . Adaptive Cross Approximation

**BA** . . . . . Born Approximation

**BEM** . . . . . Boundary Element Method

**BIE** . . . . . Boundary Integral Equation

**BIEM** . . . . . Boundary Integral Equation Method

**BM-BIE** . . . . Burton-Miller Boundary Integral Equation

**CBIE** . . . . . Conventional Boundary Integral Equation

**CFIE** . . . . . Combined-field Integral Equation

**CG** . . . . . Conjugate Gradient

**COD** . . . . . Crack-Opening Displacement

**CPV** . . . . . Cauchy Principal Value

**CTOA** . . . . . Crack-tip Opening Angle

**CTOD** . . . . . Crack-tip Opening Displacement

**DD** . . . . . Domain Decomposition

**DOF** . . . . . Degrees of Freedom

**DPS** . . . . . Distributed Point Source

**EWSP** . . . . . Elastic-wave Scattering Problem

**FBH** . . . . . Flat-bottomed Hole

**FCG** . . . . . Fatigue Crack Growth

**FEM** . . . . . Finite Element Method

**FMM** . . . . . Fast Multipole Method

**GBS** . . . . . Gaussian Beam Superposition

**GMRES** . . . . Generalized Minimal Residual Method

**GPSS** . . . . . Generalized Point Source Superposition

**GTD** . . . . . Geometrical Theory of Diffraction

**HBIE** . . . . . Hypersingular Boundary Integral Equation

**HFP** . . . . . Hadamard Finite Part

**IDP** . . . . . Interior Dirichlet Problem

**KA** . . . . . Kirchhoff Approximation

**LC-NM** . . . . Locally-corrected Nyström Method

**MAPOD** . . . Model-assisted Probability of Detection

**MG** . . . . . Multi-Gaussian (as in Multi-Gaussian beam model)

**MLFMA** . . . Multi-level Fast Multipole Algorithm

**MLFMM** . . . Multi-level Fast Multipole Method

**NDE** . . . . . Nondestructive Evaluation

**NDT** . . . . . Nondestructive Testing

**NM** . . . . . Nyström Method

**PDE** . . . . . Partial Differential Equation

**POD** . . . . . Probability of Detection

**PTD** . . . . . Physical Theory of Diffraction

**QNDE** . . . . . Quantitative Nondestructive Evaluation

**RS** . . . . . Residual Stress

**SA** . . . . . Scattering Amplitude

**SCC** . . . . . Stress Corrosion Cracking

**SDH** . . . . . Side-Drilled Hole

**SIF** . . . . . Stress Intensity Factor

**SHM** . . . . . Structural Health Monitoring

**SOV** . . . . . Separation of Variables

**SS** . . . . . Singularity-Subtraction

**TG** . . . . . Thompson-Gray (as in Thompson-Gray measurement model)

**UNDE** . . . . . Ultrasonic Nondestructive Evaluation

**WFNDEC** . . World Federation of NDE Centers

## ACKNOWLEDGMENTS

I am greatly indebted to my advisor, Dr. Jiming Song, for his help and guidance at every stage of this research work. His support was crucial for the completion of this thesis and improving its content. The interactions I had with Dr. Liang Dong through several research projects helped me in learning various aspects of academic research. I am very grateful to him for his advice in this regard. I would like to thank Dr. Leonard Bond, whose suggestions have helped me in developing the material presented in Chapter 2. I am also grateful for his direction in acquiring pulse-echo measurements. Thanks are due to my other committee members, Dr. Ron Roberts and Dr. Mani Mina, for reviewing my work and providing valuable comments.

Developing a numerical implementation of the BEM for 3D elastic wave scattering is often a challenging and time-consuming task. In this regard, I would like to thank Dr. Kun Chen for sharing his C++ code for the CBIE formulation, which has simplified the process of writing one for other formulations in this thesis. I also have to thank Dr. Yang Bao and Andy Downs for helping me at various stages of my dissertation. Andy has a significant contribution in preparing the spherical inclusion sample in Chapter 2 as well as in acquiring pulse-echo measurements from it. I very much appreciate Dr. Xiaosong Du and Dr. Seval Oren for collaborating on several projects. Finally, I would like to acknowledge financial assistance by the Center for Nondestructive Evaluation (CNDE) under the NSF I/U program, which has partly funded this project.

# ABSTRACT

The physical modeling and simulation of nondestructive evaluation (NDE) measurements has a major role in the advancement of NDE and structural health monitoring (SHM). In ultrasonic NDE (UNDE) simulations, evaluating the scattering of ultrasound by defects is a computationally-intensive process. Many UNDE system models treat the scattering process using exact analytical methods or high-frequency approximations such as the Kirchhoff approximation (KA) to make the simulation effort tractable. These methods naturally have a limited scope. This thesis aims to supplement the existing scattering models with fast and memory-efficient full-wave models that are based on the boundary element method (BEM).

For computational efficiency, such full-wave models should be applied only to those problems wherein the existing approximation methods are not suitable. Therefore, the adequacy of different scattering models for representing various test scenarios has to be studied. Although analyzing scattering models by themselves is helpful, their true adequacy is revealed only when they are combined with models of other elements of the NDE system and the resulting predictions are evaluated against measurements. Very few comprehensive studies of this nature exist, particularly for full-wave scattering models. To fill this gap, two different scattering models– the KA and a boundary-element method– are integrated into a UNDE system model in this work, and their predictions for standard measurement outputs are compared with experimental data for various benchmark problems. This quantitative comparison serves as a guideline for selecting between the KA and full-wave scattering models for performing UNDE simulations. In accordance with theoretical expectations, the KA is shown to be inappropriate for modeling penetrable (inclusion-type) defects and non-specular scattering, such as diffraction from thin cracks above certain angles of incidence.

A key challenge to the use of full-wave scattering methods in UNDE system models is the high computational cost incurred during simulations. Whereas the development of fast finite element methods (FEM) has inspired various applications of the FEM for ultrasound modeling in 3D heterogeneous and anisotropic media, very few applications of the BEM exist despite the progress in accelerated BEMs for elastodynamics. The BEM is highly efficient for modeling scattering from arbitrary shaped 3D defects in homogeneous isotropic media due to a reduction in the dimensionality of the scattering problem, and this potential has not been exploited for UNDE. Therefore, building on recent developments, this work proposes a fast and memory-efficient implementation of the BEM for elastic-wave scattering in UNDE applications.

This method features three crucial elements that provide robustness and fast convergence. They include the use of (1) high-order discretization methods for fast convergence, (2) the combined-field integral equation (CFIE) formulation for overcoming the fictitious eigenfrequency problem, and (3) the multi-level fast-multipole algorithm (MLFMA) for reducing the computational time and memory resource complexity. Although numerical implementations based on a subset of these three elements are reported in the literature, the implementation presented in this thesis is the first to combine all three. Some numerical examples are presented to demonstrate the importance of these elements in making the BEM viable for practical applications in UNDE. This thesis contains the first implementation of the diagonal-form MLFMA for solving the CFIE formulation for elastic wave scattering without using any global regularization techniques that reduce hypersingular integrals into less singular ones.

# CHAPTER 1. INTRODUCTION

In this chapter, background material on NDE modeling is presented first. Then, a general introduction to physical modeling of ultrasonic immersion testing is given to define the goals and scope of this thesis. Finally, a survey of UNDE models and simulation softwares is presented. The content of the last section establishes the context of this thesis.

## 1.1 Evolution of NDE

Nondestructive evaluation (NDE) is the process of evaluating the material properties of a structure, component or part without damaging its functionality. Its primary function is to detect anomalies (also called as defects or flaws) to ensure the integrity and reliable operation of the object under test. Initially, nondestructive testing (NDT) procedures were not required to be highly quantitative as they were concerned primarily with the detection of defects that are larger than a given threshold size. In the 1970s, the development and acceptance of the *damage tolerance* notion in engineering design philosophy created a need for more advanced inspection systems. Beyond indicating the presence of relatively large defects, inspections were required to provide quantitative information about their shape, size, location, etc. [1] [2, ch. 1]. Both NDT technology and its underlying science base evolved rapidly in response to this need. This quantitative shift is generally seen as marking the difference between NDT and NDE technologies, the latter also being referred to as quantitative NDE or QNDE.

As suggested above, the *fail-safety* of safety-critical components was ensured through inspection procedures even before the widespread adoption of the *damage tolerance* philosophy. It was accepted that defects could develop in components during service, and inspection procedures were designed to detect them before they grow to an extent as to cause component failure. However, since both the frequency of inspection and the threshold defect size for acceptance/rejection were not determined

from studies of defect propagation in materials, the inspection procedures so designed are not ideally reliable and optimally cost-efficient at the same time. For example, if inspections are not performed quite frequently, it may be highly probable for a defect to grow from the minimum detectable size to a critical size between two inspection routines, as in stress corrosion cracking (SCC) [3]. This possibility cannot be confidently ruled out without performing a study to that effect. Moreover, for any chosen threshold defect size, not every flaw that exceeds this size may need attention as some flaws may not grow to the fracture-critical size before the next maintenance routine. To overcome these problems, the philosophy of *damage tolerance* takes the rate of growth of defects into consideration while designing a component and its accompanying inspection procedures [4]. That is, an understanding of the growth of defects and their effect on the performance of components is inherent to this philosophy.

For example, the fitness-for-service analysis procedure outlined in the ASME boiler and pressure vessel code [5, §6.7.5] includes the following steps:

1. Determination of flaw size and orientation using UNDE procedures and resolving flaws into simple shapes.

2. Calculation of the applied stress and the corresponding stress intensity factor (SIF) at the flaw.

3. Determination of material toughness and crack propagation properties.

4. Assessing the acceptability of the flaw, which includes comparing material strength against the SIF and estimating the extent of crack growth until the next scheduled shutdown.

The last step in the above procedure requires knowledge of the applied stress at the crack (step 2) and the crack propagation properties (step 3), which in turn calls for knowledge of the defect size and shape (step 1). The latter is obtained from NDE methods. This example illustrates the role of NDE methods in the *damage tolerance* design philosophy.

In the ASME code cited above, design equations are recommended for the calculation of stress intensity. Experimental testing of samples of the actual material and published data for generic

materials are recommended for determination of crack propagation properties. However, by using appropriate computational analyses for crack-growth estimation and stress calculation, higher values of stress limits may be realized. Clearly, computational models benefit mostly from the utilization of accurate and complex information about the crack size and shape, which is not possible in analytical and empirical models. Therefore, to fully realize the benefits of advanced computational models, NDE methods need to provide accurate quantitative information about defects.

Apart from the progress in computational models, advances in fracture mechanics models themselves motivate the enhancement of NDE methods. The development of non-linear fracture mechanics thoeries is a case in point. In the linear elastic fracture mechanics theory, which is valid when the material conditions satisfy linear elasticity assumptions during the fracture process, the stress intensity factor (SIF) is a criteria for predicting fracture [6]. Both fatigue crack growth (FCG) and fracture criteria depend on the SIF, which in turn depends on the particular loading and crack geometry– particularly, the shape and size of the crack. However, for ductile materials such as steel, fracture is accompanied by extensive plastic deformation and the assumptions of linear elastic fracture mechanics are not valid. As the fracture mechanics discipline advanced, its principles were extended to elastic-plastic and fully plastic conditions to develop a non-linear fracture mechanics theory. In this new theory, geometrical parameters such as the crack-tip opening displacement (CTOD) and the crack-tip opening angle (CTOA) were found to be directly related to FCG and fracture [6, 7]. The development of quantitative NDE methods that accurately capture such important geometrical features of defects, beyond estimating their overall size and shape, is therefore beneficial.

Further, the advancement of quantitative NDE methods supports the practical realization of novel FCG models. For instance, consider FCG in the presence of residual stress (RS) fields, or RS-FCG in short, for brevity. While it is a common practice to induce compressive RS fields on the surfaces of components to increase their service life, the benefits of this practice are not considered during fitness-for-service analyses [8]. This is partly due to the lack of reliable models for RS-FCG, and partly due to the difficulties in determining the induced RS fields. UNDE methods may help

in resolving both the problems by providing the lacking information. For example, some RS-FCG models use the crack opening SIF to determine an effective SIF range, which is then applied in FCG prediction [8, 9]. Reliable knowledge of the crack opening SIF is thus crucial. As it is known that ultrasonic scattering is sensitive to the crack-closure effect [10], UNDE methods can be employed to estimate the crack opening SIF, for example, through an optimization approach [9]. Similarly, sensitivity of ultrasonic wave propagation and scattering to RS fields [10–12] may be exploited for accurate determination of the residual stresses, which is required for RS-FCG modeling.

In general, as FCG models evolve to account for RS fields and complex environmental factors, as in SCC and hydrogen embrittlement, additional parameters that characterize the complex environment around the cracks may be needed. It is possible to evaluate such parameters empirically if NDE measurements correlate with them. Hence, there is an extensive scope and substantial motivation for developing advanced NDE methods that not only predict the size and geometry of defects accurately in complex environments but also, if possible, determine parameters characterizing these complex environments in a way that is useful for predicting FCG.

## 1.2 Significance of NDE Modeling

Given the increasingly quantitative direction that NDE methods are taking, accurate NDE models are highly useful and, to an extent, required for the development and application of advanced NDE procedures. Some applications of NDE models are described below to justify their significance. Although they are illustrated with examples specific to UNDE, equivalent applications in other NDE modalities can be readily inferred.

- **Designing for inspectablity** [13–15]: In the preliminary stages of the design of components and parts, evaluating the ease of inspection of the designed object has significant benefits. The development of NDE models and simulation packages enables the simulation of NDE inspections in the early design phases, which may be useful for supplementing and validating inspectability guidelines that are learnt from practice. This allows the component design

to be better optimized for performing easy quantitative inspections and eliminates potential inspectability problems earlier in the design cycle.

- **Model-assisted probability of detection (MAPOD)** [16, 17]: As with any physical inspection, NDE testing involves many parameters whose values vary slightly from the respective nominal values determined or assumed for an inspection. Examples of such variables include the macroscopic electromagnetic and elastic material properties of the inspection specimen, orientation of the transducers, roughness of the defect surface, etc. Therefore, the measured defect response in an NDE test varies from its nominal value, which corresponds to the nominal values of all other parameters in the measurement. Inferences drawn from the measured defect responses, therefore, involve varying degrees of uncertainty. In the interest of characterizing the reliability of such inferences, it is required to evaluate the uncertainties present in the measurement. Typically, this involves performing a probability of detection (POD) study. A conventional POD test is performed by the experimental testing of multiple specimens with different defect sizes, defect orientations, etc. However, once the probability distributions of the fundamental parameters that influence the defect response are known either through experimental or theoretical studies, the remaining part of the POD study, which involves estimating the effect of uncertainties in the fundamental parameters on the defect response, can be performed through physical modeling and simulation. This gives the opportunity to include variables that are not easy to replicate in experimental specimens as well as the freedom to consider a larger number of testing cases with reduced time, cost and effort.

- **Inferring defect properties**: NDE measurements aim to infer properties such as the size, shape, etc., of defects from the measured signals. This is a classic inversion problem. Many inversion models are derived from the physical insight that is gained through forward models. For example, in UNDE, some flaw-sizing methods which are based on measured time-differences of pulse-echos were derived from high-frequency scattering models [18]. Some other methods were derived from weak-scattering models such as the Born approximation

(BA) [19–21]. Similarly, physical modeling of UNDE systems shows that a part of (the angular spectrum of) the scattering amplitude (SA) of a relatively small defect can be extracted from pulse-echo measurements [22, §11.2]. The extracted SA spectra allow the classification of defects according to predefined shapes. However, with an increase in the complexity of testing scenarios, many assumptions employed in deriving simple forward models become increasingly invalid and more accurate forward models are required. Accurate forward models provide insight into the process of wave scattering under highly complex test scenarios, which is essential for the development of advanced imaging and flaw-sizing algorithms. Moreover, data-driven inverse algorithms, which are black-box alternatives to physics-based models, also require accurate forward models.

- **Testing of inverse algorithms**: In addition to the development of inverse algorithms, NDE models also play an important role in their testing. As most defect sizing and imaging algorithms are developed under assumptions of ideal conditions such as the absence of surface roughness, the effect of non-idealities on the performance of these algorithms has to be studied. Specifically, for UNDE, roughness on the crack surface, crack-closure, crack-tip radius [23], residual stresses [10] and the extent of the plastic region around the crack [24] are known to affect the defect response. Ideally, the effect of such conditions should be characterized in reliability studies such as the POD analysis. However, in practice, the difficulty in finding their probability distributions precludes their inclusion in these studies. Still, the effect of non-idealities on the sizing algorithms has to be understood. Experimental studies will only indicate the overall performance of any given sizing algorithm in the presence of several non-idealities and do not reveal the effect of individual factors separately, as modeling and simulation could. With the help of appropriate models, sensitivity of sizing and imaging algorithms to various non-ideal factors can be studied individually, and the loss of performance due to the most offending factors can be potentially addressed on an ad hoc basis.

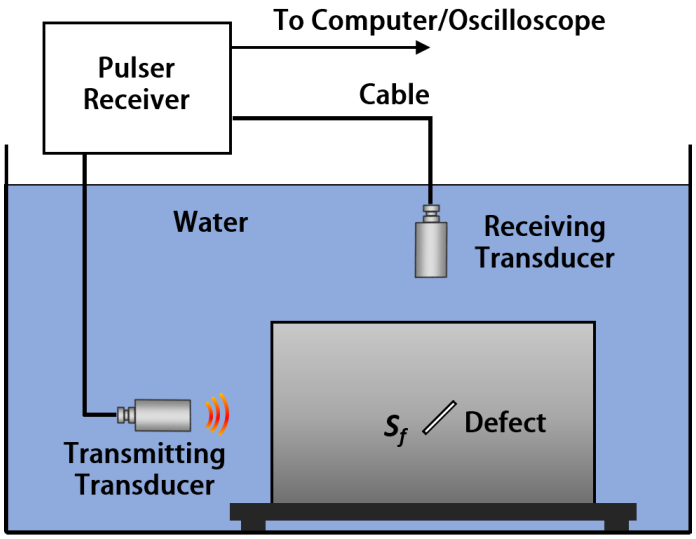


Figure 1.1: Schematic of immersion testing setup for detecting a defect inside a test block.

## 1.3 Goals and Scope of the Thesis

This section introduces a specific ultrasonic immersion testing model. The goals and scope of this thesis will be defined relative to this model. A schematic of an ultrasonic immersion test is shown in Figure 1.1. The test block is immersed in water to facilitate the coupling of ultrasound into it. The test procedure involves the following steps. A pulse generator sends a high-voltage pulse in the ultrasonic frequency range to the transmitting transducer. The pulse causes the transducer to emit an acoustic wave into water, which then propagates into the block and scatters off the defect. The scattered waves reaching the receiving transducer are converted back to a voltage pulse and sent to the receiver. Depending on the number of transducers used and their locations relative to each other, UNDE tests are classified into three distinct methods. In the pulse-echo method, a single transducer is used as both the transmitter and the receiver. In the through-transmission method, two different transducers are used, with the receiving transducer positioned on the opposite side of the transmitting transducer. When two different transducers are used in any configuration other than through-transmission, the inspection is called a pitch-catch test.

There are three common formats of data collection and representation, namely the A-scan, B-scan and C-scan. These are typically described with respect to a pulse-echo setup. In the A-scan, the voltage is depicted as a function of the time for a fixed transducer location. In the B-scan, voltage-versus-time data is collected over a line and displayed as a 2D image, with time and position on the scan line as the variables. In the C-scan, the transducer scans over an area. The voltage-versus-time data at every scan position is time-gated to select the reflections generated in a particular depth range inside the test block. The maximum value of the voltage envelope in this time-range is calculated and displayed as a 2D image, with each pixel representing one scan position.

As is evident from the above description, UNDE systems involve multiple physical processes. For example, a transducer couples electromagnetic and elastodynamic phenomena, where the exact nature of coupling depends on the type of the transducer. Within elastodynamic phenomena, we find the propagation, mode conversion and scattering of acoustic and elastic waves. UNDE models have to accurately represent all these different physical processes to guarantee overall accuracy. It is indeed possible to model the entire system with only partial differential equations (PDEs) and appropriate boundary conditions, without treating different physical processes separately. The solutions of these equations can be obtained via numerical methods such as the finite element method (FEM). However, in practice, this requires high computational effort in terms of the time and memory usage. Many UNDE models, therefore, model different physical processes individually as it allows the simulation of some processes via efficient approximations [25–27]. The interaction between the sub-models that represent different processes is handled using analytical techniques. This hybrid approach of modeling different parts of the system with different methods makes the overall simulation effort tractable. The mathematical basis for this approach is the following equation for the frequency spectrum of the receiver voltage (attributed to scattering from the defect) [22, 28] or some equivalent of it [29]

$$\Delta V_R(\omega) = \frac{2\pi\rho_2 c_{p2}^2 \beta(\omega)}{(-i\omega)\rho_1 c_1 S_R} \int_{S_f} \hat{V}^{(1)}(\mathbf{x},\omega)\ \hat{V}^{(2)}(\mathbf{x},\omega)\ \tilde{A}(\mathbf{x},\omega)\ \exp\left(ik_{p2}\mathbf{e}^{(2)}\cdot\mathbf{x}\right)\ dS(\mathbf{x}), \tag{1.1}$$

where the transducers are assumed to act like pistons, $\omega$ is the angular frequency, $\beta(\omega)$ is a quantity that models the transducers, cables and the pulser/receiver, $S_R$ is the areas of the face of the receiving transducer, $\rho_1$ is the mass density of water, $c_1$ is the speed of sound in water, $\hat{V}^{(1)}(\mathbf{x},\omega)$ and $\hat{V}^{(2)}(\mathbf{x},\omega)$ are the diffraction correction coefficients that describe the beam propagation towards and away from the defect under the paraxial approximation, $k_{p2}$ is the wavenumber of longitudinal waves in the block, $S_f$ is the surface of the defect, $\rho_2$ is the mass density of the block, $c_{p2}$ is the longitudinal wave speed in the specimen under test, $\mathbf{e}^{(2)}$ is the unit vector in the direction of the plane wave characterizing the scattered field, $\mathbf{x}$ represents the position vector with respect to a predefined coordinate system and $\tilde{A}(\mathbf{x},\omega)$ is a quantity that depends on the scattered displacement and stress fields. Only the voltage generated by scattered longitudinal waves is considered. The above equation is based on several other assumptions, which will be detailed in the next chapter. It suffices here to mention that the block is assumed to be infinite in extent for modeling wave-scattering from the defect. That is, multiple-scattering between the defect and the walls of the block is ignored.

Different quantities in Equation (1.1) model the effects of different components and processes in the immersion testing system. For example, $\beta(\omega)$ models the cables, transducers and the pulser/receiver electronics, $\hat{V}^{(1)}(\mathbf{x},\omega)$ and $\hat{V}^{(2)}(\mathbf{x},\omega)$ model the beam propagation effects in water and the block, and $\tilde{A}(\mathbf{x},\omega)$ models the scattering of ultrasound from the defect. Particularly, the quantity represented by $\tilde{A}(\mathbf{x},\omega)$ depends entirely on how plane waves are scattered by the defect. For brevity, the process of finding the scattered fields will be called the scattering problem. This work aims to obtain solutions to the scattering problem without making any approximations that restrict the physics of scattering. Such solutions are commonly known as *full-wave solutions* and the methods used to compute them are called *full-wave methods*.

Solutions to the scattering problem are usually obtained using high-frequency approximation methods, among which the Kirchhoff approximation (KA) is very popular [13, Chap. 10]. Being an approximation method, the KA is already known to be invalid for modeling scattering under certain scenarios [2, 13]. However, it is not clear a priori to what extent inaccuracies in the scattering

solutions, due to the application of KA under these scenarios, affect the overall accuracy of UNDE models. The second chapter presents an answer by applying a full-wave model and the KA to benchmark problems in UNDE modeling and comparing the predictions of both modeling techniques with measured data for standard outputs. It is shown that there are significant inaccuracies in the pulse-echo predictions of the KA if the defects are penetrable (inclusion-type defects) or if there is non-specular scattering from the defects, as in the case of diffraction from thin cracks.

Broadly speaking, this thesis aims to advance full-wave scattering models that are based on boundary integral equations (BIEs). These models are well-known alternatives to the KA for simulating scattering from defects in homogeneous, isotropic elastic media. Together with the high-frequency approximation methods, they provide accurate solutions over a much broader range of testing scenarios than what is allowed by either type of models alone. However, whereas the numerical implementation of approximation methods is computationally fast and memory-efficient, numerical methods for solving BIEs are computationally intensive and do not scale efficiently with an increase in the domain size. This is one of the major impediments to the integration of full-wave BIE methods into UNDE system models. Ensuring the uniqueness of solutions is another problem with (frequency-domain) BIEs as certain types of BIEs are known to have multiple solutions at some frequencies. In practice, the values of such "irregular" frequencies are not known a priori as they depend on the shape of the defect and elastic properties of the host medium. The conventional displacement BIE applied for modeling the scattering of ultrasound has this problem. Although alternative BIE formulations that have unique solutions at all frequencies are available, they are not very popular as they involve hypersingular integrals.

This thesis presents a numerical method for computing the scattering solutions by solving a BIE. The method relies on three crucial elements to solve the two problems stated above. These elements include the use of

- high-order discretization methods,
- the multilevel fast-multipole algorithm (MLFMA), and

- the combined-field integral equation (CFIE) formulation.

The first two choices address the problem of computational cost, and the last one solves the problem of irregular frequencies. Although numerical implementations based on a subset of these three choices are available, the implementation presented in this thesis is the first to combine all three. In the third chapter, the importance of high-order discretization is demonstrated through a numerical study of two state-of-the-art full-wave boundary element methods [30, 31] that differ only in their discretization order. It is shown that the particular high-order method considered in the study reduces the computational time and memory usage significantly. This result is non-trivial as high-order discretizations complicate the calculation of near-field matrix elements in boundary element methods, which may increase the overall simulation time.

In the fourth chapter, a boundary element method (BEM) for solving the CFIE is presented. As mentioned before, this method implements high-order geometry and field discretization. As one of the kernels in the BIE is hypersingular, the calculation of near-field BEM matrix elements involves integrating highly singular functions. Unless special analytical techniques are employed to weaken the singular nature of the integrands, computing such integrals requires a large number of quadrature points, which is problematic as it increases the computational cost. High-order geometry discretization further complicates this problem as the integrals have to be computed on curved surfaces, which naturally have lesser number of constraints than planar surfaces. In this work, the near-field matrix elements, which include both truly-singular and near-singular integrals, are computed using a singularity-subtraction (SS) technique. The SS procedure applied on truly-singular integrals is well-known whereas the one applied on nearly-singular integrals is new. Complete formulas for the SS of near-singular integrands are given to simplify replication of the method.

Application of the MLFMA to the CFIE formulation is described in the fifth chapter. The MLFMA exploits a factorization of the BIE kernels to decrease the computational complexity of solving the discretized BIE. As in the fourth chapter, complete formulas are given for factorization of the kernels. A method to simplify the calculation of radiation and receiving patterns of the kernels is also shown. The sixth chapter is devoted to the problem of irregular frequencies. The problem

is described mathematically, and several numerical examples are given for illustration. Finally, numerical examples are presented to demonstrate that the CFIE formulation has no irregular frequencies for a proper choice of the coupling coefficient.

## 1.4 Review of UNDE Models

This section presents a review of UNDE system models. As mentioned in the previous section, UNDE models typically involve semi-analytical (or equivalently, composite) modeling wherein different physical processes, such as wave propagation, scattering, etc., are treated separately. Given the large number of methods developed for modeling each of these processes individually, a multitude of possibilities exist for synthesizing different composite models. For example, a composite UNDE model that treats the scattering process via the KA can be modified by replacing the KA scattering model with any numerical method. Reviewing all such possibilities is beyond the scope of this work. Therefore, only some popular UNDE system models and simulation packages are reviewed. Since this thesis is concerned with scattering models, system models are reviewed with specific attention to how the scattering process is represented. Some promising scattering models which can be integrated into composite UNDE models are also mentioned.

### 1.4.1 CIVA

CIVA is a NDT simulation platform developed by the French Atomic Commission (CEA) [32]. The UNDE simulation tool in CIVA is based on a semi-analytical model that is derived from field reciprocity considerations and several physical assumptions [29]. This model is closely related to the Auld reciprocity equation for the flaw response [28], which is the basis for Equation (1.1). Similar to the composite model described by Equation (1.1), CIVA's model involves three separate models, one each for computing the transducer beam, flaw scattering and field reception [33].

The transducers are assumed to act like pistons. Radiation from the transducer is modeled by assuming a distribution of point velocity sources on its radiating face [34]. Each point source emits a spherical wave. The radiated field at any point is given by the sum of the contributions from

each point source. Mathematically, this sum is equivalent to the Rayleigh-Sommerfeld integral over the transducer face [35][13, §8.1.1]. In evaluating the contribution of each source, an asymptotic approximation (geometrical optics) is applied, which leads to a so-called divergence factor that describes the evolution of the wavefront as the beam propagates and refracts at material interfaces [35]. The divergence factor is evaluated using the pencil method [36], which is sufficiently general as to apply to beam propagation in heterogeneous and anisotropic media, and transmission through curved interfaces [37]. As the transducers are modeled through point sources, it is possible to simulate a wide range of transducers including angle beam probes and arrays.

Various flaw scattering models are available in CIVA. Their applicability is restricted based on the nature of the flaw. It should be noted that such restrictions within CIVA do not always follow the theoretical validity of the scattering models as they may involve specific practical limitations. The different flaw scattering models include the Kirchhoff approximation (KA), the Born approximation (BA), the geometrical theory of diffraction (GTD), the physical theory of diffraction (PTD), exact analytical models using separation-of-variables (SOV), and the finite element method (FEM) [33, 38]. Within CIVA, the KA can be applied to volumetric defects of simple shapes (but for any type of material inclusion) [39, 40] and crack-like (or equivalently, zero thickness) defects of arbitrary shape [32, 41]. The GTD and PTD can be used for simulating diffraction from edges of crack-like defects of any shape. For multifaceted and branched flaws, GTD and PTD are applied only to the free edges and not the internal (wedge-type) edges [33]. CIVA features a modified version of the BA known as the doubly-distorted wave BA [42]. It can be applied to volumetric inclusion-type defects of simple shapes. The SOV technique can handle cylindrical and spherical cavities as well as spherical inclusions [39]. The FEM can be applied to any type of 2D defect [43]. Extension of the FEM for 3D defects of canonical shapes is under development [44, 45].

Despite the impressive set of scattering models available in CIVA, arbitrary 3D volumetric defects can be handled only by the KA at the time of this writing. The KA is accurate for modeling specular and leading reflections from smooth objects. It is not accurate for edge diffractions and secondary reflections, such as internal reflections from the dark (non-insonified) side of an inclusion.

In CIVA, the drawbacks of the KA in modeling diffractions are partly resolved by combining it with the GTD, as the latter handles edge diffractions more accurately. Specifically, the GTD model in CIVA uses the GTD coefficients derived from a stress-free half-plane crack with an infinite edge, with suitable modifications to account for the finite extent of edges in practical simulation models [33, 46]. As the GTD coefficients diverge in the specular and forward transmission directions [41], a modified version of the PTD is employed to build the KA-GTD hybrid model [33]. Since this PTD model is based on the GTD coefficients of a crack (zero-thickness defect), it cannot be applied to wedge-like edges. PTD models of the above mentioned type do exist for wedges with infinite-edges [38], but they are yet to be extended to treat finite-sized edges, which will in turn allow wedges with arbitrary shaped edges to be modeled.

The simulation output in CIVA is the total force on the transducer face, that is, the integral of the pressure on its surface [29]. The pressure field at the transducer is computed using field reciprocity. The output amplitude is calibrated using the echo from a reference planar reflector. Electro-acoustic transduction is modeled implicitly by assigning the measured signal of the calibration experiment as the input signal of the scattering model. See [29] for further details on this.

### 1.4.2 UTSIM

UTSIM is a software package developed at the Center for NDE, Iowa State University, for simulating ultrasonic immersion testing [13, §14.4.1]. It was redesigned recently as an extensible software package and renamed as UTSim2 [25]. UTSim2 is based on the Thompson-Gray (TG) measurement model [47], which is valid for modeling inspections of small defects. The exact sense of smallness of the defect can be discerned by deriving the TG model from the Auld's reciprocity equation for the flaw response. When transducers are located far from the defect, application of the paraxial approximation in the Auld's reciprocity equation leads to Equation (1.1). The TG model is derived from Equation (1.1) by further assuming the velocity diffraction coefficients (resulting from the application of paraxial approximation) to be constant over the surface of the flaw. This

allows the diffraction coefficients to be factored out from the integral over the flaw surface, leading to the following mathematical expression for the voltage spectrum of the flaw response

$$\Delta V_R(\omega) = \frac{2\pi\rho_2 c_{p2}^2 \beta(\omega)}{(-i\omega)\rho_1 c_1 S_R} \hat{V}^{(1)}(\mathbf{x}_0, \omega)\ \hat{V}^{(2)}(\mathbf{x}_0, \omega) \int_{S_f} \tilde{A}(\mathbf{x}, \omega) \exp\left(ik_{p2}\mathbf{e}^{(2)} \cdot \mathbf{x}\right)\ dS(\mathbf{x}), \tag{1.2}$$

where $\mathbf{x}_0$ is the position vector of any point near the defect. The integral in the above equation can be shown to be a projection of the scattering amplitude of the defect, which doesn't depend on the amplitude of the transducer beam. Therefore, the TG measurement model is a linear time-invariant (LTI) model. UTSim2 has, in addition, a large-flaw model that computes (1.1) directly without making the small-flaw assumption [25, 48].

The beam diffraction coefficients were originally computed using Gauss-Hermite expansions [49, 50] adopted from the works of Bruce Thompson and others [49, 51, 52]. Although later versions of UTSIM employed the faster and more versatile Multi-Gaussian (MG) beam model [13, 48], UTSim2 does not seem to support this method [25]. UTSIM also has a 3D ray-tracing feature for geometries of arbitrary shape. This feature ignores beam spread but computes the ray paths of all modes using the Snell's law. Although this feature cannot predict the flaw response amplitudes, it is highly useful for predicting ray paths in complex 3D inspection parts.

The flaw scattering models in UTSIM are rather limited. For simple shapes, exact analytical models based on the SOV-technique can be used. The KA can be used for 3D defects of arbitrary shape. In the large-flaw model, the flaw geometry is discretized with small triangular elements, and the KA is applied to compute scattered fields on each triangle individually. The quantity $\tilde{A}(\mathbf{x}, \omega)$, which is required for computing the integral in Equation (1.1), is determined from the scattered fields on the flaw surface.

Unlike CIVA, UTSIM outputs the absolute value of the receiver voltage. The user, therefore, needs to input the system efficiency factor, $\beta(\omega)$, characterizing electro-acoustic transduction. Often, the system efficiency factor for realistic pulser/receiver settings is determined from a reference experiment and entered into the software. Alternatively, the system efficiency factor can be defined by specifying the parameters of a predefined family of functions [13].

### 1.4.3 UTDefect

UTDefect is a computer code developed at the Department of Mechanics at Chalmers University of Technology, for UNDE simulation. A software program called simSUNDT interfaces with UTDefect and provides post-processing capabilities [53]. Similar to UTSIM and CIVA, UTDefect also relies on field reciprocity to model the received signal. Specifically, the output of the simulation is the change in an electric field transmission coefficient (as defined by Auld [28]) due to the defect and is calculated from Auld's reciprocity equation.

The transducer is modeled by specifying the traction induced by it on the surface of the inspection component, which is assumed to be planar. The incident fields inside the component are computed by considering the surface traction fields as the boundary condition of a half-space elastodynamic wave propagation problem [54]. The solutions are obtained analytically by applying the Fourier transform and enforcing field continuity on the surface [55]. As the fields computed in this fashion are represented as double integrals, a 2D stationary-phase approximation is performed to reduce the computation cost [56]. However, the software also allows these integrals to be computed by numerical methods. Both immersion probes and contact probes can be modeled. The elastic properties of the inspection components need to be homogeneous and isotropic.

As defect scattering is also modeled using analytical techniques, only defects of a few simple shapes can be handled. The volumetric defects available in UTDefect include the spherical cavity, the spherical inclusion, the cylindrical cavity, also called as the side drilled hole (SDH), and the spheroidal cavity. All volumetric defects are handled using the T-matrix approach. In the T-matrix method, the incident and scattered fields are first expressed in a spherical wave basis [57], and the expansion coefficients of one are sought in terms of the other through the unknown T-matrix. The T-matrix can be obtained in several ways, including the null-field, SOV and integral equation approaches. SOV is used for finding the T-matrices of spherical and cylindrical defects [58], whereas the null-field method is used for spheroidal defects [56]. The T-matrix of circular cracks is determined using the integral equation approach as mentioned below.

The list of crack-like defects that can be modeled includes the circular crack, the rectangular crack and the strip-like crack. The circular crack can be open, fluid-filled or partly closed, where partial closure is modeled as a boundary condition relating the stress to the crack opening displacement (COD) via a proportionality constant [56], as originally proposed in [59]. All crack-like defects are handled using semi-analytical integral equation approaches. The integral equation is solved by expanding the COD with basis functions that account for edge singularities. Although such integral equation solutions exist for all the above mentioned cracks, the T-matrix of the circular crack is also computed (from the integral equation solution) as it allows the same methods used for spheres and spheroids to be applied for the crack also in characterizing the coupling to the transducer and the planar back-wall [56, 60]. For rectangular and strip-like cracks, surface roughness can be prescribed parametrically. The roughness is modeled as a perturbation of the boundary.

All defects except the SDH can be close to the back-wall of the component, which is assumed to be parallel to the top (scanning) surface except for strip-like surface breaking cracks, in which case the back-wall is allowed to be a tilted plane. Recently, a hybrid T-matrix/BEM method has been developed for scattering from defects close to a non-planar surface [61]. Although this method builds on the UTDefect models, there seem to be no reports on its implementation in UTDefect yet. In computational terms, the simplicity of the UTDefect models is derived from the possibility of obtaining analytical or semi-analytical solutions for scattering from simple shapes. Even for defects with complex shapes, the T-matrix can be computed numerically via the null-field method, but the computational complexity of this approach is on a similar level with the numerical methods applied for solving BIEs. Indeed, for acoustic scattering, it is known that the numerical solution of a BIE via the Petrov-Galerkin method leads to the same algebraic equations as the null-field method [62].

### 1.4.4 IZFP Models

The IZFP ultrasound simulation models were developed at the Fraunhofer Institute of Non-destructive Testing IZFP [63]. These models are based on the Auld's reciprocity relationship [13,

§14.4]. The transducers can be modeled using the generalized point source superposition (GPSS) method or the Gaussian beam superposition (GBS) method. Both the methods can be applied to anisotropic materials. In the GPSS method, the transducer field is computed by the numerical quadrature of a surface integral representation of the displacement. The Green's functions appearing in the surface integral are approximated with their (point-source) far-field forms, as described in [64]. In the final form, this method appears like an approximation by superposition of directive point sources [65]. Transmission through interfaces and scattering by defects can be modeled by applying the GPSS to similar surface integral representations characterizing these processes. For computing the scattered fields through such representation integrals, the scattered field on the surface of the scattering object needs to be known. The IZFP models apply the KA for determining these fields. See [66] for an example on how this is done for voids in general anisotropic media.

In the GBS method, a small number of Gaussian beams are superposed to synthesize the transducer beam [67, 68]. This makes the method computationally more efficient than the GPSS and other beam computation methods. The Gaussian beam coefficients in IZFP models are computed individually for each transducer, assuming a five-beam model. The reference beam profiles that the superposed Gaussian beam should match are obtained either experimentally or from simulations [65].

### 1.4.5 Distributed Point Source Model

Distributed point source (DPS) modeling was proposed by Placko and Kundu [69] first as a method to model transducer radiation in a fluid. It is very similar to the GPSS method. Indeed, in its original form, it is equivalent to computing the Rayleigh-Sommerfeld integral for the radiated pressure field by a numerical quadrature. It consists of approximating the transducer radiation by a number of point sources of equal amplitude distributed over the face of the transducer.

However, in the modified DPS formulation [70], the amplitudes of the point sources are assumed to be unknown and are sought by matching the radiated fields to known quantities at a set of test points, very similar to the approach of the BEM. When the test points are chosen on the transducer

surface, the approximation of the surface integral with a numerical quadrature makes it difficult to calculate the fields (at the test point locations) because of the singular nature of the point sources. To account for this, the point sources are distributed on a plane removed from the transducer face. This method has been extended to treat transmission at interfaces and scattering from defects [71, 72]; point sources of unknown amplitudes are placed close to the material interfaces and defect surfaces, and continuity of the fields is enforced at test points located on these surfaces to determine the amplitudes of the point sources. DPS models do not simulate electro-acoustic transduction, and hence, the output in scattering problems can be defined only in mechanical terms, such as for instance the total force received on the transducer element.

Although the DPS method appears to have been applied to three dimensional scattering problems [71, 73, 74], since no experimental comparisons are made, its accuracy is still unknown. Particularly, it remains to be seen how this method compares with the BEM in terms of accuracy since its computational efficiency (over the BEM) seems to be due to the application of approximations on some versions of the BEM. Moreover, this method is yet to be extended to three dimensional defects of arbitrary shape.

### 1.4.6 Finite Element Method

The finite element method (FEM) is a technique for solving partial differential equations by partitioning the computational domain into small regions (say, mesh elements). The fields within each mesh element are assumed to be generated by a finite-dimensional approximation. Specifically, this is achieved via "local" basis functions— that is, the domains of these functions are restricted to a few mesh elements over which they approximate the fields. The coefficients of the approximation (also called as degrees of freedom) are sought using weighted-residual or variational methods [75, Chap. 2]. Discretization of the domain as mentioned above simplifies the treatment of inhomogeneous and anisotropic media. The versatility of the method in handling different materials, therefore, makes it particularly attractive for ultrasound modeling, which often involves complex elastic media. Further, the partial differentiation operators yield sparse systems of linear equations,

which can be solved efficiently. The typical discretization length required for proper convergence of the method is about one-tenth of the wavelength. For three-dimensional problems, the required number of degrees of freedom (DOFs) increases rapidly as a function of the domain size. Therefore, application of this method to ultrasonic scattering in NDE, where defects as large as six times the shear wavelength (at the highest frequency in the bandwidth) are common, is challenging. Also, due to the exterior nature of the scattering problem, the simulation domain has to be extended beyond the defect to model an open region, and unless the extents of this domain are relatively large, the artificial boundary conditions imposed on it will lead to modeling errors.

In the context of elastodynamics, two broad techniques have evolved for handling large computational domains. Both techniques yield methods that can be efficiently parallelized. The first technique involves the use of explicit time-marching schemes in conjunction with mass-lumping. As is well known, explicit-time FEMs require the inversion of the so-called mass matrix for determination of the DOFs at the new time-step [76]. The ability to diagonalize the mass matrix using the lumped-mass approximation simplifies the matrix inversion process (see [77] and [78] for an analysis of convergence rates with the lumped mass approximation in elasticity and magnetohydrodynamics problems). Further, the whole solution process is amenable to efficient parallel computation. This technique is used in the simulation packages POGO [79], PZFlex (now called OnScale Flex) [80, 81], ABAQUS/Explicit [82, §2.4.5] [83, §3.5.3], ATHENA3D [45], and CIVA [44, 84–86]. Further, ATHENA3D utilizes the fictitious domain method to combine irregular meshes on the defect surface with a regular mesh implemented outside the defect. With this method, stability can be ensured by satisfying the CFL condition for the regular mesh [87]. This is a significant improvement over the other methods, where the small elements that approximate the irregular defect boundary impose a stringent condition on the time-step via the CFL condition. Additionally, regularity of the mesh improves efficiency of the method.

The other approach for handling large domains involves the use of the domain decomposition (DD) technique, where the computational domain is split into (in general, overlapping) subdomains. The PDE is solved independently in the sub-domains, with appropriate prescriptions

in the overlapping regions to obtain the solution over the entire domain. The most popular DD techniques are the iterative Schwarz methods, which can be viewed as preconditioned fixed-point iterative methods [88, §1.4]. The corresponding preconditioners are often used with Krylov-type iterative methods, such as the GMRES or CG algorithms [88, Chap. 3], as they are more efficient than fixed-point iteration. Therefore, it is common to refer to the DD technique as a preconditioning method for iterative solvers. The DD technique is used in the simulation packages COMSOL [89, p. 1213] [90] and CIVA [85]. Particularly, CIVA uses a macro-element strategy to efficiently handle parametrized defect shapes, where the interaction between the macro-elements that handle different formulations (acoustic, elastodynamic, etc.) is modeled using the mortar element DD technique; see [84, 86] for details. Although a DD technique is also adopted in the software ABAQUS/Explicit [83, §3.5.3], DD in that context refers to parallelization of the explicit-time solution, which is categorically different from the iterative Schwarz methods mentioned above.

All the aforementioned software packages have found applications in UNDE for modeling various physical processes. For example, see [91, 92] for studies using POGO, [44, 86] for CIVA, [93] for PZFlex, [94] for ABAQUS/Explicit, [45, 95] for ATHENA3D, and [96, 97] for COMSOL, to cite a few.

### 1.4.7 Boundary Element Method

The boundary element method (BEM) is a numerical method for solving surface integral equations. Similar to the FEM, it involves discretization of the solution domain (a finite number of disjoint surfaces for 3D problems) into small regions. The fields within these regions are approximated using local basis functions with unknown coefficients (DOFs). The DOFs are sought via weighted-residual methods. The BEM is especially well-suited for modeling exterior problems such as wave scattering since radiation conditions are built into the governing integral equations, which eliminates the need for artificial boundary conditions. Additionally, since the fields need to be discretized only on the surface(s) of the scattering object(s), the required number of DOFs increases much slowly with an increase in the scatterer size, compared to volume discretization methods

such as the FEM. However, unlike the FEM, BEM discretizations result in dense systems of linear equations, which cannot be handled as efficiently as sparse systems of the same size.

Specifically, inversion of a dense matrix of size $N$ via standard methods such as the LUD requires $\mathcal{O}(N^3)$ operations. Therefore, for large matrices, iterative methods are preferred as they need to compute only a few matrix-vector products for each iteration, which typically has an operation cost of $\mathcal{O}(N^2)$. In the context of the BEM, many fast algorithms for computing matrix-vector products have been developed to further accelerate the solution process. Among them, the most popular algorithms are the fast multipole method (FMM), the pre-corrected fast fourier transform (pFFT) and the adaptive cross approximation (ACA) (see [98] and references therein). These algorithms do not require explicit computation of the full BEM matrix; only the near-field matrix elements are explicitly computed and stored. The contribution of the far-field elements to the matrix-vector product is computed (approximately) on-the-fly during the iterative solution process using a relatively small set of pre-computed values characterizing the same. This is achieved by factorization of the kernel functions in the FMM, by low-rank approximation of the far-field matrix blocks in the ACA, and by projection of sources onto a regular grid in the pFFT.

There are very few direct applications of the BEM for UNDE modeling in recent literature. Some early work includes the application of BEM for studying elastic wave scattering from inclusions and cracks. The review papers by Beskos [99, 100] provide a nearly comprehensive list of these studies. Some notable works are due to Niwa, Budreck, Schafbuch and others [101–103]. For applications related to guided wave scattering, see [104–107], which were published in the early 2000s. BEM-based inverse methods for UNDE were developed around the same time by Rus and others [108, 109]. More recently, a fast time-domain BEM was developed for modeling air-coupled ultrasonic testing [110]. Although, recent applications of the BEM for UNDE modeling are relatively few, the work on fast BEM solvers for 3D elastodynamics has been progressing steadily [31, 111–113]. This work will be described in Chapter 5, when fast BEM algorithms for elastodynamics are introduced.

## 1.5 Summary and Organization of the Thesis

To summarize, quantitative NDE methods form an important aspect of the damage-tolerance design principle. Among other things, they support the development of fracture mechanics models and are required for realizing the full benefits of computational models for crack growth prediction and stress calculation. The advancement of such quantitative NDE methods, in turn, benefits considerably from the availability of accurate NDE models. This thesis is concerned with bettering UNDE measurement models by solving the problem of modeling elastic-wave scattering both accurately and efficiently. The primary impediment towards this not the lack of accurate models, but the computational cost incurred in using them. Indeed, it is for this reason that most simulation softwares do not handle scattering from arbitrary shaped 3D defects. The only software that does handle them uses the Kirchhoff approximation to reduce the computational burden.

This thesis presents the development of a fast and memory-efficient BEM for simulating elastic wave scattering. It is organized as follows. Chapter 2 presents a comprehensive study of the adequacy of the KA for modeling various practical test scenarios. The results serve as a quantitative guideline for selecting between the KA and full-wave methods such as the BEM while performing UNDE simulations. Chapter 3 demonstrates the importance of high-order discretization for making the BEM viable for practical applications. This is achieved through various numerical examples. In Chapter 4, a BEM is developed for solving the CFIE formulation through high-order discretization. Chapter 5 describes the application of the multilevel fast multipole method to this BEM. Chapter 6 describes the irregular frequency problem and demonstrates that the formulation developed in Chapter 4 is free from this artifact, unlike conventional methods.

# CHAPTER 2. APPLICATION OF FULL-WAVE SCATTERING MODELS TO BENCHMARK PROBLEMS

This chapter aims to study the proper use-cases of full-wave scattering models within semi-analytical (composite) UNDE measurement models. A composite UNDE measurement model wherein wave-scattering is modeled separately from other physical processes is described. Two different scattering models, namely, the Kirchhoff approximation (KA) and the boundary element method (BEM), are used within the composite model. This composite model is applied to simulate benchmark experiments. Two sets of results are obtained separately with the KA and the BEM while keeping all other elements in the model the same. The results are compared with experimental data to confirm the validity of the KA under different test scenarios as well as to understand when full-wave methods such as the BEM are required.

## 2.1 Introduction

UNDE tests involve ultrasonic phenomena within regions spanning several hundreds of wavelengths. At the same time, numerical methods for the exact modeling of ultrasound (as opposed to approximation methods) require discretization of the computational region on length-scales of the order of one-tenth of a wavelength for proper resolution of the ultrasonic fields. When such numerical methods are applied to model a UNDE test, a large number of discretization variables are required due to the relatively large size of the computational domain. Most UNDE models, therefore, treat different physical processes such as wave propagation, scattering, etc. separately, which allows the modeling of some or all of these processes via exact analytical or approximation methods, making the simulation effort tractable. Such composite models typically comprise three sub-models, including (a) an ultrasonic beam model to describe the propagation of ultrasonic waves,

(b) a scattering model to describe the scattering of ultrasonic fields by the defects, and (c) a model for electro-mechanical transduction.

The Kirchhoff approximation (KA) is a scattering model based on a ray-like approximation of waves. Similar to the geometrical optics and geometrical elastodynamics models, it works best in the high-frequency limit. Being an approximation method, it is computationally very efficient. Specifically, in terms of the computational time and memory usage, it outperforms full-wave numerical methods such as the finite element method (FEM) and the BEM by several orders of magnitude. Consequently, it is one of the widely used scattering models. Also, as seen from the survey of simulation softwares presented in Section 1.4, it is currently the only method that can handle arbitrary shaped 3D defects within UNDE simulation packages.

Due to the ray-like approximation, the KA treats specular reflections from flat surfaces accurately. Its accuracy decreases as the radius of curvature of the scattering surface becomes smaller and comparable to the wavelength. Notably, it does not model edge diffractions accurately. Further, secondary reflections and surface waves on defects are not considered in this method [22, Chap. 10]. Although the foregoing limitations of the KA are well-studied and understood, the application of the KA in UNDE measurement models raises a new question: as the scattering model is only a part of the UNDE measurement model, one might ask how the limitations of the KA affect the overall accuracy of the measurement model under various test scenarios. Clearly, the answer would depend on how sensitive the output of the measurement is to the process of scattering.

In this chapter, we look at three different measurement outputs. The accuracy of the KA in predicting these three quantities is studied by comparison with experiments under different testing scenarios. First output is the time-domain waveform of the receiver voltage. As mentioned in the previous chapter, this waveform is indeed the quantity that is represented in both A- and B-scans. However, in the C-scan and many other imaging methods, the output of interest is the maximum value of the amplitude of the receiver voltage pulse. This is the second quantity we consider. The third quantity is the far-field scattering spectra of the defect, which is obtained by deconvolving the effects of the transducers and electronics in the system. This parameter is commonly known as the

scattering amplitude (SA). For defects that are not relatively small, it is not possible to separate the effects of beam spreading and scattering. Therefore, a quantity analogous to the SA, but which includes the effects of beam spreading, is considered for relatively large defects.

One may expect to find the KA inadequate in predicting the measurements that are sensitive to the physical processes not fully represented in it. Diffraction from cracks, surface waves, secondary reflections, etc. are some examples of such processes. We try to confirm these expectations quantitatively by comparing predictions from KA-based models with measurements. Since any discrepancies observed in the model predictions may include the contributions of experimental uncertainties, such a comparison will not indicate how well exact scattering models perform over the KA. Hence, a different set of results are obtained by replacing the KA with a full-wave scattering model while keeping all other elements in the composite model the same. A *full-wave model* is defined as any model that solves the complete wave equations. The particular full-wave scattering model considered here is based on the solution of a boundary integral equation (BIE) via the Nyström method (NM), which is a boundary-element-type numerical method [114, 115]. Comparison of the NM-based model predictions with the measurement data will indicate the potential performance-gains of full-wave models over the KA.

Some studies have been conducted previously for the experimental verification of UNDE measurement models [27, 47, 63, 116–120]. In [27, 63, 116–119], UNDE models were applied to simulate some benchmark problems proposed by the World Federation of NDE Centers (WFNDEC). Experimental data for these problems were also provided by the WFNDEC. The scattering models applied in these studies include the KA and full-wave analytical methods. As only few scattering problems admit exact analytical solutions, complex defects were treated only using the KA in these studies. Predictions of full-wave scattering models known as MOOT and T-matrix method were compared with measured data in [47]. A scattering model based on the BEM was used for the prediction of experimental pulse-echo signals from spherical voids or inclusions in [120]. Both [47, 120] were restricted to defects of simple shapes only.

In this chapter, composite UNDE models based on the KA and the NM are applied to the WFNDEC benchmark problems from the years 2004 and 2005. These problems include various pulse-echo immersion tests with standard scatterers such as flat bottomed holes, spherical voids, etc. in solids. Only echos resulting from longitudinal waves were considered in the simulations, although the simulation model has no restrictions on the type of wave modes. Experimental data for the benchmark problems were obtained from the WFNDEC archives [121]. The UNDE measurement model used in the simulations follows the development in [22]. This model has three quantities that are derived independently of the scattering problem: the system efficiency factor, which characterizes the electro-acoustic transduction process, and the velocity diffraction coefficients of the transmitting and receiving transducers. The system efficiency factor corresponding to every measurement was extracted from a reference measurement performed with the same pulser and receiver settings as used in the original experiment. The velocity diffraction coefficients were calculated either using the multi-Gaussian beam model [22, 122] or by evaluating the Rayleigh-Sommerfeld integral for transducer radiation under the paraxial approximation as described in [13, Chap. 8]. In the following sections of this chapter, a description of the composite UNDE model is given first. Then, the methods employed to compute the elements of the composite model are described, which is followed by a presentation of the simulation results.

## 2.2 Measurement Model for Immersion Testing

### 2.2.1 Composite Measurement Model

A composite semi-analytical model is used for computing the receiver voltage. This model is based on a modification of the electromechanical reciprocity relation derived by Auld in [28]. The original version relates the change in the electric field transmission coefficient (of the fundamental mode in the coaxial line connected to the receiving transducer) due to the presence of a flaw, with the displacement and traction fields on a surface enclosing the flaw. A similar relation for the receiver voltage was derived by Schmerr [123] from mechanical reciprocity principles by assuming the receiver voltage to be proportional (for a fixed frequency) to the average pressure on the receiving

transducer. The model used here for computing the receiver voltage is based on a simplification of this relationship via paraxial approximations and follows the treatment in [22, §11.1]. Therefore, the reader may refer to [22] for a complete description and derivation of the model; it is described here in only as much detail as necessary for understanding the results of the simulations.

Consider an immersion testing measurement with two piston-like transducers: one transmitter and one receiver. The specimen under test is assumed to be a linear elastic material with homogeneous and isotropic elastic properties except for the presence of a few defects. A defect is defined as any region within the specimen wherein elastic material properties are different from those of the specimen. We refer to the normal velocity on the surface of a transducer, generated by its excitation alone (that is, without the echoes) as the excitation amplitude. Let the excitation amplitude of the transmitting transducer be $v_T$, which is, in general, allowed to be a function of the frequency. Also, let the receiving transducer be unexcited. This situation (state 1) is depicted in Figure 2.1a. Assume that we are interested in finding the response of a defect bounded by a surface $S_f$.

For the purpose of modeling, another scenario as shown in Figure 2.1b is considered. In this state (state 2), the receiving transducer is fired with a unit excitation amplitude, and the defect of our interest is absent. That is, within the surface defined by $S_f$, the elastic properties are same as those of the specimen. Although only one defect is shown in Figure 2.1a, if multiple defects are present in the specimen, all the defects whose response is not desired should be assumed to be present in both the states. The receiver voltage in state 1 constitutes the contribution of the wave interactions that do not involve the flaw as well as those that do. The latter component is the difference between the receiver voltages observed with and without the flaw. This component, defined as the flaw voltage response, can be expressed in terms of the velocity and traction fields on the surface $S_f$ in the states 1 and 2. This relation is based on some assumptions on the nature of the water-air and water-tank interfaces, all of which generally hold true. Assuming that the fields are time-harmonic with the factor $e^{-i\omega t}$, the result is as follows [22, §11.1]

$$\Delta V_R(\omega) = \frac{\beta(\omega)}{2\rho_1 c_1 S_R v_T} \int_{S_f} \left( \mathbf{t}^{(1)} \cdot \mathbf{v}^{(2)} - \mathbf{t}^{(2)} \cdot \mathbf{v}^{(1)} \right) \, dS \tag{2.1}$$

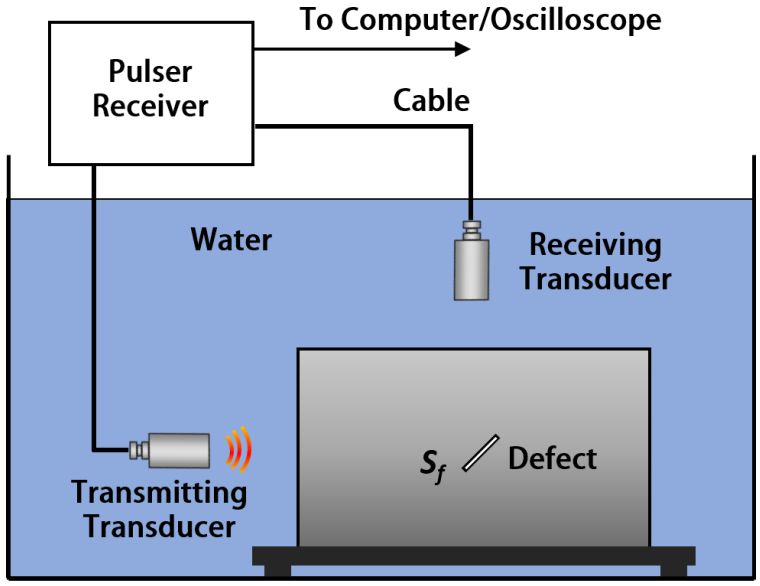


(a) State 1

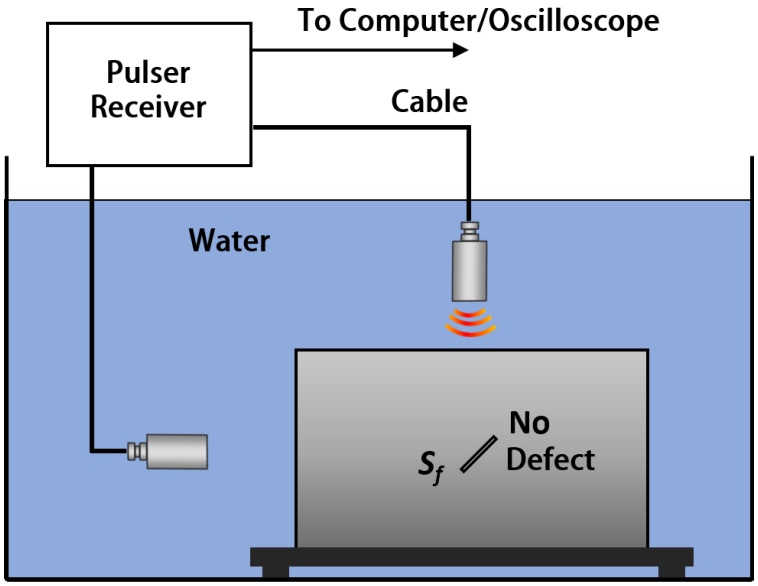


(b) State 2

Figure 2.1: Schematics of the two states considered for modeling the flaw response. State 1 is the conventional immersion testing experiment, reproduced from Figure 1.1. In state 2, the defect is absent, and the receiving transducer is excited.

where $\Delta V_R(\omega)$ is the flaw voltage response, $\mathbf{v}^{(j)}$ and $\mathbf{t}^{(j)}$ are the velocity and traction fields, respectively, in the state $j$ ($j = 1, 2$); $\beta(\omega)$ is called the system efficiency factor and depends only on the spectrum of voltage excitation in state 1 and the properties of the transducers, cables and electronic components in the system; $\rho_1$ is the mass density of water; $c_1$ is the wave speed in water; $S_R$ is the area of the face of the receiving transducer. The traction fields are defined with respect to the unit normal vector directed away from the defect ($\hat{\mathbf{n}}$). That is, $\mathbf{t}^{(j)} = \hat{\mathbf{n}} \cdot \bar{\boldsymbol{\tau}}^{(j)}$, with $\bar{\boldsymbol{\tau}}^{(j)}$ representing the stress fields in state $j$. In the above equation, the fields $\mathbf{v}^{(1)}$ and $\mathbf{t}^{(1)}$ include the contributions of the respective fields radiated by the transmitting transducer (incident fields) as well as those that are generated by scattering from the defect (scattered fields). Therefore, these fields have to be calculated by solving the elastic wave scattering problem. It may not be immediately evident that Equation (2.1) is same as that in [22, §11.1]. The only actual difference is that a unit excitation amplitude is assumed in state 2 here. There is no loss of generality due to this assumption as the fields $\mathbf{v}^{(2)}$ and $\mathbf{t}^{(2)}$ are proportional to the excitation amplitude. Other apparent differences are due to the substitution of the quantities $s(\omega)$ (system function) and $Z_r^{T;a}$ (acoustic radiation impedance) appearing in [22, §11.1] in terms of the system efficiency factor and other fundamental parameters (see [22, §7.2]).

The fields $\mathbf{v}^{(2)}$ and $\mathbf{t}^{(2)}$ are the incident fields generated at the surface $S_f$ when the receiving transducer is excited with a unit velocity amplitude. Assuming that the surface $S_f$ is located well within the specimen, these fields can be decomposed using the paraxial approximation. This assumption is valid for all the benchmark problems considered in this chapter. Applying the paraxial approximation to decompose the incident fields in state 2 is physically equivalent to applying it to the fields received at the receiving transducer due to scattering by the defect in state 1. As the results shown in this chapter are concerned with only longitudinal waves in the specimen, the formulation below will be restricted to this condition. Its extension to other wave modes is straight-forward. Under the paraxial approximation, $\mathbf{v}^{(2)}$ can be expressed as

$$\mathbf{v}^{(2)}(\mathbf{x}, \omega) = \hat{V}^{(2)}(\mathbf{x}, \omega)\ \mathbf{d}^{(2)} \exp\left[ik_{p2}\mathbf{e}^{(2)} \cdot \mathbf{x}\right] \tag{2.2}$$

where $\mathbf{d}^{(2)}$ is a unit vector in the direction of polarization of the wave, $k_{p2}$ is the longitudinal wave number in the specimen and $\mathbf{e}^{(2)}$ is the unit vector in the direction of wave propagation. The term $\hat{V}^{(2)}(\mathbf{x},\omega)$ is the diffraction correction coefficient. It can be calculated analytically for a circular piston transducer, though we use a different approach in the simulations, as mentioned later. The vector $\mathbf{x}$ represents the coordinates relative to a fixed coordinate system. Since most beam models naturally describe the transducer radiation relative to the axis of the beam, a convenient choice for the origin of the coordinate system is any point on this axis. If the origin is chosen away from the transducer and close to the defect, as is usually done, the diffraction correction factor will include a factor describing the phase accrued by the beam due to propagation from the transducer to the origin. The stress fields corresponding to the velocity fields in Equation (2.2) can be calculated from the stress-strain constitutive relation in the specimen. For a linear elastic material, the stress tensor ($\bar{\boldsymbol{\tau}}$) is related to the Cauchy strain tensor ($\bar{\boldsymbol{\varepsilon}}$) by the fourth-order stiffness tensor ($\boldsymbol{\mathcal{C}}$) as follows

$$\bar{\boldsymbol{\tau}} = \boldsymbol{\mathcal{C}} : \bar{\boldsymbol{\varepsilon}}. \tag{2.3}$$

The double dot product operator (:) is defined in the Einstein summation convention by contraction over the last two indices as follows

$$\tau_{jk} = C_{jklm}\varepsilon_{lm}, \tag{2.4}$$

where $C_{jklm}$, $\tau_{jk}$ and $\varepsilon_{lm}$ (for $j,k,l,m = 1,2,3$) are the components of $\boldsymbol{\mathcal{C}}$, the stress tensor and the strain tensor, respectively. For an isotropic material, this relation further simplifies to

$$\bar{\boldsymbol{\tau}} = \boldsymbol{\mathcal{C}} : \nabla\mathbf{u}, \tag{2.5}$$

Using this constitutive equation, we obtain the stress field $\bar{\boldsymbol{\tau}}^{(2)}$ corresponding to the velocity field $\mathbf{v}^{(2)}(\mathbf{x},\omega)$ as follows

$$\bar{\boldsymbol{\tau}}^{(2)} = -\boldsymbol{\mathcal{C}} : \frac{\nabla\mathbf{v}^{(2)}}{i\omega}. \tag{2.6}$$

Ignoring spatial variations in the diffraction correction coefficient while taking the derivative, we get

$$\bar{\boldsymbol{\tau}}^{(2)} = -\frac{1}{c_{p2}}\boldsymbol{\mathcal{C}} : (\mathbf{e}^{(2)}\mathbf{d}^{(2)})\hat{V}^{(2)}(\mathbf{x},\omega)\ \exp\left[ik_{p2}\mathbf{e}^{(2)}\cdot\mathbf{x}\right] \tag{2.7}$$

where the dyadic notation is assumed and $c_{p2}$ is the longitudinal wave speed in the specimen. Substituting Equations (2.2) and (2.7) in (2.1) yields

$$\Delta V_R(\omega) = \frac{2\pi\rho_2 c_{p2}^2\beta(\omega)}{(-i\omega)\rho_1 c_1 S_R}\int_{S_f}\hat{V}^{(2)}(\mathbf{x},\omega)\ \tilde{A}(\mathbf{x},\omega)\exp\left[ik_{p2}\mathbf{e}^{(2)}\cdot\mathbf{x}\right]\mathrm{d}S, \tag{2.8}$$

with $\tilde{A}(\mathbf{x},\omega)$ given by

$$\tilde{A}(\mathbf{x},\omega) = \frac{1}{4\pi\rho_2 c_{p2}^2}\left[\tilde{\mathbf{t}}^{(1)}\cdot\mathbf{d}^{(2)} + \frac{1}{c_{p2}}(\tilde{\mathbf{v}}^{(1)}\hat{\mathbf{n}}) : \boldsymbol{\mathcal{C}} : (\mathbf{e}^{(2)}\mathbf{d}^{(2)})\right] \tag{2.9}$$

and

$$\tilde{\mathbf{t}}^{(1)} = \frac{-i\omega\mathbf{t}^{(1)}}{v_T} \quad \text{and} \quad \tilde{\mathbf{v}}^{(1)} = \frac{-i\omega\mathbf{v}^{(1)}}{v_T} \tag{2.10}$$

In the above equations, $\rho_2$ is the mass density of the specimen. Using the explicit representation of the stiffness tensor in terms of the Lamé constants $\lambda$ and $\mu$, the term $\tilde{A}(\mathbf{x},\omega)$ can be further simplified as follows

$$\tilde{A}(\mathbf{x},\omega) = \frac{1}{4\pi\rho_2 c_{p2}^2}\left[\tilde{\mathbf{t}}^{(1)}\cdot\mathbf{d}^{(2)} + \frac{\lambda}{c_{p2}}\hat{\mathbf{n}}\cdot\tilde{\mathbf{v}}^{(1)}\mathbf{d}^{(2)}\cdot\mathbf{e}^{(2)} + \frac{\mu}{c_{p2}}\hat{\mathbf{n}}\cdot\left(\mathbf{d}^{(2)}\mathbf{e}^{(2)} + \mathbf{e}^{(2)}\mathbf{d}^{(2)}\right)\cdot\tilde{\mathbf{v}}^{(1)}\right] \tag{2.11}$$

As mentioned before, the fields $\tilde{\mathbf{v}}^{(1)}$ and $\tilde{\mathbf{t}}^{(1)}$ are obtained by solving the scattering problem. In the simulations presented here, the BEM and KA scattering models were used for this purpose. For both methods, it is necessary to compute the incident fields radiated by the transmitting transducer first. As in the case of state 2, the paraxial approximation is applied for decomposing these incident fields as follows

$$\mathbf{v}^{(1);\mathrm{inc}}(\mathbf{x},\omega) = v_T\hat{V}^{(1)}(\mathbf{x},\omega)\ \mathbf{d}^{(1)}\exp\left[ik_{p2}\mathbf{e}^{(1)}\cdot\mathbf{x}\right] \tag{2.12}$$

where $\mathbf{d}^{(1)}$ is a unit vector in the direction of polarization of the wave, $\mathbf{e}^{(1)}$ is the unit vector in the direction of wave propagation and $\mathbf{v}^{(1);\mathrm{inc}}$ is the incident field in the scattering problem. A further

approximation is possible if we assume that the fields generated due to the scattering of an incident wave in the form of Equation (2.12), are $\hat{V}^{(1)}(\mathbf{x},\omega)$ times those generated by the scattering of a plane wave of amplitude $v_T$. The differences between the solutions computed with and without this approximation indicate that the approximation holds true in most cases considered here. Therefore, we can rewrite Equation (2.8) as follows

$$\Delta V_R(\omega) = \frac{2\pi\rho_2 c_{p2}^2 \beta(\omega)}{(-i\omega)\rho_1 c_1 S_R} \int_{S_f} \hat{V}^{(1)}(\mathbf{x},\omega)\ \hat{V}^{(2)}(\mathbf{x},\omega)\ \tilde{A}(\mathbf{x},\omega) \exp\left[ik_{p2}\mathbf{e}^{(2)}\cdot\mathbf{x}\right] \mathrm{d}S \tag{2.13}$$

where $\tilde{A}(\mathbf{x},\omega)$ is still given by Equation (2.9), *but the fields* $\tilde{\mathbf{v}}^{(1)}$ *and* $\bar{\tilde{\mathbf{t}}}^{(1)}$ *in Equation* (2.10) *must be considered as those corresponding to the scattering of a plane wave of amplitude* $v_T$. When the defect size is small, such that $\hat{V}^{(1)}(\mathbf{x},\omega)$ and $\hat{V}^{(2)}(\mathbf{x},\omega)$ do not vary significantly over the surface of the defect, these two terms can be approximated by their value at a fixed point near or inside the defect and factored out of the integral. We call this the small-flaw approximation, and the resulting equation for the flaw voltage response, which is shown below, is known as the Thompson-Gray (TG) model [47]:

$$\Delta V_R(\omega) = \frac{2\pi\rho_2 c_{p2}^2 \beta(\omega)}{(-i\omega)\rho_1 c_1 S_R} \hat{V}^{(1)}(\mathbf{x_0},\omega)\ \hat{V}^{(2)}(\mathbf{x_0},\omega) \int_{S_f} \tilde{A}(\mathbf{x},\omega) \exp\left[ik_{p2}\mathbf{e}^{(2)}\cdot\mathbf{x}\right] \mathrm{d}S \tag{2.14}$$

where $\mathbf{x_0}$ is some fixed point near/inside the defect and is generally taken to be its geometric center. The integral in the above equation can be shown to be related to the far-field scattering amplitude (SA) (evaluated in the angular direction of the receiving transducer) of the defect, which is defined with respect to the scattering of a plane wave of velocity amplitude $-i\omega$ [22, §11.1]. To be more precise, the integral equals the projection of the SA along the direction opposite to the vector $\mathbf{d^{(2)}}$.

### 2.2.2 Beam Model

In the simulations where the TG model was not used, the diffraction coefficients were calculated using the multi-Gaussian (MG) beam model [22, §12.2][122]. A more accurate and computationally intensive beam model was used for evaluating the diffraction coefficients in the TG model since the evaluation needs to be done only at a single point in that case. This accurate beam model is based

on plane-wave expansion of the spherical waves generated by the point sources in the Rayleigh-Sommerfeld integral. The resulting integrals are evaluated by applying the stationary-phase and paraxial approximations as described in [13, Chap. 8].

### 2.2.3 Extraction of System Efficiency Factor

The system efficiency factor, $\beta(\omega)$, depends on the properties of the transducers and the electrical/electronic components in the system. Inherently, it also depends on the pulse generator and receiver settings. For pulse-echo measurements, it can be extracted from a calibration experiment performed with the same pulse-generator and receiver settings as used in the original experiment. Therefore, every benchmark experiment dataset provided by the WFNDEC is accompanied by a corresponding calibration dataset. The system efficiency factors were extracted from these calibration datasets as explained below.

The calibration measurements involve positioning the transducer above any block of elastic material, and measuring the pulse-echo from its front surface at normal incidence. For spherically-focused transducers, the distance between the transducer and the front surface is equal to the effective geometrical focal length. That is, the transducer is positioned such that it is focused on the surface as shown in Figure 2.2a. For planar transducers, the transducer is positioned such that the reflector lies in its far-field as shown in Figure 2.2b. The voltage measured in these scenarios can be expressed analytically with the system efficiency factor as the only unknown quantity in the expression. For spherically-focused transducers, the receiver voltage in the calibration measurement is given by [22, §8.13]

$$V_f(\omega) = -\beta(\omega) R_p \; e^{-2[\alpha(\omega) - ik_1]D} H^* \left( \frac{k_1 a^2}{2D} \right) \tag{2.15}$$

where $R_p$ is the pressure-field reflection coefficent at the interface between water and the block, $\alpha(\omega)$ is a frequency-dependent coefficient characterizing the attenuation in water, $k_1$ is the wavenumber in water, $D$ is the focus distance of the transducer, and $a$ is the radius of the radiating face of the transducer. The function $H$ is a correction factor for beam spreading, and is given by

$$H(x) = 2 - 2e^{ix}\Big[J_0(x) - iJ_1(x)\Big] \tag{2.16}$$

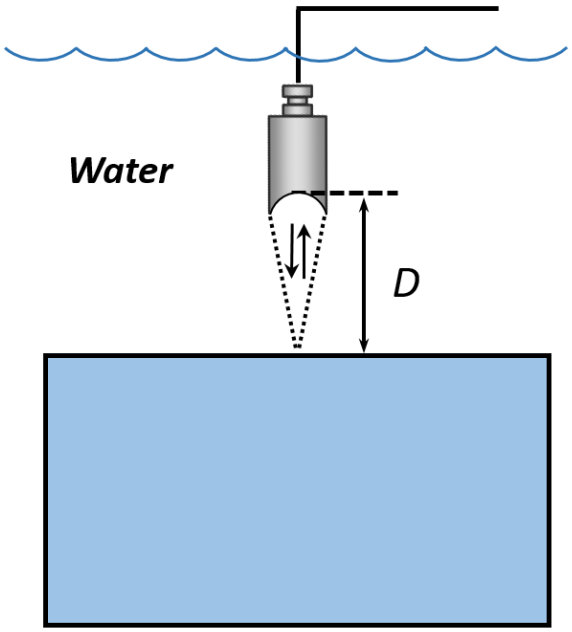


(a) Spherically focused transducer

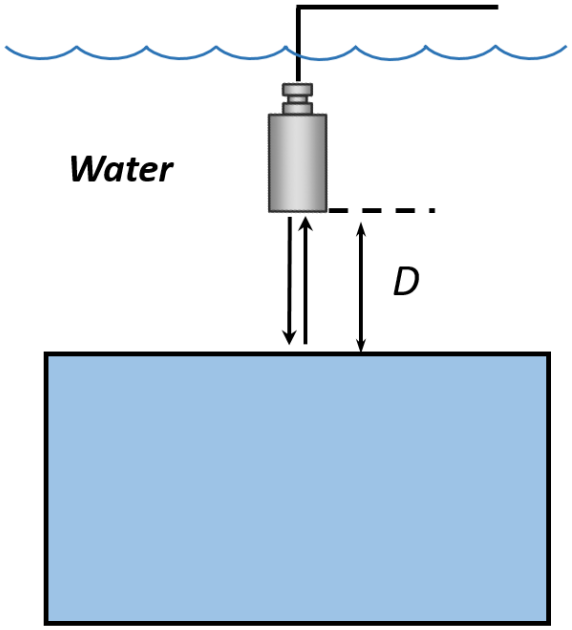


(b) Planar transducer

Figure 2.2: Schematics of calibration measurements for spherically focused transducers and planar transducers.

for any real number $x$, and $J_k$ is the Bessel function of order $k$. The superscript $(^*)$ over $H$ represents the operation of taking the complex conjugate of $H$. If the voltage spectrum is known from the calibration experiment, $\beta(\omega)$ can be extracted using a Wiener-deconvolution-type division process as shown below [13, §14.1.3]

$$\beta(\omega) = \frac{V_f(\omega)}{B(\omega)} \left( \frac{|B(\omega)|^2}{|B(\omega)|^2 + \epsilon_1^2 B_{\max}^2} \right) \tag{2.17}$$

where $B(\omega)$ denotes all factors on the right hand side of Equation (2.15) excluding $\beta(\omega)$, $B_{\max}$ is the maximum value of $|B(\omega)|$ over all frequencies, and $\epsilon_1$ is a small positive number. For a planar transducer, the corresponding expression for the receiver voltage is [124] [13, §8.13]

$$V_p(\omega) = \beta(\omega) R_p \; e^{-2[\alpha(\omega) - ik_1]D} H\left(\frac{k_1 a^2}{2D}\right) \tag{2.18}$$

where $\beta(\omega)$ now represents the system efficiency factor corresponding to the planar transducer. As in the case of the spherically focused transducer, the system efficiency factor can be extracted from the above equation by Wiener deconvolution.

To understand how the choice of $\epsilon_1$ is made, consider $V_f(\omega)$ to be a sum of the true signal and some noise. Then,

$$V_f(\omega) = B(\omega)\beta_t(\omega) + V_n(\omega) \tag{2.19}$$

where $V_n(\omega)$ is the Fourier spectrum of the measured (time-limited) noise and $\beta_t(\omega)$ is the true value of the system efficiency factor. Therefore, the system efficiency factor has to satisfy the following implicit relationship

$$\beta_t(\omega) = \frac{V_f(\omega)}{B(\omega) + \frac{V_n(\omega)}{\beta_t(\omega)}} \tag{2.20}$$

At frequencies where $|B(\omega)|$ is much greater than $|V_n(\omega)|/|\beta_t(\omega)|$, the system efficiency factor is obtained to a good approximation by dividing $V_f(\omega)$ by $B(\omega)$ as shown below

$$\beta_t(\omega) \approx \frac{V_f(\omega)}{B(\omega)} \tag{2.21}$$

The typical shape of the magnitude of the system efficiency factor is shown in Figure 2.6. It peaks at a frequency, defined as the center frequency, and decreases on either side away from it.

The magnitude of the system efficiency factor at the center frequency is typically much larger than the noise value. Therefore, the approximation (2.21) is valid at the center frequency. As we move away from the center frequency, the magnitudes of both $\beta_t(\omega)$ and $B(\omega)$ decrease usually, and beyond some point, the foregoing approximation becomes invalid. In this region, the values of the system efficiency factor extracted according to (2.21) are unreliable and uninformative. As will be mentioned later, the definition of bandwidth depends on this observation. When the system efficiency factor extracted in this fashion is used in pulse-echo calculations, the effect of the unreliable values is negligible provided their magnitudes are small. To ensure this, the division in Equation (2.21) has to be stabilised such that when $|B(\omega)|$ is very small, the extracted values of $\beta(\omega)$ will not have large magnitudes. The division process shown in Equation (2.17) achieves this purpose. The parameter $\epsilon_1$ in Equation (2.17) is chosen such that the extracted value of $\beta(\omega)$ does not have large values except in the frequency range close to the center frequency.

As an example, typical magnitudes of $B(\omega)$ and $\beta(\omega)$ are shown in Figure 2.6. Since the magnitude of $B(\omega)$ goes to zero with a decrease in the frequency (or equivalently, the wavenumber), the magnitude of $\beta(\omega)$ peaks close to the origin. The value of $\epsilon_1$ was chosen appropriately to keep this peak in $\beta(\omega)$ small. It is important to distinguish between the sensitivity of the extracted $\beta(\omega)$ to $\epsilon_1$ and its partial unreliability due to noise. For example, the effect of noise may be considered high when the normalized magnitude of $\beta(\omega)$ is below 0.5. According to the figure, this corresponds to the (normalized) wavenumbers below 1 and above 2.2. However, the magnitude of $B(\omega)$ is not small except for wavenumbers below 0.25. Therefore, $\beta(\omega)$ is not very sensitive to the value of $\epsilon_1$ for wavenumbers above 0.25, though its values may be unreliable due to the effect of noise.

### 2.2.4 Scattering Model

Two different scattering models are used in the simulations, as mentioned in Section 2.1. The full-wave scattering model is based on the solution of a BIE via the Nyström method (NM). This method is explained in detail in [30, 115]. A summary is given in Section 3.2. The second scattering model is the KA. A brief overview of this method is given in [125, §2.2.2]. Formulas for computing

the far-field SA using the KA are available in [13, §10.4]. For void-like defects, these relations can be further simplified [22, §10.2]. Further, for voids of simple shapes, such as spherical cavities and circular crack-like voids, the far-field SA can be expressed in a closed-form under the KA [126]. Appendix A lists some formulas for spherical scatterers, which will be useful for inclusion-type flaws.

## 2.3 Simulations of Benchmark Problems

### 2.3.1 Benchmark Problems of 2004

The benchmark problems from the year 2004 cover three standard defects: the spherical cavity, the flat-bottomed hole (FBH) and the side-drilled hole (SDH). The length of the SDH in these problems is larger than the beamwidth of the transducer, which typically spans over tens of wavelengths. Therefore, the NM would require a large number of discretization points to cover the entire length of the SDH. As this discretization condition exceeds what could be handled with our computational resources, only the spherical cavity and the FBH were simulated. Results for both planar and spherically-focused transducers are shown for these two defects. Interestingly, an approximate relation exists between the far-field SAs of finite-length and infinte-length SDHs when insonified by a plane wave traveling perpendicular to the SDH axis. The fields in the former case are assumed to not have any variations out of the plane of incidence in deriving this relation. Naturally, this implies that edge-effects at the ends of the SDH are neglected. Since the transducer beam in the benchmark problems is paraxial near the SDH and attenuates sufficiently ahead of its edges, this approximation holds good for these cases. Consequently, the far-field SA of a finite-length SDH can be derived from a two-dimensional scattering problem for a circular hole. This technique has been used to compare the predictions of an exact analytical scattering model with experimental data in [27, 116, 118]. The same method can be followed to get the NM solution too, but the NM simulation code used here was implemented only for three-dimensional scattering problems; its reduction to two dimensions is not possible by numerical manipulation due to the singular nature of the kernel functions in the underlying BIEs.

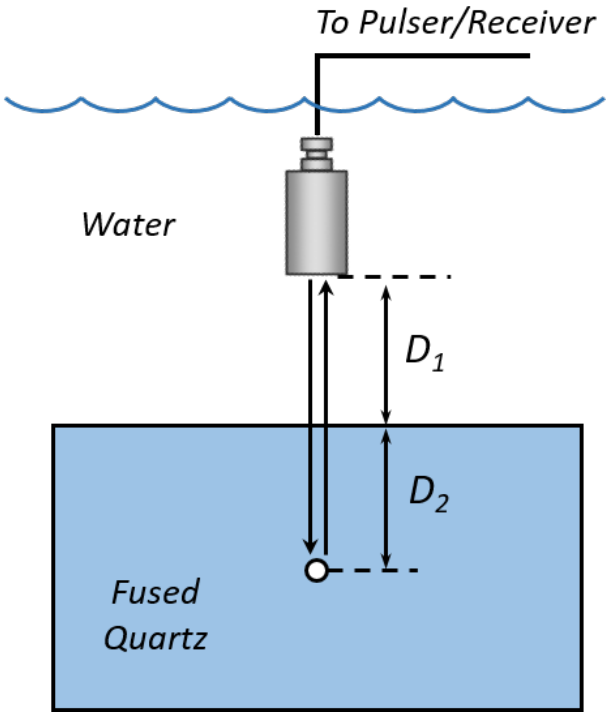


Figure 2.3: Schematic of pulse-echo measurement of a fused-quartz specimen with a spherical cavity.

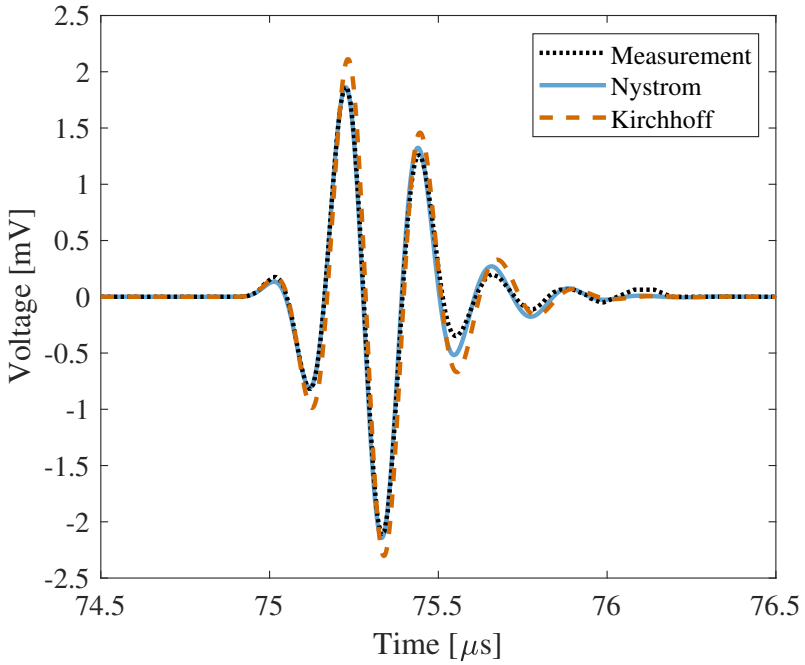


Figure 2.4: Measured and simulated pulse-echo signals for spherical cavity with planar transducer.

#### 2.3.1.1 Spherical Cavity in a Fused-Quartz Specimen

Figure 2.3 shows the schematic of the spherical cavity benchmark problem. The specimen under inspection is a fused-quartz block. Radius of the spherical cavity ($a$) is 0.346 mm. Pulse-echo measurements are obtained with both planar and spherically-focused transducers. The center frequency of both transducers is about 5 MHz. The mass density, the longitudinal and shear wave speeds of the block are 2200 kg/m$^3$, 5969.4 m/s and 3774.1 m/s, respectively. The distances $D_1$ and $D_2$ are 50.8 mm and 19.63 mm, respectively, for both planar and focused-transducer tests. Other test parameters relevant for modeling are mentioned in [121].

At the center frequency of the transducer, the wavelength of the longitudinal wave in the quartz block is 1.19 mm. Therefore, the diameter of the flaw is about half the longitudinal wavelength. The diffraction coefficient $\hat{V}^{(1)}(\mathbf{x}, \omega)$ due to radiation from the planar transducer was calculated in the region near the defect using the MG beam model. The variation of its magnitude over the surface of the spherical defect was found to be small. This is to be expected as the size of the sphere is smaller than the wavelength. Hence, pulse-echo signals were simulated using the TG model according to Equation (2.14). Specifically, the frequency response obtained from Equation (2.14) was converted to the time-domain using the inverse discrete Fourier transformation. As mentioned earlier, the system efficiency factor in Equation (2.14) was extracted from reference measurement data according to Equations (2.17) and (2.18). The parameter $\epsilon_1$ in Equation (2.17) was set to 0.03. Figure 2.4 shows the measured and predicted pulse-echo signals from the spherical void for the planar transducer.

The observed pulse-echo signal includes the leading-edge pulse as well as the contribution of the creeping wave that travels along the surface of the sphere [127]. The leading-edge pulse is the reflection from the point at which the wave contacts the sphere first. The creeping wave is a surface wave initiated at the boundary of the insonified and non-insonified (dark) regions. It travels along the surface of the sphere in the dark region and radiates away from it along the way. When it reaches the boundary of the insonified and the dark regions, it radiates in the direction opposite to the incident wave, which causes a second pulse in the receiver voltage. Due to the relatively small

size of the sphere in this benchmark problem, the contribution of the creeping wave overlaps with the leading-edge pulse. The NM, being a full-wave method, predicts the contribution of both the pulses accurately. The KA prediction also has two overlapping pulses: one from the leading-edge and another from the discontinuity between the insonified and dark regions. The latter is an artifact of the KA model. Besides, the KA does not model the creeping wave, which is another reason for its deviation from the measured signal. Further, in the KA prediction, the leading part of the signal, which is attributed primarily to the leading-edge pulse, also seems to be in slight disagreement. This is due to the small size of the defect; the KA, being a high-frequency approximation method, becomes progressively less accurate as the radius of curvature of the reflecting surface becomes smaller and comparable to the wavelength.

Table 2.1: Pulse-echo amplitudes (in mV) for the spherical cavity inspection with planar transducer.

| Amplitude | $\epsilon_1$ | Measurement | NM | KA | % Error NM | % Error KA |
|---|---|---|---|---|---|---|
| $A_1$ | 0.01 | 2.113 | 2.161 | 2.323 | 2.27 | 9.94 |
| | 0.03 | 2.113 | 2.159 | 2.321 | 2.18 | 9.84 |
| | 0.09 | 2.113 | 2.198 | 2.304 | 1.42 | 9.04 |
| $A_2$ | 0.01 | 2.180 | 2.216 | 2.411 | 1.65 | 10.60 |
| | 0.03 | 2.180 | 2.214 | 2.413 | 1.56 | 10.69 |
| | 0.09 | 2.180 | 2.198 | 2.393 | 0.83 | 9.77 |

Next, the amplitudes of the pulse-echo signals are compared. Two different definitions of the amplitude are considered: one is the maximum of the absolute value of the voltage signal, defined as $A_1$, and another is the maximum of the envelope of the voltage signal, defined as $A_2$. The envelope is defined as the magnitude of the analytic representation of the voltage signal obtained from the `envelope` function in MATLAB® [128]. In both amplitude definitions, the maximum is taken over time. Uncertainty due to the $\epsilon_1$ parameter in Equation (2.17) was taken into account by calculating the amplitudes for three different $\epsilon_1$ values, including 0.01, 0.03 and 0.09. More explicitly, three different system efficiency factors were obtained based on the three $\epsilon_1$ values, and the flaw response in Equation (2.14) was calculated for the three different system efficiency factors. The results are

shown in Table 2.1. The NM and KA have an error of about 1% and 10%, respectively, for both the amplitude definitions.

As mentioned earlier, the integral in Equation (2.14) is related to a projection of the SA. For brevity, it will be referred to as the SA itself. This quantity, represented as $A(\omega)$, is calculated for both NM and KA as a function of the frequency (equivalently, the wavenumber) and compared with the measurement in Figure 2.5. The measured SA was computed by inverting Equation (2.14) in a way similar to the extraction of the system efficiency factor. Considering $A_e(\omega)$ as the SA corresponding to the measurement, the inversion process is expressed as follows

$$A_e(\omega) = \frac{\Delta V_R(\omega)}{\tilde{B}(\omega)} \left( \frac{|\tilde{B}(\omega)|^2}{|\tilde{B}(\omega)|^2 + \epsilon_2^2 \tilde{B}_{\max}^2} \right) \tag{2.22}$$

where $\Delta V_R(\omega)$ is the measured flaw response and $\tilde{B}(\omega)$ is the product of all the terms on the right hand side of (2.14) except the SA. The parameter $\epsilon_2$ is a small positive number, which is in general different from the parameter $\epsilon_1$ used in the extraction of the system efficiency factor. The measured SA was extracted for three different values of $\epsilon_1$ and $\epsilon_2$, including 0.01, 0.03 and 0.09, leading to nine combinations. The result for $\epsilon_1 = \epsilon_2 = 0.03$ is considered as the nominal SA. The normalized magnitude of this quantity is represented by the continuous line in Figure 2.5. As $\epsilon_1$ and $\epsilon_2$ are varied within the given set of values, the magnitude of the extracted SA varies. The shaded region represents the limits of this variation.

From Equations (2.17) and (2.22), we should expect to see large variation in the extracted SA at frequencies where either $|B(\omega)|$ or $|\tilde{B}(\omega)|$ is small. The normalized values of these two quantities are plotted in Figure 2.6. The plot of $\tilde{B}(\omega)$ corresponds to $\epsilon_1 = 0.03$. The corresponding plot of $\beta(\omega)$ is also shown. We observe that the normalized magnitude of $\tilde{B}(\omega)$ is lower than that of $B(\omega)$ in most of the frequency band away from the center frequency. Therefore, the boundaries demarcating the frequency ranges with large and small sensitivities can be discerned from the values of $\tilde{B}(\omega)$. Roughly speaking, on either side of the center frequency, these boundaries occur at frequencies where the normalized value of $|\tilde{B}(\omega)|$ goes to 0.5 (-6 dB).

However, as mentioned in Section 2.2.3, the bandwidth limits are defined according to the reliability and not the sensitivity of the extracted values. Since the values of $|\beta(\omega)|$ less than half of

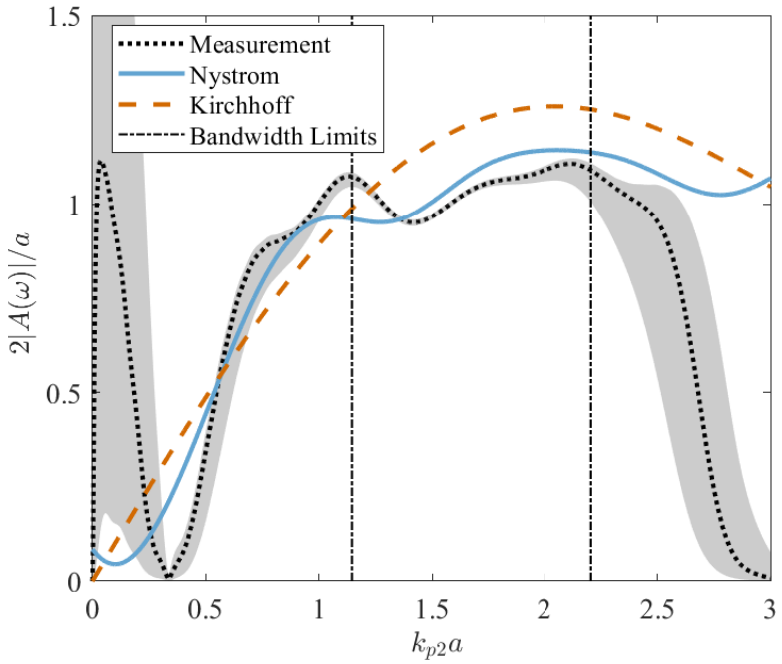


Figure 2.5: Measured and simulated scattering amplitudes of a spherical void. Measurement curve is extracted from planar transducer measurement.

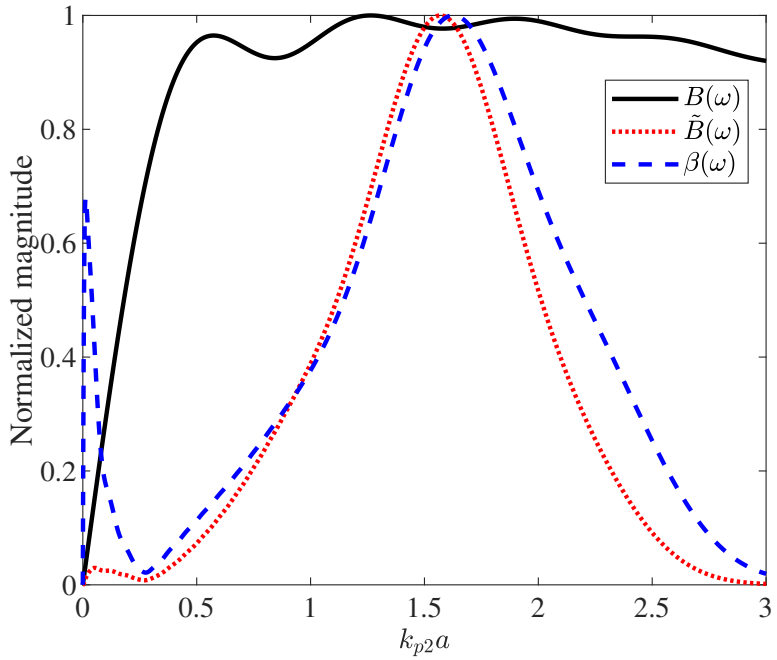


Figure 2.6: Normalized magnitudes of $B(\omega)$, $\tilde{B}(\omega)$ and $\beta(\omega)$ for spherical void with planar transducer. Each curve is normalized by its maximum value in the given frequency range. The plots of $\beta(\omega)$ and $|\tilde{B}(\omega)|$ correspond to $\epsilon_1$=0.03.

its maximum value (across all frequencies) are considered unreliable, the bandwidth limits are set accordingly. This choice agrees with the bandwidth definition in earlier works [129, §5.3]. Similarly, scattering amplitudes extracted according to Equation (2.22) are also unreliable if the extracted values are very small. However, this is not taken into account in the bandwidth definition and has to be kept in mind while interpreting Figure 2.5. Since the shape of $|\beta(\omega)|$ matches that of $|\tilde{B}(\omega)|$, the bandwidth limits appear to demarcate regions with small and large sensitivities. However, this is incidental and is not true in general as illustrated by some examples shown later.

Within the bandwidth, the NM result agrees well with the measurement. The minor difference from measurement is primarily due to uncertainties in the measured voltages and extracted model parameters (wave speed, attenuation constant, etc.), and to a lesser extent due to approximations in the TG model (small-flaw approximation, plane-wave assumption, etc.) and the beam model because the conditions required for these approximations seem to be more or less valid. The KA prediction is slightly away from the measurement due to the relatively small size of the sphere, which is evident from the values of $k_{p2}a$ in the given bandwidth range. The KA would agree well with the NM for $k_{p2}a \gg 1$, except for the contribution of the creeping wave, which is not included in the KA. For high frequencies out of the bandwidth, the SA extracted from measurement seems to diverge from the NM. This is due to the effect of the $\epsilon_2$ parameter. Indeed, for $\epsilon_2$ values much closer to zero, the measured SA lies above the NM curve.

Table 2.2: Pulse-echo amplitudes (in mV) for spherical cavity inspection with focused transducer.

| Amplitude | $\epsilon_1$ | Measurement | NM | KA | % Error NM | % Error KA |
|---|---|---|---|---|---|---|
| $A_1$ | 0.01 | 8.906 | 8.613 | 9.349 | 3.29 | 4.97 |
| | 0.03 | 8.906 | 8.604 | 9.340 | 3.39 | 4.87 |
| | 0.09 | 8.906 | 8.683 | 9.262 | 4.3 | 4 |
| $A_2$ | 0.01 | 9.123 | 8.774 | 9.534 | 4.40 | 3.88 |
| | 0.03 | 9.123 | 8.765 | 9.524 | 4.50 | 3.77 |
| | 0.09 | 9.123 | 8.683 | 9.437 | 5.40 | 2.82 |

The above procedure was repeated for the spherically-focused transducer case. The effective focal distance of the transducer in water is 172.9 mm. Other details relevant for modeling are

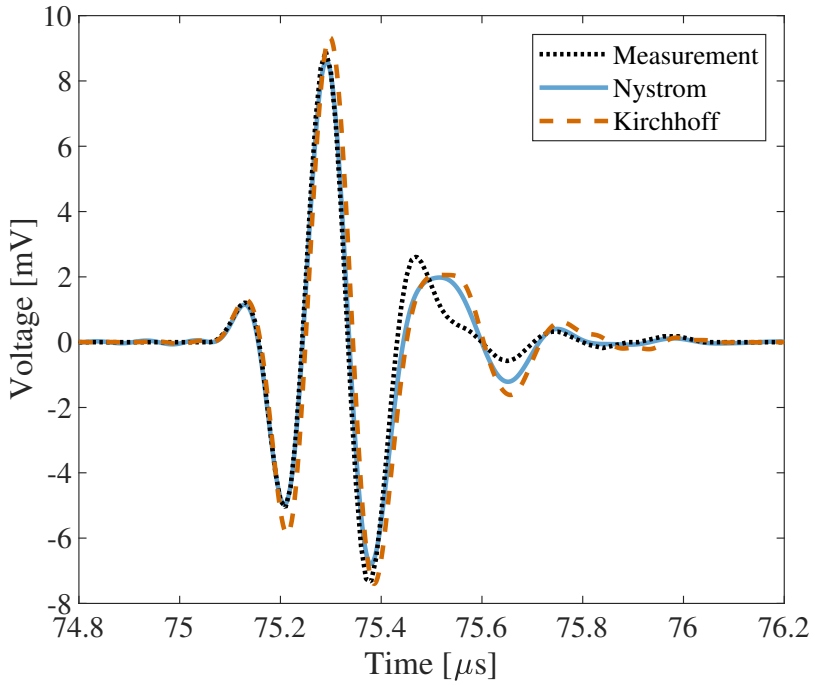


Figure 2.7: Measured and simulated pulse-echo signals for the spherical void with focused transducer.

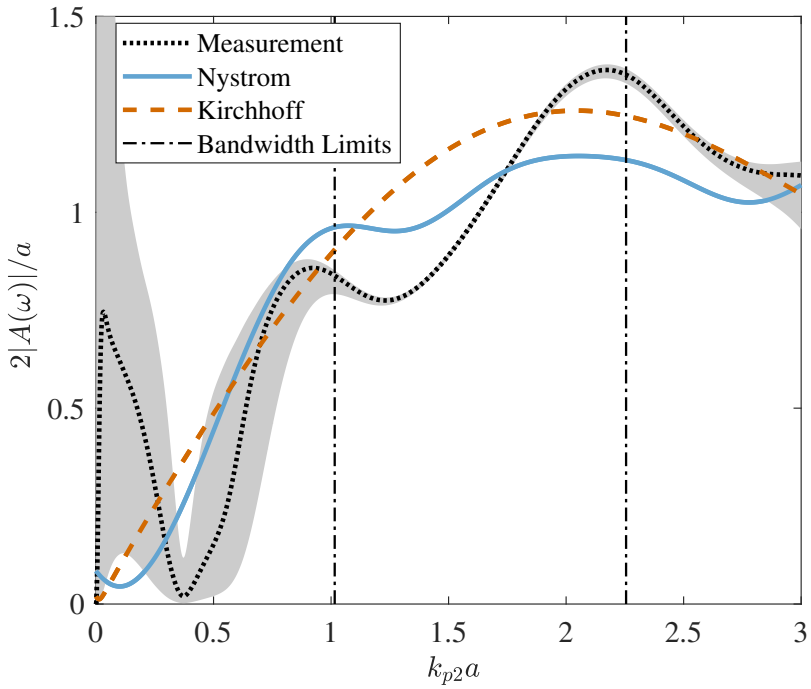


Figure 2.8: Measured and simulated scattering amplitudes of the spherical void. Measurement curve is extracted from focused transducer measurement.

available in [121]. The system efficiency factor was extracted from Equation (2.15) instead of (2.18). The three measurement outputs are shown in Figures 2.7, 2.8 and Table 2.2. The results are similar to the planar transducer case with one exception; the pulse-echo amplitudes predicted by the KA are closer to the measurement, seemingly indicating the KA to be better than the NM. However, the full pulse-echo signals in Figure 2.7 give a different picture. The NM prediction matches the measurement much better than the KA. Indeed, in the leading part of the signal, the NM prediction is more or less exact. However, as the signal amplitude peaks closer to its tail, the maximum amplitude predicted by the NM differs more significantly from the measurement. In contrast, the KA prediction incidentally matches the measured signal near the amplitude peak.

#### 2.3.1.2 FBH in a Steel Specimen

Figure 2.3 shows the schematic of the FBH benchmark problem. The specimen under inspection is a steel block. The FBH is a cylindrical hole with length much larger than the radius. The specific FBH considered here has a radius ($a$) of 1.191 mm. Similar to the spherical cavity problem, pulse-echo measurements are obtained with both planar and spherically-focused transducers. The center frequency of both transducers is about 5 MHz. The mass density, the longitudinal and shear wave speeds of the block are 7860 kg/m$^3$, 5940 m/s and 3230 m/s, respectively. The distances $D_1$ and $D_2$ are 50.8 mm and 25.4 mm, respectively, for both planar and focused-transducer tests. The length of the FBH is not specified in the benchmarks as the reflections from its far-end are ignored. However, a finite-length needs to be assigned for applying the NM scattering model. For this purpose, the length is taken to be five times the radius. This ensures proper time separation between the leading and far-end reflections such that the former can be extracted from the combined signal by time-gating.

The diameter of the FBH corresponds to about two longitudinal wavelengths at the center frequency. Therefore, variations in the beam shape over the front surface of the FBH are higher than in the case of the spherical cavity considered earlier. Figure 2.10 shows the magnitude of the diffraction coefficient of the planar transducer radiation on the front surface of the FBH. The horizontal

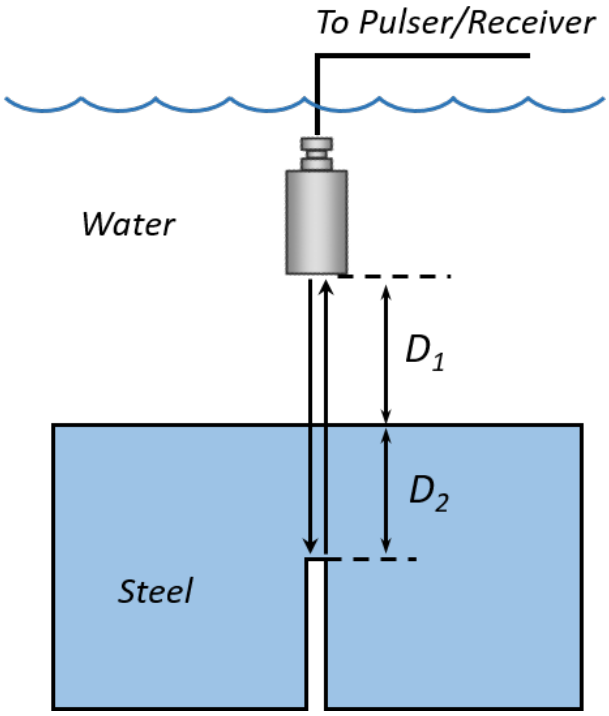


Figure 2.9: Schematic of pulse-echo measurement of a steel specimen containing an FBH.

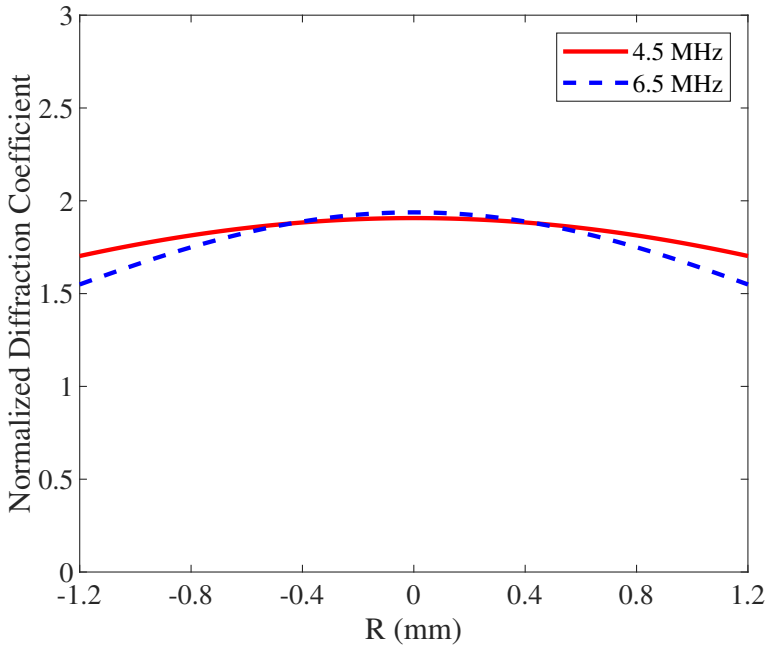


Figure 2.10: Magnitude of the diffraction coefficient corresponding to the planar transducer at the surface of the FBH.

axis represents points on a line passing through the center of the face, with $R = 0$ corresponding to the center. This figure completely characterizes beam variations over the front-surface because of the underlying axial symmetry, which is also partially represented in the figure. The two plotted curves correspond to the center frequency and the frequency at the upper bandwidth limit. Both plots are normalized by the excitation amplitude of the transducer. We recall that the TG model approximates the diffraction coefficients with their values at a fixed location on/near the flaw. If this location is chosen as the center of the front surface of the FBH, the diffraction coefficients will be larger than their true values, except at the center. Therefore, this approximation may lead to larger pulse-echo amplitudes than measurement in the model predictions.

Indeed, the pulse-echo signals simulated according the TG model in Equation (2.14) are in agreement with this conclusion as shown in Figure 2.11. The signals of both the models are shifted by 0.053 $\mu$s to match their peaks with the measured signal. To be sure, the phase variations in the diffraction coefficients also have to be considered to understand the effect of approximations in the TG model. In fact, as shown later for the focused transducer case, the TG model predictions appear to be in good agreement with the measurement despite similar variations in the magnitudes of the diffraction coefficients over the FBH surface. This difference between the planar and the focused transducer cases is explained, therefore, by the phase variations of the diffraction coefficients.

Table 2.3: Pulse-echo amplitudes (in mV) for the FBH inspection with planar transducer.

| Amplitude | $\epsilon_1$ | Measurement | NM | KA | % Error NM | % Error KA |
|---|---|---|---|---|---|---|
| $A_1$ | 0.01 | 3.08 | 3.666 | 3.423 | 9.29 | 11.1 |
| | 0.03 | 3.08 | 3.363 | 3.420 | 9.19 | 11.0 |
| | 0.09 | 3.08 | 3.339 | 3.395 | 8.41 | 10.2 |
| $A_2$ | 0.01 | 3.170 | 3.457 | 3.520 | 9.05 | 11.0 |
| | 0.03 | 3.170 | 3.454 | 3.517 | 8.96 | 10.9 |
| | 0.09 | 3.170 | 3.429 | 3.491 | 8.17 | 10.1 |

As the reflection from the front-surface is highly specular, the KA pulse-echo prediction coincides with that of the NM. The discrepancy between the models in the tail region of the pulse is due to the small contribution of surface waves excited on the front-surface of the FBH. Both model predictions

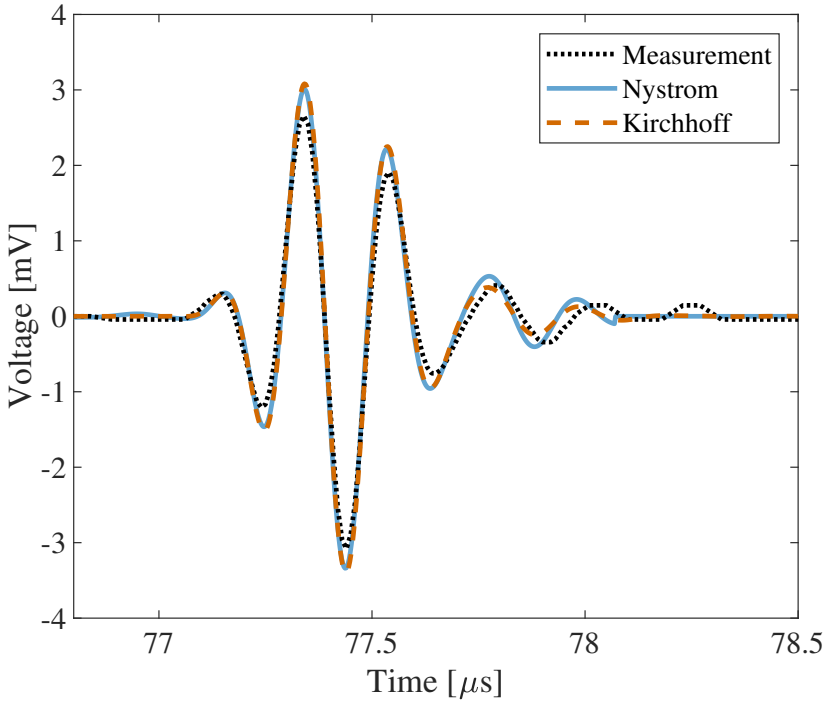


Figure 2.11: Measured and simulated pulse-echo signals for the FBH with planar transducer.

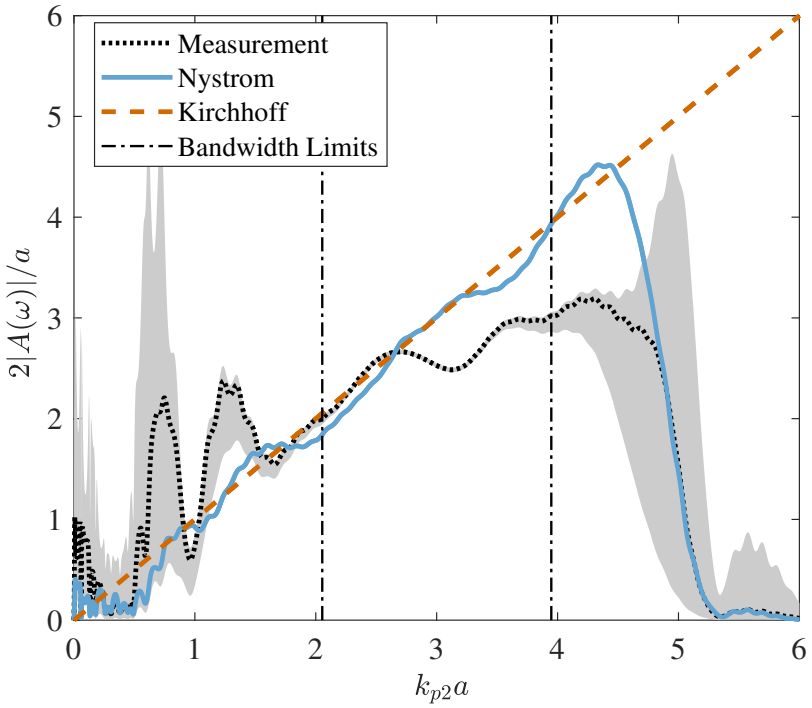


Figure 2.12: Measured and simulated scattering amplitudes of the FBH. Measurement curve is extracted from planar transducer measurement.

can be improved by relaxing the approximations made in deriving the TG model. Specifically, two different approximations were made in going from Equation (2.8) to (2.14) through Equation (2.13). First is the assumption that the scattered fields due a quasi-plane wave of the form (2.12) are obtained by multiplying the diffraction coefficient with those generated by the scattering of a plane wave of velocity amplitude $v_T$. This allows the incident-wave in the scattering problem to be replaced by a plane-wave. Therefore, this approximation will be called as the plane-wave assumption. The second approximation is the small-flaw assumption. Both the scattering models can be applied to simulate pulse-echo signals according Equation (2.13), that is, by relaxing only the small-flaw assumption. Due to the specular nature of the scattering, their predictions should be more or less same. However, only the NM can be applied for computing Equation (2.8) as the KA cannot handle scattering due to non-plane incident waves. The KA prediction corresponding to Equation (2.13) showed marginal improvement compared to Equation (2.14). Therefore, the error in the TG model is mostly explained by the plane-wave assumption.

The foregoing observation can be confirmed by applying the NM to compute (2.8). This NM result agrees well with the measurement except for an artifact which can be traced to a so-called irregular frequency problem in the BIE underlying the NM. Therefore, this result will be presented in Chapter 6, where the irregular frequency problem is discussed in detail. In short, the irregular frequency problem manifests as sharp peaks in the values of the integrals in Equations (2.8), (2.13) and (2.14) around certain frequencies. If the variation of the integral as a function of frequency is relatively smooth, this effect can be smoothed out by interpolation. This is true for the integral in Equation (2.14). Still a weak sign of the peaks in the frequency domain signal can be observed in the time domain signal derived from it; see the ripples arriving ahead of the pulse in Figure 2.11. This effect is exacerbated for the integrals in Equations (2.8) and (2.13) as their variation as a function of frequency is not smooth due to mixing of the fields scattered from the front and far ends of the FBH. Further discussion on this problem will be deferred to Chapter 6.

The pulse-echo amplitudes corresponding to the signals in Figure 2.11 are shown in Table 2.3. The errors in both models are on the same order. Next, the SAs are compared in Figure 2.12.

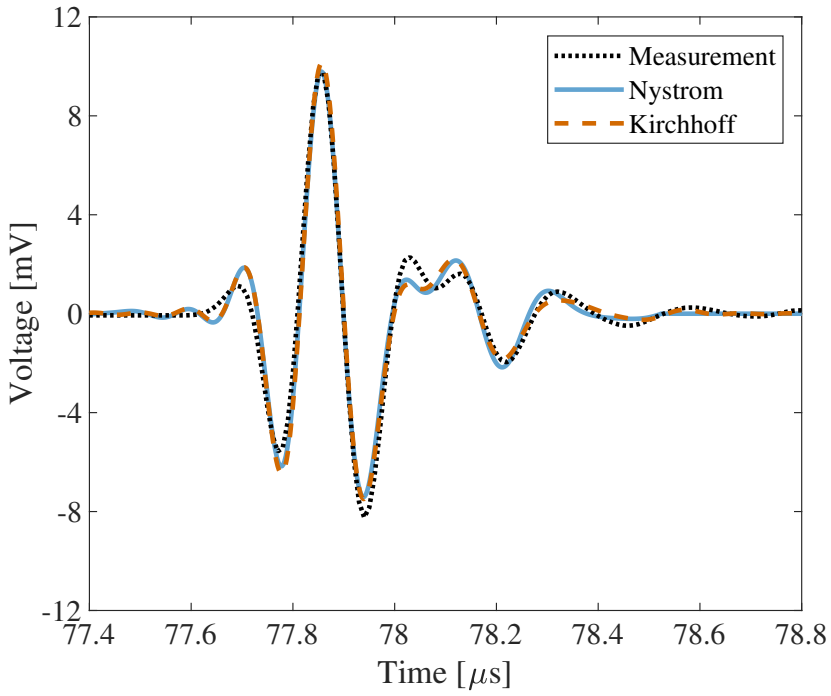


Figure 2.13: Measured and simulated pulse-echo signals for the FBH with focused transducer.

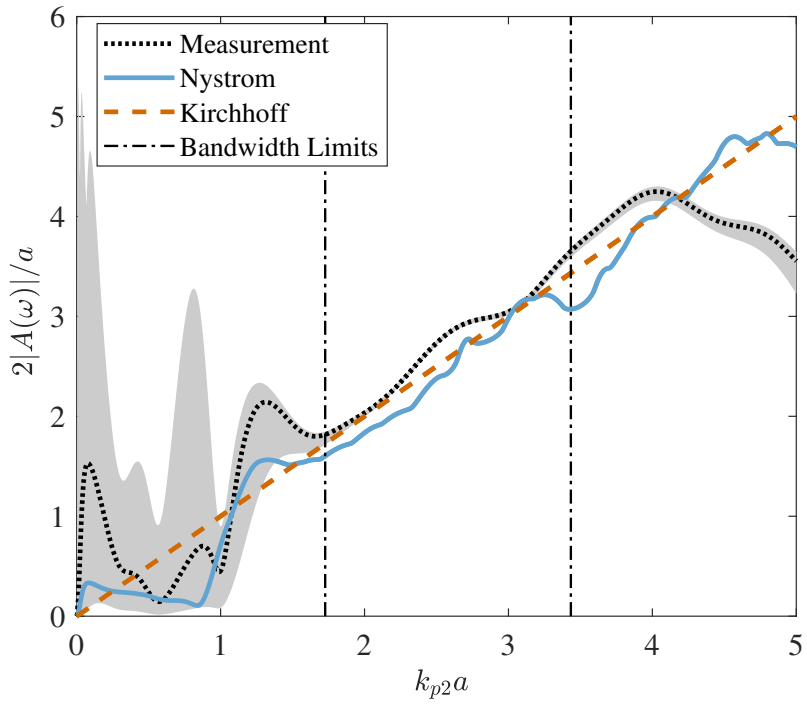


Figure 2.14: Measured and simulated scattering amplitudes of the FBH. Measurement curve is extracted from focused transducer measurement.

Since, the SA of the NM includes reflections from the far-end of the FBH, the contribution of these reflections was removed by time-gating the corresponding pulse-echo signal and then extracting the SA from the time-gated pulse-echo signal using the same procedure adopted for extracting the measured SA (see Equation (2.22)). Extraction of the SA in this fashion will involve a parameter $\epsilon_3$, which is analogous to the parameter $\epsilon_2$ that is employed in the extraction of the measured SA. For simplicity, this parameter was set to a fixed value of 0.03. Therefore, sensitivity of the SA to the value of $\epsilon_3$ is not represented in the figure. As expected from the pulse-echo observations, the NM and KA agree with each other. The agreement of both the models with the measurement is good in the lower half of the bandwidth. The divergence towards higher frequencies is explained by the small-flaw and plane-wave approximations, which get increasingly invalid as frequency gets higher. The drop in the SA corresponding to the NM at frequencies above the higher bandwidth limit is a result of the deconvolution procedure adopted in extracting it and does not reflect its true value. As the same extraction procedure was applied to compute the measured SA, the coincidence of these two results (NM and measurement) outside the bandwidth is uninformative of the agreement between the true values of the corresponding SAs.

Table 2.4: Pulse-echo amplitudes (in mV) for the FBH inspection with focused transducer.

| Amplitude | $\epsilon_1$ | Measurement | NM | KA | % Error NM | % Error KA |
|---|---|---|---|---|---|---|
| $A_1$ | 0.01 | 9.747 | 9.792 | 10.135 | 0.46 | 3.98 |
| | 0.03 | 9.747 | 9.781 | 10.124 | 0.34 | 3.87 |
| | 0.09 | 9.747 | 9.685 | 10.024 | 0.64 | 2.84 |
| $A_2$ | 0.01 | 10.117 | 9.874 | 10.199 | 2.40 | 0.81 |
| | 0.03 | 10.117 | 9.864 | 10.187 | 2.50 | 0.69 |
| | 0.09 | 10.117 | 9.767 | 10.024 | 3.46 | 0.29 |

The results for the spherically-focused transducers are shown in Figures 2.13, 2.14 and Table 2.4. The pulse-echo predictions are shifted by 0.505 $\mu$s to have them coincide with the measurement. Agreement of the models with the measurement is better than that in the case of the planar transducer. This is likely due to better validity of the approximations in the TG model. Similar to the focused transducer inspection of the spherical cavity, the seemingly better agreement of the

KA compared to the NM for the amplitude $A_2$ is incidental; the maxima of the measurement and the KA occur at different parts of the pulse. Also, in Figure 2.14, the uncertainty in the measured SA is low even outside the bandwidth at higher frequencies. As mentioned before, this is due to the disconnect between the definition of bandwidth and the sensitivity of the extracted SA to the parameters $\epsilon_1$ and $\epsilon_2$.

### 2.3.2 Benchmark Problems of 2005

The benchmark problems from the year 2005 cover two types of defects: pillbox-shaped voids and SDHs. As in the case of the benchmarks from 2004, the SDH problems were not simulated. Further, only the larger of the two pillbox voids defined in the benchmarks is considered here. The pillbox void is a cylindrical defect with a length much smaller than the radius. The diameter ($2a$) and length of the pillbox considered here are 1.908 mm and 0.089 mm, respectively. The specimen hosting the defect is made of a Titanium alloy. It has a mass density of 4420 kg/m$^3$. The longitudinal and shear wave speeds in it are 6200 m/s and 3180 m/s, respectively. Pulse-echo signals are obtained with a planar transducer with center frequency around 10 MHz at different angles of incidence. All other details relevant for modeling are mentioned in [121].

#### 2.3.2.1 Normal Incidence

Figure 2.15 shows a schematic of the test setup. The distances $D_1$ and $D_2$ are 25.4 mm and 13.0445 mm, respectively. The diameter of the pillbox corresponds to three longitudinal wavelengths at the center frequency. Due to the large size of the flaw, the TG model cannot be applied. Therefore, pulse-echo signals were simulated according to Equation (2.13). The model predictions are compared with measurement in Figure 2.16. The parameter $\epsilon_1$ was set to 0.12 in computing the system efficiency factor. The NM and KA results are time-shifted by 0.065 $\mu$s and 0.072 $\mu$s, respectively, for overlapping their peaks with the measurement. The NM prediction agrees very well with the measurement. As in the FBH benchmark, the KA prediction matches the NM because of the highly specular reflection from the flat front surface of the void. However, unlike the FBH

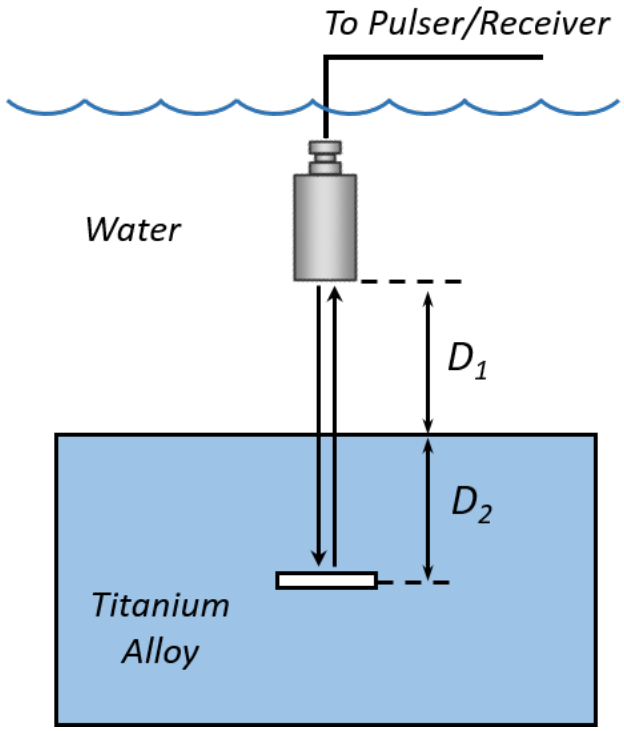


Figure 2.15: Schematic of pulse-echo measurement of a Titanium alloy containing a crack-like void.

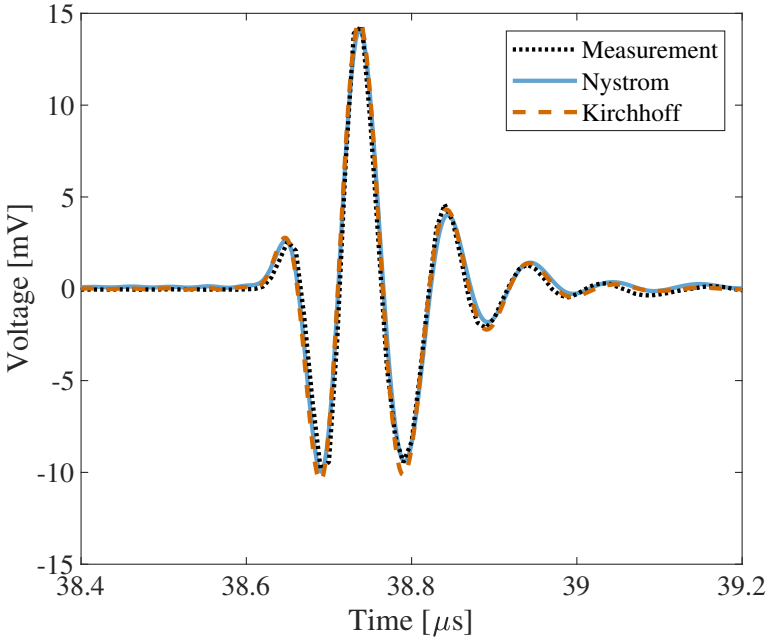


Figure 2.16: Measured and simulated pulse-echo signals for the pillbox void at normal incidence.

problem, slight differences between the KA and the NM occur even in the leading part of the signal. This is likely due to scattering from the back surface of the void, which is not represented in the KA. Due to the small thickness of the void, the voltage pulses resulting from such scattering are not well separated from the leading pulse.

Table 2.5: Pulse-echo amplitudes (in mV) from Crack C for normal incidence.

| Amplitude | $\epsilon_1$ | Measurement | NM | KA | % Error NM | % Error KA |
|---|---|---|---|---|---|---|
| $A_1$ | 0.09 | 14.296 | 14.274 | 14.592 | 0.15 | 2.07 |
| | 0.12 | 14.296 | 14.106 | 14.492 | 0.13 | 1.37 |
| | 0.18 | 14.296 | 13.781 | 14.215 | 0.36 | 0.57 |
| $A_2$ | 0.09 | 15.296 | 14.370 | 14.664 | 6.05 | 4.13 |
| | 0.12 | 15.296 | 14.189 | 14.563 | 7.24 | 4.79 |
| | 0.18 | 15.296 | 13.853 | 14.282 | 9.43 | 6.63 |

The amplitudes of the pulse-echo signals are compared in Table 2.5 for three different values of $\epsilon_1$. Relative errors for both the models are within 10 percent. Because of the large size of the defect, the scattering amplitude cannot be extracted from the measured pulse-echo signal. Therefore, instead of the SA, the integral in Equation (2.13), represented as $I(\omega)$, was extracted through a procedure similar to Equation (2.22) and compared with the corresponding model predictions in Figure 2.17. The sensitivity limits are plotted by varying $\epsilon_1$ in $\{0.09, 0.12, 0.18\}$ and $\epsilon_2$ in $\{0.01, 0.03, 0.09\}$, where the result corresponding to $\epsilon_1 = 0.12$ and $\epsilon_2 = 0.03$ is considered nominal. Both models agree well with the measurement, as expected from the pulse-echo results.

#### 2.3.2.2 Oblique Incidence at Point A

Figures 2.18 and 2.23 show the schematics of the oblique incidence benchmark problems. In the former case, the transducer beam is set to maximize the reflection from the left tip (defined as point A) of the defect. In the latter case, it is set to maximize the reflection from the right tip (defined as point B) of the defect. The transducer positions corresponding to these two setups were determined experimentally by scanning the transducer on a horizontal line and observing the amplitude of the pulse-echo as a function of the scan position. The amplitude peaks at two scan positions,

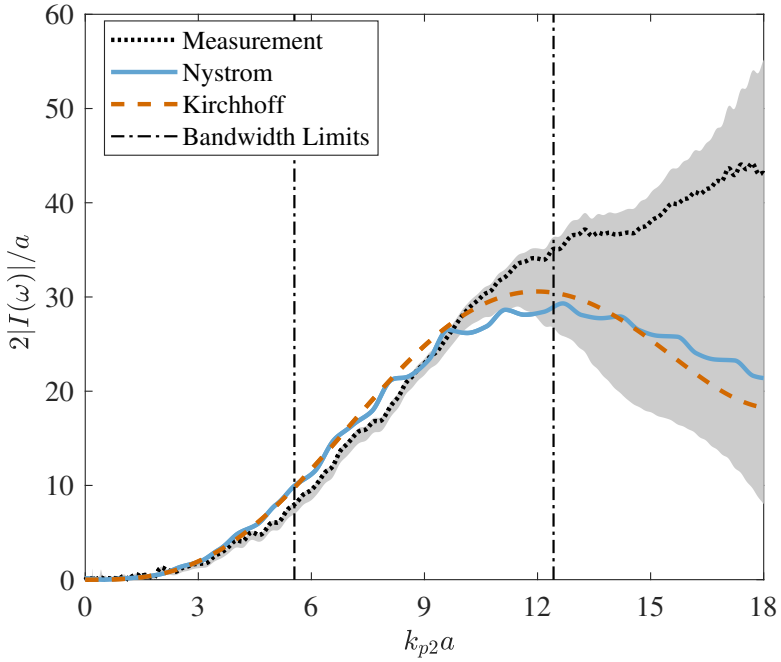


Figure 2.17: Magnitude of the integral $I(\omega)$ for the pillbox benchmark problem at normal incidence.

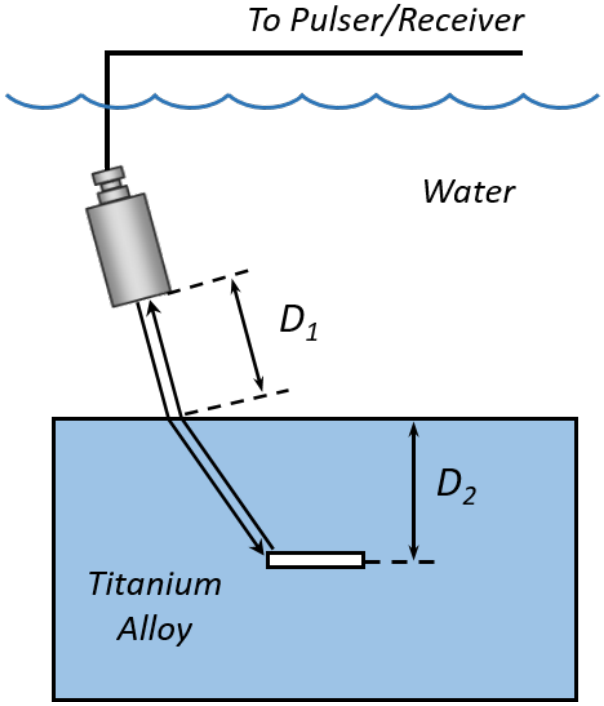


Figure 2.18: Schematic of pulse-echo measurement of a Titanium alloy containing a crack-like void. Oblique incidence on the left tip (point A).

corresponding to the two setups mentioned above. The scan coordinates for these positions are listed in the benchmark files [121]. The pulse-echo signals are obtained for two incidence angles (at the defect): 30° and 45°. For all these cases, the water path length, $D_1$, is fixed and equal to 25.4 mm. The oblique incidence results for point A are described in this subsection.

Figure 2.19 shows the NM pulse-echo results simulated according to Equation (2.13), that is, by applying the plane-wave assumption without the small-flaw approximation. The parameter $\epsilon_1$ was set to 0.12. The simulated result was shifted by 0.292 $\mu$s to let its peaks coincide with the measurement. The measured signal is similar to the theoretically predicted response of a crack (zero-thickness defect), which has three distinct pulses: two resulting from diffraction at the left and right flash points on the crack and one due to scattering of a surface wave excited on it [130, 131]. This similarity is due to the large aspect ratio of the pillbox void. However, there is an additional pulse in the pillbox response due to diffraction from the left edge on the bottom surface. This pulse overlaps with the one resulting from the edge on the top surface since the separation between the two surfaces is small. The NM model predicts the overall waveform accurately, with the largest error (among the three distinctly identifiable pulses) appearing in the leading pulse. Since this pulse includes the contribution from the bottom edge and the lateral surface of the pillbox, the observed discrepancy is possibly due to the actual shape of the defect being different from that of the pillbox. Further, since the pillbox void was fabricated in the specimen using a diffusion bonding process, there may have been additional discontinuities at the bonding surface as inferred in earlier works with similar defects [132].

Table 2.6: Pulse-echo amplitudes (in mV) for Crack C for 30° incidence at point A.

| Amplitude | $\epsilon_1$ | Measurement | NM | KA | % Error NM | % Error KA |
|---|---|---|---|---|---|---|
| $A_1$ | 0.09 | 0.53535 | 0.476 | 0.535 | 11.1 | 0.07 |
| | 0.12 | 0.53535 | 0.473 | 0.532 | 11.6 | 0.63 |
| | 0.18 | 0.53535 | 0.463 | 0.521 | 13.5 | 2.68 |
| $A_2$ | 0.09 | 0.6076 | 0.541 | 0.601 | 11.0 | 1.08 |
| | 0.12 | 0.6076 | 0.537 | 0.597 | 11.6 | 1.74 |
| | 0.18 | 0.6076 | 0.526 | 0.586 | 13.4 | 3.55 |

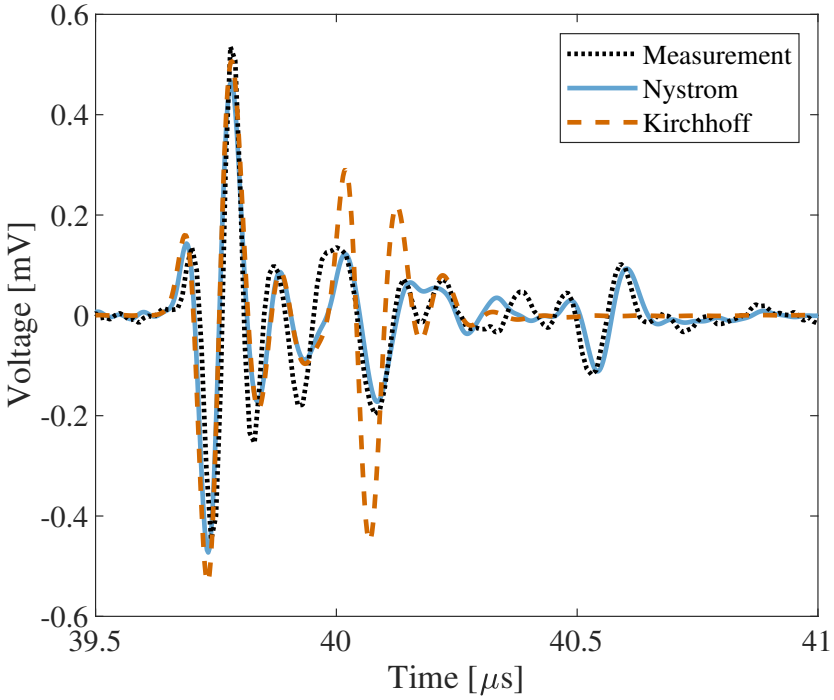


Figure 2.19: Pulse-echo signals for the pill-box flaw corresponding to 30° incidence at point A.

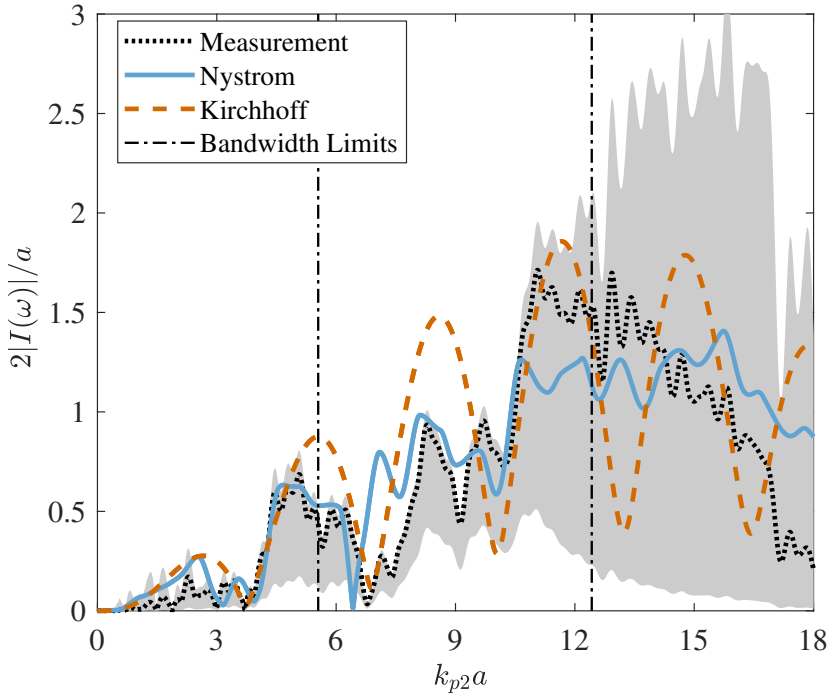


Figure 2.20: Magnitude of the integral $I(\omega)$ for the pill-box flaw for 30° incidence at point A.

Although, in general, the KA model can be applied to compute pulse-echo signals without the small-flaw approximation according to Equation (2.13) [117, 118], the KA model in this work was developed only under this approximation. Therefore, the KA result shown in Figure 2.19 was obtained using the TG model according to Equation (2.14). The KA signal was shifted by 0.456 $\mu$s for coinciding it with the measurement. We recall that in the TG model, the diffraction coefficients on the surface of the defect are approximated with their values at a fixed point ($\mathbf{x}_0$) chosen on or near the defect. If we assume that the two pulses in the KA response are generated primarily by the surface fields in the vicinity of the left and right tips of the defect, respectively, then according to Equation (2.13), the amplitudes of these two pulses are weighted by the approximate value of the diffraction coefficients near the two tips, respectively. Therefore, by taking $\mathbf{x}_0$ to be the left tip, we can minimize the error (due to the small-flaw assumption) in the KA-prediction of the leading pulse. Likewise, the error in the trailing pulse is minimized by taking $\mathbf{x}_0$ to be the right tip. A middle ground in the errors of the two pulses is achieved by choosing $\mathbf{x}_0$ as any point close to the center of the pillbox. For the KA waveform shown in Figure 2.19, $\mathbf{x}_0$ was taken as the left tip on the top surface of the pillbox to enable comparison of the amplitude of the leading pulse with the measurement.

The simulated and measured amplitudes are shown in Table 2.6. Both the KA and the measured amplitudes are higher than that of the NM. For the KA, this is due to modeling errors and for the measurement, this is due to additional scattering from the lateral and bottom surfaces. This explains the surprisingly accurate predictions of the KA. Still, so far as the amplitude of the leading pulse is concerned, either of the models can be used roughly within 10% error. For crack-like flaws of small diameter, the overlapping of the surface wave contribution with the leading pulse may lead to larger errors in the KA-predicted amplitudes. The magnitudes of the integral $I(\omega)$ computed with both the models are shown in Figure 2.20. The KA response was obtained by assuming the velocity diffraction coefficients to be constant over the defect surface (small-flaw assumption). The sensitivity limits are plotted by varying $\epsilon_1$ in $\{0.09, 0.12, 0.18\}$ and $\epsilon_2$ in $\{0.01, 0.03, 0.09\}$, where the result corresponding to $\epsilon_1 = 0.12$ and $\epsilon_2 = 0.03$ is considered nominal. The same sensitivity

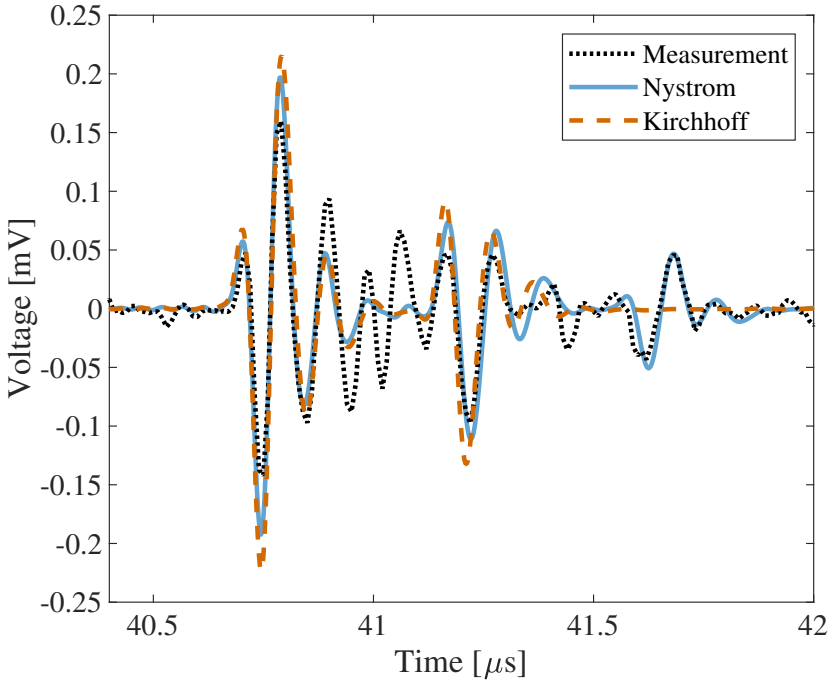


Figure 2.21: Pulse-echo signals for the pill-box flaw corresponding to 45° incidence at point A.

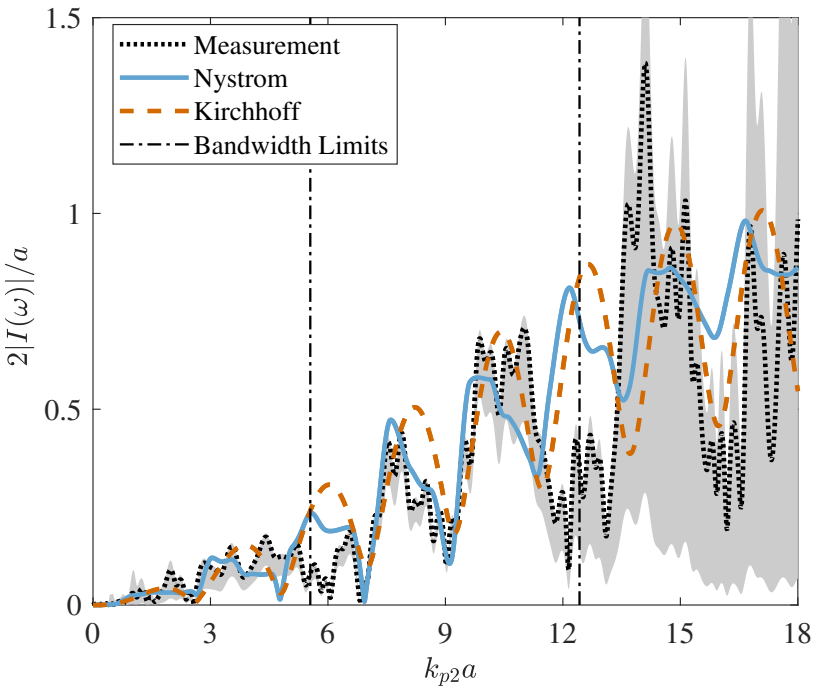


Figure 2.22: Magnitude of the integral $I(\omega)$ for the pill-box flaw for 45° incidence at point A.

parameter settings are retained for all the oblique incidence simulations. The agreement between the NM and the measurement is good, whereas the KA response differs from them. This is due to the small-flaw assumption as well as the missing surface-wave contribution in the KA. The slight discrepancy between the NM and the measurement is possibly due to experimental uncertainties, and, particularly, due to additional scattering from the lateral and bottom surfaces of the defect as explained above.

Results for the 45° incidence angle are shown in Figures 2.21, 2.22 and Table 2.7. It is well-known that the accuracy of the KA in representing edge-diffractions decreases progressively with an increase in the angle of incidence. We see this effect in the pulse-echo waveforms and the corresponding amplitudes. With an error of about 30-40% in the amplitude prediction, the KA may be considered inadequate for modeling scattering beyond 45°. As a tangential remark, the time-difference between the leading pulse and the surface wave pulse in Figure 2.19 differs from that in Figure 2.21 by a small value. This value matches that predicted under the assumption that a surface wave (which is initiated at the left tip) scatters off the defect at its right tip, serving as an empirical confirmation of the expected path of propagation of the surface wave.

Table 2.7: Pulse-echo amplitudes (in mV) for Crack C for 45° incidence at point A.

| Amplitude | $\epsilon_1$ | Measurement | NM | KA | % Error NM | % Error KA |
|---|---|---|---|---|---|---|
| $A_1$ | 0.09 | 0.15971 | 0.198 | 0.225 | 24.0 | 40.9 |
| | 0.12 | 0.15971 | 0.197 | 0.223 | 23.3 | 39.6 |
| | 0.18 | 0.15971 | 0.193 | 0.219 | 20.8 | 37.6 |
| $A_2$ | 0.09 | 0.19025 | 0.224 | 0.253 | 17.7 | 33.0 |
| | 0.12 | 0.19025 | 0.222 | 0.251 | 16.7 | 31.9 |
| | 0.18 | 0.19025 | 0.218 | 0.246 | 14.6 | 29.3 |

#### 2.3.2.3 Oblique Incidence at Point B

Figure 2.23 shows the schematic of the oblique incidence tests corresponding to point B. The results for 30° incidence angle are shown in Figures 2.24, 2.25 and Table 2.8. The KA result was obtained with the TG model, where the point $\mathbf{x}_0$ for approximation of the diffraction coefficients

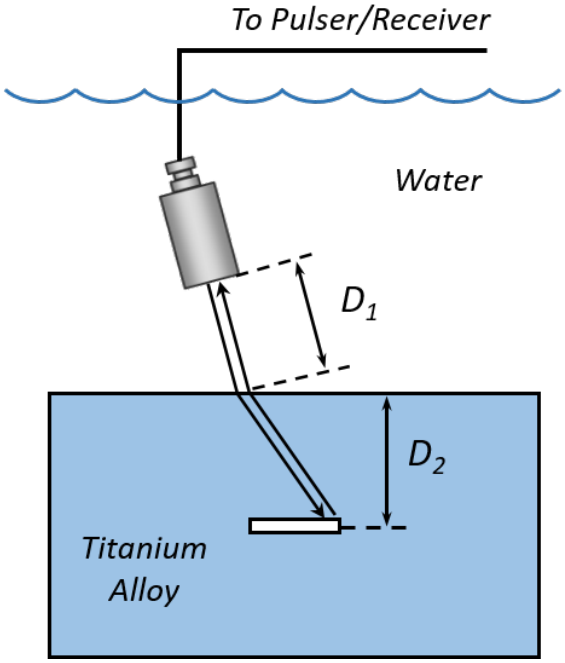


Figure 2.23: Schematic of pulse-echo measurement of a Titanium alloy containing a crack-like void. Oblique incidence on point B.

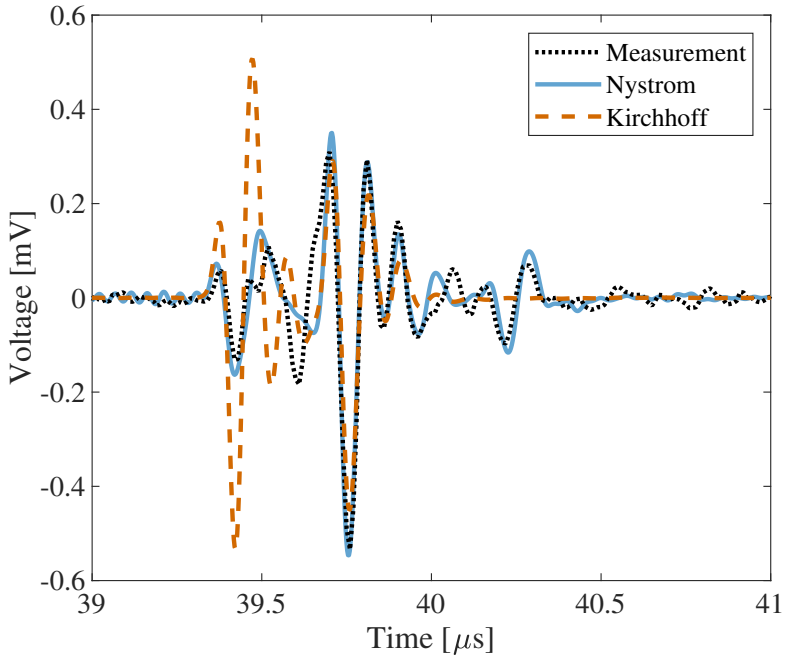


Figure 2.24: Pulse-echo signals for the pill-box flaw corresponding to 30° incidence on the right tip (point B).

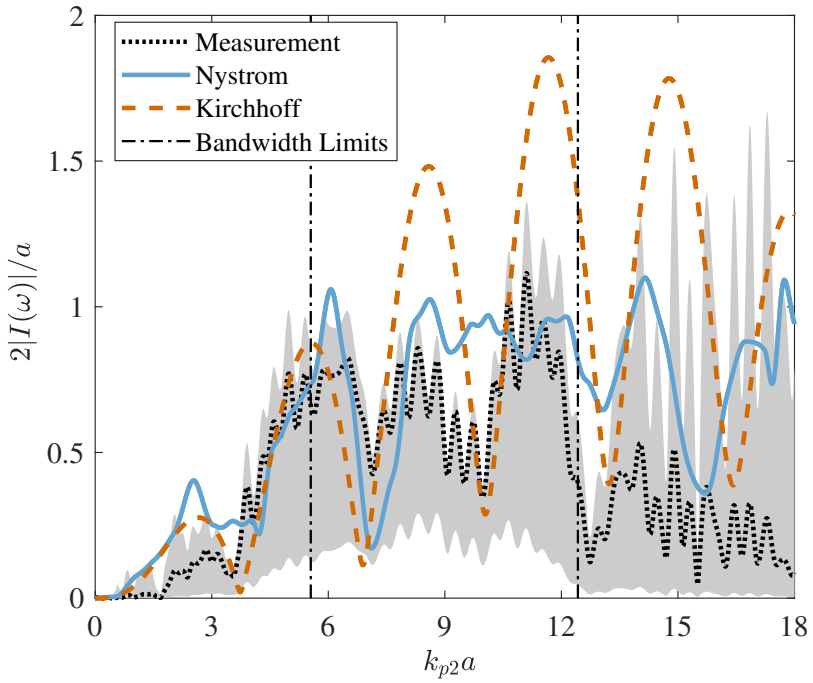


Figure 2.25: Magnitude of the integral $I(\omega)$ for the pill-box flaw for 30° incidence at point B.

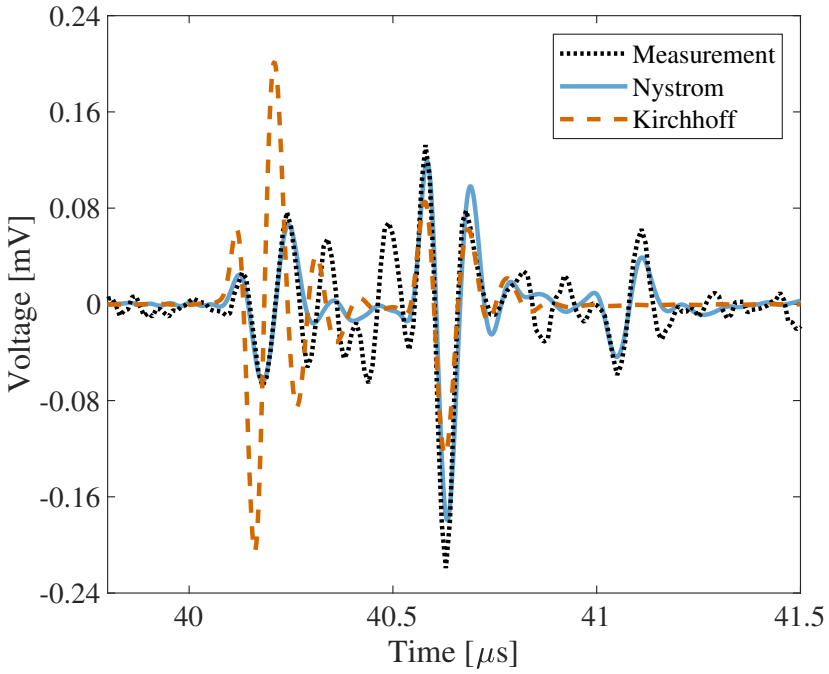


Figure 2.26: Pulse-echo signals for the pill-box flaw corresponding to 45° incidence at point B.

was chosen as the right tip on the top surface of the defect. This choice of $\mathbf{x}_0$ minimizes error (due to the small flaw assumption) in the trailing pulse of the KA pulse-echo prediction. Similar to pulse-echo results for point A, the NM agrees well with the measurement. Both the models simulate the reflection from the right tip quite accurately. In the KA signal, the leading pulse has larger amplitude than the trailing pulse because beam variations on the surface of the defect are ignored. Further, the choice of $\mathbf{x}_0$ maximizes error in the leading pulse prediction of the KA. Therefore, the leading pulse in the KA model was not considered for calculating the amplitudes in Table 2.8. We observe that both models predict the amplitudes within 15% error. The results for the 45° incidence are shown in Figures 2.26, 2.27 and Table 2.9. Again, as in the case of point A, the KA amplitudes have an error of about 40%, and, therefore, the KA model is inadequate for incidence angles above 45°.

Table 2.8: Pulse-echo amplitudes (in mV) for Crack C for 30° incidence at point B.

| Amplitude | $\epsilon_1$ | Measurement | NM | KA | % Error NM | % Error KA |
|---|---|---|---|---|---|---|
| $A_1$ | 0.09 | 0.53393 | 0.550 | 0.453 | 3.01 | 15.2 |
| | 0.12 | 0.53393 | 0.546 | 0.450 | 2.26 | 15.7 |
| | 0.18 | 0.53393 | 0.536 | 0.441 | 0.39 | 17.4 |
| $A_2$ | 0.09 | 0.53433 | 0.554 | 0.458 | 3.68 | 14.3 |
| | 0.12 | 0.53433 | 0.551 | 0.455 | 3.12 | 14.8 |
| | 0.18 | 0.53433 | 0.540 | 0.446 | 1.06 | 16.5 |

Table 2.9: Pulse-echo amplitudes (in mV) for Crack C for 45° incidence at point B.

| Amplitude | $\epsilon_1$ | Measurement | NM | KA | % Error NM | % Error KA |
|---|---|---|---|---|---|---|
| $A_1$ | 0.09 | 0.21929 | 0.181 | 0.126 | 17.5 | 42.5 |
| | 0.12 | 0.21929 | 0.180 | 0.125 | 17.9 | 43.0 |
| | 0.18 | 0.21929 | 0.176 | 0.126 | 19.7 | 43.9 |
| $A_2$ | 0.09 | 0.21738 | 0.183 | 0.128 | 15.8 | 41.1 |
| | 0.12 | 0.21738 | 0.181 | 0.127 | 16.7 | 41.6 |
| | 0.18 | 0.21738 | 0.178 | 0.125 | 18.1 | 42.5 |

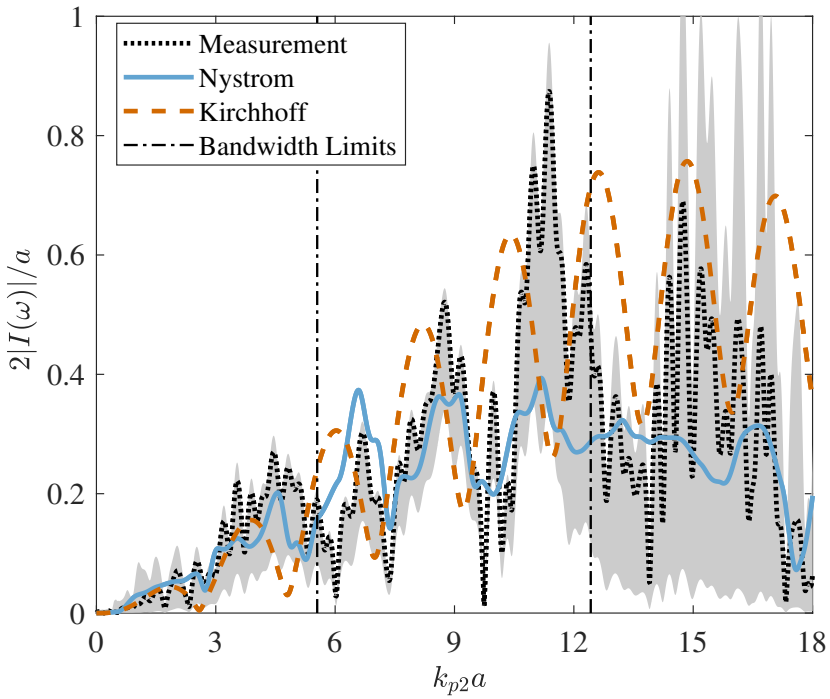


Figure 2.27: Magnitude of the integral $I(\omega)$ for the pill-box flaw for 45° incidence at point B.

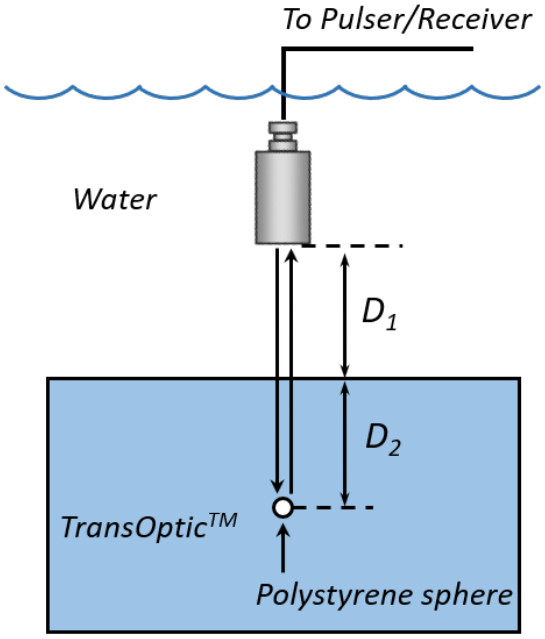


Figure 2.28: Schematic of pulse-echo measurement of a TransOptic™ specimen containing a polystyrene sphere.

### 2.3.3 Polystyrene Sphere in TransOptic Specimen

The following example does not appear in the WFNDEC benchmarks. Figure 2.28 shows a schematic of the inspection. The inspection sample is made of TransOptic$^{TM}$ material, which is a thermoplastic acrylic supplied by the company Buehler [133]. A polystyrene sphere of radius 325 $\mu$m is embedded in it. We obtained pulse-echo measurements from this sample using a spherically-focused transducer at normal incidence. The inspection parameters are listed in Table 2.10. The distances $D_1$ and $D_2$ are 86.98 mm and 6.1 mm, respectively. The process applied for determining some of the inspection parameters is described below.

The longitudinal wave speed in the sample was calculated from the time differences between the front and back-wall reflections at three different transducer heights. The value reported in Table 2.10 is the mean of the three measurements. Similarly, the shear wave speed was calculated from time differences between the first and second back-wall reflections measured with a contact shear wave transducer. Again, the reported value is a mean of three different measurements. Attenuation coefficient of the longitudinal wave in the sample was determined from the front and back wall reflections using the procedure outlined in [13, 9.2.2], with the parameter $\varepsilon$ appearing in the deconvolution process set to 0.01 times the maximum value of $|F|$ (see Equation (9.91) in [13]). Standard values for the wave speeds and mass density of polystyrene [120] were used for the flaw due to the difficulty in measuring these parameters for a small spherical sample. The effective focal length of the transducer was obtained by placing the transducer above the inspection sample and maximizing the amplitude of front-wall reflection by varying the height of the transducer face measured from the front wall. The height at which the signal is maximized is taken as the effective focal length. To be sure, this height is not equal to the true effective focal length [13, §8.2.2.1-8.2.2.3], but lies close to it. A small error is introduced by equating them.

Figure 2.29 shows the calibration reference signal obtained from the frontwall of the inspection sample. The 6 dB beamwidth at the flaw is about four times the radius of the polystyrene sphere at the upper frequency bandwidth limit. Therefore, the small-flaw model is applied to simulate pulse-echo signals. Figure 2.30 shows the simulated and measured pulse-echo signals. The measured

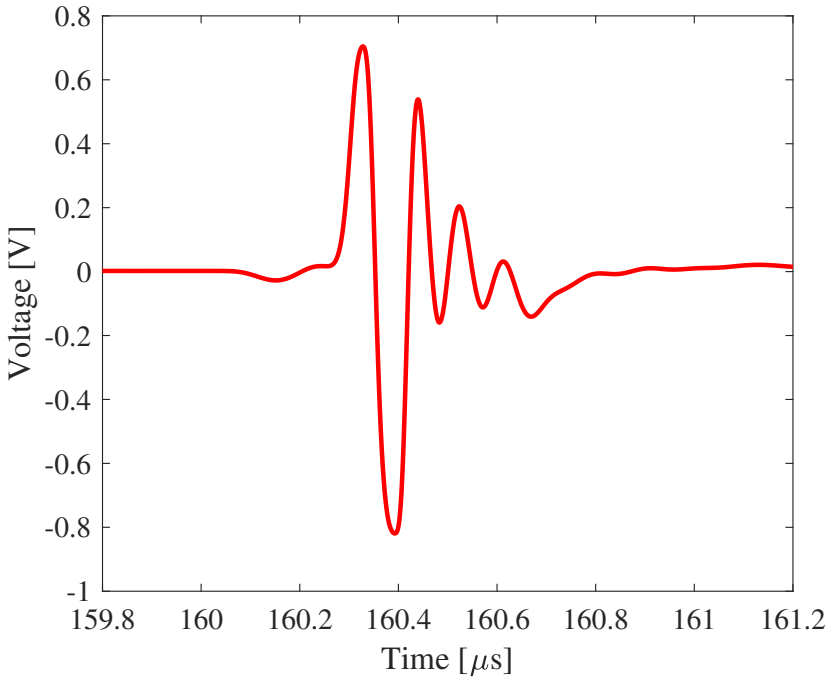


Figure 2.29: Front-wall reflection from the TransOptic$^{TM}$ sample in the calibration measurement.

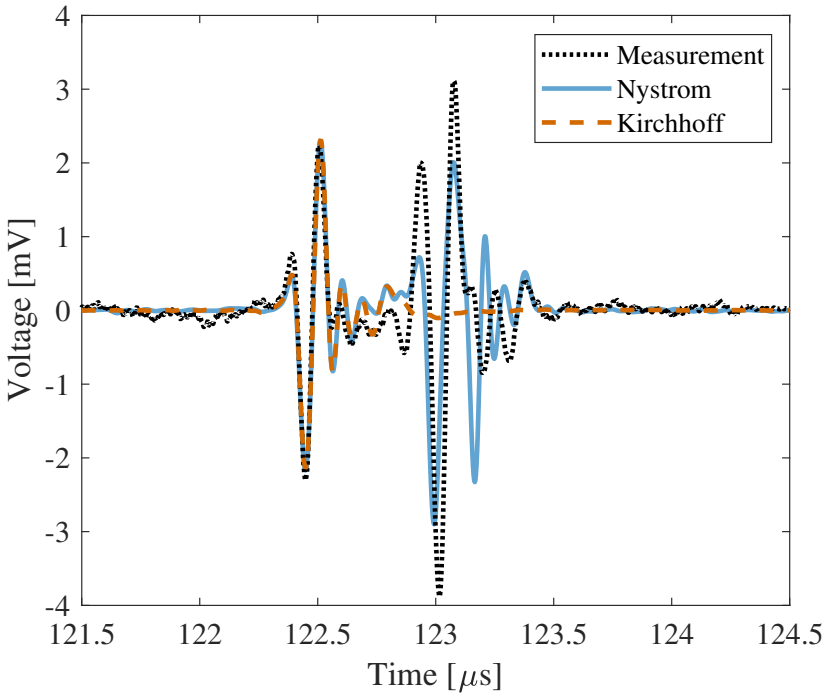


Figure 2.30: Pulse-echo signals obtained from the polystyrene sphere embedded in the TransOptic$^{TM}$ sample.

Table 2.10: Parameters for the inspection in Section 2.3.3.

| Parameter | Value |
|---|---|
| P-wave speed in water (m/s) | 1486.6 |
| Density of water (kg/m$^3$) | 1000 |
| Attenuation in water (Np/m) ($f$ in MHz) | 0.02479 $f^2$ |
| P-wave speed in block (m/s) | 2689±25 |
| S-wave speed in block (m/s) | 1340±28 |
| Density of block (kg/m$^3$) | 1171 |
| P-wave attenuation in block (Np/m) ($f$ in MHz) | 8.001654 $f^{1.0792}$ |
| P-wave speed in polystyrene (m/s) | 2400 |
| S-wave speed in polystyrene (m/s) | 1280 |
| Density of polystyrene (kg/m$^3$) | 1060 |
| Radius of transducer (mm) | 6.35 |
| Effective focal length (in) | 4.66 |

signal consists of two distinct pulses: the earlier pulse is the leading-edge reflection, and the later pulse is primarily due to reflection from the point at which the incident wave leaves the sphere (trailing-edge reflection). The contributions of internal reflections and creeping waves are also present in the later pulse. Both models predict the leading-edge reflection quite well. However, the KA models only the leading-edge reflection, and hence is inappropriate for modeling inclusions. Particularly, when the size of inclusion is relatively small, the leading-edge pulse overlaps with the signals arising from other reflections. This may lead to a large error in the KA pulse-echo amplitude, which is a key parameter in MAPOD studies.

The NM pulse-echo signal includes contributions from all reflections. However, the amplitude of the later-time pulse in NM is lower than that of the measurement. This can be explained by uncertainties in the determination of wave speeds of the inclusion and specimen. For weak scatterers particularly, it is well-known from Born approximation theory that the amplitude of reflected waves is highly sensitive to the difference in wave speeds of the scatterer and inclusion [21, 134]. For example, Figure 2.31 shows the NM pulse-echo prediction obtained when the longitudinal wave speed of the inclusion is assumed to deviate from its nominal value by -50 m/s. Compared to the previous case, we observe that the amplitude of the later-pulse fits the measurement better, with a

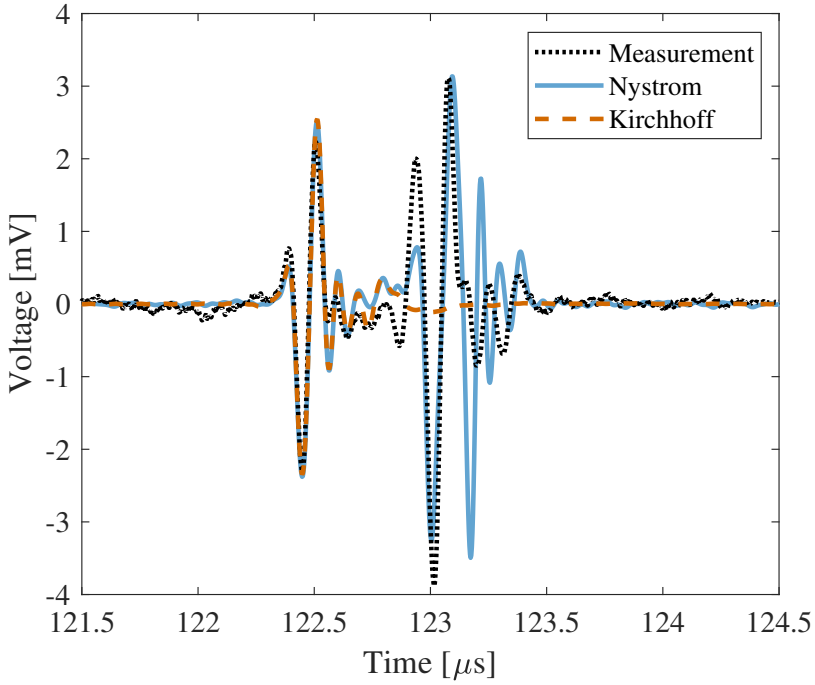


Figure 2.31: Pulse-echo signals for the TransOptic$^{TM}$ inspection with longitudinal wave speed of the inclusion modified to $c_p = 2350$ m/s.

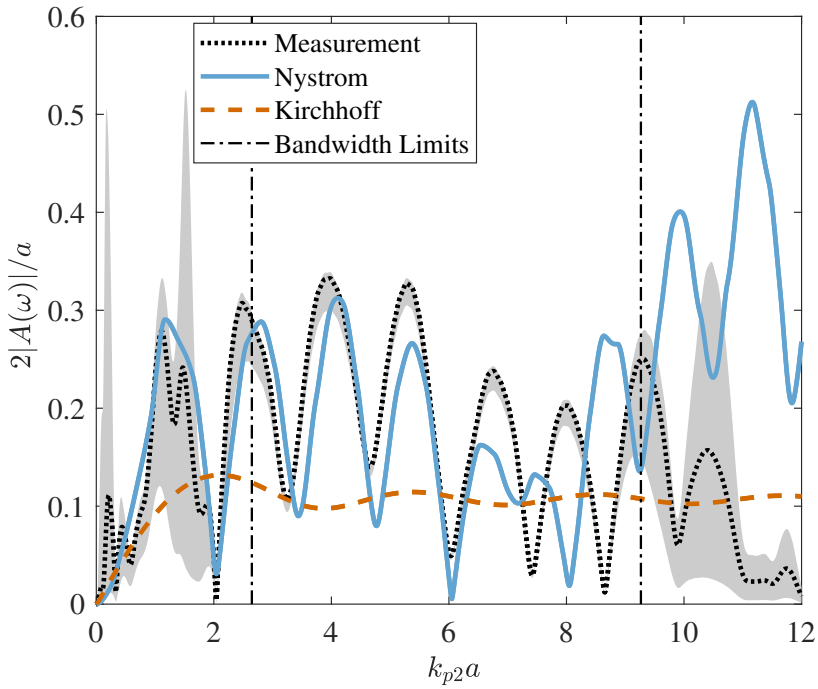


Figure 2.32: Measured and simulated scattering amplitudes for the spherical polystyrene inclusion in the TransOptic$^{TM}$ specimen.

relatively lower change in the amplitude of the leading-edge pulse. In addition, uncertainties in the measurement of the effective focal length of the transducer influence the accuracy of the system efficiency factor (see Section 2.2.3). This is possibly another reason for the deviation of NM results from measurement.

Pulse-echo amplitudes of the leading-edge pulse are compared in Table 2.11. The errors in KA and NM are similar. However, for relatively small inclusions, the amplitude predictions of KA will have large errors, as mentioned before. The measured and simulated SAs are shown in Figure 2.32. Unlike the KA result, the SAs of NM and measurement show significant oscillations. This is due to the existence of two distinct pulses in the corresponding time-domain signals. The NM result agrees well with the measurement. The disagreement towards the higher frequencies in the bandwidth is due to uncertainties in the wave speed, as mentioned above, and the small-flaw approximation applied in the simulation model.

Table 2.11: Pulse-echo amplitudes (in mV) for the TransOptic inspection.

| Amplitude | $\epsilon_1$ | Measurement | NM | KA | % Error NM | % Error KA |
|---|---|---|---|---|---|---|
| $A_1$ | 0.06 | 2.304 | 2.316 | 2.335 | 0.52 | 1.35 |
| | 0.09 | 2.304 | 2.297 | 2.314 | 0.30 | 0.43 |
| | 0.12 | 2.304 | 2.271 | 2.286 | 1.43 | 0.78 |
| $A_2$ | 0.06 | 2.625 | 2.562 | 2.511 | 2.40 | 4.34 |
| | 0.09 | 2.625 | 2.545 | 2.496 | 3.05 | 4.91 |
| | 0.12 | 2.625 | 2.521 | 2.474 | 3.96 | 5.75 |

## 2.4 Conclusions

In this chapter, KA and NM are applied to simulate various benchmark problems, and their predictions for standard measurement outputs are compared with measurements. KA is suitable for modeling specular scattering from defects. For relatively small spherical voids ($a \sim \lambda/4$), the largest error observed in KA pulse-echo amplitude predictions is around 10% of the true amplitude. A higher error is expected for smaller voids. The NM is an attractive choice for modeling such

voids since it performs consistently even with a decrease in the void size. The largest differences between the two models are observed for inclusions and for edge-diffractions from cracks at angles greater than 45°. In the latter case, amplitude errors in KA are higher than those of NM by around 20 percentage points. Therefore, full-wave models such as the NM make substantial improvements to model predictions in such cases. The scattering spectra obtained from KA differ quite distinctly from the measured response for both inclusions and non-specular crack inspections. Hence, full-wave models are the proper choice in applications that require knowledge of the scattering spectra, for example, for classifying defects.

# CHAPTER 3. NUMERICAL STUDY OF HIGH-ORDER NYSTRÖM METHOD FOR ELASTIC WAVE SCATTERING

This chapter presents an argument for the use of high-order discretization as a means to reduce the computational resource requirements of BEMs. We focus particularly on a locally-corrected Nyström method (NM) for 3D elastodynamic scattering problems. Two versions of this NM which use different discretization orders, respectively, are compared in terms of their computational time and memory usage for solving large-scale model problems in elastic-wave scattering. It is demonstrated that despite the additional computations required for second-order discretization, higher convergence rates drastically reduce the total resource requirement for achieving a given level of output error, making the NM viable for practical applications in UNDE.

## 3.1 Introduction

The computational time and memory utilization of BEMs is relatively high compared to approximation methods. A key parameter that decides the computational cost is the number of discretization variables ($N$) or degrees of freedom (DOFs) required by the BEM to achieve a given level of output accuracy. The asymptotic convergence rate is the rate at which the output error decreases with an increase in the number of DOFs (a process known as refinement) when $N$ is relatively large. The process of $h$-refinement involves decreasing the size of mesh elements as a means to increase the number of DOFs, and $p$-refinement involves increasing the degree of polynomials used for approximating the fields. Between two BEMs (more precisely, refinement methods), the method with higher convergence rate requires lower number of DOFs for a given level of error, assuming that the prescribed error is in the asymptotic regime. This does not, however, imply that higher-order methods have a lower computational resource requirement (for the same level of error) since the higher convergence rate may be achieved at a drastically higher computational cost.

In this chapter, we argue that adopting even second-order geometry and field discretizations in a locally-corrected NM (LC-NM) leads to a significant reduction in computational costs compared to methods based on lower-order discretizations. The following section gives an overview of the LC-NM considered in this thesis. Convergence rates for methods based on different discretization orders are compared in Section 3.3. Two LC-NMs with different orders of discretization are compared in Section 3.4 in terms of their computational time and memory usage for solving large-scale scattering problems. The data for the lower-order method are taken from [31].

## 3.2 High-order Nyström Method

This section provides an overview of the LC-NM considered in this thesis. The reader may refer to Section 4.3 for a full description of this method. The primary purpose of this section is to describe the sources of error in the LC-NM. This LC-NM is equivalent to a collocation-BEM in which surface fields are expanded using an interpolation technique and where the collocation and field interpolation points coincide with quadrature points on the mesh elements. Traditionally, the NM proceeds (i) by posing the underlying boundary integral equations on an exact geometric representation of the boundary, and (ii) discretizing the integrals using global quadrature rules, by which it implicitly commits to the existence of a global parametric description of the boundary. The assumption of a global parametric description is too restrictive on the types of defects that can be modeled since most CAD representations do not admit such descriptions. Restriction of the method to exact geometries excludes approximate representations of boundaries that are obtained, for example, from coarsening of features and subsequent refinements. We relax both the assumptions so as to allow the application of the NM to approximate geometric representations based on boundary-element meshes. It is in this sense that the term LC-NM is used throughout this thesis.

Consider a defect in an otherwise homogeneous unbounded elastic solid. The scattering problem involves finding the displacement and stress fields scattered from the defect in the presence of an

incident displacement field given by $\mathbf{u}^I(\mathbf{x})$. This problem can be reformulated in terms of the conventional boundary integral equations (CBIEs), which are given by (see Section 4.2.6)

$$\oint_S \left( \overline{\mathbf{G}}_+(\mathbf{x},\mathbf{x}') \cdot \mathbf{t}(\mathbf{x}') + \left[ \hat{\mathbf{n}}' \cdot \overline{\overline{\mathbf{\Sigma}}}^{(1)}_+(\mathbf{x},\mathbf{x}') \right]^T \cdot \mathbf{u}(\mathbf{x}') \right) dS(\mathbf{x}') + \frac{1}{2}\mathbf{u}(\mathbf{x}) = \mathbf{u}^I(\mathbf{x}), \tag{3.1a}$$

$$\oint_S \left( \overline{\mathbf{G}}_-(\mathbf{x},\mathbf{x}') \cdot \mathbf{t}(\mathbf{x}') + \left[ \hat{\mathbf{n}}' \cdot \overline{\overline{\mathbf{\Sigma}}}^{(1)}_-(\mathbf{x},\mathbf{x}') \right]^T \cdot \mathbf{u}(\mathbf{x}') \right) dS(\mathbf{x}') - \frac{1}{2}\mathbf{u}(\mathbf{x}) = 0. \tag{3.1b}$$

for $\mathbf{x} \in S$, where $\mathbf{u}$ and $\mathbf{t}$ are the displacement and traction fields, respectively, $S$ is the surface of the defect, and $\overline{\overline{\mathbf{\Sigma}}}^{(1)}_\pm(\mathbf{x},\mathbf{x}')$ and $\overline{\mathbf{G}}_\pm(\mathbf{x},\mathbf{x}')$ are the fundamental solutions of stress and displacement fields, respectively. The "+" and "-" subscripts distinguish fundamental solutions obtained with elastic material constants of the host and the defect, respectively.

Solutions to the CBIE-formulation provide the total displacement and traction fields on the surface of the defect. The scattered fields outside the defect can be computed from the surface fields using representation formulas. All numerical examples presented in this chapter involve the application of the LC-NM to the CBIE-formulation for solving the scattering problem. We assume a surface mesh of the defect that consists of a set of points on $S$ which can be mapped onto triangular patches through a prescribed connectivity between the points. If the surface of the defect is specified, for instance, in terms of a CAD representation, the first step involves constructing a surface mesh of the above-mentioned type from the CAD representation. Then, an approximation of $S$ is developed via patch-wise parametric interpolation using polynomial functions. Because of conformal interpolation, the resulting approximation $\tilde{S}$ consists of continuous but non-overlapping (except at the edges) curved triangular elements. Specifically, there are two interpolation parameters, $\xi_1$ and $\xi_2$, which lie in the reference triangular patch defined by $\Omega = \{(\xi_1,\xi_2) \in \mathbb{R}^2 \mid \xi_1,\xi_2 > 0, \xi_1+\xi_2 \leq 1\}$. For an interpolation scheme of order $M$, the interpolation functions are polynomials of degree $M$ in $\xi_1$ and $\xi_2$. We consider mesh interpolations of orders 1 and 2 in this implementation.

Equations (3.1) are rewritten by replacing $S$ with the approximation surface $\tilde{S}$. On each element of $\tilde{S}$, the displacement and traction fields are expanded using an interpolation technique wherein the interpolation nodes coincide with quadrature points on the element. All the quadrature points are internal to the element. Therefore, this interpolation technique can be considered as an expansion

of fields using non-conformal basis functions. The components of displacement and traction fields at the interpolation/quadrature points form the DOFs that need to be determined. According to the foregoing field interpolation, the integrals in Equation (3.1) can be written in the following form

$$\int\!\!\!\!\!\!-_{\tilde{S}} dS(\mathbf{x}')\ \overline{\mathbf{T}}^{(1)}_{+}(\mathbf{x},\mathbf{x}')\cdot\mathbf{u}(\mathbf{x}') = \sum_{p=1}^{N_p}\sum_{i=1}^{N_n}\int\!\!\!\!\!\!-_{\Delta_p} dS(\mathbf{x}')\ \overline{\mathbf{T}}^{(1)}_{+}(\mathbf{x},\mathbf{x}')\cdot\left[L_i^{(p)}(\mathbf{x}')\,u_{i\alpha}^{(p)}\mathbf{e}_\alpha^{(p)}(\mathbf{x}')\right],$$

$$\text{(sum over } \alpha = 1,2,3) \qquad (3.2)$$

where $\overline{\mathbf{T}}^{(1)}_{+}(\mathbf{x},\mathbf{x}') = \left[\hat{\mathbf{n}}'\cdot\overline{\overline{\mathbf{\Sigma}}}^{(1)}_{+}(\mathbf{x},\mathbf{x}')\right]^T$, $N_p$ is the total number of elements, $N_n$ is the number of interpolation points per element, $\Delta_p$ is the integration domain corresponding to the element with index $p$, $L_i^{(p)}:\Delta_p\to\mathbb{R}$ is an interpolation function such that $L_i^{(p)}(\mathbf{y}_j^{(p)})=\delta_{ij}$ for all interpolation nodes $\mathbf{y}_j^{(p)}$ ($j=1$ to $N_n$) in the $p^{th}$ element; $\mathbf{e}_\alpha^{(p)}(\mathbf{x}')$ for $\alpha=1,2,3$ are basis vectors at the point $\mathbf{x}'$ such that $\mathbf{u}(\mathbf{x}')=u_{i\alpha}^{(p)}\mathbf{e}_\alpha^{(p)}(\mathbf{x}')$ (sum over $\alpha$), and $u_{i\alpha}^{(p)}$ are unknowns which need to be determined. The interpolation functions $L_i^{(p)}$, when written as functions of the interpolation parameters $\xi_1$ and $\xi_2$, are polynomials of degree 0, 1, 2 or 3. See Section 4.3 for details.

Rewriting (3.1) by approximating all integrals as shown in (3.2) yields two equations containing the DOFs. These equations are valid for all $\mathbf{x}\in\tilde{S}$. A finite-dimensional system of equations is obtained by performing collocation at the interpolation/quadrature points and equating the components along the dual basis vectors. Let $\mathbf{x}_0=\mathbf{y}_j^{(q)}$ be a collocation point representing the $j^{th}$ interpolation point in the element with index $q$. Let $\tilde{\mathbf{e}}_\beta^{(q)}(\mathbf{x}_0)$, for $\beta=1,\ 2$ and 3, represent the dual basis vectors of the basis given by $\mathbf{e}_\alpha^{(q)}(\mathbf{x}_0)$. For convenience, let $\mathbf{e}_0$ represent $\tilde{\mathbf{e}}_\beta^{(q)}(\mathbf{x}_0)$. The equation corresponding to component $\beta$ at $\mathbf{x}_0$ is

$$\sum_{p=1}^{N_p}\sum_{i=1}^{N_n}\Bigg[t_{i\alpha}^{(p)}\int_{\Delta_p}\tilde{L}_i^{(p)}(\mathbf{x}')\ \mathbf{e}_0\cdot\overline{\mathbf{G}}_{+}(\mathbf{x}_0,\mathbf{x}')\cdot\mathbf{e}_\alpha^{(p)}(\mathbf{x}')\ dS(\mathbf{x}')+$$

$$u_{i\alpha}^{(p)}\int\!\!\!\!\!\!-_{\Delta_p} L_i^{(p)}(\mathbf{x}')\ \mathbf{e}_0\cdot\overline{\mathbf{T}}^{(1)}_{+}(\mathbf{x}_0,\mathbf{x}')\cdot\mathbf{e}_\alpha^{(p)}(\mathbf{x}')\ dS(\mathbf{x}')\Bigg]+\frac{1}{2}u_{j\beta}^{(q)}=\mathbf{e}_0\cdot\mathbf{u}^I(\mathbf{x}_0). \qquad (3.3)$$

Observe that the coefficients of DOFs are in the form of integrals over the domain $\Delta_p$. These coefficients constitute elements of the matrix which needs to be inverted for determining the DOFs.

If $\mathbf{x}_0$ is sufficiently away from $\Delta_p$, the coefficients can be computed using the same quadrature rule that defines the interpolation nodes, as shown below:

$$\int_{\Delta_p} dS(\mathbf{x}')\ \mathbf{e}_0 \cdot \overline{\mathbf{T}}_+^{(1)}(\mathbf{x}_0, \mathbf{x}') \cdot \left[ L_i^{(p)}(\mathbf{x}')\, \mathbf{e}_\alpha^{(p)}(\mathbf{x}') \right] = \sum_{j=1}^{N_n} w_j \mathbf{e}_0 \cdot \overline{\mathbf{T}}_+^{(1)}(\mathbf{x}_0, \mathbf{y}_j^{(p)}) \cdot \left[ L_i^{(p)}(\mathbf{y}_j^{(p)})\, \mathbf{e}_\alpha^{(p)}(\mathbf{y}_j^{(p)}) \right] \tag{3.4a}$$

$$= w_i \mathbf{e}_0 \cdot \overline{\mathbf{T}}_+^{(1)}(\mathbf{x}_0, \mathbf{y}_i^{(p)}) \cdot \mathbf{e}_\alpha^{(p)}(\mathbf{x}_i^{(p)}), \tag{3.4b}$$

where $w_j$ are the quadrature weights. Therefore, each coefficient can be computed with a single evaluation of the kernel function. More importantly, there is no interpolation error in the evaluated values of coefficients since quadrature points coincide with interpolation nodes. See Section 4.3.3 for the degree of exactness (order) of the quadrature rules used in this implementation. When $\mathbf{x}_0$ is one of the quadrature points inside $\Delta_p$, the integrand in (3.4a) is singular. Similarly, when $\mathbf{x}_0$ is close to $\Delta_p$ but not inside it, the integrand is nearly-singular. In both cases, singularity subtraction techniques are applied to compute the coefficients [30, Chap. 4]. The resulting values of coefficients have both quadrature and interpolation errors. Most UNDE applications require only the scattering spectra of the defect in the far-field. These far-field quantities can be expressed in the form of surface integrals over the defect, and computed using the same quadrature rule that is applied in field interpolation. The far-field quantities determined in this fashion have quadrature error but are free from field-interpolation error. Summing up, the primary sources of error are:

1. Interpolation error in geometry description.
2. Error in computation of matrix elements, which includes
   (a) quadrature error in near-field matrix elements,
   (b) interpolation error in near-field matrix elements, and
   (c) quadrature error in far-field matrix elements.
3. Quadrature error in calculating scattering spectra.

## 3.3 Numerical Study of Error and Convergence Rates

This section shows typical convergence rates ($h$-refinement) achieved with discretizations of various orders. First, consider scattering of a longitudinal plane wave from a spherical cavity of radius $a$. Assume a spherical coordinate system with $\theta$ denoting the polar angle. The cavity is centered at the origin, and the plane-wave is propagating along the positive $z$-axis. The mass density and Lamé constants of the host material are 3 kg/m$^3$, 1 N/m$^2$ and 1 N/m$^2$, respectively. The longitudinal-wave scattering amplitude [13, §10.2] of the cavity is calculated for 181 uniformly spaced values of $\theta$ in the range $[0, \pi]$. Let $\mathbf{A}_n$ be a vector of length 181 that stores the scattering amplitudes determined from the LC-NM. The relative error is defined as $||\mathbf{A}_n - \mathbf{A}_{\text{ref}}||_2/||\mathbf{A}_{\text{ref}}||_2$, where $\mathbf{A}_{\text{ref}}$ is the reference solution obtained from the separation-of-variables technique [13, §10.6.2].

Figure 3.1 shows the relative errors for $k_p a = \pi$, where $k_p$ is the longitudinal wave number. Let $N_g$ and $N_p$ represent the order of geometry interpolation and the degree of polynomials used in field interpolation, respectively. The nomenclature "Rule-$xy$" is used to distinguish results obtained with different discretization rules, where the numbers $x$ and $y$ represent the values of $N_g$ and $N_p$, respectively. Note that $N_p$ is related to the number of field interpolation points in each curvilinear element, and is thus related to the degree of exactness of the quadrature rule used for computing far-field matrix elements. The results for Rule-22 and Rule-23 are based on 20, 80, 320 and 1280 second-order elements, where refinement from one-level to the next is performed by refining each curvilinear triangle into four sub-triangles. The results for Rule-11 and Rule-10 are based on a similar refinement strategy, starting from 80 first-order elements. The convergence rate increases when either $N_g$ or $N_p$ is increased, except for Rule-23. For Rule-22, we observe that a relative error of 0.001 is achieved with just 8 interpolation nodes (on average) per shear wavelength, whereas methods based on first-order geometry discretization need at least twice as many nodes.

Rule-23 has the same convergence rate as Rule-22 because of the effect of geometry error (see [135, §3.2] for a similar observation in electromagnetic scattering problems). If the order of geometry interpolation and the number of elements is fixed, one would eventually reach a point where increasing the degree of polynomials used in field approximation does not lead to a significant

decrease in the error since the error in field approximation at that point would be sufficiently low compared to the effect of geometry error. This phenomena is also seen in high-order finite element methods [136, pp. 4137-4138]. If the error in scattering amplitude occurs mostly from geometry approximation, the convergence rate should depend solely on the order of geometry interpolation. This explains why Rule-23 has the same convergence rate as Rule-22.

To further support the above reasoning, the relative errors for all combinations of $N_g \in \{1,\ 2\}$ and $N_p \in \{0,\ 1,\ 2,\ 3\}$ are shown in Figure 3.2. For Rule-12 and Rule-13, we observe no further decrease in the error compared to Rule-11 for the same number of elements. However, when the order of geometry interpolation is increased to 2, we observe that the method with $N_p = 2$ gives lower error than that with $N_p = 1$ (for the same number of elements). The degree that the corresponding convergence rates differ by depends on the relative contributions of different sources of error mentioned in the previous section, where it should be noted that the total error is not additive.

The foregoing example indicates that methods with $N_p = 3$ may not be useful unless geometry interpolation is of order three or higher. This is because the error in scattering amplitude in this example occurs mostly from geometry error. Specifically, for a fixed second-order geometry representation, the error from Rule-23 is almost the same as that from Rule-22. It is indeed possible that for some other scattering problems, Rule-23 has lower error than Rule-22 for the same geometry representation. For example, consider the same scattering problem as above but at a higher frequency such that $k_p a = 2.648\pi$. The errors for different discretization rules are shown in Figure 3.3. Results for Rule-10 and Rule-11 are obtained by $h$-refinement starting from 80 first-order elements. For Rule-22 and Rule-23, the starting point is 20 second-order elements. Here, we find that for the same number of mesh elements, Rule-23 has lower error than Rule-22. However, for the same number of nodes per wavelength, $h$-refinement of Rule-22 still leads to a lower error than Rule-23.

If the wavenumber is increased further to $k_p a = 3.216\pi$, we find the opposite result: for the same number of nodes per wavelength, $h$-refinement of Rule-23 has lower error than Rule-22 when

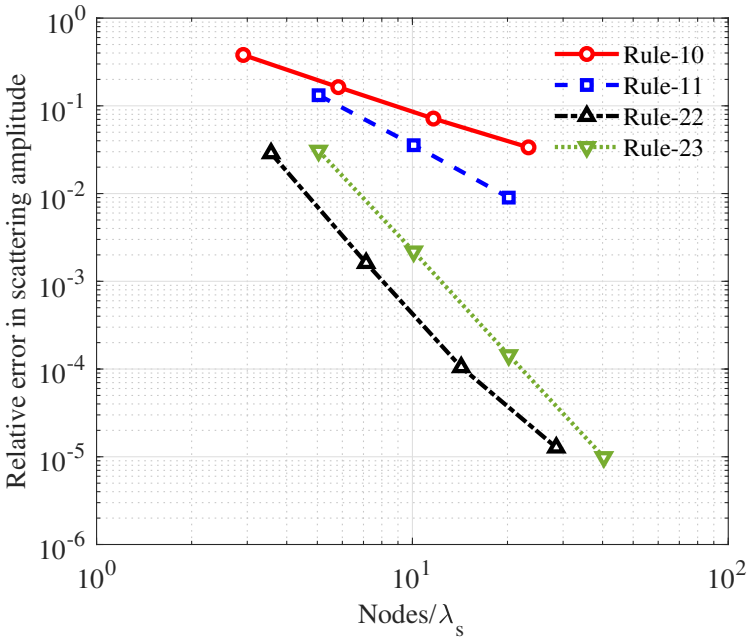


Figure 3.1: Relative error for $k_p a = \pi$ as a function of the average number of interpolation nodes per shear wavelength.

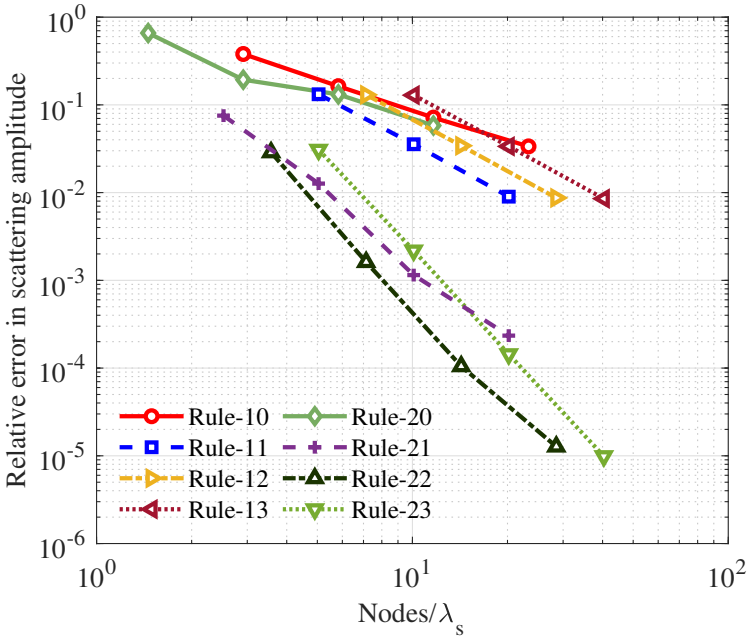


Figure 3.2: Relative error for $k_p a = \pi$ for all combinations of field and geometry discretizations.

the number of nodes is relatively high, as shown in Figure 3.4. In UNDE simulations, wavenumbers close to the above value correspond to frequencies near the upper limit of bandwidth. Therefore, rules with $N_p \geq 3$ maybe useful for simulations at the higher end of the frequency bandwidth even if geometry discretization is of order two. For scattering problems where the effect of geometry error is small, Rule-23 may indeed perform better than Rule-22 even at low frequencies. This is the case, for example, for scattering from a planar rectangular crack-like defect, where the geometry representation is exact. Planar defects of other shapes still have a geometry error because of imperfect representation of edges. Errors and convergence rates for scattering from traction-free circular cracks (open surfaces) are shown in Chapter 4 since the CBIE cannot model this scattering problem.

## 3.4 Comparison of Simulation Times and Memory Usage

In this section, the simulation times and memory usage of the foregoing LC-NM (Rule-22) are compared with those of the LC-NM in [31], which is based on first-order geometry representation and zeroth-order field discretization. For convenience, we refer to the former as the higher-order method, and the latter as the lower-order method. Both methods are accelerated using the multi-level fast multipole algorithm (MLFMA). See [30, 31, 137] for implementation details. All simulations of the higher-order method were performed on a Dell Precision T7500 workstation with two quad-core 2.13 GHz processors and 24 GB memory but using only a single core. The simulations in [31] were performed on a Dell Precision 690 workstation with two dual-core 3.0 GHz processors and 16 GB RAM but using only a single core.

The aim of the comparison in this section is to show that higher-order field and geometry discretization leads to a significant reduction in the total computational resource requirement due to higher convergence rate, despite introducing additional complexity in the calculation of singular and near-singular elements of the influence matrix. Many problems in practical UNDE modeling would remain impossible to tackle via boundary integral equation techniques without at least second-order field and geometry discretizations.

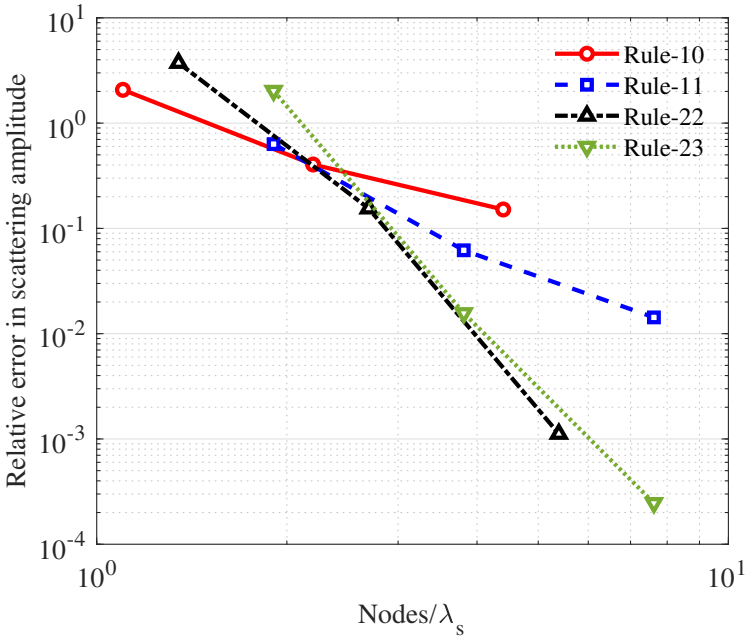


Figure 3.3: Relative error for $k_p a = 2.648\pi$ as a function of the average number of interpolation nodes per shear wavelength.

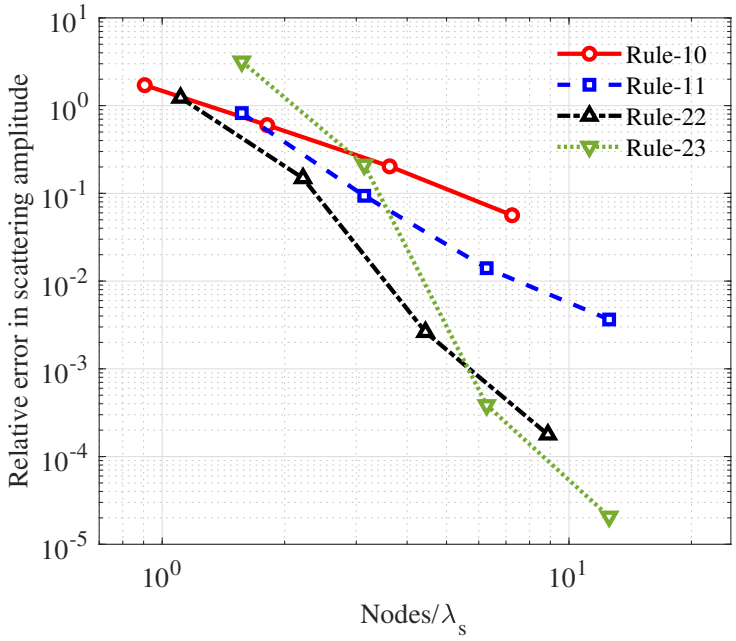


Figure 3.4: Relative error for $k_p a = 3.216\pi$ as a function of the average number of interpolation nodes per shear wavelength.

Table 3.1: CPU time and memory usage for scattering from rigid cube.

| | Reference [31] | Rule-22 |
|---|---|---|
| CPU Time (hr.) | 64.1 | 1.03 |
| Memory (GB) | - | 5.8 |
| No. of unknowns | 343,224 | 31,104 |
| MLFMA levels | 5 | 4 |

### 3.4.1 Rigid Cube

Consider scattering of a longitudinal plane-wave from a rigid cube inside an elastic solid. The mass density ($\rho$), Poisson's ratio ($\nu$) and normalized longitudinal wavenumber ($k_p a$) of the elastic solid are 1 kg/m$^3$, 0.5 and 20, respectively, where $a$ is half of the side length of the cube. The incident wave is traveling along the negative $z$-axis. The cube is centered at the origin, with its faces aligned with the coordinate planes. A standard spherical coordinate system is assumed. For the higher-order method, the number of mesh elements is 1728, leading to 31,104 DOFs. Since exact analytical solutions are not available for this problem, this number was selected based on the criteria of obtaining external fields that are visually similar to those in [31]. This enables a fair comparison between the simulation times of the two methods.

Figure 3.5 shows magnitudes of the radial and polar components of displacement at a distance of $5a$ from the origin, calculated using the higher-order method. Table 3.1 shows the CPU time and number of DOFs of both methods. The size of the cube is about six times the longitudinal wavelength inside the host material. The relative size of the defect is comparable to that observed near the higher-end of the frequency range in immersion testing measurements. The CPU time for the lower-order Nyström method is prohibitively large to be of any practical use and can be reduced by at least by a factor of 50 using second-order discretization.

### 3.4.2 Rigid Sphere

Next, we consider scattering of a longitudinal plane-wave from a rigid sphere inside an elastic solid. The mass density ($\rho$), Poisson's ratio ($\nu$) and normalized longitudinal wavenumber ($k_p a$)

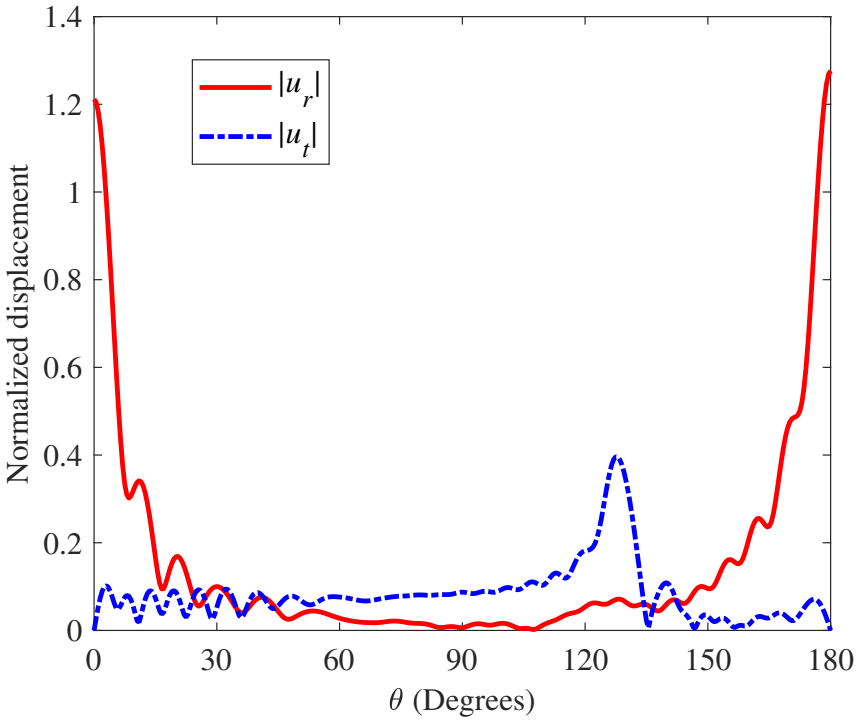


Figure 3.5: Magnitude of scattered displacement field at $r = 5a$ due to a longitudinal plane-wave incident on a rigid cube in an elastic solid ($k_p a = 20$). Radial component is $u_r$. Polar component is $u_t$. Fields are normalized by the variable $a$.

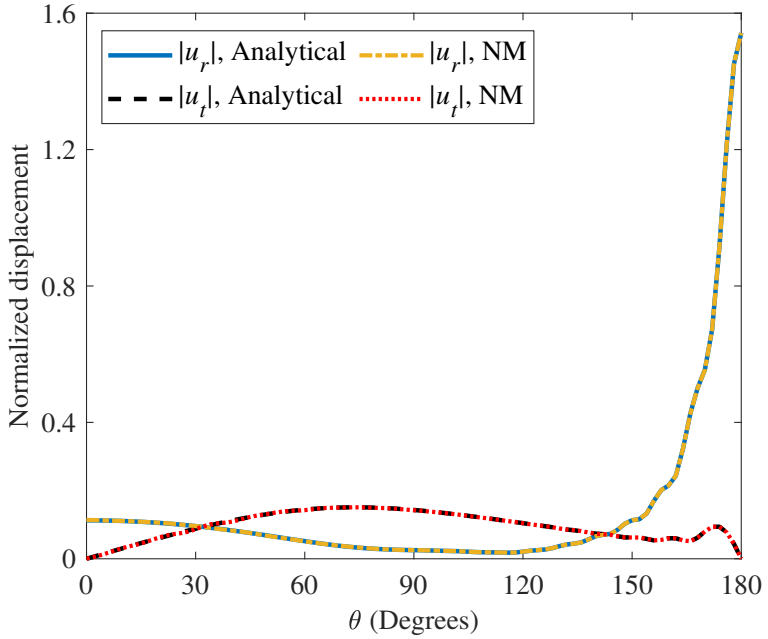


Figure 3.6: Magnitude of scattered displacement field at $r = 5a$ due to scattering from a rigid sphere in an elastic solid ($k_p a = 20$). Radial component is $u_r$. Polar component is $u_t$. Fields are normalized by the variable $a$.

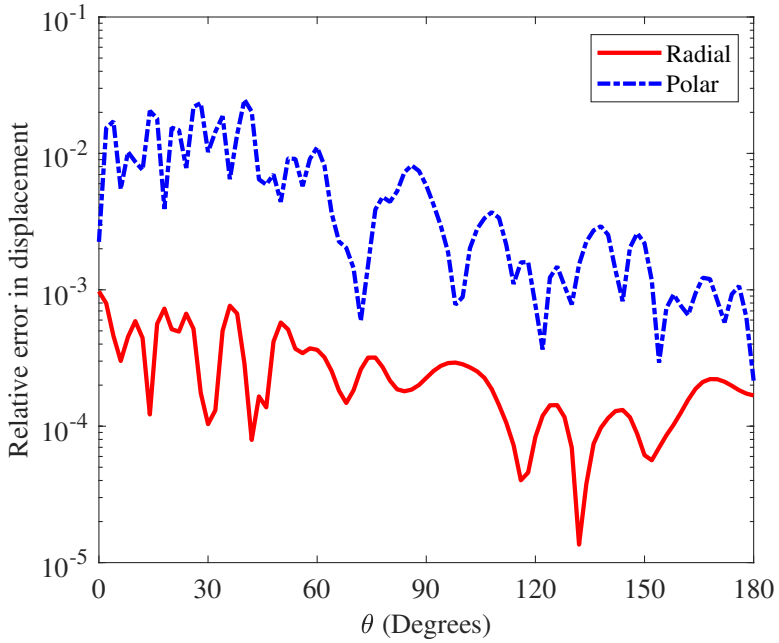


Figure 3.7: Relative errors in the radial and polar components of the displacement field for scattering from rigid sphere ($k_p a = 20$).

Table 3.2: CPU time and memory usage for scattering from rigid sphere.

| | Reference [31] | Rule-22 |
|---|---|---|
| CPU Time (hr.) | 50.7 | 1.23 |
| Memory (GB) | - | 2.9 |
| No. of unknowns | 317,196 | 23,040 |
| MLFMA levels | 5 | 5 |

of the host material are 1 kg/m$^3$, 0.1 and 20, respectively, where $a$ is the radius of the sphere. The incident wave travels along the negative $z$-axis. Magnitude of the scattered displacement field at a radial distance of $5a$, computed from the higher-order method, is shown in Figure 3.6. This solution is generated using 1280 second-order mesh elements and 23,040 DOFs. Mesh density for the higher-order method is set such that its solution matches the exact analytical solution [13, §10.6.2] at least as closely as in [31].

Since relative errors in displacement fields are not shown in [31], a quantitative comparison of the accuracy of the higher and lower-order methods is not possible. The errors in the radial and polar components of the displacement calculated from the higher-order method are shown Figure 3.7. Both errors are normalized by the maximum value of the corresponding component over $\theta \in [0, \pi]$. The error in the polar component is higher because the radial and polar components of displacement are generated exclusively by scattered longitudinal and shear waves, respectively. Since shear wavelength is smaller than the longitudinal wavelength, a higher mesh resolution is needed to capture shear waves at the same level of accuracy as longitudinal waves. Table 3.2 compares total computation time of the two methods. The higher-order Nyström method performs about 40 times faster than the lower-order method.

### 3.4.3 Elastic Sphere

The third example consists of scattering from a spherical elastic inclusion. The incident wave is same as that in the previous two examples. The mass density ($\rho$), longitudinal wave speed ($c_p$) and shear wave speed ($c_s$) of the host medium are 1 kg/m$^3$, 0.95 m/s and 0.63 m/s, respectively,

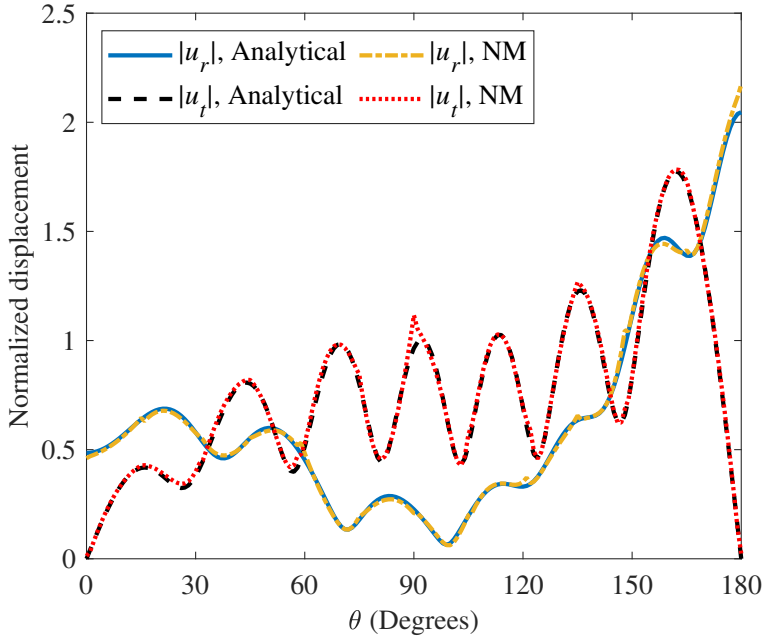


Figure 3.8: Magnitude of surface displacement field on a cut-plane for scattering from a spherical elastic inclusion in an elastic solid ($k_p a = 8$). Radial component is $u_r$. Polar component is $u_t$. Fields are normalized by the variable $a$.

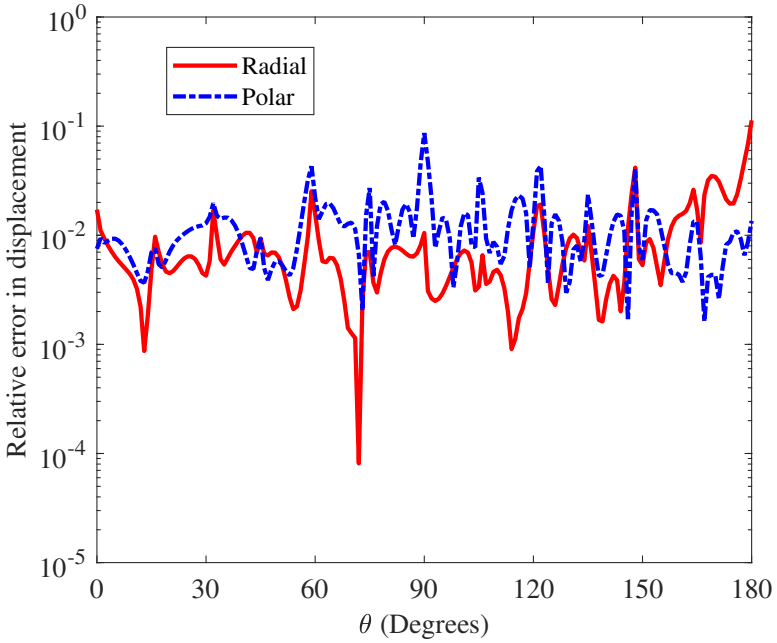


Figure 3.9: Relative errors in the radial and polar components of the surface displacement field for scattering from a spherical elastic inclusion in an elastic solid ($k_p a = 8$).

Table 3.3: CPU time and memory usage for scattering from spherical inclusion.

| | Reference [31] | Rule-22 |
|---|---|---|
| CPU Time (hr.) | 55.9 | 2.67 |
| Memory (GB) | 12 | 1.3 |
| No. of unknowns | 237,600 | 11,520 |
| MLFMA levels | 5 | 3, 4 |

and those of the embedded sphere are 2 kg/m$^3$, 0.77 m/s and 0.5 m/s, respectively. The frequency is set such that the normalized value of the longitudinal wavenumber in the host medium ($k_p a$) is 8. The surface displacement on a cut-plane calculated using the higher-order method is shown in Figure 3.8. The exact analytical solution is also shown for reference. The numerical solution is calculated using 320 second-order elements and 11,520 DOFs. As in the previous two examples, the number of mesh elements was set high enough to ensure that the solution matches the analytical result at least as closely as in [31]. Relative errors are shown in Figure 3.9.

The CPU time and memory usage of both methods are shown in Table 3.3. In the MLFMA solution of the higher-order method, the number of levels corresponding to the Green's functions of the host and scattering medium are three and four, respectively. The higher-order method leads to a significant reduction in the number of DOFs, total simulation time and memory requirement. For comparison, solutions generated using Rule-11 with 1280 and 5120 first-order elements are shown in Figures 3.10 and 3.12, respectively. Discontinuities in the NM results are due to the use of non-conforming basis functions, which are discontinuous between mesh elements. Corresponding errors are shown in Figures 3.11 and 3.13. For convenience, these two instances of Rule-11 will be called Rule-11a and Rule-11b, respectively. The number of DOFs for Rule-11a and Rule-11b are $N = 23,040$ and $N = 92,160$, respectively. In both cases, the number of DOFs is higher than that used for Rule-22.

The solution error from Rule-11a is higher than the error from Rule-22, whereas the error from Rule-11b is slightly lower than that from Rule-22. A performance comparison of Rule-11 and Rule-22 is made in Table 3.4. Rule-22 performs better than Rule-11a in memory usage, matrix filling time

Table 3.4: Comparison of performance metrics of Rule-22 and Rule-11 for the spherical inclusion problem.

| | Rule-22 | Rule-11 | |
|---|---|---|---|
| | 320 triangles $N = 11,520$ | 1280 triangles $N = 23,040$ | 5120 triangles $N = 92,160$ |
| MLFMA levels | 3, 4 | 4, 5 | 4, 5 |
| Memory (GB) | 1.35 | 1.4 | 10.39 |
| Total simulation time (sec) | 9601 | 7957 | 27090 |
| Matrix filling time (sec) | 1140 | 1429 | 5745 |
| Iterative solver time (sec) | 8333 | 6330 | 20609 |
| Average time per iteration (sec) | 11.94 | 15.22 | 42.95 |
| Total number of iterations | 675 | 401 | 463 |

and average time per iteration, despite the former being more accurate than the latter. Rule-22 still has a higher total simulation time than Rule-11a since the total time is dominated by the iterative solution process, which is in turn a result of ill-conditioning of the CBIE formulation at relatively high frequencies. This will not be a concern, therefore, for well-conditioned BIE formulations since the number of iterations required by both Rule-22 and Rule-11a would be small in that case. Comparison between Rule-22 and Rule-11b indicates that the former performs significantly better in all computational performance metrics. The matrix filling time and time per iteration are lower for Rule-22 by a factor of 5 and 3.6, respectively. This comparison shows that for the same level of output error, Rule-22 may indeed have a lower matrix filling time and average time per iteration. Particularly, complexity in the calculation of near-field matrix elements in Rule-22 does not make the method less efficient than Rule-11 since the effect of this complexity on simulation times is offset by the difference in convergence rates of the two methods.

## 3.5 Conclusions

Methods based on first-order geometry and field discretizations are quite commonly used in the BEM for solving large-scale scattering problems since computation of near-field matrix elements, which is one of the most time-consuming parts of the BEM, is simplified by low-order

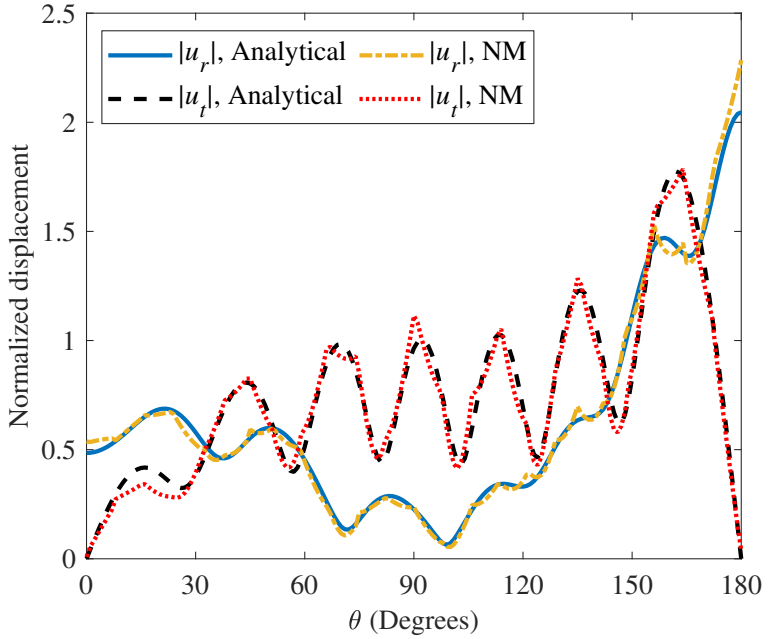


Figure 3.10: Magnitude of surface displacement field in the spherical inclusion problem ($k_p a = 8$). NM result is generated from Rule-11 with 1280 mesh elements. Radial component is $u_r$. Polar component is $u_t$. Fields are normalized by the variable $a$.

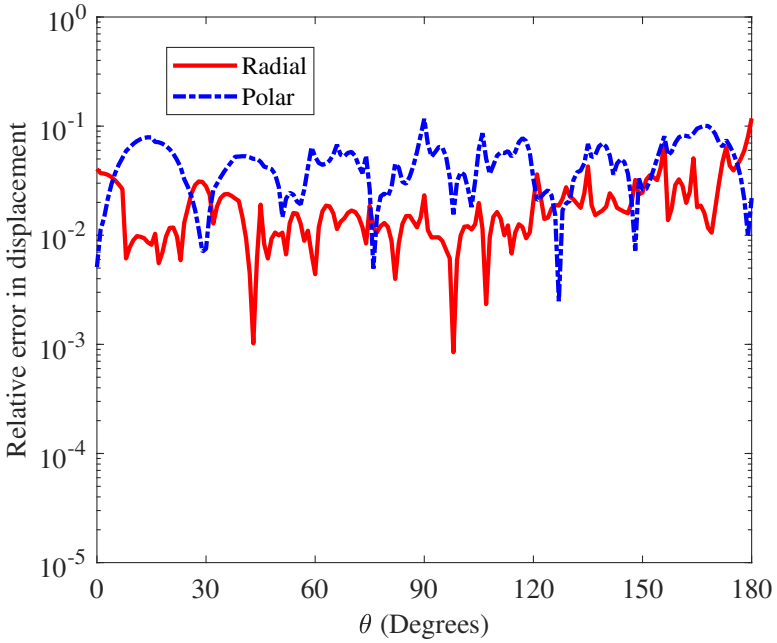


Figure 3.11: Relative errors in the radial and polar components of the surface displacement field on the spherical inclusion for Rule-11 with 1280 mesh elements.

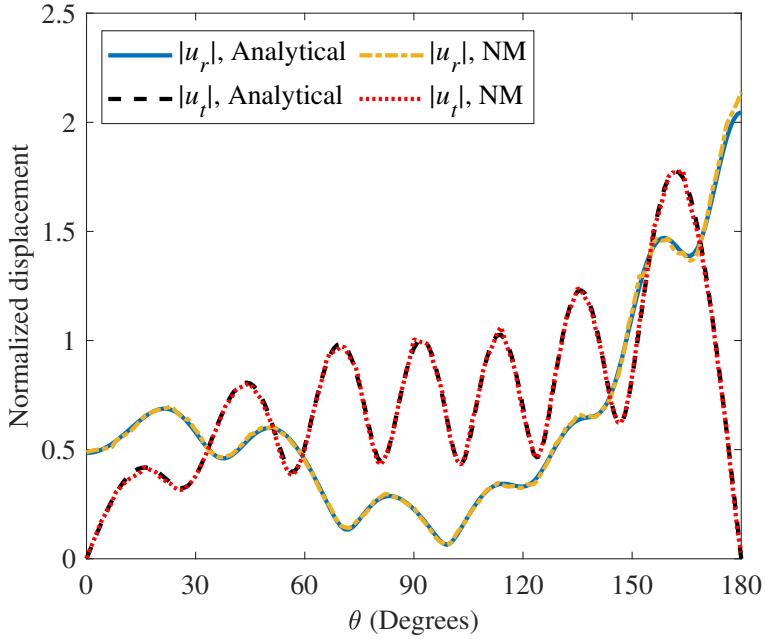


Figure 3.12: Magnitude of surface displacement field in the spherical inclusion problem ($k_p a = 8$). NM result is generated from Rule-11 with 5120 mesh elements. Radial component is $u_r$. Polar component is $u_t$. Fields are normalized by the variable $a$.

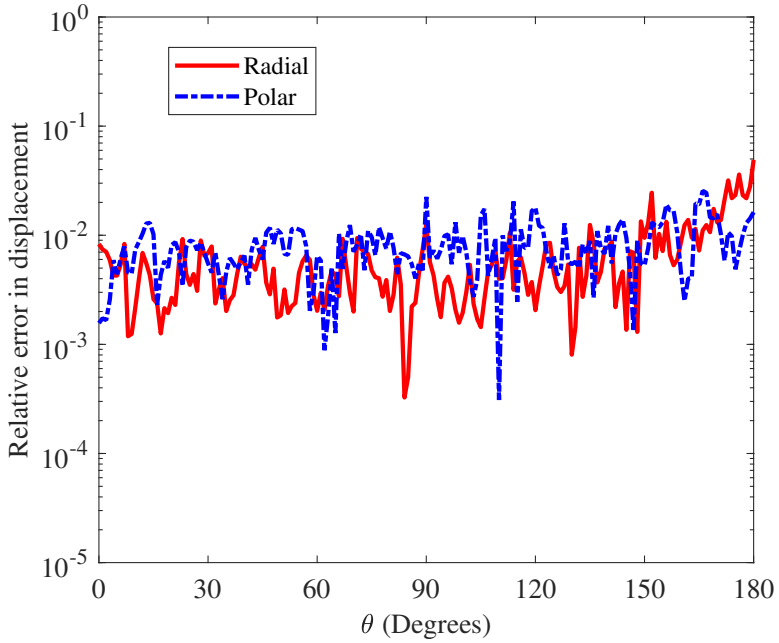


Figure 3.13: Relative errors in the radial and polar components of the surface displacement field on the spherical inclusion for Rule-11 with 5120 mesh elements.

discretizations. However, if the near-field matrix elements are evaluated efficiently using singularity subtraction techniques, such as in the LC-NM presented here, high-order discretizations lead to reduced simulation times. This is because high-order methods require a lower number of DOFs for achieving a given level of output error. We find that even if geometry discretization is of order two, increasing the degree of polynomials used in field approximation beyond two can be useful for some scattering problems: it leads to lower errors despite the asymptotic convergence rate being limited by the order of geometry interpolation. The reduction in simulation times due to high-order discretization is crucial for UNDE applications. This motivates the application of high-order LC-NM to BIE formulations other than the one considered in this chapter.

# CHAPTER 4. A HIGH-ORDER BOUNDARY ELEMENT METHOD FOR ELASTIC WAVE SCATTERING

This chapter presents a high-order boundary-element method (BEM) for simulating elastic wave scattering using the direct CFIE formulation. The first section provides a brief introduction to boundary integral equations (BIEs) and the CFIE. The following section contains a derivation of the CFIE and definitions of various kernels appearing in it. Although the derivation is inessential for following BEM-related work, it is provided for the sake of completeness. Among other things, it explains the origin and interpretation of hypersingularity and the continuity requirements of density functions. The proposed high-order BEM and its application to CFIE formulation are discussed in Section 4.3. Remaining sections are devoted to numerical results and validations.

## 4.1 Introduction

In this chapter, we define the elastic wave scattering problem and present its reformulation in terms of the conventional and hypersingular boundary integral equations (CBIEs and HBIEs, respectively). The combined-field integral equation (CFIE) formulation is obtained by combining the CBIE and HBIE formulations using a coupling parameter. Unlike the elastic wave scattering problem, both conventional and hypersingular BIE formulations admit multiple solutions at some frequencies. This artifact is known as the fictitious eigenfrequency problem. In contrast, the CFIE formulation is uniquely solvable at all frequencies and, hence, is equivalent to the elastic wave scattering problem. Therefore, it is more appropriate than the conventional and hypersingular BIEs for numerical computation of scattering solutions using BEMs or, more generally, boundary integral equation methods (BIEMs).

BIEMs for all three BIE formulations mentioned above are reported in the literature [30, 31, 103, 111–113, 137–143]. Out of these, only [113, 139, 140] are based on the CFIE formulation. Further,

only [139, 140] use discretizations of order more than one. The BIEM in [112] is high-order and can be easily extended to CFIE formulations, though it has not been done. Since this BIEM uses smooth overlapping patches to represent the boundaries of scatterers, it is not easily generalizable to arbitrary shapes (see [144] for a description of such boundary representations). In contrast to the foregoing BIEs, elastic wave scattering can also be formulated in terms of indirect BIEs, where auxiliary field variables are the unknown density functions. In [145, 146], Liu et al. developed a BEM for an indirect BIE formulation. However, this BIE is also ill-conditioned at some frequencies because of the fictitious eigenfrequency problem.

Here, we extend the high-order BEM, or equivalently the locally-corrected Nyström method (see Section 3.2), in [30] to the (direct) CFIE formulation. A key feature of this BEM is the coincidence of field interpolation and quadrature points. This leads to simplified computation of far-field (regular) elements in the influence matrix. Indeed, evaluation of a far-field matrix element requires only a single computation of a kernel function and is free from interpolation error. Also, this BEM uses second-order interpolation from triangular meshes for accurate representation of complex geometries. Evaluation of singular and near-singular integrals on the resulting curvilinear mesh elements is particularly challenging. We use singularity subtraction techniques to evaluate them efficiently.

## 4.2 Derivation of the CFIE

Direct BIEs for elastic wave scattering can be derived in the same way as their counterparts in acoustics and elastostatics. The underlying ideas are well-known, and some derivations are detailed, for example, in [147, 148] for the CBIE formulation. Alternate but equivalent BIEs follow from §13.1 in [149]. For HBIEs, [142] covers some derivations in sufficient depth. Here, we roughly follow the outline laid out in these resources, but provide more details for clarity and rigor, wherever necessary. We start with the partial differential equations governing the stress and displacement fields and derive their integral representations using the concepts of reciprocity and fundamental solutions. Specifically, reciprocity equations express the relation between two different solutions of

the governing PDE (albeit, with different body forces, or more generally, "source" terms). When one of the solutions is chosen as the fundamental solution, the reciprocity equations yield integral representations. The CFIE follows readily from these integral representations.

### 4.2.1 Equation of Motion

Consider a linear elastic solid with a uniform mass density $\rho$. Let the displacement and stress fields in the solid be represented by $\mathbf{u}(\mathbf{x}, t)$ and $\bar{\boldsymbol{\tau}}(\mathbf{x}, t)$, respectively, where $\mathbf{x}$ represents the position coordinates with respect to a fixed coordinate system and $t$ represents the time. The fields satisfy the following equation of motion inside the solid [147][13, §3.2.1]

$$\nabla \cdot \bar{\boldsymbol{\tau}}(\mathbf{x}, t) + \mathbf{f}(\mathbf{x}, t) = \rho \frac{\partial^2 \mathbf{u}(\mathbf{x}, t)}{\partial t^2}, \tag{4.1}$$

with $\mathbf{f}(\mathbf{x}, t)$ representing the body force per unit volume. Assuming that all fields are time-harmonic with the factor $e^{-i\omega t}$ ($\omega \in \mathbb{R}$), the above equation can be re-written without time dependency as follows

$$\nabla \cdot \bar{\boldsymbol{\tau}}(\mathbf{x}, \omega) + \mathbf{f}(\mathbf{x}, \omega) = -\rho\omega^2 \mathbf{u}(\mathbf{x}, \omega), \tag{4.2}$$

which is equivalent to taking the Fourier transform of Equation (4.1) in the time variable and writing the corresponding equation for the Fourier spectra of the fields. Henceforth, we will operate in the frequency domain ($\omega-$domain), and the dependence of fields on position and angular frequency will not be shown explicitly unless when necessary.

For a homogeneous, isotropic solid with Lamé parameters $\lambda$ and $\mu$, the following constitutive equation relates the stress and displacement fields

$$\bar{\boldsymbol{\tau}} = \lambda \bar{\mathbf{I}} \left( \nabla \cdot \mathbf{u} \right) + \mu \left( \nabla \mathbf{u} + \mathbf{u} \nabla \right). \tag{4.3}$$

The dyadic notation is adopted for expressing the foregoing relation compactly. The symbol $\bar{\mathbf{I}}$ represents the unit dyadic, and $\mathbf{u}\nabla$ is defined as the transpose of the dyadic $\nabla\mathbf{u}$. For example, in the index notation, the $(i, j)$ component of $\mathbf{u}\nabla$ is $[\mathbf{u}\nabla]_{ij} = \partial_j u_i$. Also, throughout this thesis, for any dyadic $\mathbf{ab}$, the notation $[\mathbf{ab}]_{ij}$ is used occasionally to represent its $(i, j)$ component. Note that

the stress tensor is symmetric, as required by the conservation of angular momentum [13, §3.2]. Substituting the constitutive relation in the equation of motion yields the following equation for the displacement field

$$(\lambda + \mu)\nabla\nabla \cdot \mathbf{u} + \mu\nabla^2\mathbf{u} + \rho\omega^2\mathbf{u} = -\mathbf{f}. \tag{4.4}$$

The displacement field inside a solid can be determined by solving this equation with appropriate boundary conditions. The corresponding stress field is obtained from (4.3).

### 4.2.2 Reciprocity Relation

Consider an elastic solid occupying a volume $V \subset \mathbb{R}^3$ that is bounded by a surface $S \subset \mathbb{R}^3$. Let the fields $\bar{\boldsymbol{\tau}}_1$ and $\mathbf{u}_1$ be such that they satisfy Equations (4.4) and (4.3) for a body force $\mathbf{f}_1$. Similarly, let $\bar{\boldsymbol{\tau}}_2$ and $\mathbf{u}_2$ be a solution to these equations for a body force $\mathbf{f}_2$. We are interested in deriving a relation involving the foregoing fields. From (4.2), we have the following two equations

$$\nabla \cdot \bar{\boldsymbol{\tau}}_1 - \rho\omega^2\mathbf{u}_1 = -\mathbf{f}_1, \tag{4.5a}$$

$$\nabla \cdot \bar{\boldsymbol{\tau}}_2 - \rho\omega^2\mathbf{u}_2 = -\mathbf{f}_2. \tag{4.5b}$$

Taking the dot product of (4.5a) with $\mathbf{u}_2$ and of (4.5b) with $\mathbf{u}_1$, and subtracting the resulting equations gives

$$(\nabla \cdot \bar{\boldsymbol{\tau}}_1) \cdot \mathbf{u}_2 - \mathbf{u}_1 \cdot (\nabla \cdot \bar{\boldsymbol{\tau}}_2) = \mathbf{u}_1 \cdot \mathbf{f}_2 - \mathbf{f}_1 \cdot \mathbf{u}_2. \tag{4.6}$$

Since the terms in the above equation are scalars, the direction in which the dot products of equations (4.5a) and (4.5b) are taken is not relevant. However, the same operations will be repeated for a tensor version of Equation (4.2) in the next section, where taking dot product from the left yields different equations than taking it from the right. To maintain consistency and to avoid having to repeat the above steps, the dot products in this section will be depicted such that they reflect the proper direction of multiplication; for example, $\mathbf{u}_2$ is multiplied from the right of Equation (4.5a) and $\mathbf{u}_1$ is multiplied from the left of Equation (4.5b).

The terms on the left hand side of (4.6) can be expressed as the divergence of a vector. The derivation of the reciprocity relation follows from an application of the Gauss-Divergence theorem to this quantity. Towards this, consider the following identities for any vector $\mathbf{u}$ and tensor $\bar{\boldsymbol{\tau}}$

$$\nabla \cdot (\bar{\boldsymbol{\tau}} \cdot \mathbf{u}) = \partial_i(\tau_{ij} u_j) = \partial_i(\tau_{ij}) u_j + \tau_{ij} \partial_i u_j = (\nabla \cdot \bar{\boldsymbol{\tau}}) \cdot \mathbf{u} + \bar{\boldsymbol{\tau}} : \nabla \mathbf{u}. \tag{4.7}$$

Similarly,

$$\nabla \cdot (\mathbf{u} \cdot \bar{\boldsymbol{\tau}}) = \partial_i(u_j \tau_{ji}) = \partial_i(u_j \tau_{ij}) = u_j \partial_i(\tau_{ij}) + (\partial_i u_j)\tau_{ij} = \mathbf{u} \cdot (\nabla \cdot \bar{\boldsymbol{\tau}}) + \nabla \mathbf{u} : \bar{\boldsymbol{\tau}}. \tag{4.8}$$

The second equality in (4.8) is due to symmetry of the stress tensor. Also, although the end result of (4.8) follows readily from (4.7), the same is not true if one of the fields in the identities is a fundamental solution that is introduced in the next section. Therefore, (4.8) is derived separately from (4.7) and expressed in a specific form, keeping the generalization of the derivations and results in mind. Notice that the first term on the right hand side in the foregoing identities is in the form of the terms on the left hand side of Equation (4.6). We can rewrite (4.6) using the above identities as follows

$$\nabla \cdot (\bar{\boldsymbol{\tau}}_1 \cdot \mathbf{u}_2 - \mathbf{u}_1 \cdot \bar{\boldsymbol{\tau}}_2) + \nabla \mathbf{u}_1 : \bar{\boldsymbol{\tau}}_2 - \bar{\boldsymbol{\tau}}_1 : \nabla \mathbf{u}_2 = \mathbf{u}_1 \cdot \mathbf{f}_2 - \mathbf{f}_1 \cdot \mathbf{u}_2. \tag{4.9}$$

The last two terms on the left hand side evaluate to zero for any linear elastic solid as a consequence of the symmetries of the stiffness tensor that relates the stress and the displacement fields [13, §5.2]. However, for isotropic solids, we can show the cancellation using the explicit expression of the constitutive equation. Using (4.3), we can write

$$\begin{aligned}
\nabla \mathbf{u}_1 : \bar{\boldsymbol{\tau}}_2 - \bar{\boldsymbol{\tau}}_1 : \nabla \mathbf{u}_2 =& \nabla \mathbf{u}_1 : \left[\lambda \bar{\mathbf{I}} (\nabla \cdot \mathbf{u}_2) + \mu (\nabla \mathbf{u}_2 + \mathbf{u}_2 \nabla)\right] - \\
& \left[\lambda \bar{\mathbf{I}} (\nabla \cdot \mathbf{u}_1) + \mu (\nabla \mathbf{u}_1 + \mathbf{u}_1 \nabla)\right] : \nabla \mathbf{u}_2 && \text{(4.10a)} \\
=& \lambda (\nabla \cdot \mathbf{u}_1)(\nabla \cdot \mathbf{u}_2) + \mu (\nabla \mathbf{u}_1 : \nabla \mathbf{u}_2 + \nabla \mathbf{u}_1 : \mathbf{u}_2 \nabla) - \\
& \lambda (\nabla \cdot \mathbf{u}_1)(\nabla \cdot \mathbf{u}_2) - \mu (\nabla \mathbf{u}_1 : \nabla \mathbf{u}_2 + \mathbf{u}_1 \nabla : \nabla \mathbf{u}_2) && \text{(4.10b)} \\
=& 0. && \text{(4.10c)}
\end{aligned}$$

Therefore, Equation (4.9) reduces to the following

$$\nabla \cdot (\bar{\boldsymbol{\tau}}_1 \cdot \mathbf{u}_2 - \mathbf{u}_1 \cdot \bar{\boldsymbol{\tau}}_2) = \mathbf{u}_1 \cdot \mathbf{f}_2 - \mathbf{f}_1 \cdot \mathbf{u}_2. \tag{4.11}$$

Integrating the above equation over $V$ and applying the Gauss-Divergence theorem yields the following reciprocity relation

$$\int_S \hat{\mathbf{n}} \cdot (\bar{\boldsymbol{\tau}}_1 \cdot \mathbf{u}_2 - \mathbf{u}_1 \cdot \bar{\boldsymbol{\tau}}_2)\, dS = \int_V (\mathbf{u}_1 \cdot \mathbf{f}_2 - \mathbf{f}_1 \cdot \mathbf{u}_2)\, dV, \tag{4.12}$$

where $\hat{\mathbf{n}}$ is the unit vector that is normal to $S$ and oriented away from $V$. In general, the unit vector $\hat{\mathbf{n}}$ is not a constant function of $\mathbf{x}$.

Equation (4.12) can be used to derive some relations analogous to the reaction theorems in electromagnetics [150, §3.8], as described below. Assume that the solid is unbounded and that the body forces $\mathbf{f}_1$ and $\mathbf{f}_2$ can be bounded within a finite region. Further, since the reciprocity relation applies to any surface $S$ that encloses the body forces, take $S$ to be a spherical surface of radius $R$ that is sufficiently large to enclose the body forces. As $R$ goes to infinity, Equation (4.26) yields asymptotic forms of the displacement fields, which, in turn, provide asymptotic forms of the stress fields via the constitutive relation. The asymptotic forms of the stress and displacement fields can be used to show that the surface integral in (4.12) vanishes (in the limit $R \to \infty$ and thus for all surfaces that completely enclose the body forces), leading to the following "reaction theorem"

$$\int_V \mathbf{u}_1 \cdot \mathbf{f}_2 \; dV = \int_V \mathbf{f}_1 \cdot \mathbf{u}_2 \; dV. \tag{4.13}$$

Applying this to the body forces $\mathbf{f}_1(\mathbf{x}) = \delta(\mathbf{x} - \mathbf{x_1})\hat{\mathbf{e}}_1$ and $\mathbf{f}_2(\mathbf{x}) = \delta(\mathbf{x} - \mathbf{x_2})\hat{\mathbf{e}}_2$, for any unit vectors $\hat{\mathbf{e}}_1$ and $\hat{\mathbf{e}}_2$, results in

$$\mathbf{u}_1(\mathbf{x}_2) \cdot \hat{\mathbf{e}}_2 = \mathbf{u}_2(\mathbf{x}_1) \cdot \hat{\mathbf{e}}_1. \tag{4.14}$$

In other words, the displacement at $\mathbf{x}_2$, in the direction $\hat{\mathbf{e}}_2$, created by the application of a point body force that is located at $\mathbf{x}_1$ and directed along $\hat{\mathbf{e}}_1$, is same as that observed when both the location and direction of the force (source) are exchanged with those of the displacement (effect).

### 4.2.3 Fundamental Solutions

The fundamental solution for displacement field is the solution of Equation (4.4) for a Dirac-delta body force (point source) in an unbounded solid with a boundary condition that is mentioned later. The corresponding solution for the stress field is obtained from the constitutive relation given by (4.3). Since body force is a vector in $\mathbb{R}^3$, to get the fundamental solution corresponding to any arbitrary direction of the body force, it is sufficient to get three sets of solutions corresponding to three cases wherein the body force points along the three axes of a rectangular coordinate system. The displacement and stress field solutions for these three cases can be represented compactly as second and third order tensors, respectively. Accordingly, we seek the solution of the following equation in an unbounded elastic solid

$$(\lambda+\mu)\nabla\nabla\cdot\overline{\mathbf{G}}(\mathbf{x},\mathbf{x}')+\mu\nabla^2\overline{\mathbf{G}}(\mathbf{x},\mathbf{x}')+\rho\omega^2\overline{\mathbf{G}}(\mathbf{x},\mathbf{x}')=-\delta(\mathbf{x}-\mathbf{x}')\bar{\mathbf{I}} \tag{4.15}$$

with the condition that $\overline{\mathbf{G}}(\mathbf{x},\mathbf{x}')$ goes to zero as $|\mathbf{x}-\mathbf{x}'|$ goes to infinity. Here, $\overline{\mathbf{G}}(\mathbf{x},\mathbf{x}')$ is a second-order tensor representing the displacements caused at point $\mathbf{x}$ individually by three point body forces that are located at $\mathbf{x}'$ and directed along the three coordinate axes. From the way the above equation is written, the second index of $\overline{\mathbf{G}}(\mathbf{x},\mathbf{x}')$ represents the direction of the body force. For example, the three elements in the $j^{th}$ column of $\overline{\mathbf{G}}(\mathbf{x},\mathbf{x}')$ are the components of the displacement in the case wherein the body force points along the $j^{th}$ coordinate axis.

It follows from Equation (4.14) that $\overline{\mathbf{G}}(\mathbf{x},\mathbf{x}')$ equals the transpose of $\overline{\mathbf{G}}(\mathbf{x}',\mathbf{x})$, that is, $\overline{\mathbf{G}}(\mathbf{x},\mathbf{x}')=\overline{\mathbf{G}}^T(\mathbf{x}',\mathbf{x})$. This can be seen by choosing $\mathbf{x}_1=\mathbf{x}$, $\mathbf{x}_2=\mathbf{x}'$ in (4.14), and setting $\hat{\mathbf{e}}_1$ and $\hat{\mathbf{e}}_2$ as each of the three unit vectors along the three axes of a rectangular coordinate system. To elaborate, we get an element-by-element equality of $\overline{\mathbf{G}}(\mathbf{x},\mathbf{x}')$ and $\overline{\mathbf{G}}^T(\mathbf{x}',\mathbf{x})$ if we set $\hat{\mathbf{e}}_1=\hat{\mathbf{a}}_i$ and $\hat{\mathbf{e}}_2=\hat{\mathbf{a}}_j$ for $i,j=1,2,3$, where $\hat{\mathbf{a}}_p$ is the unit vector along the $p^{th}$ axis of a coordinate system. Further, both (4.15) and its accompanying boundary condition are translationally and rotationally invariant because of material homogeneity and isotropy. This invariance can be used to show that $\overline{\mathbf{G}}(\mathbf{x},\mathbf{x}')=\overline{\mathbf{G}}(\mathbf{x}',\mathbf{x})$. Summing up, we have the following important relations

$$\overline{\mathbf{G}}(\mathbf{x},\mathbf{x}')=\overline{\mathbf{G}}(\mathbf{x}',\mathbf{x})=\overline{\mathbf{G}}^T(\mathbf{x},\mathbf{x}'). \tag{4.16}$$

In other words, the displacement caused by a point source remains the same if we were to exchange either the locations or the directions or both locations and directions of the source and observation.

The stress fields corresponding to $\overline{\mathbf{G}}(\mathbf{x},\mathbf{x}')$ are given by the following third order tensor

$$\overline{\overline{\mathbf{\Sigma}}}^{(1)}(\mathbf{x},\mathbf{x}') = \lambda\bar{\mathbf{I}}\left(\nabla\cdot\overline{\mathbf{G}}(\mathbf{x},\mathbf{x}')\right) + \mu\left(\nabla\overline{\mathbf{G}}(\mathbf{x},\mathbf{x}') + \overline{\mathbf{G}}(\mathbf{x},\mathbf{x}')\nabla\right), \tag{4.17}$$

where the superscript $[\ ]^{(1)}$ is used to indicate that the divergence and gradient are defined with respect to the first argument of $\overline{\overline{\mathbf{\Sigma}}}^{(1)}(\mathbf{x},\mathbf{x}')$. The notation $\overline{\mathbf{G}}(\mathbf{x},\mathbf{x}')\nabla$ represents the tensor obtained by transposing the first two indices of $\nabla\overline{\mathbf{G}}(\mathbf{x},\mathbf{x}')$. As in the case of the displacement fundamental solution, the last index of $\overline{\overline{\mathbf{\Sigma}}}^{(1)}(\mathbf{x},\mathbf{x}')$ represents the direction of the body force. Also, it is clear from (4.17) that $\overline{\overline{\mathbf{\Sigma}}}^{(1)}(\mathbf{x},\mathbf{x}')$ is symmetric with respect to its first two indices. This is a consequence of the symmetries of the second-order stress tensor corresponding to a single body force. Further, due to the notation that is adopted, $\overline{\overline{\mathbf{\Sigma}}}^{(1)}(\mathbf{x},\mathbf{x}')$ is same as $\overline{\overline{\mathbf{\Sigma}}}^{(2)}(\mathbf{x}',\mathbf{x})$ as they express the same quantity.

The fundamental solution $\overline{\mathbf{G}}(\mathbf{x},\mathbf{x}')$ can be expressed in terms of the longitudinal and shear wave speeds ($c_p$ and $c_s$, respectively) and the corresponding wavenumbers ($k_p$ and $k_s$) as follows [30]

$$\overline{\mathbf{G}}(\mathbf{x},\mathbf{x}') = \frac{C\hat{\mathbf{R}}\hat{\mathbf{R}} + D\bar{\mathbf{I}}}{4\pi\rho\omega^2R^3}, \tag{4.18a}$$

where $R = |\mathbf{x}'-\mathbf{x}|$, and

$$\hat{\mathbf{R}} = \frac{\mathbf{x}'-\mathbf{x}}{R}, \tag{4.18b}$$

$$C = \Omega_s e^{ik_sR} - \Omega_c e^{ik_pR}, \tag{4.18c}$$

$$D = [(k_sR)^2 + ik_sR - 1]e^{ik_sR} - (ik_cR - 1)e^{ik_cR}, \tag{4.18d}$$

$$\Omega_\alpha = -(k_\alpha R)^2 - 3ik_\alpha R + 3 \quad \text{for } \alpha\in\{s,p\}. \tag{4.18e}$$

The relations in (4.16) can be explicitly seen in the above expression for $\overline{\mathbf{G}}(\mathbf{x},\mathbf{x}')$. Also, $\overline{\mathbf{G}}(\mathbf{x},\mathbf{x}')$ is singular at $\mathbf{x}=\mathbf{x}'$ as can be verified using the asymptotic forms (as $R\to 0$) of $C$ and $D$ given in Appendix B.1. Also, $\overline{\mathbf{G}}(\mathbf{x},\mathbf{x}')$ is singular at $\mathbf{x}=\mathbf{x}'$ as can be verified using the asymptotic forms (as $R\to 0$) of $C$ and $D$. It follows from Equations (4.17) and (4.18) that $\overline{\overline{\mathbf{\Sigma}}}^{(1)}(\mathbf{x}',\mathbf{x}) = -\overline{\overline{\mathbf{\Sigma}}}^{(1)}(\mathbf{x},\mathbf{x}')$.

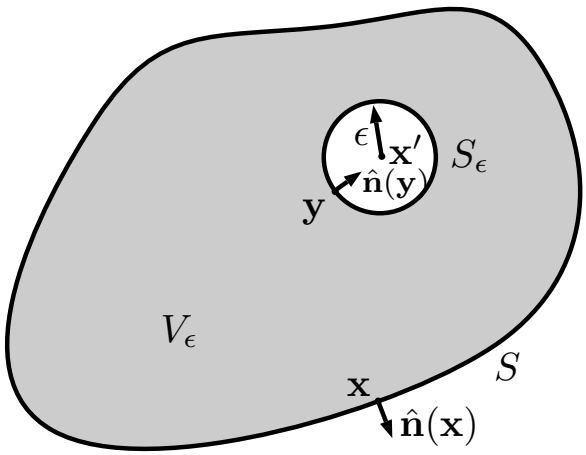


Figure 4.1: Schematic of an elastic solid occupying a volume $V$ and bounded by a surface $S$. An imaginary sphere centered at $\mathbf{x}'$ and of radius $\epsilon$ is excluded from $V$ for applying the divergence theorem. Orientations of the unit surface normal vectors on the surfaces $S$ and $S_\epsilon$ are indicated by the vectors $\hat{\mathbf{n}}(\mathbf{x})$ and $\hat{\mathbf{n}}(\mathbf{y})$, respectively. The surface $S_\epsilon$ is fictitious and does not represent material inhomogeneity.

This symmetry is due to the rotational and translational invariance of (4.15) and the boundary condition.

Since the stress and displacement fundamental solutions are derived from the equation of motion given by (4.2), they satisfy the following equation

$$\nabla \cdot \overline{\overline{\mathbf{\Sigma}}}^{(1)}(\mathbf{x}, \mathbf{x}') + \rho\omega^2 \overline{\mathbf{G}}(\mathbf{x}, \mathbf{x}') = -\delta(\mathbf{x} - \mathbf{x}')\bar{\mathbf{I}}. \tag{4.19}$$

In place of Equation (4.5b), if we consider the above equation to be the starting point of the derivation of the reciprocity relation, all the steps until Equation (4.11) hold true if $\mathbf{u}_2(\mathbf{x})$, $\bar{\boldsymbol{\tau}}_2(\mathbf{x})$ and $\mathbf{f}_2(\mathbf{x})$ are replaced with $\overline{\mathbf{G}}(\mathbf{x}, \mathbf{x}')$, $\overline{\overline{\mathbf{\Sigma}}}^{(1)}(\mathbf{x}, \mathbf{x}')$ and $\delta(\mathbf{x}-\mathbf{x}')\bar{\mathbf{I}}$, respectively. Dropping the subscript in $\mathbf{u}_1$, $\bar{\boldsymbol{\tau}}_1$ and $\mathbf{f}_1$, an equation analogous to (4.11) can be written as shown below

$$\nabla \cdot \left( \bar{\boldsymbol{\tau}}(\mathbf{x}) \cdot \overline{\mathbf{G}}(\mathbf{x}, \mathbf{x}') - \mathbf{u}(\mathbf{x}) \cdot \overline{\overline{\mathbf{\Sigma}}}^{(1)}(\mathbf{x}, \mathbf{x}') \right) = \mathbf{u}(\mathbf{x})\delta(\mathbf{x} - \mathbf{x}') - \mathbf{f}(\mathbf{x}) \cdot \overline{\mathbf{G}}(\mathbf{x}, \mathbf{x}'). \tag{4.20}$$

### 4.2.4 Integral Representation

An integral representation of displacement field can be derived by applying the Gauss-divergence theorem to Equation (4.20). However, the theorem cannot be applied directly in the volume $V$ as

the fields $\overline{\mathbf{G}}(\mathbf{x},\mathbf{x}')$ and $\overline{\overline{\boldsymbol{\Sigma}}}^{(1)}(\mathbf{x},\mathbf{x}')$ are singular at $\mathbf{x}=\mathbf{x}'$. To exclude the singularities, consider a modified volume $V_\epsilon \subset V$ formed by the removal of a sphere of radius $\epsilon$ from $V$ as shown in Figure 4.1. Applying the divergence theorem to (4.20) in the volume $V_\epsilon$ gives

$$\int_{S+S_\epsilon} \hat{\mathbf{n}}(\mathbf{x}) \cdot \left( \bar{\boldsymbol{\tau}}(\mathbf{x}) \cdot \overline{\mathbf{G}}(\mathbf{x},\mathbf{x}') - \mathbf{u}(\mathbf{x}) \cdot \overline{\overline{\boldsymbol{\Sigma}}}^{(1)}(\mathbf{x},\mathbf{x}') \right) dS(\mathbf{x}) \;=\; -\int_{V_\epsilon} \mathbf{f}(\mathbf{x}) \cdot \overline{\mathbf{G}}(\mathbf{x},\mathbf{x}') dV(\mathbf{x}), \quad (4.21)$$

where $dS(\mathbf{x})$ and $dV(\mathbf{x})$ are the area and volume elements, respectively, in the corresponding domains of integration. Here, for $\mathbf{x} \in S \cup S_\epsilon$, $\hat{\mathbf{n}}(\mathbf{x})$ represents the unit vector that is normal to the boundaries of $V_\epsilon$ and directed away from it. Replacing the stress field $\bar{\boldsymbol{\tau}}$ on $S$ and $S_\epsilon$ with the corresponding traction field $\mathbf{t}(\mathbf{x}) = \hat{\mathbf{n}} \cdot \bar{\boldsymbol{\tau}}$, we get

$$\begin{aligned} &\int_S \left( \mathbf{t}(\mathbf{x}) \cdot \overline{\mathbf{G}}(\mathbf{x},\mathbf{x}') - \mathbf{u}(\mathbf{x}) \cdot \left[ \hat{\mathbf{n}}(\mathbf{x}) \cdot \overline{\overline{\boldsymbol{\Sigma}}}^{(1)}(\mathbf{x},\mathbf{x}') \right] \right) dS(\mathbf{x}) = \\ &\qquad \int_{S_\epsilon} \left( \mathbf{u}(\mathbf{x}) \cdot \left[ \hat{\mathbf{n}}(\mathbf{x}) \cdot \overline{\overline{\boldsymbol{\Sigma}}}^{(1)}(\mathbf{x},\mathbf{x}') \right] - \mathbf{t}(\mathbf{x}) \cdot \overline{\mathbf{G}}(\mathbf{x},\mathbf{x}') \right) dS(\mathbf{x}) - \int_{V_\epsilon} \mathbf{f}(\mathbf{x}) \cdot \overline{\mathbf{G}}(\mathbf{x},\mathbf{x}') dV(\mathbf{x}). \end{aligned} \quad (4.22)$$

The symmetry of $\overline{\overline{\boldsymbol{\Sigma}}}^{(1)}(\mathbf{x},\mathbf{x}')$ in the first two indices was used in the above to interchange the order of multiplication of $\mathbf{u}(\mathbf{x})$ and $\hat{\mathbf{n}}(\mathbf{x})$. In the limit $\epsilon \to 0$, the first term on the right-hand side evaluates to $\mathbf{u}(\mathbf{x}')$, and the second term evaluates to zero for a sufficiently smooth $\mathbf{u}(\mathbf{x})$, as shown in Appendix B.1. Also, the limit of the last term exists for a sufficiently smooth $\mathbf{f}(\mathbf{x})$ and is represented as the integral over the whole domain $V$. Thus, the displacement at any point $\mathbf{x}'$ in $V$ can be written as follows

$$\mathbf{u}(\mathbf{x}') = \int_S \left( \mathbf{t}(\mathbf{x}) \cdot \overline{\mathbf{G}}(\mathbf{x},\mathbf{x}') - \mathbf{u}(\mathbf{x}) \cdot \left[ \hat{\mathbf{n}}(\mathbf{x}) \cdot \overline{\overline{\boldsymbol{\Sigma}}}^{(1)}(\mathbf{x},\mathbf{x}') \right] \right) dS(\mathbf{x}) + \int_V \mathbf{f}(\mathbf{x}) \cdot \overline{\mathbf{G}}(\mathbf{x},\mathbf{x}') dV(\mathbf{x}). \quad (4.23)$$

An explicit expression of $\hat{\mathbf{n}} \cdot \overline{\overline{\boldsymbol{\Sigma}}}^{(1)}(\mathbf{x},\mathbf{x}')$ which can be used for evaluating one of the foregoing limits is shown below [30, §4.1]

$$\hat{\mathbf{n}} \cdot \overline{\overline{\boldsymbol{\Sigma}}}^{(1)}(\mathbf{x},\mathbf{x}') = -\frac{(\lambda\psi_p + 2\mu C)\hat{\mathbf{n}}\hat{\mathbf{R}} + \mu(\psi_s + 2C)\left(\hat{\mathbf{R}}\hat{\mathbf{n}} + \hat{\mathbf{n}} \cdot \hat{\mathbf{R}}\bar{\mathbf{I}}\right) + 2\mu F(\hat{\mathbf{n}} \cdot \hat{\mathbf{R}})\hat{\mathbf{R}}\hat{\mathbf{R}}}{4\pi\rho\omega^2 R^4}, \quad (4.24a)$$

with the terms appearing in the above expression defined according to (4.18) and as shown below

$$F = H_p e^{ik_p R} - H_s e^{ik_p R}, \quad (4.24b)$$

$$H_\alpha = i(k_\alpha R)^3 - 6(k_\alpha R)^2 - 15ik_\alpha R + 15, \quad (4.24c)$$

$$\psi_\alpha = (k_\alpha R)^2(ik_\alpha R - 1)e^{ik_\alpha R} \tag{4.24d}$$

for $\alpha \in \{s, p\}$. An alternate expression for $\hat{\mathbf{n}} \cdot \overline{\overline{\boldsymbol{\Sigma}}}^{(1)}(\mathbf{x}, \mathbf{x}')$ is [112]

$$\hat{\mathbf{n}} \cdot \overline{\overline{\boldsymbol{\Sigma}}}^{(1)}(\mathbf{x}, \mathbf{x}') = -\frac{\left(A_1 \hat{\mathbf{R}}\hat{\mathbf{R}} + A_2 \bar{\mathbf{I}}\right) \hat{\mathbf{R}} \cdot \hat{\mathbf{n}} + \left(A_3 \hat{\mathbf{n}}\hat{\mathbf{R}} + A_2 \hat{\mathbf{R}}\hat{\mathbf{n}}\right)}{2\pi R^2}, \tag{4.25a}$$

where

$$\mathbf{R} = \mathbf{x}' - \mathbf{x}, \qquad R = |\mathbf{R}|, \qquad \hat{\mathbf{R}} = \frac{\mathbf{R}}{R}, \tag{4.25b}$$

$$\tau = ik_s R, \qquad \alpha = \frac{k_p}{k_s}, \tag{4.25c}$$

$$M(\tau) = \frac{e^{\alpha\tau}(1 - \alpha\tau) - e^{\tau}(1 - \tau)}{\tau^2} \tag{4.25d}$$

$$\psi(\tau) = e^{\tau} - M(\tau), \tag{4.25e}$$

$$\chi(\tau) = e^{\alpha\tau}\alpha^2 - e^{\tau} + 3M(\tau), \tag{4.25f}$$

$$A_1(\tau) = \tau\chi'(\tau) - 3\chi(\tau), \tag{4.25g}$$

$$A_2(\tau) = \frac{\tau\psi'(\tau) - \psi(\tau) + \chi(\tau)}{2}, \tag{4.25h}$$

$$A_3(\tau) = \chi(\tau) + \left(\frac{1}{2\alpha^2} - 1\right)[A_1 + 2A_2 + 3\chi(\tau)]. \tag{4.25i}$$

Note that the dependence of $A_1$, $A_2$ and $A_3$ on $\tau$ is not shown explicitly in (4.25a). For notational convenience, we shall interchange $\mathbf{x}$ and $\mathbf{x}'$ in Equation (4.23) so that $\mathbf{x}$ represents the location of field observation. This gives

$$\mathbf{u}(\mathbf{x}) = \int_S \left(\mathbf{t}(\mathbf{x}') \cdot \overline{\mathbf{G}}(\mathbf{x}, \mathbf{x}') + \mathbf{u}(\mathbf{x}') \cdot \left[\hat{\mathbf{n}}(\mathbf{x}') \cdot \overline{\overline{\boldsymbol{\Sigma}}}^{(1)}(\mathbf{x}, \mathbf{x}')\right]\right) dS(\mathbf{x}') + \int_V \mathbf{f}(\mathbf{x}) \cdot \overline{\mathbf{G}}(\mathbf{x}, \mathbf{x}') dV(\mathbf{x}), \tag{4.26}$$

where we have used the fact that $\overline{\mathbf{G}}(\mathbf{x}', \mathbf{x}) = \overline{\mathbf{G}}(\mathbf{x}, \mathbf{x}')$ and $\overline{\overline{\boldsymbol{\Sigma}}}^{(1)}(\mathbf{x}', \mathbf{x}) = -\overline{\overline{\boldsymbol{\Sigma}}}^{(1)}(\mathbf{x}, \mathbf{x}')$. The above equation, known as the integral representation formula, expresses the displacement at any point $\mathbf{x}$ in the volume $V$ as the sum of an integral involving the displacement and traction fields on the boundaries and a volume integral involving the body force density.

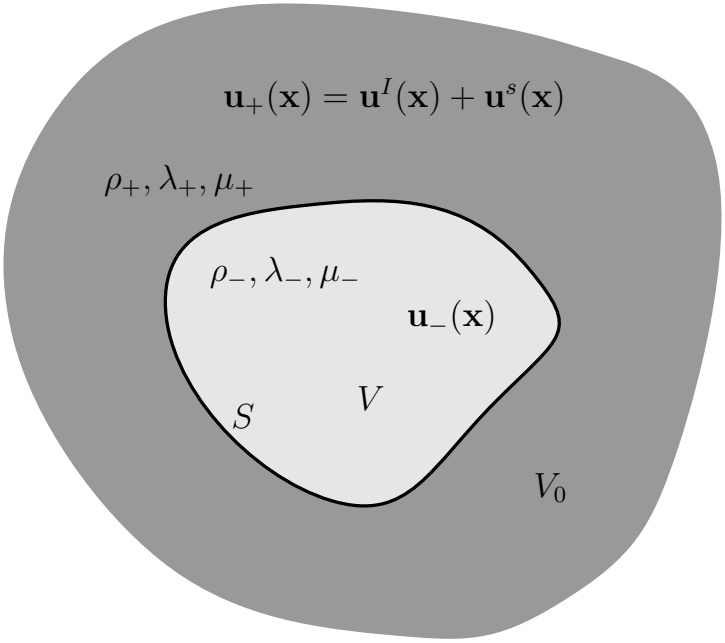


Figure 4.2: An unbounded and otherwise homogeneous elastic solid containing an inclusion.

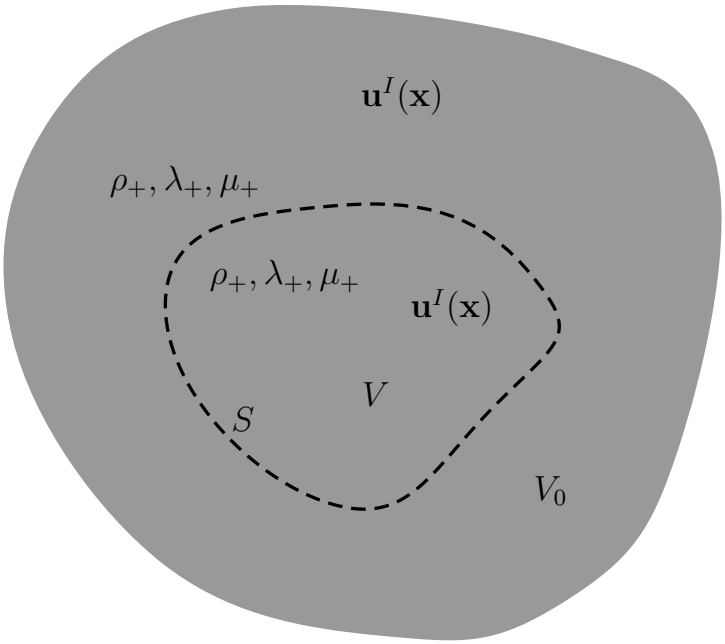


Figure 4.3: An unbounded and homogeneous elastic solid with a background displacement field $\mathbf{u}^I(\mathbf{x})$. Dashed line represents the surface $S$.

### 4.2.5 Elastic Wave Scattering Problem

The conventional (displacement) BIE for elastic wave scattering can be derived either by taking a limit of the integral representation formula (4.26) or by applying the divergence theorem to Equation (4.20) in a modified volume, as done in the previous section. It is, however, required to define the elastic wave scattering problem first. Consider two homogeneous, isotropic elastic solids, one embedded inside the other, as shown in Figure 4.2. The embedded solid occupies the region $V \in \mathbb{R}^3$ and is bounded by the surface $S$, whereas the external solid is unbounded and occupies the region $V_0 = \mathbb{R}^3 \setminus (V \cup S)$. Assume that an elastic wave, defined in terms of displacement and stress fields, impinges on the embedded solid. The idea of impingement is inherently a time-domain notion. In the frequency domain, the impinging (or incident) wave should be considered as a background field, that is, a field that would be present in $\mathbb{R}^3$ in the absence of the embedded solid as shown in Figure 4.3.

The embedded solid scatters the incident wave, or equivalently (in the frequency domain), modifies the background field. Therefore, we shall refer to the embedded solid as the scatterer. Let the mass density and Lamé constants of the scatterer be $\rho_-$, $\lambda_-$ and $\mu_-$, respectively, and those of the surrounding medium be $\rho_+$, $\lambda_+$ and $\mu_+$, respectively. Let the incident displacement field be given by $\mathbf{u}^I(\mathbf{x})$ for $\mathbf{x} \in \mathbb{R}^3$. Then, the elastic wave scattering problem is defined as follows: given an incident field that satisfies the wave Equation (4.4) in $\mathbb{R}^3$ with the material constants $\rho_+$, $\lambda_+$, $\mu_+$ and a body force $\mathbf{f}(\mathbf{x})$ (where $\mathbf{f}(\mathbf{x}) = 0$ for $\mathbf{x} \in V$), find the fields $\mathbf{u}^s(\mathbf{x})$ and $\mathbf{u}_-(\mathbf{x})$ such that the equations of motion (4.27), transmission conditions (4.28) and radiation conditions (4.29) are satisfied simultaneously. The equations of motion in $V$ and $V_0$ are as follows:

$$(\lambda_+ + \mu_+)\nabla\nabla \cdot \mathbf{u}^s(\mathbf{x}) + \mu_+\nabla^2\mathbf{u}^s(\mathbf{x}) + \rho_+\omega^2\mathbf{u}^s(\mathbf{x}) = 0 \quad \text{for } \mathbf{x} \in V_0, \tag{4.27a}$$

$$(\lambda_- + \mu_-)\nabla\nabla \cdot \mathbf{u}_-(\mathbf{x}) + \mu_-\nabla^2\mathbf{u}_-(\mathbf{x}) + \rho_-\omega^2\mathbf{u}_-(\mathbf{x}) = 0 \quad \text{for } \mathbf{x} \in V. \tag{4.27b}$$

The transmission conditions are defined according to continuity of displacement and traction fields on the interface $S$ as shown below:

$$\mathbf{u}^I(\mathbf{x}) + \mathbf{u}^s(\mathbf{x}) = \mathbf{u}_-(\mathbf{x}), \tag{4.28a}$$

$$\mathbf{t}^I(\mathbf{x}) + \mathbf{t}^s(\mathbf{x}) = \mathbf{t}_-(\mathbf{x}) \tag{4.28b}$$

for $\mathbf{x} \in S$, where $\mathbf{t}^I(\mathbf{x})$, $\mathbf{t}^s(\mathbf{x})$ and $\mathbf{t}_-(\mathbf{x})$ are the traction fields on $S$. We assume that the traction fields are defined using the exterior unit normal vector on $S$, although Equation (4.28b) does not depend on the choice of orientation of the unit normal. The radiation conditions are as follows:

$$\lim_{r\to\infty} \mathbf{u}_p(\mathbf{x}) = 0, \tag{4.29a}$$

$$\lim_{r\to\infty} \mathbf{u}_s(\mathbf{x}) = 0, \tag{4.29b}$$

$$\lim_{r\to\infty} r\left(\frac{\partial \mathbf{u}_p(\mathbf{x})}{\partial r} - ik_p\mathbf{u}_p(\mathbf{x})\right) = 0, \tag{4.29c}$$

$$\lim_{r\to\infty} r\left(\frac{\partial \mathbf{u}_s(\mathbf{x})}{\partial r} - ik_s\mathbf{u}_s(\mathbf{x})\right) = 0, \tag{4.29d}$$

where $r$ is the radius of a sphere that is centered at an arbitrary but fixed location, and the limits are approached uniformly in all directions around the sphere. The quantities $\mathbf{u}_p(\mathbf{x})$ and $\mathbf{u}_s(\mathbf{x})$ are the irrotational (curl-free) and solenoidal (divergence-free) components of $\mathbf{u}^s(\mathbf{x})$, respectively, and are uniquely given by

$$\mathbf{u}_p(\mathbf{x}) = \frac{-1}{k_p^2}\nabla\nabla\cdot\mathbf{u}^s(\mathbf{x}), \tag{4.30a}$$

$$\mathbf{u}_s(\mathbf{x}) = \mathbf{u}^s(\mathbf{x}) - \mathbf{u}_p(\mathbf{x}) = \frac{1}{k_p^2}\nabla\nabla\cdot\mathbf{u}^s(\mathbf{x}) + \mathbf{u}^s(\mathbf{x}). \tag{4.30b}$$

Equations (4.29a, 4.29b) are called regularity conditions and Equations (4.29c, 4.29d) are called the Sommerfeld-Kupradze radiation conditions [151] [152, §3.2].

**Remark 4.1** The following limiting cases of the material properties $\lambda_-$ and $\mu_-$ are of interest for scattering problems: when $\lambda_-, \mu_- \to \infty$, the displacement inside the material tends to zero, and hence the scatterer is called a *rigid* scatterer. Similarly, when $\lambda_-, \mu_- \to 0$, the stress field inside the material tends to zero, and hence the scatterer is called a *soft* scatterer. In the former case, the scattering problem reduces to a boundary-value problem with the Dirichlet boundary conditions obtained by setting $\mathbf{u}_-(\mathbf{x}) = 0$ in Equation (4.28a). Likewise, in the latter case, we get a boundary-value problem wherein the traction field on $S$ is prescribed according to Equation (4.28b) with $\mathbf{t}_-(\mathbf{x}) = 0$.

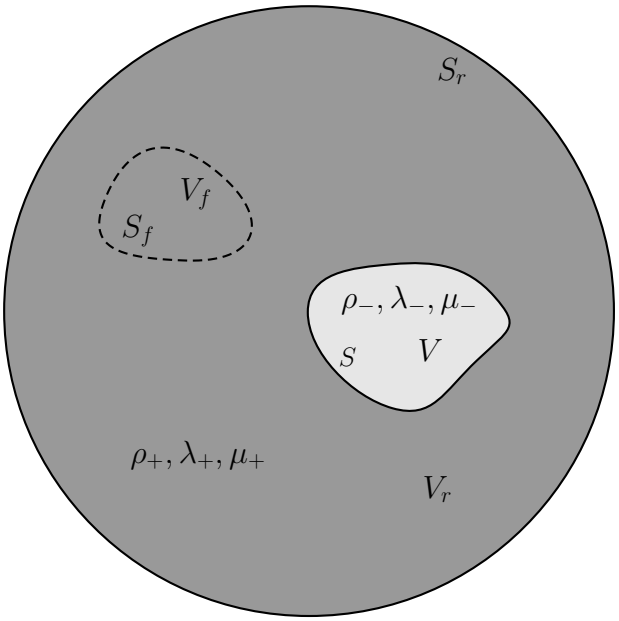


Figure 4.4: A model for elastic wave scattering in UNDE applications. The incident field is assumed to be generated by body forces present inside $V_f$.

**Remark 4.2** Some remarks are due on the use of the above formulation for modeling the scattering of ultrasound from defects in NDE. First, we assume that the defects are located relatively far from the walls of the inspection specimen. Then, due to the finite speed of propagation of waves, the interaction of incident waves with a defect is temporally separated from the interactions involving the boundaries of the specimen: that is, the time-domain voltage signals arising due to these two effects appear as distinct pulses separated in time. Since NDE measurements often require only the former, it is sufficient to model the problem such that it captures this initial response accurately. Any late time response present in the solution can be removed using window functions in the time-domain. For the same reason, it is also sufficient to model the source of the incident field using body forces that are placed far away from the defect; the only requirements on the body forces are: (a) the incident field generated by them near the defect should match that generated by the transducers, and (b) any additional scattering caused by the interaction of incident fields with specimen boundaries should be well-separated (in time) from the initial defect response.

According to these assumptions, consider the model shown in Figure 4.4. The body force density $\mathbf{f}(\mathbf{x})$ which creates the incident field is assumed to be bounded within the volume $V_f \subset V_r$, that is, $\mathbf{f}(\mathbf{x}) = 0$ for $\mathbf{x} \notin V_f$. The inspection specimen is modeled as a sphere of radius $r$ such that the boundaries are relatively far from both the defect and the body forces. The total displacement field should satisfy the following equation of motion inside $V_r$, which is the region inside the sphere excluding $V \cup S$

$$(\lambda_+ + \mu_+)\nabla\nabla \cdot \mathbf{u}(\mathbf{x}) + \mu_+\nabla^2\mathbf{u}(\mathbf{x}) + \rho_+\omega^2\mathbf{u}(\mathbf{x}) = -\mathbf{f}(\mathbf{x}). \tag{4.31}$$

The incident displacement field satisfies the following equation for the whole region in the sphere

$$(\lambda_+ + \mu_+)\nabla\nabla \cdot \mathbf{u}^I(\mathbf{x}) + \mu_+\nabla^2\mathbf{u}^I(\mathbf{x}) + \rho_+\omega^2\mathbf{u}^I(\mathbf{x}) = -\mathbf{f}(\mathbf{x}). \tag{4.32}$$

By eliminating $\mathbf{f}(\mathbf{x})$ from the above equations, we get the following equation for $\mathbf{x} \in V_r$

$$(\lambda_+ + \mu_+)\nabla\nabla \cdot \mathbf{u}^s(\mathbf{x}) + \mu_+\nabla^2\mathbf{u}^s(\mathbf{x}) + \rho_+\omega^2\mathbf{u}^s(\mathbf{x}) = 0, \tag{4.33}$$

where $\mathbf{u}^s(\mathbf{x}) \coloneqq \mathbf{u}(\mathbf{x}) - \mathbf{u}^I(\mathbf{x})$ is defined as the scattered field. We should note that the above equation, along with the equation of motion inside the defect (4.27b) and the transmission conditions (4.28), is not sufficient for finding a solution unless appropriate boundary conditions are prescribed on $S_r$. For any choice of the boundary condition, we should ensure that a solution exists in an appropriate function space and that it approximates the desired solution sufficiently well. Further, boundary conditions that yield unique solutions are preferred over those that give more than one solution, even if all such solutions are equally good approximations of the desired one, since they simplify the process of finding a solution. The radiation conditions prescribed in Equations (4.29) were shown to yield at least one solution by Kupradze et al. [153, §12.2, §12.5.9] [154] [155, §7.4]. The proof is rather complicated. Simpler proofs are available for scattering from soft and rigid bodies [155, §6.12][156]. Note that the radiation conditions in [156] are equivalent to (4.29), as shown in [157]. Uniqueness of the solution follows from Corollary 2.12 in [153]. Also, see [155, §2.4] for uniqueness proofs for scattering from rigid and soft solids.

A physical interpretation of the scattered-field decomposition and radiation conditions is as follows: notice that from Equation (4.23), one can write the scattered field as an integral over

$S$. Therefore, the total displacement field is a sum of the incident field and an integral over $S$. Further, this integral can be interpreted as the radiation due to fictitious *single layer* and *double layer* body forces distributed over $S$ (see [158, pp. 377-378] for an analogous description for the vector Helmholtz equation). Therefore, the scattered field decomposition is indeed a mathematical expression of the Huygen's principle [147], where the total field is assumed to be a superposition of the incident field created by primary sources and the scattered field created by secondary sources located on $S$. The radiation conditions are, then, a prescription that the scattered field generated by the secondary sources does not propagate back towards the scatterer from infinity [152, §3.1] [158, pp. 380-381]. This is a sufficiently good approximation for modeling scattering from defects that are relatively far from the walls of the inspection specimen.

### 4.2.6 Conventional Boundary Integral Equation

The conventional boundary integral equation (CBIE) [140] for elastic wave scattering is a direct BIE that can be derived from the representation formula (4.26). Recall that the representation formula gives the displacement field only at points $\mathbf{x}$ inside the volume $V$ and not on the surface $S$. This is because the derivation of the formula assumes the exclusion of a small spherical volume around $\mathbf{x}$ as illustrated in Figure 4.1. However, a similar formula can be derived for points $\mathbf{x} \in S$ if the surface $S$ is sufficiently smooth at $\mathbf{x}$.

For this, consider the exclusion of volumes around $\mathbf{x}$ as shown in Figures 4.5 and 4.6. The scatterer occupies a region $V$ and the complementary region $V_0 = \mathbb{R}^3 \setminus (V \cup S)$ is occupied by the solid embedding the scatterer. An imaginary surface $S_r$ formed by a large sphere of radius $r$ is assumed for applying the radiation conditions under $r \to \infty$. For fields satisfying the equations of motion in the domain $V_0$ and the radiation conditions on $S_r$ (as $r \to \infty$), we use Figure 4.5 as a reference. Likewise, for fields satisfying equations of motion in $V$, we refer to Figure 4.6. The excluded regions ($V_\epsilon$) are defined by the intersection of the surface $S$ with a sphere of radius $\epsilon$ centered at $\mathbf{x}$: that is, $V_\epsilon = \{\mathbf{x}' \in V_0 \ni |\mathbf{x}' - \mathbf{x}| < \epsilon\}$ in Figure 4.5 and $V_\epsilon = \{\mathbf{x}' \in V \ni |\mathbf{x}' - \mathbf{x}| < \epsilon\}$

in Figure 4.6. Also, let the set of points on $S$ that lie inside $V_\epsilon$ be $\Omega_\epsilon = \{\mathbf{x}' \in S \cap V_\epsilon\}$. Note that the surfaces $S_r$ and $S_\epsilon$ are imaginary and do not represent material boundaries.

Since the scattered field satisfies the equation of motion (4.27a) in $V_r \setminus V_\epsilon$, an equation similar to (4.22) can be written as follows:

$$\int_{(S\setminus\Omega_\epsilon)\cup S_r} \left(\mathbf{t}^s(\mathbf{x}') \cdot \overline{\mathbf{G}}_+(\mathbf{x},\mathbf{x}') + \mathbf{u}^s(\mathbf{x}') \cdot \left[\hat{\mathbf{n}}' \cdot \overline{\overline{\mathbf{\Sigma}}}^{(1)}_+(\mathbf{x},\mathbf{x}')\right]\right) dS(\mathbf{x}') + \int_{S_\epsilon} \left(\mathbf{u}^s(\mathbf{x}') \cdot \left[\hat{\mathbf{n}}' \cdot \overline{\overline{\mathbf{\Sigma}}}^{(1)}_+(\mathbf{x},\mathbf{x}')\right] + \mathbf{t}^s(\mathbf{x}') \cdot \overline{\mathbf{G}}_+(\mathbf{x},\mathbf{x}')\right) dS(\mathbf{x}') = 0, \quad (4.34)$$

where the traction field is defined with respect to the unit normal oriented into $V_r$, which is given by $\hat{\mathbf{n}}' = \hat{\mathbf{n}}(\mathbf{x}')$. The $+$ subscript in the fundamental solutions indicates that they correspond to the material properties of the external medium. Also, notice that $\mathbf{x}$ and $\mathbf{x}'$ have been interchanged in writing the above equation from (4.22). The integral over $S_r$ vanishes as $r \to \infty$ because of the radiation conditions [152, §3.3]. In the limit $\epsilon \to 0$, the first term in (4.34) converges to the corresponding Riemann integral over the surface $S$, which is guaranteed to exist since the kernel is only weakly-singular, and the fourth term converges to zero. If the surface $S$ is smooth at $\mathbf{x}$ and the displacement $\mathbf{u}^s(\mathbf{x})$ is Hölder continuous in a neighbourhood of $\mathbf{x}$, then the second term also converges, and the limiting value is defined as a Cauchy principal value (CPV) integral over $S$. A proof for the convergence of the CPV integral is discussed in Appendix B.2. The third term converges to $\mathbf{u}^s(\mathbf{x})/2$, again assuming that $\mathbf{u}^s(\mathbf{x})$ is Hölder continuous around $\mathbf{x}$. This result follows directly from the derivation in Appendix B.1, where we consider a similar limit. Therefore, we get the following equation:

$$\fint_S \left(\mathbf{t}^s(\mathbf{x}') \cdot \overline{\mathbf{G}}_+(\mathbf{x},\mathbf{x}') + \mathbf{u}^s(\mathbf{x}') \cdot \left[\hat{\mathbf{n}}' \cdot \overline{\overline{\mathbf{\Sigma}}}^{(1)}_+(\mathbf{x},\mathbf{x}')\right]\right) dS(\mathbf{x}') = -\frac{1}{2}\mathbf{u}^s(\mathbf{x}), \quad (4.35)$$

where the integral sign with a horizontal line is defined as the CPV integral obtained by taking the limit $\epsilon \to 0$.

For the incident field, we will consider Figure 4.6, assuming, however, that the region $V$ consists of the medium with material properties $\rho_+$, $\lambda_+$ and $\mu_+$, instead of the scatterer. Since the incident field satisfies the equation of motion in $V \setminus V_\epsilon$, we obtain the following equation similar to (4.22)

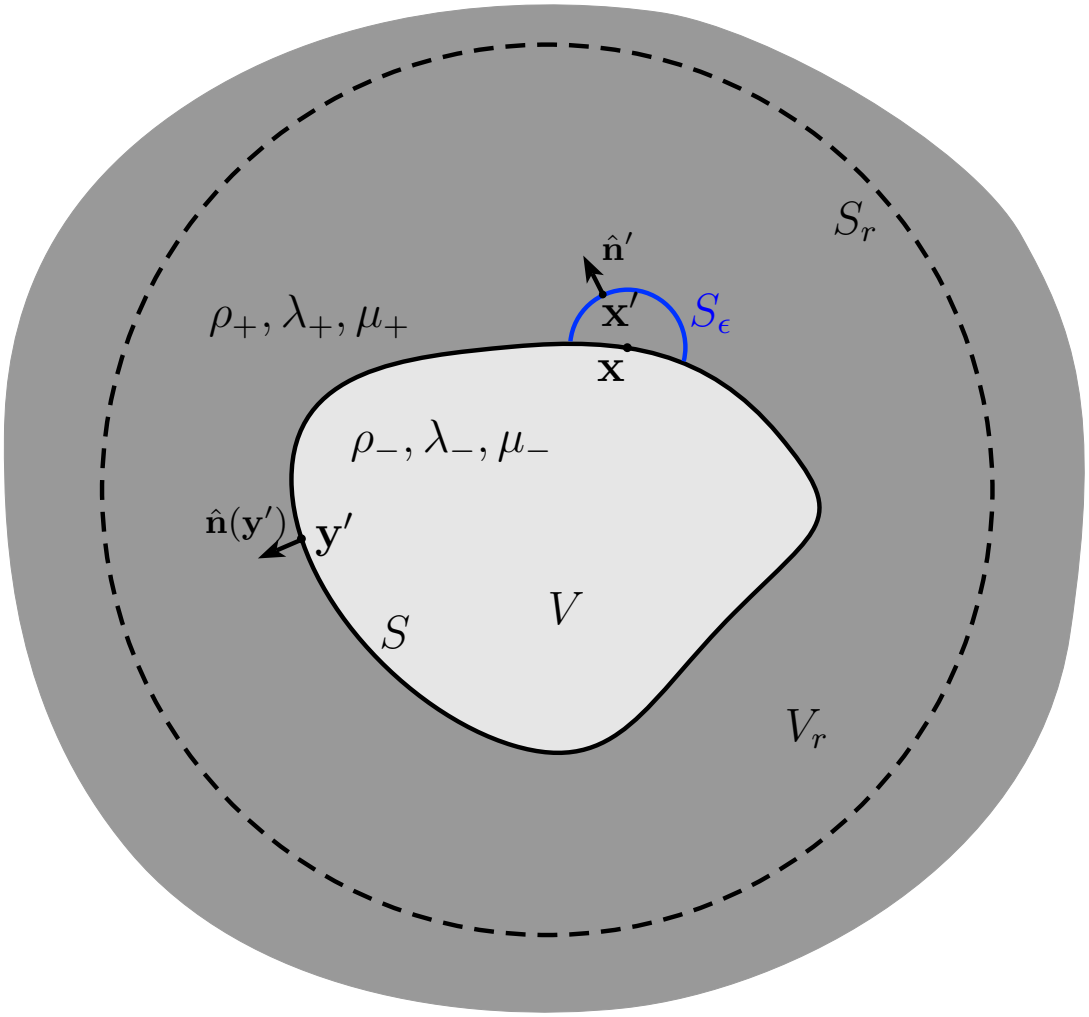


Figure 4.5: An imaginary surface $S_\epsilon$ is used to exclude the point $\mathbf{x}$ from the volume in which the divergence theorem is applied.

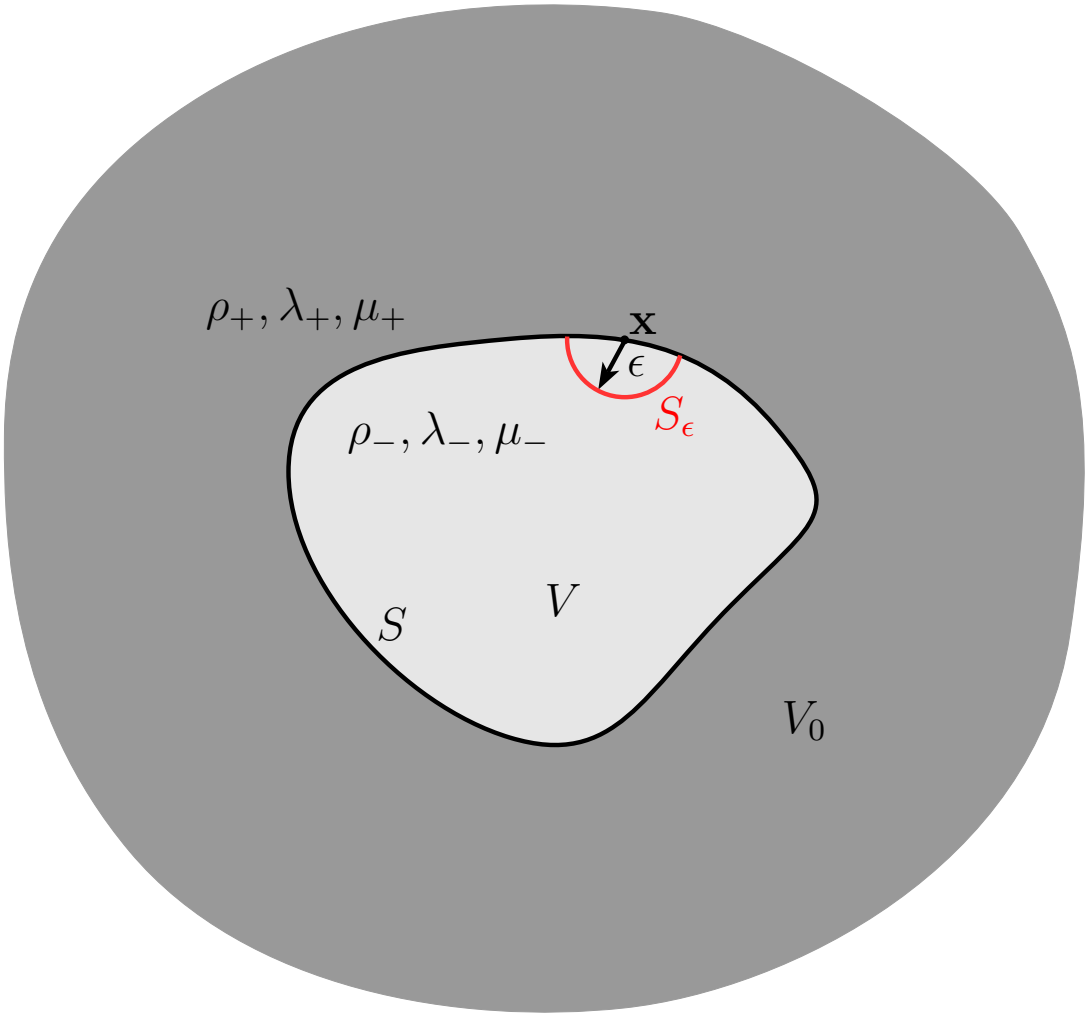


Figure 4.6: The imaginary surface $S_\epsilon$ projects into the scatterer. Divergence theorem can be applied inside the scatterer minus the volume excluded by $S_\epsilon$.

$$\int_{S\setminus\Omega_\epsilon} \left(\mathbf{t}^I(\mathbf{x}')\cdot\overline{\mathbf{G}}_+(\mathbf{x},\mathbf{x}')+\mathbf{u}^I(\mathbf{x}')\cdot\left[\hat{\mathbf{n}}'\cdot\overline{\overline{\boldsymbol{\Sigma}}}^{(1)}_+(\mathbf{x},\mathbf{x}')\right]\right)dS(\mathbf{x}') + \int_{S_\epsilon}\left(\mathbf{t}^I(\mathbf{x}')\cdot\overline{\mathbf{G}}_+(\mathbf{x},\mathbf{x}')+\mathbf{u}^I(\mathbf{x}')\cdot\left[\hat{\mathbf{n}}'\cdot\overline{\overline{\boldsymbol{\Sigma}}}^{(1)}_+(\mathbf{x},\mathbf{x}')\right]\right)dS(\mathbf{x}')=0, \quad (4.36)$$

where the unit normal is still chosen to point away from $V$ and the traction fields are defined according to this choice. Again, in the limit $\epsilon\to 0$, the first two terms converge to the corresponding CPV integrals, and the third and fourth terms evaluate to 0 and $-\mathbf{u}^I(\mathbf{x})/2$, respectively. This gives

$$\oint_S \left(\mathbf{t}^I(\mathbf{x}')\cdot\overline{\mathbf{G}}_+(\mathbf{x},\mathbf{x}')+\mathbf{u}^I(\mathbf{x}')\cdot\left[\hat{\mathbf{n}}'\cdot\overline{\overline{\boldsymbol{\Sigma}}}^{(1)}_+(\mathbf{x},\mathbf{x}')\right]\right)dS(\mathbf{x}')=\frac{1}{2}\mathbf{u}^I(\mathbf{x}). \quad (4.37)$$

Adding Equations (4.35) and (4.37) and noting that the total fields $\mathbf{u}(\mathbf{x})$ and $\mathbf{t}(\mathbf{x}')$ are given by the sum of the respective scattered and incident fields, we have

$$\oint_S \left(\mathbf{t}(\mathbf{x}')\cdot\overline{\mathbf{G}}_+(\mathbf{x},\mathbf{x}')+\mathbf{u}(\mathbf{x}')\cdot\left[\hat{\mathbf{n}}'\cdot\overline{\overline{\boldsymbol{\Sigma}}}^{(1)}_+(\mathbf{x},\mathbf{x}')\right]\right)dS(\mathbf{x}')+\frac{1}{2}\mathbf{u}(\mathbf{x})=\mathbf{u}^I(\mathbf{x}). \quad (4.38)$$

Repeating the derivation of (4.36), but considering the total fields inside $V\setminus V_\epsilon$ in the presence of the scatterer (instead of the incident fields), we get the following equation

$$\oint_S \left(\mathbf{t}(\mathbf{x}')\cdot\overline{\mathbf{G}}_-(\mathbf{x},\mathbf{x}')+\mathbf{u}(\mathbf{x}')\cdot\left[\hat{\mathbf{n}}'\cdot\overline{\overline{\boldsymbol{\Sigma}}}^{(1)}_-(\mathbf{x},\mathbf{x}')\right]\right)dS(\mathbf{x}')=\frac{1}{2}\mathbf{u}(\mathbf{x}). \quad (4.39)$$

Note that the fundamental solutions now correspond to the material properties of the scatterer. Equations (4.38) and (4.39) form the CBIE-formulation of elastic wave scattering. Once the displacement and traction fields on the surface $S$ are determined from this formulation, the fields in other regions can be obtained using the representation formula (4.26), thus solving the elastic wave scattering problem defined in the previous section. Observe that although the CBIE-formulation is implied by the scattering problem, the converse is not true. In other words, not every solution of the CBIE-formulation is a solution to the elastic wave scattering problem, as will be demonstrated in Chapter 6. Finally, the above equations can be derived alternatively by taking the limit of the representation formula as $\mathbf{x}$ approaches the surface $S$, as shown in Section 4.2.9.

### 4.2.7 Hypersingular Boundary Integral Equation

The hypersingular boundary integral equation (HBIE) is a direct BIE similar to the CBIE. It is also referred by the name traction BIE in the literature [159], particularly when regularization

techniques are applied on it to get rid of hypersingular characteristics. To derive the HBIE from the CBIE, we apply the boundary traction operator to the CBIE as described below. The following definitions will be helpful in simplifying the notation:

$$\overline{\mathbf{U}}_{\pm}(\mathbf{x},\mathbf{x}') \coloneqq \overline{\mathbf{G}}^{T}_{\pm}(\mathbf{x},\mathbf{x}') = \overline{\mathbf{G}}_{\pm}(\mathbf{x},\mathbf{x}'), \tag{4.40}$$

$$\overline{\mathbf{T}}^{(\alpha)}_{\pm}(\mathbf{x},\mathbf{x}') \coloneqq \left[\hat{\mathbf{n}}(\mathbf{x}')\cdot\overline{\overline{\mathbf{\Sigma}}}^{(\alpha)}_{\pm}(\mathbf{x},\mathbf{x}')\right]^{T} \tag{4.41}$$

for $\alpha = 1$ and 2. For $q = 1, 2$ and 3, differentiating the first equation in the CBIE-formulation (4.38) by the coordinate $x_q$ gives

$$\lim_{\epsilon\to 0}\left[\frac{\partial}{\partial x_q}\int_{S\setminus\Omega_\epsilon}\overline{\mathbf{U}}_{+}(\mathbf{x},\mathbf{x}')\cdot\mathbf{t}(\mathbf{x}')\,dS(\mathbf{x}') + \frac{\partial}{\partial x_q}\int_{S\setminus\Omega_\epsilon}\overline{\mathbf{T}}^{(1)}_{+}(\mathbf{x},\mathbf{x}')\cdot\mathbf{u}(\mathbf{x}')\,dS(\mathbf{x}')\right] + \frac{1}{2}\frac{\partial\mathbf{u}(\mathbf{x})}{\partial x_q} = \frac{\partial\mathbf{u}^{I}(\mathbf{x})}{\partial x_q}. \tag{4.42}$$

Note that the order of the derivative and the limit are interchanged assuming that the derivatives are uniformly convergent as $\epsilon \to 0$. However, the order of the integral and the derivative cannot be interchanged because the integration domain is a function of $\mathbf{x}$.

One way to evaluate the derivative is to rewrite the integral such that the domain of integration includes the entire surface $S$. Taking the example of the second integral on the left hand side of (4.42), one can write

$$\int_{S\setminus\Omega_\epsilon}\overline{\mathbf{T}}^{(1)}_{+}(\mathbf{x},\mathbf{x}')\cdot\mathbf{u}(\mathbf{x}')\,dS(\mathbf{x}') = \int_{S}\Big[1-\eta_\epsilon(\mathbf{x},\mathbf{x}')\Big]\overline{\mathbf{T}}^{(1)}_{+}(\mathbf{x},\mathbf{x}')\cdot\mathbf{u}(\mathbf{x}')\,dS(\mathbf{x}'), \tag{4.43}$$

where $\eta_\epsilon(\mathbf{x},\mathbf{x}')\colon \mathbb{R}^3\times\mathbb{R}^3 \to \mathbb{R}$ is a function that evaluates to one when $|\mathbf{x}-\mathbf{x}'| < \epsilon$ and zero otherwise. The derivative can then be moved inside the integral as shown below

$$\frac{\partial}{\partial x_q}\int_{S\setminus\Omega_\epsilon}\overline{\mathbf{T}}^{(1)}_{+}(\mathbf{x},\mathbf{x}')\cdot\mathbf{u}(\mathbf{x}')\,dS(\mathbf{x}') = \frac{\partial}{\partial x_q}\int_{S}\Big[1-\eta_\epsilon(\mathbf{x},\mathbf{x}')\Big]\overline{\mathbf{T}}^{(1)}_{+}(\mathbf{x},\mathbf{x}')\cdot\mathbf{u}(\mathbf{x}')\,dS(\mathbf{x}') \tag{4.44a}$$

$$= \int_{S}\left\{\Big[1-\eta_\epsilon(\mathbf{x},\mathbf{x}')\Big]\frac{\partial\overline{\mathbf{T}}^{(1)}_{+}(\mathbf{x},\mathbf{x}')}{\partial x_q}\cdot\mathbf{u}(\mathbf{x}') - \overline{\mathbf{T}}^{(1)}_{+}(\mathbf{x},\mathbf{x}')\cdot\mathbf{u}(\mathbf{x}')\frac{\partial\eta_\epsilon(\mathbf{x},\mathbf{x}')}{\partial x_q}\right\}dS(\mathbf{x}') \tag{4.44b}$$

$$= \int_{S\setminus\Omega_\epsilon}\frac{\partial\overline{\mathbf{T}}^{(1)}_{+}(\mathbf{x},\mathbf{x}')}{\partial x_q}\cdot\mathbf{u}(\mathbf{x}')\,dS(\mathbf{x}') - \mathbf{\Phi}_\epsilon(\mathbf{x}). \tag{4.44c}$$

The last term in the integrand in (4.44b) evaluates to a Dirac delta function on the closed curve $\Gamma_\epsilon = \{\mathbf{x}'\in S \ni |\mathbf{x}-\mathbf{x}'| = \epsilon\}$ which forms the boundary of $\Omega_\epsilon$, and thus $\mathbf{\Phi}_\epsilon(\mathbf{x})$ consists only of values

of the kernel $\overline{\mathbf{T}}^{(1)}_{+}(\mathbf{x},\mathbf{x}')$ evaluated on $\Gamma_\epsilon$. In the limit $\epsilon \to 0$, the terms in (4.44c) do not converge individually, but the limit exists when the two terms are considered together. Further, $\mathbf{\Phi}_\epsilon(\mathbf{x})$ does not have any non-divergent terms when written as a Laurent series in the variable $\epsilon$. Therefore, the order of the integral and the derivative can be interchanged if only the finite (non-divergent) part in the Laurent series expansion of the integral in Equation (4.44c) is retained. In contrast, for the first term on the left hand side of Equation (4.42), decomposition of the derivative as in Equation (4.44c) leads to a $\mathbf{\Phi}_\epsilon(\mathbf{x})$ which converges to zero as $\epsilon \to 0$. Using the above arguments, Equation (4.42) then leads to the following

$$\lim_{\epsilon\to 0}\int_{S\setminus\Omega_\epsilon} \frac{\partial \overline{\mathbf{U}}_{+}(\mathbf{x},\mathbf{x}')}{\partial x_q}\cdot\mathbf{t}(\mathbf{x}')\; dS(\mathbf{x}') + FP\left\{\lim_{\epsilon\to 0}\int_{S\setminus\Omega_\epsilon} \frac{\partial \overline{\mathbf{T}}^{(1)}_{+}(\mathbf{x},\mathbf{x}')}{\partial x_q}\cdot\mathbf{u}(\mathbf{x}')\; dS(\mathbf{x}')\right\} + \frac{1}{2}\frac{\partial \mathbf{u}(\mathbf{x})}{\partial x_q} = \frac{\partial \mathbf{u}^I(\mathbf{x})}{\partial x_q}, \quad (4.45)$$

where $FP\{\ldots\}$ denotes the finite part of the terms inside the parentheses as described above.

With the definitions of the Hadamard finite part (HFP) and CPV integrals, the above equation can be rewritten as follows in a coordinate-free notation

$$\int_S \nabla\overline{\mathbf{U}}_{+}(\mathbf{x},\mathbf{x}')\cdot\mathbf{t}(\mathbf{x}')\; dS(\mathbf{x}') + \fint_S \nabla\overline{\mathbf{T}}^{(1)}_{+}(\mathbf{x},\mathbf{x}')\cdot\mathbf{u}(\mathbf{x}')\; dS(\mathbf{x}') + \frac{1}{2}\nabla\mathbf{u}(\mathbf{x}) = \nabla\mathbf{u}^I(\mathbf{x}). \quad (4.46)$$

Here, the integral with two horizontal lines is the HFP integral. Multiplying the above by the fourth-order stiffness tensor $\mathcal{C}^+$ and the unit normal vector $\mathbf{n}(\mathbf{x})$, we get

$$\int_S \mathbf{n}(\mathbf{x})\cdot\mathcal{C}^+\colon\nabla\overline{\mathbf{U}}_{+}(\mathbf{x},\mathbf{x}')\cdot\mathbf{t}(\mathbf{x}')\; dS(\mathbf{x}') + \fint_S \mathbf{n}(\mathbf{x})\cdot\mathcal{C}^+\colon\nabla\overline{\mathbf{T}}^{(1)}_{+}(\mathbf{x},\mathbf{x}')\cdot\mathbf{u}(\mathbf{x}')\; dS(\mathbf{x}') + \frac{1}{2}\mathbf{n}(\mathbf{x})\cdot\mathcal{C}^+\colon\nabla\mathbf{u}(\mathbf{x}) = \mathbf{n}(\mathbf{x})\cdot\mathcal{C}^+\colon\nabla\mathbf{u}^I(\mathbf{x}), \quad (4.47)$$

where the double dot product is defined according to Equation (2.4), which is reproduced below for convenience:

$$\left[\mathcal{C}\colon\overline{\mathbf{E}}\right]_{ik} = C_{ikpq}E_{pq} \quad (4.48)$$

for any fourth-order tensor $\mathcal{C}$ and second-order tensor $\overline{\mathbf{E}}$.

To simplify the kernels in the above equation, consider the following definitions

$$\overline{\mathbf{K}}_{\pm}^{(\alpha)}(\mathbf{x},\mathbf{x}') \coloneqq \mathbf{n}(\mathbf{x}) \cdot \mathcal{C}^{\pm} \colon \nabla_{\alpha} \overline{\mathbf{U}}_{\pm}(\mathbf{x},\mathbf{x}'), \tag{4.49a}$$

$$\overline{\mathbf{H}}_{\pm}^{(\alpha)}(\mathbf{x},\mathbf{x}') \coloneqq \mathbf{n}(\mathbf{x}) \cdot \mathcal{C}^{\pm} \colon \nabla_{\alpha} \overline{\mathbf{T}}_{\pm}^{(\alpha)}(\mathbf{x},\mathbf{x}') \tag{4.49b}$$

for $\alpha = 1$ and 2, where the index $\alpha$ indicates that the gradient $\nabla_{\alpha}$ is taken with respect to argument $\alpha$ of $\overline{\mathbf{K}}_{\pm}^{(\alpha)}(\mathbf{x},\mathbf{x}')$ and $\overline{\mathbf{H}}_{\pm}^{(\alpha)}(\mathbf{x},\mathbf{x}')$. For example, in $\overline{\mathbf{K}}_{\pm}^{(1)}(\mathbf{x},\mathbf{x}')$, the gradient is taken with respect to the variable $\mathbf{x}$. Note that from the definition of $\overline{\mathbf{T}}_{\pm}^{(2)}(\mathbf{x}',\mathbf{x})$ in (4.41) and Equation (4.17), it follows that $\overline{\mathbf{K}}_{\pm}^{(2)}(\mathbf{x}',\mathbf{x}) = \left[\overline{\mathbf{T}}_{\pm}^{(1)}(\mathbf{x},\mathbf{x}')\right]^{T}$ and $\left[\overline{\mathbf{T}}_{\pm}^{(2)}(\mathbf{x}',\mathbf{x})\right]^{T} = \overline{\mathbf{K}}_{\pm}^{(1)}(\mathbf{x},\mathbf{x}')$. Also, since $\overline{\mathbf{H}}_{\pm}^{(1)}(\mathbf{x},\mathbf{x}') = \overline{\mathbf{H}}_{\pm}^{(2)}(\mathbf{x},\mathbf{x}')$, the superscript of this kernel is dropped hereafter. Using the above definitions, Equation (4.47) can be expressed as follows

$$\fint_S \overline{\mathbf{K}}_{+}^{(1)}(\mathbf{x},\mathbf{x}') \cdot \mathbf{t}(\mathbf{x}')\, dS(\mathbf{x}') + \fint_S \overline{\mathbf{H}}_{+}(\mathbf{x},\mathbf{x}') \cdot \mathbf{u}(\mathbf{x}')\, dS(\mathbf{x}') + \frac{1}{2}\mathbf{t}(\mathbf{x}) = \mathbf{t}^{I}(\mathbf{x}), \tag{4.50}$$

Equivalently, by switching the variable with respect to which the gradient is taken in kernel $\overline{\mathbf{K}}_{+}^{(1)}(\mathbf{x},\mathbf{x}')$, we have

$$-\fint_S \overline{\mathbf{K}}_{+}^{(2)}(\mathbf{x},\mathbf{x}') \cdot \mathbf{t}(\mathbf{x}')\, dS(\mathbf{x}') + \fint_S \overline{\mathbf{H}}_{+}(\mathbf{x},\mathbf{x}') \cdot \mathbf{u}(\mathbf{x}')\, dS(\mathbf{x}') + \frac{1}{2}\mathbf{t}(\mathbf{x}) = \mathbf{t}^{I}(\mathbf{x}), \tag{4.51}$$

This is the first equation in the HBIE formulation. One may notice that the above procedure from (4.42) to (4.47) is nothing but the application of the boundary traction operator to the first equation in the CBIE-formulation. Repeating this process on the second equation in the CBIE formulation, we get

$$-\fint_S \overline{\mathbf{K}}_{-}^{(2)}(\mathbf{x},\mathbf{x}') \cdot \mathbf{t}(\mathbf{x}')\, dS(\mathbf{x}') + \fint_S \overline{\mathbf{H}}_{-}(\mathbf{x},\mathbf{x}') \cdot \mathbf{u}(\mathbf{x}')\, dS(\mathbf{x}') - \frac{1}{2}\mathbf{t}(\mathbf{x}) = 0. \tag{4.52}$$

Equations (4.51) and (4.52) together form the HBIE formulation for elastic wave scattering. The HBIE formulation as expressed in these two equations is in a form that enables direct comparison with [139]. The HBIE formulation requires that the displacement field be $C^{1,\alpha}$ Hölder continuous. This requirement is more stringent than the one in the CBIE formulation and arises from the fact the we rely on constructing a Laurent series of the hypersingular integrand to eliminate divergent terms in the formulation. See Appendix B.3 for details.

The kernel $\overline{\mathbf{H}}_{\pm}(\mathbf{x},\mathbf{x}')$ can be evaluated from the following expression [112]

$$\begin{aligned}\overline{\mathbf{H}}_{\pm}(\mathbf{x},\mathbf{x}') = \frac{\mu_{\pm}}{\pi R^3}\Big\{\hat{\mathbf{R}}\cdot\hat{\mathbf{n}}'\left[\left(B_1\hat{\mathbf{R}}\hat{\mathbf{R}}+B_2\bar{\mathbf{I}}\right)\hat{\mathbf{R}}\cdot\hat{\mathbf{n}}+B_2\hat{\mathbf{R}}\hat{\mathbf{n}}+B_3\hat{\mathbf{n}}\hat{\mathbf{R}}\right]+\\ \hat{\mathbf{R}}\cdot\hat{\mathbf{n}}\left[B_2\hat{\mathbf{n}}'\hat{\mathbf{R}}+B_5\hat{\mathbf{R}}\hat{\mathbf{n}}'\right]+\hat{\mathbf{n}}\cdot\hat{\mathbf{n}}'\left[B_2\hat{\mathbf{R}}\hat{\mathbf{R}}+B_4\bar{\mathbf{I}}\right]+\\ \left[B_4\hat{\mathbf{n}}'\hat{\mathbf{n}}+B_6\hat{\mathbf{n}}\hat{\mathbf{n}}'\right]\Big\},\end{aligned} \tag{4.53}$$

where $\hat{\mathbf{n}}=\hat{\mathbf{n}}(\mathbf{x})$, $\hat{\mathbf{n}}'=\hat{\mathbf{n}}(\mathbf{x}')$, and

$$B_1 = A_1'\tau - 5A_1, \tag{4.54a}$$

$$B_2 = (A_2'\tau - 3A_2 + A_1)/2, \tag{4.54b}$$

$$B_3 = A_1 + \left(\frac{1}{2\alpha^2}-1\right)(A_1'\tau + 2A_2'\tau - 6A_2), \tag{4.54c}$$

$$B_4 = A_2, \tag{4.54d}$$

$$B_5 = A_3'\tau - 3A_3 = B_3, \tag{4.54e}$$

$$B_6 = A_3 + \left(\frac{1}{2\alpha^2}-1\right)(A_3'\tau + 2A_2). \tag{4.54f}$$

Since $B_5 = B_3$, it follows that $\overline{\mathbf{H}}_{\pm}(\mathbf{x},\mathbf{x}') = \overline{\mathbf{H}}_{\pm}^{T}(\mathbf{x}',\mathbf{x})$.

### 4.2.8 Combined Field Integral Equation

As the name suggests, the combined field integral equation (CFIE) involves the combination of the CBIE and the HBIE via a coupling parameter. The following operator definitions will be useful in writing the CFIE formulation compactly

$$\mathcal{U}_S^{\pm}\boldsymbol{\Psi}(\mathbf{x}) \coloneqq \int_S \overline{\mathbf{U}}_{\pm}(\mathbf{x},\mathbf{x}')\cdot\boldsymbol{\Psi}(\mathbf{x}')\,dS(\mathbf{x}'), \tag{4.55a}$$

$${}^{\alpha}\mathcal{T}_S^{\pm}\boldsymbol{\Psi}(\mathbf{x}) \coloneqq \int_S \overline{\mathbf{T}}_{\pm}^{(\alpha)}(\mathbf{x},\mathbf{x}')\cdot\boldsymbol{\Psi}(\mathbf{x}')\,dS(\mathbf{x}'), \tag{4.55b}$$

$${}^{\alpha}\mathcal{K}_S^{\pm}\boldsymbol{\Psi}(\mathbf{x}) \coloneqq \int_S \overline{\mathbf{K}}_{\pm}^{(\alpha)}(\mathbf{x},\mathbf{x}')\cdot\boldsymbol{\Psi}(\mathbf{x}')\,dS(\mathbf{x}'), \tag{4.55c}$$

$$\mathcal{H}_S^{\pm}\boldsymbol{\Psi}(\mathbf{x}) \coloneqq \int_S \overline{\mathbf{H}}_{\pm}(\mathbf{x},\mathbf{x}')\cdot\boldsymbol{\Psi}(\mathbf{x}')\,dS(\mathbf{x}') \tag{4.55d}$$

for $\alpha = 1$ and 2, where $\boldsymbol{\Psi}(\mathbf{x})$ is a vector field that represents either the displacement or traction, and $\mathbf{x}$ is assumed to lie on the surface $S$. When $\mathbf{x}\notin S$, the CPV and HFP integrals have to be

replaced with Riemann integrals. With these operator definitions, the CBIE formulation reads as follows

$$-\mathcal{U}_S^+\mathbf{t}(\mathbf{x}) + {}^2\mathcal{T}_S^+\mathbf{u}(\mathbf{x}) - \frac{\mathbf{u}(\mathbf{x})}{2} = -\mathbf{u}^I(\mathbf{x}), \tag{4.56a}$$

$$-\mathcal{U}_S^-\mathbf{t}(\mathbf{x}) + {}^2\mathcal{T}_S^-\mathbf{u}(\mathbf{x}) + \frac{\mathbf{u}(\mathbf{x})}{2} = 0. \tag{4.56b}$$

The same can be expressed in a matrix form as shown below

$$\begin{bmatrix} -\mathcal{U}_S^+ & {}^2\mathcal{T}_S^+ - \dfrac{\mathcal{I}}{2} \\ -\mathcal{U}_S^- & {}^2\mathcal{T}_S^- + \dfrac{\mathcal{I}}{2} \end{bmatrix} \begin{bmatrix} \mathbf{t}(\mathbf{x}) \\ \mathbf{u}(\mathbf{x}) \end{bmatrix} = \begin{bmatrix} -\mathbf{u}^I(\mathbf{x}) \\ \mathbf{0} \end{bmatrix}. \tag{4.57}$$

Similarly, the HBIE formulation is

$$\begin{bmatrix} -{}^2\mathcal{K}_S^+ + \dfrac{\mathcal{I}}{2} & \mathcal{H}_S^+ \\ -{}^2\mathcal{K}_S^- - \dfrac{\mathcal{I}}{2} & \mathcal{H}_S^- \end{bmatrix} \begin{bmatrix} \mathbf{t}(\mathbf{x}) \\ \mathbf{u}(\mathbf{x}) \end{bmatrix} = \begin{bmatrix} \mathbf{t}^I(\mathbf{x}) \\ \mathbf{0} \end{bmatrix}. \tag{4.58}$$

The CFIE formulation is defined using a coupling parameter $\alpha \in \mathbb{C}$ as follows

$$\alpha(4.57) + \frac{(1-\alpha)}{k_p^+\gamma^+}(4.58), \tag{4.59}$$

where $k_p^+$ is the wavenumber of the longitudinal wave in the exterior medium and $\gamma^+ = \lambda_+ + 2\mu_+$. Division of (4.58) by the constant $k_p^+\gamma^+$ ensures that the terms in (4.59) have the same dimensions. Equation (4.59) reduces to the conventional and hypersingular BIE formulations, when $\alpha = 1$ and 0, respectively. An alternate way of representing the CFIE formulation is as follows

$$(4.57) + \frac{\beta}{k_p^+\gamma^+}(4.58), \tag{4.60}$$

for $\beta \in \mathbb{C}$. The following relations are helpful for converting from one representation to the other

$$\beta = \frac{1-\alpha}{\alpha}, \tag{4.61a}$$

$$\alpha = \frac{1}{1+\beta}. \tag{4.61b}$$

### 4.2.9 Limit-to-the-Boundary Approach

The derivation of CBIE in Section 4.2.6 requires the exclusion of a spherical volume centered at $\mathbf{x}$. An alternative to this approach is to start with the representation formula for $\mathbf{x} \notin S$ and derive its limit as $\mathbf{x}$ goes to some point on $S$. The results of this limiting process are also applied in deriving integral equations for objects of zero thickness such as "cracks", as we will see in the next section. Consider Figure 4.5 in the case when $\mathbf{x}$ lies in $V_r$ instead of $S$. Then, from the representation formula (4.26), we have

$$-\mathbf{u}^s(\mathbf{x}) = \int_{S \cup S_r} \mathbf{t}^s(\mathbf{x}') \cdot \overline{\mathbf{G}}_+(\mathbf{x}, \mathbf{x}')\, dS(\mathbf{x}') + \int_{S \cup S_r} \mathbf{u}^s(\mathbf{x}') \cdot \left[\hat{\mathbf{n}}' \cdot \overline{\overline{\mathbf{\Sigma}}}^{(1)}_+(\mathbf{x}, \mathbf{x}')\right] dS(\mathbf{x}'). \tag{4.62}$$

The integral over $S_r$ tends to zero as $r \to \infty$ due to the radiation conditions. We are interested in the limit as $\mathbf{x}$ goes to a point $\mathbf{y} \in S$. The first term on the right hand side of the above equation is continuous at $\mathbf{y}$, whereas the second term is discontinuous and leads to a "jump term", that is

$$\lim_{\mathbf{x} \to \mathbf{y}} \int_S \mathbf{t}^s(\mathbf{x}') \cdot \overline{\mathbf{G}}_+(\mathbf{x}, \mathbf{x}')\, dS(\mathbf{x}') = \int_S \mathbf{t}^s(\mathbf{x}') \cdot \overline{\mathbf{G}}_+(\mathbf{y}, \mathbf{x}')\, dS(\mathbf{x}'), \tag{4.63a}$$

$$\lim_{\mathbf{x} \to \mathbf{y}} \int_S \mathbf{u}^s(\mathbf{x}') \cdot \left[\hat{\mathbf{n}}' \cdot \overline{\overline{\mathbf{\Sigma}}}^{(1)}_+(\mathbf{x}, \mathbf{x}')\right] dS(\mathbf{x}') = \barint_S \mathbf{u}^s(\mathbf{x}') \cdot \left[\hat{\mathbf{n}}' \cdot \overline{\overline{\mathbf{\Sigma}}}^{(1)}_+(\mathbf{y}, \mathbf{x}')\right] dS(\mathbf{x}') - \frac{\mathbf{u}^s(\mathbf{y})}{2}. \tag{4.63b}$$

Notice that the integral on the right hand side of Equation (4.63b) is a CPV integral and that $\mathbf{x}$ approaches $\mathbf{y}$ in the direction opposite to $\mathbf{n}'$. The sign of the jump term changes if the orientation of the unit normal is flipped. The proof of (4.63b), given in Appendix B.4, assumes that the displacement field is Hölder continuous in a neighbourhood of $\mathbf{y}$ and that the surface $S$ is smooth. Therefore, for any $\mathbf{x} \in S$, we have

$$-\frac{\mathbf{u}^s(\mathbf{x})}{2} = \int_S \mathbf{t}^s(\mathbf{x}') \cdot \overline{\mathbf{G}}_+(\mathbf{x}, \mathbf{x}')\, dS(\mathbf{x}') + \barint_S \mathbf{u}^s(\mathbf{x}') \cdot \left[\hat{\mathbf{n}}' \cdot \overline{\overline{\mathbf{\Sigma}}}^{(1)}_+(\mathbf{x}, \mathbf{x}')\right] dS(\mathbf{x}'), \tag{4.64}$$

which is same as Equation (4.35). It is clear that Equations (4.37) and (4.39) for $\mathbf{u}^I(\mathbf{x})$ and $\mathbf{u}_-(\mathbf{x})$, respectively, can be derived in a similar fashion, which leads to the CBIE formulation.

### 4.2.10 Boundary Integral Equations for Scattering from Thin Bodies

UNDE modeling often deals with very thin defects, such as cracks in metals. These defects may be modeled either using their exact geometries or by idealizations such as open surfaces of zero-

thickness. This section describes the application of BIE formulations to both of these cases, and this description will itself clarify why this topic warrants a special discussion. First, define a thin body as an object that has two compact surfaces ($S_{h1}$, $S_{h2} \in \mathbb{R}^3$) separated by a small thickness ($h$), which represents the largest normal distance from $S_{h1}$ to $S_{h2}$, such that there exists a bijective map between the two surfaces and that they converge to a surface $S_0 \in \mathbb{R}^3$ uniformly as the thickness goes to zero. Further, assume that $S_0$ is smooth and that the tangential vectors at points on $S_{h1}$ and their images in $S_{h2}$ converge (except for a factor of -1) to those at the corresponding points in $S_0$ uniformly. Note that the surfaces $S_{h1}$, $S_{h2}$ and $S_0$ include their respective boundaries. Unless mentioned otherwise, a thin object is assumed to be of non-zero thickness.

When the CBIE or HBIE formulation is applied to a thin body, any collocation scheme used for solving the resulting equations will have to avoid the problem of ill-conditioning arising from the fact that for any point $\mathbf{x}_1 \in S_{h1}$, there exists a point $\mathbf{x}_2 \in S_{h2}$ that is very close to $\mathbf{x}_1$. Therefore, collocation at $\mathbf{x}_1$ and $\mathbf{x}_2$ will yield approximately the same equations, barring a factor of -1 in case of the HBIE which results from the normal vectors being in opposite directions at $\mathbf{x}_1$ and $\mathbf{x}_2$. It is not difficult to see that boundary element methods that do not use collocation are also ill-conditioned in a similar fashion. Therefore, both conventional and hypersingular BIEs are not well-suited for modeling scattering from thin bodies. However, since the HBIE leads to equations that differ by a factor of -1 at $\mathbf{x}_1$ and $\mathbf{x}_2$ whereas the CBIE leads to the same equations, a combination of CBIE and HBIE can be made non-degenerate [140, 160]. Also, in the limit of zero thickness and for some special cases, the CBIE or HBIE can be solved to obtain the scattered fields without having to determine the fields on the surface completely, as detailed later in this section.

To mathematically demonstrate the degeneracy of the CBIE for thin bodies, distribute the integrals on $S$ in (4.56) over $S_{h1}$ and $S_{h2}$ as shown below

$$\mathcal{U}^+_{S_{h1}}\mathbf{t}(\mathbf{x}) + \mathcal{U}^+_{S_{h2}}\mathbf{t}(\mathbf{x}) - {}^2\mathcal{T}^+_{S_{h1}}\mathbf{u}(\mathbf{x}) - {}^2\mathcal{T}^+_{S_{h2}}\mathbf{u}(\mathbf{x}) + \frac{1}{2}\mathbf{u}(\mathbf{x}) = \mathbf{u}^I(\mathbf{x}), \tag{4.65a}$$

$$\mathcal{U}^-_{S_{h1}}\mathbf{t}(\mathbf{x}) + \mathcal{U}^-_{S_{h2}}\mathbf{t}(\mathbf{x}) - {}^2\mathcal{T}^-_{S_{h1}}\mathbf{u}(\mathbf{x}) - {}^2\mathcal{T}^-_{S_{h2}}\mathbf{u}(\mathbf{x}) = \frac{1}{2}\mathbf{u}(\mathbf{x}). \tag{4.65b}$$

Here, $S$ is assumed to be formed by $S_{h1}$ and $S_{h2}$ alone. The description below can be trivially generalized to the scenarios where this is not the case. Assume points $\mathbf{x}_1 \in S_{h1}$ and $\mathbf{x}_2 \in S_{h2}$, such

that $\mathbf{x}_1$ and $\mathbf{x}_2$ converge to the point $\mathbf{x}_0 \in S_0$ as $h \to 0$. Rewriting the above equations at $\mathbf{x} = \mathbf{x}_1$, we get

$$\mathcal{U}^+_{S_{h1}}\mathbf{t}(\mathbf{x}_1) + \mathcal{U}^+_{S_{h2}}\mathbf{t}(\mathbf{x}_1) - {}^2\mathcal{T}^+_{S_{h1}}\mathbf{u}(\mathbf{x}_1) - {}^2\mathcal{T}^+_{S_{h2}}\mathbf{u}(\mathbf{x}_1) + \frac{1}{2}\mathbf{u}(\mathbf{x}_1) = \mathbf{u}^I(\mathbf{x}_1), \tag{4.66a}$$

$$\mathcal{U}^-_{S_{h1}}\mathbf{t}(\mathbf{x}_1) + \mathcal{U}^-_{S_{h2}}\mathbf{t}(\mathbf{x}_1) - {}^2\mathcal{T}^-_{S_{h1}}\mathbf{u}(\mathbf{x}_1) - {}^2\mathcal{T}^-_{S_{h2}}\mathbf{u}(\mathbf{x}_1) = \frac{1}{2}\mathbf{u}(\mathbf{x}_1). \tag{4.66b}$$

Noting that in the limit $h \to 0$, the incident displacement field is continuous at $\mathbf{x}$ and that the total displacement and traction fields are discontinuous, define

$$\boldsymbol{\Psi}_1(\mathbf{y}_0) \coloneqq \lim_{h\to 0} \boldsymbol{\Psi}(\mathbf{y}_1), \tag{4.67a}$$

$$\boldsymbol{\Psi}_2(\mathbf{y}_0) \coloneqq \lim_{h\to 0} \boldsymbol{\Psi}(\mathbf{y}_2), \tag{4.67b}$$

$$\hat{\mathbf{n}}_1(\mathbf{y}_0) \coloneqq \lim_{h\to 0} \hat{\mathbf{n}}(\mathbf{y}_1) = -\lim_{h\to 0} \hat{\mathbf{n}}(\mathbf{y}_2), \tag{4.67c}$$

assuming that $\mathbf{y}_1 \in S_{h1}$, $\mathbf{y}_1 \in S_{h2}$ such that both $\mathbf{y}_1$ and $\mathbf{y}_2$ go to $\mathbf{y}_0$ as $h \to 0$, and where $\boldsymbol{\Psi}$ is a vector field that represents either the displacement or traction. The unit vector $\hat{\mathbf{n}}$ is the outward pointing normal vector on $S$, and the vector $\hat{\mathbf{n}}_1$ is defined as the unit normal vector on $S_0$. Then, Equations (4.63a) and (4.63b) imply the following limits

$$\lim_{h\to 0} \mathcal{U}^\pm_{S_{h2}}\mathbf{t}(\mathbf{x}_1) = \mathcal{U}^\pm_{S_0}\mathbf{t}_2(\mathbf{x}), \tag{4.68}$$

$$\lim_{h\to 0} {}^2\mathcal{T}^\pm_{S_{h2}}\mathbf{u}(\mathbf{x}_1) = -{}^2\mathcal{T}^\pm_{S_0}\mathbf{u}_2(\mathbf{x}) - \frac{1}{2}\mathbf{u}_2(\mathbf{x}). \tag{4.69}$$

The negative sign in the first term on the right hand side of (4.69) is due to the difference in the orientation of the unit normal vectors on $S_{h2}$ and $S_0$ according to (4.67c). The sign of the jump term in (4.69) is adjusted according to the fact that $\mathbf{x}_1$ approaches the surface $S_{h2}$ in the same direction as the unit normal, unlike in (4.63b). Also, we have

$$\lim_{h\to 0} \mathcal{U}^\pm_{S_{h1}}\mathbf{t}(\mathbf{x}_1) = \mathcal{U}^\pm_{S_0}\mathbf{t}_1(\mathbf{x}), \tag{4.70}$$

$$\lim_{h\to 0} {}^2\mathcal{T}^\pm_{S_{h1}}\mathbf{u}(\mathbf{x}_1) = {}^2\mathcal{T}^\pm_{S_0}\mathbf{u}_1(\mathbf{x}). \tag{4.71}$$

Therefore, in the limit $h \to 0$, Equations (4.66a) and (4.66b) become

$$\mathcal{U}^+_{S_0}\mathbf{t}_\Sigma(\mathbf{x}_0) - {}^2\mathcal{T}^+_{S_0}\mathbf{u}_\Delta(\mathbf{x}_0) + \frac{1}{2}\mathbf{u}_\Sigma(\mathbf{x}_0) = \mathbf{u}^I(\mathbf{x}_0), \tag{4.72a}$$

$$\mathcal{U}^{-}_{S_0}\mathbf{t}_\Sigma(\mathbf{x}_0) - {}^2\mathcal{T}^{-}_{S_0}\mathbf{u}_\Delta(\mathbf{x}_0) = \frac{1}{2}\mathbf{u}_\Delta(\mathbf{x}_0), \tag{4.72b}$$

where $\mathbf{\Psi}_\Sigma(\mathbf{x}_0) \coloneqq \mathbf{\Psi}_1(\mathbf{x}_0) + \mathbf{\Psi}_2(\mathbf{x}_0)$ and $\mathbf{\Psi}_\Delta(\mathbf{x}_0) \coloneqq \mathbf{\Psi}_1(\mathbf{x}_0) - \mathbf{\Psi}_2(\mathbf{x}_0)$, and $\mathbf{\Psi}$ is either the displacement or traction field. The same equation is obtained if the above steps are repeated for the case wherein collocation is performed at $\mathbf{x}_2$, which indicates that as $h$ goes to zero, the CBIE formulation becomes increasingly ill-conditioned due to near-degeneracy. In the limit $h \to 0$, observe that both $\mathbf{u}_\Delta(\mathbf{x})$ and $\mathbf{u}_\Sigma(\mathbf{x})$ are unknowns in Equations (4.72). If the term containing $\mathbf{u}_\Sigma(\mathbf{x})$ was not present, an indirect BEM could be applied to solve for the auxiliary variables $\mathbf{u}_\Delta(\mathbf{x})$ and $\mathbf{t}_\Sigma(\mathbf{x})$ on the surface $S_0$, from which the scattered field could be obtained. The presence of the $\mathbf{u}_\Sigma(\mathbf{x})$ term, though, makes such BEM formulations under-determined. However, for rigid bodies, the total displacement on $S$ vanishes, and the CBIE formulation reduces to

$$\mathcal{U}^{+}_{S_0}\mathbf{t}_\Sigma(\mathbf{x}_0) = \mathbf{u}^I(\mathbf{x}_0). \tag{4.73}$$

Therefore, the CBIE for zero-thickness rigid bodies can be solved using BEMs of the above-mentioned type. The HBIE-formulation for bodies of zero thickness follows from the application of the boundary-traction operator to (4.72), similar to the procedure described in Section 4.2.7. The end result is as follows

$$-{}^2\mathcal{K}^{+}_{S_0}\mathbf{t}_\Sigma(\mathbf{x}_0) + \mathcal{H}^{+}_{S_0}\mathbf{u}_\Delta(\mathbf{x}_0) + \frac{1}{2}\mathbf{t}_\Sigma(\mathbf{x}_0) = \mathbf{t}^I(\mathbf{x}_0), \tag{4.74a}$$

$$-{}^2\mathcal{K}^{-}_{S_0}\mathbf{t}_\Sigma(\mathbf{x}_0) + \mathcal{H}^{-}_{S_0}\mathbf{u}_\Delta(\mathbf{x}_0) = \frac{1}{2}\mathbf{t}_\Delta(\mathbf{x}_0). \tag{4.74b}$$

For soft scatterers, the traction field $\mathbf{t}_\Sigma$ is zero on $S_0$, and the formulation reduces to

$$\mathcal{H}^{+}_{S_0}\mathbf{u}_\Delta(\mathbf{x}_0) = \mathbf{t}^I(\mathbf{x}_0). \tag{4.75}$$

This equation can be solved using BEM by considering the *crack-opening displacement* $\mathbf{u}_\Delta(\mathbf{x}_0)$ as the unknown field.

## 4.3 Discretization

This section describes a collocation-based BEM for solving the CFIE-formulation. The surface of the scatterrer is described by a curvilinear triangular mesh. The displacement and traction fields are

approximated using non-conforming elements (basis functions) defined on the curvilinear triangular mesh. The coefficients of the basis functions form the degrees of freedom. They are determined by performing collocation at quadrature points on the triangles and solving the resulting linear system. This BEM can also be viewed as a locally-corrected Nyström method due to the specific choice of basis functions that define the boundary elements. The method presented here closely follows [30, Chap. 4].

### 4.3.1 Mesh Interpolation

Given a triangular mesh, defined by a list of points (nodes) on the actual surface of the scatterer and a prescription of their connectivity (in the form of triangles), one can construct an approximation of that surface by parametric interpolation over the mesh. The solution of the CFIE-formulation is obtained over this surface approximation ($S \subset \mathbb{R}^3$). Assume a Cartesian coordinate system wherein the position vectors are described by $\mathbf{x} = (x_1, x_2, x_3)$. Let the mesh consist of $N_P$ triangular patches with $N$ mesh nodes per each patch. Let the position vectors of the $N$ points for the patch indexed by the integer $p$ be given by $\mathbf{r}_1^{(p)}, \mathbf{r}_2^{(p)} \ldots \mathbf{r}_N^{(p)}$. Consider interpolation parameters $\xi_1$ and $\xi_2$ lying in the set $\Omega = \{\boldsymbol{\xi} = (\xi_1, \xi_2) \in \mathbb{R}^2 \mid \xi_1 + \xi_2 \leq 1\}$. The interpolation scheme is defined using polynomial functions of the interpolation parameters. An interpolation scheme is said to be of order $M$ if it exactly interpolates all surfaces whose coordinates can all be represented in terms of bivariate-polynomials (of the same two parameters) of degree less than or equal to $M$.

We need $(M+1)(M+2)/2$ points per patch for an interpolation of order $M$. This gives $N = 3$, 6, 10, etc. for interpolations of order $M = 1$, 2, 3, etc., respectively. Further, according to the prescribed mesh connectivity and node ordering (within a triangle), we associate the $N$ mesh nodes with the following $N$ points in the parameter space

$$\tilde{\boldsymbol{\xi}}_{jk} = \left(\frac{j}{M}, \frac{k}{M}\right) \tag{4.76}$$

for $0 \leq j, k \leq M$ and $j + k \leq M$. Therefore, the mesh nodes $\mathbf{r}_1^{(p)}$, $\mathbf{r}_2^{(p)} \ldots \mathbf{r}_N^{(p)}$ can be renamed as $\mathbf{r}_{jk}^{(p)}$, for $j$, $k$ in the foregoing range. The interpolation function corresponding to the patch with index $p$, represented by $\mathbf{x}^{(p)} \colon \Omega \to \mathbb{R}^3$, is defined as follows

$$\mathbf{x}^{(p)}(\boldsymbol{\xi}) = \sum_{j=0}^{M} \sum_{k \leq M-j} \mathcal{P}_{jk}(\boldsymbol{\xi}) \mathbf{r}_{jk}^{(p)}, \tag{4.77}$$

where the interpolation polynomial $\mathcal{P}_{jk}(\boldsymbol{\xi})$ is given by

$$\mathcal{P}_{jk}(\boldsymbol{\xi}) \coloneqq Q_j(\xi_1)\ Q_k(\xi_2)\ Q_l(\xi_3), \tag{4.78}$$

with $l = M - j - k$, $\xi_3 = 1 - \xi_1 - \xi_2$, and

$$Q_s(\xi) \coloneqq \frac{1}{s!} \prod_{k=0}^{s-1} (M\xi - k) \text{ for } 0 < s \leq M, \quad Q_0(\xi) = 1. \tag{4.79}$$

It can be verified that

$$\mathbf{x}^{(p)}(\tilde{\boldsymbol{\xi}}_{jk}) = \mathbf{r}_{jk}^{(p)}. \tag{4.80}$$

Discretizations of order upto (and including) two are considered in the implementation presented in this thesis.

From the above interpolation function, we get the following interpolation surface corresponding to the patch $p$

$$S_p = \{\, \mathbf{x} \in \mathbb{R}^3 \mid \mathbf{x} = \mathbf{x}^{(p)}(\boldsymbol{\xi}) \text{ for some } \boldsymbol{\xi} \in \Omega \}. \tag{4.81}$$

The surface approximation of the scatterer is then obtained by the union of all patch-wise interpolation surfaces:

$$S = \bigcup_{p=1}^{N_p} S_p. \tag{4.82}$$

Note that this is not a disjoint union since for any two adjacent patches indexed by $p$ and $q$, $S_p$ and $S_q$ overlap at the common edge. In other words, the surface $S$ is made up of continuous, or conformal, curvilinear triangles. Finally, define two tangent vectors $\mathbf{e}_j^{(p)}(\boldsymbol{\xi})$, for $j = 1, 2$, and a normal vector $\mathbf{e}_3^{(p)}(\boldsymbol{\xi})$ on $S_p$ as follows

$$\mathbf{e}_1^{(p)}(\boldsymbol{\xi}) \coloneqq \frac{\partial \mathbf{x}^{(p)}(\boldsymbol{\xi})}{\partial \xi_1}, \tag{4.83a}$$

$$\mathbf{e}_2^{(p)}(\boldsymbol{\xi}) \coloneqq \frac{\partial \mathbf{x}^{(p)}(\boldsymbol{\xi})}{\partial \xi_2}, \tag{4.83b}$$

$$\mathbf{e}_3^{(p)}(\boldsymbol{\xi}) \coloneqq \mathbf{e}_1^{(p)}(\boldsymbol{\xi}) \times \mathbf{e}_2^{(p)}(\boldsymbol{\xi}). \tag{4.83c}$$

These three vectors are linearly independent and, thus, form a basis in $\mathbb{R}^3$. The fields on $S_p$ are expressed in terms of these vectors, as shown in the next section. The Jacobian matrix of $\mathbf{x}^{(p)}(\boldsymbol{\xi})$ is given by

$$\mathbf{J}_m(\boldsymbol{\xi}) = \left[\frac{\partial \mathbf{x}^{(p)}(\boldsymbol{\xi})}{\partial \xi_1} \quad \frac{\partial \mathbf{x}^{(p)}(\boldsymbol{\xi})}{\partial \xi_2}\right] = \left[\mathbf{e}_1^{(p)}(\boldsymbol{\xi}) \quad \mathbf{e}_2^{(p)}(\boldsymbol{\xi})\right], \tag{4.84}$$

assuming that the components of $\mathbf{x}^{(p)}(\boldsymbol{\xi})$ are written as column vectors. We define the "Jacobian" as the positive square root of the determinant of $\mathbf{J}_m^T(\boldsymbol{\xi})\mathbf{J}_m(\boldsymbol{\xi})$, which can be expressed as

$$\mathcal{J}(\boldsymbol{\xi}) = \sqrt{g_{11}(\boldsymbol{\xi})g_{22}(\boldsymbol{\xi}) - g_{12}(\boldsymbol{\xi})g_{21}(\boldsymbol{\xi})}, \tag{4.85}$$

where $g_{jk}(\boldsymbol{\xi}) = \mathbf{e}_j^{(p)}(\boldsymbol{\xi}) \cdot \mathbf{e}_k^{(p)}(\boldsymbol{\xi})$ for $j, k \in \{1, 2\}$. One may observe that the Jacobian is the vector magnitude of $\mathbf{e}_3^{(p)}(\boldsymbol{\xi})$.

### 4.3.2 Field Expansion

The displacement and traction fields on a triangle are defined using interpolation from $N_n$ points *inside* it. The values of the fields at the interpolation nodes are the degrees of freedom (DOFs) which need to be determined in the BEM. This can be viewed as a basis function expansion wherein the values of the fields at the interpolation nodes are the expansion coefficients. Since the fields are vectors, three components are needed to express the field at every interpolation node. Therefore, in every triangle, there are $3N_n$ vector basis functions each for the displacement and traction fields.

Consider the displacement field $\mathbf{u}(\mathbf{x})$ for $\mathbf{x} \in S$. The triangles are assumed to be indexed by the variable $p$. Quantities that vary across triangles are superscripted by $p$. Let the displacement field on triangle $p$ be given by

$$\mathbf{u}^{(p)}(\mathbf{x}) = \begin{cases} \mathbf{u}(\mathbf{x}) & \text{if } \mathbf{x} \in S_p \\ 0 & \text{otherwise} \end{cases}. \tag{4.86}$$

Note that if $\mathbf{x} \in S_p$, then there exists a $\boldsymbol{\xi} \in \Omega$ such that $\mathbf{x} = \mathbf{x}^{(p)}(\boldsymbol{\xi})$. Consider $N_n$ field interpolation points whose positions in the parameter space are defined, independently of $p$, by $\boldsymbol{\xi}_i = (\xi_{i1}, \xi_{i2}, \xi_{i3}) \in \Omega$ for $i = 1, 2, \ldots N_n$. The corresponding position vectors are given by $\mathbf{y}_i^{(p)} = \mathbf{x}^{(p)}(\boldsymbol{\xi}_i)$.

We first write the fields at each field interpolation point inside the triangle as a linear combination of the basis vectors defined in (4.83), that is,

$$\mathbf{u}_i^{(p)} \coloneqq \mathbf{u}^{(p)}(\mathbf{y}_i^{(p)}) = u_{i1}^{(p)}\mathbf{e}_1^{(p)}(\boldsymbol{\xi}_i) + u_{i2}^{(p)}\mathbf{e}_2^{(p)}(\boldsymbol{\xi}_i) + u_{i3}^{(p)}\mathbf{e}_3^{(p)}(\boldsymbol{\xi}_i), \tag{4.87}$$

where the coefficients $u_{i1}^{(p)}$, $u_{i2}^{(p)}$ and $u_{i3}^{(p)}$ are the components of the displacement vector in the given basis. Associating one vector basis function to each component of the displacement at each interpolation point, and writing the displacement field as a linear combination of these components gives

$$\mathbf{u}^{(p)}(\mathbf{x}) = \sum_{i=1}^{N_n} \left[ u_{i1}^{(p)}\mathbf{b}_{i1}^{(p)}(\mathbf{x}) + u_{i2}^{(p)}\mathbf{b}_{i2}^{(p)}(\mathbf{x}) + u_{i3}^{(p)}\mathbf{b}_{i3}^{(p)}(\mathbf{x}) \right], \tag{4.88}$$

where $\mathbf{b}_{i\alpha}^{(p)} : S_p \to \mathbb{R}^3$ (for $\alpha = 1, 2, 3$) is the basis function corresponding to the $\alpha^{th}$ field component at the $i^{th}$ field interpolation point in triangle $p$. The same can be expressed in the dyadic notation as

$$\mathbf{u}^{(p)}(\mathbf{x}) = \sum_{i=1}^{N_n} \bar{\mathbf{L}}_i^{(p)}(\mathbf{x}) \cdot \mathbf{u}_i^{(p)}, \tag{4.89}$$

where $\bar{\mathbf{L}}_i^{(p)}(\mathbf{x})$ is a field interpolation dyad which satisfies the relation $\bar{\mathbf{L}}_i^{(p)}(\mathbf{x}) \cdot \mathbf{e}_\alpha^{(p)}(\boldsymbol{\xi}_i) = \mathbf{b}_{i\alpha}^{(p)}(\mathbf{r})$.

The basis functions $\mathbf{b}_{i\alpha}^{(p)}(\mathbf{r})$ (for $\alpha = 1, 2, 3$) corresponding to the point $i$ are chosen such that they vanish for $\mathbf{x} = \mathbf{y}_j^{(p)}$, $j \neq i$, and are equal to $\mathbf{e}_\alpha^{(p)}(\boldsymbol{\xi}_i)$ at $\mathbf{x} = \mathbf{y}_i^{(p)}$. In terms of $\bar{\mathbf{L}}_i^{(p)}(\mathbf{x})$, this means that

$$\bar{\mathbf{L}}_i^{(p)}(\mathbf{y}_j^{(p)}) = \bar{\mathbf{I}}\delta_{ij} \tag{4.90}$$

for $i, j = 1, 2, 3 \ldots N_n$. This can be achieved by setting

$$\mathbf{b}_{i\alpha}^{(p)}(\mathbf{x}) = L_i(\boldsymbol{\xi})\mathbf{e}_\alpha^{(p)}(\boldsymbol{\xi}), \tag{4.91}$$

Table 4.1: Quadrature rules

| Rule | Order | Number of Points |
|---|---|---|
| 0 | 1 | 1 |
| 1 | 2 | 3 |
| 2 | 4 | 6 |
| 3 | 6 | 12 |

where $\boldsymbol{\xi}$ is such that $\mathbf{x} = \mathbf{x}^{(p)}(\boldsymbol{\xi})$, and $L_i : \Omega \to \mathbb{R}$ are functions such that

$$L_i(\boldsymbol{\xi}_j) = \delta_{ij} \tag{4.92}$$

for $i, j = 1, 2 \ldots N_n$. For traction fields, the functions $\tilde{L}_i(\boldsymbol{\xi})$, defined according to (4.93), are used in place of $L_i(\boldsymbol{\xi})$.

$$\tilde{L}_i(\boldsymbol{\xi}) = \frac{\mathcal{J}(\boldsymbol{\xi}_i)}{\mathcal{J}(\boldsymbol{\xi})} L_i(\boldsymbol{\xi}), \tag{4.93}$$

where $\mathcal{J}(\boldsymbol{\xi})$ is the Jacobian function defined in (4.85). The reason for this rather odd choice is to allow cancellation of the Jacobian in singular integrals and is explained in Appendix C.1. It remains to specify the construction of the functions $L_i(\boldsymbol{\xi})$. This requires a description of the choice of the field interpolation points.

### 4.3.3 Field Interpolation Points

The field interpolation points in a triangle are chosen to coincide with quadrature points on it. Therefore, corresponding to different quadrature rules, we get different number of interpolation points. This implementation is based on the symmetric Gaussian quadrature rules due to Dunavant [161]. It is not difficult to extend the method to other quadrature rules. Table 4.1 gives the order (degree of exactness) and corresponding number of points for the four quadrature rules considered in this work.

The interpolation functions $L_i(\boldsymbol{\xi})$ are constructed using polynomials in the variables $\xi_1$ and $\xi_2$. The natural, though not the best, choice for such a construction is by the linear combination of

monomials. Consider the set of monomials in two variables ($\xi_1, \xi_2 \in \mathbb{R}$) of degree less than or equal to $M$

$$B_M^2 = \{\xi_1^a \xi_2^b \mid a, b \in \mathbb{Z}^{\geq 0}, a + b \leq M\}. \tag{4.94}$$

The number of elements in $B_M^2$ is given by

$$N_b = \frac{(M+1)(M+2)}{2}. \tag{4.95}$$

For $M = 0, 1, 2$ and 3, we get $N_b = 1, 3, 6$ and 10, respectively. Constructing the functions $L_i(\boldsymbol{\xi})$ from a linear combination of the elements of $B_M^2$ gives

$$L_i(\boldsymbol{\xi}) = \sum_{k=1}^{N_b} A_{ik} P_k(\xi_1, \xi_2), \tag{4.96}$$

where $P_k(\xi_1, \xi_2)$ are the elements of $B_M^2$ and $A_{ik} \in \mathbb{R}$ are the coefficients. There are $N_b$ coefficients for each of the $N_n$ functions. But Equation (4.90) prescribes $N_n$ conditions for each function. To be able to uniquely determine the coefficients, we need $N_n$ to equal $N_b$. Table (4.1) indicates that this condition is obtained only for Rules 0, 1 and 2. For Rule 3, the number of coefficients is 10, whereas the number of conditions is 12, and a solution for the coefficients may not exist. Therefore, set $B_3^2$ is augmented with two fourth-degree monomials – $\xi_1^3 \xi_2$ and $\xi_1 \xi_2^3$. The coefficients are, then, determined according to the following equation:

$$L_i(\boldsymbol{\xi}_j) = \sum_{k=1}^{N_n} A_{ik} P_k(\xi_{j1}, \xi_{j2}) = \delta_{ij} \tag{4.97}$$

for $j = 1, 2, 3 \ldots N_n$. This can be expressed compactly in the Einstein summation convention as follows

$$L_{ij} = A_{ik} P_{kj} = \delta_{ij}, \tag{4.98}$$

where $L_{ij} = L_i(\boldsymbol{\xi}_j)$ and $P_{kj} = P_k(\xi_{j1}, \xi_{j2})$. The condition number of the matrix $P_{kj}$ depends on the choice of functions used for constructing the interpolation polynomials. When the number of quadrature (equivalently, interpolation) points is large, monomial sets are not suitable for constructing interpolation functions as they lead to matrices with high condition numbers. Additionally in

that case, the resultant coefficients involve very large numbers, which increases cancellation errors in the evaluation of interpolation functions. The choice of the quadrature rule is also crucial as the distribution of quadrature (interpolation) points affects the accuracy of interpolation schemes involving high-degree polynomials.

### 4.3.4 Matrix Equations

This section describes discretization of the CFIE-formulation according to the mesh and field interpolations mentioned above. Equation (4.51) in the HBIE-formulation is used to illustrate the discretization procedure. The integrals over $S$ in (4.51) can be decomposed over the curvilinear triangles, as shown below using the example of one of the integrals:

$$\neq_S \overline{\mathbf{H}}_+(\mathbf{x},\mathbf{x}')\cdot\mathbf{u}(\mathbf{x}')\ dS(\mathbf{x}') = \sum_{p=1}^{N_P} \neq_{S_p} \overline{\mathbf{H}}_+(\mathbf{x},\mathbf{x}')\cdot\mathbf{u}(\mathbf{x}')\ dS(\mathbf{x}'). \tag{4.99}$$

The displacement field on triangle $p$ is

$$\mathbf{u}^{(p)}(\mathbf{x}') = \sum_{i=1}^{N_n} L_i(\boldsymbol{\xi}) \left[ u_{i1}^{(p)}\mathbf{e}_1^{(p)}(\boldsymbol{\xi}) + u_{i2}^{(p)}\mathbf{e}_2^{(p)}(\boldsymbol{\xi}) + u_{i3}^{(p)}\mathbf{e}_3^{(p)}(\boldsymbol{\xi}) \right], \tag{4.100}$$

where $\boldsymbol{\xi}\in\Omega$ is such that $\mathbf{x}' = \mathbf{x}^{(p)}(\boldsymbol{\xi})$. Therefore,

$$\neq_S \overline{\mathbf{H}}_+(\mathbf{x},\mathbf{x}')\cdot\mathbf{u}(\mathbf{x}')\ dS(\mathbf{x}') = \sum_{p=1}^{N_P}\sum_{i=1}^{N_n} u_{i\alpha}^{(p)} \neq_{S_p} L_i(\boldsymbol{\xi})\ \overline{\mathbf{H}}_+(\mathbf{x},\mathbf{x}')\cdot\mathbf{e}_\alpha^{(p)}(\boldsymbol{\xi})\ dS(\mathbf{x}'), \tag{4.101}$$

where summation over $\alpha = 1,2,3$ is implied. Noting that the area element on $S_p$ is given by

$$dS(\mathbf{x}') = \left\| \frac{\partial \mathbf{x}^{(p)}(\boldsymbol{\xi})}{\partial \xi_1} \times \frac{\partial \mathbf{x}^{(p)}(\boldsymbol{\xi})}{\partial \xi_2} \right\| d\xi_1 d\xi_2 = \mathcal{J}(\boldsymbol{\xi}) d\xi_1 d\xi_2, \tag{4.102}$$

the integration can be performed in the parametric space $\Omega$ as follows

$$\neq_S \overline{\mathbf{H}}_+(\mathbf{x},\mathbf{x}')\cdot\mathbf{u}(\mathbf{x}')\ dS(\mathbf{x}') = \sum_{p=1}^{N_P}\sum_{i=1}^{N_n} u_{i\alpha}^{(p)} \neq_{\Omega} L_i(\boldsymbol{\xi})\ \overline{\mathbf{H}}_+(\mathbf{x},\mathbf{x}')\cdot\mathbf{e}_\alpha^{(p)}(\boldsymbol{\xi})\mathcal{J}(\boldsymbol{\xi})\ d\xi_1 d\xi_2, \tag{4.103}$$

where $\mathbf{x}' = \mathbf{x}^{(p)}(\boldsymbol{\xi})$.

Applying the above procedure to all the integrals in Equation (4.51) yields the following equation

$$\sum_{p=1}^{N_p}\sum_{i=1}^{N_n} \Bigg[ - t_{i\alpha}^{(p)} \int_\Omega \tilde{L}_i(\boldsymbol{\xi})\ \overline{\mathbf{K}}_+^{(2)}(\mathbf{x},\mathbf{x}')\cdot\mathbf{e}_\alpha^{(p)}(\boldsymbol{\xi})\mathcal{J}(\boldsymbol{\xi})\ d\xi_1 d\xi_2 + u_{i\alpha}^{(p)} \neq_\Omega L_i(\boldsymbol{\xi})\ \overline{\mathbf{H}}_+(\mathbf{x},\mathbf{x}')\cdot\mathbf{e}_\alpha^{(p)}(\boldsymbol{\xi})\mathcal{J}(\boldsymbol{\xi})\ d\xi_1 d\xi_2 \Bigg] + \frac{1}{2}\mathbf{t}(\mathbf{x}) = \mathbf{t}^I(\mathbf{x}) \tag{4.104}$$

for $\mathbf{x} \in S$. We discretize this equation by performing collocation at the field interpolation points. Therefore,

$$\sum_{p=1}^{N_p}\sum_{i=1}^{N_n}\Bigg[ - t_{i\alpha}^{(p)} \fint_{\Omega} \tilde{L}_i(\boldsymbol{\xi})\ \overline{\mathbf{K}}_{+}^{(2)}(\mathbf{y}_j^{(q)},\mathbf{x}')\cdot\mathbf{e}_\alpha^{(p)}(\boldsymbol{\xi})\mathcal{J}(\boldsymbol{\xi})\ d\xi_1 d\xi_2 + u_{i\alpha}^{(p)} \fint_{\Omega} L_i(\boldsymbol{\xi})\ \overline{\mathbf{H}}_{+}(\mathbf{y}_j^{(q)},\mathbf{x}')\cdot\mathbf{e}_\alpha^{(p)}(\boldsymbol{\xi})\mathcal{J}(\boldsymbol{\xi})\ d\xi_1 d\xi_2\Bigg] + \frac{1}{2}\mathbf{t}(\mathbf{y}_j^{(q)}) = \mathbf{t}^I(\mathbf{y}_j^{(q)}) \quad (4.105)$$

for each $q \in \{1,2,\dots N_p\}$ and $j \in \{1,2,\dots N\}$ and where $\mathbf{y}_j^{(p)}$ is the $j^{th}$ field interpolation point on triangle $q$. Note that the above equation is a vector equation. To obtain a linear system of equations with $t_{i\alpha}^{(p)}$ and $u_{i\alpha}^{(p)}$ as unknowns, we take its dot product with $\tilde{\mathbf{e}}_\beta^{(q)}(\boldsymbol{\xi}_j)$ for $\beta \in \{1,2,3\}$, where $\tilde{\mathbf{e}}_\beta^{(q)}(\boldsymbol{\xi}_j)$ are vectors that satisfy $\tilde{\mathbf{e}}_\beta^{(q)}(\boldsymbol{\xi}_j)\cdot\mathbf{e}_\alpha^{(p)}(\boldsymbol{\xi}_j) = \delta_{\alpha\beta}$ for $\alpha,\beta \in \{1,2,3\}$. Note that this definition of $\tilde{\mathbf{e}}_\beta^{(q)}(\boldsymbol{\xi}_j)$ guarantees uniqueness of these vectors. Also, since $\mathbf{e}_1^{(p)}(\boldsymbol{\xi}_j)$ and $\mathbf{e}_2^{(p)}(\boldsymbol{\xi}_j)$ span the tangent space at $\boldsymbol{\xi}_j$, the vector $\tilde{\mathbf{e}}_3^{(p)}(\boldsymbol{\xi}_j)$ is normal to the surface. Similarly, $\tilde{\mathbf{e}}_1^{(p)}(\boldsymbol{\xi}_j)$ and $\tilde{\mathbf{e}}_2^{(p)}(\boldsymbol{\xi}_j)$ lie in the tangent space. We know that

$$\mathbf{t}(\mathbf{y}_j^{(q)}) = \mathbf{t}^{(q)}(\mathbf{y}_j^{(q)}) = \sum_{i=1}^{N_n}\tilde{L}_i(\boldsymbol{\xi}_j)\left[t_{i1}^{(q)}\mathbf{e}_1^{(q)}(\boldsymbol{\xi}_j) + t_{i2}^{(q)}\mathbf{e}_2^{(q)}(\boldsymbol{\xi}_j) + t_{i3}^{(q)}\mathbf{e}_3^{(q)}(\boldsymbol{\xi}_j)\right] \quad (4.106a)$$

$$= \sum_{i=1}^{N_n}\delta_{ij}\left[t_{i1}^{(q)}\mathbf{e}_1^{(q)}(\boldsymbol{\xi}_j) + t_{i2}^{(q)}\mathbf{e}_2^{(q)}(\boldsymbol{\xi}_j) + t_{i3}^{(q)}\mathbf{e}_3^{(q)}(\boldsymbol{\xi}_j)\right] \quad (4.106b)$$

$$= t_{j1}^{(q)}\mathbf{e}_1^{(q)}(\boldsymbol{\xi}_j) + t_{j2}^{(q)}\mathbf{e}_2^{(q)}(\boldsymbol{\xi}_j) + t_{j3}^{(q)}\mathbf{e}_3^{(q)}(\boldsymbol{\xi}_j). \quad (4.106c)$$

Equation (4.106b) follows from (4.106a) due to coincidence of the collocation and field interpolation points. Therefore (4.105) can be written as

$$\sum_{p=1}^{N_p}\sum_{i=1}^{N_n}\Bigg[ - t_{i\alpha}^{(p)} \fint_{\Omega} \tilde{L}_i(\boldsymbol{\xi})\ \tilde{\mathbf{e}}_\beta^{(q)}(\boldsymbol{\xi}_j)\cdot\overline{\mathbf{K}}_{+}^{(2)}(\mathbf{y}_j^{(q)},\mathbf{x}')\cdot\mathbf{e}_\alpha^{(p)}(\boldsymbol{\xi})\mathcal{J}(\boldsymbol{\xi})\ d\xi_1 d\xi_2 + u_{i\alpha}^{(p)} \fint_{\Omega} L_i(\boldsymbol{\xi})\ \tilde{\mathbf{e}}_\beta^{(q)}(\boldsymbol{\xi}_j)\cdot\overline{\mathbf{H}}_{+}(\mathbf{y}_j^{(q)},\mathbf{x}')\cdot\mathbf{e}_\alpha^{(p)}(\boldsymbol{\xi})\mathcal{J}(\boldsymbol{\xi})\ d\xi_1 d\xi_2\Bigg] + \frac{1}{2}t_{j\beta}^{(q)} = \tilde{\mathbf{e}}_\beta^{(q)}(\boldsymbol{\xi}_j)\cdot\mathbf{t}^I(\mathbf{y}_j^{(q)}). \quad (4.107)$$

Arrange the unknown displacement and traction coefficients separately into lists with a single index determined from $p,i,\alpha$. Then, define the integrals

$$Z_{K_{mn}}^{\pm} \coloneqq \fint_{\Omega} \tilde{L}_i(\boldsymbol{\xi})\ \tilde{\mathbf{e}}_\beta^{(q)}(\boldsymbol{\xi}_j)\cdot\overline{\mathbf{K}}_{\pm}^{(2)}(\mathbf{y}_j^{(q)},\mathbf{x}')\cdot\mathbf{e}_\alpha^{(p)}(\boldsymbol{\xi})\mathcal{J}(\boldsymbol{\xi})\ d\xi_1 d\xi_2, \quad (4.108a)$$

$$Z^{\pm}_{H_{mn}} \coloneqq \oint\!\!\!\!\!\!- \int_{\Omega} L_i(\boldsymbol{\xi})\ \tilde{\mathbf{e}}^{(q)}_{\beta}(\boldsymbol{\xi}_j) \cdot \overline{\mathbf{H}}_{\pm}(\mathbf{y}^{(q)}_j, \mathbf{x}') \cdot \mathbf{e}^{(p)}_{\alpha}(\boldsymbol{\xi}) \mathcal{J}(\boldsymbol{\xi})\ d\xi_1 d\xi_2, \tag{4.108b}$$

where the index $n$ is determined from $p$, $i$, $\alpha$, and $m$ is determined from $q$, $j$, $\beta$ according the above-mentioned ordering of the unknown coefficients. The HBIE-formulation, then, leads to the following matrix equation

$$\begin{bmatrix} -\overline{\mathbf{Z}}^{+}_{K} + \frac{1}{2}\bar{\mathbf{I}} & \overline{\mathbf{Z}}^{+}_{H} \\ -\overline{\mathbf{Z}}^{-}_{K} - \frac{1}{2}\bar{\mathbf{I}} & \overline{\mathbf{Z}}^{+}_{H} \end{bmatrix} \begin{bmatrix} \tilde{\mathbf{t}} \\ \tilde{\mathbf{u}} \end{bmatrix} = \begin{bmatrix} \tilde{\mathbf{t}}^{I} \\ 0 \end{bmatrix}, \tag{4.109}$$

where $\overline{\mathbf{Z}}^{\pm}_{K}$ and $\overline{\mathbf{Z}}^{\pm}_{H}$ are square sub-matrices of size $3N_P N_n$ whose elements are defined by (4.108). The vectors $\tilde{\mathbf{t}}$ and $\tilde{\mathbf{u}}$ of size $3N_P N_n \times 1$ store the unknown traction and displacement coefficients, respectively, in the above-mentioned order, and $\bar{\mathbf{I}}$ is the identity matrix of size $3N_P N_n$. The matrix formed by the sub-matrices $\overline{\mathbf{Z}}^{\pm}_{K}$ and $\overline{\mathbf{Z}}^{\pm}_{H}$ is known as the influence matrix. Numerical evaluation of the influence matrix is explained in the following sections. Note that every element of the influence matrix involves an integral associated with a collocation point $\mathbf{y}^{(q)}_j$ and a triangle $S_p$ on which the integration is performed.

### 4.3.5 Far-field Matrix Elements

When the collocation point $\mathbf{y}^{(p)}_j$ is not close to $S_p$, the integral is regular and is evaluated using the same quadrature rule that defines the field interpolation points, as shown below:

$$Z^{\pm}_{K_{mn}} = \sum_{k=1}^{N_n} w_k \tilde{L}_i(\boldsymbol{\xi}_k)\ \tilde{\mathbf{e}}^{(q)}_{\beta}(\boldsymbol{\xi}_j) \cdot \overline{\mathbf{K}}^{(2)}_{\pm}(\mathbf{y}^{(q)}_j, \mathbf{y}^{(p)}_k) \cdot \mathbf{e}^{(p)}_{\alpha}(\boldsymbol{\xi}_k) \mathcal{J}(\boldsymbol{\xi}_k) \tag{4.110a}$$

$$= \sum_{k=1}^{N_n} w_k \delta_{ik}\ \tilde{\mathbf{e}}^{(q)}_{\beta}(\boldsymbol{\xi}_j) \cdot \overline{\mathbf{K}}^{(2)}_{\pm}(\mathbf{y}^{(q)}_j, \mathbf{y}^{(p)}_k) \cdot \mathbf{e}^{(p)}_{\alpha}(\boldsymbol{\xi}_k) \mathcal{J}(\boldsymbol{\xi}_k) \tag{4.110b}$$

$$= w_i\ \tilde{\mathbf{e}}^{(q)}_{\beta}(\boldsymbol{\xi}_j) \cdot \overline{\mathbf{K}}^{(2)}_{\pm}(\mathbf{y}^{(q)}_j, \mathbf{y}^{(p)}_i) \cdot \mathbf{e}^{(p)}_{\alpha}(\boldsymbol{\xi}_i) \mathcal{J}(\boldsymbol{\xi}_i) \tag{4.110c}$$

Similarly,

$$Z^{\pm}_{H_{mn}} = w_i\ \tilde{\mathbf{e}}^{(q)}_{\beta}(\boldsymbol{\xi}_j) \cdot \overline{\mathbf{H}}_{\pm}(\mathbf{y}^{(q)}_j, \mathbf{y}^{(p)}_i) \cdot \mathbf{e}^{(p)}_{\alpha}(\boldsymbol{\xi}_i) \mathcal{J}(\boldsymbol{\xi}_i). \tag{4.111}$$

### 4.3.6 Near-field Matrix Elements

#### 4.3.6.1 Singular Integrals

When the collocation point lies inside $S_p$, the integral is singular, and can be expressed in the following general form

$$I = \fint_{\Omega} F(\xi_1, \xi_2)\ d\xi_1 d\xi_2. \tag{4.112}$$

Here, the function $F : \Omega \to \mathbb{C}$ is assumed to be hypersingular. Strongly-singular and weakly-singular integrands occur as special cases of the hypersingular function. When $F(\xi_1, \xi_2)$ is strongly-singular, the foregoing HFP integral coincides with the corresponding CPV integral. Similarly, when $F(\xi_1, \xi_2)$ is weakly-singular, the HFP integral coincides with the Riemann integral. Generally, a change of variables transformation is applied from $(\xi_1, \xi_2)$ to new variables $(\eta_1, \eta_2)$ for evaluating the integrals. The reason for this is mentioned later. Since the case wherein no transformation is applied can be considered as an instance of application of the identity transformation, the general form of above integral can be rewritten as follows

$$I = \fint_{\Omega_\eta} F(\eta_1, \eta_2)\ d\eta_1 d\eta_2, \tag{4.113}$$

where the Jacobian of the transformation is absorbed into the integrand. The function $F$ in the above equation is not the same as in (4.112); the letter $F$ is reused to represent the integrand. Note that $F$ is singular at some point $(\eta_{01}, \eta_{02}) \in \Omega_\eta$ if there is no singularity cancellation due to the Jacobian of the transformation from $(\xi_1, \xi_2)$ to $(\eta_1, \eta_2)$, which is the case for all the transformations considered here.

Transform the integral into polar coordinates $(\rho, \theta)$ centered at the point of singularity and defined according to (4.114).

$$\rho = \sqrt{(\eta_1 - \eta_{01})^2 + (\eta_2 - \eta_{02})^2}, \tag{4.114a}$$

$$\theta = \arctan\left(\frac{\eta_1 - \eta_{01}}{\eta_2 - \eta_{02}}\right). \tag{4.114b}$$

The integral $I$ can, then, be expressed as

$$I = \fint_{\Gamma} F(\rho, \theta)\, d\rho\, d\theta. \tag{4.115}$$

Again, the Jacobian of the polar coordinate transformation is absorbed into the integrand, which is still represented by the letter $F$. The domain $\Gamma$ is defined according to the location of the singularity point $(\eta_{01}, \eta_{02})$ relative to the boundaries of the triangle. The integrals in the general form given by (4.115) are evaluated using the singularity subtraction technique developed in [162], as shown below. Assume that $F(\rho, \theta)$ satisfies the following Laurent series expansion

$$F(\rho,\theta) = \frac{F_{-2}(\theta)}{\rho^2} + \frac{F_{-1}(\theta)}{\rho} + O(1). \tag{4.116}$$

For strongly-singular integrands, $F_{-2}(\theta) = 0$, and for weakly-singular integrands, both $F_{-2}(\theta)$ and $F_{-1}(\theta)$ are zero. Therefore, in the weakly-singular case, the integral in (4.115) is evaluated directly without any singularity subtraction. In all other cases, the divergent terms are subtracted from the integrand and integrated separately, as shown below

$$\begin{aligned} \oint\!\!\!\!\!\!-_{\Gamma} F(\rho,\theta)\, d\rho\, d\theta = FP\Bigg\{ \lim_{\epsilon\to 0^+} \Bigg( & \int_0^{2\pi} \int_{\alpha(\epsilon,\theta)}^{\hat{\rho}(\theta)} \left[ F(\rho,\theta) - \frac{F_{-2}(\theta)}{\rho^2} - \frac{F_{-1}(\theta)}{\rho} \right] d\rho\, d\theta \\ & + \int_0^{2\pi} \int_{\alpha(\epsilon,\theta)}^{\hat{\rho}(\theta)} \frac{F_{-1}(\theta)}{\rho} d\rho\, d\theta + \int_0^{2\pi} \int_{\alpha(\epsilon,\theta)}^{\hat{\rho}(\theta)} \frac{F_{-2}(\theta)}{\rho^2} d\rho\, d\theta \Bigg) \Bigg\} \end{aligned} \tag{4.117a}$$

$$:= I_0 + I_{-1} + I_{-2}. \tag{4.117b}$$

Here, $\alpha(\epsilon, \theta)$ is the value of $\rho$ on the boundary of $\Omega_\epsilon$ in the transformed coordinates, and $\hat{\rho}(\theta)$ is a function of $\theta$ that represents the distance to the edges of the triangular integration domain.

The integral over $\rho$ in $I_0$ is regular and can be evaluated using Gaussian quadrature rules. The Taylor series expansion of $\alpha(\epsilon, \theta)$ in the variable $\epsilon$ is required to evaluate the other $\rho$-integrals.

$$\alpha(\epsilon,\theta) = \alpha(0,\theta) + \epsilon \left.\frac{\partial \alpha(\epsilon,\theta)}{\partial \epsilon}\right|_{\epsilon=0} + \frac{\epsilon^2}{2} \left.\frac{\partial^2 \alpha(\epsilon,\theta)}{\partial \epsilon^2}\right|_{\epsilon=0} + O(\epsilon^3) \tag{4.118a}$$

$$= \epsilon\beta(\theta) + \epsilon^2\gamma(\theta) + O(\epsilon^3). \tag{4.118b}$$

The functions $\beta(\theta)$ and $\gamma(\theta)$ can be obtained by inversion of the Taylor series of the curve $|\mathbf{x}' - \mathbf{x}| = \epsilon$ about $\rho = 0$ [162]. Then,

$$I_{-1} = \lim_{\epsilon\to 0^+} \int_0^{2\pi} F_{-1}(\theta) \left[ \ln(\hat{\rho}(\theta)) - \ln(\alpha(\epsilon,\theta)) \right] d\theta \tag{4.119a}$$

$$= \int_0^{2\pi} F_{-1}(\theta) \ln(\hat{\rho}(\theta)) d\theta - \lim_{\epsilon \to 0^+} \int_0^{2\pi} F_{-1}(\theta) \ln(\epsilon \beta(\theta)) d\theta \tag{4.119b}$$

$$= \int_0^{2\pi} F_{-1}(\theta) \ln\left(\frac{\hat{\rho}(\theta)}{\beta(\theta)}\right) d\theta - \lim_{\epsilon \to 0^+} \ln \epsilon \int_0^{2\pi} F_{-1}(\theta) d\theta = \int_0^{2\pi} F_{-1}(\theta) \ln\left(\frac{\hat{\rho}(\theta)}{\beta(\theta)}\right) d\theta. \tag{4.119c}$$

The last equality follows from the fact that $F_{-1}(\theta) = -F_{-1}(\theta + \pi)$ for the kernels under consideration. Similarly,

$$I_{-2} = FP \left\{ \lim_{\epsilon \to 0^+} \int_0^{2\pi} F_{-2}(\theta) \left[ -\frac{1}{\hat{\rho}(\theta)} + \frac{1}{\alpha(\epsilon, \theta)} \right] d\theta \right\} \tag{4.120}$$

$$= -\int_0^{2\pi} \frac{F_{-2}(\theta)}{\hat{\rho}(\theta)} d\theta + FP \left\{ \lim_{\epsilon \to 0^+} \int_0^{2\pi} \frac{F_{-2}(\theta)}{\epsilon \beta(\theta)} \left(1 - \epsilon \frac{\gamma(\theta)}{\beta(\theta)}\right) d\theta \right\} \tag{4.121}$$

$$= -\int_0^{2\pi} F_{-2}(\theta) \left[ \frac{1}{\hat{\rho}(\theta)} + \frac{\gamma(\theta)}{\beta^2(\theta)} \right] d\theta + FP \left\{ \lim_{\epsilon \to 0^+} \frac{1}{\epsilon} \int_0^{2\pi} \frac{F_{-2}(\theta)}{\beta(\theta)} d\theta \right\} \tag{4.122}$$

$$= -\int_0^{2\pi} F_{-2}(\theta) \left[ \frac{1}{\hat{\rho}(\theta)} + \frac{\gamma(\theta)}{\beta^2(\theta)} \right] d\theta. \tag{4.123}$$

The Laurent series expansions corresponding to various kernels in the CFIE-formulation are given in Appendix C.1.

The integrals over $\theta$ are nearly-singular when the aspect ratio of the triangle $S_p$ is large or when the collocation point lies very close to the edges of $S_p$ [163]. The methods proposed in [163] are adopted for overcoming the near-singularity problem in both of these cases. The following transformation from $\boldsymbol{\xi}$ to $\boldsymbol{\eta}$ solves the problem due to triangles of large aspect ratios:

$$\begin{bmatrix} \eta_1 \\ \eta_2 \end{bmatrix} = \overline{\mathbf{T}}_0 \begin{bmatrix} \xi_1 \\ \xi_2 \end{bmatrix}, \tag{4.124}$$

where the transformation matrix $\overline{\mathbf{T}}_0$ is given by

$$\overline{\mathbf{T}}_0 = \begin{bmatrix} 1 & \eta_1^{(2)} \\ 0 & \eta_2^{(2)} \end{bmatrix}, \qquad \eta_1^{(2)} = \frac{g_{12}(\boldsymbol{\xi}_0)}{g_{11}(\boldsymbol{\xi}_0)}, \quad \eta_2^{(2)} = \frac{\mathcal{J}(\boldsymbol{\xi}_0)}{g_{11}(\boldsymbol{\xi}_0)} \tag{4.125}$$

and $\boldsymbol{\xi}_0 \in \Omega$ corresponds to the collocation point. The functions $g_{ij}$ $(i, j = 1, 2)$ are defined according to (4.85). The inverse transformation is

$$\mathbf{T}_0^{-1} = \begin{bmatrix} 1 & -\dfrac{\eta_1^{(2)}}{\eta_2^{(2)}} \\ 0 & \dfrac{1}{\eta_2^{(2)}} \end{bmatrix} \tag{4.126a}$$

$$= \begin{bmatrix} 1 & -\dfrac{g_{12}(\boldsymbol{\xi}_0)}{\mathcal{J}(\boldsymbol{\xi}_0)} \\ 0 & \dfrac{g_{11}(\boldsymbol{\xi}_0)}{\mathcal{J}(\boldsymbol{\xi}_0)} \end{bmatrix}. \tag{4.126b}$$

The Jacobian of the transformation from $\boldsymbol{\xi}$ to $\boldsymbol{\eta}$, which is the determinant of $\mathbf{T}_0^{-1}$, is therefore a constant and given by

$$\tilde{\mathcal{J}}(\boldsymbol{\eta}) = |\mathbf{T}_0^{-1}| = \frac{g_{11}(\boldsymbol{\xi}_0)}{\mathcal{J}(\boldsymbol{\xi}_0)}. \tag{4.127}$$

Near-singularity due to the collocation point being close to the edges is resolved by the application of a sigmoidal transformation [163].

#### 4.3.6.2 Nearly-singular Integrals

When the collocation point lies very close to $S_p$ but not inside it, the BEM integral is nearly-singular. Evaluation of such integrals is tougher than that of singular integrals since the apparent order of singularity can be very large, as shown later. For this reason, singularity cancellation schemes such as the ones considered in [164, 165] cannot be applied here. Indeed, for elastodynamic BIEs, this topic is not well-addressed in the literature. For example, there is no mention of nearly-singular integrals in [112, 166, 167]. An analysis of three integration methods was presented in [168] wherein the authors conclude that conversion of nearly hypersingular integrals to nearly weakly-singular integrals is the most efficient among the three examined methods. This conversion is based on the subtraction of some terms resulting from the Taylor series expansion of the density function and integrating them separately. However, this method does not account for all the apparent orders of singularity, as will be clear from the analysis presented this section. The singularity subtraction

procedure described here is more complicated as it involves constructing series expansions of the whole integrand. The fundamental idea underlying this method is rather simple and well-known. The complexity is in the details.

The singularity subtraction procedure for the integrals corresponding to the $\overline{\mathbf{H}}_{\pm}(\mathbf{x}, \mathbf{x}')$ kernel is described here. It is extended to other kernels in Appendix C.2. Nearly-singular integrals involving the $\overline{\mathbf{H}}_{\pm}(\mathbf{x}, \mathbf{x}')$ kernel can be expressed in the following form

$$I_H = \int_{\Omega} \mathbf{H}(\mathbf{x}_0, \boldsymbol{\xi}) \cdot \boldsymbol{\phi}(\boldsymbol{\xi}) \mathcal{J}(\boldsymbol{\xi}) \, d\xi_1 d\xi_2, \tag{4.128}$$

where $\mathbf{x}_0 = \mathbf{x}^{(q)}(\boldsymbol{\xi}_j)$ is the collocation point and

$$\mathbf{H}(\mathbf{x}_0, \boldsymbol{\xi}) \coloneqq \tilde{\mathbf{e}}_{\beta}^{(q)}(\boldsymbol{\xi}_j) \cdot \overline{\mathbf{H}}_{\pm}(\mathbf{x}_0, \mathbf{x}^{(p)}(\boldsymbol{\xi})), \tag{4.129a}$$

$$\boldsymbol{\phi}(\boldsymbol{\xi}) \coloneqq L_i(\boldsymbol{\xi}) \mathbf{e}_{\alpha}^{(p)}(\boldsymbol{\xi}). \tag{4.129b}$$

The collocation point is very close to triangle $S_p$. Also, the hypersingular integral is replaced with a Riemann integral since the integral is not truly singular. Let triangle $S_p$ be extended to $\tilde{S}_p$ as defined below

$$\tilde{S}_p = \{ \mathbf{x} \in \mathbb{R}^3 \mid \mathbf{x} = \mathbf{x}^{(p)}(\boldsymbol{\xi}) \text{ for some } \boldsymbol{\xi} \in \mathbb{R}^3 \}. \tag{4.130}$$

Let the projection of $\mathbf{x}_0$ on $\tilde{S}_p$ be $\tilde{\mathbf{x}} = \mathbf{x}^{(p)}(\tilde{\boldsymbol{\xi}})$ for some $\tilde{\boldsymbol{\xi}} \in \mathbb{R}^2$. Define a transformation from $\boldsymbol{\xi}$ to $\boldsymbol{\eta}$ by replacing $\boldsymbol{\xi}_0$ in Equation (4.125) with $\tilde{\boldsymbol{\xi}}$. According to this transformation, there exists a point $\tilde{\boldsymbol{\eta}} \in \mathbb{R}^2$ which corresponds to $\tilde{\boldsymbol{\xi}}$. Transforming the integral into polar coordinates centered at $\tilde{\boldsymbol{\eta}}$ yields

$$I_H = \int_{\Gamma} \tilde{F}(\rho, \theta) d\rho d\theta, \tag{4.131}$$

with $\tilde{F}(\rho, \theta) = \mathbf{H} \cdot \boldsymbol{\phi} J \rho$, where $J(\boldsymbol{\eta}) = \mathcal{J}(\boldsymbol{\xi}(\boldsymbol{\eta})) \, \tilde{\mathcal{J}}(\boldsymbol{\eta})$, and $\mathbf{H}$, $\boldsymbol{\phi}$ and $J$ should be seen as functions of $\rho$ and $\theta$. Note that if the point of projection lies outside the triangle, then the $\rho$-limits for $\Gamma$ are defined using only two subtriangles similar to the procedure in Appendix C.2.5 (see Figure C.1). If the conventional method of dividing the domain into three subtriangles is applied, the integral becomes hypersingular when $d = 0$, which typically happens when the scatterer is flat. Then the integral has to be treated according to the methods in Section 4.3.6.1.

Recall that, from (4.53), the kernel $\overline{\mathbf{H}}_{\pm}(\mathbf{x},\mathbf{x}')$ is given by

$$\overline{\mathbf{H}}_{\pm}(\mathbf{x},\mathbf{x}') = \frac{\mu_{\pm}}{\pi R^3}\Big\{\hat{\mathbf{R}}\cdot\hat{\mathbf{n}}'\left[\left(B_1\hat{\mathbf{R}}\hat{\mathbf{R}}+B_2\bar{\mathbf{I}}\right)\hat{\mathbf{R}}\cdot\hat{\mathbf{n}}+B_2\hat{\mathbf{R}}\hat{\mathbf{n}}+B_3\hat{\mathbf{n}}\hat{\mathbf{R}}\right]+ \hat{\mathbf{R}}\cdot\hat{\mathbf{n}}\left[B_2\hat{\mathbf{n}}'\hat{\mathbf{R}}+B_5\hat{\mathbf{R}}\hat{\mathbf{n}}'\right]+\hat{\mathbf{n}}\cdot\hat{\mathbf{n}}'\left[B_2\hat{\mathbf{R}}\hat{\mathbf{R}}+B_4\bar{\mathbf{I}}\right]+ \left[B_4\hat{\mathbf{n}}'\hat{\mathbf{n}}+B_6\hat{\mathbf{n}}\hat{\mathbf{n}}'\right]\Big\}. \tag{4.132}$$

Therefore, $\tilde{F}(\rho,\theta)=\mathbf{H}\cdot\boldsymbol{\phi}J\rho$ is in the general form

$$\tilde{F}(\rho,\theta)=\tilde{\mathbf{e}}\cdot\overline{\mathbf{H}}(\mathbf{x},\mathbf{x}')\cdot\boldsymbol{\phi}J\rho=\frac{\mu}{\pi R^3}\tilde{\mathbf{e}}\cdot\Big\{\hat{\mathbf{R}}\cdot\hat{\mathbf{n}}'\left[\left(B_1\hat{\mathbf{R}}\hat{\mathbf{R}}+B_2\bar{\mathbf{I}}\right)\hat{\mathbf{R}}\cdot\hat{\mathbf{n}}+B_2\hat{\mathbf{R}}\hat{\mathbf{n}}+B_3\hat{\mathbf{n}}\hat{\mathbf{R}}\right]+ \hat{\mathbf{R}}\cdot\hat{\mathbf{n}}\left[B_2\hat{\mathbf{n}}'\hat{\mathbf{R}}+B_5\hat{\mathbf{R}}\hat{\mathbf{n}}'\right]+\hat{\mathbf{n}}\cdot\hat{\mathbf{n}}'\left[B_2\hat{\mathbf{R}}\hat{\mathbf{R}}+B_4\bar{\mathbf{I}}\right]+ \left[B_4\hat{\mathbf{n}}'\hat{\mathbf{n}}+B_6\hat{\mathbf{n}}\hat{\mathbf{n}}'\right]\Big\}\cdot\boldsymbol{\phi}J\rho. \tag{4.133}$$

Series expansions of each term about $\rho=0$ are obtained separately and subtracted from the integrand to make it smooth. The subtracted terms are integrated analytically in the $\rho$-direction.

***First term.*** Consider the first term for example

$$\tilde{F}_1(\rho,\theta)=\frac{\mu}{\pi R^3}B_1(\hat{\mathbf{R}}\cdot\hat{\mathbf{n}}')(\tilde{\mathbf{e}}\cdot\hat{\mathbf{R}})(\hat{\mathbf{R}}\cdot\boldsymbol{\phi})(\hat{\mathbf{R}}\cdot\hat{\mathbf{n}})\;J\rho \tag{4.134a}$$

$$=\frac{\mu}{\pi R^7}B_1(\mathbf{R}\cdot\hat{\mathbf{n}}')(\tilde{\mathbf{e}}\cdot\mathbf{R})(\mathbf{R}\cdot\boldsymbol{\phi})(\mathbf{R}\cdot\hat{\mathbf{n}})\;J\rho \tag{4.134b}$$

$$=\frac{\mu}{\pi R^7}B_1(\mathbf{R}\cdot\mathbf{e}_3)(\tilde{\mathbf{e}}\cdot\mathbf{R})(\mathbf{R}\cdot\boldsymbol{\phi})(\mathbf{R}\cdot\hat{\mathbf{n}})\;\tilde{\mathcal{J}}(\boldsymbol{\eta})\rho, \tag{4.134c}$$

where a factor of $J$ was combined with the unit vector at $\mathbf{x}'$ to obtain the basis vector $\mathbf{e}_3$. Expand each of the quantities in the above expression in terms of their Taylor series expansions about $\rho=0$

$$\mathbf{R}=\mathbf{d}+\rho\mathbf{C}+\rho^2\mathbf{D}+O(\rho^3), \tag{4.135a}$$

$$B_j=\tilde{B}_{j,0}+\rho\tilde{B}_{j,1}+\rho^2\tilde{B}_{j,2}+O(\rho^3)\quad(j=1,2,\ldots 6), \tag{4.135b}$$

$$\boldsymbol{\phi}=\boldsymbol{\Phi_0}+\rho\boldsymbol{\Phi_1}+\rho^2\boldsymbol{\Phi_2}+O(\rho^3), \tag{4.135c}$$

$$\mathbf{e}_3=\mathbf{P_0}+\rho\mathbf{P_1}+\rho^2\mathbf{P_2}+O(\rho^3), \tag{4.135d}$$

where the `tilde` accent is used for coefficients of the Taylor series of $B_j$ to distinguish them from those defined about $\mathbf{R} = 0$. Note that when $\rho = 0$, the vector $\mathbf{R}$ represents the vector between the collocation point and the projection point $\tilde{\mathbf{x}}$. The following definitions will be useful in deriving the series expansions

$$\mathbf{R} \cdot \mathbf{e}_3 = \left[\mathbf{d} + \rho\mathbf{C} + \rho^2\mathbf{D} + O(\rho^3)\right] \cdot \left[\mathbf{P_0} + \rho\mathbf{P_1} + \rho^2\mathbf{P_2} + O(\rho^3)\right] \tag{4.136a}$$

$$= \mathbf{d} \cdot \mathbf{P_0} + \rho\mathbf{d} \cdot \mathbf{P_1} + \rho^2 \left(\mathbf{d} \cdot \mathbf{P_2} + \mathbf{D} \cdot \mathbf{P_0}\right) + O(\rho^3) \tag{4.136b}$$

$$\coloneqq M_{0,0} + \rho M_{0,1} + \rho^2 M_{0,2} + O(\rho^3), \tag{4.136c}$$

$$\tilde{\mathbf{e}} \cdot \mathbf{R} = \tilde{\mathbf{e}} \cdot \mathbf{d} + \rho\tilde{\mathbf{e}} \cdot \mathbf{C} + \rho^2\tilde{\mathbf{e}} \cdot \mathbf{D} + O(\rho^3) \tag{4.136d}$$

$$\coloneqq M_{1,0} + \rho M_{1,1} + \rho^2 M_{1,2} + O(\rho^3), \tag{4.136e}$$

$$\mathbf{R} \cdot \boldsymbol{\phi} = \mathbf{d} \cdot \mathbf{\Phi}_0 + \rho \left(\mathbf{d} \cdot \mathbf{\Phi}_1 + \mathbf{C} \cdot \mathbf{\Phi}_0\right) + \rho^2 \left(\mathbf{d} \cdot \mathbf{\Phi_2} + \mathbf{\Phi_0} \cdot \mathbf{D} + \mathbf{C} \cdot \mathbf{\Phi_1}\right) + O(\rho^3) \tag{4.136f}$$

$$\coloneqq M_{2,0} + \rho M_{2,1} + \rho^2 M_{2,2} + O(\rho^3), \tag{4.136g}$$

$$\hat{\mathbf{n}} \cdot \mathbf{R} = \hat{\mathbf{n}} \cdot \mathbf{d} + \rho\hat{\mathbf{n}} \cdot \mathbf{C} + \rho^2\hat{\mathbf{n}} \cdot \mathbf{D} + O(\rho^3) \tag{4.136h}$$

$$\coloneqq M_{3,0} + \rho M_{3,1} + \rho^2 M_{3,2} + O(\rho^3), \tag{4.136i}$$

$$\tilde{\mathbf{e}} \cdot \boldsymbol{\phi} = \tilde{\mathbf{e}} \cdot \mathbf{\Phi}_0 + \rho\tilde{\mathbf{e}} \cdot \mathbf{\Phi}_1 + \rho^2\tilde{\mathbf{e}} \cdot \mathbf{\Phi}_2 + O(\rho^3) \tag{4.136j}$$

$$\coloneqq M_{4,0} + \rho M_{4,1} + \rho^2 M_{4,2} + O(\rho^3), \tag{4.136k}$$

$$\hat{\mathbf{n}} \cdot \boldsymbol{\phi} = \hat{\mathbf{n}} \cdot \mathbf{\Phi_0} + \rho\hat{\mathbf{n}} \cdot \mathbf{\Phi_1} + \rho^2\hat{\mathbf{n}} \cdot \mathbf{\Phi_2} + O(\rho^3) \tag{4.136l}$$

$$\coloneqq M_{5,0} + \rho M_{5,1} + \rho^2 M_{5,2} + O(\rho^3), \tag{4.136m}$$

$$\tilde{\mathbf{e}} \cdot \mathbf{e}_3 = \tilde{\mathbf{e}} \cdot \mathbf{P}_0 + \rho\tilde{\mathbf{e}} \cdot \mathbf{P}_1 + \rho^2\tilde{\mathbf{e}} \cdot \mathbf{P}_2 + O(\rho^3) \tag{4.136n}$$

$$\coloneqq M_{6,0} + \rho M_{6,1} + \rho^2 M_{6,2} + O(\rho^3), \tag{4.136o}$$

$$\mathbf{e}_3 \cdot \boldsymbol{\phi} = \left[\mathbf{P_0} + \rho\mathbf{P_1} + \rho^2\mathbf{P_2} + O(\rho^3)\right] \cdot \left[\mathbf{\Phi_0} + \rho\mathbf{\Phi_1} + \rho^2\mathbf{\Phi_2} + O(\rho^3)\right] \tag{4.136p}$$

$$= \mathbf{P_0} \cdot \mathbf{\Phi_0} + \rho \left[\mathbf{P_0} \cdot \mathbf{\Phi_1} + \mathbf{\Phi_0} \cdot \mathbf{P_1}\right] + \rho^2 \left[\mathbf{P_0} \cdot \mathbf{\Phi_2} + \mathbf{P_2} \cdot \mathbf{\Phi_0} + \mathbf{P_1} \cdot \mathbf{\Phi_1}\right] + O(\rho^3) \tag{4.136q}$$

$$\coloneqq M_{7,0} + \rho M_{7,1} + \rho^2 M_{7,2} + O(\rho^3), \tag{4.136r}$$

$$\hat{\mathbf{n}} \cdot \mathbf{e}_3 = \hat{\mathbf{n}} \cdot \mathbf{P_0} + \rho\hat{\mathbf{n}} \cdot \mathbf{P_1} + \rho^2\hat{\mathbf{n}} \cdot \mathbf{P_2} + O(\rho^3) \tag{4.136s}$$

$$\coloneqq M_{8,0} + \rho M_{8,1} + \rho^2 M_{8,2} + O(\rho^3). \tag{4.136t}$$

In the Taylor series of $\mathbf{R}\cdot\mathbf{e}_3$, we have $\mathbf{C}\cdot\mathbf{e_3}=0$ because $\mathbf{C}$ is a linear combination of the basis vectors $\mathbf{e}_1$ and $\mathbf{e}_2$, which are tangential to the surface. As a result, coefficients of the first two terms in that Taylor series are proportional to $d=|\mathbf{d}|$. Define the polynomials

$$M_k(\rho)=M_{k,0}+M_{k,1}\rho+M_{k,2}\rho^2 \tag{4.137}$$

for $k=0,1,\ldots 8$, and

$$\tilde{B}_k(\rho)=\tilde{B}_{k,0}+\tilde{B}_{k,1}\rho+\tilde{B}_{k,2}\rho^2 \tag{4.138}$$

for $k=1,\ldots 6$.

Using the expansions (4.136) and (4.135), the terms in the numerator of (4.134c) can be expanded as follows

$$B_1(\mathbf{R}\cdot\mathbf{e}_3)(\tilde{\mathbf{e}}\cdot\mathbf{R})(\mathbf{R}\cdot\boldsymbol{\phi})(\hat{\mathbf{n}}\cdot\mathbf{R})=\sum_{k=0}^{5}H_{0,k}\rho^k+O(\rho^3), \tag{4.139}$$

where the coefficients $H_{0,k}$ are evaluated from the product of the polynomials $\tilde{B}_1$, $M_0$, $M_1$, $M_2$ and $M_3$. In the above expansion, the coefficients upto, but not including, order five are proportional to some polynomial in $d$ of degree less than 5 with no constant term. Henceforth, such coefficients will be said to be proportional to $d$, as a shorthand for the above idea. The fifth order term is not proportional to $d$ because of the term $\rho^5 B_{1,0}M_{0,2}M_{1,1}M_{2,1}M_{3,1}$ obtained in the multiplication of the polynomials. The above expansion is truncated such that this term can be retained. If this term is subtracted from (4.139), all terms of order less than or equal to five in the resultant difference will be proportional to $d$. We will see why this is useful later. We now have

$$\tilde{F}_1(\rho,\theta)=\frac{\mu}{\pi R^7}\left[\sum_{k=0}^{5}H_{0,k}\rho^{k+1}+O(\rho^4)\right]\tilde{\mathcal{J}}(\boldsymbol{\eta}). \tag{4.140}$$

If we define $R_a\coloneqq\sqrt{d^2+\rho 2\mathbf{d}\cdot\mathbf{C}+\rho^2\left[C^2+2\mathbf{d}\cdot\mathbf{D}\right]}$, then

$$R=|\mathbf{R}|=\left[\left(\mathbf{d}+\rho\mathbf{C}+\rho^2\mathbf{D}+O(\rho^3)\right)\cdot\left(\mathbf{d}+\rho\mathbf{C}+\rho^2\mathbf{D}+O(\rho^3)\right)\right]^{1/2} \tag{4.141a}$$

$$=\left[d^2+\rho 2\mathbf{d}\cdot\mathbf{C}+\rho^2\left[C^2+2\mathbf{d}\cdot\mathbf{D}\right]+O(\rho^3)\right]^{1/2} \tag{4.141b}$$

$$=R_a\left[1+\frac{R_e}{R_a^2}\right]^{1/2}\quad\text{for some } R_e \text{ such that } R_e=O(\rho^3) \tag{4.141c}$$

$$= R_a \left[1 + O\left(\frac{R_e}{R_a^2}\right)\right] \quad \text{as } \frac{R_e}{R_a^2} \text{ goes to } 0 \tag{4.141d}$$

$$= R_a + O\left(\frac{\rho^3}{R_a}\right) \text{ as } \rho \text{ goes to } 0. \tag{4.141e}$$

We will assume that $R - R_a$ goes to zero at least as fast as $\rho^3/R_a$ *in most of the* domain of integration. Similarly,

$$\frac{1}{R^n} \approx \frac{1}{R_a^n}\left[1 - \frac{n}{2} O\left(\frac{\rho^3}{R_a^2}\right)\right]. \tag{4.142}$$

Therefore,

$$\tilde{F}_1(\rho,\theta) = \frac{\mu}{\pi R_a^7}\left[1 - O\left(\frac{\rho^3}{R_a^2}\right)\right]\left[\sum_{k=0}^{5} H_{0,k}\rho^{k+1} + O(\rho^4)\right]\tilde{\mathcal{J}}(\boldsymbol{\eta}) \tag{4.143}$$

$$= \frac{\mu}{\pi R_a^7}\left[\sum_{k=0}^{5} H_{0,k}\rho^{k+1} + G(\rho,\theta)\right]\tilde{\mathcal{J}}(\boldsymbol{\eta}), \tag{4.144}$$

where $G(\rho,\theta)$ is either $O(\rho^4)$ or $O(\rho^4/R_a^2)$. We consider the worst case, which is $O(\rho^4/R_a^2)$. Consider decomposition of the integral over $\tilde{F}_1(\rho,\theta)$ as follows

$$\int_\Gamma \tilde{F}_1(\rho,\theta)d\rho d\theta = \int_\Gamma \tilde{F}_1^S(\rho,\theta)d\rho d\theta + \int_\Gamma \tilde{F}_1^R(\rho,\theta)d\rho d\theta, \tag{4.145}$$

where

$$\tilde{F}_1^S(\rho,\theta) = \tilde{F}_1(\rho,\theta) - \frac{\mu}{\pi R_a^7}\left[\sum_{k=0}^{5} H_{0,k}\rho^{k+1}\right]\tilde{\mathcal{J}}(\boldsymbol{\eta}). \tag{4.146}$$

The $\rho$-integral over $\tilde{F}_1^R(\rho,\theta)$ can be evaluated analytically, as shown in Appendix C.2.5, and that over $\tilde{F}_1^S(\rho,\theta)$ can be evaluated using Gaussian quadrature since $\tilde{F}_1^S(\rho,\theta)$ is relatively smooth, as explained below. The integral over $\theta$ is computed simultaneously for $\tilde{F}_1^S(\rho,\theta)$ and $\tilde{F}_1^R(\rho,\theta)$ using Gaussian quadrature. The sigmoidal transformation mentioned on Page 134 is still applied.

When $d$ is relatively small, $R_a$ varies as $\rho$ in the worst case. Therefore, some terms in $\tilde{F}_1^S(\rho,\theta)$ vary as $1/\rho^3$. However, this is not a problem because such the terms go to zero as $d$ goes to zero. As noted before, the lowest order term in the numerator of $\tilde{F}_1(\rho,\theta)$ that is not proportional to $d$ varies as $\rho^6$. Since this term is subtracted in (4.146), all terms in $\tilde{F}_1^S(\rho,\theta)$ whose coefficient is not proportional to $d$ vary at least as slowly as $\rho^7/R_a^7$, which is on the order of a constant. When $d$ is

much larger than $\sqrt{(2\mathbf{d}\cdot\mathbf{D})/\rho + C^2}\rho$ in the domain of integration, which is not generally the case, $R_a$ varies as $\sqrt{\rho}$. Therefore, $\tilde{F}_1^S(\rho,\theta)$ is on the same order as $1/\sqrt{\rho}$ in the domain of integration and non-smoothness of the integrand is significantly reduced. Note that to guarantee smoothness of $\tilde{F}_1^S(\rho,\theta)$ under all cases, one would have to retain terms of order $\rho^3$ in the expansions (4.136) and then subtract some of the additional terms resulting from them from the integrand. However, constructing these expansions is computationally intensive. Therefore, it can be ignored since the condition that $d$ be large enough as mentioned above is rarely satisfied.

***Second term.*** The foregoing approach can be applied for integrating other terms in Equation (4.133). Consider the second term in Equation (4.133),

$$\tilde{F}_2(\rho,\theta) = \frac{\mu}{\pi R^3} B_2(\hat{\mathbf{R}}\cdot\hat{\mathbf{n}}')(\hat{\mathbf{R}}\cdot\hat{\mathbf{n}})(\tilde{\mathbf{e}}\cdot\boldsymbol{\phi})\ J\rho \tag{4.147a}$$

$$= \frac{\mu}{\pi R^5} B_2(\mathbf{R}\cdot\mathbf{e}_3)(\mathbf{R}\cdot\hat{\mathbf{n}})(\tilde{\mathbf{e}}\cdot\boldsymbol{\phi})\ \tilde{\mathcal{J}}(\boldsymbol{\eta})\rho. \tag{4.147b}$$

Then, from the expansions (4.136) and (4.135), we have

$$B_2(\mathbf{R}\cdot\mathbf{e}_3)(\mathbf{R}\cdot\hat{\mathbf{n}})(\tilde{\mathbf{e}}\cdot\boldsymbol{\phi}) = \sum_{k=0}^{3} H_{1,k}\rho^k + O(\rho^2), \tag{4.148}$$

where the coefficients $H_{1,k}$ are obtained by multiplication of the polynomials $\tilde{B}_2$, $M_0$, $M_3$ and $M_4$, without considering the coefficient $\tilde{B}_{2,2}$ (for reasons mentioned at the end of this section). The coefficients of terms of order less than 3 are proportional to $d$.

$$\tilde{F}_2(\rho,\theta) = \frac{\mu}{\pi R^5}\left[\sum_{k=0}^{3} H_{1,k}\rho^{k+1} + O(\rho^3)\right]\tilde{\mathcal{J}}(\boldsymbol{\eta}) \tag{4.149}$$

$$= \frac{\mu}{\pi R_a^5}\left[1 - O\left(\frac{\rho^3}{R_a^2}\right)\right]\left[\sum_{k=0}^{3} H_{1,k}\rho^{k+1} + O(\rho^3)\right]\tilde{\mathcal{J}}(\boldsymbol{\eta}) \tag{4.150}$$

$$= \frac{\mu}{\pi R_a^5}\left[\sum_{k=0}^{3} H_{1,k}\rho^{k+1} + G(\rho,\theta)\right]\tilde{\mathcal{J}}(\boldsymbol{\eta}), \tag{4.151}$$

where $G(\rho,\theta)$ is either $O(\rho^3)$ or $O(\rho^4/R_a^2)$. The term obtained from singularity subtraction is

$$\tilde{F}_2^S(\rho,\theta) = \tilde{F}_2(\rho,\theta) - \frac{\mu}{\pi R_a^5}\left[\sum_{k=0}^{3} H_{1,k}\rho^{k+1}\right]\tilde{\mathcal{J}}(\boldsymbol{\eta}). \tag{4.152}$$

When $d$ is small, $\tilde{F}_2^S(\rho,\theta)$ varies at least as slowly as $\rho^5/R_a^5$, which in turn varies as a constant, and thus, $\tilde{F}_2^S(\rho,\theta)$ is smooth. This is because the only terms in $\tilde{F}_2^S(\rho,\theta)$ that vary faster include those that are proportional to $d$, which is small by assumption. Note that the above argument works because the expansion in (4.148) is truncated such that it can generate all terms up to (and including) order three that are not proportional to $d$. It is not required to retain terms of order three in the expansions in (4.136) for this. When $d$ is not small, which is rarely the case, $\tilde{F}_2^S(\rho,\theta)$ varies as $G(\rho,\theta)/R_a^5$ in the domain of integration, which in turn varies as $\rho^3/\rho^{2.5} = \sqrt{\rho}$. Hence, $\tilde{F}_2^S(\rho,\theta)$ is always smooth and can be integrated numerically. The same idea is applied for singularity subtraction of other terms and kernels. Details are mentioned in Appendix C.2.

One may notice that the above argument for smoothness of the subtracted integrand works even if terms of order two are not retained for some of the expansions in (4.136) and (4.135). This is indeed true. However, retaining these additional terms provides better accuracy in the quadrature. In the computer code developed based on this work, only the second order terms in (4.135b) for $j = 2$ to 6 are dropped when the $\overline{\overline{\mathbf{H}}}(\mathbf{x},\mathbf{x}')$ kernel is required in the simulation. For problems where this kernel is not needed, such as for scattering from rigid objects, only terms up to and including order one in (4.136) are used. Finally, we also apply the following transformation from $\rho$ to $t$ to compute the $\rho$-integral, which helps in further cancelling the near-singularity

$$t = \ln\left(\rho + \frac{b}{2c} + \frac{R_a}{\sqrt{c}}\right), \tag{4.153}$$

where $b$ and $c$ are the coefficients obtained by writing $R_a$ as $R_a = \sqrt{a + b\rho + c\rho^2}$.

## 4.4 Incident Field Calculation

When the incident field is a plane wave with unit displacement amplitude, the incident displacement is given by

$$\mathbf{u}^I(\mathbf{x}) = \mathbf{d}\; e^{i\mathbf{k}\cdot\mathbf{x}}, \tag{4.154}$$

where $\mathbf{d}$ is a unit vector denoting the polarization of the wave and $\mathbf{k}$ is the wavevector. The corresponding traction field on the surface of the scatterer is given by

$$\mathbf{t}^I(\mathbf{x}) = \bar{\boldsymbol{\tau}}^I \cdot \hat{\mathbf{n}} = \lambda \nabla \cdot \mathbf{u}^I \ \hat{\mathbf{n}} + \mu(\nabla \mathbf{u}^I + \mathbf{u}^I \nabla) \cdot \hat{\mathbf{n}} \tag{4.155a}$$

$$= i\lambda(\mathbf{k} \cdot \mathbf{u}^I)\hat{\mathbf{n}} + i\mu \left[\mathbf{k}(\mathbf{u}^I \cdot \hat{\mathbf{n}}) + \mathbf{u}^I(\mathbf{k} \cdot \hat{\mathbf{n}})\right], \tag{4.155b}$$

where $\hat{\mathbf{n}}$ is the outward oriented unit normal vector on the surface of the scatterer, and all quantities except the Lamé constants, $\mathbf{k}$ and $\mathbf{d}$ are, in general, functions of $\mathbf{x}$.

## 4.5 Semi-Analytical Solution for Scattering from a Circular Crack

For the purpose of validating the BEM, we will show several numerical results in Section 4.6. One of the validation examples is the circular crack scattering problem. This section details the process of computing a reference semi-analytical solution for this problem for the purpose of comparison. Consider a circular crack (open surface of zero thickness) of unit radius in an otherwise homogeneous elastic solid. The crack is assumed to be traction-free. Let the crack lie on the $xy$-plane. Assume that a plane wave with displacement field

$$\mathbf{u}^I(\mathbf{x}) = ik_1 \tilde{A}_0 e^{ik_1 z} \hat{\mathbf{z}} \tag{4.156}$$

is impinged on the crack, where $k_1$ is the longitudinal wavenumber in the host medium and $\tilde{A}_0$ is a constant. Let $\sigma = k_1/k_2$ and $B = -ik_1^3$, with $k_2$ representing the shear wavenumber, and assume a spherical coordinate system centered at the crack.

Mal showed that the scattered displacement field in the far-field can be expressed as [169]

$$u_r(r,\theta) = B\frac{e^{ik_1 r}}{k_1 r}\left(\sin^2\theta - \frac{1}{2\sigma^2}\right)\frac{P(k_1 \sin\theta)}{\sin\theta}, \quad (\sin\theta \neq 0) \tag{4.157a}$$

$$u_\theta(r,\theta) = \frac{B}{\sigma^3}\frac{e^{ik_2 r}}{k_2 r}\cos\theta P(k_2 \sin\theta), \tag{4.157b}$$

where

$$P(k) = \frac{2\tilde{A}_0}{\pi(1-\sigma^2)}\int_0^1 p(\xi)\sin(k\xi)d\xi, \tag{4.158}$$

and $p(\xi)$ is a continuous function with bounded first derivative in $[0,1]$ that satisfies the integral equation (4.159).

$$p(\xi) + \int_0^1 F(\xi,\eta)p(\eta)d\eta = \xi \tag{4.159}$$

for $\xi \in [0,1]$, where

$$F(\xi,\eta) = \frac{-2ik_2\sigma^3}{\pi(1-\sigma^2)} \int_0^1 \left[ \frac{\left(k^2 - 1/(2\sigma^2)\right)^2}{k\sqrt{1-k^2}} \left( e^{ikk_1|\xi-\eta|} - e^{ikk_1(\xi+\eta)} \right) + \right.$$
$$\left. \frac{k\sqrt{1-k^2}}{\sigma^3} \left( e^{ikk_2|\xi-\eta|} - e^{ikk_2(\xi+\eta)} \right) \right] dk. \tag{4.160}$$

When $\sin\theta$ is zero, $u_r$ can be calculated from the limiting form of (4.157a):

$$u_r(r,\theta) = -B\frac{e^{ik_1 r}}{2k_1 r\sigma^2} \left[ \lim_{\sin\theta\to 0} \frac{P(k_1\sin\theta)}{\sin\theta} \right], \tag{4.161}$$

$$\lim_{\sin\theta\to 0} \frac{P(k_1\sin\theta)}{\sin\theta} = \frac{2\tilde{A}_0 k_1}{\pi(1-\sigma^2)} \int_0^1 p(\xi)\xi d\xi. \tag{4.162}$$

The scattering amplitudes for scattered longitudinal and shear waves can be extracted by setting $\tilde{A}_0 = -i/k_1$:

$$A_p(\theta) = re^{-ik_1 r}u_r(r,\theta), \tag{4.163a}$$

$$A_s(\theta) = re^{-ik_2 r}u_\theta(r,\theta), \tag{4.163b}$$

where $A_p$ and $A_s$ are the scattering amplitudes for longitudinal and shear waves, respectively. To compute the scattering amplitudes, the integral equation in (4.159) has to be solved. We use the Nyström method for this. For $m = 1,\ 2\ldots N_q$, let $\xi_m$ and $w_m$ be the points and weights of a quadrature rule in the interval $[0,1]$. Then, for $m = 1$ to $N_q$, we have

$$p(\xi_m) + \int_0^1 F(\xi_m,\eta)p(\eta)d\eta = \xi_m. \tag{4.164}$$

In the Nyström method, the integral in the above equation is discretized using the foregoing quadrature rule to obtain a linear system of equations for determining the values of $p(\xi)$ at the quadrature

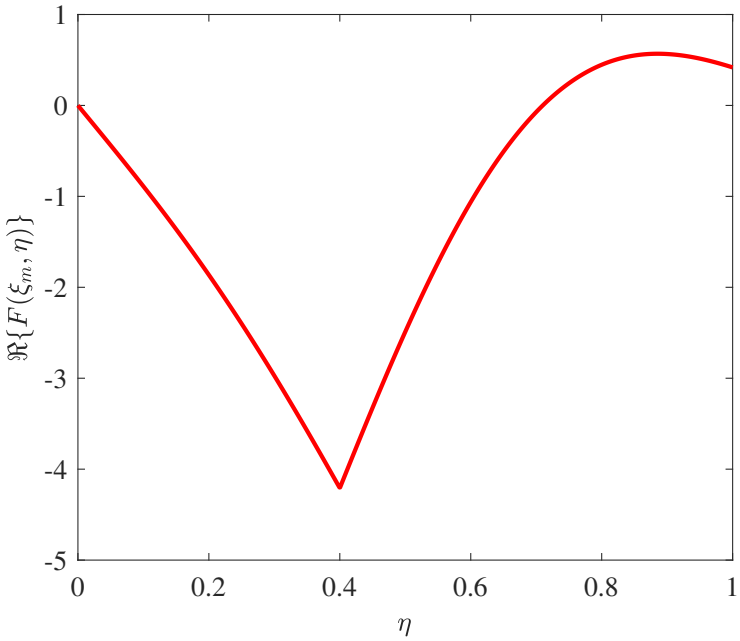


Figure 4.7: Real part of $F(\xi_m, \eta)$ as a function of $\eta$ ($\xi_m = 0.4$). Derivative is discontinuous at $\eta = \xi_m$.

points. The choice of the quadrature rule affects the rate at which the solution (for the scattering amplitude) converges as a function of $N_q$ because the first derivative of the real part of $F(\xi_m, \eta)$ is discontinuous at $\eta = \xi_m$, as shown in Figure 4.7. Because of this discontinuity, the trapezoidal rule performs better than the Gauss-Legendre rule (for the same number of quadrature points) even though the latter has a lower error in computing the integral in (4.158).

Discretizing the integral in (4.164) using the preferred quadrature rule, we get

$$p(\xi_m) + \sum_{n=1}^{N_q} w_n F(\xi_m, \xi_n) p(\xi_n) = \xi_m, \tag{4.165}$$

which leads to a linear system of equations for determining $p(\xi_m)$ for $m = 1$ to $N_q$. After solving this system, $P(k)$ in (4.158) can be computed as follows

$$P(k) = \frac{2\tilde{A}_0}{\pi(1-\sigma^2)} \sum_{m=1}^{N_q} w_m p(\xi_m) \sin(k\xi_m). \tag{4.166}$$

Table 4.2: Convergence of semi-analytical solution for $\Sigma_p/\pi$ with increasing $N_q$ ($k_2 = 6,\ \nu = 0.25$).

| No. of quadrature points ($N_q$) | Normalized scattering cross section ($\Sigma_p/\pi$) | Relative Error |
|---|---|---|
| 10 | 1.8570398127 | 0.011 |
| 20 | 1.8734260844 | 0.0022 |
| 50 | 1.8769418518 | 0.00032 |
| 100 | 1.8773975290 | 7.8e-05 |
| 200 | 1.8775082919 | 1.9e-05 |
| 500 | 1.8775388932 | 3.1e-06 |
| 1000 | 1.8775432353 | 7.7e-07 |
| 2000 | 1.8775443182 | 1.9e-07 |
| 3000 | 1.8775445186 | 8.3e-08 |
| 4000 | 1.8775445886 | 4.6e-08 |
| 5000 | 1.8775446211 | 2.9e-08 |
| 6000 | 1.8775446387 | 1.9e-08 |
| 7000 | 1.8775446493 | 1.4e-08 |
| 8000 | 1.8775446562 | 1.0e-08 |
| 9000 | 1.8775446609 | 7.6e-09 |
| 10000 | 1.8775446643 | 5.8e-09 |

For estimating the number of quadrature points required to achieve less than 0.0001% of error in the scattering amplitudes, the scattering cross section of the P-wave [170, 171], defined in (4.167), is computed for several values of $N_q$ and listed in Table 4.2.

$$\Sigma_p = \frac{4\pi}{k_1}\Im\left\{A_p(\theta_i)\right\}, \tag{4.167}$$

where $\Im\{\ \}$ represents the imaginary part and $\theta_i$ represents the propagation direction of the incident wave, which equals zero in this case. Solutions in the table correspond to the case with Poisson's ratio $\nu = 0.25$ (i.e., $\sigma = 1/\sqrt{3}$) and $k_2 = 6$, and are computed using the trapezoidal rule. The relative error is calculated by taking the solution for $N_q = 20,000$ as reference. For $k_2 > 6$, more quadrature points are required to achieve the same relative errors. The foregoing analysis indicates that the solution for $N_q = 10,000$ can be reasonably assumed to achieve an accuracy of at least 0.0001%, even for slightly higher values of $k_2$.

## 4.6 Numerical Results

In this section, simulation results for a spherical cavity and some penny-shaped cracks are compared with the respective reference solutions to validate the BEM model. Convergence results ($h$-refinement) for different discretization rules are also shown.

### 4.6.1 Convergence Rates

#### 4.6.1.1 Spherical Cavity Problem

Consider scattering of a longitudinal plane wave from a spherical cavity of radius $a$ in an unbounded elastic solid. The material properties of the host medium and the properties of the incident wave are same as those in Section 3.3. The frequency is such that $k_p a = \pi$. This problem is simulated using the CFIE formulation with coupling parameter $\beta = -(1+i)$. The scattering amplitudes of longitudinal and shear waves are calculated at 181 uniformly spaced values of $\theta$ in $[0, \pi]$. The relative error in scattering amplitude is defined in the same way as in Section 3.3. Figure 4.8 shows the relative errors in scattered longitudinal wave for different discretization rules as a function of the average number of interpolation nodes per shear wavelength. Recall that Rule-$xy$ represents the case wherein mesh interpolation is of order $x$ and the degree of polynomials used in field interpolation is $y$.

The results for Rule-10 and Rule-11 are obtained by starting with 80 first-order triangular elements and dividing each triangle into four sub-triangles at each refinement step. For Rule-22 and Rule-23, the starting point is 20 second-order triangles. We find that the convergence rate increases with an increase in the discretization order. For Rule-23, the errors are on the same level as that of Rule-22 because of the effect of geometry error, as explained in Section 3.3. The relative errors for scattered shear wave are shown in Figure 4.9. We observe higher errors than in the case of the longitudinal wave. This is because shear wavelength is smaller than the longitudinal wavelength, and hence for the same mesh, the error in approximating shear waves is higher. Another difference between longitudinal and shear waves is that Rule-33 converges faster than Rule-22 in the latter

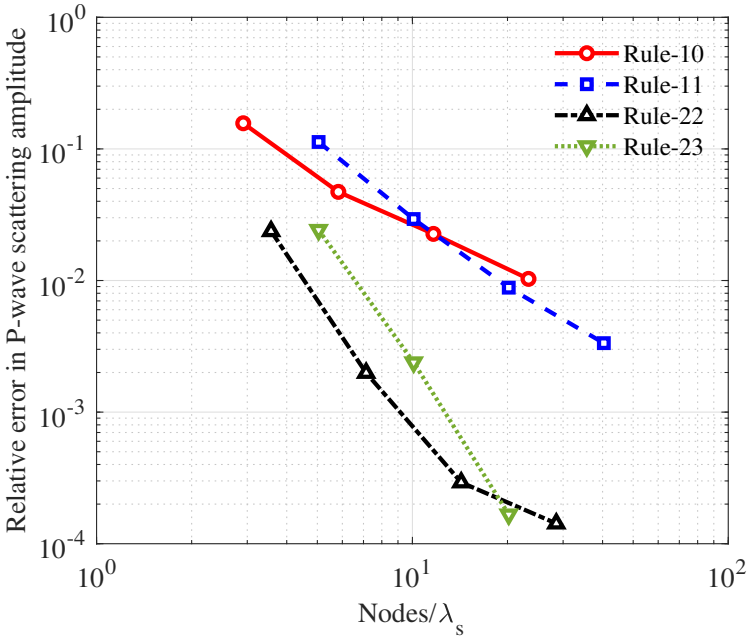


Figure 4.8: Relative error in scattering amplitude of longitudinal wave for a spherical cavity ($k_p a = \pi$) as a function of the average number of interpolation nodes per shear wavelength. Simulation results are based on the CFIE formulation with coupling parameter $\beta = -(1+i)$.

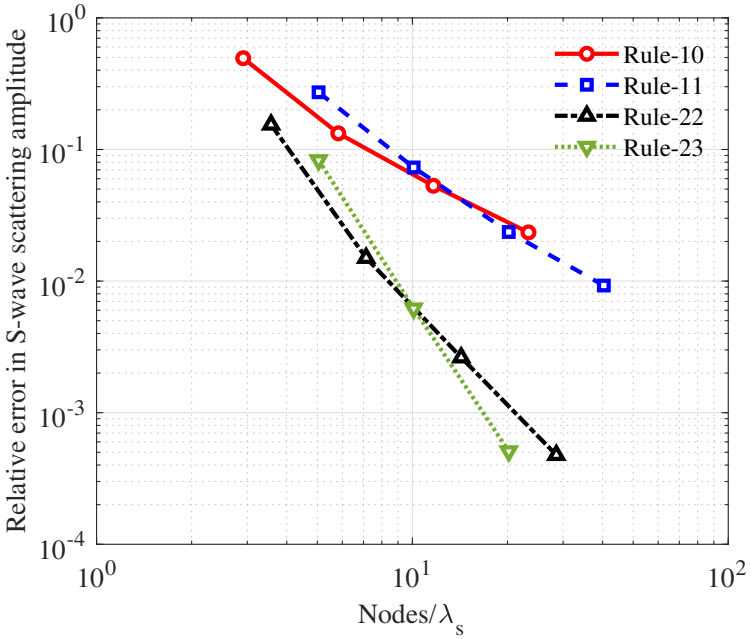


Figure 4.9: Relative error in scattering amplitude of shear wave for a spherical cavity ($k_p a = \pi$) as a function of the average number of interpolation nodes per shear wavelength. Simulation results are based on the CFIE formulation with coupling parameter $\beta = -(1+i)$.

case. This is possible because compared to geometry error, error from field approximation may have a higher influence on the total error in case of the shear wave.

#### 4.6.1.2 Circular Crack Problem

Consider a circular traction-free crack of radius $a$ in a material with Poisson's ratio $\nu = 0.25$, as described in Section 4.5. A longitudinal plane wave travelling in the positive $z$-direction is incident on the crack. The frequency is such that $k_s a = 4\pi$. This problem is solved using the HBIE formulation, and scattering amplitudes of the longitudinal and shear waves are calculated at 181 uniformly spaced values of $\theta$ in $[0, \pi]$. The reference solution is computed as described in Section 4.5. Figure 4.10 shows the convergence results for the longitudinal wave. Results of Rule-10 and Rule-11 are obtained by starting with 80 first-order elements and performing $h$-refinement. The starting point of other rules is 20 second-order elements. Unlike the spherical cavity problem, Rule-23 has lower error and converges faster than Rule-22. However, geometry error begins to dominate with further $h$-refinement, as previously noted in the spherical cavity problem.

Although Rule-11 has lower error than Rule-10 for the same mesh representation, the latter seems to converge faster than Rule-11. This seems to be an anomaly specific to some frequencies since the opposite behaviour is observed at some other frequencies. Rule-24 is based on a 15-point symmetric quadrature rule with order (degree of exactness) seven. The points and weights of this quadrature rule for a standard reference triangle $\Omega = \{(\xi_1, \xi_2) \ni \xi_1, \xi_2 \in [0, 1] \text{ and } \xi_1 + \xi_2 \leq 1\}$ are given in Table 4.3. The results for shear wave are shown in Figure 4.11. As in the case of the spherical cavity, the errors for shear wave are higher than those of the longitudinal wave. Rule-24 shows lower errors and higher convergence rate than Rule-23, except for the last point.

### 4.6.2 Scattering Cross Section for a Circular Crack

We now compare simulation results for the scattering cross section with the reference solution over a range of frequencies. All parameters except the frequency remain unchanged from Section 4.6.1.2. Figure 4.12 shows the scattering cross section as a function of the shear wavenumber

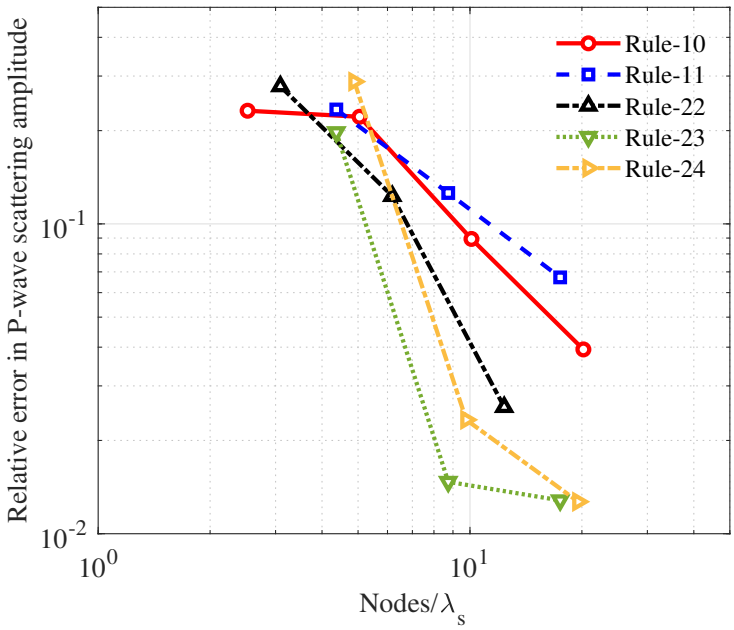


Figure 4.10: Relative error in scattering amplitude of longitudinal wave for a circular crack ($\nu = 0.25$, $k_s a = 4\pi$) as a function of the average number of interpolation nodes per shear wavelength. Simulation results are are based on the HBIE formulation.

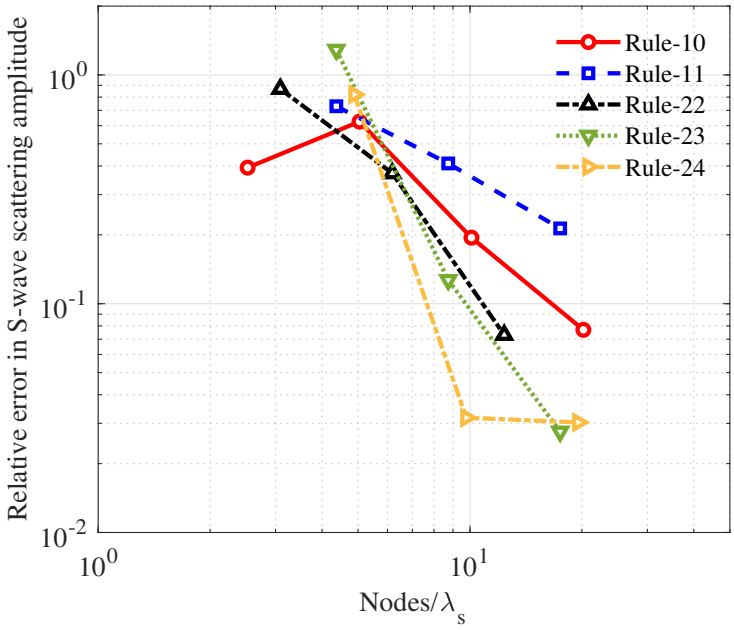


Figure 4.11: Relative error in scattering amplitude of shear wave for a circular crack ($\nu = 0.25$, $k_s a = 4\pi$) as a function of the average number of interpolation nodes per shear wavelength. Simulation results are are based on the HBIE formulation.

Table 4.3: Symmetric quadrature rule used in Rule-24.

| Weight | $\xi_1$ | $\xi_2$ |
|---|---|---|
| 0.02229067600526 | 0.43530466960355 | 0.43530466960355 |
| 0.12046117216372 | 0.23927997518879 | 0.23927997518879 |
| 0.05237092590776 | 0.06453787138293 | 0.06453787138293 |
| 0.06910527962829 | 0.31072360003490 | 0.64514575889900 |

from $k_s a = 0$ to $k_s a = 8$. The reference solution for $k_s a \geq 2$ is calculated using the semi-analytical solution with 10,000 quadrature points. For $k_s a < 2$, the number of quadrature points is scaled down by the factor $8/(k_s a)$ to reduce the computational cost. Assuming that the function $p(\xi)$ in Equation (4.159) oscillates at the frequency of the shear wave, this scaling factor ensures that the discretization "density" is same as that at $k_s a = 8$. Hence, the accuracy of reference solution is unaffected by decreasing the number of quadrature points. The BEM results are obtained by solving the HBIE formulation with Rule-22 and 80 second-order triangles. There is good agreement between the simulated and reference solutions. The Kirchhoff approximation (KA) solution is also shown for reference. Both reference and BEM solutions converge to the KA result asymptotically. Figure 4.13 shows that the relative error in the scattering cross section is less than 5% at almost all frequencies. The error does not show an increasing trend with the frequency since it is calculated using the scattering cross section in a single direction. Indeed, when the error is defined by taking all angles into consideration, we will observe an increasing trend with frequency, as implied by the results in Section 4.6.1.2.

## 4.7 Summary

In this chapter, we presented a high-order BEM for solving the CFIE formulation for elastic wave scattering. The development of such methods is especially challenging because of the presence of highly singular kernels. Special quadrature schemes are required to integrate singular and nearly-singular integrals in the BEM matrix, which has a significant impact on the matrix filling time. While some methods to convert hypersingular kernels to weakly-singular ones are available in the

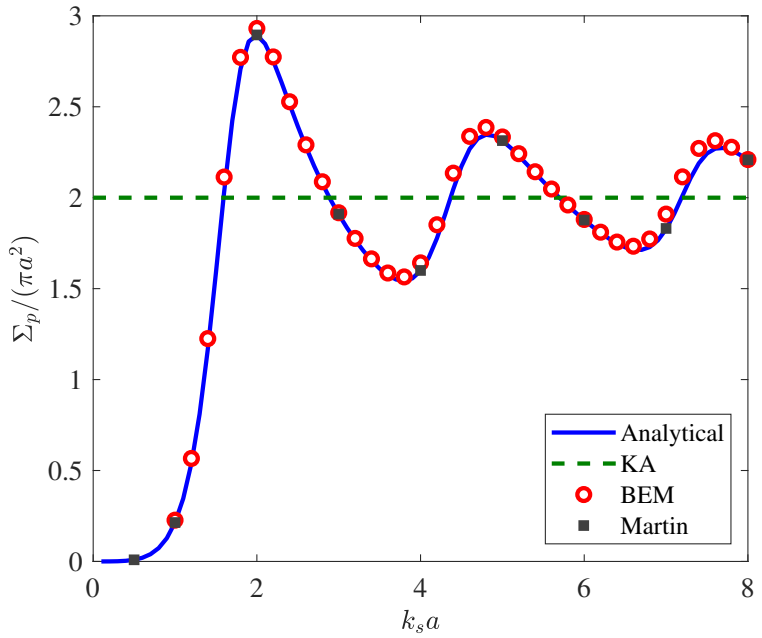


Figure 4.12: Normalized scattering cross section of a circular crack as a function of the shear wavelength. BEM results are generated using 80 second-order triangles with Rule-22 discretization. KA refers to the Kirchhoff approximation. Martin's results are from [170].

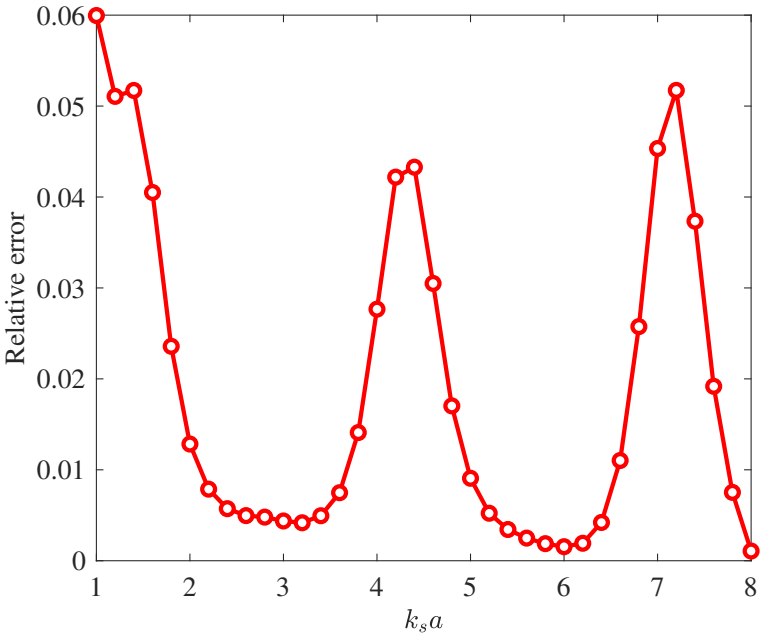


Figure 4.13: Relative error in the scattering cross section computed using BEM.

literature, they may be less efficient since they can be viewed as "global" regularization methods wherein any additional calculations introduced in the formulation apply even to far-field matrix elements. Here, we use "local" regularization methods based on singularity subtraction.

The use of high-order discretization and the coincidence of field interpolation and quadrature points are other key features of this method. Because of highly singular kernels, it seems more beneficial to use high-order geometry discretizations as they lead to larger mesh elements; the use of small mesh elements (for resolving geometries accurately) drastically increases the number of matrix elements which need to be treated as nearly-singular integrals, thus affecting the computational performance. Moreover, numerical results for scattering from spherical cavities and traction-free cracks show the benefits of using even second-order geometry representations (in conjunction with high-order field interpolation) in terms of convergence rates. In the case of the CFIE and HBIE, field interpolation with polynomials of degree more than two may not be particularly useful unless when the geometry representation is accurate. Scattering from rectangular crack-like objects, for example, is a problem where high-order field discretizations are independently useful.

# CHAPTER 5. MULTILEVEL FAST MULTIPOLE METHOD FOR COMBINED FIELD FORMULATION

The first two sections of this chapter serve as an introduction to fast algorithms and the fast-multipole method (FMM). The following two sections derive diagonal-form multipole expansions of the CFIE kernels and the resulting factorizations of far-field elements in the influence matrix. Section 5.5 details a multilevel implementation of the FMM for calculating matrix-vector products. The last section contains numerical results for computational time and memory complexity as well as some validation examples.

## 5.1 Introduction

In BEM, the degrees of freedom (DOFs) are determined by solving a linear system of equations defined by the BEM influence matrix. Solutions can be obtained either by inversion of the influence matrix (direct methods) or by iterative methods that start with a trial solution and iteratively converge to the true solution. Since the influence matrix is dense, standard methods such as the LU decomposition need to be applied in the former case. For a matrix of size $N \times N$, this requires $\mathcal{O}(N^3)$ computational time and $\mathcal{O}(N^2)$ storage memory. On the other hand, standard iterative methods such as the Krylov-subspace techniques typically require $\mathcal{O}(N^2)$ computational time per iteration as matrix-vector multiplications form the bottleneck. If the matrix is well-conditioned, solutions can be obtained to a good accuracy within a few iterations. Hence, iterative methods are preferred when the matrix dimension $N$ is large. However, their storage memory requirement is still $\mathcal{O}(N^2)$ since the whole influence matrix needs to be stored. For very large values of $N$, the number of computations required for both computing the elements of the influence matrix and solving the linear system is practically prohibitive.

Fast BEM algorithms require the computation of near-field matrix elements only. They exploit the properties of the influence matrix to represent the far-field elements in a way that enables fast solution of linear systems approximately. Fast direct methods, for example, store a small number of precomputed values that enable fast computation of the product of the inverse matrix with a vector. Likewise, fast iterative methods enable fast computation of the product of the influence matrix with a vector. The fast multipole method is a fast iterative method that is based on analytical factorization of the BEM kernels wherein the factors that depend on the "source" location are independent of the "observation" location, and vice-versa.

**Related work.** In the last two decades, several fast boundary integral equation methods (BIEMs) have been investigated for 3D elastodynamics. Fujiwara [172] published the first implementation of the high-frequency (diagonal-form) FMM to 3D elastodynamics problems in the year 2000. In the same year, Yoshida et al. [173, 174] applied the low-frequency FMM to the traction BIE formulation for modeling crack scattering problems. Subsequently, they developed a diagonal-form FMM for the same problem [175]. The traction BIE considered in these works is derived from a "global" regularization of the hypersingular BIE in Equation (4.75). Chaillat, Sanz and others [111, 166, 176] published several extensive studies and applications of the high-frequency FMM for 3D elastodynamics starting from the year 2008. Around the same time, Tong and Chew [31] developed a similar technique for the Nyström method. Yan et al. [177] developed a kernel-independent method based on the precorrected-FFT technique [178]. Isakari [179] developed a low-frequency FMM for 3D periodic problems based on a combined-field formulation (Burton-Miller BIE). Fanbin et al. [112] proposed an FFT method for accelerating a high-order BIEM. This method is based on an unconventional choice of the BIE formulation which, even if free from fictitious eigenfrequencies for transmission problems, is not extensible to Dirichlet and Neumann scattering problems. Liu et al. [145] applied the FMM to an indirect (displacement) BIE formulation for multi-domain problems. Chaillat, Desidario and Ciarlet [180, 181] studied $\mathcal{H}-$matrix based iterative and direct solvers for high-frequency elastodynamics problems.

All the above mentioned works solve the conventional (displacement) BIE except when mentioned otherwise. The combined-field formulation is better than the conventional (displacement) and hypersingular (traction) BIEs for modeling scattering problems since it is free from fictitious eigenfrequencies. However, applying it at relatively high frequencies is problematic since it becomes progressively less regular with an increase in the frequency. Therefore, at high frequencies, fast iterative BIEMs based on the combined-field formulation require a relatively large number of iterations to obtain a solution within a given level of residual error. Recently, some preconditioned combined-field formulations have been proposed for both Dirichlet and Neumann scattering problems to address this difficulty [182–184]. In case of the Dirchlet scattering problem, a fast-multipole BEM has also been applied to such a preconditioned formulation [113].

In this chapter, we develop a multilevel implementation of the diagonal-form FMM for the (direct) CFIE formulation where the hypersingular kernel is evaluated using "local" regularization. To our knowledge, this is the first implementation of the diagonal-form FMM for the CFIE formulation wherein the hypersingular kernels not evaluated by means of global regularization. Local regularization leads to a simplification in far-field evaluations since the kernels of the CBIE and HBIE formulations share their radiation patterns, as shown in Section 5.4.

## 5.2 Principle of the Fast Multipole Method

For illustrating the principle of the FMM, consider the following matrix-vector product, assuming $x_i, x'_j \in \mathbb{R}^2$, $u_j \in \mathbb{R}$ and $g : \mathbb{R}^2 \times \mathbb{R}^2 \to \mathbb{R}$:

$$I_i = \sum_{j=1}^{N} g(x_i, x'_j) u_j \tag{5.1}$$

for $i = 1, 2, \ldots N$, where $g(x_i, x'_j)$ form the elements of a matrix and $u_j$ form the elements of a vector. The points $x'_i$ and $x_i$ will be called source and observation points, respectively. Direct evaluation of this product requires $N^2$ computations of the function $g$ and $\mathcal{O}(N^2)$ elementary computations. If there exists a factorization of $g$ as in Equation (5.2), then only $\mathcal{O}(N)$ elementary computations and $2N$ evaluations of the functions $k$ and $l$ are required since the product can be evaluated as

shown in (5.3). Further, only $2N$ quantities are sufficient to represent the whole matrix insofar as computing its products with vectors is concerned.

$$g(x, x') = k(x)l(x'), \tag{5.2}$$

$$I_i = k(x_i) \sum_{j=1}^{N} l(x'_j)u_j. \tag{5.3}$$

Equation (5.2) represents a factorization of $g$ that is separable in the variables $x$ and $x'$. Factorizations of this form are quite elementary and rarely exist for the elements of influence matrices in BEMs. A more complex representation includes a truncated series expansion of $g$ wherein each term of the series admits a separable factorization. Such expansions are known as *degenerate expansions*, and are illustrated in (5.4).

$$g(x, x') = \sum_{p=1}^{P} T_p k_p(x) l_p(x') = \bar{k}^T(x) \cdot \bar{\bar{T}} \cdot \bar{l}(x'), \tag{5.4}$$

where the column vectors $\bar{k}(x)$, $\bar{l}(x') \in \mathbb{R}^P$ are formed by $k_p(x)$ and $l_p(x')$, respectively, for $p = 1, 2, \ldots P$. Similarly, the diagonal matrix $\bar{\bar{T}}$ is formed by $T_p$. In this case, the matrix-vector product can be evaluated as shown below:

$$I_i = \sum_{p=1}^{P} T_p k_p(x_i) \sum_{j=1}^{N} l_p(x'_j)u_j \tag{5.5}$$

for $i = 1, 2, \ldots N$. This requires $2NP + P$ function evaluations, assuming that the coefficients $T_p$ are also functions. The number of quantities that need to be stored for computing products of the matrix with vectors is also $2NP + P$. If $P$ is small compared to $N$, the computational cost involved in the above factorization compares favorably with direct computation according to (5.1). Equation (5.4) can be viewed as a *diagonal-form* factorization as it readily yields the following generalization:

$$g(x, x') = \sum_{p=1}^{P} k_p(x) \sum_{q=1}^{Q} T_{pq} l_q(x') = \bar{k}^T(x) \cdot \bar{\bar{T}} \cdot \bar{l}(x'), \tag{5.6}$$

where the matrix $\bar{\bar{T}}$ is now dense and non-square. The matrix-vector product then simplifies to

$$I_i = \sum_{p=1}^{P} k_p(x_i) \sum_{q=1}^{Q} T_{pq} \sum_{j=1}^{N} l_q(x'_j)u_j \tag{5.7}$$

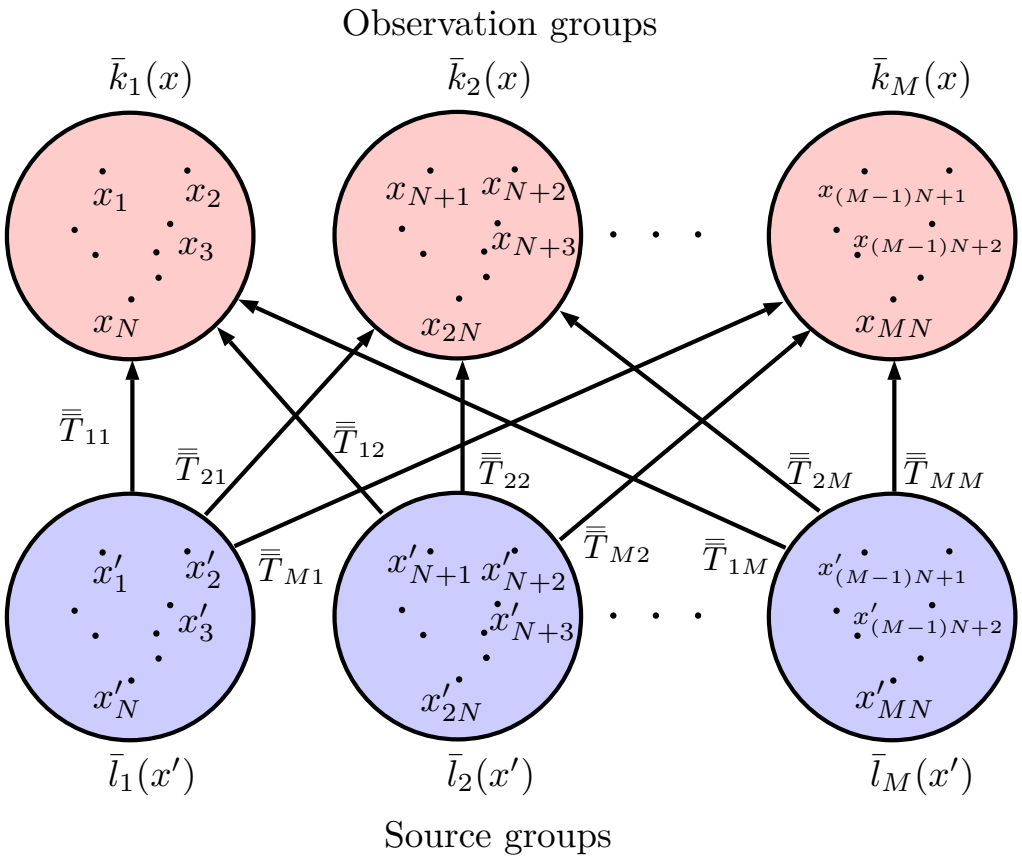


Figure 5.1: A representation of $M$ groups of source and observation points.

for $i = 1, 2, \ldots N$. Assuming that $P = Q$, this requires $2NP$ function evaluations resulting from $\bar{k}(x)$ and $\bar{l}(x')$, and $P^2$ evaluations resulting from $\bar{\bar{T}}$. In other words, the number of quantities required for representing the matrix is $2NP + P^2$. The number of elementary operations required is $\mathcal{O}(NP)$ or $\mathcal{O}(P^2)$, depending on whichever is higher.

An important difference between the diagonal and non-diagonal factorizations is revealed when the foregoing concepts are extended to $M$ groups of source and observation points. For this, consider Figure 5.1 and the following matrix-vector product

$$I_i = \sum_{j=1}^{MN} g(x_i, x'_j) u_j \tag{5.8}$$

for $i = 1, 2 \ldots MN$. First, assume that each pair of source and observation groups satisfies an expansion of the form (5.4) such that all expansions involving a given source group share the same

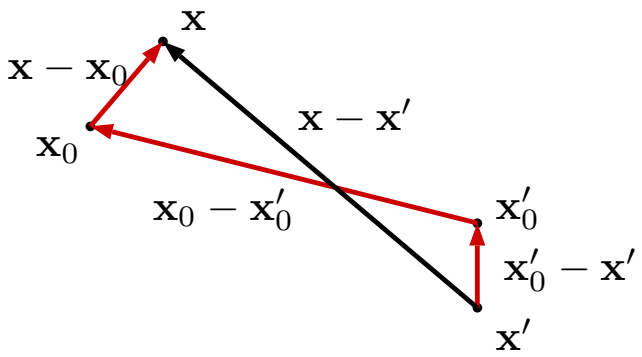


Figure 5.2: An illustration of source and observation points in Equation (5.10). The source point is $\mathbf{x}'$, observation point is $\mathbf{x}$, and multipole and local expansion centers are $\mathbf{x}'_0$ and $\mathbf{x}_0$, respectively.

vector $\bar{l}(x')$. Similarly, assume that all expansions involving a given observation group share the same vector $\bar{k}(x)$. To elaborate, associate $M$ vectors represented by $\bar{l}_\alpha(x')$ for $\alpha = 1, 2 \ldots M$ with the $M$ source groups and another $M$ vectors represented by $\bar{k}_\beta(x)$ for $\beta = 1, 2 \ldots M$ with the $M$ observation groups. If the points $x'$ and $x$ belong to the source and observation groups $\alpha_0$ and $\beta_0$, respectively, then the following expansion is assumed to hold:

$$g(x, x') = \bar{k}^T_{\beta_0}(x) \cdot \bar{\bar{T}}_{\alpha_0\beta_0} \cdot \bar{l}_{\alpha_0}(x'). \tag{5.9}$$

Therefore, to compute the matrix-vector product in (5.8) according to these expansions, the number of function evaluations involved in computing the vectors $\bar{k}_\beta(x_i)$ and $\bar{l}_\alpha(x'_i)$ for $i = 1, 2 \ldots NM$ is $\mathcal{O}(NMP)$. The number of function evaluations required for computing the diagonal matrices $\bar{\bar{T}}_{\alpha\beta}$ is $\mathcal{O}(M^2P)$. If $\bar{\bar{T}}_{\alpha\beta}$ was not diagonal, which is the case for non-diagonal expansions of the form given by (5.6), then the function evaluations required is $\mathcal{O}(M^2P^2)$. Therefore, if $P \sim N$, the total number of function evaluations required for non-diagonal expansions is $\mathcal{O}((NM)^2)$, which is on the same order as that required for direct computation of the matrix-vector product. Therefore, non-diagonal factorizations are useful only when the number of terms in the expansion ($P$) is much less than number of points in each group ($N$).

In the FMM, expansions of the above type are derived for far-field blocks of the influence matrix using multipole expansions of the BEM kernels. Non-diagonal expansions are used at low frequencies (static and quasi-static regimes), whereas diagonal-form expansions are used at high

frequencies. This is because the number of terms required in non-diagonal expansions is relatively small only at low frequencies, and the known diagonal-form expansions fail at low frequencies [185, Chap. 5]. The multipole expansions derive their name from the observation that they approximate radiation from a point source by that from a number of multipole sources that are located away from it. This can be seen with the help of Figure 5.2. Using the notation of the earlier example, a kernel function $g(\mathbf{x}, \mathbf{x}')$ which represents the radiation at an observation point $\mathbf{x}$ due to a point source located at $\mathbf{x}'$ is factorized in the form of (5.6) such that the vectors $\bar{l}$ and $\bar{k}$ depend on $\mathbf{x}_0' - \mathbf{x}'$ and $\mathbf{x} - \mathbf{x}_0$, respectively, and the matrix $\bar{\bar{T}}$ depends on $\mathbf{x}_0 - \mathbf{x}_0'$. Furthermore, $g(\mathbf{x}, \mathbf{x})$ can be written as

$$g(\mathbf{x}, \mathbf{x}') = \sum_{p=1}^{\infty} k_p(\mathbf{x} - \mathbf{x}_0) \sum_{q=1}^{\infty} T_{pq}(\mathbf{x}_0 - \mathbf{x}_0') l_q(\mathbf{x}_0' - \mathbf{x}') \tag{5.10a}$$

$$= \sum_{q=1}^{\infty} \gamma_q(\mathbf{x}, \mathbf{x}_0') l_q(\mathbf{x}_0' - \mathbf{x}') = \bar{\gamma}^T(\mathbf{x}, \mathbf{x}_0') \cdot \bar{l}(\mathbf{x}_0' - \mathbf{x}') \tag{5.10b}$$

$$= \sum_{p=1}^{\infty} k_p(\mathbf{x} - \mathbf{x}_0) \Gamma_p(\mathbf{x}_0, \mathbf{x}') = \bar{k}^T(\mathbf{x} - \mathbf{x}_0) \cdot \bar{\Gamma}(\mathbf{x}_0, \mathbf{x}'), \tag{5.10c}$$

where $\gamma_q(\mathbf{x}, \mathbf{x}_0')$ and $\Gamma_p(\mathbf{x_0}, \mathbf{x'})$ are defined by contraction of the appropriate summations. Each element of $\bar{\gamma}(\mathbf{x}, \mathbf{x}_0')$ can be expressed in the form of the radiation field due to a multipole centered at $\mathbf{x}_0'$ and evaluated at $\mathbf{x}$. Therefore, Equation (5.10b) is called *multipole expansion*, and the elements of $\bar{l}(\mathbf{x}_0' - \mathbf{x}')$ are called *multipole moments*. By symmetry, Equation (5.10c) can also be viewed as a multipole expansion. However, it is more common to view the elements of $\bar{k}(\mathbf{x} - \mathbf{x}_0)$ as the expansion (basis) functions and those of $\bar{\Gamma}(\mathbf{x}_0, \mathbf{x}')$ as the coefficients, and hence (5.10c) is called *local expansion*. The coefficients $T_{pq}(\mathbf{x}_0 - \mathbf{x}_0')$ are called *transfer functions*.

## 5.3 Multipole Expansions of CFIE Kernels

Multipole expansions of the kernels in the CFIE formulation are given in this section. The CFIE includes kernels from both the CBIE and the HBIE. Diagonal-form expansions of CBIE kernels are

well-known [30]. Similar expansions of HBIE kernels are derived here. Consider the Helmholtz equation corresponding to the wavenumber $k$

$$(\nabla^2 + k^2)\phi(\mathbf{x}) = 0. \tag{5.11}$$

The fundamental solution (i.e., Green's function with regularity condition imposed at infinity) of the Helmholtz equation is

$$g(\mathbf{x}, \mathbf{x}') = \frac{e^{ikR}}{4\pi R}, \tag{5.12}$$

where $R = |\mathbf{x} - \mathbf{x}'|$ and $\mathbf{x}'$ is the location of the Dirac-delta source. A diagonal-form multipole expansion is available for this Green's function. Multipole expansions of the HBIE kernels can be derived by expressing them in terms of the Helmholtz Green's functions corresponding to the longitudinal ($k_c$) and shear wavenumbers ($k_s$). The subscripts $s$ and $c$, standing for shear and compressional (longitudinal) wavenumbers, respectively, are used to distinguish between the two Green's functions when necessary. Assuming that there exist vectors $\mathbf{d}, \mathbf{D} \in \mathbb{R}^3$ such that $|\mathbf{d}| < |\mathbf{D}|$ and $|\mathbf{x} - \mathbf{x}'| = |\mathbf{d} + \mathbf{D}|$, the Helmholtz Green's function can be decomposed as follows [185, p. 80] [186, p. 16]

$$g(\mathbf{x}, \mathbf{x}') = \frac{ik}{(4\pi)^2} \sum_{l=0}^{\infty} i^l (2l+1) h_l^{(1)}(kD)\ j_l(kd)\ P_l(\hat{\mathbf{d}} \cdot \hat{\mathbf{D}}), \tag{5.13}$$

where $d = |\mathbf{d}|$, $D = |\mathbf{D}|$, $\hat{\mathbf{d}}$ and $\hat{\mathbf{D}}$ are the unit vectors along $\mathbf{d}$ and $\mathbf{D}$, respectively, $P_l(x)$ is the Legendre polynomial of order $l$, and $h_l(x)$ and $j_l(x)$ are the spherical Hankel and Bessel functions of the first kind of order $l$, respectively. The above equation is known as Gegenbauer's addition theorem. If we choose $\mathbf{d} = \mathbf{x}_0' - \mathbf{x}'$ and $\mathbf{D} = \mathbf{x} - \mathbf{x}_0'$, then this theorem represents a multipole expansion about the point $\mathbf{x}_0'$ for a point source located at $\mathbf{x}'$. However, a different choice of $\mathbf{d}$ and $\mathbf{D}$ is used to derive a diagonal-form expansion, as mentioned later.

The following identity, which is an instance of the Funk-Hecke theorem, is applied to rewrite the above expression [186, p. 16] [187, p. 7]:

$$4\pi i^l j_l(\lambda) P_l(\hat{\mathbf{d}} \cdot \hat{\mathbf{s}}) = \int_{\mathbb{S}^2} d\sigma(\hat{\mathbf{k}})\ e^{i\lambda \hat{\mathbf{k}} \cdot \hat{\mathbf{d}}} P_l(\hat{\mathbf{k}} \cdot \hat{\mathbf{s}}), \tag{5.14}$$

for all $\hat{\mathbf{s}}, \hat{\mathbf{d}} \in \mathbb{S}^2$, $l \in \mathbb{N}$, and $\lambda \in \mathbb{C}$, where $\mathbb{S}^2 \subset \mathbb{R}^3$ is the 2-sphere and $d\sigma$ is the area element on $\mathbb{S}^2$. Note that the points in $\mathbb{S}^2$ are considered to be dimensionless and hence all unit vectors naturally lie in this space. Choosing $\hat{\mathbf{s}} = \hat{\mathbf{D}}$ and $\lambda = kd$, we get

$$4\pi i^l j_l(kd) P_l(\hat{\mathbf{d}} \cdot \hat{\mathbf{D}}) = \int_{\mathbb{S}^2} d^2\hat{\mathbf{k}}\; e^{i\mathbf{k}\cdot\mathbf{d}} P_l(\hat{\mathbf{k}} \cdot \hat{\mathbf{D}}), \tag{5.15}$$

where $\mathbf{k} = k\hat{\mathbf{k}}$ and the area element is represented by $d^2\hat{\mathbf{k}}$. Substituting the above equation into (5.13) yields

$$g(\mathbf{x}, \mathbf{x}') = \frac{ik}{(4\pi)^2} \sum_{l=0}^{\infty} i^l (2l+1) h_l^{(1)}(kD) \int_{\mathbb{S}^2} d^2\hat{\mathbf{k}}\; e^{i\mathbf{k}\cdot\mathbf{d}} P_l(\hat{\mathbf{k}} \cdot \hat{\mathbf{D}}) \tag{5.16a}$$

$$\approx \frac{ik}{(4\pi)^2} \int_{\mathbb{S}^2} d^2\hat{\mathbf{k}}\; e^{i\mathbf{k}\cdot\mathbf{d}} \sum_{l=0}^{L_T} i^l (2l+1) h_l^{(1)}(kD) P_l(\hat{\mathbf{k}} \cdot \hat{\mathbf{D}}), \tag{5.16b}$$

where the integral is interchanged with the summation after truncating the sum at $L_T + 1$ terms. With reference to Figure 5.2, choose $\mathbf{x}_0,\ \mathbf{x}_0' \in \mathbb{R}^3$ such that $|\mathbf{x}_0 - \mathbf{x}_0'| > |\mathbf{x} - \mathbf{x}_0 + \mathbf{x}_0' - \mathbf{x}'|$. Let $\mathbf{r}_0 = \mathbf{x}_0 - \mathbf{x}_0'$. We have

$$\mathbf{x} - \mathbf{x}' = \mathbf{x} - \mathbf{x}_0 + \mathbf{r}_0 + \mathbf{x}_0' - \mathbf{x}'. \tag{5.17}$$

Substituting $\mathbf{d} = \mathbf{x} - \mathbf{x}_0 + \mathbf{x}_0' - \mathbf{x}'$ and $\mathbf{D} = \mathbf{r}_0$ in (5.16b) gives

$$g(\mathbf{x}, \mathbf{x}') \approx \frac{ik}{(4\pi)^2} \int_{\mathbb{S}^2} d^2\hat{\mathbf{k}}\; e^{i\mathbf{k}\cdot(\mathbf{x}-\mathbf{x}_0)} \mathcal{L}(\mathbf{k}, \mathbf{r}_0) e^{-i\mathbf{k}\cdot(\mathbf{x}'-\mathbf{x}_0')}, \tag{5.18}$$

where

$$\mathcal{L}(\mathbf{k}, \mathbf{r}_0) = \frac{ik}{(4\pi)^2} \sum_{l=0}^{L_T} i^l (2l+1) h_l^{(1)}(kr_0) P_l(\hat{\mathbf{k}} \cdot \hat{\mathbf{r}}_0), \tag{5.19}$$

$r_0 = |\mathbf{r}_0|$ and $\hat{\mathbf{r}} = \mathbf{r}/r_0$. More concisely, we can write

$$g(\mathbf{x}, \mathbf{x}') \approx \int_{\mathbb{S}^2} d^2\hat{\mathbf{k}}\; \mathcal{G}(\mathbf{k}), \tag{5.20}$$

with $\mathcal{G}(\mathbf{k})$ is given by

$$\mathcal{G}(\mathbf{k}) = \mathcal{M}(\mathbf{k}, \mathbf{x} - \mathbf{x}_0)\; \mathcal{L}(\mathbf{k}, \mathbf{r}_0)\; \mathcal{M}(\mathbf{k}, \mathbf{x}_0' - \mathbf{x}'), \tag{5.21}$$

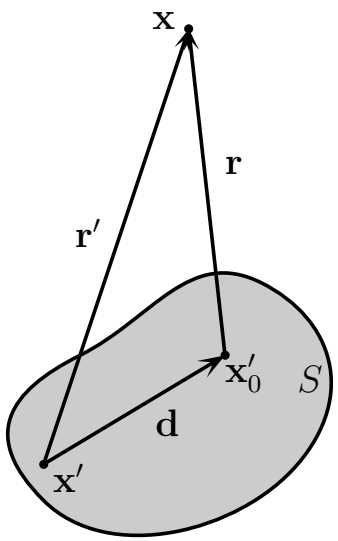


Figure 5.3: A representation of a closed surface $S$ with a single-layer source $h(\mathbf{x})$. The point $\mathbf{x}$ represents the location where the radiated field is evaluated.

and $\mathcal{M}(\mathbf{k}, \mathbf{x}-\mathbf{y}) = e^{i\mathbf{k}\cdot(\mathbf{x}-\mathbf{y})}$ for $\mathbf{x}, \mathbf{y} \in \mathbb{R}^3$. For brevity, the dependence of $\mathcal{G}(\mathbf{k})$ on $\mathbf{x}$, $\mathbf{x}'$, and $\mathbf{r}_0$ is not shown explicitly. Discretizing the integral in (5.20) using a quadrature rule yields a diagonal-form expansion of the type given by (5.4):

$$g(\mathbf{x}, \mathbf{x}') \approx \sum_{q=1}^{Q} w_q \mathcal{M}(\mathbf{k}^{(q)}, \mathbf{x}-\mathbf{x}_0)\ \mathcal{L}(\mathbf{k}^{(q)}, \mathbf{r}_0)\ \mathcal{M}(\mathbf{k}^{(q)}, \mathbf{x}_0'-\mathbf{x}'), \tag{5.22}$$

where $Q$ is the number of quadrature points, $w_q$ and $\mathbf{k}^{(q)}$ are the quadrature weights and points (scaled by $k$), respectively.

Notice that the term $\mathcal{M}(\mathbf{k}^{(q)}, \mathbf{x}_0'-\mathbf{x}')$ expresses the phase shift from $\mathbf{x}'$ to $\mathbf{x}_0'$ due to a plane-wave with wavevector $\mathbf{k}^{(q)}$. It lends a physical meaning to some components in the matrix-vector product, as shown below. First, consider the evaluation of a matrix-vector product as in Equation (5.1) by replacing $g(x_j, x_i')$ with the 3D Helmholtz Green's function $g(\mathbf{x}_i, \mathbf{x}_j')$. This product can be evaluated using the factorization (5.22) as

$$I_j = \sum_{q=1}^{Q} w_q \mathcal{M}(\mathbf{k}^{(q)}, \mathbf{x}_j-\mathbf{x}_0)\ \mathcal{L}(\mathbf{k}^{(q)}, \mathbf{r}_0) \left( \sum_{k=1}^{N} \mathcal{M}(\mathbf{k}^{(q)}, \mathbf{x}_0'-\mathbf{x}_k') u_k \right). \tag{5.23}$$

The term in the parentheses can be interpreted as the radiation field in the direction $\hat{\mathbf{k}}^{(q)}$ due to single-layer sources located at $\mathbf{x}_k'$ for $k = 1, 2, \ldots N$. The reason for this can be discerned by

calculating the radiated field at a point $\mathbf{x}$ due to single-layer sources $h(\mathbf{x}')$ located on a closed surface $S$, as shown in Figure 5.3. The radiated field at $\mathbf{x}$ is given by

$$\phi(\mathbf{x}) = \int_S g(\mathbf{x}, \mathbf{x}') h(\mathbf{x}') dS(\mathbf{x}'). \tag{5.24}$$

When $\mathbf{x}$ is far from $S$, the radiated field can be approximated by

$$\phi(\mathbf{x}) \approx \frac{e^{ikr}}{r} \int_S e^{ik\mathbf{d}\cdot\hat{\mathbf{r}}} h(\mathbf{x}') dS(\mathbf{x}') \approx \frac{e^{ikr}}{r} \sum_{k=1}^{N} e^{ik(\mathbf{x}_0' - \mathbf{x}_k')\cdot\hat{\mathbf{r}}} u(\mathbf{x}_k'), \tag{5.25}$$

where $r$ and $\hat{\mathbf{r}}$ are the magnitude and direction of $\mathbf{r}$, and the integral is discretized using $N$ quadrature points. The function $u(\mathbf{x}_k')$ is the product of the density function and the quadrature weights. Therefore, the far-field pattern of the radiated field is given by the integral in (5.25), which is approximated by a summation. The quantity in the parantheses in Equation (5.23) is in the same form as the summation in the above equation, and hence, for different values of $q$, it can be considered as representing a radiation pattern. Analogously, the term $\mathcal{M}(\mathbf{k}^{(q)}, \mathbf{x} - \mathbf{x}_0)$ leads to a receiving pattern. In case of collocation-based BEMs, the receiving pattern is that of a (in general, directive) point source. Finally, by analogy with (5.10b), we shall refer to $\mathcal{M}(\mathbf{k}^{(q)}, \mathbf{x}_0' - \mathbf{x}')$ as a multipole-moment. It should be kept in mind, however, that it does not truly represent a multipole-moment because of a change of basis from multipole expansions to plane-wave expansions (see [185, §2.2.5]).

The CBIE and HBIE kernels can be expressed as derivatives of the Helmholtz Green's functions as follows

$$\overline{\mathbf{U}}(\mathbf{x}, \mathbf{x}') = \left(\bar{\mathbf{I}} + \frac{\nabla\nabla}{k_s^2}\frac{1}{\mu}\right) g_s(\mathbf{x}, \mathbf{x}') - \frac{\nabla\nabla}{k_c^2}\frac{1}{\gamma} g_c(\mathbf{x}, \mathbf{x}'), \tag{5.26a}$$

$$\overline{\mathbf{T}}^{(1)}(\mathbf{x}, \mathbf{x}') = [\hat{\mathbf{n}}' \cdot \overline{\overline{\mathbf{\Sigma}}}^{(1)}(\mathbf{x}, \mathbf{x}')]^T \tag{5.26b}$$

$$= \lambda \left(\nabla_x \cdot \overline{\mathbf{U}}(\mathbf{x}, \mathbf{x}')\right) \hat{\mathbf{n}}' + \mu(\hat{\mathbf{n}}' \cdot \nabla_x \overline{\mathbf{U}}^T(\mathbf{x}, \mathbf{x}') + [\hat{\mathbf{n}}' \cdot (\overline{\mathbf{U}}(\mathbf{x}, \mathbf{x}')\nabla_x)]^T), \tag{5.26c}$$

$$\overline{\mathbf{K}}^{(2)}(\mathbf{x}, \mathbf{x}') = -\hat{\mathbf{n}} \cdot \overline{\overline{\mathbf{\Sigma}}}^{(1)}(\mathbf{x}, \mathbf{x}') = -\lambda\hat{\mathbf{n}}\nabla_x \cdot \overline{\mathbf{U}}(\mathbf{x}, \mathbf{x}') - \mu\hat{\mathbf{n}} \cdot (\nabla_x \overline{\mathbf{U}}(\mathbf{x}, \mathbf{x}') + \overline{\mathbf{U}}(\mathbf{x}, \mathbf{x}')\nabla_x), \tag{5.26d}$$

$$\overline{\mathbf{H}}(\mathbf{x}, \mathbf{x}') = \lambda\hat{\mathbf{n}} \left(\nabla_x \cdot \overline{\mathbf{T}}^{(1)}(\mathbf{x}, \mathbf{x}')\right) + \mu\hat{\mathbf{n}} \cdot (\nabla_x \overline{\mathbf{T}}^{(1)}(\mathbf{x}, \mathbf{x}') + \overline{\mathbf{T}}^{(1)}(\mathbf{x}, \mathbf{x}')\nabla_x), \tag{5.26e}$$

where $\gamma := \lambda + 2\mu$, $k_s$ and $k_c$ are the shear and longitudinal wavenumbers, respectively, and $g_s$ and $g_c$ are the Helmholtz Green's functions with wavenumbers $k_s$ and $k_c$, respectively. Both $g_s(\mathbf{x}, \mathbf{x}')$ and $g_c(\mathbf{x}, \mathbf{x}')$ can be factorized in the form of (5.20), as shown below

$$g_s(\mathbf{x}, \mathbf{x}') \approx \int_{\mathbb{S}^2} d^2\hat{\mathbf{k}}\ \mathcal{G}(\mathbf{k}_s), \tag{5.27}$$

$$g_c(\mathbf{x}, \mathbf{x}') \approx \int_{\mathbb{S}^2} d^2\hat{\mathbf{k}}\ \mathcal{G}(\mathbf{k}_c). \tag{5.28}$$

Similar factorizations of the HBIE kernels are obtained by substituting the above expressions for $g_s(\mathbf{x}, \mathbf{x}')$ and $g_c(\mathbf{x}, \mathbf{x}')$ into Equations (5.26a) through (5.26e) and moving the derivatives inside the integrals over $\mathbb{S}^2$. Assume that the factorizations are in the following form

$$\overline{\mathbf{F}}(\mathbf{x}, \mathbf{x}') \approx \int_{\mathbb{S}^2} d^2\hat{\mathbf{k}}\ \widetilde{\overline{\mathbf{F}}}(\mathbf{k}_c, \mathbf{k}_s), \tag{5.29}$$

where $\overline{\mathbf{F}}$ represents the kernel $\overline{\mathbf{U}}$, $\overline{\mathbf{T}}^{(1)}$, $\overline{\mathbf{K}}^{(2)}$ or $\overline{\mathbf{H}}$. Let $\mathcal{G}_m = \mathcal{G}(\mathbf{k}_m)$ for $m = s, c$. Noting that $\nabla_x \mathcal{G}(\mathbf{k}) = i\mathbf{k}\mathcal{G}(\mathbf{k})$ and $\nabla_x \cdot (\overline{\mathbf{P}}\mathcal{G}(\mathbf{k})) = i\mathbf{k} \cdot \overline{\mathbf{P}}\mathcal{G}(\mathbf{k})$ for any tensor $\overline{\mathbf{P}} \in \mathbb{R}^3 \otimes \mathbb{R}^3$, we have

$$\widetilde{\overline{\mathbf{U}}} = \frac{1}{\mu}\left(\bar{\mathbf{I}} - \hat{\mathbf{k}}\hat{\mathbf{k}}\right)\mathcal{G}_s + \frac{1}{\gamma}\hat{\mathbf{k}}\hat{\mathbf{k}}\mathcal{G}_c. \tag{5.30}$$

Furthermore,

$$\nabla_x \cdot \widetilde{\overline{\mathbf{U}}} = \frac{1}{\gamma} i\mathbf{k}_c \mathcal{G}_c, \tag{5.31a}$$

$$\hat{\mathbf{n}}' \cdot \nabla_x \widetilde{\overline{\mathbf{U}}}^T = \frac{i\hat{\mathbf{n}}' \cdot \mathbf{k}_s}{\mu}\left(\bar{\mathbf{I}} - \hat{\mathbf{k}}\hat{\mathbf{k}}\right)\mathcal{G}_s + \frac{i\hat{\mathbf{n}}' \cdot \mathbf{k}_c}{\gamma}\hat{\mathbf{k}}\hat{\mathbf{k}}\mathcal{G}_c, \tag{5.31b}$$

$$[\hat{\mathbf{n}}' \cdot (\widetilde{\overline{\mathbf{U}}}\nabla_x)]^T = \frac{i}{\mu}\left(\hat{\mathbf{n}}' - (\hat{\mathbf{n}}' \cdot \hat{\mathbf{k}})\hat{\mathbf{k}}\right)\mathbf{k}_s\mathcal{G}_s + \frac{i}{\gamma}(\hat{\mathbf{n}}' \cdot \hat{\mathbf{k}})\hat{\mathbf{k}}\mathbf{k}_c\mathcal{G}_c \tag{5.31c}$$

$$= \frac{i}{\mu}\hat{\mathbf{n}}' \cdot \left(\bar{\mathbf{I}} - \hat{\mathbf{k}}\hat{\mathbf{k}}\right)\mathbf{k}_s\mathcal{G}_s + \frac{i}{\gamma}(\hat{\mathbf{n}}' \cdot \mathbf{k}_c)\hat{\mathbf{k}}\hat{\mathbf{k}}\mathcal{G}_c. \tag{5.31d}$$

Therefore,

$$\widetilde{\overline{\mathbf{T}}}^{(1)} = \frac{ik_c}{\gamma}\hat{\mathbf{k}}\left(\lambda\hat{\mathbf{n}}' + 2\mu\hat{\mathbf{n}}' \cdot \hat{\mathbf{k}}\hat{\mathbf{k}}\right)\mathcal{G}_c + ik_s\left[\hat{\mathbf{n}}' \cdot \hat{\mathbf{k}}\left(\bar{\mathbf{I}} - \hat{\mathbf{k}}\hat{\mathbf{k}}\right) + \hat{\mathbf{n}}' \cdot \left(\bar{\mathbf{I}} - \hat{\mathbf{k}}\hat{\mathbf{k}}\right)\hat{\mathbf{k}}\right]\mathcal{G}_s. \tag{5.32}$$

Similarly,

$$\widetilde{\overline{\mathbf{K}}}^{(2)} = -\frac{ik_c}{\gamma}\left(\lambda\hat{\mathbf{n}} + 2\mu\hat{\mathbf{n}} \cdot \hat{\mathbf{k}}\hat{\mathbf{k}}\right)\hat{\mathbf{k}}\mathcal{G}_c - ik_s\left[\hat{\mathbf{n}} \cdot \hat{\mathbf{k}}\left(\bar{\mathbf{I}} - \hat{\mathbf{k}}\hat{\mathbf{k}}\right) + \hat{\mathbf{k}}\hat{\mathbf{n}} \cdot \left(\bar{\mathbf{I}} - \hat{\mathbf{k}}\hat{\mathbf{k}}\right)\right]\mathcal{G}_s. \tag{5.33}$$

The derivatives of $\widetilde{\overline{\mathbf{T}}}^{(1)}$ that are required for computing $\widetilde{\overline{\mathbf{H}}}$ are given by

$$\nabla_x \cdot \widetilde{\overline{\mathbf{T}}}^{(1)} = -\frac{k_c^2}{\gamma}\left(\lambda\hat{\mathbf{n}}' + 2\mu\hat{\mathbf{n}}'\cdot\hat{\mathbf{k}}\hat{\mathbf{k}}\right)\mathcal{G}_c, \tag{5.34a}$$

$$\begin{aligned}\hat{\mathbf{n}}\cdot\nabla_x\widetilde{\overline{\mathbf{T}}}^{(1)} &= -\frac{k_c^2}{\gamma}(\hat{\mathbf{n}}\cdot\hat{\mathbf{k}})\hat{\mathbf{k}}\left(\lambda\hat{\mathbf{n}}' + 2\mu\hat{\mathbf{n}}'\cdot\hat{\mathbf{k}}\hat{\mathbf{k}}\right)\mathcal{G}_c \\ &\quad - k_s^2\hat{\mathbf{n}}\cdot\hat{\mathbf{k}}\left[\hat{\mathbf{n}}'\cdot\hat{\mathbf{k}}\left(\bar{\mathbf{I}} - \hat{\mathbf{k}}\hat{\mathbf{k}}\right) + \hat{\mathbf{n}}'\cdot\left(\bar{\mathbf{I}} - \hat{\mathbf{k}}\hat{\mathbf{k}}\right)\hat{\mathbf{k}}\right]\mathcal{G}_s,\end{aligned} \tag{5.34b}$$

$$\begin{aligned}\hat{\mathbf{n}}\cdot\widetilde{\overline{\mathbf{T}}}^{(1)}\nabla_x &= -\frac{k_c^2}{\gamma}(\hat{\mathbf{n}}\cdot\hat{\mathbf{k}})\hat{\mathbf{k}}\left(\lambda\hat{\mathbf{n}}' + 2\mu\hat{\mathbf{n}}'\cdot\hat{\mathbf{k}}\hat{\mathbf{k}}\right)\mathcal{G}_c \\ &\quad - k_s^2\left[(\hat{\mathbf{n}}'\cdot\hat{\mathbf{k}})\hat{\mathbf{k}}\left(\bar{\mathbf{I}} - \hat{\mathbf{k}}\hat{\mathbf{k}}\right)\cdot\hat{\mathbf{n}} + \hat{\mathbf{n}}'\cdot\left(\bar{\mathbf{I}} - \hat{\mathbf{k}}\hat{\mathbf{k}}\right)\cdot\hat{\mathbf{n}}\hat{\mathbf{k}}\hat{\mathbf{k}}\right]\mathcal{G}_s \qquad (5.34c)\\ &= -\frac{k_c^2}{\gamma}(\hat{\mathbf{n}}\cdot\hat{\mathbf{k}})\hat{\mathbf{k}}\left(\lambda\hat{\mathbf{n}}' + 2\mu\hat{\mathbf{n}}'\cdot\hat{\mathbf{k}}\hat{\mathbf{k}}\right)\mathcal{G}_c \\ &\quad - k_s^2\left[(\hat{\mathbf{n}}'\cdot\hat{\mathbf{k}})\hat{\mathbf{k}}\left(\bar{\mathbf{I}} - \hat{\mathbf{k}}\hat{\mathbf{k}}\right)\cdot\hat{\mathbf{n}} + \hat{\mathbf{n}}\cdot\left(\bar{\mathbf{I}} - \hat{\mathbf{k}}\hat{\mathbf{k}}\right)\cdot\hat{\mathbf{n}}'\hat{\mathbf{k}}\hat{\mathbf{k}}\right]\mathcal{G}_s. \qquad (5.34d)\end{aligned}$$

Therefore,

$$\begin{aligned}\widetilde{\overline{\mathbf{H}}} = -\frac{k_c^2}{\gamma}&\left[\lambda\hat{\mathbf{n}}\left(\lambda\hat{\mathbf{n}}' + 2\mu(\hat{\mathbf{n}}'\cdot\hat{\mathbf{k}})\hat{\mathbf{k}}\right) + 2\mu(\hat{\mathbf{n}}\cdot\hat{\mathbf{k}})\hat{\mathbf{k}}\left(\lambda\hat{\mathbf{n}}' + 2\mu(\hat{\mathbf{n}}'\cdot\hat{\mathbf{k}})\hat{\mathbf{k}}\right)\right]\mathcal{G}_c - k_s^2\mu \\ &\left[(\hat{\mathbf{n}}\cdot\hat{\mathbf{k}})(\bar{\mathbf{I}} - \hat{\mathbf{k}}\hat{\mathbf{k}})(\hat{\mathbf{n}}'\cdot\hat{\mathbf{k}}) + (\hat{\mathbf{n}}\cdot\hat{\mathbf{k}})\hat{\mathbf{n}}'\cdot(\bar{\mathbf{I}} - \hat{\mathbf{k}}\hat{\mathbf{k}})\hat{\mathbf{k}} + \hat{\mathbf{k}}(\bar{\mathbf{I}} - \hat{\mathbf{k}}\hat{\mathbf{k}})\cdot\hat{\mathbf{n}}(\hat{\mathbf{n}}'\cdot\hat{\mathbf{k}}) + \hat{\mathbf{n}}\cdot(\bar{\mathbf{I}} - \hat{\mathbf{k}}\hat{\mathbf{k}})\cdot\hat{\mathbf{n}}'\hat{\mathbf{k}}\hat{\mathbf{k}}\right]\mathcal{G}_s,\end{aligned} \tag{5.35}$$

which can be further simplified as

$$\begin{aligned}\widetilde{\overline{\mathbf{H}}} = -\frac{k_c^2}{\gamma}&\left[\left(\lambda\hat{\mathbf{n}} + 2\mu(\hat{\mathbf{n}}\cdot\hat{\mathbf{k}})\hat{\mathbf{k}}\right)\left(\lambda\hat{\mathbf{n}}' + 2\mu(\hat{\mathbf{n}}'\cdot\hat{\mathbf{k}})\hat{\mathbf{k}}\right)\right]\mathcal{G}_c - k_s^2\mu \\ &\left[(\hat{\mathbf{n}}\cdot\hat{\mathbf{k}})(\bar{\mathbf{I}} - \hat{\mathbf{k}}\hat{\mathbf{k}})(\hat{\mathbf{n}}'\cdot\hat{\mathbf{k}}) + (\hat{\mathbf{n}}\cdot\hat{\mathbf{k}})\hat{\mathbf{n}}'\cdot(\bar{\mathbf{I}} - \hat{\mathbf{k}}\hat{\mathbf{k}})\hat{\mathbf{k}} + \hat{\mathbf{k}}(\bar{\mathbf{I}} - \hat{\mathbf{k}}\hat{\mathbf{k}})\cdot\hat{\mathbf{n}}(\hat{\mathbf{n}}'\cdot\hat{\mathbf{k}}) + \hat{\mathbf{n}}\cdot(\bar{\mathbf{I}} - \hat{\mathbf{k}}\hat{\mathbf{k}})\cdot\hat{\mathbf{n}}'\hat{\mathbf{k}}\hat{\mathbf{k}}\right]\mathcal{G}_s.\end{aligned} \tag{5.36}$$

When the integral in (5.29) is discretized, diagonal form expansions of the HBIE kernels can be derived using (5.33) and (5.36) along with (5.21). Rather than deriving these expansions and then obtaining the expansions of far-field matrix elements defined in Chapter 4, the latter are derived directly in the next section.

## 5.4 Factorization of Far-field Matrix Elements

Recall that according to (4.110c), all far-field matrix elements can be written in the following form

$$Z^F_{\beta,\alpha}(\mathbf{y}^{(q)}_j, \mathbf{y}^{(p)}_i) = w_i \; \tilde{\mathbf{e}}^{(q)}_\beta(\boldsymbol{\xi}_j) \cdot \overline{\mathbf{F}}(\mathbf{y}^{(q)}_j, \mathbf{y}^{(p)}_i) \cdot \mathbf{e}^{(p)}_\alpha(\boldsymbol{\xi}_i) \mathcal{J}(\boldsymbol{\xi}_i). \tag{5.37}$$

Thus, every far-field matrix element is a function of two position vectors– one corresponding to the interpolation basis and another to the collocation point. Let these two position vectors be referred by $\mathbf{x}'$ and $\mathbf{x}$, respectively. We can rewrite the above in the following simplified notation

$$Z^F_{\beta,\alpha}(\mathbf{x}, \mathbf{x}') = \tilde{\mathbf{e}}_\beta(\mathbf{x}) \cdot \overline{\mathbf{F}}(\mathbf{x}, \mathbf{x}') \cdot \mathbf{e}_\alpha(\mathbf{x}') W(\mathbf{x}'). \tag{5.38}$$

Henceforth, the dependence of quantities on $\mathbf{x}$ and $\mathbf{x}'$ will not be shown explicitly unless when necessary. Substituting the factorizations of the kernels derived in the previous section into the above equation, we obtain factorizations for the matrix elements in the following form

$$Z^F_{\beta,\alpha}(\mathbf{x}, \mathbf{x}') \approx \int_{\mathbb{S}^2} d^2\hat{\mathbf{k}} \; \mathcal{Z}^F_{\beta,\alpha}(\mathbf{k}_c, \mathbf{k}_s). \tag{5.39}$$

For the $\overline{\mathbf{K}}^{(2)}$ kernel, Equation (5.33) yields

$$\mathcal{Z}^K_{\beta,\alpha}(\mathbf{k}_c, \mathbf{k}_s) = \tilde{\mathbf{e}}_\beta \cdot \overset{\sim}{\overline{\mathbf{K}}}^{(2)} \cdot \mathbf{e}_\alpha W = \mathcal{Z}^{K,s}_{\beta,\alpha}(\mathbf{k}_s) + \mathcal{Z}^{K,c}_{\beta,\alpha}(\mathbf{k}_c), \tag{5.40}$$

where

$$\begin{aligned}
\mathcal{Z}^{K,c}_{\beta,\alpha}(\mathbf{k}_c) &= -ik_c \tilde{\mathbf{e}}_\beta \cdot e^{i\mathbf{k}_c \cdot (\mathbf{x}-\mathbf{x}_0)} \mathcal{L}(\mathbf{k}_c, \mathbf{r}_0) \left\{ \left[ \hat{\mathbf{n}} \left( \frac{\lambda}{\gamma} \hat{\mathbf{k}} \cdot \mathbf{e}_\alpha \right) + \hat{\mathbf{k}} \left( \frac{2\mu}{\gamma} (\hat{\mathbf{n}} \cdot \hat{\mathbf{k}})(\hat{\mathbf{k}} \cdot \mathbf{e}_\alpha) \right) \right] e^{i\mathbf{k}_c \cdot (\mathbf{x}'_0 - \mathbf{x}')} W \right\} \\
&= -ik_c \left[ \left( (\tilde{\mathbf{e}}_\beta \cdot \hat{\mathbf{n}}) \frac{\lambda}{\gamma} + (\tilde{\mathbf{e}}_\beta \cdot \hat{\mathbf{k}})(\hat{\mathbf{n}} \cdot \hat{\mathbf{k}}) \frac{2\mu}{\gamma} \right) e^{i\mathbf{k}_c \cdot (\mathbf{x}-\mathbf{x}_0)} \right] \mathcal{L}(\mathbf{k}_c, \mathbf{r}_0) \left[ \hat{\mathbf{k}} \cdot \mathbf{e}_\alpha e^{i\mathbf{k}_c \cdot (\mathbf{x}'_0 - \mathbf{x}')} W \right]
\end{aligned} \tag{5.41}$$

and

$$\begin{aligned}
\mathcal{Z}^{K,s}_{\beta,\alpha}(\mathbf{k}_s) = -ik_s \tilde{\mathbf{e}}_\beta \cdot e^{i\mathbf{k}_s \cdot (\mathbf{x}-\mathbf{x}_0)} \mathcal{L}(\mathbf{k}_s, \mathbf{r}_0) \Big\{ \Big[ (\hat{\mathbf{k}} \cdot \hat{\mathbf{n}}) \left( \hat{\boldsymbol{\theta}}\hat{\boldsymbol{\theta}} + \hat{\boldsymbol{\phi}}\hat{\boldsymbol{\phi}} \right) \cdot \mathbf{e}_\alpha + \\
\hat{\mathbf{k}}\hat{\mathbf{n}} \cdot \left( \hat{\boldsymbol{\theta}}\hat{\boldsymbol{\theta}} + \hat{\boldsymbol{\phi}}\hat{\boldsymbol{\phi}} \right) \cdot \mathbf{e}_\alpha \Big] e^{i\mathbf{k}_s \cdot (\mathbf{x}'_0 - \mathbf{x}')} W \Big\}.
\end{aligned} \tag{5.42}$$

We have used the fact that $\bar{\mathbf{I}} - \hat{\mathbf{k}}\hat{\mathbf{k}} = \hat{\boldsymbol{\theta}}\hat{\boldsymbol{\theta}} + \hat{\boldsymbol{\phi}}\hat{\boldsymbol{\phi}}$ in the above, where $\hat{\boldsymbol{\theta}}$ and $\hat{\boldsymbol{\phi}}$ are polar and azimuthal unit vectors defined on $\mathbb{S}^2$. Separating the terms dependent on $\mathbf{x}$ and $\mathbf{x}'$, we get

$$\mathcal{Z}^{K,s}_{\beta,\alpha}(\mathbf{k}_s) = -ik_s \left[\left(\tilde{\mathbf{e}}_\beta(\hat{\mathbf{k}}\cdot\hat{\mathbf{n}}) + \tilde{\mathbf{e}}_\beta\cdot\hat{\mathbf{k}}\hat{\mathbf{n}}\right) e^{i\mathbf{k}_s\cdot(\mathbf{x}-\mathbf{x}_0)}\right]\cdot\mathcal{L}(\mathbf{k}_s,\mathbf{r}_0)\left[\left(\hat{\boldsymbol{\theta}}\hat{\boldsymbol{\theta}}+\hat{\boldsymbol{\phi}}\hat{\boldsymbol{\phi}}\right)\cdot\mathbf{e}_\alpha e^{i\mathbf{k}_s\cdot(\mathbf{x}'_0-\mathbf{x}')}W\right]. \tag{5.43}$$

Similarly, the $\overline{\mathbf{H}}$ kernel factorization is given by

$$\mathcal{Z}^{H}_{\beta,\alpha}(\mathbf{k}_c,\mathbf{k}_s) = \tilde{\mathbf{e}}_\beta\cdot\widetilde{\overline{\mathbf{H}}}\cdot\mathbf{e}_\alpha W = \mathcal{Z}^{H,s}_{\beta,\alpha}(\mathbf{k}_s) + \mathcal{Z}^{H,c}_{\beta,\alpha}(\mathbf{k}_c), \tag{5.44}$$

where

$$\mathcal{Z}^{H,c}_{\beta,\alpha}(\mathbf{k}_c) = -k_c^2\left[\left((\tilde{\mathbf{e}}_\beta\cdot\hat{\mathbf{n}})\frac{\lambda}{\gamma} + (\tilde{\mathbf{e}}_\beta\cdot\hat{\mathbf{k}})(\hat{\mathbf{n}}\cdot\hat{\mathbf{k}})\frac{2\mu}{\gamma}\right)e^{i\mathbf{k}_c\cdot(\mathbf{x}-\mathbf{x}_0)}\right]\mathcal{L}(\mathbf{k}_c,\mathbf{r}_0)$$
$$\left[\left(\lambda(\hat{\mathbf{n}}'\cdot\mathbf{e}_\alpha) + 2\mu(\hat{\mathbf{n}}'\cdot\hat{\mathbf{k}})(\hat{\mathbf{k}}\cdot\mathbf{e}_\alpha)\right)e^{i\mathbf{k}_c\cdot(\mathbf{x}'_0-\mathbf{x}')}W\right] \tag{5.45}$$

and

$$\mathcal{Z}^{H,s}_{\beta,\alpha}(\mathbf{k}_s) = -k_s^2\mu\tilde{\mathbf{e}}_\beta\cdot e^{i\mathbf{k}_s\cdot(\mathbf{x}-\mathbf{x}_0)}\mathcal{L}(\mathbf{k}_s,\mathbf{r}_0)\Bigg\{\Big[(\hat{\mathbf{n}}\cdot\hat{\mathbf{k}})(\hat{\boldsymbol{\theta}}\hat{\boldsymbol{\theta}}+\hat{\boldsymbol{\phi}}\hat{\boldsymbol{\phi}})\cdot\mathbf{e}_\alpha(\hat{\mathbf{n}}'\cdot\hat{\mathbf{k}}) + (\hat{\mathbf{n}}\cdot\hat{\mathbf{k}})(\hat{\boldsymbol{\theta}}\hat{\boldsymbol{\theta}}+\hat{\boldsymbol{\phi}}\hat{\boldsymbol{\phi}})\cdot\hat{\mathbf{n}}'(\hat{\mathbf{k}}\cdot\mathbf{e}_\alpha) +$$
$$\hat{\mathbf{k}}\hat{\mathbf{n}}\cdot(\hat{\boldsymbol{\theta}}\hat{\boldsymbol{\theta}}+\hat{\boldsymbol{\phi}}\hat{\boldsymbol{\phi}})\cdot\mathbf{e}_\alpha(\hat{\mathbf{n}}'\cdot\hat{\mathbf{k}}) + \hat{\mathbf{k}}\hat{\mathbf{n}}\cdot(\hat{\boldsymbol{\theta}}\hat{\boldsymbol{\theta}}+\hat{\boldsymbol{\phi}}\hat{\boldsymbol{\phi}})\cdot\hat{\mathbf{n}}'(\hat{\mathbf{k}}\cdot\mathbf{e}_\alpha)\Big]e^{i\mathbf{k}_s\cdot(\mathbf{x}'_0-\mathbf{x}')}W\Bigg\}. \tag{5.46}$$

Separating the terms dependent on $\mathbf{x}$ and $\mathbf{x}'$ in the above equation, we get

$$\mathcal{Z}^{H,s}_{\beta,\alpha}(\mathbf{k}_s) = -k_s^2\mu\left[\left(\tilde{\mathbf{e}}_\beta(\hat{\mathbf{k}}\cdot\hat{\mathbf{n}}) + \tilde{\mathbf{e}}_\beta\cdot\hat{\mathbf{k}}\hat{\mathbf{n}}\right)e^{i\mathbf{k}_s\cdot(\mathbf{x}-\mathbf{x}_0)}\right]\cdot\mathcal{L}(\mathbf{k}_s,\mathbf{r}_0)$$
$$\left[\left(\hat{\boldsymbol{\theta}}\hat{\boldsymbol{\theta}}+\hat{\boldsymbol{\phi}}\hat{\boldsymbol{\phi}}\right)\cdot\left(\mathbf{e}_\alpha\hat{\mathbf{n}}'\cdot\hat{\mathbf{k}} + \hat{\mathbf{n}}'\hat{\mathbf{k}}\cdot\mathbf{e}_\alpha\right)e^{i\mathbf{k}_s\cdot(\mathbf{x}'_0-\mathbf{x}')}W\right]. \tag{5.47}$$

For any $\mathbf{x},\mathbf{y},\mathbf{r}_0\in\mathbb{R}^3$, let $\mathcal{M}_p(\mathbf{x}-\mathbf{y}) \coloneqq e^{i\mathbf{k}_p\cdot(\mathbf{x}-\mathbf{y})}$ and $\mathcal{L}_p(\mathbf{r}_0) = \mathcal{L}(\mathbf{k}_p,\mathbf{r}_0)$ for $p = s,c$. Summarizing the above results by writing quantities as functions of space coordinates only, we have the following equations:

$$\mathcal{Z}^{K,c}_{\beta,\alpha}(\mathbf{x},\mathbf{x}') = -ik_c\mathcal{V}^\beta(\mathbf{x},\mathbf{x}_0)\ \mathcal{L}_c(\mathbf{r}_0)\ \mathcal{V}_\alpha(\mathbf{x}',\mathbf{x}'_0), \tag{5.48a}$$

$$\mathcal{Z}^{K,s}_{\beta,\alpha}(\mathbf{x},\mathbf{x}') = -ik_s\mathbf{V}^\beta(\mathbf{x},\mathbf{x}_0)\cdot\mathcal{L}_s(\mathbf{r}_0)\ \mathbf{V}_\alpha(\mathbf{x}',\mathbf{x}'_0), \tag{5.48b}$$

where

$$\mathcal{V}^{\beta}(\mathbf{x},\mathbf{x}_0) = \frac{1}{\gamma}\tilde{\mathbf{e}}_{\beta}\cdot\left(\hat{\mathbf{n}}\lambda + \hat{\mathbf{k}}(\hat{\mathbf{n}}\cdot\hat{\mathbf{k}})2\mu\right)\mathcal{M}_c(\mathbf{x}-\mathbf{x}_0), \tag{5.49a}$$

$$\mathcal{V}_{\alpha}(\mathbf{x}',\mathbf{x}'_0) = W\ (\hat{\mathbf{k}}\cdot\mathbf{e}_{\alpha})\mathcal{M}_c(\mathbf{x}'_0-\mathbf{x}'), \tag{5.49b}$$

$$\mathbf{V}^{\beta}(\mathbf{x},\mathbf{x}_0) = \hat{\mathbf{k}}\cdot(\tilde{\mathbf{e}}_{\beta}\hat{\mathbf{n}} + \hat{\mathbf{n}}\tilde{\mathbf{e}}_{\beta})\,\mathcal{M}_s(\mathbf{x}-\mathbf{x}_0), \tag{5.49c}$$

$$\mathbf{V}_{\alpha}(\mathbf{x}',\mathbf{x}'_0) = W\ (\hat{\boldsymbol{\theta}}\hat{\boldsymbol{\theta}} + \hat{\boldsymbol{\phi}}\hat{\boldsymbol{\phi}})\cdot\mathbf{e}_{\alpha}\mathcal{M}_s(\mathbf{x}'_0-\mathbf{x}'). \tag{5.49d}$$

Using the fact that $\mathbf{e}_3(\mathbf{x}') = \mathcal{J}(\mathbf{x}')\mathbf{n}(\mathbf{x}') = \hat{\mathbf{n}}'$ for the chosen discretization basis functions,

$$\mathcal{Z}^{H,c}_{\beta,\alpha}(\mathbf{x},\mathbf{x}') = -k_c^2\mathcal{V}^{\beta}(\mathbf{x},\mathbf{x}_0)\ \mathcal{L}_c(\mathbf{r}_0)\ \left(\lambda\mathcal{J}(\mathbf{x}')\delta_{3\alpha}W\mathcal{M}_c(\mathbf{x}'_0-\mathbf{x}') + 2\mu(\hat{\mathbf{k}}\cdot\hat{\mathbf{n}}')\mathcal{V}_{\alpha}(\mathbf{x}',\mathbf{x}'_0)\right), \tag{5.50a}$$

$$\mathcal{Z}^{H,s}_{\beta,\alpha}(\mathbf{x},\mathbf{x}') = -\mu k_s^2\mathbf{V}^{\beta}(\mathbf{x},\mathbf{x}_0)\cdot\mathcal{L}_s(\mathbf{r}_0)\ \left(b_3(\mathbf{x}')\mathbf{V}_{\alpha}(\mathbf{x}',\mathbf{x}'_0) + b_{\alpha}(\mathbf{x}')\mathbf{V}_3(\mathbf{x}',\mathbf{x}'_0)\right), \tag{5.50b}$$

where

$$b_{\alpha}(\mathbf{x}') = \frac{\hat{\mathbf{k}}\cdot\mathbf{e}_{\alpha}(\mathbf{x}')}{\mathcal{J}(\mathbf{x}')}. \tag{5.51}$$

Notice that only the $\hat{\boldsymbol{\theta}}$ and $\hat{\boldsymbol{\phi}}$ components of the vectors $\mathbf{V}^{\beta}(\mathbf{x},\mathbf{x}_0)$ and $\mathbf{V}_{\alpha}(\mathbf{x}',\mathbf{x}'_0)$ need to be stored, whereas three components of each vector would be required if Cartesian coordinates were used. This leads to about 20 percent reduction in the memory required for storing the radiation and receiving patterns [30, §5.3]. The factorizations in (5.48) and (5.50) lead to diagonal-form expansions when the integral in (5.39) is discretized. Comparing the foregoing expansions with the expansions for the CBIE kernels in [30, §5.3], we observe that they share the same radiation patterns. Therefore, so far as the computation of radiation and receiving patterns is concerned, the CFIE formulation requires additional operations (over CBIE) only in the calculation of receiving patterns. Furthermore, the memory requirement for storing the patterns is the same irrespective of the formulation (CBIE, HBIE or CFIE.)

## 5.5 Application of FMM to Matrix-Vector Products of Influence Matrix

This section explains how the FMM is applied for computing the product of the influence matrix obtained in Chapter 4 with a vector. Note that every element in the matrix-vector product

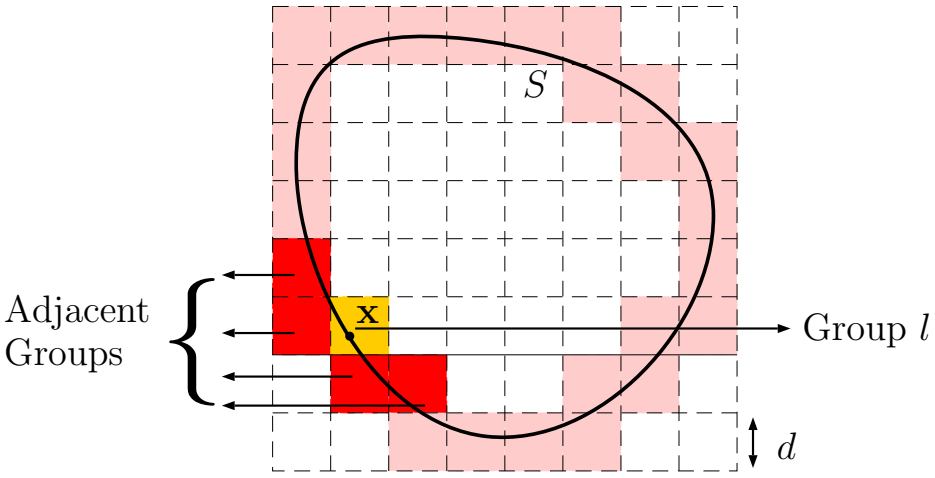


Figure 5.4: The two-dimensional scatterer, represented by the boundary $S$, is embedded in a fictitious grid. Collocation point $\mathbf{x}$ lies in the group with index $l$. Groups that are adjacent to group $l$ are marked in red.

corresponds to one collocation point and is a sum involving both near-field and far-field matrix elements.

### 5.5.1 Single Level Implementation

The expansions derived in the previous section apply only to the far-field matrix elements, which are proportional to the kernel functions defined for a combination of a source point $\mathbf{x}'$ and an observation point $\mathbf{x}$. Furthermore, they are valid only when the distance criteria $|\mathbf{x}_0 - \mathbf{x}'_0| > |\mathbf{x} - \mathbf{x}_0 + \mathbf{x}'_0 - \mathbf{x}'|$ is satisfied (see Figure 5.2). At the same time, for ideal efficiency of FMM, we require the same transfer function to hold for all source and observation points (i.e., for all far-field matrix elements). In other words, the points $\mathbf{x}_0$ and $\mathbf{x}'_0$ need to be fixed for all combinations of source and observation points. The two conditions stated above express opposing requirements. If $\mathbf{x}_0$ and $\mathbf{x}'_0$ are held fixed, the distance criteria holds only for some combinations of source and observation points. A compromise is achieved by dividing the scatterer into groups such that $\mathbf{x}'_0$ and $\mathbf{x}_0$ are the same for all points in a group. The groups are generally defined by embedding the scatterer into a fictitious three dimensional cubic grid, and the points $\mathbf{x}'_0$ and $\mathbf{x}_0$ are chosen to lie at the centroids of the cubes.

Figure 5.4 illustrates the grouping scheme in two-dimensions. Consider a collocation point $\mathbf{x}$ lying in a group with index $l$. The groups which share a vertex with group $l$ are called its adjacent groups. For calculating the element in the matrix-vector product which corresponds to $\mathbf{x}$, the contributions from the part of the boundary lying in the adjacent groups are computed directly since the distance criteria fails for some combinations of source and observation points lying in adjacent groups. The contributions from non-adjacent groups are computed using multipole expansions. Using the terminology from Section 5.3 and Equation (5.23) as an example, the procedure can be described broadly in three steps:

1. For every group and for every direction given by $q$, evaluate the radiation pattern due to the source points inside the group.

2. For every group and for every direction, evaluate the incoming radiation from its non-adjacent groups by multiplying the corresponding transfer functions and radiation patterns, and summing the resulting products.

3. For every collocation point and for every direction, multiply its receiving pattern with the incoming radiation associated with its group center. Performing the summation over all directions (as shown, for example, in (5.22)) gives the contribution from the non-adjacent groups to the given collocation point.

The multipole moments and receiving patterns corresponding to every source and collocation point, respectively, are precalculated. The transfer functions between all non-adjacent groups are also precalculated. Since far-field expansions are decomposed into longitudinal and shear components (see (5.40)), the above steps have to be performed separately for the two components. The truncation parameter $L_T$ in (5.16b) is defined in terms of the size of cubes ($d$) in the grid as follows [185, §3.4.1]

$$L_T = kd + 1.8 d_0^{2/3} (kd)^{1/3}, \tag{5.52}$$

where $d_0 = \log(1/\epsilon)$ with $\epsilon$ representing the relative error due to truncation. In this implementation, $\epsilon$ is set to 0.001 unless specified otherwise. The variable $k$ is the wavenumber and is different

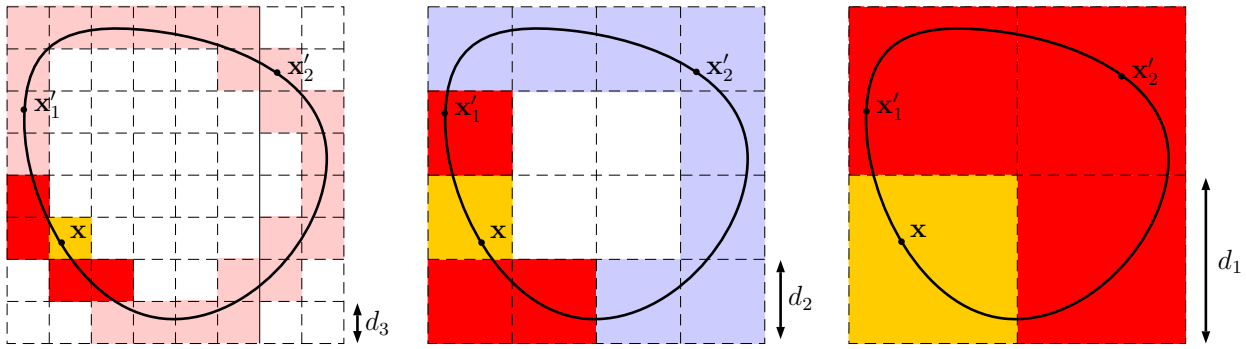


Figure 5.5: An illustration of a multilevel grouping scheme in two dimensions. Collocation point is $\mathbf{x}$

for shear and longitudinal components. The integration over $\mathbb{S}^2$ is performed using the $L_T + 1$ point Gauss-Legendre rule in the polar ($\theta$) direction and the $2L_T + 1$ point trapezoidal rule in the azimuthal ($\phi$) direction [185, §3.4.3][166, §2.4.3]. Therefore, the number of quadrature points (directions or modes) is dependent on the wavenumber through the truncation parameter and hence is different for the longitudinal and shear components.

### 5.5.2 Multilevel Implementation

Multilevel implementation of the FMM is based on the observation that the multipole expansion in (5.22) can be recentered at two new points $\mathbf{y}_0$ and $\mathbf{y}'_0$ by translating the multipole moments. Letting $\mathbf{r}'_0 = \mathbf{y}_0 - \mathbf{y}'_0$, we have

$$g(\mathbf{x}, \mathbf{x}') \approx \sum_{q=1}^{Q} w_q \mathcal{M}(\mathbf{k}^{(q)}, \mathbf{x} - \mathbf{x}_0)\ \mathcal{L}(\mathbf{k}^{(q)}, \mathbf{r}_0)\ \mathcal{M}(\mathbf{k}^{(q)}, \mathbf{x}'_0 - \mathbf{x}') \tag{5.53a}$$

$$\approx \sum_{q=1}^{Q} w_q \mathcal{M}(\mathbf{k}^{(q)}, \mathbf{x} - \mathbf{x}_0 + \mathbf{x}_0 - \mathbf{y}_0)\ \mathcal{L}(\mathbf{k}^{(q)}, \mathbf{r}'_0)\ \mathcal{M}(\mathbf{k}^{(q)}, \mathbf{y}'_0 - \mathbf{x}'_0 + \mathbf{x}'_0 - \mathbf{x}') \tag{5.53b}$$

$$= \sum_{q=1}^{Q} w_q \mathcal{M}(\mathbf{k}^{(q)}, \mathbf{x} - \mathbf{x}_0) \mathcal{M}(\mathbf{k}^{(q)}, \mathbf{x}_0 - \mathbf{y}_0)$$

$$\mathcal{L}(\mathbf{k}^{(q)}, \mathbf{r}'_0) \mathcal{M}(\mathbf{k}^{(q)}, \mathbf{y}'_0 - \mathbf{x}'_0) \mathcal{M}(\mathbf{k}^{(q)}, \mathbf{x}'_0 - \mathbf{x}'), \tag{5.53c}$$

where we have assumed that the truncation parameter and the number of modes are the same after recentering. For the expansion to be accurate and efficient, these parameters have to depend on the locations of the centers of expansion. However, this requirement is relaxed for illustrating the multilevel implementation procedure. An interpolation technique is applied to account for the level-dependence of parameters, as mentioned at the end of this section.

In general, an $L$-level implementation consists of $L$ levels without counting level 0. A three-level implementation in two dimensions is illustrated in Figure 5.5. The coarsest level (level 0) consists of a bounding box enclosing the scatterer, forming a single group. Finer levels are obtained by dividing each group into four subgroups. In three-dimensions, this leads to an octree structure. At any level, say $l$, the interaction list of a group (whose index is $j$) is defined as the set of groups that are not adjacent to group $j$ and whose parent groups at level $l-1$ are adjacent the parent group of group $j$. The procedure for calculating the matrix-vector product can be described in the following steps:

1. For every group in the finest level (level $L$) and for every direction, evaluate the radiation patterns due to the source points in the group.

2. For every group from level $L-1$ to level 2, and for every direction, calculate the corresponding radiation patterns by performing translations as indicated by (5.53c).

3. At level 2, for every group and for every direction, evaluate the incoming radiation from non-adjacent groups by multiplying the corresponding transfer functions and radiation patterns, and summing the resulting products.

4. From level 3 to level $L$, for every group and for every direction, evaluate its incoming radiation by (a) computing the incoming radiation from its interaction list as in step 3, (b) computing the incoming radiation from its parent group as indicated by (5.53c), and (c) summing the contributions from (a) and (b).

5. For every collocation point and for every direction, multiply its receiving pattern with the incoming radiation associated with its group center. Performing the summation over all directions gives the contribution from the non-adjacent groups to the given collocation point.

The transfer functions at every level, the multipole moments, and receiving patterns are pre-computed. Note that because of the regularity of the grid and translational symmetry of the transfer function, there is only a small number of $\mathbf{r}_0$ values for which the transfer function needs to be evaluated at every level. The multilevel implementation is more efficient than the single-level method because of reduction in the required number of transfer functions. For instance, in the example in Figure 5.5, let $K^{(l)}(\mathbf{x})$ represent the index of the group that the point $\mathbf{x}$ lies in at level $l$. The interaction between source points in the group $K^{(2)}(\mathbf{x}_2')$ on one hand and collocation points in the group $K^{(2)}(\mathbf{x})$ on the other are evaluated by mutlipole expansion between groups of size $d_2$. Whereas interactions between source points in the group $K^{(3)}(\mathbf{x}_1')$ and collocation points in the group $K^{(3)}(\mathbf{x})$ are evaluated by multipole expansion between groups of size $d_3$. In a single-level implementation using the grid of level 3, the group size is fixed at $d_3$ even in the calculation of interactions between $\mathbf{x}$ and $\mathbf{x}_2'$.

The foregoing description is based on the assumption that the number of modes does not change with the level. This assumption is, however, invalid as the number of modes depends on the group size through the truncation parameter $L_T$. Both the number of modes and their directions ($\hat{\mathbf{k}}^{(q)}$)– in other words, the number of quadrature points and their locations– vary across levels, with coarser levels requiring more number of modes. Therefore, local polynomial interpolation using six points each in the $\theta$ and $\phi$ directions is used to perform steps 2 and 4 in the above procedure [185, 3.4.4][188]. In our implementation, a collocation or field interpolation point on a mesh triangle is assumed to lie in a group if the centroid of the first-order triangle formed by the vertices lies in the group. Unless mentioned otherwise, the box size at the finest level is set to $0.31\lambda_s$ or $1.5L_t$, whichever is higher, where $\lambda_s$ is the shear wavelength and $L_t$ is the maximum edge length in the triangular mesh (for curvilinear triangles, the curved edge length is approximated by the distance between the respective vertices). The size of bounding box at level 0 is adjusted slightly so that

it is possible to achieve the specified (finest level) box size exactly upon refinement. Also, a block Jacobi preconditioner is used wherein the DOFs are partitioned according to the grid at the finest level [189, §3.2].

## 5.6 Numerical Results

### 5.6.1 Helical Strip

The first validation example consists of a traction-free helical strip (open surface) as shown in Figure 5.6. The strip is embedded in an otherwise homogeneous material with mass density ($\rho$) and Lamé constants ($\lambda$, $\mu$) given by 1 kg/m$^3$, 1 N/m$^2$ and 1 N/m$^2$, respectively. A longitudinal plane-wave traveling in the $+z$-direction with frequency 1 Hz is incident on the strip. The dimensions of the strip are: $L_s = 4\lambda_s$, $H = 2.148\lambda_s$, $E = 0.195\lambda_s$, $R = 0.542\lambda_s$, where $L_s$ is the length along the strip and $\lambda_s$ is the shear wavelength. The strip is discretized with 40 first-order nearly-equilateral triangles, and the first column in the BEM influence matrix is calculated (separately) with and without MLFMM (with Rule-12 discretization, see Section 3.3 for nomenclature). In the MLFMM calculation, the box size of the finest level is set to $0.28\lambda_s$, which gives $L = 4$ levels. The relative errors for elements in the first column are shown in Figure 5.7, where the values obtained without MLFMM are taken as reference. The matrix elements computed using MLFMM are within about 1% error compared to the reference. Note that the relative error is smaller if the diagonal element is used as reference.

### 5.6.2 Traction-free Sphere

The second validation example involves a traction-free sphere embedded in an otherwise homogeneous medium with the following material properties: $\rho = 1$ N/m$^2$, $\lambda = 2$ N/m$^2$ and $\mu = 1$ N/m$^2$. The sphere is assumed to be centered at the origin, and a longitudinal plane wave travelling in the $+z$-direction is incident on it. A spherical coordinate is assumed, with $\theta$ denoting the polar angle. The frequency of the incident wave is 1 Hz. This scattering problem is solved using MLFMM with Rule-22 BEM discretization. The number of mesh elements is 320, and the CFIE formulation with

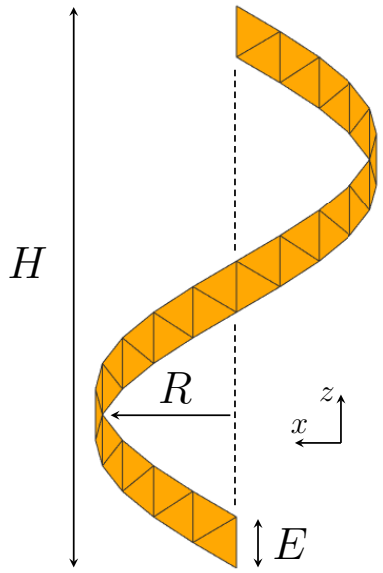


Figure 5.6: A traction-free helical strip.

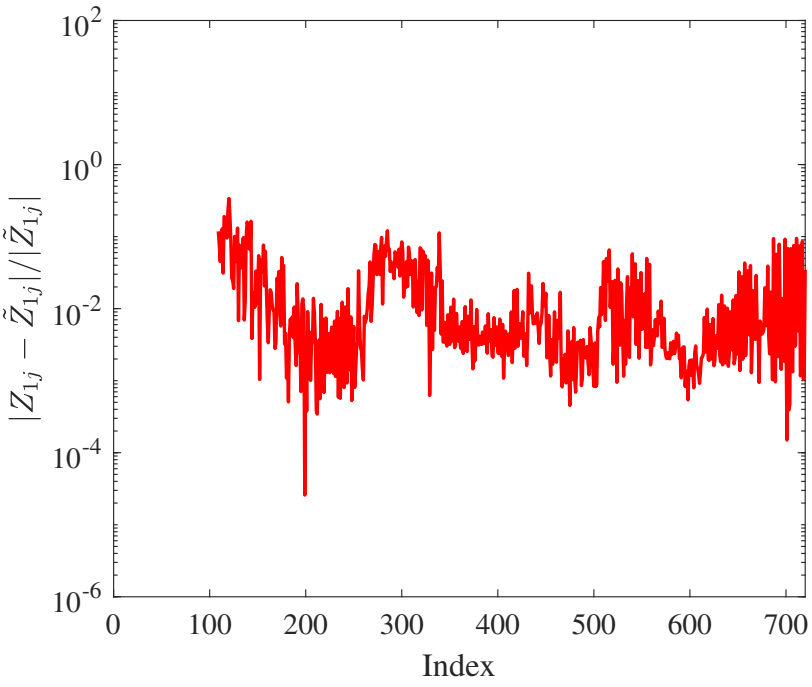


Figure 5.7: Relative error for elements in the first column of influence matrix. For any index $j$, $Z_{1j}$ represents the matrix element in column 1 and row $j$.

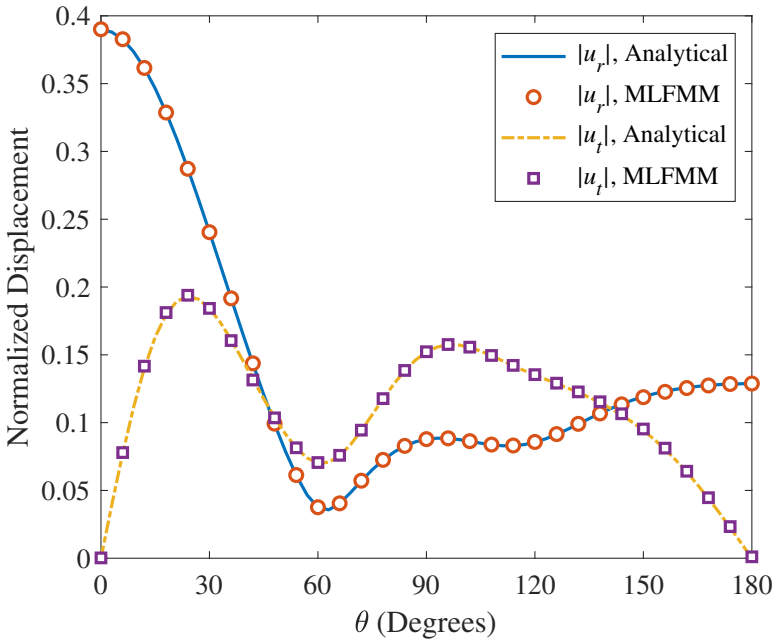


Figure 5.8: Magnitude of scattered displacement field at $r = 5a$. Radial and polar components are represented as $u_r$ and $u_t$, respectively. All fields are normalized by the radius of the sphere.

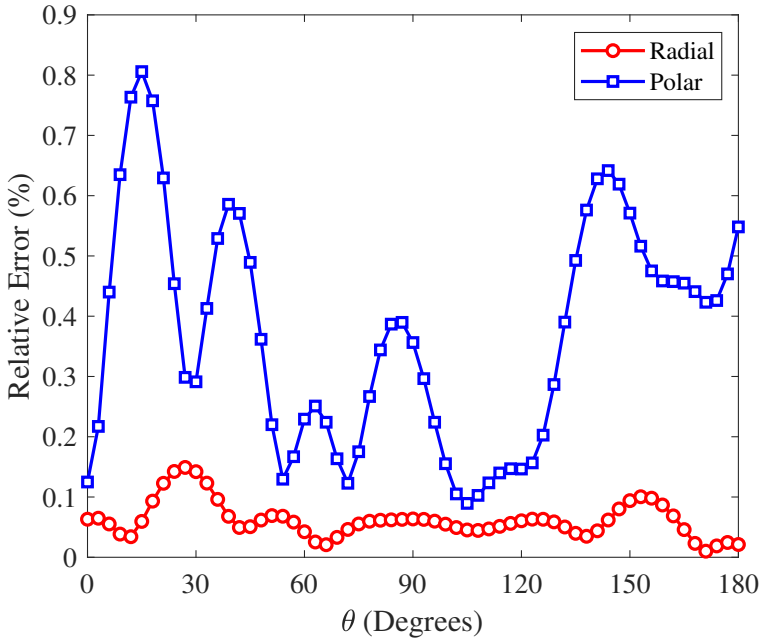


Figure 5.9: Relative error in the scattered displacement at $r = 5a$.

coupling coefficient $\beta = i$ is used. Box size at the finest level ($L = 3$) is $0.49\lambda_s$. Figure 5.8 shows the radial and polar components of scattered displacement field at a distance $r = 5a$, where $a$ is the radius of the sphere. The analytical solution calculated from the separation-of-variables technique is also shown for reference [13, §10.6.2]. The relative error is defined as $|u_\alpha - u_{\text{ref}}|/\max_\theta |u_{\text{ref}}|$, where $\alpha = r,\ s$ and $u_{\text{ref}}$ is the corresponding reference solution. The relative errors are shown in Figure 5.9. The error in the polar component is higher than that of the radial component because the contribution from shear waves (relative to longitudinal waves) is higher for the polar component. Figure 5.10 shows the relative errors separately for the longitudinal and shear wave components of both radial and polar displacement fields. Shear wave components have higher errors than the longitudinal waves.

### 5.6.3 CPU Time and Memory Scaling

Consider a traction-free sphere as in the previous section. The host material parameters are: $\rho = 3$ N/m$^2$, $\lambda = 1$ N/m$^2$ and $\mu = 1$ N/m$^2$. We consider four different scattering problems wherein the frequency is 0.5 Hz, 1 Hz, 2 Hz, and 4 Hz, respectively. They are solved by applying the MLFMM-accelerated BEM (Rule-22 discretization) to the HBIE formulation. The number of mesh elements is set such that the average number of nodes per shear wavelength is around 13. Therefore, number of DOFs increases by a factor of four when the frequency is doubled. In all cases, the box size at the finest level is around $0.85\lambda_s$. Figure 5.11 shows the CPU time per iteration and the memory requirement as a function of the number of DOFs. The simulation results were obtained by means of a C++ numerical implementation on a Dell Precision T7500 workstation with two quad-core 2.13 GHz processors and 24 GB memory but using only a single core. As expected, both CPU time and memory requirement show an $\mathcal{O}(N \log N)$ behaviour.

## 5.7 Concluding Remarks

In this chapter, MLFMM is applied to the high-order BEM developed in Chapter 4. The diagonal-form expansions derived for the CFIE kernels are new. Evaluation of the contribution

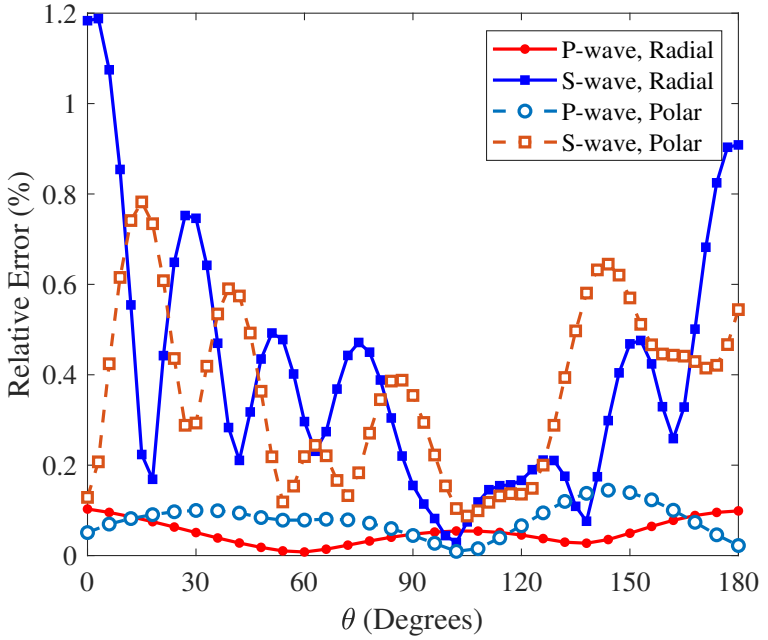


Figure 5.10: Relative errors for the longitudinal and shear wave components of the scattered displacement field at $r = 5a$.

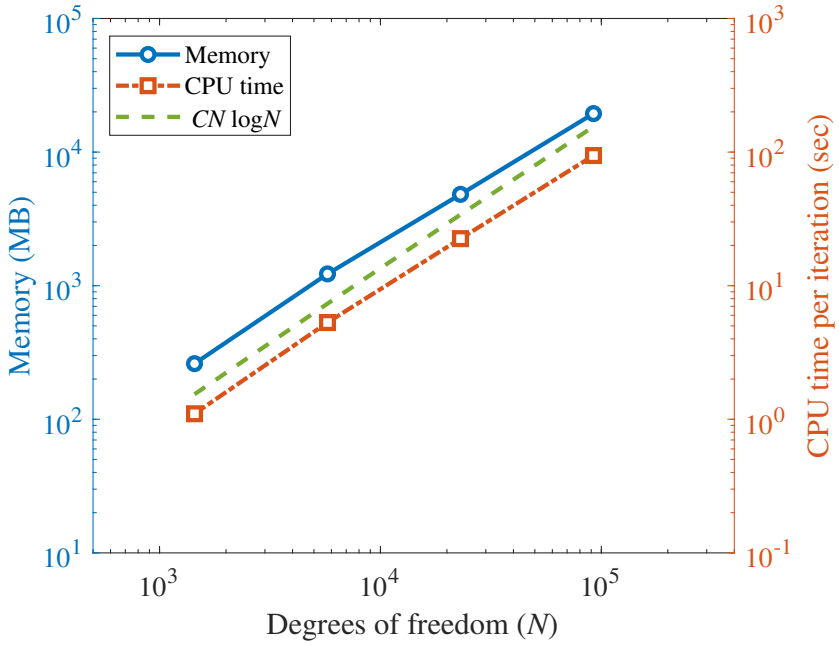


Figure 5.11: CPU time per iteration and memory requirement as a function of the number of DOFs for solving a scattering from a traction-free sphere using HBIE formulation. An $\mathcal{O}(N \log N)$ curve is shown for reference.

of far-field elements to the matrix-vector product is simplified since the CBIE and HBIE kernels share the same radiation patterns. Also, the memory storage cost associated with the far-field contribution is the same regardless of which formulation– CBIE, HBIE or CFIE– is used. Numerical results presented here demonstrate the validity of the method. The next chapter will include some applications to practical UNDE problems.

# CHAPTER 6. IRREGULAR FREQUENCIES IN ELASTODYNAMIC BOUNDARY INTEGRAL EQUATIONS

Despite the elastic-wave scattering problem (EWSP) being well-conditioned at all frequencies, the CBIE and HBIE reformulations of the EWSP admit multiple solutions at some frequencies. This artifact is known as the fictitious eigenfrequency problem. The frequencies where it occurs are known as irregular frequencies or fictitious eigenfrequencies. This chapter provides a mathematical description of this problem and illustrates it using numerical examples. It demonstrates the relevance of this ill-conditioning to ultrasonic NDE modeling using examples from practical testing scenarios. It is well-known that the CFIE-formulation is free from irregular frequencies for a proper choice of the coupling constant. Since the fast-multipole BEM model proposed in this thesis is based on the CFIE-formulation, it models the EWSP more accurately and efficiently than models based on CBIE and HBIE formulations. Some numerical examples are shown at the end of this chapter for validating this.

## 6.1 Introduction

Recall that the EWSP introduced in Chapter 4 has unique solutions at all frequencies. The EWSP entails the conventional and hypersingular BIEs, but the converse is not always true. In other words, although all solutions of the EWSP are solutions to the BIEs, not every solution of the BIEs is a solution to the EWSP. Both conventional and hypersingular BIEs have multiple solutions at some frequencies called irregular frequencies. The next section presents a partial proof for this phenomenon. For the two-dimensional case, Martin [190] proved that the irregular frequencies of the CBIE coincide with the eigenfrequencies of an interior Dirichlet problem defined using the scatterer and vice-versa. Similar proofs for the three-dimensional case are not available as far as we know. However, it is well-known from numerical evidence that this result extends to three-

dimensional problems. Similarly, the irregular frequencies of the HBIE are the eigenfrequencies of an interior boundary-value problem with traction-free boundary conditions. Parallels with BIEs outside elastodynamics further support these results. See [191–193] for example.

Ill-conditioning due to irregular frequencies is a serious impediment to the application of BIEs for modeling elastic-wave scattering. The BEM influence matrix is singular at the irregular frequencies, which implies the existence of multiple solutions. In this case, it is not easy to find even a single solution. Even if a solution was found, it may not be the one that solves the EWSP. This situation, however, is rare since it occurs only at a few distinct frequency points in a whole frequency range. In practice, it is more likely that a given simulation frequency lies close to but not exactly at an irregular frequency. In that case, the influence matrix has a high condition number. This affects the accuracy of the solutions even when direct methods are used. The error may be higher for iterative methods since they may be viewed as solving a linear system with a perturbed right-hand side; thus, small changes in the right-hand side may lead to large errors in the solution. Also, computational performance deteriorates as a large number of iterations are required for convergence.

Since UNDE applications require solutions over multiple frequencies in a given bandwidth range, it is practically impossible to avoid simulating the model close to the irregular frequencies owing to the following reasons. First, although the irregular frequencies are known to be the eigenfrequencies of certain problems, it takes much computational effort to compute them. Therefore, a priori knowldge of the irregular frequencies comes only at a significant expense. Second, even if the locations of the irregular frequencies are known, it is possible to avoid simulating close to them only if they are located sparsely in the frequency range of our interest. This condition is satisfied only if the scatterer is relatively small compared to the wavelengths in the given frequency range since eigenfrequencies become more closely spaced with an increase in the relative size of the scatterer. Therefore, UNDE scattering models should be based on well-conditioned BIE formulations. The CFIE formulation described in Section 4.2.8 is well-conditioned if the coupling constant $\beta$ is chosen as the complex number $i$. The resulting BIE is known as the Burton-Miller BIE (BM-BIE) [194, 195] (by analogy with acoustics problems). The previous two chapters describe the application of a fast-

multipole BEM to the BM-BIE, and, more generally, to the CFIE. Numerical examples presented in this chapter will validate that this implementation is free from irregular frequencies. The importance of BM-BIE in UNDE applications is revealed by contrasting some of these results with those of ill-conditioned formulations.

## 6.2 Mathematical Description

The CBIE formulation from Section 4.2.8 is reproduced in Equation (6.1). This formulation is derived from the EWSP, and thus every solution of the EWSP is also a solution to (6.1). Since a unique solution for the EWSP exists at all frequencies, the CBIE also admits at least one solution at all frequencies. Therefore, for any frequency, the CBIE is equivalent to the EWSP if it has a unique solution for that frequency. In other words, the CBIE is not equivalent to the EWSP for any frequency if and only if it has multiple solutions.

$$\begin{bmatrix} -\mathcal{U}_S^+ & {}^2\mathcal{T}_S^+ - \dfrac{\mathcal{I}}{2} \\ -\mathcal{U}_S^- & {}^2\mathcal{T}_S^- + \dfrac{\mathcal{I}}{2} \end{bmatrix} \begin{bmatrix} \mathbf{t}(\mathbf{x}) \\ \mathbf{u}(\mathbf{x}) \end{bmatrix} = \begin{bmatrix} -\mathbf{u}^I(\mathbf{x}) \\ \mathbf{0} \end{bmatrix}. \tag{6.1}$$

A necessary and sufficient condition for the existence of multiple solutions for (6.1) is that there exist non-zero fields $\mathbf{t}(\mathbf{x})$ and $\mathbf{u}(\mathbf{x})$ defined on the surface $S$ of the scatterer such that

$$\begin{bmatrix} -\mathcal{U}_S^+ & {}^2\mathcal{T}_S^+ - \dfrac{\mathcal{I}}{2} \\ -\mathcal{U}_S^- & {}^2\mathcal{T}_S^- + \dfrac{\mathcal{I}}{2} \end{bmatrix} \begin{bmatrix} \mathbf{t}(\mathbf{x}) \\ \mathbf{u}(\mathbf{x}) \end{bmatrix} = \begin{bmatrix} \mathbf{0} \\ \mathbf{0} \end{bmatrix} \tag{6.2}$$

for $\mathbf{x} \in S$. The reason for this is that if there exist two distinct sets of solutions given by $\mathbf{t}_1(\mathbf{x})$, $\mathbf{u}_1(\mathbf{x})$ and $\mathbf{t}_2(\mathbf{x})$, $\mathbf{u}_2(\mathbf{x})$, then the fields $\mathbf{t}_1(\mathbf{x}) - \mathbf{t}_2(\mathbf{x})$ and $\mathbf{u}_1(\mathbf{x}) - \mathbf{u}_2(\mathbf{x})$ satisfy (6.2). Conversely, if there exists a solution for (6.2), it can be added to the solution of the EWSP to get a different solution for the CBIE. Numerical evidence indicates that non-trivial fields satisfying (6.2) exist at all the frequencies that coincide with the eigenfrequencies of the following interior Dirichlet problem (IDP):

$$(\lambda_+ + \mu_+)\nabla\nabla \cdot \mathbf{u}_d(\mathbf{x}) + \mu_+ \nabla^2 \mathbf{u}_d(\mathbf{x}) + \rho_+ \omega^2 \mathbf{u}_d(\mathbf{x}) = 0 \text{ for } \mathbf{x} \in V, \tag{6.3a}$$

$$\mathbf{u}_d(\mathbf{x}) = 0 \text{ for } \mathbf{x} \in S, \tag{6.3b}$$

where $V$ is the region inside the scatterer. It is easy to show the coincidence of the irregular frequencies determined from (6.2) and the eigenfrequencies of the IDP in the special case wherein the scatterer is rigid. It is much harder to show this in the general case. Alternatively, using a proof similar to [190, Theorem 1], the solutions of (6.1) can be shown to solve the EWSP at all frequencies except the eigenfrequencies of the IDP. This proves the required result partially as it shows that non-unique solutions to the CBIE can exist only at the eigenfrequencies of the IDP. Proving that non-unique solutions do indeed exist at every eigenfrequency is difficult.

Now consider the special case of a rigid scatterer. The CBIE in Equation (6.1) reduces to

$$-\mathcal{U}_S^+ \tilde{\mathbf{t}}(\mathbf{x}) = -\mathbf{u}^I(\mathbf{x}). \tag{6.4}$$

Similarly, Equation (6.2) reduces to

$$-\mathcal{U}_S^+ \mathbf{t}(\mathbf{x}) = 0. \tag{6.5}$$

It follows from Section 4.2.6 that any field satisfying (6.3a) should also satisfy the second equation in the CBIE formulation given by (6.1), with the operators redefined using the material parameters in (6.3a). Therefore,

$$-\mathcal{U}_S^+ \mathbf{t}_d(\mathbf{x}) + \left( {}^2\mathcal{T}_S^+ + \frac{\mathcal{I}}{2} \right) \mathbf{u}_d(\mathbf{x}) = 0, \tag{6.6}$$

where $\mathbf{t}_d(\mathbf{x})$ is the traction field obtained from $\mathbf{u}_d(\mathbf{x})$. Using (6.3b), this further reduces to

$$-\mathcal{U}_S^+ \mathbf{t}_d(\mathbf{x}) = 0. \tag{6.7}$$

This shows that (6.5) is satisfied by choosing $\mathbf{t}(\mathbf{x})$ as $\mathbf{t}_d(\mathbf{x})$. Therefore, the CBIE for the rigid scatterer has non-unique solutions at every eigenfrequency of the IDP. Conversely, if (6.5) is given, we are allowed to choose $\mathbf{t}_d(\mathbf{x}) = \mathbf{t}(\mathbf{x})$ and $\mathbf{u}_d(\mathbf{x}) = 0$ for $\mathbf{x} \in S$ since these fields on the boundary are consistent with (6.6). Then, the representation theorem (4.26) gives the displacement field for $\mathbf{x} \in V$ as

$$\mathbf{u}_d(\mathbf{x}) = \int_S \mathbf{t}_d(\mathbf{x}') \cdot \overline{\mathbf{G}}_+(\mathbf{x}, \mathbf{x}') \, dS(\mathbf{x}'). \tag{6.8}$$

The field $\mathbf{u}_d(\mathbf{x})$ as defined above can be verified to satisfy (6.3a) using (4.17) and (4.19). Therefore, irregular frequencies occur only at the eigenfrequencies of the IDP. This proves the coincidence between irregular frequencies of the CBIE and eigenfrequencies of the IDP for rigid scatterers.

The HBIE is reproduced below:

$$\begin{bmatrix} -^2\mathcal{K}_S^+ + \dfrac{\mathcal{I}}{2} & \mathcal{H}_S^+ \\ -^2\mathcal{K}_S^- - \dfrac{\mathcal{I}}{2} & \mathcal{H}_S^- \end{bmatrix} \begin{bmatrix} \mathbf{t}(\mathbf{x}) \\ \mathbf{u}(\mathbf{x}) \end{bmatrix} = \begin{bmatrix} \mathbf{t}^I(\mathbf{x}) \\ \mathbf{0} \end{bmatrix}. \tag{6.9}$$

As in the case of the CBIE, a necessary and sufficient condition for non-uniqueness of the solutions of HBIE is that there exist non-trivial fields $\mathbf{t}(\mathbf{x})$ and $\mathbf{u}(\mathbf{x})$ on $S$ such that

$$\begin{bmatrix} -^2\mathcal{K}_S^+ + \dfrac{\mathcal{I}}{2} & \mathcal{H}_S^+ \\ -^2\mathcal{K}_S^- - \dfrac{\mathcal{I}}{2} & \mathcal{H}_S^- \end{bmatrix} \begin{bmatrix} \mathbf{t}(\mathbf{x}) \\ \mathbf{u}(\mathbf{x}) \end{bmatrix} = \begin{bmatrix} \mathbf{0} \\ \mathbf{0} \end{bmatrix}. \tag{6.10}$$

This condition is satisfied at all and only the eigenfrequencies of the following interior boundary-value problem:

$$(\lambda_+ + \mu_+)\nabla\nabla\cdot\mathbf{u}_n(\mathbf{x}) + \mu_+\nabla^2\mathbf{u}_n(\mathbf{x}) + \rho_+\omega^2\mathbf{u}_n(\mathbf{x}) = 0 \text{ for } \mathbf{x}\in V, \tag{6.11a}$$

$$\mathbf{t}_n(\mathbf{x}) = 0 \text{ for } \mathbf{x}\in S, \tag{6.11b}$$

where $\mathbf{t}_n(\mathbf{x})$ is the traction field on S corresponding to the displacement $\mathbf{u}_n(\mathbf{x})$. When the scatterer is soft, (6.9) and (6.10) reduce to the following equations

$$\mathcal{H}_S^+\tilde{\mathbf{u}}(\mathbf{x}) = \mathbf{t}^I(\mathbf{x}), \tag{6.12}$$

$$\mathcal{H}_S^+\mathbf{u}(\mathbf{x}) = 0, \tag{6.13}$$

respectively. Since the displacement and traction fields that satisfy (6.11) should also satisfy the second equation in (6.9), with the operators redefined using the material parameters in (6.11), we have

$$\mathcal{H}_S^+\mathbf{u}_n(\mathbf{x}) = 0. \tag{6.14}$$

Therefore, every eigenfrequency of (6.10) is an irregular frequency. Conversely, if (6.10) is given, we can choose $\mathbf{u}_n(\mathbf{x}) = \mathbf{u}(\mathbf{x})$ and $\mathbf{t}_n(\mathbf{x}) = 0$ for $\mathbf{x} \in S$. The displacement field in $V$ is given by the representation formula as

$$\mathbf{u}_n(\mathbf{x}) = \int_S \mathbf{u}_n(\mathbf{x}') \cdot \left[\hat{\mathbf{n}}(\mathbf{x}') \cdot \overline{\overline{\mathbf{\Sigma}}}^{(1)}(\mathbf{x}, \mathbf{x}')\right] dS(\mathbf{x}'), \tag{6.15}$$

which can be shown to satisfy (6.11) by applying the operator $\lambda_+ \bar{\mathbf{I}} \nabla \cdot + \mu_+ \left(\nabla + \nabla^T\right)$ on (4.19), knowing that $\mathbf{x}' \neq \mathbf{x}$. Therefore, irregular frequencies occur only at the eigenfrequencies of the interior boundary value problem with traction-free boundary condition.

## 6.3 Eigenfrequencies of Sphere

The next section illustrates the irregular frequency problem by numerically solving the CBIE and HBIE formulations for scattering from a sphere. Analytical solutions for the eigenfrequencies of a sphere are derived in this section for comparison with the irregular frequencies. We consider a homogeneous, isotropic elastic sphere under both traction-free and rigid boundary conditions. In the rigid boundary case, the eigenfrequency problem consists of finding non-trivial solutions for the displacement field $\mathbf{u}(\mathbf{x})$ which simultaneously satisfies (6.16a) and (6.16b).

$$\mu \nabla^2 \mathbf{u}(\mathbf{x}) + (\lambda + \mu) \nabla \nabla \cdot \mathbf{u}(\mathbf{x}) = -\rho \omega^2 \mathbf{u}(\mathbf{x}) \text{ for } \mathbf{x} \in V, \tag{6.16a}$$

$$\mathbf{u}(\mathbf{x}) = 0 \text{ for } \mathbf{x} \in S, \tag{6.16b}$$

where $\lambda$, $\mu$ are the Lamé constants, $\rho$ is the mass density, $\omega$ is the radian frequency, $V$ is the region inside the sphere and $S$ is its boundary. In the soft boundary condition case, (6.16b) is replaced with (6.17).

$$\mathbf{t}(\mathbf{x}) = 0 \text{ for } \mathbf{x} \in S, \tag{6.17}$$

where $\mathbf{t}(\mathbf{x})$ is the traction field on $S$. In the following, the radius of the sphere is represented by the letter $a$. A spherical coordinate system with the position vector given by $\mathbf{r} = (r, \theta, \varphi)$ and unit vectors given by $\hat{\mathbf{r}}$, $\hat{\boldsymbol{\theta}}$, $\hat{\boldsymbol{\varphi}}$ is assumed.

By Helmholtz decomposition of the vector field $\mathbf{u}$, there exist scalar and vector fields $\gamma$ and $\mathbf{\Gamma}$, respectively, such that

$$\mathbf{u}(\mathbf{x}) = \nabla\gamma(\mathbf{r}) + \nabla \times \mathbf{\Gamma}(\mathbf{r}). \tag{6.18}$$

By substituting (6.18) in (6.16a), it can be shown that (6.16a) is satisfied only if the potentials satisfy the following wave equations [158, §5.4]:

$$\nabla^2\gamma + k_p^2\gamma = 0, \tag{6.19a}$$

$$\nabla^2\mathbf{\Gamma} + k_s^2\mathbf{\Gamma} = 0. \tag{6.19b}$$

Here, $k_p = \omega/c_p$ and $k_s = \omega/c_s$, with $c_p$ and $c_s$ representing the longitudinal and shear wave speeds in the material, respectively. The above result does not depend on the choice of a gauge condition such as $\nabla \cdot \mathbf{\Gamma} = 0$. Conversely, if there exist fields $\gamma$ and $\mathbf{\Gamma}$ satisfying (6.19), then the displacement field defined using (6.18) satisfies (6.16a). From this, it can be shown that every field that satisfies (6.16a) can be decomposed into a linearly independent set of modes, where the modes correspond to an ordered pair of positive integers ($n$,$m$) with $m < n$, and where the displacement corresponding to the mode ($n$,$m$) is given by:

$$\mathbf{u}_{nm} = \frac{a_1}{k_p}\nabla\phi_{nm} + a_2\mathbf{M}_{nm} + a_3\mathbf{N}_{nm}, \tag{6.20a}$$

$$\mathbf{M}_{nm} = \nabla \times (\psi_{nm} r\hat{\mathbf{r}}) = \nabla\psi_{nm} \times r\hat{\mathbf{r}}, \tag{6.20b}$$

$$\mathbf{N}_{nm} = \frac{1}{k_s}\nabla \times \nabla \times (\psi_{nm} r\hat{\mathbf{r}}) = \frac{1}{k_s}\nabla \times \mathbf{M}_{nm}. \tag{6.20c}$$

In the above, $a_i$ for $i \in \{1,\ 2,\ 3\}$ represent coefficients that depend on the boundary conditions. In general, they vary from one mode to the other. The fields $\phi_{nm}$ and $\psi_{nm}$ are given by

$$\phi_{nm} = j_n(k_p r)P_n^m(\cos\theta)\begin{Bmatrix}\sin(m\varphi)\\ \cos(m\varphi)\end{Bmatrix}, \tag{6.21a}$$

$$\psi_{nm} = j_n(k_s r)P_n^m(\cos\theta)\begin{Bmatrix}\sin(m\varphi)\\ \cos(m\varphi)\end{Bmatrix}, \tag{6.21b}$$

where $j_n$ is the spherical Bessel function of the first kind of order $n$ and $P_n^m$ is an associated Legendre function. For different values of $n$ and $m$, Equations (6.21) represent the general solutions to scalar Helmholtz equations with wavenumbers $k_p$ and $k_s$, respectively.

In the following derivation, the subscripts of the fields are dropped for convenience. Substituting (6.21) into (6.20), the longitudinal component of the displacement for mode $(m,n)$ is simplified to

$$\frac{a_1}{k_p}\nabla\phi = a_1\left[\hat{\mathbf{r}}j_n'(k_pr)P_n^m(\cos\theta)+\frac{1}{k_pr}\hat{\boldsymbol{\theta}}j_n(k_pr)\frac{dP_n^m(\cos\theta)}{d\theta}\right]\begin{Bmatrix}\sin(m\varphi)\\ \cos(m\varphi)\end{Bmatrix} + \frac{a_1m}{k_pr}\hat{\boldsymbol{\varphi}}j_n(k_pr)\frac{P_n^m(\cos\theta)}{\sin\theta}\begin{Bmatrix}\cos(m\varphi)\\ -\sin(m\varphi)\end{Bmatrix}. \tag{6.22}$$

Similarly, the shear components are given by

$$a_2\mathbf{M} = a_2\nabla\psi\times r\hat{\mathbf{r}} = \hat{\boldsymbol{\theta}}a_2mj_n(k_sr)\frac{P_n^m(\cos\theta)}{\sin\theta}\begin{Bmatrix}\cos(m\varphi)\\ -\sin(m\varphi)\end{Bmatrix} - \hat{\boldsymbol{\varphi}}a_2j_n(k_sr)\frac{dP_n^m(\cos\theta)}{d\theta}\begin{Bmatrix}\sin(m\varphi)\\ \cos(m\varphi)\end{Bmatrix}, \tag{6.23}$$

$$\begin{aligned}a_3\mathbf{N} = \frac{a_3}{k_s}\nabla\times\mathbf{M} =& \hat{\boldsymbol{\varphi}}a_3m\left[k_srj_n(k_sr)\right]'\frac{P_n^m(\cos\theta)}{\sin\theta}\begin{Bmatrix}\cos(m\varphi)\\ -\sin(m\varphi)\end{Bmatrix}\\ &+\frac{a_3}{k_sr}\left[\hat{\mathbf{r}}n(n+1)j_n(k_sr)P_n^m(\cos\theta)+\hat{\boldsymbol{\theta}}\left[k_srj_n(k_sr)\right]'\frac{dP_n^m(\cos\theta)}{d\theta}\right]\begin{Bmatrix}\sin(m\varphi)\\ \cos(m\varphi)\end{Bmatrix}.\end{aligned} \tag{6.24}$$

Therefore, the components of displacement in spherical coordinates are

$$u_r = \left[a_1j_n'(k_pr)+\frac{a_3}{k_sr}n(n+1)j_n(k_sr)\right]P_n^m(\cos\theta)\begin{Bmatrix}\sin(m\varphi)\\ \cos(m\varphi)\end{Bmatrix}, \tag{6.25a}$$

$$\begin{aligned}u_\theta =& a_2\ m\ j_n(k_sr)\frac{P_n^m(\cos\theta)}{\sin\theta}\begin{Bmatrix}\cos(m\varphi)\\ -\sin(m\varphi)\end{Bmatrix}+\\ &\left[\frac{a_1}{k_pr}j_n(k_pr)+\frac{a_3}{k_sr}\left[k_srj_n(k_sr)\right]'\right]\frac{dP_n^m(\cos\theta)}{d\theta}\begin{Bmatrix}\sin(m\varphi)\\ \cos(m\varphi)\end{Bmatrix},\end{aligned} \tag{6.25b}$$

$$\begin{aligned}u_\varphi =& -a_2\ j_n(k_sr)\frac{dP_n^m(\cos\theta)}{d\theta}\begin{Bmatrix}\sin(m\varphi)\\ \cos(m\varphi)\end{Bmatrix}+\\ &m\left[\frac{a_1}{k_pr}j_n(k_pr)+\frac{a_3}{k_sr}\left[k_srj_n(k_sr)\right]'\right]\frac{P_n^m(\cos\theta)}{\sin\theta}\begin{Bmatrix}\cos(m\varphi)\\ -\sin(m\varphi)\end{Bmatrix}.\end{aligned} \tag{6.25c}$$

The traction field is determined from the following constitutive relation:

$$\mathbf{t} = \lambda\hat{\mathbf{n}}\nabla\cdot\mathbf{u}+\mu\hat{\mathbf{n}}\cdot\left(\nabla\mathbf{u}+(\nabla\mathbf{u})^T\right), \tag{6.26}$$

where $\hat{\mathbf{n}}$ is the outward unit normal vector on the surface of the sphere, which is, hence, equal to $\hat{\mathbf{r}}$. Since

$$\nabla\cdot\mathbf{u} = \frac{a_1}{k_p}\nabla^2\phi = -a_1k_p\phi, \tag{6.27a}$$

$$\hat{\mathbf{r}}\cdot\left(\nabla\mathbf{u}+(\nabla\mathbf{u})^T\right)=\hat{\mathbf{r}}2\frac{\partial u_r}{\partial r}+\hat{\boldsymbol{\theta}}\left[\frac{\partial u_\theta}{\partial r}+\frac{1}{r}\left(\frac{\partial u_r}{\partial\theta}-u_\theta\right)\right]+\hat{\boldsymbol{\varphi}}\left[\frac{\partial u_\varphi}{\partial r}+\frac{1}{r}\left(\frac{1}{\sin\theta}\frac{\partial u_r}{\partial\varphi}-u_\varphi\right)\right], \tag{6.27b}$$

we have

$$t_r=-\lambda k_p\phi+2\mu\frac{\partial u_r}{\partial r}. \tag{6.28}$$

For any real number $z$, let $\hat{J}_n(z)=zj_n(z)$ and $\tilde{J}_n(z)=j_n(z)/z$. The components of the traction field can be simplified to the following:

$$\frac{t_r}{2\mu}=\left(a_1k_p\left[j_n''(k_pr)-\frac{\lambda}{2\mu}j_n(k_pr)\right]+a_3k_sn(n+1)\tilde{J}_n'(k_sr)\right)P_n^m(\cos\theta)\begin{Bmatrix}\sin(m\varphi)\\\cos(m\varphi)\end{Bmatrix}, \tag{6.29a}$$

$$\begin{aligned}\frac{t_\theta}{2\mu}=&\frac{\partial u_\theta}{\partial r}+\frac{1}{r}\left(\frac{\partial u_r}{\partial\theta}-u_\theta\right)\\=&ma_2k_s\left[j_n'(k_sr)-\tilde{J}_n(k_sr)\right]\frac{P_n^m(\cos\theta)}{\sin\theta}\begin{Bmatrix}\cos(m\varphi)\\-\sin(m\varphi)\end{Bmatrix}+\\&\left(\frac{2a_1}{r}\left[j_n'(k_pr)-\tilde{J}_n(k_pr)\right]+\frac{a_3}{r}\left[\left[n(n+1)-2\right]\tilde{J}_n(k_sr)+k_srj_n''(k_sr)\right]\right)\\&\frac{dP_n^m(\cos\theta)}{d\theta}\begin{Bmatrix}\sin(m\varphi)\\\cos(m\varphi)\end{Bmatrix},\end{aligned} \tag{6.29b}$$

$$\begin{aligned}\frac{t_\varphi}{2\mu}=&\frac{\partial u_\varphi}{\partial r}+\frac{1}{r}\left(\frac{1}{\sin\theta}\frac{\partial u_r}{\partial\varphi}-u_\varphi\right)\\=&a_2k_s\left[\tilde{J}_n(k_sr)-j_n'(k_sr)\right]\frac{dP_n^m(\cos\theta)}{d\theta}\begin{Bmatrix}\sin(m\varphi)\\\cos(m\varphi)\end{Bmatrix}+\\&m\left(\frac{2a_1}{r}\left[j_n'(k_pr)-\tilde{J}_n(k_pr)\right]+\frac{a_3}{r}\left[\left[n(n+1)-2\right]\tilde{J}_n(k_sr)+k_srj_n''(k_sr)\right]\right)\\&\frac{P_n^m(\cos\theta)}{\sin\theta}\begin{Bmatrix}\cos(m\varphi)\\-\sin(m\varphi)\end{Bmatrix}.\end{aligned} \tag{6.29c}$$

Due to linear independence between the modes, each mode needs to separately satisfy the boundary conditions for it to contribute to the total fields non-trivially.

### 6.3.1 Rigid Boundary

We apply the boundary condition (6.16b) by setting the displacement field at $r=a$ to zero, and seek the frequencies (or, equivalently, the wavenumbers) at which non-trivial solutions for

the displacement (or, equivalently, the coefficients $a_1$, $a_2$ and $a_3$) occur. Note that $k_s$ and $k_p$ are related to each other by the elastic constants of the material. Equating each component of the displacement to zero over all angles (assuming $n \neq 0$), we get the following conditions which must be simultaneously satisfied

$$a_1 j_n'(k_p a) + \frac{a_3}{k_s a} n(n+1) j_n(k_s a) = 0, \tag{6.30a}$$

$$a_2 m j_n(k_s a) = 0, \qquad \frac{a_1}{k_p a} j_n(k_p a) + \frac{a_3}{k_s a} \left[k_s a j_n(k_s a)\right]' = 0, \tag{6.30b}$$

$$a_2 j_n(k_s a) = 0, \qquad m\left[\frac{a_1}{k_p a} j_n(k_p a) + \frac{a_3}{k_s a} \left[k_s a j_n(k_s a)\right]'\right] = 0. \tag{6.30c}$$

The above equations can be reduced to the following system of independent equations

$$a_1 j_n'(k_p a) + \frac{a_3}{k_s a} n(n+1) j_n(k_s a) = 0, \tag{6.31a}$$

$$a_2 j_n(k_s a) = 0, \tag{6.31b}$$

$$\frac{a_1}{k_p a} j_n(k_p a) + \frac{a_3}{k_s a} \left[k_s a j_n(k_s a)\right]' = 0. \tag{6.31c}$$

Rewriting the above in a matrix form yields

$$\begin{bmatrix} j_n'(k_p a) & 0 & \frac{1}{k_s a} n(n+1) j_n(k_s a) \\ 0 & j_n(k_s a) & 0 \\ \frac{1}{k_p a} j_n(k_p a) & 0 & \frac{1}{k_s a}\left[k_s a j_n(k_s a)\right]' \end{bmatrix} \begin{bmatrix} a_1 \\ a_2 \\ a_3 \end{bmatrix} = 0. \tag{6.32}$$

Observe that the equations involving $a_1$ and $a_3$ are not coupled to the equation involving $a_2$. From this, one can show that the eigen frequencies split into two distinct classes: one for which $a_1 = a_3 = 0$ and another for which $a_2 = 0$.

#### 6.3.1.1 Class 1 Modes

For Class 1 modes, $a_1 = a_3 = 0$ and $a_2 \neq 0$, and the displacement is given by

$$\mathbf{u} = j_n(k_s r)\left[\hat{\boldsymbol{\theta}} m \frac{P_n^m(\cos\theta)}{\sin\theta} \begin{Bmatrix} \cos(m\varphi) \\ -\sin(m\varphi) \end{Bmatrix} - \hat{\boldsymbol{\varphi}} \frac{dP_n^m(\cos\theta)}{d\theta} \begin{Bmatrix} \sin(m\varphi) \\ \cos(m\varphi) \end{Bmatrix}\right]. \tag{6.33}$$

For $n = 0$, $m$ has to be zero. Also, since $P_0^0(\cos\theta) = 1$, the displacement vanishes for $n = 0$. Therefore, non-trivial solutions exist only for $n \neq 0$. For $n \neq 0$, eigenfrequencies are determined from the following equation

$$j_n(k_s a) = 0. \tag{6.34}$$

Let the zeros of $j_n(k_s a)$ occur at $\zeta_{nq}$ for $q = 1, 2, 3 \ldots \infty$. The corresponding eigenfrequencies are $\omega_{nq}^{(1)} = \zeta_{nq} c_s / a$. Observe that Class 1 modes are independent of the Poisson's ratio if the shear wave speed is specified.

#### 6.3.1.2 Class 2 Modes

For Class 2 modes, $a_1, a_3 \neq 0$ and $a_2 = 0$, and the displacement field is

$$\begin{aligned}
\mathbf{u} =& \hat{\mathbf{r}} \left[ a_1 j_n'(k_p r) + \frac{a_3}{k_s r} n(n+1) j_n(k_s r) \right] P_n^m(\cos\theta) \begin{Bmatrix} \sin(m\varphi) \\ \cos(m\varphi) \end{Bmatrix} + \\
& \hat{\boldsymbol{\theta}} \left[ \frac{a_1}{k_p r} j_n(k_p r) + \frac{a_3}{k_s r} \left[ k_s r j_n(k_s r) \right]' \right] \frac{dP_n^m(\cos\theta)}{d\theta} \begin{Bmatrix} \sin(m\varphi) \\ \cos(m\varphi) \end{Bmatrix} + \\
& \hat{\boldsymbol{\varphi}} m \left[ \frac{a_1}{k_p r} j_n(k_p r) + \frac{a_3}{k_s r} \left[ k_s r j_n(k_s r) \right]' \right] \frac{P_n^m(\cos\theta)}{\sin\theta} \begin{Bmatrix} \cos(m\varphi) \\ -\sin(m\varphi) \end{Bmatrix}.
\end{aligned} \tag{6.35}$$

Using identity (6.45b) to replace the derivatives, we get

$$\begin{aligned}
\mathbf{u} =& \hat{\mathbf{r}} \left[ a_1 \left( j_{n-1}(k_p r) - \frac{n+1}{k_p r} j_n(k_p r) \right) + \frac{a_3}{k_s r} n(n+1) j_n(k_s r) \right] P_n^m(\cos\theta) \begin{Bmatrix} \sin(m\varphi) \\ \cos(m\varphi) \end{Bmatrix} + \\
& \left[ \frac{a_1}{k_p r} j_n(k_p r) + \frac{a_3}{k_s r} \left( k_s r j_{n-1}(k_s r) - n j_n(k_s r) \right) \right] \\
& \left[ \hat{\boldsymbol{\theta}} \frac{dP_n^m(\cos\theta)}{d\theta} \begin{Bmatrix} \sin(m\varphi) \\ \cos(m\varphi) \end{Bmatrix} + \hat{\boldsymbol{\varphi}} m \frac{P_n^m(\cos\theta)}{\sin\theta} \begin{Bmatrix} \cos(m\varphi) \\ -\sin(m\varphi) \end{Bmatrix} \right].
\end{aligned} \tag{6.36}$$

The eigen frequencies are determined from the following equation (assuming $n \neq 0$)

$$j_n'(k_p a) \left[ k_s a j_n(k_s a) \right]' = \frac{n(n+1)}{k_p a} j_n(k_s a) j_n(k_p a), \tag{6.37}$$

which simplifies to

$$\left[ k_p a j_{n-1}(k_p a) - (n+1) j_n(k_p a) \right] \left[ k_s a j_{n-1}(k_s a) - n j_n(k_s a) \right] = n(n+1) j_n(k_s a) j_n(k_p a). \tag{6.38}$$

For $n = 0$, the displacement reduces to

$$\mathbf{u} = a_1 j_0'(k_p r)\ \hat{\mathbf{r}} = -a_1 j_1(k_p r)\ \hat{\mathbf{r}}. \tag{6.39}$$

The corresponding eigenfrequencies are obtained from the condition

$$j_0'(k_p a) = 0. \tag{6.40}$$

Since $j_0'(k_p a) = -j_1(k_p a) = \sin(k_p a)/(k_p a)^2 - \cos(k_p a)/k_p a$, the eigen frequencies are obtained from solutions of the following equation:

$$\tan(k_p a) = k_p a. \tag{6.41}$$

Let $k_p a = \xi_{0q}$ (for $q = 1, 2, \dots$) be the solutions of this equation. Note that according to the definition of $\zeta_{nq}$ in Section 6.3.1.1, $\xi_{0q} = \zeta_{1q}$. The shear wavenumbers are given by $k_s a = \zeta_{1q} c_p/c_s$. The first twenty Class 1 and Class 2 eigenfrequenices for the rigid boundary case are listed in Table 6.1, where Class 2 eigenfrequencies for $n = 0$ correspond to $\zeta_{11} = 4.49340945790906$ and $\zeta_{12} = 7.72525183693771$.

### 6.3.2 Traction-free Boundary

For traction-free boundary condition, $\mathbf{t} = 0$ at $r = a$ for all angles. As in the case of the rigid boundary condition, setting each component of traction to zero yields three independent equations. These are

$$a_1 k_p \left[ j_n''(k_p a) - \frac{\lambda}{2\mu} j_n(k_p a) \right] + a_3 k_s n(n+1) \tilde{J}_n'(k_s a) = 0. \tag{6.42a}$$

$$\frac{2a_1}{a} \left[ j_n'(k_p a) - \tilde{J}_n(k_p a) \right] + \frac{a_3}{a} \left[ \Big( n(n+1) - 2 \Big) \tilde{J}_n(k_s a) + k_s a j_n''(k_s a) \right] = 0. \tag{6.42b}$$

$$a_2 k_s \left[ \tilde{J}_n(k_s a) - j_n'(k_s a) \right] = 0. \tag{6.42c}$$

Simplifying the above into a matrix form, we can write

$$\begin{bmatrix} c_{11} & 0 & c_{13} \\ c_{21} & 0 & c_{23} \\ 0 & c_{32} & 0 \end{bmatrix} \begin{bmatrix} a_1 \\ a_2 \\ a_3 \end{bmatrix} = 0, \tag{6.43}$$

Table 6.1: Eigenfrequencies for rigid boundary condition.

| Class 1 | | | Class 2 | | | | | |
|---|---|---|---|---|---|---|---|---|
| | | | $\nu = 0.1$ | | | $\nu = 0.25$ | | |
| $k_s a$ | $n$ | $q$ | $k_s a$ | $n$ | $q$ | $k_s a$ | $n$ | $q$ |
| 4.4934094579 | 1 | 1 | 3.7090232164 | 1 | 1 | 3.9897788303 | 1 | 1 |
| 5.7634591969 | 2 | 1 | 5.3924416817 | 2 | 1 | 5.7750982326 | 2 | 1 |
| 6.9879320005 | 3 | 1 | 6.1482576116 | 1 | 2 | 6.2029629965 | 1 | 2 |
| 7.7252518369 | 1 | 2 | 6.7401141869 | 0 | 1 | 7.2928444987 | 3 | 1 |
| 8.1825614526 | 4 | 1 | 6.8965368890 | 3 | 1 | 7.7359420389 | 2 | 2 |
| 9.0950113305 | 2 | 2 | 7.5682016314 | 2 | 2 | 7.7828134803 | 0 | 1 |
| 9.3558121110 | 5 | 1 | 8.2857012396 | 4 | 1 | 8.6533116453 | 4 | 1 |
| 10.4171185474 | 3 | 2 | 8.8005097416 | 1 | 3 | 9.2585575331 | 1 | 3 |
| 10.5128354081 | 6 | 1 | 8.9961365547 | 3 | 2 | 9.3225153930 | 3 | 2 |
| 10.9041216594 | 1 | 3 | 9.4247779608 | 1 | 4 | 9.9237449673 | 5 | 1 |
| 11.6570321925 | 7 | 1 | 9.5949205388 | 5 | 1 | 10.3278157116 | 1 | 4 |
| 11.7049071546 | 4 | 2 | 10.4343585735 | 4 | 2 | 10.6701294368 | 2 | 3 |
| 12.3229409706 | 2 | 3 | 10.4419342460 | 2 | 3 | 10.9225361933 | 4 | 2 |
| 12.7907817120 | 8 | 1 | 10.8481610844 | 6 | 1 | 11.1413141242 | 6 | 1 |
| 12.9665301728 | 5 | 2 | 11.1878413384 | 2 | 4 | 12.0668676568 | 3 | 3 |
| 13.6980231532 | 3 | 3 | 11.5878777554 | 0 | 2 | 12.3255962825 | 7 | 1 |
| 13.9158226105 | 9 | 1 | 11.8666791855 | 3 | 3 | 12.4914680586 | 5 | 2 |
| 14.0661939128 | 1 | 4 | 11.8747644290 | 5 | 2 | 12.4975549688 | 1 | 5 |
| 14.2073924588 | 6 | 2 | 12.0619160438 | 7 | 1 | 12.5914424974 | 2 | 4 |
| 15.0334693037 | 10 | 1 | 12.4717985040 | 1 | 5 | 13.3805286828 | 0 | 2 |

where

$$c_{11} = k_p \left[ j_n''(k_p a) - \frac{\lambda}{2\mu} j_n(k_p a) \right], \tag{6.44a}$$

$$c_{13} = k_s n(n+1) \tilde{J}_n'(k_s a), \tag{6.44b}$$

$$c_{21} = 2 \left[ j_n'(k_p a) - \tilde{J}_n(k_p a) \right], \tag{6.44c}$$

$$c_{23} = \left[ n(n+1) - 2 \right] \tilde{J}_n(k_s a) + k_s a j_n''(k_s a), \tag{6.44d}$$

$$c_{32} = \tilde{J}_n(k_s a) - j_n'(k_s a). \tag{6.44e}$$

These matrix elements can be simplified further and written only in terms of the spherical Bessel functions of various orders without involving their derivatives. To this end, the following identities will be useful

$$z \tilde{J}_n'(z) = j_n'(z) - \tilde{J}_n(z), \tag{6.45a}$$

$$j_n'(z) = \frac{n}{z} j_n(z) - j_{n+1}(z) = j_{n-1}(z) - \frac{n+1}{z} j_n(z), \tag{6.45b}$$

$$j_n''(z) = \frac{n(n+1) - z^2}{z^2} j_n(z) - \frac{2}{z} j_n'(z) = \frac{n(n-1) - z^2}{z^2} j_n(z) + \frac{2}{z} j_{n+1}(z) \tag{6.45c}$$

$$= \frac{(n+1)(n+2) - z^2}{z^2} j_n(z) - \frac{2}{z} j_{n-1}(z) \tag{6.45d}$$

for any real number $z$, and

$$\left[ n(n+1) - 2 \right] \tilde{J}_n(k_s r) + k_s r j_n''(k_s r) = \frac{2(n^2+n-1) - (k_s r)^2}{k_s r} j_n(k_s r) - 2 j_n'(k_s r) \tag{6.45e}$$

$$= \frac{2\left(n^2-1\right) - (k_s r)^2}{k_s r} j_n(k_s r) + 2 j_{n+1}(k_s r) \tag{6.45f}$$

$$= \frac{2n\left(n+2\right) - (k_s r)^2}{k_s r} j_n(k_s r) - 2 j_{n-1}(k_s r) \tag{6.45g}$$

for any real number $r$. Also,

$$\frac{\lambda}{2\mu} = \frac{\nu}{1-2\nu} = \frac{k_s^2}{2k_p^2} - 1, \tag{6.45h}$$

where $\nu$ is the Poisson's ratio.

For the purpose of normalization, the first equation is multiplied with the radius of the sphere. Therefore, both $c_{11}$ and $c_{13}$ are scaled up by the factor $a$. The normalized quantities are represented by $\tilde{c}_{11}$ and $\tilde{c}_{13}$. Substituting identities (6.45c) and (6.45h) into (6.44a), we get

$$\tilde{c}_{11} = \frac{2n(n-1) - (k_s a)^2}{2k_p a} j_n(k_p a) + 2j_{n+1}(k_p a) \tag{6.46a}$$

$$= \frac{2(n+1)(n+2) - (k_s a)^2}{2k_p a} j_n(k_p a) - 2j_{n-1}(k_p a). \tag{6.46b}$$

Note that an extra factor of $a$ in the denominator is canceled due to normalization. Similarly, using (6.45a) and (6.45b) in (6.44b), we get

$$\frac{\tilde{c}_{13}}{n(n+1)} = \frac{n-1}{k_s a} j_n(k_s a) - j_{n+1}(k_s a) = j_{n-1}(k_s a) - \frac{n+2}{k_s a} j_n(k_s a). \tag{6.46c}$$

Likewise, for the other matrix elements, we have

$$\frac{c_{21}}{2} = \frac{n-1}{k_p a} j_n(k_p a) - j_{n+1}(k_p a) = j_{n-1}(k_p a) - \frac{n+2}{k_p a} j_n(k_p a), \tag{6.46d}$$

$$c_{23} = \frac{2\left(n^2-1\right) - (k_s a)^2}{k_s a} j_n(k_s a) + 2j_{n+1}(k_s a) \tag{6.46e}$$

$$= \frac{2n\left(n+2\right) - (k_s a)^2}{k_s a} j_n(k_s a) - 2j_{n-1}(k_s a), \tag{6.46f}$$

$$c_{32} = -k_s a \tilde{J}_n'(k_s a) = -\frac{\tilde{c}_{13}}{n(n+1)}. \tag{6.46g}$$

Equation (6.43) indicates that the eigenfrequencies split into two distinct classes: one for which $a_1 = a_3 = 0$ and another for which $a_2 = 0$.

#### 6.3.2.1 Class 1 Modes

For Class 1 modes, $a_1 = a_3 = 0$ and $a_2 \neq 0$, and the traction field is given by

$$\frac{\mathbf{t}}{2\mu} = a_2 k_s \left[j_n'(k_s r) - \tilde{J}_n(k_s r)\right] \left[\hat{\boldsymbol{\theta}} m \frac{P_n^m(\cos\theta)}{\sin\theta} \begin{Bmatrix} \cos(m\varphi) \\ -\sin(m\varphi) \end{Bmatrix} - \hat{\boldsymbol{\varphi}} k_s \frac{dP_n^m(\cos\theta)}{d\theta} \begin{Bmatrix} \sin(m\varphi) \\ \cos(m\varphi) \end{Bmatrix}\right] \tag{6.47a}$$

$$= a_2 k_s \left[\frac{n+2}{k_s a} j_n(k_s r) - j_{n-1}(k_s r)\right] \left[\hat{\boldsymbol{\theta}} m \frac{P_n^m(\cos\theta)}{\sin\theta} \begin{Bmatrix} \cos(m\varphi) \\ -\sin(m\varphi) \end{Bmatrix} - \hat{\boldsymbol{\varphi}} k_s \frac{dP_n^m(\cos\theta)}{d\theta} \begin{Bmatrix} \sin(m\varphi) \\ \cos(m\varphi) \end{Bmatrix}\right]. \tag{6.47b}$$

The traction field vanishes for $n = 0$. For $n \neq 0$, the eigenfrequencies are obtained by solving

$$\frac{n-1}{k_s a} j_n(k_s a) - j_{n+1}(k_s a) = j_{n-1}(k_s a) - \frac{n+2}{k_s a} j_n(k_s a) = 0, \tag{6.48}$$

where (6.46g) and (6.46c) are used. For $n = 1$, this simplifies to

$$j_2(k_s a) = 0, \tag{6.49}$$

which is same as

$$\tan(k_s a) = \frac{3 k_s a}{3 - (k_s a)^2}. \tag{6.50}$$

According to the definition of $\zeta_{nq}$ in Section 6.3.1.1, the solutions of this equation are $k_s a = \zeta_{2q}$ (for $q = 1, 2, \ldots$). Note that $\zeta_{2q}$ are independent of the Poisson's ratio. The first two solutions are: $\zeta_{21} = 5.76345919689455$ and $\zeta_{22} = 9.09501133047636$.

#### 6.3.2.2 Class 2 Modes

For Class 2 modes, $a_2 \neq 0$ and $a_1, a_3 \neq 0$, and the traction field is given by

$$\begin{aligned}\frac{\mathbf{t}}{2\mu} = \hat{\mathbf{r}} &\left( a_1 k_p \left[ j_n''(k_p r) - \frac{\lambda}{2\mu} j_n(k_p r) \right] + a_3 k_s n(n+1) \tilde{J}_n'(k_s r) \right) P_n^m(\cos\theta) \begin{Bmatrix} \sin(m\varphi) \\ \cos(m\varphi) \end{Bmatrix} + \\ &\left( \frac{2a_1}{r} \left[ j_n'(k_p r) - \tilde{J}_n(k_p r) \right] + \frac{a_3}{r} \left[ [n(n+1) - 2] \tilde{J}_n(k_s r) + k_s r j_n''(k_s r) \right] \right) \\ &\left( \hat{\boldsymbol{\theta}} \frac{dP_n^m(\cos\theta)}{d\theta} \begin{Bmatrix} \sin(m\varphi) \\ \cos(m\varphi) \end{Bmatrix} + \hat{\boldsymbol{\varphi}} m \frac{P_n^m(\cos\theta)}{\sin\theta} \begin{Bmatrix} \cos(m\varphi) \\ -\sin(m\varphi) \end{Bmatrix} \right). \end{aligned} \tag{6.51}$$

This can be rewritten as

$$\begin{aligned}\frac{\mathbf{t}}{2\mu} = \hat{\mathbf{r}} &\Big( a_1 k_p T_1 + a_3 k_s n(n+1) T_3 \Big) P_n^m(\cos\theta) \begin{Bmatrix} \sin(m\varphi) \\ \cos(m\varphi) \end{Bmatrix} + \\ &\left( \frac{2a_1}{r} \widetilde{T}_1 + \frac{a_3}{r} \widetilde{T}_3 \right) \left( \hat{\boldsymbol{\theta}} \frac{dP_n^m(\cos\theta)}{d\theta} \begin{Bmatrix} \sin(m\varphi) \\ \cos(m\varphi) \end{Bmatrix} + \hat{\boldsymbol{\varphi}} m \frac{P_n^m(\cos\theta)}{\sin\theta} \begin{Bmatrix} \cos(m\varphi) \\ -\sin(m\varphi) \end{Bmatrix} \right), \end{aligned} \tag{6.52}$$

where

$$T_1 = \frac{2(n+1)(n+2) - (k_s r)^2}{2(k_p r)^2} j_n(k_p r) - \frac{2 j_{n-1}(k_p r)}{k_p r} \tag{6.53}$$

$$= \frac{2n(n-1) - (k_s r)^2}{2(k_p r)^2} j_n(k_p r) + \frac{2 j_{n+1}(k_p r)}{k_p r}, \tag{6.54}$$

$$T_3 = \frac{j_{n-1}(k_s r)}{k_s r} - \frac{n+2}{(k_s r)^2} j_n(k_s r), \tag{6.55}$$

$$\widetilde{T}_1 = j_{n-1}(k_p r) - \frac{n+2}{k_p r} j_n(k_p r), \tag{6.56}$$

$$\widetilde{T}_3 = \frac{2n\,(n+2) - (k_s r)^2}{k_s r} j_n(k_s r) - 2 j_{n-1}(k_s r). \tag{6.57}$$

The eigenfrequencies are determined by solving

$$\tilde{c}_{11} c_{23} - c_{21} \tilde{c}_{13} = 0, \tag{6.58}$$

which can be expressed in terms of spherical Bessel functions using (6.46). For the special case of $n = 0$, the traction reduces to

$$\frac{\mathbf{t}}{2\mu} = \hat{\mathbf{r}} a_1 k_p T_1. \tag{6.59}$$

The equation for eigenfrequencies reduces to

$$\tan(k_p a) = \frac{4 k_p a}{4 - (k_s a)^2}. \tag{6.60}$$

The first twenty Class 1 and Class 2 eigenfrequenices for the traction-free boundary case are listed in Table 6.2.

## 6.4 Numerical Examples

In all examples, the incident wave is a longitudinal plane wave traveling in the $+z$-direction. For problems with spherical scatterers, we assume spherical coordinates centered at the sphere, with $r$ denoting the radial distance and $\theta$, $\phi$ denoting the polar and azimuthal angles, respectively. The variable $a$ represents the radius of the sphere. The mass density and Lamé constants of the host medium are represented by $\rho_+$, $\lambda_+$ and $\mu_+$, respectively, and those of the scatterer are represented by $\rho_-$, $\lambda_-$ and $\mu_-$, respectively.

### 6.4.1 Condition Number of BEM Matrix

Consider a spherical scatterer embedded in a medium with $\rho_+ = 1$ kg/m$^3$, $\lambda_+ = 1$ N/m$^2$ and $\mu_+ = 4$ N/m$^2$. The corresponding Poisson's ratio is $\nu = 0.1$. For both hard and soft scatterers,

Table 6.2: Eigenfrequencies for traction-free boundary condition.

| Class 1 | | | Class 2 | | | | | |
|---|---|---|---|---|---|---|---|---|
| | | | $\nu = 0.1$ | | | $\nu = 0.25$ | | |
| $k_s a$ | $n$ | $q$ | $k_s a$ | $n$ | $q$ | $k_s a$ | $n$ | $q$ |
| 2.5011326204 | 2 | 1 | 2.6152347452 | 2 | 1 | 2.6398692779 | 2 | 1 |
| 3.8646997782 | 3 | 1 | 3.0737426518 | 1 | 1 | 3.4245297320 | 1 | 1 |
| 5.0946156324 | 4 | 1 | 3.3977140284 | 0 | 1 | 3.9163370211 | 3 | 1 |
| 5.7634591969 | 1 | 1 | 3.8360119016 | 3 | 1 | 4.4399982124 | 0 | 1 |
| 6.2657678453 | 5 | 1 | 4.4129182959 | 2 | 2 | 4.8652728499 | 2 | 2 |
| 7.1360087922 | 2 | 2 | 4.8746628215 | 4 | 1 | 5.0093128642 | 4 | 1 |
| 7.4035969273 | 6 | 1 | 5.8511419592 | 5 | 1 | 6.0326988865 | 5 | 1 |
| 8.4449220200 | 3 | 2 | 5.8950839279 | 1 | 2 | 6.4543692537 | 3 | 2 |
| 8.5198681240 | 7 | 1 | 5.9597389993 | 3 | 2 | 6.7712913674 | 1 | 2 |
| 9.0950113305 | 1 | 2 | 6.7999936321 | 6 | 1 | 7.0229729764 | 6 | 1 |
| 9.6209990706 | 8 | 1 | 7.5373408953 | 1 | 3 | 7.7452144006 | 1 | 3 |
| 9.7125043954 | 4 | 2 | 7.5474590658 | 4 | 2 | 7.9948299123 | 7 | 1 |
| 10.5146010554 | 2 | 3 | 7.6339863287 | 2 | 3 | 8.0614966838 | 4 | 2 |
| 10.7108802591 | 9 | 1 | 7.7340204822 | 7 | 1 | 8.3291954591 | 2 | 3 |
| 10.9506107192 | 5 | 2 | 8.6590055204 | 8 | 1 | 8.9552528042 | 8 | 1 |
| 11.7920513847 | 10 | 1 | 8.9699858306 | 0 | 2 | 9.6357585373 | 5 | 2 |
| 11.8817466328 | 3 | 3 | 9.1068642770 | 3 | 3 | 9.7049056999 | 3 | 3 |
| 12.1664025691 | 6 | 2 | 9.1231792165 | 5 | 2 | 9.7801634603 | 2 | 4 |
| 12.3229409706 | 1 | 3 | 9.1699304284 | 2 | 4 | 9.9079944498 | 9 | 1 |
| 12.8662640580 | 11 | 1 | 9.5779666312 | 9 | 1 | 10.4939244112 | 0 | 2 |

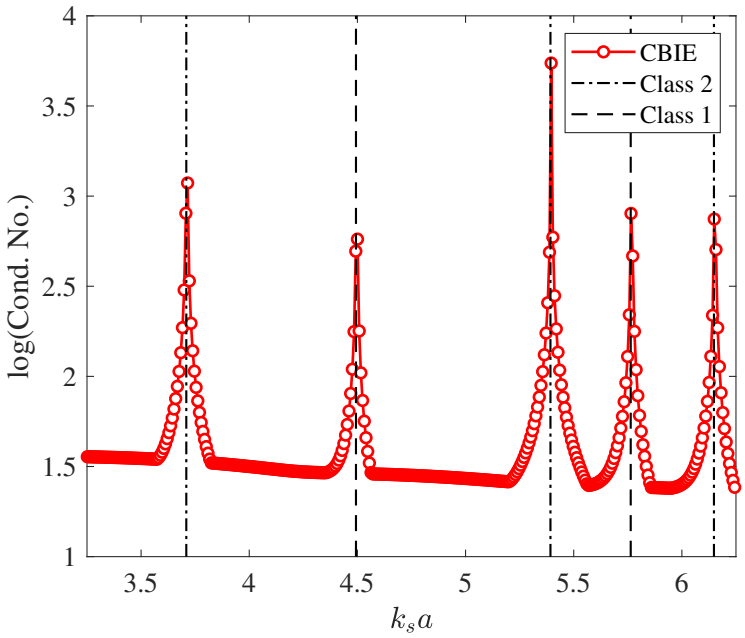


Figure 6.1: Condition number of BEM matrix for the CBIE formulation and rigid spherical scatterer. Vertical lines mark the positions of Class 1 and Class 2 eigenfrequencies of a rigid sphere.

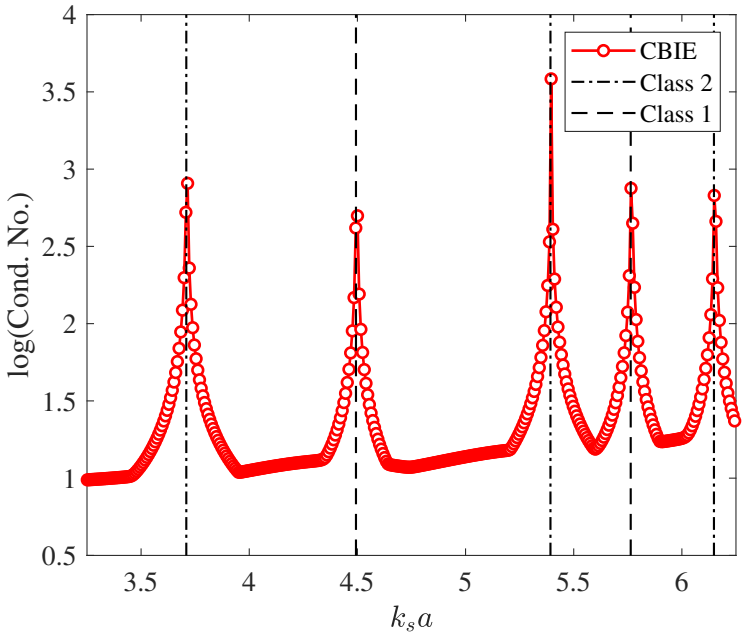


Figure 6.2: Condition number of BEM matrix for the CBIE formulation and soft spherical scatterer. Vertical lines mark the positions of Class 1 and Class 2 eigenfrequencies of a rigid sphere.

BEM matrices corresponding to CBIE, HBIE and CFIE formulations are obtained over a range of frequencies. Figures 6.1 and 6.2 show the condition number of the CBIE matrix as function of the the frequency for hard and soft scatterers, respectively. The eigenfrequencies of a rigid sphere are also shown for reference. The frequency sweep is performed at 401 points in the displayed range. As expected, the condition number increases near the eigenfrequencies. The BEM matrices are obtained with 80 second-order mesh elements with Rule-22 discretization. Because of discretization error, the numerical eigenfrequencies lie slightly away from the theoretical ones, although this discrepancy is unnoticeable in the foregoing cases. The number of mesh elements is set such that all the eigenfrequencies are resolved without any noticeable error.

The condition numbers for the HBIE formulation are shown in Figures 6.3 and 6.4. The fictitious eigenfrequencies coincide with the eigenfrequencies of traction-free sphere. In the soft scatterer case, the number of mesh elements is increased to 320 for $k_s a > 4.83$ because the discretization error for 80 elements was large beyond this frequency. Unlike the foregoing cases, Figure 6.5 shows that there are no eigenfrequencies in the CFIE formulation with coupling coefficient $\beta = i$.

### 6.4.2 Scattering Amplitude

We will now consider scattering amplitude solutions for the foregoing spherical scatterer problems. Figures 6.6 and 6.7 show the longitudinal wave scattering amplitude obtained by solving the CBIE formulation for soft and rigid scatterer cases, respectively. The exact analytical solution computed using the separtion of variables technique [13, §10.6.2] is used as reference. In the rigid scatterer case, we observe that scattering amplitude exhibits sharp peaks at Class 2 eigenfrequencies. However, no such peaks are observed in the scattering amplitude in the soft scatterer case. This phenomena is similar to that observed for the electric field integral equation (EFIE) for electromagnetic scattering, where the resonant surface currents do not radiate away from the scatterer [192]. Therefore, although the surface fields are in error, the radiated fields still match the exact solution.

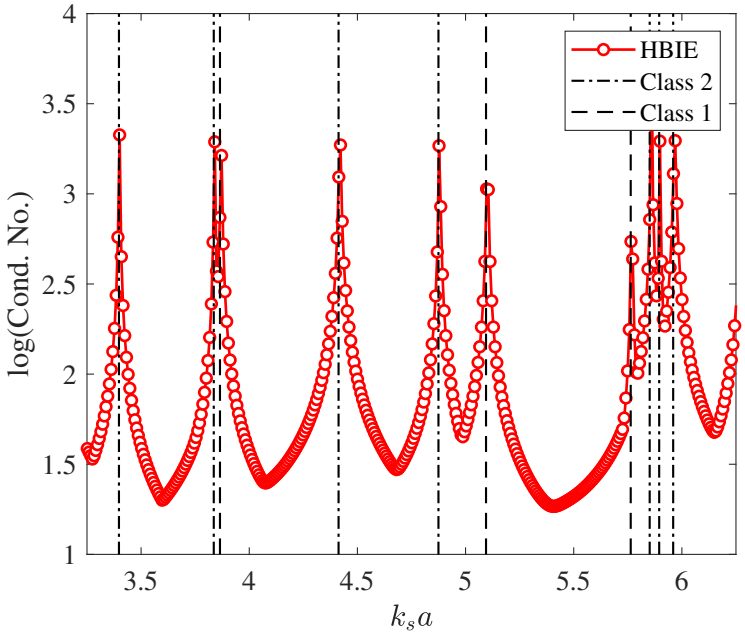


Figure 6.3: Condition number of BEM matrix for the HBIE formulation and rigid spherical scatterer. Vertical lines mark the positions of Class 1 and Class 2 eigenfrequencies of a traction-free sphere.

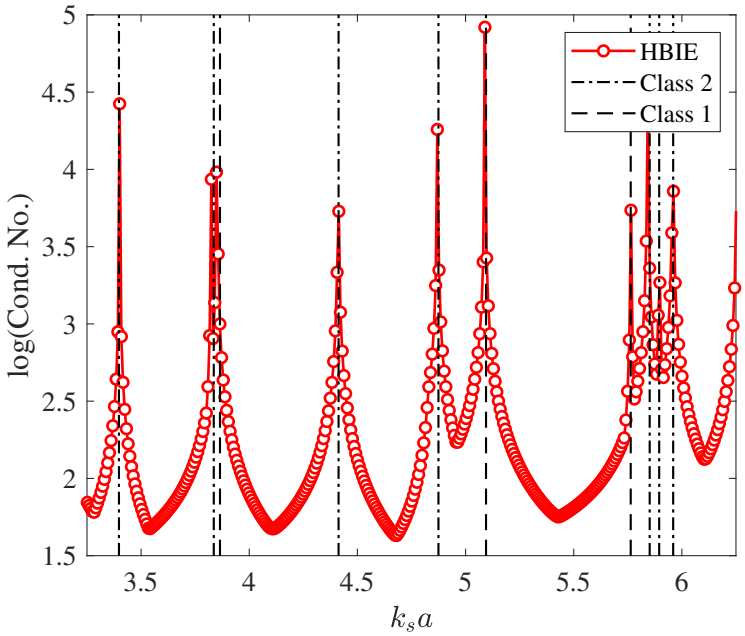


Figure 6.4: Condition number of BEM matrix for the HBIE formulation and soft spherical scatterer. Vertical lines mark the positions of Class 1 and Class 2 eigenfrequencies of a traction-free sphere.

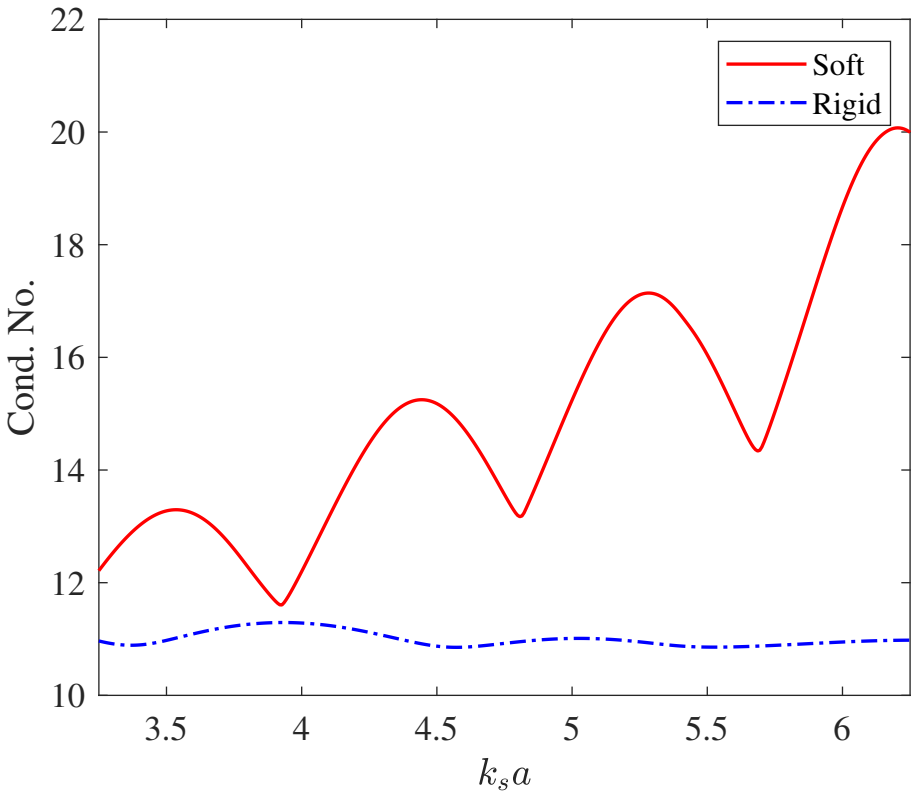


Figure 6.5: Condition number of BEM matrix for the CFIE formulation ($\beta = i$) in case of both soft and rigid spherical scatterers.

The scattering amplitudes computed using the HBIE formulation are shown in Figures 6.8 and 6.9. The rigid scatterer case exhibits large errors whereas the soft scatterer case has very small error near some of the eigenfrequencies. This indicates that for the HBIE formulation, the presence of eigenfrequencies may not be problematic since their effect on the accuracy of the scattering amplitude solution occurs in a very narrow-band centered at the eigenfrequencies. Recall that for the soft scatterer case, 320 mesh elements are used for $k_s a > 4.83$ whereas 80 mesh elements are used for $k_s a < 4.83$. The discontinuity around $k_s a = 4.83$ is due to the use of different meshes. The solution for $k_s a < 4.83$ has a higher error because of the use of a coarser mesh. The scattering amplitudes obtained with the CFIE formulation ($\beta = i$) are shown in Figures 6.10 and 6.11. No peaks in the scattering amplitude are observed because of the absence of eigenfrequencies.

Next, we consider a spherical void problem proposed in [139] for testing the CFIE formulation. The host material properties are: $\rho_+ = 1$ kg/m$^3$, $\lambda_+ = 2$ N/m$^2$ and $\mu_+ = 1$ N/m$^2$. This scattering problem is solved using the CBIE, HBIE and CFIE ($\beta = i$) formulations. In all cases, Rule-22 discretization is applied in the BEM, with 80 mesh elements. In [139], the frequency of the incident wave is set to 1 Hz, which coincides with a Class 2 eigenfrequency of a rigid sphere. To account for discretization error in the location of the irregular frequency, we calculated the condition number of the BEM matrix using CBIE formulation at several frequencies close to 1 Hz and selected the frequency that maximized the condition number. Therefore, the frequency is set to 1.00074 Hz. The magnitude of radial dispkacement at $r = 5a$ is shown as function of the polar angle in Figure 6.12. Since the simulation frequency coincides with an irregular frequency of the CBIE formulation, we observe a large error in the corresponding solution. On the other hand, both HBIE and CFIE formulations lead to small errors, as also indicated by the relative errors in Figure 6.13. The relative error in this figure is defined as $|u_r - u_{\text{ref}}| / \max_\theta |u_{\text{ref}}|$, where $u_{\text{ref}}$ is the reference solution.

To further confirm these results, we modify the host material properties to $\rho_+ = 1$ kg/m$^3$, $\lambda_+ = 1$ N/m$^2$ and $\mu_+ = 4$ N/m$^2$ and compute the longitudinal wave scattering amplitude at the first four eigenfrequencies (of a rigid sphere). These frequencies correspond to $k_p a = 2.4746$, 2.9979, 3.5977, 3.8453. The first and the third eigenfrequencies belong to Class 2, whereas the other two

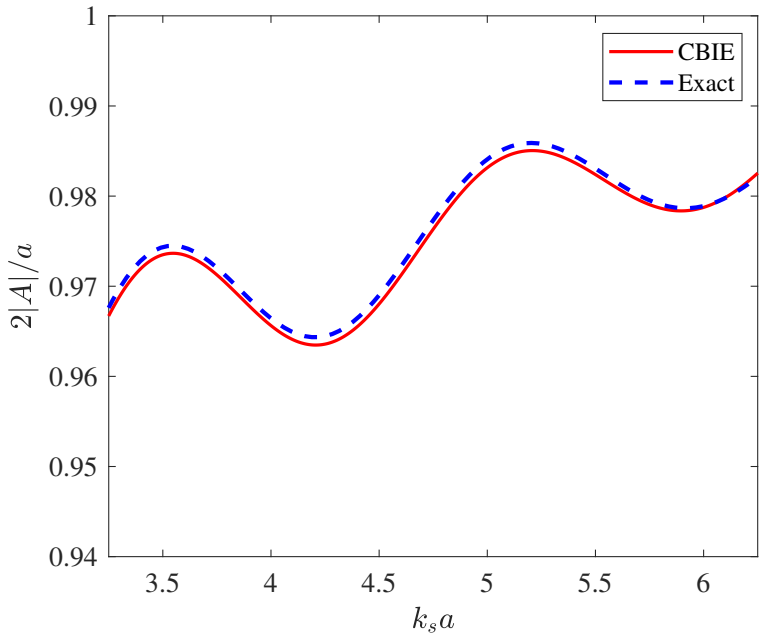


Figure 6.6: Magnitude of longitudinal wave scattering amplitude for the rigid spherical scatterer computed using the CBIE formulation.

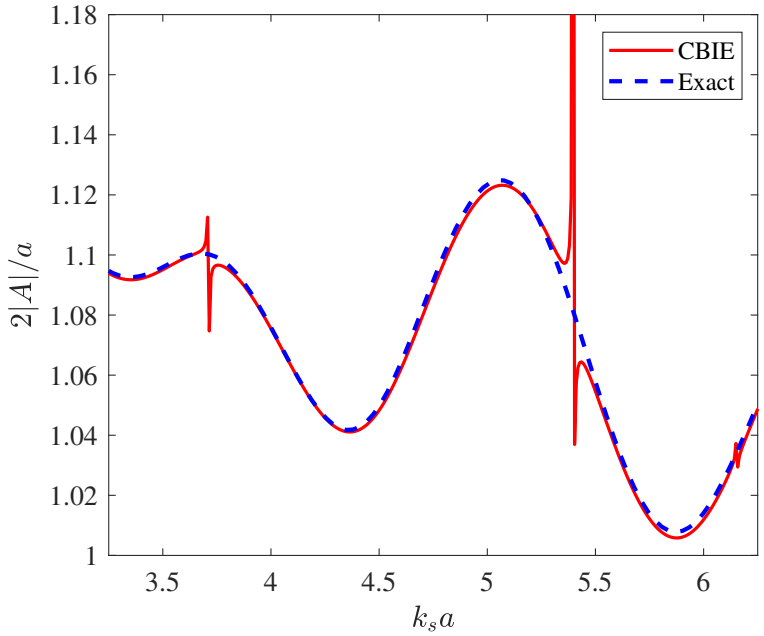


Figure 6.7: Magnitude of longitudinal wave scattering amplitude for the soft spherical scatterer computed using the CBIE formulation.

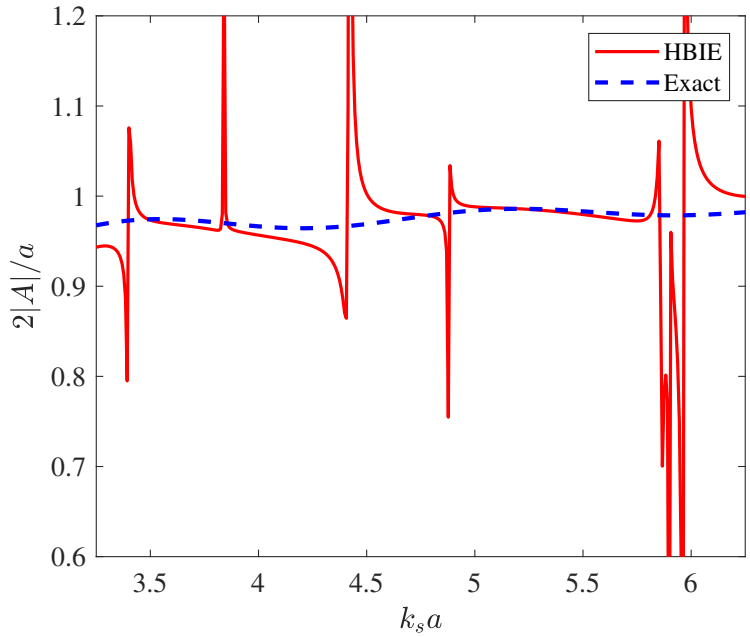


Figure 6.8: Magnitude of longitudinal wave scattering amplitude for the rigid spherical scatterer computed using the HBIE formulation.

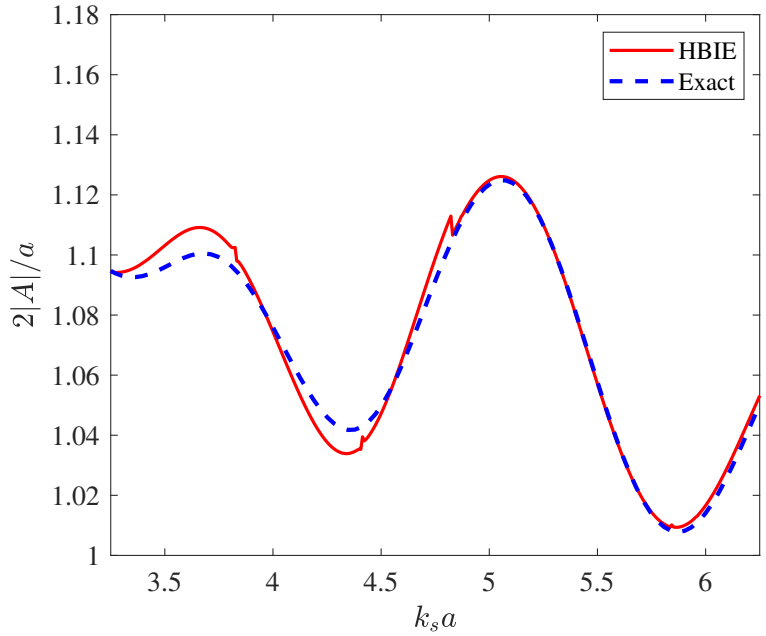


Figure 6.9: Magnitude of longitudinal wave scattering amplitude for the soft spherical scatterer computed using the HBIE formulation.

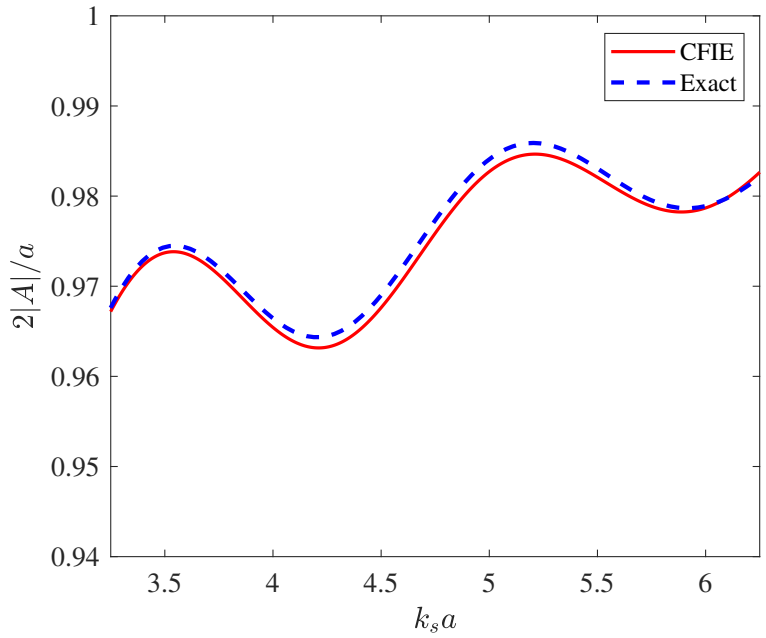


Figure 6.10: Magnitude of longitudinal wave scattering amplitude for the rigid spherical scatterer computed using the CFIE formulation ($\beta = i$).

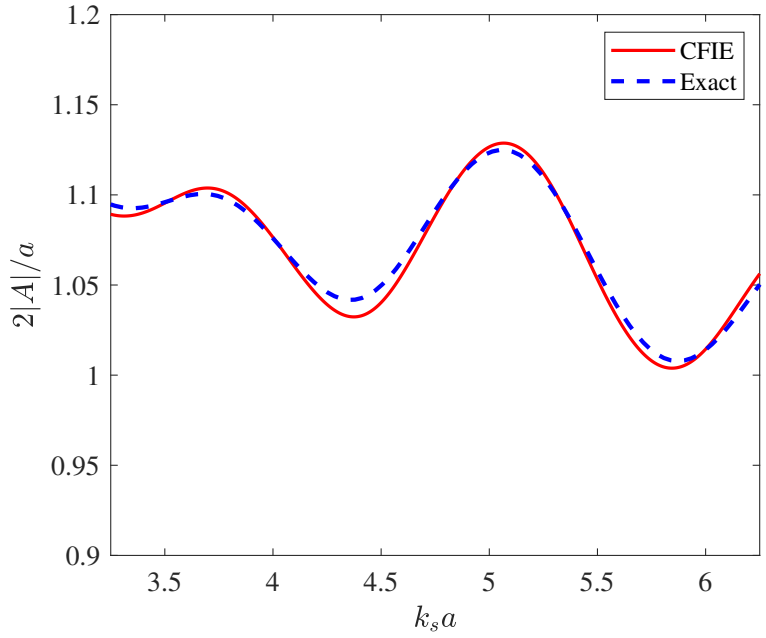


Figure 6.11: Magnitude of longitudinal wave scattering amplitude for the soft spherical scatterer computed using the CFIE formulation ($\beta = i$).

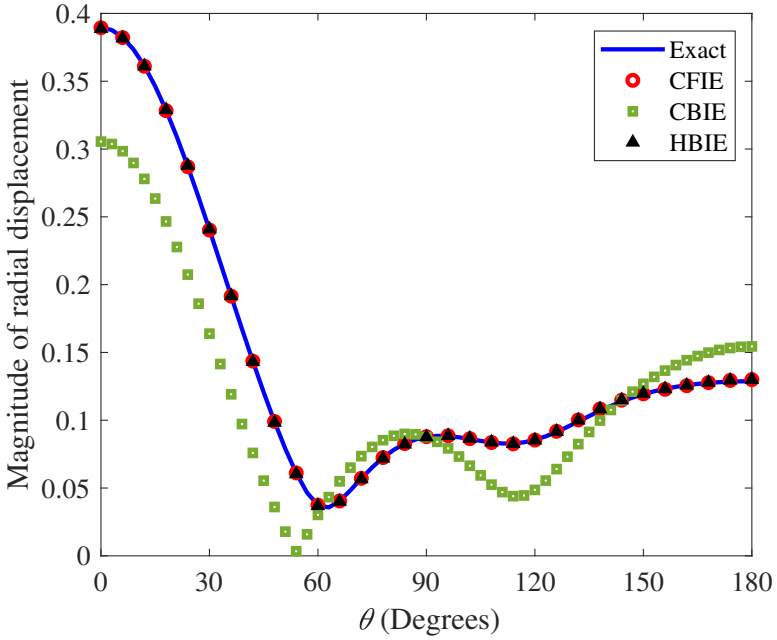


Figure 6.12: Magnitude of scattered radial displacement at $r = 5a$ for a soft spherical scatterer ($k_s a = 2\pi$). Coupling coefficient in CFIE formulation is $\beta = i$.

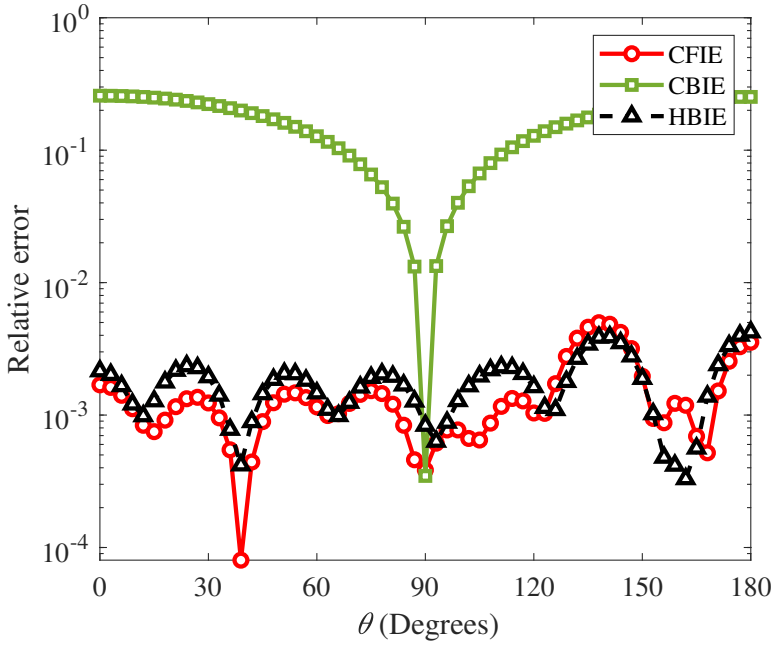


Figure 6.13: Relative error in scattered radial displacement at $r = 5a$ for a soft spherical scatterer ($k_s a = 2\pi$). Coupling coefficient in CFIE formulation is $\beta = i$.

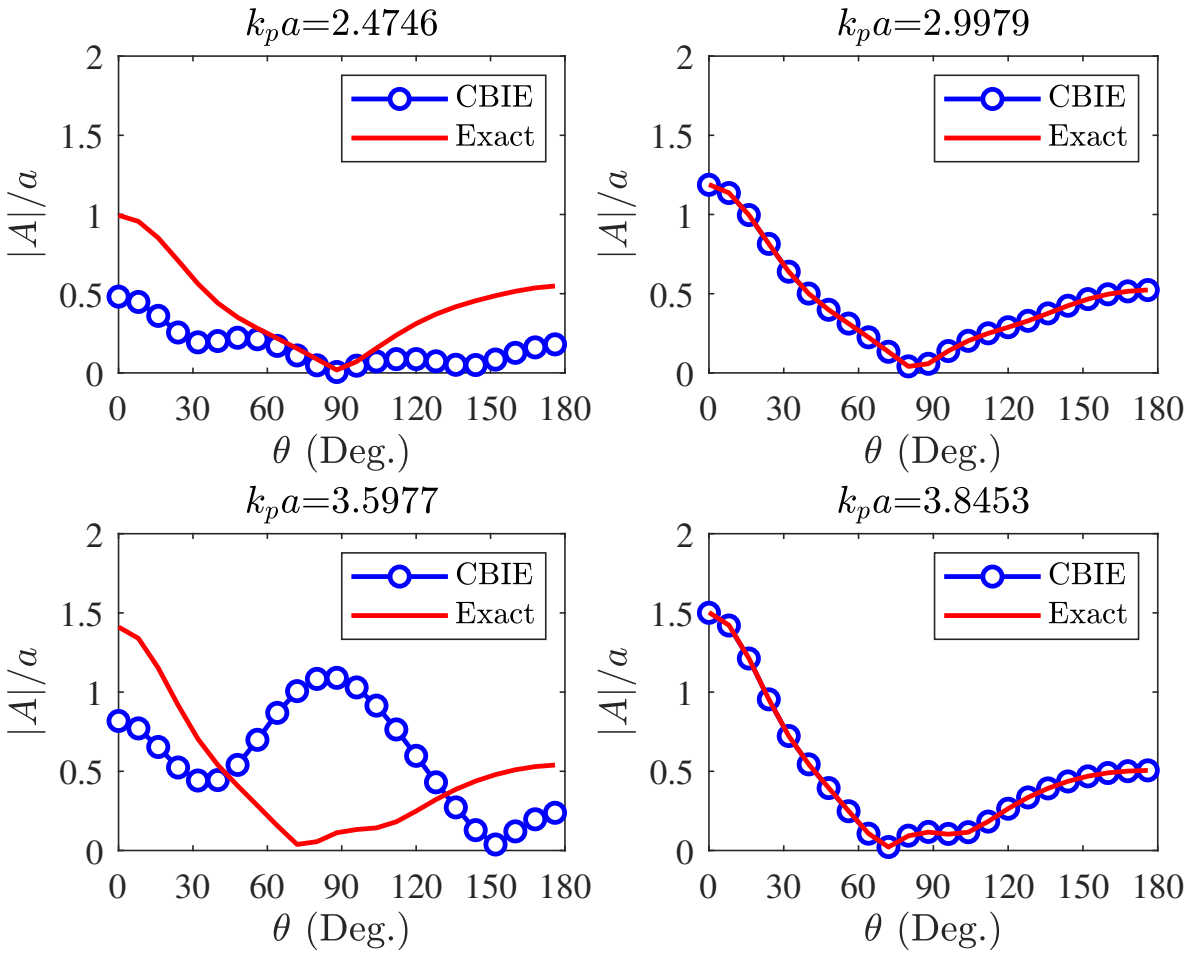


Figure 6.14: Longitudinal wave scattering amplitude for a spherical cavity at the first four Class 2 eigenfrequencies.

belong to Class 1. Accordingly, we find in Figure 6.14 that the solution calculated using the CBIE formulation is in error at the first and the third eigenfrequencies. On the other hand, the CFIE ($\beta = i$) results shown in Figure 6.15 are accurate.

### 6.4.3 Convergence Rate of Iterative Solution

Although the coupling coefficient $\beta = i$ makes the CFIE well-conditioned, it may not be an optimal choice for reducing the number of iterations required when the BEM linear system is solved using an iterative method. To illustrate this, we consider the spherical cavity problem mentioned above (Figure 6.12) with $\rho_+ = 1$ kg/m$^3$, $\lambda_+ = 2$ N/m$^2$ and $\mu_+ = 1$ N/m$^2$. However, instead

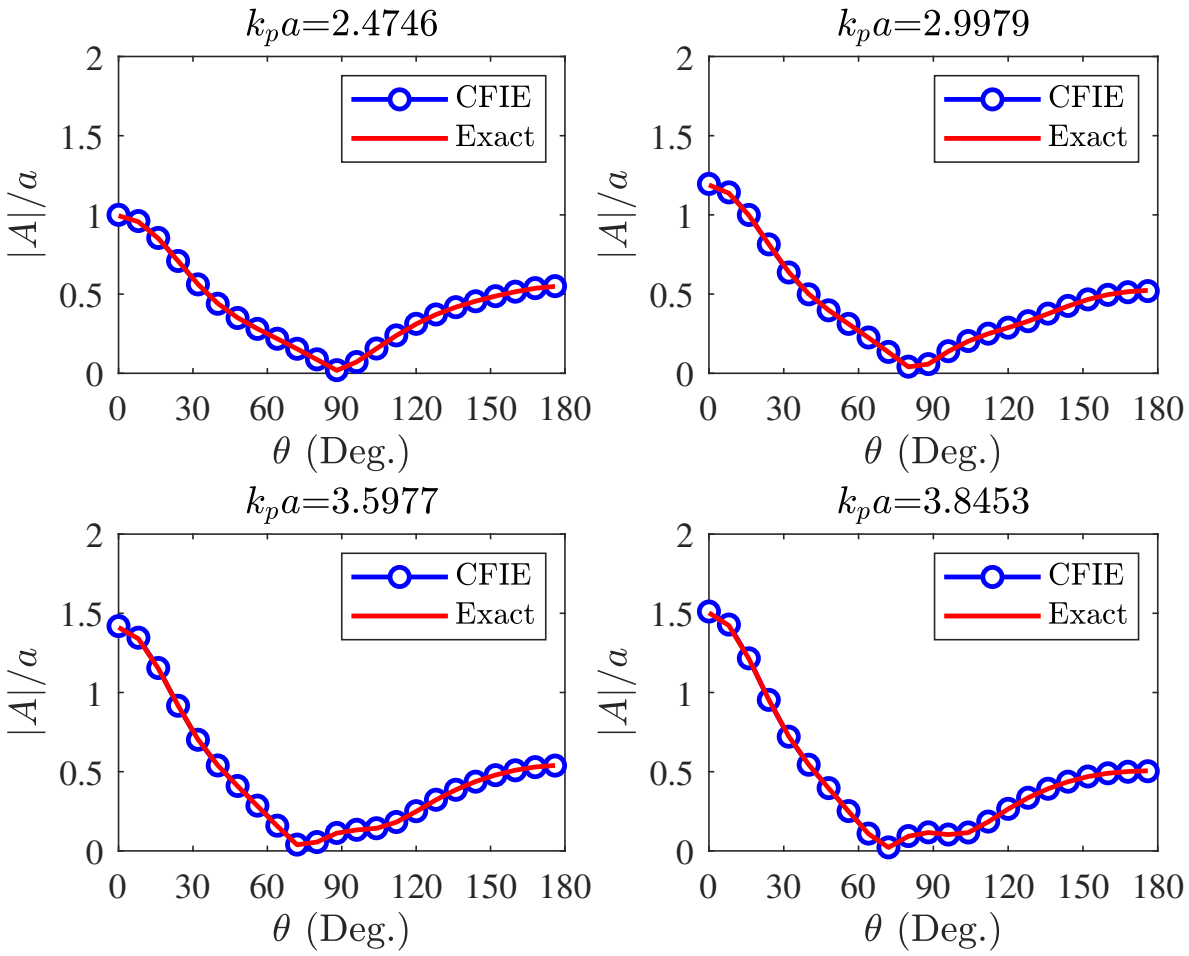


Figure 6.15: Longitudinal wave scattering amplitude for spherical cavity at the first four Class 2 eigenfrequencies. Coupling coefficient in CFIE formulation is $\beta = i$.

Table 6.3: Comparison of number of iterations and relative errors of different BIE formulations for scattering from a spherical cavity.

| | $k_s a = 2.00148\pi$ | | $k_s a = 16\pi$ | |
|---|---|---|---|---|
| | Iterations | Rel. err. | Iterations | Rel. err. |
| CBIE | 27 | 0.204 | $> 1000$ | – |
| HBIE | 255 | $4.4\times10^{-3}$ | $> 1000$ | – |
| CFIE ($\beta = i$) | 205 | $4.1\times10^{-3}$ | $> 1000$ | – |
| CFIE ($\beta = -1 - i$) | 13 | $4.2\times10^{-3}$ | 84 | $1.45 \times 10^{-2}$ |

of solving the BEM linear system by direct inversion, we obtain the solution using the GMRES method with a block Jacobi preconditioner [189, §3.2]. The residual error is set to $10^{-4}$. Table 6.3 shows the number of iterations and the relative error, which is defined as $||\mathbf{A}_n - \mathbf{A}_{\text{ref}}||_2/||\mathbf{A}_{\text{ref}}||_2$, where $\mathbf{A}_n$ is a vector that stores the longitudinal wave scattering amplitudes for different values of $\theta$ and $\mathbf{A}_{\text{ref}}$ is the reference solution.

Although the CFIE converges faster than the HBIE and BM-BIE formulations, it has a large relative error because of ill-conditioning. The CFIE formulation with $\beta = -1 - i$ converges in the least number of iterations and has slightly higher error than the BM-BIE formulation. We find similar observations when the frequency is increased to $k_s a = 16\pi$, which corresponds to another Class 2 eigenfrequency. The number of mesh elements is 1280, and MLFMM with $L = 4$ levels is applied. Only the CFIE formulation with $\beta = -1 - i$ converges to the required tolerance. Other formulations do not converge even after 1000 iterations. This suggests a need to study the affect of coupling parameter on the convergence rate. The residual errors after 1000 iterations for the CBIE, HBIE and BM-BIE formulations are 0.014, 0.022 and 0.357, respectively. The corresponding relative errors are 0.215, $2.1 \times 10^{-2}$ and 0.725, respectively.

### 6.4.4 Pulse-echo from FBH

We revisit the FBH benchmark problem analysed in Section 2.3.1.2. We mentioned that the pulse-echo simulated using the BEM matches the measurement more closely if the plane-wave approximation is not used. Since the variation of the integral in (2.8) ($I(\omega)$) as a function of

frequency is not as smooth as that of the scattering amplitude in (2.14), the frequency sweep for the large-flaw model needs more points than the one with the small-flaw model. This increases the chances of simulating the model close to a fictitious eigenfrequency. Also, although the scattering amplitude of the FBH may not be effected by some eigenfrequencies, as in the case of the spherical scatterer at Class 1 eigenfrequencies, the same may not be true for the integral $I(\omega)$. Therefore, BEM results are more prone to the eigenfrequency problem when the large flaw model is used.

Indeed, as Figure 6.16 demonstrates, the pulse-echo simulated using the CBIE and the large flaw model shows artifacts in the form of large ripples that exist outside the time-range of the measured pulse-echo, unlike the same result in case of the small-flaw model, where this artifact is less pronounced. Figure 6.17 shows the normalized magnitude of $I(\omega)$. The ripple-like artifacts in the pulse-echo signal are due to the sharp peaks in the CBIE response in this figure. The FBH model is also simulated using the CFIE formulation with $\beta = -(1+i)$. Unlike the CBIE case, the frequency domain response of the CFIE formulation exhibits no peaks. Therefore, we find no artifacts in the corresponding pulse-echo result. Also, as expected, this result matches the measured pulse-echo more closely than the one generated using the small flaw model (see Figure 2.12) since it does not include the plane-wave approximation.

## 6.5 Conclusions

This chapter illustrates the fictitious eigenfrequency problem in the conventional and hyper-singular BIE formulations. Scattering amplitudes calculated with these formulations exhibit sharp peaks at some eigenfrequencies. Similar to the internal resonance frequency phenomena in the EFIE for electromagnetics, radiated fields are unaffected by resonant surface fields at some eigenfrequencies for both HBIE and CBIE formulations. Particularly, longitudinal wave scattering amplitudes can be calculated accurately for rigid spherical scatterers in case of CBIE and soft spherical scatterers in case of HBIE, despite the presence of eigenfrequencies. However, for other types of scatterers, the longitudinal wave scattering amplitudes may be in error, particularly at high frequencies, where the density of eigenfrequencies is relatively high. The CFIE is proposed as an alternative well-

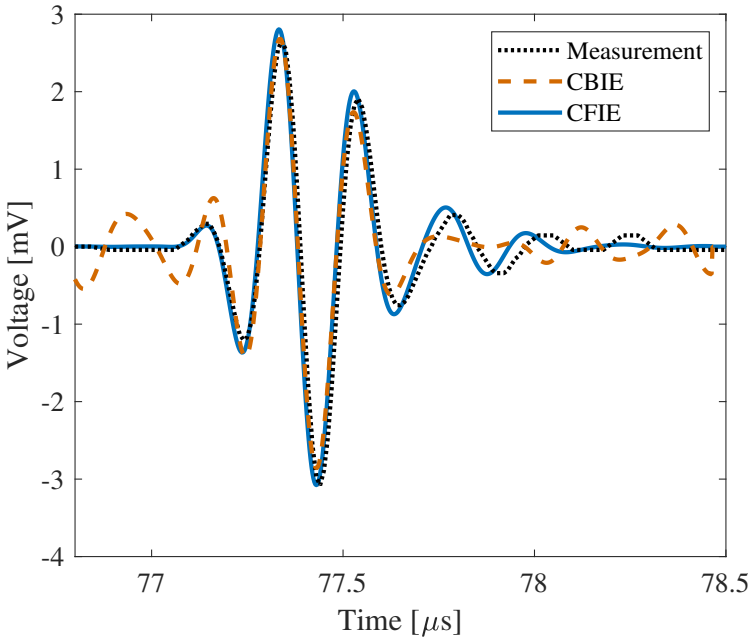


Figure 6.16: Measured and simulated pulse-echo signals for the FBH benchmark problem with planar transducer. Coupling coefficient in CFIE formulation is $\beta = -(1+i)$.

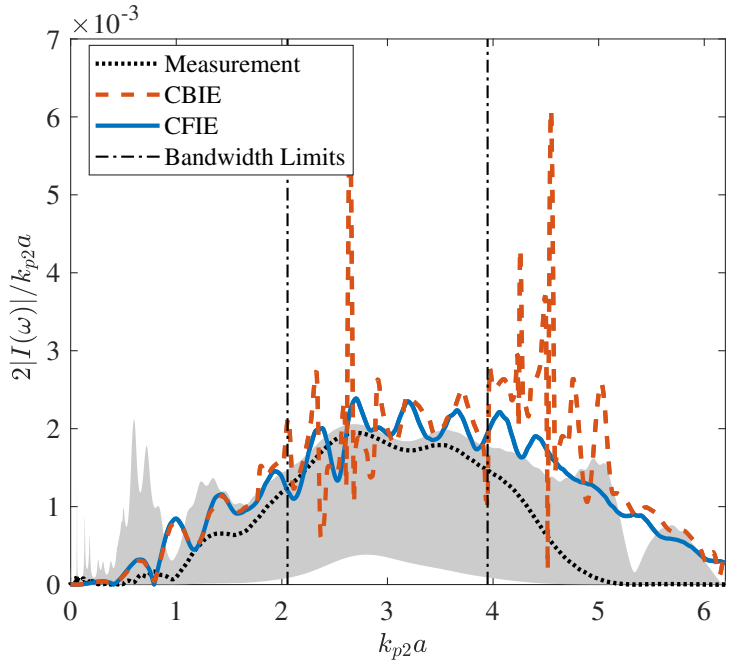


Figure 6.17: Magnitude of the integral $I(\omega)$ for the FBH benchmark problem. Coupling coefficient in CFIE formulation is $\beta = -(i+1)$. Measurement response is extracted from the pulse-echo signal. Shaded region represents the sensitivity of the extracted value to the parameters $\epsilon_1$ and $\epsilon_2$ (see Section 2.3.1.2.)

conditioned formulation for modeling ultrasonic scattering problems. Numerical examples indicate that the CFIE formulation is free from the ficititious eigenfrequency problem when the coupling coefficient $\beta$ is set to $i$. However, the convergence rate in iterative solution process is sensitive to the choice of the coupling coefficient, and a further analysis is required to study this effect.

# CHAPTER 7. CONCLUSIONS AND DIRECTIONS FOR FUTURE WORK

State-of-the-art ultrasonic NDE modeling involves the use of a composite modeling technique wherein different processes in the system are modeled separately and the system output response is synthesized by combining the outputs of sub-models using analytical techniques. This allows the use of efficient approximations and empirical models to treat processes such as transduction, wave propagation, etc., which in turn makes the simulation effort tractable. In view of computational efficiency, UNDE simulation packages use full-wave scattering models only for simple defect shapes that admit exact analytical solutions and handle more complex defects using approximation models, with the most popular one being the Kirchhoff approximation (KA). It is well-known that the KA does not capture some salient processes underlying ultrasonic scattering, such as creeping wave phenomena and multiple reflections. This thesis advances the BEM to address the lack of efficient high-fidelity (full-wave) solvers for ultrasonic scattering in UNDE applications. To inform the judicious use of BEM (or full-wave solvers, in general), a comprehensive study is conducted in Chapter 2 using immersion testing benchmarks. Small inclusion-type defects and edge-diffractions at angles of incidence greater than 45° were identified as the cases that showed the largest differences between KA and full-wave model predictions, with the predicted pulse-echo amplitudes differing by around 20 percentage points in the latter case.

This thesis proposes the use of three crucial implementation choices, namely, high-order discretization, multilevel fast multipole algorithm (MLFMA) and the direct combined-field integral equation (CFIE), as a means to reduce the computational costs of BEM. Chapter 3 compared the total simulation times and output errors of BEMs of different orders of discretizations applied to the conventional boundary integral equation (CBIE) and demonstrated that the use of second-order geometry and field discretizations leads to faster simulations (over first and zeroth order) due to reduction in the number of degrees of freedom required for converging to a given level of error. A

high-order BEM for the CFIE formulation was developed in Chapter 4. A key contribution from this chapter is the singularity subtraction method applied for handling near-singular integrals. The high-order BEM is validated using analytical results for circular traction-free cracks and spherical scatterers. Diagonal-form expansions of the CFIE kernels are given in Chapter 5. Since the unregularized HBIE and CBIE kernels share their radiation patterns, the compute-time and memory overheads (due to the use of combined-field formulation) in evaluating the far-field contributions in MLFMA are minimized. Chapter 6 analyzes the fictitious eigenfrequency problem associated with the CBIE and HBIE formulations. The CFIE formulation is free from this artifact for a proper choice of the coupling constant. An example of a practical UNDE test reveals that the eigenfrequency problem in the CBIE may be more pronounced with the use of large flaw scattering models as opposed to small flaw models, which provide scattering amplitudes as outputs.

Although the CFIE formulation leads to well-conditioned linear systems that are more suitable for iterative solution methods than those from the CBIE and HBIE formulations, it still requires a relatively large number of iterations at high frequencies. Therefore, efficient preconditioners for combined-field formulations need to be explored to further reduce the iterative solution times [182–184]. The most time-consuming part of the BEM is the matrix filling process. For near-singular integrals arising from strongly singular kernels, singularity cancellation schemes have been developed [164, 196] which may be more efficient than the singularity subtraction procedures applied here. A performance comparison between the two methods will be helpful. Also, the development of efficient singularity cancellation schemes for near-hypersingular integrals will probably have the highest impact in reducing the matrix-filling times. Since surface fields on crack-like defects exhibit singular behaviour, the performance of BEM for such defects can be improved by using non-uniform boundary elements. However, non-uniform discretizations lead to highly ill-conditioned linear systems. Therefore, preconditioners for linear systems resulting from such discretizations should be considered [197].

On the application side, meta-modeling based model-assisted probability of detection (MAPOD) approaches have seen promising developments recently [198, 199]. Multifidelity metamodeling tech-

niques fuse data from a high-fidelity full-wave solver with low-fidelity (approximation) solvers to provide efficient and accurate surrogates of the full-wave solver [200]. In this way, MAPOD-approaches based on the BEM can be realized with a relatively smaller number of evaluations of the BEM model than what is possible by direct application. Also, it is worth noting that the computational cost of near-field matrix filling is amortized by the fact that changes in parameters related to the transducer orientation, location, etc. only change the incident field vector in the linear system. Therefore, the near-field matrix does not have to be re-evaluated for parametric variations of such variables.

# BIBLIOGRAPHY

[1] W. D. Rummel, "Probability of detection (POD) is not NDT/E reliability," in *AIP Conference Proceedings*, vol. 1511, pp. 1809–1816, AIP, 2013.

[2] D. Ensminger and L. J. Bond, *Ultrasonics: fundamentals, technologies, and applications*. CRC press, 2011.

[3] R. M. Meyer, P. Ramuhalli, M. B. Toloczko, L. J. Bond, and R. O. Montgomery, "Assessment of NDE technologies for detection and characterization of stress corrosion cracking in LWRs," Tech. Rep. IAEA-CN–194, International Atomic Energy Agency (IAEA), 2012.

[4] H. K. Reddick Jr., "Safe-life and damage-tolerant design approaches for helicopter structures," in *Failure Analysis and Mechanisms of Failure of Fibrous Composite Structures* (A. K. Noor, M. J. Shuart, J. H. Starnes Jr., and J. G. Williams, eds.), vol. NASA-CP-2278, pp. 129–152, NASA, USA, 1983.

[5] M. Stewart and O. T. Lewis, *Pressure Vessels Field Manual - Common Operating Problems and Practical Solutions*. Elsevier, 2013.

[6] S. D. Antolovich, A. Saxena, and W. W. Gerberich, "Fracture mechanics–an interpretive technical history," *Mechanics Research Communications*, vol. 91, pp. 46–86, 2018.

[7] J. Wang and J. Shuai, "Measurement and analysis of crack tip opening angle in pipeline steels," *Engineering Fracture Mechanics*, vol. 79, pp. 36–49, 2012.

[8] C. Garcia, T. Lotz, M. Martinez, A. Artemev, R. Alderliesten, and R. Benedictus, "Fatigue crack growth in residual stress fields," *International Journal of Fatigue*, vol. 87, pp. 326–338, 2016.

[9] M. Saka and M. S. Akanda, "Ultrasonic measurement of the crack depth and the crack opening stress intensity factor under a no load condition," *Journal of Nondestructive Evaluation*, vol. 23, no. 2, pp. 49–63, 2004.

[10] M. Kemppainen and I. Virkkunen, "Crack characteristics and their importance to NDE," *Journal of Nondestructive Evaluation*, vol. 30, no. 3, pp. 143–157, 2011.

[11] C. Ruud, "A review of selected non-destructive methods for residual stress measurement," *NDT International*, vol. 15, no. 1, pp. 15–23, 1982.

[12] N. Pei and L. J. Bond, "Higher order acoustoelastic lamb wave propagation in stressed plates," *The Journal of the Acoustical Society of America*, vol. 140, no. 5, pp. 3834–3843, 2016.

[13] L. W. Schmerr Jr., *Fundamentals of ultrasonic nondestructive evaluation: a modeling approach*. Springer Science & Business Media, 2016.

[14] R. Stolt, F. Elgh, and P. Andersson, "Design for inspection-evaluating the inspectability of aerospace components in the early stages of design," *Procedia Manufacturing*, vol. 11, pp. 1193–1199, 2017.

[15] C. Latiolais and F. Becker, "Guidelines for inspectability for new plant components," Tech. Rep. 1015139, EPRI, Palo Alto, CA, 2007.

[16] J. C. Aldrin, "Overview of mathematical modeling in nondestructive evaluation (NDE)," tech. rep., Nondestructive Testing Information Analysis Center, Austin, TX, 2002.

[17] R. M. Meyer, S. L. Crawford, J. P. Lareau, and M. T. Anderson, "Review of literature for model assisted probability of detection," Tech. Rep. PNNL-23714, Pacific Northwest National Lab.(PNNL), Richland, WA (United States), 2014.

[18] A. Sedov and L. W. Schmerr Jr., "The time domain elastodynamic Kirchhoff approximation for cracks: the inverse problem," *Wave Motion*, vol. 8, no. 1, pp. 15–26, 1986.

[19] D. Hsu, J. Rose, and D. Thompson, "Reconstruction of inclusions in solids using ultrasonic born inversion," *Journal of Applied Physics*, vol. 55, no. 1, pp. 162–168, 1984.

[20] C. Chaloner and L. Bond, "Ultrasonic signal processing using Born inversion," *NDT International*, vol. 19, no. 3, pp. 133–140, 1986.

[21] C. Chaloner and L. Bond, "Investigation of the 1-D inverse Born technique," *IEE Proceedings A (Physical Science, Measurement and Instrumentation, Management and Education, Reviews)*, vol. 134, no. 3, pp. 257–265, 1987.

[22] L. Schmerr Jr. and J. S. Song, *Ultrasonic Nondestructive Evaluation Systems*. Springer, 2007.

[23] H. Wirdelius and E. Oesterberg, "Study of defect characteristics essential for NDT testing methods ET, UT and RT," Tech. Rep. SKI-R–00-42, Swedish Nuclear Power Inspectorate, 2000.

[24] M. Saka and Y. Fukuda, "NDT of closed cracks by ultrasonic propagation along the crack surface," *NDT & E International*, vol. 24, no. 4, pp. 191–194, 1991.

[25] R. Grandin and T. Gray, "UTSim2 validation," in *AIP Conference Proceedings*, vol. 1806, p. 150007, AIP Publishing, 2017.

[26] F. Foucher, S. Lonné, G. Toullelan, S. Mahaut, and S. Chatillon, "An overview of validation campaigns of the CIVA simulation software," ECNDT, 2018.

[27] L. W. Schmerr Jr., H. J. Kim, A. L. Lopez, and A. Sedov, "Simulating the experiments of the 2004 ultrasonic benchmark study," in *Review of Progress in Quantitative Nondestructive Evaluation* (D. O. Thompson and D. E. Chimenti, eds.), vol. 760, pp. 1880–1887, American Institute of Physics, Melville, NY, 2005.

[28] B. Auld, "General electromechanical reciprocity relations applied to the calculation of elastic wave scattering coefficients," *Wave Motion*, vol. 1, no. 1, pp. 3–10, 1979.

[29] M. Darmon and S. Chatillon, "Main features of a complete ultrasonic measurement model: formal aspects of modeling of both transducers radiation and ultrasonic flaws responses," *Open J. Acoust*, vol. 3, no. 3A, pp. 43–53, 2013.

[30] K. Chen, *Boundary integral equation method for electromagnetic and elastic waves.* PhD thesis, Iowa State University, 2016.

[31] M. S. Tong and W. C. Chew, "Multilevel fast multipole algorithm for elastic wave scattering by large three-dimensional objects," *Journal of Computational Physics*, vol. 228, no. 3, pp. 921–932, 2009.

[32] S. Mahaut, S. Chatillon, M. Darmon, N. Leymarie, R. Raillon, and P. Calmon, "An overview of ultrasonic beam propagation and flaw scattering models in the CIVA software," in *AIP Conference Proceedings*, vol. 1211, pp. 2133–2140, AIP, 2010.

[33] M. Darmon, V. Dorval, A. K. Djakou, L. Fradkin, and S. Chatillon, "A system model for ultrasonic NDT based on the physical theory of diffraction (PTD)," *Ultrasonics*, vol. 64, pp. 115–127, 2016.

[34] P. Calmon, S. Mahaut, S. Chatillon, and R. Raillon, "CIVA: An expertise platform for simulation and processing NDT data," *Ultrasonics*, vol. 44, pp. e975–e979, 2006.

[35] P. Calmon, A. Lhémery, I. Lecœur-Taıbi, R. Raillon, and L. Paradis, "Models for the computation of ultrasonic fields and their interaction with defects in realistic NDT configurations," *Nuclear Engineering and Design*, vol. 180, no. 3, pp. 271–283, 1998.

[36] N. Gengembre and A. Lhémery, "Pencil method in elastodynamics: application to ultrasonic field computation," *Ultrasonics*, vol. 38, no. 1-8, pp. 495–499, 2000.

[37] N. Gengembre and A. Lhémery, "Calculation of wideband ultrasonic fields radiated by water-coupled transducers into heterogeneous and anisotropic media," in *AIP Conference Proceedings*, vol. 509, pp. 977–984, AIP, 2000.

[38] V. Zernov, L. Fradkin, and M. Darmon, "A refinement of the Kirchhoff approximation to the scattered elastic fields," *Ultrasonics*, vol. 52, no. 7, pp. 830–835, 2012.

[39] M. Darmon, R. Raillon, V. Dorval, S. Chatillon, and F. L. Fradkin, "Generic GTD-Kirchhoff scattering model for the ultrasonic response of planar defects," in *10th International Conference on NDE in Relation to Structural Integrity for Nuclear and Pressurized Components, 1-3 October 2013, Cannes, France (JRC-NDE 2013)*, vol. 2015-12, NDT.net, 2016.

[40] V. Dorval, S. Chatillon, B. Lu, M. Darmon, and S. Mahaut, "A general Kirchhoff approximation for echo simulation in ultrasonic NDT," in *AIP Conference Proceedings*, vol. 1430, pp. 193–200, AIP, 2012.

[41] V. Dorval, M. Darmon, S. Chatillon, and L. Fradkin, "Simulation of the UT inspection of planar defects using a generic GTD-Kirchhoff approach," in *AIP Conference Proceedings*, vol. 1650, pp. 1750–1756, AIP, 2015.

[42] M. Darmon, P. Calmon, and B. Bèle, "An integrated model to simulate the scattering of ultrasounds by inclusions in steels," *Ultrasonics*, vol. 42, no. 1-9, pp. 237–241, 2004.

[43] N. Leymarie, P. Calmon, T. Fouquet, and A. Schumm, "A semi-analytical FEM hybrid model for ultrasonic simulation of complicated wave defect interaction," in *Procedings of the 5th I Int. Conf. on NDE in Relation to Structural Integrity for Nuclear and Pressurised components, edited by M. Bièth, J. Whittle, DG JRC Institute of Energy, San Diego, USA*, pp. 554–562, 2006.

[44] A. Imperiale, S. Chatillon, M. Darmon, N. Leymarie, and E. Demaldent, "UT simulation using a fully automated 3D hybrid model: application to planar backwall breaking defects inspection," in *AIP Conference Proceedings*, vol. 1949, p. 050004, AIP Publishing, 2018.

[45] C. Rose, F. Rupin, T. Fouquet, and B. Chassignole, "ATHENA 3D: A finite element code for ultrasonic wave propagation," in *Journal of Physics: Conference Series*, vol. 498, p. 012009, IOP Publishing, 2014.

[46] A. K. Djakou, M. Darmon, and C. Potel, "Elastodynamic models for extending GTD to penumbra and finite size flaws," in *Journal of Physics: Conference Series*, vol. 684, p. 012002, IOP Publishing, 2016.

[47] R. B. Thompson and T. Gray, "A model relating ultrasonic scattering measurements through liquid–solid interfaces to unbounded medium scattering amplitudes," *The Journal of the Acoustical Society of America*, vol. 74, no. 4, pp. 1279–1290, 1983.

[48] M. Garton, T. Gray, R. B. Thompson, and I. Gray, "UTSim: overview and application," in *AIP Conference Proceedings*, vol. 1211, pp. 2141–2148, AIP, 2010.

[49] M. S. Garton, "Refining automated ultrasonic inspections with simulation models," Master's thesis, Iowa State University, 1997.

[50] M. Garton, "Refining automated ultrasonic inspections with simulation models," in *Review of Progress in Quantitative Nondestructive Evaluation*, pp. 1825–1829, Springer, 1998.

[51] R. Thompson and E. Lopes, "The effects of focusing and refraction on Gaussian ultrasonic beams," *Journal of Nondestructive Evaluation*, vol. 4, no. 2, pp. 107–123, 1984.

[52] R. B. Thompson, T. Gray, J. Rose, V. Kogan, and E. Lopes, "The radiation of elliptical and bicylindrically focused piston transducers," *The Journal of The Acoustical Society of America*, vol. 82, no. 5, pp. 1818–1828, 1987.

[53] G. Persson and H. Wirdelius, "Recent survey and application of the simSUNDT software," in *AIP Conference Proceedings*, vol. 1211, pp. 2125–2132, AIP, 2010.

[54] H. Wirdelius and G. Persson, "Simulation based validation of the detection capacity of an ultrasonic inspection procedure," *International Journal of Fatigue*, vol. 41, pp. 23–29, 2012.

[55] A. Boström and H. Wirdelius, "Ultrasonic probe modeling and nondestructive crack detection," *The Journal of the Acoustical Society of America*, vol. 97, no. 5, pp. 2836–2848, 1995.

[56] B. Anders, "User guide to UTDefect, version 3," tech. rep., SKI Report 00:44, 2000.

[57] P. Waterman, "Matrix theory of elastic wave scattering," *The Journal of the Acoustical Society of America*, vol. 60, no. 3, pp. 567–580, 1976.

[58] A. Boström and P. Bövik, "Ultrasonic scattering by a side-drilled hole," *International Journal of Solids and Structures*, vol. 40, no. 13-14, pp. 3493–3505, 2003.

[59] A. Boström and G. Wickham, "On the boundary conditions for ultrasonic transmission by partially closed cracks," *Journal of Nondestructive Evaluation*, vol. 10, no. 4, pp. 139–149, 1991.

[60] A. Boström and A. S. Eriksson, "Scattering by two penny-shaped cracks with spring boundary conditions," *Proceedings of the Royal Society of London. Series A: Mathematical and Physical Sciences*, vol. 443, no. 1917, pp. 183–201, 1993.

[61] J. Westlund and A. Boström, "A hybrid T matrix/boundary element method for elastic wave scattering from a defect near a non-planar surface," *Journal of Nondestructive Evaluation*, vol. 31, no. 2, pp. 148–156, 2012.

[62] P. Martin, "On connections between boundary integral equations and T-matrix methods," *Engineering Analysis with Boundary Elements*, vol. 27, no. 7, pp. 771–777, 2003.

[63] R. Raillon, S. Chatillon, S. Mahaut, M. Spies, D. O. Thompson, and D. E. Chimenti, "Results of the 2007 UT modeling benchmark using two semi-analytical beam propagation and flaw scattering model," in *Review of Progress in Quantitative Nondestructive Evaluation* (D. O. Thompson and D. E. Chimenti, eds.), vol. 975, pp. 1759–1766, American Institute of Physics, Melville, NY, 2008.

[64] M. Spies, "Semi-analytical elastic wave-field modeling applied to arbitrarily oriented orthotropic media," *The Journal of the Acoustical Society of America*, vol. 110, no. 1, pp. 68–79, 2001.

[65] M. Spies, A. Dillhöfer, H. Rieder, and D. Dobrovolskij, "Real-time 3D-simulation tool for ultrasonic transducers used in aeroengine component inspections," in *4th International Symposium on NDT in Aerospace 2012, Nov 13-14, Augsburg, Germany (AeroNDT 2012)*, vol. 2013-02, NDT.net, 2013.

[66] M. Spies, "Kirchhoff evaluation of scattered elastic wavefields in anisotropic media," *The Journal of the Acoustical Society of America*, vol. 107, no. 5, pp. 2755–2759, 2000.

[67] M. Spies, "Ultrasonic field modeling for immersed components using Gaussian beam superposition," *Ultrasonics*, vol. 46, no. 2, pp. 138–147, 2007.

[68] M. Spies and W. Feist, "Application and validation of the Gaussian beam superposition technique to simulate the inspection of aero engine components," in *AIP Conference Proceedings*, vol. 894, pp. 886–893, AIP, 2007.

[69] D. Placko and T. Kundu, "Theoretical study of magnetic and ultrasonic sensors: dependence of magnetic potential and acoustic pressure on the sensor geometry," in *Advanced Nondestructive Evaluation for Structural and Biological Health Monitoring*, vol. 4335, pp. 52–62, International Society for Optics and Photonics, 2001.

[70] D. Placko and T. Kundu, *Basic Theory of Distributed Point Source Method (DPSM) and Its Application to Some Simple Problems*, ch. 1, pp. 1–58. John Wiley & Sons, Ltd, 2006.

[71] S. Das, S. Banerjee, and T. Kundu, "Elastic wave scattering in a solid half-space with a circular cylindrical hole using the distributed point source method," *International Journal of Solids and Structures*, vol. 45, no. 16, pp. 4498–4508, 2008.

[72] A. Shelke, S. Das, and T. Kundu, "Distributed point source method for modeling scattered ultrasonic fields in the presence of an elliptical cavity," *Structural Health Monitoring*, vol. 9, no. 6, pp. 527–539, 2010.

[73] D. Placko, T. Yanagita, E. K. Rahani, and T. Kundu, "Mesh-free modeling of the interaction between a point-focused acoustic lens and a cavity," *IEEE Transactions on Ultrasonics, Ferroelectrics, and Frequency Control*, vol. 57, no. 6, pp. 1396–1404, 2010.

[74] T. Hajzargarbashi, E. K. Rahani, and T. Kundu, "Scattering of focused ultrasonic beams by two spherical cavities in close proximity," *IEEE Transactions on Ultrasonics, Ferroelectrics, and Frequency Control*, vol. 58, no. 8, pp. 1619–1627, 2011.

[75] J. Reddy, *An introduction to the finite element method*, vol. 1221. McGraw-Hill New York, USA, 2004.

[76] S. R. Wu, "A priori error estimates for explicit finite element for linear elasto-dynamics by galerkin method and central difference method," *Computer Methods in Applied Mechanics and Engineering*, vol. 192, no. 51-52, pp. 5329–5353, 2003.

[77] S. R. Wu, "Lumped mass matrix in explicit finite element method for transient dynamics of elasticity," *Computer Methods in Applied Mechanics and Engineering*, vol. 195, no. 44-47, pp. 5983–5994, 2006.

[78] N. Murphy and C. Sovinec, "An analysis of mass matrix lumping in NIMROD," tech. rep., UW-CPTC 05-1, 2005.

[79] P. Huthwaite, "Accelerated finite element elastodynamic simulations using the GPU," *Journal of Computational Physics*, vol. 257, pp. 687–707, 2014.

[80] G. L. Wojcik, D. Vaughan, N. Abboud, and J. J. Mould, "Electromechanical modeling using explicit time-domain finite elements," in *1993 Proceedings IEEE Ultrasonics Symposium*, pp. 1107–1112, IEEE, 1993.

[81] G. Wojcik, D. Vaughan, V. Murray, and J. J. Mould, "Time-domain modeling of composite arrays for underwater imaging," in *1994 Proceedings of IEEE Ultrasonics Symposium*, vol. 2, pp. 1027–1032, IEEE, 1994.

[82] Dassault Systemes SE, *Abaqus Theory Guide*, 2016.

[83] Dassault Systemes SE, *Abaqus Analysis User Guide*, 2016.

[84] A. Imperiale and E. Demaldent, "A macro-element strategy based upon spectral finite elements and mortar elements for transient wave propagation modeling. Application to ultrasonic testing of laminate composite materials," *International Journal for Numerical Methods in Engineering*, vol. 119, no. 10, pp. 964–990, 2019.

[85] A. Imperiale, S. Chatillon, P. Calmon, N. Leymarie, S. Imperiale, and E. Demaldent, "UT simulation of embedded parametric defects using a hybrid model based upon spectral finite element and domain decomposition methods," in *19th World Conference on Non-Destructive Testing*, vol. 1, pp. 2184–2189, 2016.

[86] A. Imperiale, E. Demaldent, N. Leymarie, S. Chatillon, and P. Calmon, "Smart numerical tools for the modelling of ultrasonic testing on curved composite structures," in *AIP Conference Proceedings*, vol. 2102, p. 130004, AIP Publishing, 2019.

[87] E. Becache, P. Joly, and C. Tsogka, "Fictitious domains, mixed finite elements and perfectly matched layers for 2-D elastic wave propagation," *Journal of Computational Acoustics*, vol. 9, no. 03, pp. 1175–1201, 2001.

[88] V. Dolean, P. Jolivet, and F. Nataf, *An introduction to domain decomposition methods: algorithms, theory, and parallel implementation*, vol. 144. SIAM, 2015.

[89] COMSOL Inc., *COMSOL Multiphysics Reference Manual*, 2018.

[90] J.-P. Weiss, "Using the domain decomposition solver in COMSOL multiphysics." https://www.comsol.com/blogs/using-the-domain-decomposition-solver-in-comsol-multiphysics/, 2016. [Online; accessed 01-October-2019].

[91] A. Van Pamel, C. R. Brett, P. Huthwaite, and M. J. Lowe, "Finite element modelling of elastic wave scattering within a polycrystalline material in two and three dimensions," *The Journal of the Acoustical Society of America*, vol. 138, no. 4, pp. 2326–2336, 2015.

[92] A. Van Pamel, G. Sha, S. Rokhlin, and M. Lowe, "Finite-element modelling of elastic wave propagation and scattering within heterogeneous media," *Proceedings of the Royal Society A: Mathematical, Physical and Engineering Sciences*, vol. 473, no. 2197, p. 20160738, 2017.

[93] J. Dobson, A. Tweedie, G. Harvey, R. OLeary, A. Mulholland, K. Tant, and A. Gachagan, "Finite element analysis simulations for ultrasonic array NDE inspections," in *AIP Conference Proceedings*, vol. 1706, p. 040005, AIP Publishing, 2016.

[94] J. Zhang, B. W. Drinkwater, and P. D. Wilcox, "Defect characterization using an ultrasonic array to measure the scattering coefficient matrix," *IEEE Transactions on Ultrasonics, Ferroelectrics, and Frequency Control*, vol. 55, no. 10, pp. 2254–2265, 2008.

[95] S. Bannouf, D. Elbaz, B. Chassignole, N. Leymarie, and P. Recolin, "Validation of simulation tools for ultrasonic inspection of austenitic welds in the framework of the MOSAICS project," in *Proceedings of 11th European Conference on Non-Destructive Testing (ECNDT 2014)*, 2014.

[96] H. Taheri, L. Koester, T. Bigelow, and L. J. Bond, "Finite element simulation and experimental verification of ultrasonic non-destructive inspection of defects in additively manufactured materials," in *AIP Conference Proceedings*, vol. 1949, p. 020011, AIP Publishing, 2018.

[97] C. Boller, D. R. Mahapatra, R. Sridaran Venkat, N. B. Ravi, N. Chakraborty, R. Shivamurthy, and K. M. Simon, "Integration of non-destructive evaluation-based ultrasonic simulation: A means for simulation in structural health monitoring," *Structural Health Monitoring*, vol. 16, no. 5, pp. 611–629, 2017.

[98] Y. Liu, S. Mukherjee, N. Nishimura, M. Schanz, W. Ye, A. Sutradhar, E. Pan, N. Dumont, A. Frangi, and A. Saez, "Recent advances and emerging applications of the boundary element method," *Applied Mechanics Reviews*, vol. 64, no. 3, p. 030802, 2011.

[99] D. E. Beskos, "Boundary element methods in dynamic analysis," *Applied Mechanics Reviews*, vol. 40, no. 1, pp. 1–23, 1987.

[100] D. E. Beskos, "Boundary element methods in dynamic analysis: Part II (1986-1996)," *Applied Mechanics Reviews*, vol. 50, no. 3, pp. 149–197, 1997.

[101] Y. Niwa, S. Hirose, and M. Kitahara, "Application of the boundary integral equation (BIE) method to transient response analysis of inclusions in a half space," *Wave Motion*, vol. 8, no. 1, pp. 77–91, 1986.

[102] D. Budreck and J. Achenbach, "Scattering from three-dimensional planar cracks by the boundary integral equation method," *Journal of Applied Mechanics*, vol. 55, no. 2, pp. 405–412, 1988.

[103] P. Schafbuch, F. Rizzo, and R. Thompson, "Boundary element method solutions for elastic wave scattering in 3D," *International Journal for Numerical Methods in Engineering*, vol. 36, no. 3, pp. 437–455, 1993.

[104] Y. Cho and J. L. Rose, "A boundary element solution for a mode conversion study on the edge reflection of lamb waves," *The Journal of the Acoustical Society of America*, vol. 99, no. 4, pp. 2097–2109, 1996.

[105] Y. Cho and J. L. Rose, "An elastodynamic hybrid boundary element study for elastic guided wave interactions with a surface breaking defect," *International Journal of Solids and Structures*, vol. 37, no. 30, pp. 4103–4124, 2000.

[106] J. Rose, S. Pelts, and Y. Cho, "Modeling for flaw sizing potential with guided waves," *Journal of Nondestructive Evaluation*, vol. 19, no. 2, pp. 55–66, 2000.

[107] J. L. Rose *et al.*, "Boundary element modeling for defect characterization potential in a wave guide," *International Journal of Solids and Structures*, vol. 40, no. 11, pp. 2645–2658, 2003.

[108] G. Rus, S.-C. Wooh, and R. Gallego, "QNDE using complete frequency information from ultrasound," *WIT Transactions on Modelling and Simulation*, vol. 37, 2004.

[109] G. Rus, S.-Y. Lee, and R. Gallego, "Defect identification in laminated composite structures by BEM from incomplete static data," *International Journal of Solids and Structures*, vol. 42, no. 5-6, pp. 1743–1758, 2005.

[110] T. Maruyama, T. Saitoh, and S. Hirose, "Simulation for air-coupled ultrasound testing using time-domain BEM," in *AIP Conference Proceedings*, vol. 1581, pp. 550–555, AIP, 2014.

[111] S. Chaillat, M. Bonnet, and J.-F. Semblat, "A multi-level fast multipole BEM for 3-d elastodynamics in the frequency domain," *Computer Methods in Applied Mechanics and Engineering*, vol. 197, no. 49-50, pp. 4233–4249, 2008.

[112] F. Bu, J. Lin, and F. Reitich, "A fast and high-order method for the three-dimensional elastic wave scattering problem," *Journal of Computational Physics*, vol. 258, pp. 856–870, 2014.

[113] S. Chaillat, M. Darbas, and F. Le Louër, "Fast iterative boundary element methods for high-frequency scattering problems in 3d elastodynamics," *Journal of Computational Physics*, vol. 341, pp. 429–446, 2017.

[114] K. Chen, S. Yang, J. Song, and R. Roberts, "High order nystrom method for acoustic scattering," in *41st Annual Review of Progress in Quantitative Nondestructive Evaluation* (D. E. Chimenti and L. J. Bond, eds.), vol. 1650, pp. 1744–1749, American Institute of Physics, Melville, NY, 2015.

[115] K. Chen, P. Gurrala, J. Song, and R. Roberts, "High order nyström method for elastodynamic scattering," in *42nd Annual Review of Progress in Quantitative Nondestructive Evaluation* (D. E. Chimenti and L. J. Bond, eds.), vol. 1706, p. 050003, American Institute of Physics, Melville, NY, 2016.

[116] S. J. Song, J. S. Park, Y. H. Choi, S. C. Kang, and K. J. Kim, "Model predictions to the 2004 ultrasonic benchmark problems," in *Review of Progress in Quantitative Nondestructive Evaluation* (D. O. Thompson and D. E. Chimenti, eds.), vol. 760, pp. 1872–1879, American Institute of Physics, Melville, NY, 2005.

[117] H. J. Kim, S. J. Song, and J. S. Park, "Model predictions to the 2005 ultrasonic benchmark problems," in *Review of Progress in Quantitative Nondestructive Evaluation* (D. O. Thompson and D. E. Chimenti, eds.), vol. 820, pp. 1836–1843, American Institute of Physics, Melville, NY, 2006.

[118] L. W. Schmerr Jr., T. A. Gray, A. Lopez Sanchez, and R. Huang, "Simulating the experiments of the 2005 ultrasonic benchmark study," in *Review of Progress in Quantitative Nondestructive Evaluation* (D. O. Thompson and D. E. Chimenti, eds.), vol. 820, pp. 1813–1819, American Institute of Physics, Melville, NY, 2006.

[119] G. Toullelan, R. Raillon, S. Chatillon, and S. Lonne, "Results of the 2013 UT modeling benchmark obtained with models implemented in CIVA," in *40th Annual Review of Progress in Quantitative Nondestructive Evaluation* (D. O. Thompson, L. J. Bond and D. E. Chimenti, ed.), vol. 1581, pp. 2093–2100, American Institute of Physics, Melville, NY, 2014.

[120] J. K. Ness, *Efficient inversion of Fourier and Laplace domain boundary element solutions for elastodynamic scattering*. PhD thesis, Iowa State University, 1994.

[121] https://www.wfndec.org/benchmark-problems/. [Last accessed 11-August-2019].

[122] J. J. Wen and M. Breazeale, "Computer optimization of the Gaussian beam description of an ultrasonic field," *Computational Acoustics*, vol. 2, p. 181, 1990.

[123] L. W. Schmerr Jr. and A. Sedov, "Mechanical reciprocity principles and ultrasonic measurement models," in *Review of Progress in Quantitative Nondestructive Evaluation*, pp. 65–71, Springer, 1996.

[124] P. H. Rogers and A. L. Van Buren, "An exact expression for the lommel-diffraction correction integral," *The Journal of the Acoustical Society of America*, vol. 55, no. 4, pp. 724–728, 1974.

[125] J. R. Pettit, *Modelling the ultrasonic response from rough defects using efficient finite element modelling techniques*. PhD thesis, Imperial College London, 2014.

[126] R. Huang, L. W. Schmerr Jr., A. Sedov, and T. A. Gray, "Kirchhoff approximation revisitedsome new results for scattering in isotropic and anisotropic elastic solids," *Research in Nondestructive Evaluation*, vol. 17, no. 3, pp. 137–160, 2006.

[127] H. Zhang and L. Bond, "Ultrasonic scattering by spherical voids," *Ultrasonics*, vol. 27, no. 2, pp. 116–119, 1989.

[128] "MATLAB online documentation." https://www.mathworks.com/help/signal/ref/envelope.html, 2020. [Online; accessed 18-March-2020].

[129] T. J. Eason, *Ultrasonic thickness structural health monitoring of steel pipe for internal corrosion*. PhD thesis, Iowa State University, 2017.

[130] C.-P. Chiou and L. W. Schmerr Jr., "New approaches to model-based ultrasonic flaw sizing," *The Journal of the Acoustical Society of America*, vol. 92, no. 1, pp. 435–444, 1992.

[131] S. Ayter and B. A. Auld, "Elastic wave scattering from rough surfaces and cracks," in *Review of Progress in Quantitative Nondestructive Evaluation*, pp. 611–624, Springer, 1983.

[132] T. A. Gray, R. B. Thompson, and B. Newberry, "Improvements in ultrasonic measurement modeling with applications to ultrasonic reliability," in *Review of Progress in Quantitative Nondestructive Evaluation*, pp. 11–17, Springer, 1985.

[133] https://web.archive.org/web/20200309000033/https://www.buehler.com/assets/SDS/US/1339940_A_TransOptic_EN.PDF. [Last accessed 08-March-2020].

[134] J. Gubernatis, E. Domany, J. Krumhansl, and M. Huberman, "The Born approximation in the theory of the scattering of elastic waves by flaws," *Journal of Applied Physics*, vol. 48, no. 7, pp. 2812–2819, 1977.

[135] A. Peterson and M. Bibby, *An Introduction to the Locally-Corrected Nystrom Method*. Morgan & Claypool, 2009.

[136] T. J. Hughes, J. A. Cottrell, and Y. Bazilevs, "Isogeometric analysis: CAD, finite elements, NURBS, exact geometry and mesh refinement," *Computer Methods in Applied Mechanics and Engineering*, vol. 194, no. 39-41, pp. 4135–4195, 2005.

[137] M. S. Tong and W. C. Chew, "Nyström method for elastic wave scattering by three-dimensional obstacles," *Journal of Computational Physics*, vol. 226, no. 2, pp. 1845–1858, 2007.

[138] F. Rizzo, D. Shippy, and M. Rezayat, "A boundary integral equation method for radiation and scattering of elastic waves in three dimensions," *International Journal for Numerical Methods in Engineering*, vol. 21, no. 1, pp. 115–129, 1985.

[139] Y. Liu and F. Rizzo, "Hypersingular boundary integral equations for radiation and scattering of elastic waves in three dimensions," *Computer Methods in Applied Mechanics and Engineering*, vol. 107, no. 1-2, pp. 131–144, 1993.

[140] Y. Liu and F. J. Rizzo, "Scattering of elastic waves from thin shapes in three dimensions using the composite boundary integral equation formulation," *The Journal of the Acoustical Society of America*, vol. 102, no. 2, pp. 926–932, 1997.

[141] P. J. Schafbuch, *Application of the boundary element method to elastic wave scattering problems in ultrasonic nondestructive evaluation*. PhD thesis, Iowa State University, 1991.

[142] G. Krishnasamy, F. Rizzo, T. Rudolphi, *et al.*, "Hypersingular boundary integral equations: their occurrence, interpretation, regularization and computation," *Developments in Boundary Element Methods*, vol. 7, pp. 207–252, 1991.

[143] G. Krishnasamy, L. W. Schmerr, T. J. Rudolphi, and F. J. Rizzo, "Hypersingular Boundary Integral Equations: Some Applications in Acoustic and Elastic Wave Scattering," *Journal of Applied Mechanics*, vol. 57, no. 2, pp. 404–414, 1990.

[144] O. P. Bruno and L. A. Kunyansky, "A fast, high-order algorithm for the solution of surface scattering problems: basic implementation, tests, and applications," *Journal of Computational Physics*, vol. 169, no. 1, pp. 80–110, 2001.

[145] Z. Liu, F. Wu, and D. Wang, "The multi-domain FMM-IBEM to model elastic wave scattering by three-dimensional inclusions in infinite domain," *Engineering Analysis with Boundary Elements*, vol. 60, pp. 95–105, 2015.

[146] Z. Liu, D. Wang, J. Liang, F. Wu, and C. Wu, "The fast multi-pole indirect bem for solving high-frequency seismic wave scattering by three-dimensional superficial irregularities," *Engineering Analysis with Boundary Elements*, vol. 90, pp. 86–99, 2018.

[147] Y.-H. Pao and V. Varatharajulu, "Huygens principle, radiation conditions, and integral formulas for the scattering of elastic waves," *The Journal of the Acoustical Society of America*, vol. 59, no. 6, pp. 1361–1371, 1976.

[148] W. C. Chew, M. S. Tong, and B. Hu, "Integral equation methods for electromagnetic and elastic waves," *Synthesis Lectures on Computational Electromagnetics*, vol. 3, no. 1, pp. 1–241, 2008.

[149] P. M. Morse, H. Feshbach, and H. Feshbach, *Methods of theoretical physics*. New York: McGraw-Hill, 1953.

[150] C. A. Balanis, *Antenna theory: analysis and design*. John Wiley & Sons, 3rd ed., 2011.

[151] J. Bramble, J. Pasciak, and D. Trenev, "Analysis of a finite PML approximation to the three dimensional elastic wave scattering problem," *Mathematics of Computation*, vol. 79, no. 272, pp. 2079–2101, 2010.

[152] V. D. Kupradze, "Dynamical problems in elasticity," *Progress in Solid Mechanics*, vol. 3, pp. 1–259, 1963.

[153] V. Kupradze, T. Gegelia, M. Basheleishvili, and T. V. Burchuladze, *Three-dimensional problems of the mathematical theory of elasticity and thermoelasticity*. North-Holland Publishing Company, 1979.

[154] P. Martin, "On the scattering of elastic waves by an elastic inclusion in two dimensions," *The Quarterly Journal of Mechanics and Applied Mathematics*, vol. 43, no. 3, pp. 275–291, 1990.

[155] V. D. Kupradze, *Potential methods in the theory of elasticity*. (Translated from Russian by H. Gutfreund and I. Meroz). Israel Program for Scientific Translations, 1965.

[156] P. Hahner and G. C. Hsiao, "Uniqueness theorems in inverse obstacle scattering of elastic waves," *Inverse Problems*, vol. 9, no. 5, p. 525, 1993.

[157] J. H. Bramble and J. E. Pasciak, "A note on the existence and uniqueness of solutions of frequency domain elastic wave problems: A priori estimates in H1," *Journal of Mathematical Analysis and Applications*, vol. 345, no. 1, pp. 396–404, 2008.

[158] A. Eringen and E. Suhubi, *Elastodynamics, Volume II: Linear Theory*. Academic Press, New York, 1975.

[159] J. Domınguez and M. Ariza, "A direct traction BIE approach for three-dimensional crack problems," *Engineering Analysis with Boundary Elements*, vol. 24, no. 10, pp. 727–738, 2000.

[160] G. Krishnasamy, F. J. Rizzo, and Y. Liu, "Boundary integral equations for thin bodies," *International Journal for Numerical Methods in Engineering*, vol. 37, no. 1, pp. 107–121, 1994.

[161] D. Dunavant, "High degree efficient symmetrical Gaussian quadrature rules for the triangle," *International Journal for Numerical Methods in Engineering*, vol. 21, no. 6, pp. 1129–1148, 1985.

[162] M. Guiggiani, G. Krishnasamy, T. J. Rudolphi, and F. Rizzo, "A general algorithm for the numerical solution of hypersingular boundary integral equations," *Journal of Applied Mechanics*, vol. 59, no. 3, pp. 604–614, 1992.

[163] J. Rong, L. Wen, and J. Xiao, "An efficient method for evaluating BEM singular integrals on curved elements with application in acoustic analysis," *arXiv preprint arXiv:1306.0282*, 2013.

[164] M. M. Botha, "Evaluation of near-singularity cancellation quadrature schemes for the Green function gradient on higher-order triangles," in *2015 9th European Conference on Antennas and Propagation (EuCAP)*, pp. 1–4, IEEE, 2015.

[165] P. Fink, D. Wilton, and M. Khayat, "New method for handling near-hypersingular integrals in BEM formulations," in *2007 International Conference on Electromagnetics in Advanced Applications*, pp. 978–981, IEEE, 2007.

[166] S. Chaillat, *Fast Multipole Method for 3-D elastodynamic boundary integral equations. Application to seismic wave propagation*. PhD thesis, École des Ponts ParisTech, 2008.

[167] Y. Mi and M. Aliabadi, "Dual boundary element method for three-dimensional fracture mechanics analysis," *Engineering Analysis with Boundary Elements*, vol. 10, no. 2, pp. 161–171, 1992.

[168] Y. Liu, D. Zhang, and F. J. Rizzo, "Nearly singular and hypersingular integrals in the boundary element method," *WIT Transactions on Modelling and Simulation*, vol. 1, pp. 453–468, 1993.

[169] A. Mal, "Interaction of elastic waves with a penny-shaped crack," *International Journal of Engineering Science*, vol. 8, no. 5, pp. 381–388, 1970.

[170] P. Martin and G. Wickham, "Diffraction of elastic waves by a penny-shaped crack: analytical and numerical results," *Proc. R. Soc. Lond. A*, vol. 390, no. 1798, pp. 91–129, 1983.

[171] P. Barratt and W. Collins, "The scattering cross-section of an obstacle in an elastic solid for plane harmonic waves," in *Mathematical Proceedings of the Cambridge Philosophical Society*, vol. 61, pp. 969–981, Cambridge University Press, 1965.

[172] H. Fujiwara, "The fast multipole method for solving integral equations of three-dimensional topography and basin problems," *Geophysical Journal International*, vol. 140, no. 1, pp. 198–210, 2000.

[173] K. Yoshida, N. Nishimura, and S. Kobayashi, "Analysis of three dimensional scattering of elastic waves by a crack with fast multipole boundary integral equation method," *Journal of Applied Mechanics*, vol. 3, pp. 143–150, 2000.

[174] K. Yoshida, *Applications of fast multipole method to boundary integral equation method*. PhD thesis, 2001.

[175] K. Yoshida, N. Nishimura, and S. Kobayashi, "Application of a diagonal form fast multipole BIEM to the analysis of three dimensional scattering of elastic waves by cracks," *Trans. JASCOME*, vol. 18, pp. 77–80, 2001.

[176] J. A. Sanz, M. Bonnet, and J. Dominguez, "Fast multipole method applied to 3-D frequency domain elastodynamics," *Engineering Analysis with Boundary Elements*, vol. 32, no. 10, pp. 787–795, 2008.

[177] Z. Yan, J. Zhang, and W. Ye, "Rapid solution of 3-D oscillatory elastodynamics using the pFFT accelerated BEM," *Engineering Analysis with Boundary Elements*, vol. 34, no. 11, pp. 956–962, 2010.

[178] J. Phillips and J. White, "A precorrected-FFT method for capacitance extraction of complicated 3-D structures," in *ICCAD*, vol. 94, pp. 268–271, Citeseer, 1994.

[179] H. Isakari, *Periodic FMMs and Calderon's preconditioning in acoustics and elastodynamics*. PhD thesis, Kyoto University, 2012.

[180] S. Chaillat, L. Desiderio, and P. Ciarlet, "Theory and implementation of H-matrix based iterative and direct solvers for helmholtz and elastodynamic oscillatory kernels," *Journal of Computational Physics*, vol. 351, pp. 165–186, 2017.

[181] L. Desiderio, *H-matrix based Solver for 3D Elastodynamics Boundary Integral Equations*. PhD thesis, University of Paris-Saclay, 2017.

[182] M. Darbas and F. Le Louër, "Well-conditioned boundary integral formulations for high-frequency elastic scattering problems in three dimensions," *Mathematical Methods in the Applied Sciences*, vol. 38, no. 9, pp. 1705–1733, 2015.

[183] O. P. Bruno and T. Yin, "Regularized integral equation methods for elastic scattering problems in three dimensions," *Journal of Computational Physics*, p. 109350, 2020.

[184] S. Chaillat, M. Darbas, and F. Le Louër, "Analytical preconditioners for Neumann elastodynamic boundary element methods." preprint, HAL ID: hal-02512652, Mar. 2020.

[185] W. C. Chew, E. Michielssen, J. Song, and J.-M. Jin, "Fast and efficient algorithms in computational electromagnetics," *Artech House Inc., Norwood, MA*, 2001.

[186] M. Kachanovska, "Hierarchical matrices and the high-frequency fast multipole method for the helmholtz equation with decay," Tech. Rep. 13, Max-Planck-Institut für Mathematik in den Naturwissenschaften, Leipzig (Germany), 2014.

[187] C. Oliveira and J. Buescu, "Integral identities derived from the complex Funk-Hecke formula," *arXiv preprint, arXiv:1404.1030*, 2014.

[188] S. Koc, J. Song, and W. C. Chew, "Error analysis for the numerical evaluation of the diagonal forms of the scalar spherical addition theorem," *SIAM Journal on Numerical Analysis*, vol. 36, no. 3, pp. 906–921, 1999.

[189] R. Barrett, M. W. Berry, T. F. Chan, J. Demmel, J. Donato, J. Dongarra, V. Eijkhout, R. Pozo, C. Romine, and H. Van der Vorst, *Templates for the solution of linear systems: building blocks for iterative methods*, vol. 43. Philadelphia, PA: SIAM, 1994.

[190] P. Martin, "Identification of irregular frequencies in simple direct integral-equation methods for scattering by homogeneous inclusions," *Wave Motion*, vol. 13, no. 2, pp. 185–192, 1991.

[191] S. Amini and P. Harris, "A comparison between various boundary integral formulations of the exterior acoustic problem," *Computer Methods in Applied Mechanics and Engineering*, vol. 84, no. 1, pp. 59–75, 1990.

[192] A. F. Peterson, "The "interior resonance problem associated with surface integral equations of electromagnetics: Numerical consequences and a survey of remedies," *Electromagnetics*, vol. 10, no. 3, pp. 293–312, 1990.

[193] S. M. Rao and D. R. Wilton, "E-field, H-field, and combined field solution for arbitrarily shaped three-dimensional dielectric bodies," *Electromagnetics*, vol. 10, no. 4, pp. 407–421, 1990.

[194] A. Burton and G. Miller, "The application of integral equation methods to the numerical solution of some exterior boundary-value problems," *Proceedings of the Royal Society of London. A. Mathematical and Physical Sciences*, vol. 323, no. 1553, pp. 201–210, 1971.

[195] C.-J. Zheng, H.-B. Chen, H.-F. Gao, and L. Du, "Is the Burton-Miller formulation really free of fictitious eigenfrequencies?," *Engineering Analysis with Boundary Elements*, vol. 59, pp. 43–51, 2015.

[196] M. M. Botha, "Numerical integration scheme for the near-singular Green function gradient on general triangles," *IEEE Transactions on Antennas and Propagation*, vol. 63, no. 10, pp. 4435–4445, 2015.

[197] F. Amlani, S. Chaillat, and A. Loseille, "An efficient preconditioner for adaptive fast multipole accelerated boundary element methods to model time-harmonic 3D wave propagation," *Computer Methods in Applied Mechanics and Engineering*, vol. 352, pp. 189–210, 2019.

[198] X. Du, L. Leifsson, W. Meeker, P. Gurrala, J. Song, and R. Roberts, "Efficient model-assisted probability of detection and sensitivity analysis for ultrasonic testing simulations using stochastic metamodeling," *Journal of Nondestructive Evaluation, Diagnostics and Prognostics of Engineering Systems*, vol. 2, no. 4, 2019. 041002 (13 pages).

[199] X. Du, P. Gurrala, L. Leifsson, J. Song, W. Meeker, R. Roberts, S. Koziel, and Y. Tesfahunegn, "Stochastic-expansions-based model-assisted probability of detection analysis of the spherically-void-defect benchmark problem," in *International Conference on Computational Science*, pp. 593–603, Springer, 2018.

[200] X. Du and L. Leifsson, "Multifidelity model-assisted probability of detection via Cokriging," *NDT & E International*, vol. 108, 2019. 102156.

[201] F. Rizzo and D. Shippy, "An advanced boundary integral equation method for three-dimensional thermoelasticity," *International Journal for Numerical Methods in Engineering*, vol. 11, no. 11, pp. 1753–1768, 1977.

[202] Wolfram Research, Inc., "Mathematica, Version 10.4.1.0." Champaign, IL, 2016.

[203] I. Gradshteyn and I. Ryzhik, *Table of Integrals, Series, and Products*. San Diego: Academic Press, sixth ed., 2000.

# APPENDIX A. KIRCHHOFF APPROXIMATION FORMULAS FOR SPHERICAL SCATTERER

With reference to Figure A.1, define the following quantities:

$$\tilde{\mathbf{e}}^{\beta} = \mathbf{e}_i^{\beta}, \tag{A.1a}$$

$$\mathbf{e}^{\beta} = \mathbf{e}_s^{\beta}, \tag{A.1b}$$

$$\dot{\mathbf{e}}^{\beta} = \mathbf{e}_r^{\beta}, \tag{A.1c}$$

$$\tilde{\mathbf{d}}^{\beta} = \mathbf{d}_i^{\beta}, \tag{A.1d}$$

$$\mathbf{d}^{\beta} = \mathbf{d}_s^{\beta}, \tag{A.1e}$$

$$\dot{\mathbf{d}}^{\beta} = \mathbf{d}_r^{\beta} \tag{A.1f}$$

for $\beta = P, SV, SH$. The scattering amplitude of longitudinal wave incidence is [13, §10.4.1]

$$A_n^{P;\beta}(\tilde{\mathbf{e}}^{\beta}, \mathbf{e}^{P}) = \frac{i\omega e_n^P e_l^P C_{lkpj}}{4\pi\rho c_1^2} \int_{S_{\text{lit}}} D_{pjk}^{P;\beta} e^{(ik_\beta \tilde{\mathbf{e}}^{\beta} - ik_1 \mathbf{e}^{P})\cdot \mathbf{x}_s} dS(\mathbf{x}_s), \tag{A.2}$$

where

$$D_{pjk}^{P;\beta} = \frac{\tilde{d}_p^{\beta} \tilde{e}_j^{\beta} n_k}{c_\beta} + \frac{e_k^P \tilde{d}_j^{\beta} n_p}{c_p} + \sum_{m=P,SV,SH} R_{12}^{m;\beta} \left( \frac{\dot{d}_p^m \dot{e}_j^m n_k}{c_m} + \frac{e_k^P \dot{d}_j^m n_p}{c_p} \right). \tag{A.3}$$

Here, $R_{12}^{m;\beta}$ represents the reflection coefficient calculated by assuming that the scattering surface is an infinite plane that coincides with the tangent plane at the point where the incident ray strikes the scatterer. For a linear elastic solid with Lamé parameters $\lambda$ and $\mu$, we have

$$C_{lkpj} = \lambda \delta_{lk} \delta_{pj} + \mu(\delta_{lp}\delta_{kj} + \delta_{lj}\delta_{kp}). \tag{A.4}$$

Therefore,

$$A_n^{P;P}(\tilde{\mathbf{e}}^{P}, \mathbf{e}^{P}) = \frac{-i\omega e_n^P e_l^P \left[\lambda \delta_{lk}\delta_{pj} + \mu(\delta_{lp}\delta_{kj} + \delta_{lj}\delta_{kp})\right]}{4\pi\rho c_1^2} \int_{S_{lit}} D_{pjk}^{P;P} e^{(ik_P \tilde{\mathbf{e}}^{P} - ik_1 \mathbf{e}^{P})\cdot \mathbf{x}_s} dS(\mathbf{x}_s) \tag{A.5}$$

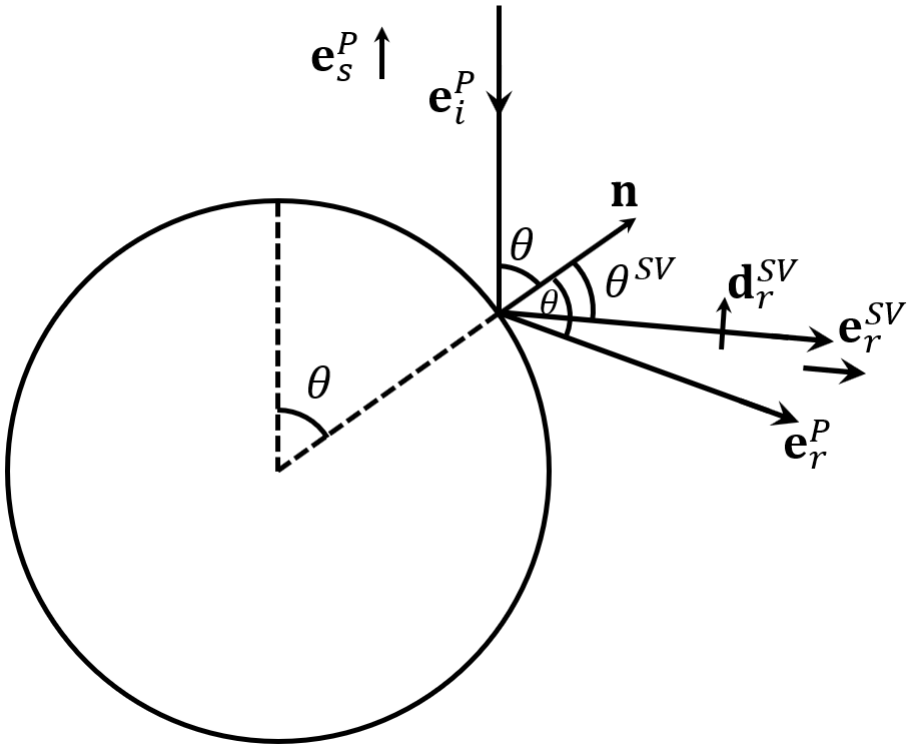


Figure A.1: KA for scattering from a sphere.

$$= \frac{-i\omega e_n^P}{4\pi\rho c_1^2}\int_{S_{lit}} \left(\lambda e_l^P D_{ppl}^{P;P} + \mu e_l^P D_{lkk}^{P;P} + \mu e_l^P D_{klk}^{P;P}\right) e^{(ik_P\tilde{\mathbf{e}}^P - ik_1\mathbf{e}^P)\cdot\mathbf{x}_s} dS(\mathbf{x}_s), \quad \text{(A.6)}$$

$$D_{pjk}^{P;P} = \frac{1}{c_p}\left(\tilde{e}_p^P\tilde{e}_j^P n_k - e_k^P\tilde{e}_j^P n_p + R_{12}^{P;P}\dot{e}_p^P\dot{e}_j^P n_k + R_{12}^{P;P} n_p\dot{e}_j^P e_k^P\right) + R_{12}^{SV;P}\left(\frac{\dot{d}_p^{SV}\dot{e}_j^{SV} n_k}{c_s} + \frac{n_p\dot{d}_j^{SV} e_k^P}{c_p}\right), \quad \text{(A.7)}$$

$$\begin{aligned} D_{ppl}^{P;P} &= \frac{1}{c_p}\left(n_l - e_l^P\cos\theta + R_{12}^{P;P} n_l + e_l^P\cos\theta R_{12}^{P;P}\right) + \frac{R_{12}^{SV;P} e_l^P\sin\theta^{SV}}{c_p} \\ &= \frac{1}{c_p}\left[n_l\left(1 + R_{12}^{P;P}\right) - e_l^P\cos\theta\left(1 - R_{12}^{P;P}\right) + R_{12}^{SV;P} e_l^P\sin\theta^{SV}\right], \end{aligned} \quad \text{(A.8)}$$

$$\begin{aligned} D_{lkk}^{P;P} &= \frac{1}{c_p}\left(-\tilde{e}_l^P\cos\theta - n_l + R_{12}^{P;P}\dot{e}_l\cos\theta + R_{12}^{P;P} n_l\cos 2\theta\right) \\ &\quad + R_{12}^{SV;P}\left(\frac{\dot{d}_l^{SV}\cos\theta^{SV}}{c_s} + \frac{n_l\sin(\theta+\theta^{SV})}{c_p}\right) \\ &= \frac{1}{c_p}\left[-\tilde{e}_l^P\cos\theta - n_l\left(1 - R_{12}^{P;P}\cos 2\theta\right) + R_{12}^{P;P}\dot{e}_l\cos\theta + R_{12}^{SV;P} n_l\sin(\theta+\theta^{SV})\right] \\ &\quad + \frac{R_{12}^{SV;P}\dot{d}_l^{SV}\cos\theta^{SV}}{c_s}, \end{aligned} \quad \text{(A.9)}$$

$$\begin{aligned} D_{klk}^{P;P} &= \frac{R_{12}^{P;P}}{c_p}\left(\dot{e}_l\cos\theta + \dot{e}_l\cos\theta\right) + R_{12}^{SV;P}\left(\frac{\dot{e}_l^{SV}\sin\theta^{SV}}{c_s} + \frac{\dot{d}_l^{SV}\cos\theta}{c_p}\right) \\ &= \frac{2R_{12}^{P;P}\dot{e}_l\cos\theta}{c_p} + R_{12}^{SV;P}\left(\frac{\dot{e}_l^{SV}\sin\theta^{SV}}{c_s} + \frac{\dot{d}_l^{SV}\cos\theta}{c_p}\right). \end{aligned} \quad \text{(A.10)}$$

# APPENDIX B. EVALUATION OF LIMITS IN THE DERIVATIONS OF INTEGRAL REPRESENTATION AND CBIE

Section B.1 contains a derivation of some limits in Equation (4.22). Section B.2 discusses the convergence of CPV integrals encountered in Section 4.2.6. Section B.3 discusses contintuity requirements of the displacement fields in the HBIE formulation. Section B.4 proves the limit in Equation (4.63b), which appears in the derivation of the CBIE via the limit-to-the-boundary approach (Section 4.2.9).

## B.1 Limits in the Derivation of Integral Representation

With reference to Figure 4.1 and Equation (4.22), we are interested in the following limits:

$$I_1 = \lim_{\epsilon \to 0} \int_{S_\epsilon} \mathbf{u}(\mathbf{x}) \cdot \left[ \hat{\mathbf{n}}(\mathbf{x}) \cdot \overline{\overline{\mathbf{\Sigma}}}^{(1)}(\mathbf{x}, \mathbf{x}') \right] dS(\mathbf{x}), \tag{B.1}$$

$$I_2 = \lim_{\epsilon \to 0} \int_{S_\epsilon} \mathbf{t}(\mathbf{x}) \cdot \overline{\mathbf{G}}(\mathbf{x}, \mathbf{x}') \; dS(\mathbf{x}). \tag{B.2}$$

To derive these limits, we will use the expressions in Equations (4.18) and (4.24) for kernels $\overline{\mathbf{G}}(\mathbf{x}, \mathbf{x}')$ and $\overline{\overline{\mathbf{\Sigma}}}^{(1)}(\mathbf{x}, \mathbf{x}')$, respectively, noting that the following limits hold true [30, §4.1] as $R \to 0$:

$$C = \frac{1}{2}(k_s^2 - k_p^2)R^2 + O(R^4), \tag{B.3a}$$

$$D = \frac{1}{2}(k_s^2 + k_p^2)R^2 + O(R^3), \tag{B.3b}$$

$$F = \frac{3}{2}(k_p^2 - k_s^2)R^2 + O(R^4), \tag{B.3c}$$

$$\lambda\psi_p + 2\mu C = \mu k_p^2 R^2 + O(R^4), \tag{B.3d}$$

$$\psi_s + 2C = -k_p^2 R^2 + O(R^4). \tag{B.3e}$$

According to the above limits, the vector magnitude of the integrand of $I_2$ varies as $1/R$ as $\epsilon$ goes to zero. Since $dS(\mathbf{x})$ varies as $R^2$, the integral $I_2$ evaluates to zero.

To evaluate $I_1$, note that $\hat{\mathbf{n}}(\mathbf{x}) = \hat{\mathbf{R}}$ for $\mathbf{x} \in S_\epsilon$. Using the (4.24) and (B.3), we have

$$I_1 = -\lim_{\epsilon\to 0}\int_{S_\epsilon} \mathbf{u}(\mathbf{x}) \cdot \left[\frac{\mu k_p^2 \hat{\mathbf{R}}\hat{\mathbf{R}} - \mu k_p^2\left(\hat{\mathbf{R}}\hat{\mathbf{R}} + \bar{\mathbf{I}}\right) + 3\mu(k_p^2 - k_s^2)\hat{\mathbf{R}}\hat{\mathbf{R}}}{4\pi\rho\omega^2 R^2}\right] dS(\mathbf{x}), \tag{B.4a}$$

$$= \lim_{\epsilon\to 0}\int_{S_\epsilon} \mathbf{u}(\mathbf{x}) \cdot \left[\frac{k_p^2\bar{\mathbf{I}} - 3(k_p^2 - k_s^2)\hat{\mathbf{R}}\hat{\mathbf{R}}}{4\pi\rho\omega^2}\right] \mu \sin\theta \, d\theta d\phi, \tag{B.4b}$$

where we assume polar coordinates centered at $\mathbf{x}'$ in the last step. Integral $I_1$ further reduces to

$$I_1 = \lim_{\epsilon\to 0}\int_{S_\epsilon} \left[\frac{k_p^2\mathbf{u}(\mathbf{x}) - 3(k_p^2 - k_s^2)\left(\hat{\mathbf{R}}\cdot\mathbf{u}(\mathbf{x})\right)\hat{\mathbf{R}}}{4\pi\rho\omega^2}\right] \mu \sin\theta \, d\theta d\phi, \tag{B.5}$$

Assuming that $\mathbf{u}(\mathbf{x})$ is Hölder continuous in a neighborhood of $\mathbf{x}$, the limits of the two terms in the integrand can be shown to exist independently, as detailed below. Consider the first term:

$$\lim_{\epsilon\to 0}\int_{S_\epsilon} \frac{\mu k_p^2 \sin\theta}{4\pi\rho\omega^2}\mathbf{u}(\mathbf{x}) \, d\theta d\phi = \lim_{\epsilon\to 0}\int_{S_\epsilon} \frac{\mu k_p^2 \sin\theta}{4\pi\rho\omega^2}\left[\mathbf{u}(\mathbf{x}) - \mathbf{u}(\mathbf{x}') + \mathbf{u}(\mathbf{x}')\right] \, d\theta d\phi. \tag{B.6}$$

By the assumption of Hölder continuity, there exist $C$, $\alpha \in \mathbb{R}$ ($C$, $\alpha > 0$) such that $|\mathbf{u}(\mathbf{x}) - \mathbf{u}(\mathbf{x}')| < CR^\alpha$. Therefore,

$$\lim_{\epsilon\to 0}\int_{S_\epsilon} \frac{\mu k_p^2 \sin\theta}{4\pi\rho\omega^2}\left[\mathbf{u}(\mathbf{x}) - \mathbf{u}(\mathbf{x}')\right] \, d\theta d\phi = 0, \tag{B.7}$$

and (B.6) reduces to

$$\lim_{\epsilon\to 0}\int_{S_\epsilon} \frac{\mu k_p^2 \sin\theta}{4\pi\rho\omega^2}\mathbf{u}(\mathbf{x}) \, d\theta d\phi = \lim_{\epsilon\to 0}\int_{S_\epsilon} \frac{\mu k_p^2 \sin\theta}{4\pi\rho\omega^2}\mathbf{u}(\mathbf{x}') \, d\theta d\phi = \frac{\mu k_p^2 \sin\theta}{\rho\omega^2}\mathbf{u}(\mathbf{x}'). \tag{B.8}$$

Similarly,

$$\lim_{\epsilon\to 0}\int_{S_\epsilon} \frac{-3\mu(k_p^2 - k_s^2)\sin\theta}{4\pi\rho\omega^2}\hat{\mathbf{R}}\hat{\mathbf{R}}\cdot\mathbf{u}(\mathbf{x}) \, d\theta d\phi = \lim_{\epsilon\to 0}\int_{S_\epsilon} \frac{-3\mu(k_p^2 - k_s^2)\sin\theta}{4\pi\rho\omega^2}\hat{\mathbf{R}}\hat{\mathbf{R}}\cdot\mathbf{u}(\mathbf{x}') \, d\theta d\phi. \tag{B.9}$$

Writing $\hat{\mathbf{R}}$ and $\mathbf{u}(\mathbf{x}')$ as their components in the underlying Cartesian coordinate basis, we have

$$\sin\theta\hat{\mathbf{R}}\hat{\mathbf{R}}\cdot\mathbf{u}(\mathbf{x}') = \sin\theta \begin{bmatrix} \sin^2\theta\cos^2\phi & \sin^2\theta\sin\phi\cos\phi & \cos\theta\sin\theta\cos\phi \\ \sin^2\theta\cos\phi\sin\phi & \sin^2\theta\sin^2\phi & \cos\theta\sin\theta\sin\phi \\ \sin\theta\cos\theta\cos\phi & \sin\theta\cos\theta\sin\phi & \cos^2\theta \end{bmatrix} \begin{bmatrix} u_1(\mathbf{x}')\hat{\mathbf{a}}_1 \\ u_2(\mathbf{x}')\hat{\mathbf{a}}_2 \\ u_3(\mathbf{x}')\hat{\mathbf{a}}_3 \end{bmatrix} \tag{B.10}$$

Then, using the following identities

$$\int_0^{2\pi} \sin t \cos t dt = 0, \tag{B.11a}$$

$$\int_0^\pi \sin^3 t dt = \frac{4}{3}, \tag{B.11b}$$

$$\int_0^\pi \sin t \cos^2 t dt = \frac{2}{3}, \tag{B.11c}$$

$$\int_0^\pi \sin^2 t dt = \int_0^\pi \cos^2 t dt = \frac{\pi}{2}, \tag{B.11d}$$

we can the right-hand side of (B.9) as follows:

$$\lim_{\epsilon \to 0} \int_{S_\epsilon} \frac{-3\mu(k_p^2 - k_s^2)\sin\theta}{4\pi\rho\omega^2} \hat{\mathbf{R}}\hat{\mathbf{R}} \cdot \mathbf{u}(\mathbf{x}')\, d\theta d\phi = \frac{-3\mu(k_p^2 - k_s^2)}{4\pi\rho\omega^2} \frac{4\pi}{3} \mathbf{u}(\mathbf{x}') = -\frac{\mu k_p^2}{\rho\omega^2}\mathbf{u}(\mathbf{x}') + \mathbf{u}(\mathbf{x}'). \tag{B.12}$$

In the last step, we have used the fact that $\rho\omega^2/\mu = k_s^2$. From (B.8), (B.12) and (B.5), we get $I_1 = \mathbf{u}(\mathbf{x}')$.

## B.2 Convergence of CPV Integrals

We prove the convergence of the following CPV integral:

$$I = \int\!\!\!\!\!\!-_S \mathbf{u}(\mathbf{x}') \cdot \left[\hat{\mathbf{n}}' \cdot \overline{\overline{\mathbf{\Sigma}}}_+^{(1)}(\mathbf{x}, \mathbf{x}')\right] dS(\mathbf{x}'). \tag{B.13}$$

We assume that the displacement field $\mathbf{u}(\mathbf{x}')$ is Hölder continuous. First, decompose the integration domain into two parts: one including a very small neighborhood of $\mathbf{x}$ and another including the rest of the surface $S$. The latter part is regular since its integration domain is away from the point of singularity. To evaluate the former part, we can transform the integral into polar coordinates defined on the tangent plane at $\mathbf{x}$, with the origin coinciding with $\mathbf{x}$.

Then, the integral can be evaluated in the form shown in Equations (4.117). Note that we need to set the coefficient $F_{-2}(\theta)$ to zero since the kernel in the above integral is not hypersingular. With reference to this equation, we note that the integrand of $I_0$ is regular if $\mathbf{u}(\mathbf{x}')$ is at least Hölder continuous (see equations (C.7) and (C.8)). The integral $I_{-1}$ is also convergent, as shown in (4.119). This proves that all parts resulting from the decomposition of the integration domain, as mentioned above, are convergent, and hence the CPV integral is convergent.

## B.3 Continuity Requirements of Displacement Field in HBIE

Recall that in the HBIE formulation, we construct a Laurent series of the hypersingular integrand to eliminate divergent terms. From Equation (C.14), we notice that this requires the displacement field to have a continuous first derivative on the boundary $S$. Also, an argument similar to the one in Section B.2 suggests that the displacement field needs to be at least $C^{1,\alpha}$ Hölder continuous for the integrand of $I_0$ in (4.117) to be regular.

## B.4 Jump Relation

We are interested in deriving the following limit:

$$\lim_{\mathbf{x}\to\mathbf{y}} \int_S \mathbf{u}(\mathbf{x}') \cdot \left[\hat{\mathbf{n}}' \cdot \overline{\overline{\mathbf{\Sigma}}}_{+}^{(1)}(\mathbf{x},\mathbf{x}')\right] dS(\mathbf{x}') = \fint_S \mathbf{u}(\mathbf{x}') \cdot \left[\hat{\mathbf{n}}' \cdot \overline{\overline{\mathbf{\Sigma}}}_{+}^{(1)}(\mathbf{y},\mathbf{x}')\right] dS(\mathbf{x}') - \frac{\mathbf{u}(\mathbf{y})}{2}. \tag{B.14}$$

Let $\overline{\overline{\mathbf{\Sigma}}}_{\pm s}^{(\alpha)}(\mathbf{x},\mathbf{x}')$ and $\overline{\mathbf{G}}_{\pm s}^{(\alpha)}(\mathbf{x},\mathbf{x}')$ $(\alpha = 1, 2)$ represent the fundamental solutions in the static case $(\omega = 0)$. Using the expressions for the static fundamental solutions in [201], one can prove the following lemma:

**Lemma B.4.1** (Limiting form of static fundamental solution)**.** *As $|\mathbf{x} - \mathbf{x}'| \to 0$, the static and (respective) dynamic fundamental solutions converge to the same expressions.*

**Lemma B.4.2.** *Equations (4.38) and (4.39), which represent the CBIE formulation, and Equation (4.26), which represents the representation formula, hold true even if the dynamic fundamental solutions are replaced with the static ones.*

*Proof.* This result follows from the derivation of the CBIE formulation from Sections 4.2.1 through Section 4.2.6 by setting the frequency $\omega = 0$ and using Lemma B.4.1. □

**Lemma B.4.3** (Rigid translation is a static solution)**.** *A rigid translation given by the displacement field $\mathbf{u}(\mathbf{x}) = \mathbf{u}_0$ for $\mathbf{x} \in \mathbb{R}^3$, where $\mathbf{u}_0$ is a constant vector, is a solution of the elastostatic equations of motion for a infinite elastic solid in the absence of body forces.*

*Proof.* From Equation (4.2), the equation of motion in the static case with no body forces is

$$\nabla \cdot \bar{\boldsymbol{\tau}}(\mathbf{x}, \omega) = 0. \tag{B.15}$$

When $\mathbf{u}(\mathbf{x})$ is constant for all $\mathbf{x} \in \mathbb{R}^3$, the traction field vanishes. Thus, any rigid translation is a solution of the equations of motion. □

As a corollary, the foregoing result holds even when an elastic object is embedded in the solid as long the displacement is continuous at their interface.

**Lemma B.4.4** (Identities of static fundamental solution)**.** *Let $S$ be the surface of an elastic object embedded in an elastic solid. Let the volume occupied by the object excluding its surface be $V_-$. The volume outside the object is $V_+ = \mathbb{R}^3 \setminus (S \cup V_-)$. If $\mathbf{u}(\mathbf{x})$ is a constant (say $\mathbf{u}_0$) for $\mathbf{x} \in \mathbb{R}^3$, then*

$$\int_S \mathbf{u}_0 \cdot \left[\hat{\mathbf{n}}' \cdot \bar{\bar{\boldsymbol{\Sigma}}}^{(1)}_{\pm s}(\mathbf{x}, \mathbf{x}')\right] dS(\mathbf{x}') = \begin{cases} \mp \mathbf{u}_0 & \text{if } \mathbf{x} \in V_\pm \\ \mp \frac{1}{2}\mathbf{u}_0 & \text{if } \mathbf{x} \in S \end{cases}. \tag{B.16}$$

*Proof.* From Lemmas B.4.2 and B.4.3, the fields corresponding to a rigid translation satisfy Equations (4.38) and (4.39) (CBIE formulation) if the fundamental solutions are replaced with their static counterparts. Then, substitute $\mathbf{u}(\mathbf{x}) = \mathbf{u}_0$ and $\mathbf{t}(\mathbf{x}) = 0$, where $\mathbf{u}_0$ is a constant vector, into these equations and replace the fundamental solutions with the static ones. This proves the lemma partially. To prove the equations inside $V_+$ and $V_-$, we apply the representation formula (4.26) in these volumes, again by replacing the dynamic fundamental solutions with the static ones. When applying the representation formula in $V_+$, we assume a sphere that bounds $S$ and let its radius go to infinity, as detailed in Section 4.2.6 (see Figure 4.5). The integral over $S_r$ can be shown to vanish as the radius of the sphere goes to infinity. This yields the required results. □

**Definition 1.** *Assume that an elastic object with closed surface $S$ is embedded in a host material, as in Lemma B.4.4. Let $\mathbf{u}(\mathbf{x})$ be a displacement field defined in $\mathbf{x} \in \mathbb{R}^3$. Define the dyad $\bar{\mathbf{L}}^{(\alpha)}_{\pm}(\mathbf{x}, \mathbf{x}')$ and operator ${}^{\alpha}\mathcal{L}^{\pm}_S$ as follows:*

$$\bar{\mathbf{L}}^{\alpha}_{\pm}(\mathbf{x}, \mathbf{x}') := \hat{\mathbf{n}}(\mathbf{x}') \cdot \bar{\bar{\boldsymbol{\Sigma}}}^{(\alpha)}_{\pm}(\mathbf{x}, \mathbf{x}'), \tag{B.17}$$

$$ {}^{\alpha}\mathcal{L}_S^{\pm}\mathbf{u}(\mathbf{x}) \coloneqq \fint_S \mathbf{u}(\mathbf{x}') \cdot \bar{\mathbf{L}}_{\pm}^{(\alpha)}(\mathbf{x},\mathbf{x}')\, dS(\mathbf{x}') \tag{B.18} $$

*for* $\mathbf{x} \in \mathbb{R}^3$*. For the points* $\mathbf{x} \notin S$*, the CPV integral reduces to a Riemann integral.*

**Theorem B.4.5** (Jump relation)**.** *Assume that for* $\mathbf{x} \in S$*, there exists a neighborhood of* $\mathbf{x}$ *in which* $\mathbf{u}(\mathbf{x})$ *is Hölder continuous. Let* $\mathbf{x}_0$ *be a point in* $S$*. Then,*

$$ \lim_{\mathbf{x}\in V_+\to\mathbf{x}_0} {}^{1}\mathcal{L}_S^{+}\mathbf{u}(\mathbf{x}) = -\frac{1}{2}\mathbf{u}(\mathbf{x}_0) + {}^{1}\mathcal{L}_S^{+}\mathbf{u}(\mathbf{x}_0), \tag{B.19} $$

$$ \lim_{\mathbf{x}\in V_-\to\mathbf{x}_0} {}^{1}\mathcal{L}_S^{-}\mathbf{u}(\mathbf{x}) = \frac{1}{2}\mathbf{u}(\mathbf{x}_0) + {}^{1}\mathcal{L}_S^{-}\mathbf{u}(\mathbf{x}_0). \tag{B.20} $$

*Proof.* Notice that (B.20) follows trivially from (B.19) by flipping the direction of the unit normal. To prove Equation (B.19), first let $\mathbf{x} \in S$. Then,

$$ {}^{1}\mathcal{L}_S^{+}\mathbf{u}(\mathbf{x}) = \fint_S \mathbf{u}(\mathbf{x}') \cdot \bar{\mathbf{L}}_{+}^{(1)}(\mathbf{x},\mathbf{x}')\, dS(\mathbf{x}') \tag{B.21a} $$

$$ = \int_S \mathbf{u}(\mathbf{x}') \cdot \bar{\mathbf{L}}_{+}^{(1)}(\mathbf{x},\mathbf{x}')\, dS(\mathbf{x}') - \int_S \mathbf{u}(\mathbf{x}_0) \cdot \bar{\mathbf{L}}_{+s}^{(1)}(\mathbf{x},\mathbf{x}')\, dS(\mathbf{x}') + \int_S \mathbf{u}(\mathbf{x}_0) \cdot \bar{\mathbf{L}}_{+s}^{(1)}(\mathbf{x},\mathbf{x}')\, dS(\mathbf{x}') \tag{B.21b} $$

$$ = \int_S \mathbf{u}(\mathbf{x}') \cdot \bar{\mathbf{L}}_{+}^{(1)}(\mathbf{x},\mathbf{x}')\, dS(\mathbf{x}') - \int_S \mathbf{u}(\mathbf{x}_0) \cdot \bar{\mathbf{L}}_{+s}^{(1)}(\mathbf{x},\mathbf{x}')\, dS(\mathbf{x}') - \mathbf{u}(\mathbf{x}_0), \tag{B.21c} $$

where $\bar{\mathbf{L}}_{+s}^{(1)}(\mathbf{x},\mathbf{x}')$ is the dyad corresponding to the static fundamental solution and the last step follows from Lemma B.4.4. By adding and subtracting some terms, the above equation can be rewritten as

$$ {}^{1}\mathcal{L}_S^{+}\mathbf{u}(\mathbf{x}) = \int_S \left[\mathbf{u}(\mathbf{x}') - \mathbf{u}(\mathbf{x}_0)\right] \cdot \bar{\mathbf{L}}_{+}^{(1)}(\mathbf{x},\mathbf{x}')\, dS(\mathbf{x}') + \int_S \mathbf{u}(\mathbf{x}_0) \cdot \left[\bar{\mathbf{L}}_{+}^{(1)}(\mathbf{x},\mathbf{x}') - \bar{\mathbf{L}}_{+s}^{(1)}(\mathbf{x},\mathbf{x}')\right] dS(\mathbf{x}') - \mathbf{u}(\mathbf{x}_0). \tag{B.22a} $$

Define

$$ I_1(\mathbf{x}) \coloneqq \int_S \left[\mathbf{u}(\mathbf{x}') - \mathbf{u}(\mathbf{x}_0)\right] \cdot \bar{\mathbf{L}}_{+}^{(1)}(\mathbf{x},\mathbf{x}')\, dS(\mathbf{x}'), \tag{B.23a} $$

$$ I_2(\mathbf{x}) \coloneqq \int_S \mathbf{u}(\mathbf{x}_0) \cdot \left[\bar{\mathbf{L}}_{+}^{(1)}(\mathbf{x},\mathbf{x}') - \bar{\mathbf{L}}_{+s}^{(1)}(\mathbf{x},\mathbf{x}')\right] dS(\mathbf{x}'). \tag{B.23b} $$

Then,

$$ {}^{1}\mathcal{L}_S^{+}\mathbf{u}(\mathbf{x}) = I_1(\mathbf{x}) + I_2(\mathbf{x}) - \mathbf{u}(\mathbf{x}_0). \tag{B.24} $$

Repeating the foregoing process for $\mathbf{x}_0 \in S$ yields

$$ {}^1\mathcal{L}_S^+\mathbf{u}(\mathbf{x}_0) = \tilde{I}_1(\mathbf{x}_0) + \tilde{I}_2(\mathbf{x}_0) - \frac{1}{2}\mathbf{u}(\mathbf{x}_0), \tag{B.25} $$

where $\tilde{I}_1(\mathbf{x}_0)$ and $\tilde{I}_2(\mathbf{x}_0)$ are obtained substituting $\mathbf{x} = \mathbf{x}_0$ in Equations (B.23), respectively and replacing the integrals with CPV integrals. Here, we note that the addition and subtraction of CPV integrals containing the integrands $\mathbf{u}(\mathbf{x}_0) \cdot \bar{\mathbf{L}}_+^{(1)}(\mathbf{x}_0, \mathbf{x}')$ and $\mathbf{u}(\mathbf{x}_0) \cdot \bar{\mathbf{L}}_{+s}^{(1)}(\mathbf{x}_0, \mathbf{x}')$ is possible because these integrals exist individually, given that the displacement field is Hölder continuous. Subtracting (B.25) from (B.24), we get

$$ {}^1\mathcal{L}_S^+\mathbf{u}(\mathbf{x}) - {}^1\mathcal{L}_S^+\mathbf{u}(\mathbf{x}_0) = I_1(\mathbf{x}) - \tilde{I}_1(\mathbf{x}_0) + I_2(\mathbf{x}) - \tilde{I}_2(\mathbf{x}_0) - \frac{1}{2}\mathbf{u}(\mathbf{x}_0). \tag{B.26} $$

We need to show that

$$ \lim_{\mathbf{x} \in V_+ \to \mathbf{x}_0} \left[ I_1(\mathbf{x}) - \tilde{I}_1(\mathbf{x}_0) + I_2(\mathbf{x}) - \tilde{I}_2(\mathbf{x}_0) \right] = 0. \tag{B.27} $$

We will prove the limits separately, as follows:

$$ \lim_{\mathbf{x} \in V_+ \to \mathbf{x}_0} \left[ I_1(\mathbf{x}) - \tilde{I}_1(\mathbf{x}_0) \right] = 0, \tag{B.28a} $$

$$ \lim_{\mathbf{x} \in V_+ \to \mathbf{x}_0} \left[ I_2(\mathbf{x}) - \tilde{I}_2(\mathbf{x}_0) \right] = 0. \tag{B.28b} $$

First, consider Equation (B.28a). For $\delta_1 > 0$, let $B_{\delta_1}^{\mathbf{x}_0} = B(\mathbf{x}_0, \delta_1)$ be the $\delta_1$-neighborhood of $\mathbf{x}_0$, that is, a ball of radius $\delta_1$ centered at $\mathbf{x}_0$. Also, let $S_{\delta_1} = B_{\delta_1}^{\mathbf{x}_0} \cap S$. Then, according to the definition of the CPV integral, we have

$$ I_1(\mathbf{x}) - \tilde{I}_1(\mathbf{x}_0) = \fint_S \left[ \mathbf{u}(\mathbf{x}') - \mathbf{u}(\mathbf{x}_0) \right] \cdot \left[ \bar{\mathbf{L}}_+^{(1)}(\mathbf{x}, \mathbf{x}') - \bar{\mathbf{L}}_+^{(1)}(\mathbf{x}_0, \mathbf{x}') \right] \, dS(\mathbf{x}') + \lim_{\delta_1 \to 0} \int_{S_{\delta_1}} \left[ \mathbf{u}(\mathbf{x}') - \mathbf{u}(\mathbf{x}_0) \right] \cdot \bar{\mathbf{L}}_+^{(1)}(\mathbf{x}, \mathbf{x}') \, dS(\mathbf{x}'). \tag{B.29} $$

Therefore,

$$ \lim_{\mathbf{x} \to \mathbf{x}_0} \left[ I_1(\mathbf{x}) - \tilde{I}_1(\mathbf{x}_0) \right] = \lim_{\mathbf{x} \to \mathbf{x}_0} \lim_{\delta_1 \to 0} \left\{ \int_{S \setminus S_{\delta_1}} \left[ \mathbf{u}(\mathbf{x}') - \mathbf{u}(\mathbf{x}_0) \right] \cdot \left[ \bar{\mathbf{L}}_+^{(1)}(\mathbf{x}, \mathbf{x}') - \bar{\mathbf{L}}_+^{(1)}(\mathbf{x}_0, \mathbf{x}') \right] dS(\mathbf{x}') + \int_{S_{\delta_1}} \left[ \mathbf{u}(\mathbf{x}') - \mathbf{u}(\mathbf{x}_0) \right] \cdot \bar{\mathbf{L}}_+^{(1)}(\mathbf{x}, \mathbf{x}') \, dS(\mathbf{x}') \right\}. \tag{B.30} $$

First note that when $\mathbf{x} = \mathbf{x}_0$, the first integral in the parentheses is trivially zero. In the second integral, the integrand is singular. We can show that this integral vanishes in the limit $\delta_1 \to 0$ despite the singularity, as follows. Assuming that $S$ is smooth at $\mathbf{x}_0$, we transform the integral into polar coordinates $(\rho, \theta)$ that are defined on the tangent plane of $S$ at $\mathbf{x}_0$, with the origin placed at $\mathbf{x}_0$. The singularity of the integrand leads to integrals of the following type:

$$\int_{\theta_{\min}}^{\theta_{\max}} \int_0^{\rho_0} \rho^\alpha \frac{1}{\rho^2} \, \rho \, d\rho d\theta = \int_{\theta_{\min}}^{\theta_{\max}} \frac{\rho_0^\alpha}{\alpha} d\theta, \tag{B.31}$$

which converges to zero as $\delta_1$ goes to zero since $\alpha > 0$.

When $\mathbf{x} \notin S$, we need to show that given $\epsilon > 0$, there exist positive numbers $d_0$ and $d_1$ such that for $\delta_1 < d_0$ and $|\mathbf{x} - \mathbf{x}_0| < d_1$

$$\left| P(\mathbf{x}, \delta_1) + Q(\mathbf{x}, \delta_1) \right| < \epsilon, \tag{B.32}$$

where $P(\mathbf{x}, \delta_1)$ and $Q(\mathbf{x}, \delta_1)$ are the two integrals in (B.30) and $d_0$ can depend on $\mathbf{x}$. First consider the integral $Q(\mathbf{x}, \delta_1)$. Since the distance $|\mathbf{x}' - \mathbf{x}|$ is bounded below for a fixed $\mathbf{x}$, there exists $M > 0$ such that

$$\max_{j,k} \left\{ \sup_{\mathbf{x}' \in S} \left| L^{(1)}_{+jk}(\mathbf{x}, \mathbf{x}') \right| \right\} < M. \tag{B.33}$$

Because of Hölder continuity of the displacement field, there exist positive real numbers $\alpha$, $\delta_1'$ and $C_1'$ such that

$$|\mathbf{u}(\mathbf{x}') - \mathbf{u}(\mathbf{x}_0)| < C_1' |\mathbf{x}' - \mathbf{x}_0|^\alpha < C_1' {\delta_1'}^\alpha \tag{B.34}$$

for $|\mathbf{x}' - \mathbf{x}_0| < \delta_1'$. Furthermore, since

$$\left| \int_{S_{\delta_1}} dS(\mathbf{x}') \right| \to 0 \text{ as } \delta_1 \to 0, \tag{B.35}$$

there exists $\delta_1'' > 0$ such that

$$\left| \int_{S_{\delta_1}} dS(\mathbf{x}') \right| < M \tag{B.36}$$

for $\delta_1 < \delta_1''$.

Given $\epsilon_1 > 0$, choose

$$\delta_1 < \min\left\{\delta_1', \delta_1'', \left(\frac{\epsilon_1}{M^2 C_1'}\right)^{1/\alpha}\right\}. \tag{B.37}$$

Then,

$$|Q(\mathbf{x},\delta_1)| \leq \int_{S_{\delta_1}} \left|\left[\mathbf{u}(\mathbf{x}') - \mathbf{u}(\mathbf{x}_0)\right] \cdot \bar{\mathbf{L}}_+^{(1)}(\mathbf{x},\mathbf{x}')\right| dS(\mathbf{x}') \tag{B.38a}$$

$$\leq \sqrt{3} M \int_{S_{\delta_1}} \left|\mathbf{u}(\mathbf{x}') - \mathbf{u}(\mathbf{x}_0)\right| dS(\mathbf{x}') \tag{B.38b}$$

$$< M C_1' {\delta_1'}^{\alpha} \int_{S_{\delta_1}} dS(\mathbf{x}') \tag{B.38c}$$

$$< M^2 C_1' {\delta_1'}^{\alpha} < \epsilon_1. \tag{B.38d}$$

Now consider the integral $P(\mathbf{x},\delta_1)$:

$$|P(\mathbf{x},\delta_1)| < \left|\int_{S\setminus S_{\delta_1}} \left[\mathbf{u}(\mathbf{x}') - \mathbf{u}(\mathbf{x}_0)\right] \cdot \left[\bar{\mathbf{L}}_+^{(1)}(\mathbf{x},\mathbf{x}') - \bar{\mathbf{L}}_+^{(1)}(\mathbf{x}_0,\mathbf{x}')\right] dS(\mathbf{x}')\right| \tag{B.39a}$$

$$< \int_{S\setminus S_{\delta_1}} \left|\left[\mathbf{u}(\mathbf{x}') - \mathbf{u}(\mathbf{x}_0)\right] \cdot \left[\bar{\mathbf{L}}_+^{(1)}(\mathbf{x},\mathbf{x}') - \bar{\mathbf{L}}_+^{(1)}(\mathbf{x}_0,\mathbf{x}')\right]\right| dS(\mathbf{x}'). \tag{B.39b}$$

The integrand in the inequality above is bounded because of the Hölder continuity property of the displacement field, although $\bar{\mathbf{L}}_+^{(1)}(\mathbf{x}_0,\mathbf{x}')$ itself cannot be bounded as $\delta_1$ approaches zero. Therefore, the supremum of this integrand over $S$ exists. Let us define

$$U(\mathbf{x}) \coloneqq \sup_{\mathbf{x}'\in S} \left|\left[\mathbf{u}(\mathbf{x}') - \mathbf{u}(\mathbf{x}_0)\right] \cdot \left[\bar{\mathbf{L}}_+^{(1)}(\mathbf{x},\mathbf{x}') - \bar{\mathbf{L}}_+^{(1)}(\mathbf{x}_0,\mathbf{x}')\right]\right|. \tag{B.40}$$

Since $\bar{\mathbf{L}}_+^{(1)}(\mathbf{x},\mathbf{x}')$ converges to $\bar{\mathbf{L}}_+^{(1)}(\mathbf{x}_0,\mathbf{x}')$, the function $U(\mathbf{x})$ must converge to zero as $\mathbf{x} \to \mathbf{x}_0$. Therefore, given a positive constant $\epsilon_1$, we can always find $d_1 > 0$ such that $U(\mathbf{x}) < \epsilon_1$ for $|\mathbf{x} - \mathbf{x}_0| < d_1$. We can now reduce the inequality in (B.39) further, as shown below:

$$|P(\mathbf{x},\delta_1)| < U(\mathbf{x}) \int_{S\setminus S_{\delta_1}} dS(\mathbf{x}') < K\epsilon_1 \tag{B.41}$$

for some constant $K > 0$ and $|\mathbf{x} - \mathbf{x}_0| < d_1$. Note that $K$ is chosen to be independent of $\delta_1$.

We shall now prove (B.32) from the foregoing results. Given $\epsilon > 0$, select $\epsilon_1$ such that

$$\epsilon_1 + K\epsilon_1 < \epsilon. \tag{B.42}$$

Then, choose $d_1 > 0$ such that

$$|P(\mathbf{x}, \delta_1)| < K\epsilon_1. \tag{B.43}$$

For any $\mathbf{x}$ satisfying $|\mathbf{x} - \mathbf{x}_0| < d_1$, we can then choose $d_0 > 0$ such that

$$|Q(\mathbf{x}, \delta_1)| < \epsilon_1 \tag{B.44}$$

for $\delta_1 < d_0$. Therefore,

$$|P(\mathbf{x}, \delta_1) + Q(\mathbf{x}, \delta_1)| < \epsilon_1 + K\epsilon_1 < \epsilon. \tag{B.45}$$

This completes the proof of Equation (B.28a). Equation (B.28b) can be proved in a similar fashion.

□

# APPENDIX C. EVALUATION OF SINGULAR AND NEAR-SINGULAR INTEGRALS

## C.1 Singular Integrals

The Laurent series expansions of the integrands corresponding to various kernels are given in this section. These expansions were originally derived in [112]. There are four different kernels, including $\overline{\mathbf{U}}_{\pm}(\mathbf{x},\mathbf{x}')$, $\overline{\mathbf{T}}^{(2)}_{\pm}(\mathbf{x},\mathbf{x}')$, $\overline{\mathbf{K}}^{(2)}_{\pm}(\mathbf{x},\mathbf{x}')$ and $\overline{\mathbf{H}}_{\pm}(\mathbf{x},\mathbf{x}')$. For brevity, these will be called the U-kernel, T-kernel, K-kernel and H-kernel, respectively.

### C.1.1 Laurent Series Expansions

For the K-kernel, we have the following integral

$$Z^{\pm}_{K_{mn}} = \int\!\!\!\!\!\!-_{\Omega} \tilde{L}_i(\boldsymbol{\xi})\ \tilde{\mathbf{e}}^{(q)}_{\beta}(\boldsymbol{\xi}_j)\cdot\overline{\mathbf{K}}^{(2)}_{\pm}(\mathbf{y}^{(q)}_j,\mathbf{x}^{(p)}(\boldsymbol{\xi}))\cdot\mathbf{e}^{(p)}_{\alpha}(\boldsymbol{\xi})\mathcal{J}(\boldsymbol{\xi})\ d\xi_1 d\xi_2, \tag{C.1}$$

When the collocation point lies on triangle $p$, on which the integration is performed, the integrand is singular. We then have $q=p$ and $\mathbf{y}^{(q)}_j = \mathbf{x}^{(p)}(\boldsymbol{\xi}_j)$. Therefore, the integral can be rewritten, generally, as

$$I_K = \int\!\!\!\!\!\!-_{\Omega} \mathbf{K}(\boldsymbol{\xi}_j,\boldsymbol{\xi})\cdot\boldsymbol{\phi}(\boldsymbol{\xi})\mathcal{J}(\boldsymbol{\xi}_i)\ d\xi_1 d\xi_2, \tag{C.2}$$

where

$$\begin{aligned}\mathbf{K}(\boldsymbol{\xi}_j,\boldsymbol{\xi}) &\coloneqq \tilde{\mathbf{e}}^{(q)}_{\beta}(\boldsymbol{\xi}_j)\cdot\overline{\mathbf{K}}^{(2)}_{\pm}(\mathbf{x}^{(p)}(\boldsymbol{\xi}_j),\mathbf{x}^{(p)}(\boldsymbol{\xi})),\\ \boldsymbol{\phi}(\boldsymbol{\xi}) &\coloneqq L_i(\boldsymbol{\xi})\mathbf{e}^{(p)}_{\alpha}(\boldsymbol{\xi}).\end{aligned} \tag{C.3}$$

Note that $\mathbf{K}^{(2)}(\boldsymbol{\xi}_j,\boldsymbol{\xi})$ is singular at $\boldsymbol{\xi}=\boldsymbol{\xi}_j$. Also, the Jacobian $\mathcal{J}(\boldsymbol{\xi})$ in the integral cancels with the one in the denominator of $\tilde{L}_i(\boldsymbol{\xi})$. Therefore, defining the interpolation function $\tilde{L}_i(\boldsymbol{\xi})$ as in (4.93) enables more accurate evaluation of the integral since the Jacobian, which is a non-polynomial

function, is eliminated. Transform the integral into new variables given by $\boldsymbol{\eta} = (\eta_1, \eta_2)$, with $\boldsymbol{\xi}_j$ mapping to $\boldsymbol{\eta}_0$

$$I_K = \oint_{\Omega_\eta} \mathbf{K}(\boldsymbol{\xi}_j(\boldsymbol{\eta}_0), \boldsymbol{\xi}(\boldsymbol{\eta})) \cdot \boldsymbol{\phi}(\boldsymbol{\xi}(\boldsymbol{\eta}))\ \tilde{J}(\boldsymbol{\eta})\ d\eta_1 d\eta_2, \tag{C.4}$$

where $\tilde{J}(\boldsymbol{\eta}) = \mathcal{J}(\boldsymbol{\xi}_i)\ \tilde{\mathcal{J}}(\boldsymbol{\eta})$, with $\tilde{\mathcal{J}}(\boldsymbol{\eta})$ being the Jacobian of the transformation from $\boldsymbol{\xi}$ to $\boldsymbol{\eta}$. Transform the integral further into polar coordinates centered at $\boldsymbol{\eta}_0$.

$$I_K = \oint_{\Gamma} F(\rho, \theta) d\rho d\theta, \tag{C.5}$$

with $F(\rho, \theta) = \mathbf{K} \cdot \boldsymbol{\phi} \tilde{J} \rho$, where $\mathbf{K}$, $\boldsymbol{\phi}$ and $\tilde{J}$ should be seen as functions of $\rho$ and $\theta$.

Let the Laurent series expansion of $F(\rho, \theta)$ in terms of $\rho$ be

$$F(\rho, \theta) = \frac{F_{-2}(\theta)}{\rho^2} + \frac{F_{-1}(\theta)}{\rho} + O(1). \tag{C.6}$$

Then $F_{-2}(\theta) = 0$ and

$$F_{-1}(\theta) = \frac{J_0}{2\pi C^3} \left\{ A_{3,0} \left( \boldsymbol{\phi}_0 \cdot \mathbf{C} \right) (\mathbf{e}_0 \cdot \hat{\mathbf{n}}) + A_{2,0} \left( \boldsymbol{\phi}_0 \cdot \hat{\mathbf{n}} \right) (\mathbf{e}_0 \cdot \mathbf{C}) \right\}, \tag{C.7}$$

where

$$\tilde{J} = J_0 + \rho J_1 + O(\rho^2), \tag{C.8a}$$

$$\boldsymbol{\phi} = \boldsymbol{\phi}_0 + \rho \boldsymbol{\phi}_1 + O(\rho^2), \tag{C.8b}$$

$$A_j = A_{j,0} + \rho A_{j,1} + O(\rho^2) \quad (j = 1, 2, 3), \tag{C.8c}$$

$$\mathbf{R} = \rho \mathbf{C} + \rho^2 \mathbf{D} + O(\rho^3). \tag{C.8d}$$

Here, $\mathbf{e}_0 = \mathbf{e}_\beta^{(q)}(\boldsymbol{\xi}_j)$ and $\hat{\mathbf{n}} = \hat{\mathbf{n}}(\mathbf{y}_j^{(p)})$. The coefficients in the foregoing expansions are evaluated at $\rho = 0$, i.e., at $\boldsymbol{\xi} = \boldsymbol{\xi}_j$. In general, all the coefficients are functions of $\theta$. The term $\mathbf{e}_0 \cdot \hat{\mathbf{n}}$ is zero when $\mathbf{e}_0$ is a tangent vector at $\boldsymbol{\xi}_j$ because $\hat{\mathbf{n}}$ is the unit normal at $\boldsymbol{\xi}_j$. This is indeed the case when the testing function is either $\tilde{\mathbf{e}}_1^{(p)}(\boldsymbol{\xi}_j)$ or $\tilde{\mathbf{e}}_2^{(p)}(\boldsymbol{\xi}_j)$. Similarly, $\boldsymbol{\phi}_0 \cdot \mathbf{C}$ becomes zero when the expansion function is $\mathbf{e}_3^{(p)}(\boldsymbol{\xi}_j)$. Similar observations can be made for the quantities in the last term of (C.7). Also, when $i \neq j$, $\boldsymbol{\phi}_0$ is zero since $L_i(\boldsymbol{\xi}_\mathbf{j}) = \delta_{ij}$. Therefore, $F_{-1}(\theta)$ is zero in that case. According to these observations, singularity subtraction needs to be performed only for a few combinations of the testing and expansion functions.

For the H-kernel, we have the following integral

$$Z^{\pm}_{H_{mn}} := \fint_{\Omega} L_i(\boldsymbol{\xi})\ \tilde{\mathbf{e}}^{(q)}_{\beta}(\boldsymbol{\xi}_j)\cdot\overline{\mathbf{H}}_{\pm}(\mathbf{y}^{(q)}_j,\mathbf{x}')\cdot\mathbf{e}^{(p)}_{\alpha}(\boldsymbol{\xi})\mathcal{J}(\boldsymbol{\xi})\ d\xi_1 d\xi_2. \tag{C.9}$$

Following the same process that is applied for the K-kernel, the general form of this integral is

$$I_H = \fint_{\Omega_\eta} \mathbf{H}(\boldsymbol{\xi}_j(\boldsymbol{\eta}_0),\boldsymbol{\xi}(\boldsymbol{\eta}))\cdot\boldsymbol{\phi}(\boldsymbol{\xi}(\boldsymbol{\eta}))\ J(\boldsymbol{\eta})\ d\eta_1 d\eta_2, \tag{C.10}$$

where $J(\boldsymbol{\eta}) = \mathcal{J}(\boldsymbol{\xi}(\boldsymbol{\eta}))\ \tilde{\mathcal{J}}(\boldsymbol{\eta})$. This integral can be transformed into polar coordinates as follows

$$I_H = \fint_{\Gamma} \tilde{F}(\rho,\theta)d\rho d\theta, \tag{C.11}$$

with $\tilde{F}(\rho,\theta) = \mathbf{H}\cdot\boldsymbol{\phi}J\rho$, where $\mathbf{H}$, $\boldsymbol{\phi}$ and $J$ should be seen as functions of $\rho$ and $\theta$. Let the Laurent series expansion of $\tilde{F}(\rho,\theta)$ in terms of $\rho$ be

$$\tilde{F}(\rho,\theta) = \frac{\tilde{F}_{-2}(\theta)}{\rho^2} + \frac{\tilde{F}_{-1}(\theta)}{\rho} + O(1). \tag{C.12}$$

The coefficients of the expansion are

$$\tilde{F}_{-2}(\theta) = \frac{\mu}{\pi C^3}(\mathbf{V}_0\cdot\boldsymbol{\phi}_0), \tag{C.13}$$

$$\tilde{F}_{-1}(\theta) = \frac{\mu}{\pi C^3}\left\{-\frac{3E}{C^2}(\mathbf{V}_0\cdot\boldsymbol{\phi}_0) + \mathbf{V}_1\cdot\boldsymbol{\phi}_0 + \mathbf{V}_0\cdot\boldsymbol{\phi}_1\right\}, \tag{C.14}$$

where

$$\mathbf{V}_0 = B_{2,0}(\mathbf{N}_0\cdot\hat{\mathbf{n}})(\mathbf{e}_0\cdot\mathbf{d}_0)\mathbf{d}_0 + B_{4,0}(\mathbf{N}_0\cdot\hat{\mathbf{n}})\mathbf{e}_0 + B_{4,0}(\mathbf{e}_0\cdot\mathbf{N}_0)\hat{\mathbf{n}} + B_{6,0}(\mathbf{e}_0\cdot\hat{\mathbf{n}})\mathbf{N}_0, \tag{C.15}$$

$$\begin{aligned}\mathbf{V}_1 =& [\mathbf{d}_0\cdot\mathbf{N}_1 + \mathbf{d}_1\cdot\mathbf{N}_0]\left\{B_{1,0}(\mathbf{e}_0\cdot\mathbf{d}_0)(\mathbf{d}_0\cdot\hat{\mathbf{n}})\mathbf{d}_0 + B_{2,0}(\mathbf{e}_0\cdot\mathbf{d}_0)\hat{\mathbf{n}} + B_{3,0}(\mathbf{e}_0\cdot\hat{\mathbf{n}})\mathbf{d}_0\right\} + \\ & \left\{B_{2,0}(\mathbf{e}_0\cdot\mathbf{N}_0)\mathbf{d}_0 + B_{5,0}(\mathbf{e}_0\cdot\mathbf{d}_0)\mathbf{d}_0\right\}(\mathbf{d}_1\cdot\hat{\mathbf{n}}) + \sum_{\substack{l_i\geq 0\ \ni \\ \sum_i l_i = 1}} B_{2,l_1}(\mathbf{e}_0\cdot\mathbf{d}_{l_2})(\mathbf{N}_{l_4}\cdot\hat{\mathbf{n}})\mathbf{d}_{l_3} \\ & \left\{B_{4,1}\mathbf{N}_0 + B_{4,0}\mathbf{N}_1\right\}\cdot\hat{\mathbf{n}}\mathbf{e}_0 + \left\{B_{4,1}\mathbf{e}_0\cdot\mathbf{N}_0 + B_{4,0}\mathbf{e}_0\cdot\mathbf{N}_1\right\}\hat{\mathbf{n}} + \left\{B_{6,1}\mathbf{N}_0 + B_{6,0}\mathbf{N}_1\right\}\mathbf{e}_0\cdot\hat{\mathbf{n}},\end{aligned} \tag{C.16}$$

and

$$B_j = B_{j,0} + \rho B_{j,1} + O(\rho^2) \quad (j = 1, 2, \ldots 6), \tag{C.17a}$$

$$J\hat{\mathbf{n}}' = \mathbf{N}_0 + \rho\mathbf{N}_1 + O(\rho^2), \tag{C.17b}$$

$$\hat{\mathbf{R}} = \frac{\mathbf{C}}{C} + \rho\left(\frac{\mathbf{D}}{C} - \frac{\mathbf{C}E}{C^3}\right) + O(\rho^2) \tag{C.17c}$$

$$= \mathbf{d}_0 + \rho\mathbf{d}_1 + O(\rho^2), \tag{C.17d}$$

$$C = |\mathbf{C}|, \quad E = \mathbf{C}\cdot\mathbf{D}. \tag{C.17e}$$

Since $\overline{\mathbf{U}}_{\pm}(\mathbf{x},\mathbf{x}')$ is weakly-singular, the integrals corresponding to this kernel can be integrated without singularity subtraction. Specifically, these integrals can be written in the form of Equation (C.5) using polar-coordinate transformation. The corresponding integrand is regular due to cancellation of the $1/\rho$ singularity by the Jacobian of the polar-coordinate transformation. Integrals corresponding to the T-kernel are evaluated in the same way as the H-kernel. The steps from (C.9) through (C.12) can be repeated by replacing $\overline{\mathbf{H}}_{\pm}(\mathbf{x},\mathbf{x}')$ with $\overline{\mathbf{T}}^{(2)}_{\pm}(\mathbf{x},\mathbf{x}')$. The Laurent series corresponding to the T-kernel has $\tilde{F}_{-2}(\theta) = 0$. The coefficient $\tilde{F}_{-1}(\theta)$ is given by

$$\tilde{F}_{-1}(\theta) = \frac{1}{2\pi C^3}\left\{A_{2,0}\,(\boldsymbol{\phi}_0\cdot\mathbf{C})(\mathbf{e}_0\cdot\mathbf{N}_0) + A_{3,0}\,(\boldsymbol{\phi}_0\cdot\mathbf{N}_0)(\mathbf{e}_0\cdot\mathbf{C})\right\}. \tag{C.18}$$

### C.1.2 Coefficients of Taylor Series Expansions

It is required to obtain coefficients of the Taylor series expansions in (C.8) and (C.17). Consider a function $h(\boldsymbol{\xi})$ that is transformed into the variables $\boldsymbol{\eta} = (\eta_1, \eta_2)$ via the transformation (4.125) and then into polar coordinates centered at $\boldsymbol{\eta}_0$ via (4.114). Assume that $\boldsymbol{\xi}_0 \in \Omega$ corresponds to the point $\boldsymbol{\eta}_0$. Then, the Taylor series of this function about $\rho = 0$ is obtained as follows:

$$\begin{aligned} h(\boldsymbol{\xi}) =& h(\boldsymbol{\xi}_0) + \rho\left[\frac{\partial h(\boldsymbol{\xi_0})}{\partial\eta_1}\cos\theta + \frac{\partial h(\boldsymbol{\xi_0})}{\partial\eta_2}\sin\theta\right] + \\ & \rho^2\left[\frac{\partial^2 h(\boldsymbol{\xi_0})}{\partial\eta_1^2}\frac{\cos^2\theta}{2} + \frac{\partial^2 h(\boldsymbol{\xi_0})}{\partial\eta_1\partial\eta_2}\cos\theta\sin\theta + \frac{\partial^2 h(\boldsymbol{\xi_0})}{\partial\eta_2^2}\frac{\sin^2\theta}{2}\right] + O(\rho^3), \end{aligned} \tag{C.19}$$

where

$$\frac{\partial h(\boldsymbol{\xi_0})}{\partial\eta_1} = \frac{\partial h(\boldsymbol{\xi_0})}{\partial\xi_1}\frac{\partial\xi_1}{\partial\eta_1} + \frac{\partial h(\boldsymbol{\xi_0})}{\partial\xi_2}\frac{\partial\xi_2}{\partial\eta_1} \tag{C.20a}$$

$$= \frac{\partial h(\boldsymbol{\xi_0})}{\partial\xi_1}(1) + \frac{\partial h(\boldsymbol{\xi_0})}{\partial\xi_2}(0) \tag{C.20b}$$

$$= \frac{\partial h(\boldsymbol{\xi_0})}{\partial\xi_1}, \tag{C.20c}$$

$$\frac{\partial h(\boldsymbol{\xi_0})}{\partial \eta_2} = \frac{\partial h(\boldsymbol{\xi_0})}{\partial \xi_1}\frac{\partial \xi_1}{\partial \eta_2} + \frac{\partial h(\boldsymbol{\xi_0})}{\partial \xi_2}\frac{\partial \xi_2}{\partial \eta_2} \tag{C.20d}$$

$$= \frac{\partial h(\boldsymbol{\xi_0})}{\partial \xi_1}\left(\frac{-g_{12}(\boldsymbol{\xi_0})}{\mathcal{J}(\boldsymbol{\xi}_0)}\right) + \frac{\partial h(\boldsymbol{\xi_0})}{\partial \xi_2}\left(\frac{g_{11}(\boldsymbol{\xi_0})}{\mathcal{J}(\boldsymbol{\xi}_0)}\right) \tag{C.20e}$$

$$= \frac{1}{\mathcal{J}(\boldsymbol{\xi}_0)}\left[-g_{12}(\boldsymbol{\xi_0})\frac{\partial h(\boldsymbol{\xi_0})}{\partial \xi_1} + g_{11}(\boldsymbol{\xi_0})\frac{\partial h(\boldsymbol{\xi_0})}{\partial \xi_2}\right], \tag{C.20f}$$

$$\frac{\partial^2 h(\boldsymbol{\xi_0})}{\partial \eta_1^2} = \frac{\partial^2 h(\boldsymbol{\xi_0})}{\partial \xi_1^2}, \tag{C.20g}$$

$$\frac{\partial^2 h(\boldsymbol{\xi_0})}{\partial \eta_1 \partial \eta_2} = \frac{1}{\mathcal{J}(\boldsymbol{\xi}_0)}\left[-g_{12}(\boldsymbol{\xi_0})\frac{\partial^2 h(\boldsymbol{\xi_0})}{\partial^2 \xi_1} + g_{11}(\boldsymbol{\xi_0})\frac{\partial^2 h(\boldsymbol{\xi_0})}{\partial \xi_1 \partial \xi_2}\right], \tag{C.20h}$$

$$\frac{\partial^2 h(\boldsymbol{\xi_0})}{\partial \eta_2^2} = \frac{1}{\mathcal{J}^2(\boldsymbol{\xi}_0)}\left[-g_{12}\left(-g_{12}\frac{\partial^2 h(\boldsymbol{\xi_0})}{\partial^2 \xi_1} + g_{11}\frac{\partial^2 h(\boldsymbol{\xi_0})}{\partial \xi_1 \partial \xi_2}\right) + g_{11}\left(-g_{12}\frac{\partial^2 h(\boldsymbol{\xi_0})}{\partial \xi_1 \partial \xi_2} + g_{11}\frac{\partial^2 h(\boldsymbol{\xi_0})}{\partial^2 \xi_2}\right)\right] \tag{C.20i}$$

$$= \frac{1}{\mathcal{J}^2(\boldsymbol{\xi}_0)}\left[g_{12}^2\frac{\partial^2 h(\boldsymbol{\xi_0})}{\partial^2 \xi_1} - 2g_{12}g_{11}\frac{\partial^2 h(\boldsymbol{\xi_0})}{\partial \xi_1 \partial \xi_2} + g_{11}^2\frac{\partial^2 h(\boldsymbol{\xi_0})}{\partial^2 \xi_2}\right]. \tag{C.20j}$$

Therefore, if the derivatives of $h(\boldsymbol{\xi})$ with respect to $\xi_1$ and $\xi_2$ are obtained, the coefficients of its Taylor series expansion can be readily calculated. When the variation of $h$ as a function of $\tau = ik_sR$ is known, as it is for the quantities $B_j$ and $A_k$ ($j = 1, 2, \ldots 6$ and $k = 1, 2, 3$), it is easier to compute these derivatives as follows

$$\frac{\partial h}{\partial \xi_i} = \frac{\mathrm{d}h}{\mathrm{d}\tau}\frac{\partial \tau}{\partial \xi_i} = \frac{\mathrm{d}h}{\mathrm{d}\tau}\left(ik_s\frac{\partial R}{\partial \xi_i}\right) = \frac{ik_s}{2R}\left(2\mathbf{R}\cdot\frac{\partial \mathbf{x}'}{\partial \xi_i}\right)\frac{\mathrm{d}h}{\mathrm{d}\tau} = ik_s(\hat{\mathbf{R}}\cdot\mathbf{e}_i)\frac{\mathrm{d}h}{\mathrm{d}\tau} \quad (i = 1, 2). \tag{C.21}$$

From the above, we find that the derivative of $h(\tau)$ needs to be calculated. Only the first derivative is required for calculating the singular integrals. The second derivative will be used for calculating the near-singular integrals.

The functions $B_j(\tau)$, $A_k(\tau)$ and their derivatives are evaluated as shown below. From (4.25), we have

$$M(\tau) = \frac{e^{\alpha\tau}(1-\alpha\tau) - e^{\tau}(1-\tau)}{\tau^2}, \quad \psi(\tau) = e^{\tau} - M(\tau), \quad \chi(\tau) = e^{\alpha\tau}\alpha^2 - e^{\tau} + 3M(\tau). \tag{C.22}$$

Let $\gamma(\tau)$ be defined as follows

$$\gamma(\tau) \coloneqq \frac{e^{\tau}(1-\tau)}{\tau^2}. \tag{C.23}$$

Let the derivative of a function with respect to its argument be represented by the prime superscript. Multiple derivatives are represented using double and triple prime superscripts. Taking the derivative of $e^\tau(1-\tau)$ with respect to $\tau$, we get

$$[e^\tau(1-\tau)]' = e^\tau(1-\tau) - e^\tau = -\tau e^\tau. \tag{C.24}$$

The derivatives of $\gamma(\tau)$ can be expressed as follows

$$\gamma'(\tau) = \frac{[e^\tau(1-\tau)]'}{\tau^2} - \frac{2e^\tau(1-\tau)}{\tau^3} \tag{C.25a}$$
$$= \frac{-\tau e^\tau}{\tau^2} - \frac{2e^\tau(1-\tau)}{\tau^3} \tag{C.25b}$$
$$= -\frac{e^\tau}{\tau} - \frac{2\gamma(\tau)}{\tau}, \tag{C.25c}$$

$$\gamma''(\tau) = -\frac{e^\tau}{\tau} + \frac{e^\tau}{\tau^2} - \frac{2\gamma'(\tau)}{\tau} + \frac{2\gamma(\tau)}{\tau^2} \tag{C.25d}$$
$$= \frac{e^\tau(1-\tau)}{\tau^2} - \frac{2\gamma'(\tau)}{\tau} + \frac{2\gamma(\tau)}{\tau^2} \tag{C.25e}$$
$$= \gamma(\tau) - \frac{2\gamma'(\tau)}{\tau} + \frac{2\gamma(\tau)}{\tau^2}, \tag{C.25f}$$

$$\gamma'''(\tau) = \gamma'(\tau) - \frac{2\gamma''(\tau)}{\tau} + \frac{2\gamma'(\tau)}{\tau^2} + \frac{2\gamma'(\tau)}{\tau^2} - \frac{4\gamma(\tau)}{\tau^3} \tag{C.25g}$$
$$= \gamma'(\tau) - \frac{2\gamma''(\tau)}{\tau} + \frac{4\gamma'(\tau)}{\tau^2} - \frac{4\gamma(\tau)}{\tau^3}. \tag{C.25h}$$

Then, the functional forms of all the required quantities can be derived as shown below

$$M(\tau) = \alpha^2\gamma(\alpha\tau) - \gamma(\tau), \tag{C.26a}$$
$$M'(\tau) = \alpha^3\gamma'(\alpha\tau) - \gamma'(\tau), \tag{C.26b}$$
$$M''(\tau) = \alpha^4\gamma''(\alpha\tau) - \gamma''(\tau), \tag{C.26c}$$
$$M'''(\tau) = \alpha^5\gamma'''(\alpha\tau) - \gamma'''(\tau). \tag{C.26d}$$

$$\chi'(\tau) = \alpha^3 e^{\alpha\tau} - e^\tau + 3M'(\tau), \tag{C.26e}$$
$$\chi''(\tau) = \alpha^4 e^{\alpha\tau} - e^\tau + 3M''(\tau), \tag{C.26f}$$

$$\chi'''(\tau) = \alpha^5 e^{\alpha\tau} - e^{\tau} + 3M'''(\tau). \tag{C.26g}$$

$$\psi'(\tau) \ = e^{\tau} - M'(\tau), \tag{C.26h}$$

$$\psi''(\tau) \ = e^{\tau} - M''(\tau), \tag{C.26i}$$

$$\psi'''(\tau) = e^{\tau} - M'''(\tau). \tag{C.26j}$$

$$A_1(\tau) = \tau\chi'(\tau) - 3\chi(\tau), \tag{C.27a}$$

$$A_1'(\tau) = \tau\chi''(\tau) + \chi'(\tau) - 3\chi'(\tau) = \tau\chi''(\tau) - 2\chi'(\tau), \tag{C.27b}$$

$$A_1''(\tau) = \tau\chi'''(\tau) + \chi''(\tau) - 2\chi''(\tau) = \tau\chi'''(\tau) - \chi''(\tau). \tag{C.27c}$$

$$A_2(\tau) = \frac{\tau\psi'(\tau) - \psi(\tau) + \chi(\tau)}{2}, \tag{C.27d}$$

$$A_2'(\tau) = \frac{\tau\psi''(\tau) + \psi'(\tau) - \psi'(\tau) + \chi'(\tau)}{2} = \frac{\tau\psi''(\tau) + \chi'(\tau)}{2}, \tag{C.27e}$$

$$A_2''(\tau) = \frac{\tau\psi'''(\tau) + \psi''(\tau) + \chi''(\tau)}{2}. \tag{C.27f}$$

$$A_3(\tau) = \chi(\tau) + \left(\frac{1}{2\alpha^2} - 1\right)[A_1 + 2A_2 + 3\chi(\tau)], \tag{C.27g}$$

$$A_3'(\tau) = \chi'(\tau) + \left(\frac{1}{2\alpha^2} - 1\right)[A_1' + 2A_2' + 3\chi'(\tau)], \tag{C.27h}$$

$$A_3''(\tau) = \chi''(\tau) + \left(\frac{1}{2\alpha^2} - 1\right)[A_1'' + 2A_2'' + 3\chi''(\tau)]. \tag{C.27i}$$

The functions $B_j(\tau)$ and their derivatives are given by (C.28). The first derivatives of only $B_2(\tau)$, $B_4(\tau)$ and $B_6(\tau)$ are needed.

$$B_1(\tau) = A_1'\tau - 5A_1, \tag{C.28a}$$

$$B_2(\tau) = (A_2'\tau - 3A_2 + A_1)/2, \tag{C.28b}$$

$$B_3(\tau) = A_1 + \left(\frac{1}{2\alpha^2} - 1\right)(A_1'\tau + 2A_2'\tau - 6A_2), \tag{C.28c}$$

$$B_4(\tau) = A_2, \tag{C.28d}$$

$$B_5(\tau) = A_3'\tau - 3A_3, \tag{C.28e}$$

$$B_6(\tau) = A_3 + \left(\frac{1}{2\alpha^2} - 1\right)(A_3'\tau + 2A_2). \tag{C.28f}$$

$$B_2'(\tau) = (A_2''\tau + A_2' - 3A_2' + A_1')/2 = (A_2''\tau - 2A_2' + A_1')/2, \tag{C.28g}$$

$$B_4'(\tau) = A_2', \tag{C.28h}$$

$$B_6'(\tau) = A_3' + \left(\frac{1}{2\alpha^2} - 1\right)(A_3''\tau + A_3' + 2A_2'). \tag{C.28i}$$

The above expressions can be used for direct evaluation of the functions only when $\tau$ is not equal to zero. This is the case for the nearly-singular integrals. However, for singular integrals, the limits as $\tau \to 0$ have to be obtained as shown below. All the following expressions have been verified using symbolic computations in Wolfram Mathematica [202].

$$\gamma(\tau) = \frac{e^\tau(1-\tau)}{\tau^2} \tag{C.29a}$$

$$= \frac{1}{\tau^2} - \frac{1}{2} - \frac{\tau}{3} - \frac{\tau^2}{8} - \frac{\tau^3}{30} + O(\tau^4), \tag{C.29b}$$

$$\gamma'(\tau) = -\frac{e^\tau}{\tau} - \frac{2\gamma(\tau)}{\tau} \tag{C.29c}$$

$$= -\frac{1+\tau+\tau^2/2+\tau^3/6}{\tau} - \frac{2}{\tau}\left(\frac{1}{\tau^2} - \frac{1}{2} - \frac{\tau}{3} - \frac{\tau^2}{8} - \frac{\tau^3}{30}\right) + O(\tau^3) \tag{C.29d}$$

$$= -\frac{2}{\tau^3} - \frac{1}{3} - \frac{\tau}{4} - \frac{\tau^2}{10} + O(\tau^3), \tag{C.29e}$$

$$\gamma''(\tau) = \gamma(\tau) - \frac{2\gamma'(\tau)}{\tau} + \frac{2\gamma(\tau)}{\tau^2} \tag{C.29f}$$

$$= \frac{1}{\tau^2} - \frac{1}{2} - \frac{\tau}{3} - \frac{2}{\tau}\left(-\frac{2}{\tau^3} - \frac{1}{3} - \frac{\tau}{4} - \frac{\tau^2}{10}\right) + \frac{2}{\tau^2}\left(\frac{1}{\tau^2} - \frac{1}{2} - \frac{\tau}{3} - \frac{\tau^2}{8} - \frac{\tau^3}{30}\right) + O(\tau^2) \tag{C.29g}$$

$$= \frac{6}{\tau^4} - \frac{1}{4} - \frac{\tau}{5} + O(\tau^2), \tag{C.29h}$$

$$\gamma'''(\tau) = \gamma'(\tau) - \frac{2\gamma''(\tau)}{\tau} + \frac{4\gamma'(\tau)}{\tau^2} - \frac{4\gamma(\tau)}{\tau^3} \tag{C.29i}$$

$$= -\frac{24}{\tau^5} - \frac{1}{5} + O(\tau). \tag{C.29j}$$

$$\lim_{\tau\to 0} M(\tau) = \lim_{\tau\to 0}\ \alpha^2\gamma(\alpha\tau) - \gamma(\tau) \tag{C.30a}$$
$$= \lim_{\tau\to 0} \alpha^2\left(\frac{1}{(\alpha\tau)^2} - \frac{1}{2}\right) - \left(\frac{1}{\tau^2} - \frac{1}{2}\right) \tag{C.30b}$$
$$= \frac{1-\alpha^2}{2}, \tag{C.30c}$$

$$\lim_{\tau\to 0} M'(\tau) = \lim_{\tau\to 0}\ \alpha^3\gamma'(\alpha\tau) - \gamma'(\tau) \tag{C.30d}$$
$$= \lim_{\tau\to 0}\ \left(\frac{1}{3} + \frac{2}{\tau^3}\right) - \alpha^3\left(\frac{1}{3} + \frac{2}{(\alpha\tau)^3}\right) \tag{C.30e}$$
$$= \frac{1-\alpha^3}{3}, \tag{C.30f}$$

$$\lim_{\tau\to 0} M''(\tau) = \lim_{\tau\to 0}\ \alpha^4\gamma''(\alpha\tau) - \gamma''(\tau) \tag{C.30g}$$
$$= \lim_{\tau\to 0}\ \alpha^4\left(\frac{6}{(\alpha\tau)^4} - \frac{1}{4}\right) - \left(\frac{6}{\tau^4} - \frac{1}{4}\right) \tag{C.30h}$$
$$= \frac{1-\alpha^4}{4}, \tag{C.30i}$$

$$\lim_{\tau\to 0} M'''(\tau) = \lim_{\tau\to 0}\ \alpha^5\gamma'''(\alpha\tau) - \gamma'''(\tau) \tag{C.30j}$$
$$= \lim_{\tau\to 0}\ \left(\frac{24}{\tau^5} + \frac{1}{5}\right) - \alpha^5\left(\frac{24}{(\alpha\tau)^5} + \frac{1}{5}\right) \tag{C.30k}$$
$$= \frac{1-\alpha^5}{5}. \tag{C.30l}$$

$$\lim_{\tau\to 0} \chi(\tau) = \lim_{\tau\to 0}\ e^{\alpha\tau}\alpha^2 - e^{\tau} + 3M(\tau) \tag{C.31a}$$
$$= (\alpha^2 - 1) + \frac{3}{2}(1-\alpha^2) \tag{C.31b}$$
$$= \frac{1-\alpha^2}{2}, \tag{C.31c}$$
$$\lim_{\tau\to 0} \chi'(\tau) = \lim_{\tau\to 0}\ \alpha^3 e^{\alpha\tau} - e^{\tau} + 3M'(\tau) \tag{C.31d}$$
$$= (\alpha^3 - 1) + (1-\alpha^3) = 0, \tag{C.31e}$$
$$\lim_{\tau\to 0} \chi''(\tau) = \lim_{\tau\to 0}\ \alpha^4 e^{\alpha\tau} - e^{\tau} + 3M''(\tau) \tag{C.31f}$$

$$= \lim_{\tau \to 0} \alpha^4 - 1 + 3\left(\frac{1-\alpha^4}{4}\right) \tag{C.31g}$$

$$= \frac{\alpha^4 - 1}{4}, \tag{C.31h}$$

$$\lim_{\tau \to 0} \chi'''(\tau) = \lim_{\tau \to 0} \alpha^5 e^{\alpha\tau} - e^{\tau} + 3M'''(\tau) \tag{C.31i}$$

$$= \lim_{\tau \to 0} \alpha^5 - 1 + 3\left(\frac{1-\alpha^5}{5}\right) \tag{C.31j}$$

$$= \frac{2(\alpha^5 - 1)}{5}. \tag{C.31k}$$

$$\lim_{\tau \to 0} \psi(\tau) = \lim_{\tau \to 0} e^{\tau} - M(\tau) \tag{C.32a}$$

$$= 1 - \frac{1-\alpha^2}{2} = \frac{1+\alpha^2}{2}, \tag{C.32b}$$

$$\lim_{\tau \to 0} \psi'(\tau) = \lim_{\tau \to 0} e^{\tau} - M'(\tau) \tag{C.32c}$$

$$= 1 - \frac{1-\alpha^3}{3} = \frac{2+\alpha^3}{3}, \tag{C.32d}$$

$$\lim_{\tau \to 0} \psi''(\tau) = \lim_{\tau \to 0} e^{\tau} - M''(\tau) \tag{C.32e}$$

$$= \lim_{\tau \to 0} 1 - \frac{1-\alpha^4}{4} = \frac{3+\alpha^4}{4}, \tag{C.32f}$$

$$\lim_{\tau \to 0} \psi'''(\tau) = \lim_{\tau \to 0} e^{\tau} - M'''(\tau) \tag{C.32g}$$

$$= \lim_{\tau \to 0} 1 - \frac{1-\alpha^5}{5} = \frac{4+\alpha^5}{5}. \tag{C.32h}$$

$$\lim_{\tau \to 0} A_1(\tau) = \lim_{\tau \to 0} \tau\chi'(\tau) - 3\chi(\tau) \tag{C.33a}$$

$$= \lim_{\tau \to 0} 0 - \frac{3}{2}(1-\alpha^2) \tag{C.33b}$$

$$= \frac{3}{2}(\alpha^2 - 1), \tag{C.33c}$$

$$\lim_{\tau \to 0} A_1'(\tau) = \lim_{\tau \to 0} \tau\chi''(\tau) - 2\chi'(\tau) \tag{C.33d}$$

$$= \lim_{\tau \to 0} \tau\frac{\alpha^4 - 1}{4} - 0 \tag{C.33e}$$

$$= 0, \tag{C.33f}$$

$$\lim_{\tau\to 0} A_1''(\tau) = \lim_{\tau\to 0} \tau\chi'''(\tau) - \chi''(\tau) \tag{C.33g}$$
$$= \lim_{\tau\to 0} \tau\frac{2(\alpha^5-1)}{5} - \frac{\alpha^4-1}{4} \tag{C.33h}$$
$$= \frac{1-\alpha^4}{4}. \tag{C.33i}$$

$$\lim_{\tau\to 0} A_2(\tau) = \lim_{\tau\to 0} \frac{\tau\psi'(\tau) - \psi(\tau) + \chi(\tau)}{2} \tag{C.34a}$$
$$= \lim_{\tau\to 0} \frac{1}{2}\left(\frac{\tau(2+\alpha^3)}{3} - \frac{(1+\alpha^2)}{2} + \frac{1-\alpha^2}{2}\right) = -\alpha^2/2, \tag{C.34b}$$
$$\lim_{\tau\to 0} A_2'(\tau) = \lim_{\tau\to 0} \frac{\tau\psi''(\tau) + \chi'(\tau)}{2} \tag{C.34c}$$
$$= 0, \tag{C.34d}$$
$$\lim_{\tau\to 0} A_2''(\tau) = \lim_{\tau\to 0} \frac{\tau\psi'''(\tau) + \psi''(\tau) + \chi''(\tau)}{2} \tag{C.34e}$$
$$= \lim_{\tau\to 0} \frac{1}{2}\left(\frac{\tau(4+\alpha^5)}{5} + \frac{(3+\alpha^4)}{4} + \frac{(\alpha^4-1)}{4}\right) \tag{C.34f}$$
$$= \frac{1+\alpha^4}{4}. \tag{C.34g}$$

$$\lim_{\tau\to 0} A_3(\tau) = \lim_{\tau\to 0} \chi(\tau) + \left(\frac{1}{2\alpha^2} - 1\right)[A_1 + 2A_2 + 3\chi(\tau)] \tag{C.35a}$$
$$= \lim_{\tau\to 0} \frac{1-\alpha^2}{2} + \left(\frac{1}{2\alpha^2} - 1\right)\left(\frac{3(\alpha^2-1)}{2} - \alpha^2 + \frac{3(1-\alpha^2)}{2}\right) \tag{C.35b}$$
$$= \lim_{\tau\to 0} \frac{1-\alpha^2}{2} - \frac{1}{2} + \alpha^2 = \frac{\alpha^2}{2}, \tag{C.35c}$$
$$\lim_{\tau\to 0} A_3'(\tau) = \lim_{\tau\to 0} \chi'(\tau) + \left(\frac{1}{2\alpha^2} - 1\right)[A_1' + 2A_2' + 3\chi'(\tau)] \tag{C.35d}$$
$$= 0 + \left(\frac{1}{2\alpha^2} - 1\right)(0+0+0) \tag{C.35e}$$
$$= 0, \tag{C.35f}$$
$$\lim_{\tau\to 0} A_3''(\tau) = \lim_{\tau\to 0} \chi''(\tau) + \left(\frac{1}{2\alpha^2} - 1\right)[A_1'' + 2A_2'' + 3\chi''(\tau)] \tag{C.35g}$$
$$= \frac{\alpha^4-1}{4} + \left(\frac{1}{2\alpha^2} - 1\right)\left(\frac{1-\alpha^4}{4} + \frac{1+\alpha^4}{2} + \frac{3(\alpha^4-1)}{4}\right) \tag{C.35h}$$
$$= \frac{\alpha^4-1}{4} + \frac{\alpha^2}{2} - \alpha^4 = \frac{-1+2\alpha^2-3\alpha^4}{4}. \tag{C.35i}$$

$$\lim_{\tau\to 0} B_1 = \lim_{\tau\to 0}\ A_1'\tau - 5A_1 = \frac{15}{2}(1-\alpha^2), \tag{C.36a}$$

$$\lim_{\tau\to 0} B_2 = \lim_{\tau\to 0}\ (A_2'\tau - 3A_2 + A_1)/2 = \frac{3\alpha^2}{4} + \frac{3}{4}(\alpha^2-1) = \frac{3\alpha^2}{2} - \frac{3}{4}, \tag{C.36b}$$

$$\lim_{\tau\to 0} B_2' = \lim_{\tau\to 0}\ (A_2''\tau - 2A_2' + A_1')/2 = 0, \tag{C.36c}$$

$$\lim_{\tau\to 0} B_3 = \lim_{\tau\to 0}\ A_1 + \left(\frac{1}{2\alpha^2} - 1\right)(A_1'\tau + 2A_2'\tau - 6A_2) = \frac{3}{2}(\alpha^2-1) + \left(\frac{1}{2\alpha^2}-1\right)3\alpha^2 = -\frac{3\alpha^2}{2}, \tag{C.36d}$$

$$\lim_{\tau\to 0} B_4 = \lim_{\tau\to 0} A_2 = -\alpha^2/2, \tag{C.36e}$$

$$\lim_{\tau\to 0} B_4' = \lim_{\tau\to 0} A_2' = 0, \tag{C.36f}$$

$$\lim_{\tau\to 0} B_5 = \lim_{\tau\to 0}\ A_3'\tau - 3A_3 = -\frac{3\alpha^2}{2}, \tag{C.36g}$$

$$\lim_{\tau\to 0} B_6 = \lim_{\tau\to 0}\ A_3 + \left(\frac{1}{2\alpha^2} - 1\right)(A_3'\tau + 2A_2) = \frac{\alpha^2}{2} + \left(\frac{1}{2\alpha^2}-1\right)(-\alpha^2) = \frac{3\alpha^2-1}{2}, \tag{C.36h}$$

$$\lim_{\tau\to 0} B_6' = \lim_{\tau\to 0}\ A_3' + \left(\frac{1}{2\alpha^2} - 1\right)(A_3''\tau + A_3' + 2A_2') = 0. \tag{C.36i}$$

Observe that the first derivatives of the functions $A_k$ and $B_j$ $(j = 2, 4, 6)$ are zero, and hence, the coefficients $A_{k,1}$ and $B_{j,1}$ are zero.

The $\xi_1$ and $\xi_2$ derivatives of $J(\boldsymbol{\eta})$, $\mathbf{R}$ and $\boldsymbol{\phi}(\boldsymbol{\xi})$ are derived below. Recall that $J(\boldsymbol{\eta}) = \mathcal{J}(\boldsymbol{\xi})\tilde{\mathcal{J}}$, where $\tilde{\mathcal{J}}$ is a constant. Also, $\mathbf{R} = \mathbf{x}' - \mathbf{x}$, where $\mathbf{x}'$ is a function of $\boldsymbol{\xi}$ and $\mathbf{x}$ is a constant. We have

$$\mathcal{J}(\boldsymbol{\xi}) = \sqrt{(\mathbf{e}_1\cdot\mathbf{e}_1)(\mathbf{e}_2\cdot\mathbf{e}_2) - (\mathbf{e}_1\cdot\mathbf{e}_2)^2}. \tag{C.37}$$

Therefore, the derivative of $\mathcal{J}(\boldsymbol{\xi})$ with respect to $\xi_i$ is given by

$$\frac{\partial\mathcal{J}}{\partial\xi_i} = \frac{1}{2\mathcal{J}}\left[|\mathbf{e}_2|^2\left(2\frac{\partial\mathbf{e}_1}{\partial\xi_i}\cdot\mathbf{e}_1\right) + |\mathbf{e}_1|^2\left(2\frac{\partial\mathbf{e}_2}{\partial\xi_i}\cdot\mathbf{e}_2\right) - 2(\mathbf{e}_1\cdot\mathbf{e}_2)\left(\frac{\partial\mathbf{e}_1}{\partial\xi_i}\cdot\mathbf{e}_2 + \mathbf{e}_1\cdot\frac{\partial\mathbf{e}_2}{\partial\xi_i}\right)\right]. \tag{C.38}$$

Next, note that the vector $\boldsymbol{\phi}(\boldsymbol{\xi})$ is of the form $\boldsymbol{\phi}(\boldsymbol{\xi}) = L_i(\boldsymbol{\xi})\mathbf{e}_\alpha^{(p)}(\boldsymbol{\xi})$ for basis function indexed by $\alpha$ at the $i^{th}$ node on triangle $p$. Therefore,

$$\frac{\partial\boldsymbol{\phi}}{\partial\xi_j} = \frac{\partial L_i(\boldsymbol{\xi})}{\partial\xi_j}\mathbf{e}_\alpha^{(p)}(\boldsymbol{\xi}) + L_i(\boldsymbol{\xi})\frac{\partial\mathbf{e}_\alpha^{(p)}(\boldsymbol{\xi})}{\partial\xi_j}. \tag{C.39}$$

The first derivatives of $\mathbf{R}$ with respect to $\boldsymbol{\xi}_1$ and $\boldsymbol{\xi}_2$ are the basis vectors $\mathbf{e}_1$ and $\mathbf{e}_2$, and the second derivatives of $\mathbf{R}$ are the derivatives of these basis vectors, which can determined easily. The coefficients of the Taylor series expansion of $\hat{\mathbf{R}}$ are determined from those of $\mathbf{R}$ according to (C.17). To determine the coefficients of the following expansion

$$J\hat{\mathbf{n}}' = \mathbf{N}_0 + \rho\mathbf{N}_1 + O(\rho^2), \tag{C.40}$$

we first observe that $J\hat{\mathbf{n}}' = \tilde{\mathcal{J}}(\boldsymbol{\eta})\mathbf{e}_3(\boldsymbol{\xi}) = \tilde{\mathcal{J}}(\boldsymbol{\eta})\ \mathbf{e}_1(\boldsymbol{\xi}) \times \mathbf{e}_2(\boldsymbol{\xi})$. Since $\tilde{\mathcal{J}}(\boldsymbol{\eta})$ is constant, we need only the following derivative

$$\frac{\partial \mathbf{e}_3(\boldsymbol{\xi})}{\partial \xi_j} = \frac{\partial \mathbf{e}_1(\boldsymbol{\xi})}{\partial \xi_j} \times \mathbf{e}_2(\boldsymbol{\xi}) + \mathbf{e}_1(\boldsymbol{\xi}) \times \frac{\partial \mathbf{e}_2(\boldsymbol{\xi})}{\partial \xi_j}. \tag{C.41}$$

## C.2 Nearly-Singular Integrals

### C.2.1 H-kernel

***Third term.*** The third term in Equation (4.133) is

$$\tilde{F}_3(\rho,\theta) = \frac{\mu}{\pi R^3} B_2(\hat{\mathbf{R}}\cdot\hat{\mathbf{n}}')(\hat{\mathbf{R}}\cdot\tilde{\mathbf{e}})(\hat{\mathbf{n}}\cdot\boldsymbol{\phi})\ J\rho \tag{C.42a}$$

$$= \frac{\mu}{\pi R^5} B_2(\mathbf{R}\cdot\mathbf{e}_3)(\mathbf{R}\cdot\tilde{\mathbf{e}})(\hat{\mathbf{n}}\cdot\boldsymbol{\phi})\ \tilde{\mathcal{J}}(\boldsymbol{\eta})\rho, \tag{C.42b}$$

which is in same form as Equation (4.147a), with $\hat{\mathbf{n}}$ and $\tilde{\mathbf{e}}$ interchanging positions.

$$B_2(\mathbf{R}\cdot\mathbf{e}_3)(\mathbf{R}\cdot\tilde{\mathbf{e}})(\hat{\mathbf{n}}\cdot\boldsymbol{\phi}) = \sum_{k=0}^{3} H_{2,k}\rho^k + O(\rho^2), \tag{C.43}$$

where the coefficients $H_{2,k}$ are obtained by multiplication of the polynomials $\tilde{B}_2$, $M_0$, $M_1$ and $M_5$. Then

$$\tilde{F}_3(\rho,\theta) = \frac{\mu}{\pi R_a^5}\left[\sum_{k=0}^{3} H_{2,k}\rho^{k+1} + G(\rho,\theta)\right]\tilde{\mathcal{J}}(\boldsymbol{\eta}), \tag{C.44}$$

where $G(\rho,\theta)$ is either $O(\rho^3)$ or $O(\rho^4/R_a^2)$. The following part of the integrand is smooth and can be integrated numerically

$$\tilde{F}_3^S(\rho,\theta) = \tilde{F}_3(\rho,\theta) - \frac{\mu}{\pi R_a^5}\left[\sum_{k=0}^{3} H_{2,k}\rho^{k+1}\right]\tilde{\mathcal{J}}(\boldsymbol{\eta}). \tag{C.45}$$

***Fourth term.*** The fourth term in Equation (4.133) is

$$\tilde{F}_4(\rho,\theta) = \frac{\mu}{\pi R^3} B_3(\hat{\mathbf{R}}\cdot\hat{\mathbf{n}}')(\tilde{\mathbf{e}}\cdot\hat{\mathbf{n}})(\hat{\mathbf{R}}\cdot\boldsymbol{\phi})\ J\rho \tag{C.46a}$$

$$= \frac{\mu}{\pi R^5} B_3(\mathbf{R}\cdot\mathbf{e}_3)(\tilde{\mathbf{e}}\cdot\hat{\mathbf{n}})(\mathbf{R}\cdot\boldsymbol{\phi})\ \tilde{\mathcal{J}}(\boldsymbol{\eta})\rho. \tag{C.46b}$$

$$B_3(\tilde{\mathbf{e}}\cdot\hat{\mathbf{n}})(\mathbf{R}\cdot\mathbf{e}_3)(\mathbf{R}\cdot\boldsymbol{\phi}) = \sum_{k=0}^{3} H_{3,k}\rho^k + O(\rho^2), \tag{C.47}$$

where the coefficients $H_{3,k}$ are obtained by multiplication of the polynomials $\tilde{B}_3$, $M_0$ and $M_2$. Note that $\tilde{\mathbf{e}}\cdot\hat{\mathbf{n}}$ is a constant and is factored into the coefficients.

$$\tilde{F}_4(\rho,\theta) = \frac{\mu}{\pi R_a^5}\left[\sum_{k=0}^{3} H_{3,k}\rho^{k+1} + G(\rho,\theta)\right]\tilde{\mathcal{J}}(\boldsymbol{\eta}), \tag{C.48}$$

where $G(\rho,\theta)$ is either $O(\rho^3)$ or $O(\rho^4/R_a^2)$. The subtracted integrand is

$$\tilde{F}_4^S(\rho,\theta) = \tilde{F}_4(\rho,\theta) - \frac{\mu}{\pi R_a^5}\left[\sum_{k=0}^{3} H_{3,k}\rho^{k+1}\right]\tilde{\mathcal{J}}(\boldsymbol{\eta}). \tag{C.49}$$

***Fifth term.*** Now consider the fifth term in Equation (4.133)

$$\tilde{F}_5(\rho,\theta) = \frac{\mu}{\pi R^3} B_2(\hat{\mathbf{R}}\cdot\hat{\mathbf{n}})(\tilde{\mathbf{e}}\cdot\hat{\mathbf{n}}')(\hat{\mathbf{R}}\cdot\boldsymbol{\phi})\ J\rho \tag{C.50a}$$

$$= \frac{\mu}{\pi R^5} B_2(\mathbf{R}\cdot\hat{\mathbf{n}})(\tilde{\mathbf{e}}\cdot\mathbf{e}_3)(\mathbf{R}\cdot\boldsymbol{\phi})\ \tilde{\mathcal{J}}(\boldsymbol{\eta})\rho. \tag{C.50b}$$

$$B_2(\mathbf{R}\cdot\boldsymbol{\phi})(\mathbf{R}\cdot\hat{\mathbf{n}})(\tilde{\mathbf{e}}\cdot\mathbf{e}_3) = \sum_{k=0}^{3} H_{4,k}\rho^k + O(\rho^2), \tag{C.51}$$

where the coefficients $H_{4,k}$ are obtained by multiplication of the polynomials $\tilde{B}_2$, $M_2$, $M_3$ and $M_6$. Then

$$\tilde{F}_5(\rho,\theta) = \frac{\mu}{\pi R_a^5}\left[\sum_{k=0}^{3} H_{4,k}\rho^{k+1} + G(\rho,\theta)\right]\tilde{\mathcal{J}}(\boldsymbol{\eta}), \tag{C.52}$$

where $G(\rho,\theta)$ is either $O(\rho^3)$ or $O(\rho^4/R_a^2)$.

$$\tilde{F}_5^S(\rho,\theta) = \tilde{F}_5(\rho,\theta) - \frac{\mu}{\pi R_a^5}\left[\sum_{k=0}^{3} H_{4,k}\rho^{k+1}\right]\tilde{\mathcal{J}}(\boldsymbol{\eta}). \tag{C.53}$$

***Sixth term.*** The sixth term in Equation (4.133) is

$$\tilde{F}_6(\rho,\theta) = \frac{\mu}{\pi R^3} B_5(\hat{\mathbf{R}}\cdot\hat{\mathbf{n}})(\hat{\mathbf{R}}\cdot\tilde{\mathbf{e}})(\hat{\mathbf{n}}'\cdot\boldsymbol{\phi})\ J\rho \tag{C.54a}$$

$$= \frac{\mu}{\pi R^5} B_5(\mathbf{R}\cdot\hat{\mathbf{n}})(\mathbf{R}\cdot\tilde{\mathbf{e}})(\boldsymbol{\phi}\cdot\mathbf{e}_3)\ \tilde{\mathcal{J}}(\boldsymbol{\eta})\rho. \tag{C.54b}$$

$$B_5(\mathbf{R}\cdot\tilde{\mathbf{e}})(\mathbf{R}\cdot\hat{\mathbf{n}})(\boldsymbol{\phi}\cdot\mathbf{e}_3) = \sum_{k=0}^{3} H_{5,k}\rho^k + O(\rho^2), \tag{C.55}$$

where the coefficients $H_{5,k}$ are obtained by multiplication of the polynomials $\tilde{B}_5$, $M_1$, $M_3$ and $M_7$. Then

$$\tilde{F}_6(\rho,\theta) = \frac{\mu}{\pi R_a^5}\left[\sum_{k=0}^{3} H_{5,k}\rho^{k+1} + G(\rho,\theta)\right]\tilde{\mathcal{J}}(\boldsymbol{\eta}), \tag{C.56}$$

where $G(\rho,\theta)$ is either $O(\rho^3)$ or $O(\rho^4/R_a^2)$. The subtracted integrand is

$$\tilde{F}_6^S(\rho,\theta) = \tilde{F}_6(\rho,\theta) - \frac{\mu}{\pi R_a^5}\left[\sum_{k=0}^{3} H_{5,k}\rho^{k+1}\right]\tilde{\mathcal{J}}(\boldsymbol{\eta}). \tag{C.57}$$

***Seventh term.*** The seventh term in Equation (4.133) is

$$\tilde{F}_7(\rho,\theta) = \frac{\mu}{\pi R^3} B_2(\hat{\mathbf{R}}\cdot\tilde{\mathbf{e}})(\hat{\mathbf{R}}\cdot\boldsymbol{\phi})(\hat{\mathbf{n}}\cdot\hat{\mathbf{n}}')\ J\rho \tag{C.58a}$$

$$= \frac{\mu}{\pi R^5} B_2(\mathbf{R}\cdot\tilde{\mathbf{e}})(\mathbf{R}\cdot\boldsymbol{\phi})(\hat{\mathbf{n}}\cdot\mathbf{e}_3)\ \tilde{\mathcal{J}}(\boldsymbol{\eta})\rho. \tag{C.58b}$$

$$B_2(\mathbf{R}\cdot\tilde{\mathbf{e}})(\mathbf{R}\cdot\boldsymbol{\phi})(\hat{\mathbf{n}}\cdot\mathbf{e}_3) = \sum_{k=0}^{3} H_{6,k}\rho^k + O(\rho^2), \tag{C.59}$$

where the coefficients $H_{6,k}$ are obtained by multiplication of the polynomials $\tilde{B}_2$, $M_1$, $M_2$ and $M_8$. Then

$$\tilde{F}_7(\rho,\theta) = \frac{\mu}{\pi R_a^5}\left[\sum_{k=0}^{3} H_{6,k}\rho^{k+1} + G(\rho,\theta)\right]\tilde{\mathcal{J}}(\boldsymbol{\eta}), \tag{C.60}$$

where $G(\rho,\theta)$ is either $O(\rho^3)$ or $O(\rho^4/R_a^2)$. The subtracted integrand is

$$\tilde{F}_7^S(\rho,\theta) = \tilde{F}_7(\rho,\theta) - \frac{\mu}{\pi R_a^5}\left[\sum_{k=0}^{3} H_{6,k}\rho^{k+1}\right]\tilde{\mathcal{J}}(\boldsymbol{\eta}). \tag{C.61}$$

***Eighth term.*** The eighth term in Equation (4.133) is

$$\tilde{F}_8(\rho,\theta) = \frac{\mu}{\pi R^3} B_4(\hat{\mathbf{n}}\cdot\hat{\mathbf{n}}')(\tilde{\mathbf{e}}\cdot\boldsymbol{\phi})\ J\rho \tag{C.62a}$$

$$= \frac{\mu}{\pi R^3} B_4(\hat{\mathbf{n}}\cdot\mathbf{e}_3)(\tilde{\mathbf{e}}\cdot\boldsymbol{\phi})\ \tilde{\mathcal{J}}(\boldsymbol{\eta})\rho. \tag{C.62b}$$

$$B_4(\hat{\mathbf{n}}\cdot\mathbf{e}_3)(\tilde{\mathbf{e}}\cdot\boldsymbol{\phi}) = \sum_{k=0}^{1} H_{7,k}\rho^k + O(\rho^2), \tag{C.63}$$

where the coefficients $H_{7,k}$ are obtained by multiplication of the polynomials $\tilde{B}_4$, $M_4$ and $M_8$. Then

$$\tilde{F}_8(\rho,\theta) = \frac{\mu}{\pi R_a^3}\left[\sum_{k=0}^{1} H_{7,k}\rho^{k+1} + G(\rho,\theta)\right]\tilde{\mathcal{J}}(\boldsymbol{\eta}), \tag{C.64}$$

where $G(\rho,\theta)$ is either $O(\rho^3)$ or $O(\rho^4/R_a^2)$. The subtracted integrand is

$$\tilde{F}_8^S(\rho,\theta) = \tilde{F}_8(\rho,\theta) - \frac{\mu}{\pi R_a^3}\left[\sum_{k=0}^{1} H_{7,k}\rho^{k+1}\right]\tilde{\mathcal{J}}(\boldsymbol{\eta}). \tag{C.65}$$

***Ninth term.*** The ninth term in Equation (4.133) is

$$\tilde{F}_9(\rho,\theta) = \frac{\mu}{\pi R^3} B_4(\tilde{\mathbf{e}}\cdot\hat{\mathbf{n}}')(\hat{\mathbf{n}}\cdot\boldsymbol{\phi})\ J\rho \tag{C.66a}$$

$$= \frac{\mu}{\pi R^3} B_4(\tilde{\mathbf{e}}\cdot\mathbf{e}_3)(\hat{\mathbf{n}}\cdot\boldsymbol{\phi})\ \tilde{\mathcal{J}}(\boldsymbol{\eta})\rho. \tag{C.66b}$$

$$B_4(\hat{\mathbf{n}}\cdot\boldsymbol{\phi})(\tilde{\mathbf{e}}\cdot\mathbf{e}_3) = \sum_{k=0}^{1} H_{8,k}\rho^k + O(\rho^2), \tag{C.67}$$

where the coefficients $H_{8,k}$ are obtained by multiplication of the polynomials $\tilde{B}_4$, $M_5$ and $M_6$. Then

$$\tilde{F}_9(\rho,\theta) = \frac{\mu}{\pi R_a^3}\left[\sum_{k=0}^{1} H_{8,k}\rho^{k+1} + G(\rho,\theta)\right]\tilde{\mathcal{J}}(\boldsymbol{\eta}), \tag{C.68}$$

where $G(\rho,\theta)$ is either $O(\rho^3)$ or $O(\rho^4/R_a^2)$. The subtracted integrand is

$$\tilde{F}_9^S(\rho,\theta) = \tilde{F}_9(\rho,\theta) - \frac{\mu}{\pi R_a^3}\left[\sum_{k=0}^{1} H_{8,k}\rho^{k+1}\right]\tilde{\mathcal{J}}(\boldsymbol{\eta}). \tag{C.69}$$

***Tenth term.*** The tenth term in Equation (4.133) is

$$\tilde{F}_{10}(\rho,\theta) = \frac{\mu}{\pi R^3} B_6(\tilde{\mathbf{e}}\cdot\hat{\mathbf{n}})(\boldsymbol{\phi}\cdot\hat{\mathbf{n}}')\ J\rho \tag{C.70a}$$

$$= \frac{\mu}{\pi R^3} B_6(\tilde{\mathbf{e}}\cdot\hat{\mathbf{n}})(\boldsymbol{\phi}\cdot\mathbf{e}_3)\ \tilde{\mathcal{J}}(\boldsymbol{\eta})\rho. \tag{C.70b}$$

$$B_6(\boldsymbol{\phi}\cdot\mathbf{e}_3)(\tilde{\mathbf{e}}\cdot\hat{\mathbf{n}}) = \sum_{k=0}^{1} H_{9,k}\rho^k + O(\rho^2), \tag{C.71}$$

where the coefficients $H_{9,k}$ are obtained by multiplication of the polynomials $\tilde{B}_6$ and $M_7$. The constant $\tilde{\mathbf{e}}\cdot\hat{\mathbf{n}}$ is factored into the coefficients. Then

$$\tilde{F}_{10}(\rho,\theta) = \frac{\mu}{\pi R_a^3}\left[\sum_{k=0}^{1} H_{9,k}\rho^{k+1} + G(\rho,\theta)\right]\tilde{\mathcal{J}}(\boldsymbol{\eta}), \tag{C.72}$$

where $G(\rho,\theta)$ is either $O(\rho^3)$ or $O(\rho^4/R_a^2)$. The subtracted integrand is

$$\tilde{F}_{10}^S(\rho,\theta) = \tilde{F}_{10}(\rho,\theta) - \frac{\mu}{\pi R_a^3}\left[\sum_{k=0}^{1} H_{9,k}\rho^{k+1}\right]\tilde{\mathcal{J}}(\boldsymbol{\eta}). \tag{C.73}$$

### C.2.2 K-Kernel

Nearly-singular integrals of the K-kernel can be reduced to a general form similar to the H-kernel. The general form of these integrals is

$$I_K = \int_\Gamma \tilde{G}(\rho,\theta)d\rho d\theta, \tag{C.74}$$

with $\tilde{G}(\rho,\theta) = \mathbf{K}\cdot\boldsymbol{\phi}\tilde{J}\rho$, where $\tilde{J}$ is as defined in (C.4) and $\mathbf{K}$, $\boldsymbol{\phi}$, and $\tilde{J}$ should be seen as functions of $\rho$ and $\theta$. Recall that the kernel $\overline{\mathbf{K}}_{\pm}^{(2)}(\mathbf{x},\mathbf{x}')$ is given by

$$\overline{\mathbf{K}}_{\pm}^{(2)}(\mathbf{x},\mathbf{x}') = \frac{1}{2\pi R^2}\left\{\left(A_1\hat{\mathbf{R}}\hat{\mathbf{R}} + A_2\bar{\mathbf{I}}\right)\hat{\mathbf{R}}\cdot\hat{\mathbf{n}} + \left(A_3\hat{\mathbf{n}}\hat{\mathbf{R}} + A_2\hat{\mathbf{R}}\hat{\mathbf{n}}\right)\right\}. \tag{C.75}$$

Therefore $\tilde{G}(\rho,\theta)$ is in the general form

$$\tilde{G}(\rho,\theta) = \tilde{\mathbf{e}}\cdot\overline{\mathbf{K}}(\mathbf{x},\mathbf{x}')\cdot\boldsymbol{\phi}\tilde{J}\rho \tag{C.76a}$$

$$= \frac{1}{2\pi R^2}\tilde{\mathbf{e}}\cdot\left\{\hat{\mathbf{R}}\cdot\hat{\mathbf{n}}\left(A_1\hat{\mathbf{R}}\hat{\mathbf{R}} + A_2\bar{\mathbf{I}}\right) + \left(A_3\hat{\mathbf{n}}\hat{\mathbf{R}} + A_2\hat{\mathbf{R}}\hat{\mathbf{n}}\right)\right\}\cdot\boldsymbol{\phi}\tilde{J}\rho. \tag{C.76b}$$

***First term.*** The first term in Equation (C.76b) is

$$\tilde{G}_1(\rho,\theta) = \frac{1}{2\pi R^2} A_1(\tilde{\mathbf{e}}\cdot\hat{\mathbf{R}})(\boldsymbol{\phi}\cdot\hat{\mathbf{R}})(\hat{\mathbf{R}}\cdot\hat{\mathbf{n}})\ \tilde{J}\rho \tag{C.77a}$$

$$= \frac{1}{2\pi R^5} A_1(\tilde{\mathbf{e}}\cdot\mathbf{R})(\boldsymbol{\phi}\cdot\mathbf{R})(\mathbf{R}\cdot\hat{\mathbf{n}})\tilde{J}\rho. \tag{C.77b}$$

Define the Taylor series expansions $\tilde{J} = M_{9,0} + \rho M_{9,1} + O(\rho^2)$ and $A_j = \tilde{A}_{j,1} + \rho\tilde{A}_{j,1} + O(\rho^2)$ for $j = 1,2,3$. Also, define polynomials $\tilde{A}_k$ from the respective coefficients of the Taylor series expansions. From the expansions (4.136), we have

$$A_1(\tilde{\mathbf{e}}\cdot\mathbf{R})(\boldsymbol{\phi}\cdot\mathbf{R})(\mathbf{R}\cdot\hat{\mathbf{n}})\tilde{J} = \sum_{k=0}^{3} K_{0,k}\rho^k + O(\rho^2), \tag{C.78}$$

where the coefficients $K_{0,k}$ are obtained by multiplication of the polynomials $\tilde{A}_1$, $M_1$, $M_2$, $M_3$ and $M_9$.

Then

$$\tilde{G}_1(\rho,\theta) = \frac{1}{2\pi R_a^5}\left[\sum_{k=0}^{3} K_{0,k}\rho^{k+1} + G(\rho,\theta)\right], \tag{C.79}$$

where $G(\rho,\theta)$ is either $O(\rho^3)$ or $O(\rho^4/R_a^2)$. The subtracted integrand is

$$\tilde{G}_1^S(\rho,\theta) = \tilde{G}_1(\rho,\theta) - \frac{1}{2\pi R_a^5}\left[\sum_{k=0}^{3} K_{0,k}\rho^{k+1}\right]. \tag{C.80}$$

***Second term.*** The second term in Equation (C.76b) is

$$\tilde{G}_2(\rho,\theta) = \frac{1}{2\pi R^2} A_2(\tilde{\mathbf{e}}\cdot\boldsymbol{\phi})(\hat{\mathbf{R}}\cdot\hat{\mathbf{n}})\ \tilde{J}\rho \tag{C.81a}$$

$$= \frac{1}{2\pi R^3} A_2(\tilde{\mathbf{e}}\cdot\boldsymbol{\phi})(\mathbf{R}\cdot\hat{\mathbf{n}})\tilde{J}\rho. \tag{C.81b}$$

$$A_2(\mathbf{R}\cdot\hat{\mathbf{n}})(\tilde{\mathbf{e}}\cdot\boldsymbol{\phi})\tilde{J} = \sum_{k=0}^{1} K_{1,k}\rho^k + O(\rho^2), \tag{C.82}$$

where the coefficients $K_{1,k}$ are obtained by multiplication of the polynomials $\tilde{A}_2$, $M_3$, $M_4$ and $M_9$. Then

$$\tilde{G}_2(\rho,\theta) = \frac{1}{2\pi R_a^3}\left[\sum_{k=0}^{1} K_{1,k}\rho^{k+1} + G(\rho,\theta)\right], \tag{C.83}$$

where $G(\rho,\theta)$ is either $O(\rho^3)$ or $O(\rho^4/R_a^2)$. The subtracted integrand is

$$\tilde{G}_2^S(\rho,\theta) = \tilde{G}_2(\rho,\theta) - \frac{1}{2\pi R_a^3}\left[\sum_{k=0}^{1} K_{1,k}\rho^{k+1}\right]. \tag{C.84}$$

***Third term.*** The third term in Equation (C.76b) is

$$\tilde{G}_3(\rho,\theta) = \frac{1}{2\pi R^2} A_3(\tilde{\mathbf{e}}\cdot\hat{\mathbf{n}})(\hat{\mathbf{R}}\cdot\boldsymbol{\phi})\ \tilde{J}\rho \tag{C.85a}$$

$$= \frac{1}{2\pi R^3} A_3(\tilde{\mathbf{e}}\cdot\hat{\mathbf{n}})(\mathbf{R}\cdot\boldsymbol{\phi})\tilde{J}\rho. \tag{C.85b}$$

$$A_3(\mathbf{R}\cdot\boldsymbol{\phi})(\tilde{\mathbf{e}}\cdot\hat{\mathbf{n}})\tilde{J} = \sum_{k=0}^{1} K_{2,k}\rho^k + O(\rho^2), \tag{C.86}$$

where the coefficients $K_{2,k}$ are obtained by multiplication of the polynomials $\tilde{A}_3$, $M_2$ and $M_9$. The constant $\tilde{\mathbf{e}}\cdot\hat{\mathbf{n}}$ is absorbed into the coefficients. Then

$$\tilde{G}_3(\rho,\theta) = \frac{1}{2\pi R_a^3}\left[\sum_{k=0}^{1} K_{2,k}\rho^{k+1} + G(\rho,\theta)\right], \tag{C.87}$$

where $G(\rho,\theta)$ is either $O(\rho^3)$ or $O(\rho^4/R_a^2)$. The subtracted integrand is

$$\tilde{G}_3^S(\rho,\theta) = \tilde{G}_3(\rho,\theta) - \frac{1}{2\pi R_a^3}\left[\sum_{k=0}^{1} K_{2,k}\rho^{k+1}\right]. \tag{C.88}$$

***Fourth term.*** The fourth term in Equation (C.76b) is

$$\tilde{G}_4(\rho,\theta) = \frac{1}{2\pi R^2} A_2(\tilde{\mathbf{e}}\cdot\hat{\mathbf{R}})(\hat{\mathbf{n}}\cdot\boldsymbol{\phi})\ \tilde{J}\rho \tag{C.89a}$$

$$= \frac{1}{2\pi R^3} A_2(\tilde{\mathbf{e}}\cdot\mathbf{R})(\hat{\mathbf{n}}\cdot\boldsymbol{\phi})\tilde{J}\rho. \tag{C.89b}$$

$$A_2(\mathbf{e}\cdot\mathbf{R})(\hat{\mathbf{n}}\cdot\boldsymbol{\phi})\tilde{J} = \sum_{k=0}^{1} K_{3,k}\rho^k + O(\rho^2), \tag{C.90}$$

where the coefficients $K_{3,k}$ are obtained by multiplication of the polynomials $\tilde{A}_2$, $M_1$, $M_5$ and $M_9$. Then

$$\tilde{G}_4(\rho,\theta) = \frac{1}{2\pi R_a^3}\left[\sum_{k=0}^{1} K_{3,k}\rho^{k+1} + G(\rho,\theta)\right], \tag{C.91}$$

where $G(\rho,\theta)$ is either $O(\rho^3)$ or $O(\rho^4/R_a^2)$. The subtracted integrand is

$$\tilde{G}_4^S(\rho,\theta) = \tilde{G}_4(\rho,\theta) - \frac{1}{2\pi R_a^3}\left[\sum_{k=0}^{1} K_{3,k}\rho^{k+1}\right]. \tag{C.92}$$

### C.2.3 U-Kernel

The general form of the integrals of the U-kernel can be obtained directly from that of the K-kernel by switching the kernels. An alternate expression for $\overline{\mathbf{U}}_{\pm}(\mathbf{x},\mathbf{x}')$ is used for singularity subtraction:

$$\overline{\mathbf{U}}_{\pm}(\mathbf{x},\mathbf{x}') = \frac{1}{4\pi\mu_{\pm}R}\left(A_4\hat{\mathbf{R}}\hat{\mathbf{R}} + A_5\bar{\mathbf{I}}\right), \tag{C.93}$$

where

$$A_4 = \frac{(\alpha\tau^2 - 3\alpha\tau + 3)e^{\alpha\tau} - (\tau^2 - 3\tau + 3)e^{\tau}}{\tau^2}, \tag{C.94}$$

$$A_5 = \frac{(\alpha\tau - 1)e^{\alpha\tau} - (-\tau^2 + \tau - 1)e^{\tau}}{\tau^2}. \tag{C.95}$$

All other quantities are defined as in (4.25). Therefore, the general form of the integrand $\tilde{Y}(\rho,\theta) = \mathbf{U}\cdot\boldsymbol{\phi}\tilde{J}$ is given by

$$\tilde{Y}(\rho,\theta) = \tilde{\mathbf{e}}\cdot\overline{\mathbf{U}}(\mathbf{x},\mathbf{x}')\cdot\boldsymbol{\phi}\tilde{J}\rho = \frac{1}{4\pi\mu R}\tilde{\mathbf{e}}\cdot\left(A_4\hat{\mathbf{R}}\hat{\mathbf{R}} + A_5\bar{\mathbf{I}}\right)\cdot\boldsymbol{\phi}\tilde{J}\rho. \tag{C.96}$$

Define the Taylor series expansions and $A_j = \tilde{A}_{j,1} + \rho\tilde{A}_{j,1} + O(\rho^2)$ for $j = 4, 5$. Also, define the respective Taylor polynomials as $\tilde{A}_j$.

***First term.*** The first term in Equation (C.96) is

$$\tilde{Y}_1(\rho,\theta) = \frac{1}{4\pi\mu R}A_4(\tilde{\mathbf{e}}\cdot\hat{\mathbf{R}})(\hat{\mathbf{R}}\cdot\boldsymbol{\phi})\ \tilde{J}\rho \tag{C.97a}$$

$$= \frac{1}{4\pi\mu R^3}A_4(\tilde{\mathbf{e}}\cdot\mathbf{R})(\mathbf{R}\cdot\boldsymbol{\phi})\tilde{J}\rho. \tag{C.97b}$$

$$A_4(\tilde{\mathbf{e}}\cdot\mathbf{R})(\mathbf{R}\cdot\boldsymbol{\phi})\tilde{J} = \sum_{k=0}^{1} G_{0,k}\rho^k + O(\rho^2), \tag{C.98}$$

where the coefficients $G_{0,k}$ are obtained by multiplication of the polynomials $\tilde{A}_4$, $M_1$, $M_2$ and $M_9$. Then

$$\tilde{Y}_1(\rho,\theta) = \frac{1}{4\pi\mu R_a^3}\left[\sum_{k=0}^{1} G_{0,k}\rho^{k+1} + G(\rho,\theta)\right], \tag{C.99}$$

where $G(\rho,\theta)$ is either $O(\rho^3)$ or $O(\rho^4/R_a^2)$. The subtracted integrand is

$$\tilde{Y}_1^S(\rho,\theta) = \tilde{Y}_1(\rho,\theta) - \frac{1}{4\pi\mu R_a^3}\left[\sum_{k=0}^{1} G_{0,k}\rho^{k+1}\right]. \tag{C.100}$$

The second term is not nearly-singular. Therefore, no subtraction is required.

### C.2.4 T-Kernel

The general form of the nearly-singular integrals of the T-kernel can be obtained directly from that of the H-kernel by switching the kernels. Recall that $\overline{\mathbf{T}}_{\pm}^{(2)}(\mathbf{x},\mathbf{x}')$ is given by

$$\overline{\mathbf{T}}_{\pm}^{(2)}(\mathbf{x},\mathbf{x}') = \frac{1}{2\pi R^2}\left\{\left(A_1\hat{\mathbf{R}}\hat{\mathbf{R}} + A_2\bar{\mathbf{I}}\right)\hat{\mathbf{R}}\cdot\hat{\mathbf{n}}' + \left(A_2\hat{\mathbf{n}}'\hat{\mathbf{R}} + A_3\hat{\mathbf{R}}\hat{\mathbf{n}}'\right)\right\}. \tag{C.101}$$

Therefore, the general form of the integrand $\tilde{Z}(\rho,\theta) = \mathbf{T}\cdot\boldsymbol{\phi}J$ is given by

$$\tilde{Z}(\rho,\theta) = \tilde{\mathbf{e}}\cdot\overline{\mathbf{T}}(\mathbf{x},\mathbf{x}')\cdot\boldsymbol{\phi}J\rho \tag{C.102}$$

$$= \frac{1}{2\pi R^2}\tilde{\mathbf{e}}\cdot\left\{\hat{\mathbf{R}}\cdot\hat{\mathbf{n}}'\left(A_1\hat{\mathbf{R}}\hat{\mathbf{R}} + A_2\bar{\mathbf{I}}\right) + \left(A_2\hat{\mathbf{n}}'\hat{\mathbf{R}} + A_3\hat{\mathbf{R}}\hat{\mathbf{n}}'\right)\right\}\cdot\boldsymbol{\phi}J\rho. \tag{C.103}$$

***First term.*** The first term in Equation (C.103) is

$$\tilde{Z}_1(\rho,\theta) = \frac{1}{2\pi R^2}A_1(\tilde{\mathbf{e}}\cdot\hat{\mathbf{R}})(\boldsymbol{\phi}\cdot\hat{\mathbf{R}})(\hat{\mathbf{R}}\cdot\hat{\mathbf{n}}')\ J\rho \tag{C.104a}$$

$$= \frac{1}{2\pi R^5}A_1(\tilde{\mathbf{e}}\cdot\mathbf{R})(\boldsymbol{\phi}\cdot\mathbf{R})(\mathbf{R}\cdot\mathbf{e}_3)\tilde{\mathcal{J}}(\boldsymbol{\eta})\rho. \tag{C.104b}$$

$$A_1(\tilde{\mathbf{e}}\cdot\mathbf{R})(\boldsymbol{\phi}\cdot\mathbf{R})(\mathbf{R}\cdot\mathbf{e}_3) = \sum_{k=0}^{3} T_{0,k}\rho^k + O(\rho^2), \tag{C.105}$$

where the coefficients $T_{0,k}$ are obtained by multiplication of the polynomials $\tilde{A}_1$, $M_0$, $M_1$ and $M_2$. Then

$$\tilde{Z}_1(\rho,\theta) = \frac{1}{2\pi R_a^5}\left[\sum_{k=0}^{3} T_{0,k}\rho^{k+1} + G(\rho,\theta)\right]\tilde{\mathcal{J}}(\boldsymbol{\eta}), \tag{C.106}$$

where $G(\rho,\theta)$ is either $O(\rho^3)$ or $O(\rho^4/R_a^2)$. The subtracted integrand is

$$\tilde{Z}_1^S(\rho,\theta) = \tilde{Z}_1(\rho,\theta) - \frac{1}{2\pi R_a^5}\left[\sum_{k=0}^{3} T_{0,k}\rho^{k+1}\right]\tilde{\mathcal{J}}(\boldsymbol{\eta}). \tag{C.107}$$

***Second term.*** The second term in Equation (C.103) is

$$\tilde{Z}_2(\rho,\theta) = \frac{1}{2\pi R^2} A_2(\tilde{\mathbf{e}}\cdot\boldsymbol{\phi})(\hat{\mathbf{R}}\cdot\hat{\mathbf{n}}')\ J\rho \tag{C.108a}$$

$$= \frac{1}{2\pi R^3} A_2(\tilde{\mathbf{e}}\cdot\boldsymbol{\phi})(\mathbf{R}\cdot\mathbf{e}_3)\tilde{\mathcal{J}}(\boldsymbol{\eta})\rho. \tag{C.108b}$$

$$A_2(\mathbf{R}\cdot\mathbf{e}_3)(\tilde{\mathbf{e}}\cdot\boldsymbol{\phi}) = \sum_{k=0}^{1} T_{1,k}\rho^k + O(\rho^2), \tag{C.109}$$

where the coefficients $T_{1,k}$ are obtained by multiplication of the polynomials $\tilde{A}_2$, $M_0$ and $M_4$. Then

$$\tilde{Z}_2(\rho,\theta) = \frac{1}{2\pi R_a^3}\left[\sum_{k=0}^{1} T_{1,k}\rho^{k+1} + G(\rho,\theta)\right]\tilde{\mathcal{J}}(\boldsymbol{\eta}), \tag{C.110}$$

where $G(\rho,\theta)$ is either $O(\rho^3)$ or $O(\rho^4/R_a^2)$. The subtracted integrand is

$$\tilde{Z}_2^S(\rho,\theta) = \tilde{Z}_2(\rho,\theta) - \frac{1}{2\pi R_a^3}\left[\sum_{k=0}^{1} T_{1,k}\rho^{k+1}\right]\tilde{\mathcal{J}}(\boldsymbol{\eta}). \tag{C.111}$$

***Third term.*** The third term in Equation (C.103) is

$$\tilde{Z}_3(\rho,\theta) = \frac{1}{2\pi R^2} A_2(\tilde{\mathbf{e}}\cdot\hat{\mathbf{n}}')(\hat{\mathbf{R}}\cdot\boldsymbol{\phi})\ \tilde{J}\rho \tag{C.112a}$$

$$= \frac{1}{2\pi R^3} A_2(\tilde{\mathbf{e}}\cdot\mathbf{e_3})(\mathbf{R}\cdot\boldsymbol{\phi})\tilde{\mathcal{J}}(\boldsymbol{\eta})\rho. \tag{C.112b}$$

$$A_2(\mathbf{R}\cdot\boldsymbol{\phi})(\tilde{\mathbf{e}}\cdot\mathbf{e_3}) = \sum_{k=0}^{1} T_{2,k}\rho^k + O(\rho^2), \tag{C.113}$$

where the coefficients $T_{2,k}$ are obtained by multiplication of the polynomials $\tilde{A}_2$, $M_2$ and $M_6$. Then

$$\tilde{Z}_3(\rho,\theta) = \frac{1}{2\pi R_a^3}\left[\sum_{k=0}^{1} T_{2,k}\rho^{k+1} + G(\rho,\theta)\right]\tilde{\mathcal{J}}(\boldsymbol{\eta}), \tag{C.114}$$

where $G(\rho,\theta)$ is either $O(\rho^3)$ or $O(\rho^4/R_a^2)$. The subtracted integrand is

$$\tilde{Z}_3^S(\rho,\theta) = \tilde{Z}_3(\rho,\theta) - \frac{1}{2\pi R_a^3}\left[\sum_{k=0}^{1} T_{2,k}\rho^{k+1}\right]\tilde{\mathcal{J}}(\boldsymbol{\eta}). \tag{C.115}$$

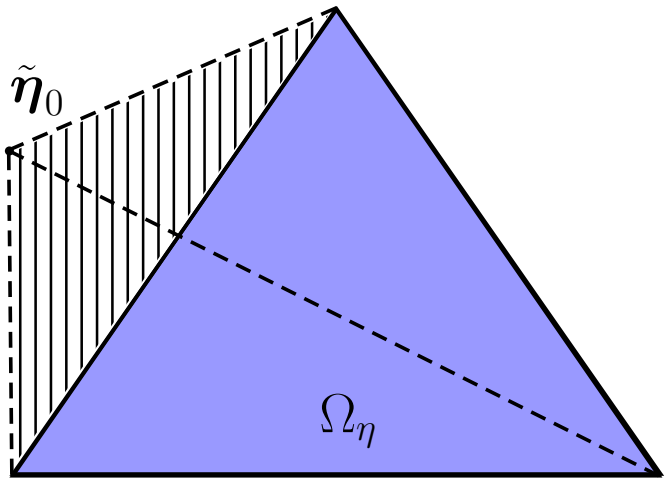


Figure C.1: Analytical integration of nearly-singular integrals. Projection point $\boldsymbol{\eta}_0$ is assumed to lie outside the triangular integration domain.

***Fourth term.*** The fourth term in Equation (C.103) is

$$\tilde{Z}_4(\rho,\theta) = \frac{1}{2\pi R^2} A_3(\tilde{\mathbf{e}}\cdot\hat{\mathbf{R}})(\hat{\mathbf{n}}'\cdot\boldsymbol{\phi})\ \tilde{J}\rho \tag{C.116a}$$

$$= \frac{1}{2\pi R^3} A_3(\tilde{\mathbf{e}}\cdot\mathbf{R})(\mathbf{e}_3\cdot\boldsymbol{\phi})\tilde{\mathcal{J}}(\boldsymbol{\eta})\rho. \tag{C.116b}$$

$$A_3(\tilde{\mathbf{e}}\cdot\mathbf{R})(\mathbf{e}_3\cdot\boldsymbol{\phi}) = \sum_{k=0}^{1} T_{3,k}\rho^k + O(\rho^2), \tag{C.117}$$

where the coefficients $T_{3,k}$ are obtained by multiplication of the polynomials $\tilde{A}_3$, $M_1$ and $M_7$. Then

$$\tilde{Z}_4(\rho,\theta) = \frac{1}{2\pi R_a^3}\left[\sum_{k=0}^{1} T_{3,k}\rho^{k+1} + G(\rho,\theta)\right]\tilde{\mathcal{J}}(\boldsymbol{\eta}), \tag{C.118}$$

where $G(\rho,\theta)$ is either $O(\rho^3)$ or $O(\rho^4/R_a^2)$. The subtracted integrand is

$$\tilde{Z}_4^S(\rho,\theta) = \tilde{Z}_4(\rho,\theta) - \frac{1}{2\pi R_a^3}\left[\sum_{k=0}^{1} T_{3,k}\rho^{k+1}\right]\tilde{\mathcal{J}}(\boldsymbol{\eta}). \tag{C.119}$$

### C.2.5 Analytical Integration of Nearly-Singular Terms

The integral over $\tilde{F}_1^R(\rho,\theta)$ in (4.145) is reproduced below

$$I_R = \int_\Gamma \tilde{F}_1^R(\rho,\theta)\ d\rho d\theta. \tag{C.120}$$

The $\rho$-integral in $I_R$ is evaluated analytically by summing the contributions from the three sub-triangles that are formed by the vertices of the reference triangle $\Omega_\eta$ and the projection point $\boldsymbol{\eta}_0$, as shown in Figure C.1. The contributions from the hatched region in the figure will cancel out in the sum. The limits of the variable $\rho$ are determined according to the foregoing decomposition of the integration domain. For thin scatterers, the assumption that $\boldsymbol{\eta}_0$ lies outside the reference triangle may not be valid. However, as we will see, this assumption is only used for the case when $a = b = 0$. Since the variable $a$ is non-zero when $\boldsymbol{\eta}_0$ lies inside the reference triangle, the foregoing assumption is valid for the purpose of computing the near-singular integrals in this section. Barring constants, the general form of the $\rho$-integrals is as follows

$$I_n^m = \int_0^{\rho_0} \frac{\rho^m}{R_a^{2n+1}} d\rho, \tag{C.121}$$

where $m$ and $n$ are integers with $n = 1, 2, 3$ and $m < 2n + 1$. Recall that $R_a$ is given by

$$R_a = \sqrt{d^2 + \rho 2\mathbf{d} \cdot \mathbf{C} + \rho^2 \left[C^2 + 2\mathbf{d} \cdot \mathbf{D}\right]}, \tag{C.122}$$

where $d$ is the distance between the projection point and the extended surface of the triangle, and $C > 0$. The subscript of $R_a$ will be dropped henceforth for convenience. Therefore, $R$ is in the following general form

$$R = \sqrt{a + b\rho + c\rho^2}, \tag{C.123}$$

where $a \geq 0$, and $b, c \in \mathbb{R}$. When the distance $d$ is zero, $a = b = 0$. In that case, $c$ is always greater than zero. When $d \neq 0$, $c$ can be zero in some instances. The integral is evaluated differently for the following four cases

1. $a = b = 0$, $c > 0$,
2. $a \neq 0$, $b \in \mathbb{R}$, $c \neq 0$,
3. $a \neq 0$, $b \neq 0$, $c = 0$,
4. $a \neq 0$, $b = 0$, $c = 0$.

In the first case, the integral reduces to

$$I_n^m = \int_0^{\rho_0} \frac{\rho^m}{c^{\frac{2n+1}{2}} \rho^{2n+1}} d\rho. \tag{C.124}$$

This integral is hypersingular for $m \neq 2n$ and strongly-singular, otherwise. The singularity occurs due to decomposition of the integral domain in (C.120) into three subtriangles and evaluating integrals over them separately. If $I_R$ is computed without including the hatched region in Figure C.1 in any of the integrals, there would be no need to deal with singularities. One can verify that dropping the terms resulting from the lower limit in (C.124) is equivalent to computing $I_R$ in this fashion. Therefore, we have

$$I_n^m = \begin{cases} \dfrac{\rho_0^{m-2n}}{c^{\frac{2n+1}{2}}(m-2n)} & (m \neq 2n) \\ \dfrac{1}{c^{\frac{2n+1}{2}}} \ln \rho_0 & (m = 2n) \end{cases} \tag{C.125}$$

plus divergent terms which can be ignored.

In the second case, the integral is evaluated using the following recursive relations [203, §2.261, §2.263]

$$I_n^m = \frac{\rho_0^{m-1}}{(m-2n)c\sqrt{R_0^{2n-1}}} - \frac{(2m-2n-1)b}{2(m-2n)c} I_n^{m-1} - \frac{(m-1)a}{(m-2n)c} I_n^{m-2} \quad \text{for } m \neq 2n,\ n \geq 1, \tag{C.126a}$$

$$I_n^m = \frac{-\rho_0^{m-1}}{(m-1)c\sqrt{R_0^{2n-1}}} - \frac{b}{2c} I_n^{m-1} + \frac{1}{c} I_n^{m-2} \quad \text{for } m = 2n,\ n \geq 1, \tag{C.126b}$$

$$I_n^0 = \frac{2(2c\rho_0 + b)}{(2n-1)\Delta\sqrt{R_0^{2n-1}}} + \frac{8(n-1)c}{(2n-1)\Delta} I_{n-1}^0 \quad \text{for } n \geq 1, \tag{C.126c}$$

$$I_0^0 = \frac{1}{c} \ln \left( \frac{2\sqrt{cR_0} + 2c\rho_0 + b}{2\sqrt{ca} + b} \right) \quad \text{for } c > 0, \tag{C.126d}$$

$$= \frac{-1}{\sqrt{-c}} \left( \arcsin \frac{2c\rho_0 + b}{\sqrt{-\Delta}} - \arcsin \frac{b}{\sqrt{-\Delta}} \right) \quad \text{for } c < 0, \Delta < 0, \tag{C.126e}$$

where $R_0 = a + b\rho_0 + c\rho_0^2$ and $\Delta = 4ac - b^2$.

In the third case, the integral can be written as

$$I_n^m = \int_0^{\rho_0} \frac{\rho^m}{\left(\sqrt{a + b\rho}\right)^{2n+1}} d\rho. \tag{C.127}$$

Integrating this by parts, we get

$$I_n^m = \frac{-2\rho_0^m}{(2n-1)b\left(\sqrt{a+b\rho_0}\right)^{2n-1}} + \int_0^{\rho_0} \frac{2m\rho^{m-1}}{(2n-1)b\left(\sqrt{a+b\rho}\right)^{2n-1}} d\rho \tag{C.128}$$

$$= \frac{-2\rho_0^m}{(2n-1)b\left(\sqrt{a+b\rho_0}\right)^{2n-1}} + \int_0^{\rho_0} \frac{2m\rho^{m-1}(a+b\rho)}{(2n-1)b\left(\sqrt{a+b\rho}\right)^{2n+1}} d\rho \tag{C.129}$$

$$= \frac{-2\rho_0^m}{(2n-1)b\left(\sqrt{a+b\rho_0}\right)^{2n-1}} + \frac{2am}{(2n-1)b} I_n^{m-1} + \frac{2m}{2n-1} I_n^m. \tag{C.130}$$

Therefore, $I_n^m$ satisfies the following recursive relation

$$I_n^m = \frac{-2\rho_0^m}{(2n-2m-1)b\left(\sqrt{a+b\rho_0}\right)^{2n-1}} + \frac{2ma}{(2n-2m-1)b} I_n^{m-1}. \tag{C.131}$$

For $m = 0$, the integral is evaluated using the following closed-form expression

$$I_n^0 = \frac{2}{(2n-1)ba^{2n-1}} - \frac{2}{(2n-1)bR_0^{2n-1}}. \tag{C.132}$$

Case four is trivial since $R_0$ is then a constant.